

Lecture Notes in Control and Information Sciences

292

Editors: M. Thoma · M. Morari

Springer

Berlin

Heidelberg

New York

Hong Kong

London

Milan

Paris

Tokyo



Guanrong Chen · Xinghuo Yu (Eds.)

Chaos Control

Theory and Applications

With 151 Figures



Springer

Series Advisory Board

A. Bensoussan · P. Fleming · M.J. Grimble · P. Kokotovic ·
A.B. Kurzhanski · H. Kwakernaak · J.N. Tsitsiklis

Editors

Prof. Guanrong Chen
City University of Hong Kong
Department of Electronic Engineering
83 Tat Chee Avenue, Kowloon
Hong Kong SAR
P.R. China

Prof. Xinghuo Yu
Faculty of Engineering
Royal Melbourne Institute of Technology
GPO Box 2476V
Melbourne VIC 3001
Australia

ISSN 0170-8643

ISBN 3-540-40405-8 Springer-Verlag Berlin Heidelberg New York

Cataloging-in-Publication Data applied for
A catalog record for this book is available from the Library of Congress.
Bibliographic information published by Die Deutsche Bibliothek
Die Deutsche Bibliothek lists this publication in the Deutsche Nationalbibliografie; detailed bibliographic data is available in the Internet at <<http://dnb.ddb.de>>.

This work is subject to copyright. All rights are reserved, whether the whole or part of the material is concerned, specifically the rights of translation, reprinting, reuse of illustrations, recitation, broadcasting, reproduction on microfilm or in other ways, and storage in data banks. Duplication of this publication or parts thereof is permitted only under the provisions of the German Copyright Law of September 9, 1965, in its current version, and permission for use must always be obtained from Springer-Verlag. Violations are liable for prosecution under German Copyright Law.

Springer-Verlag Berlin Heidelberg New York
a member of BertelsmannSpringer Science + Business Media GmbH

<http://www.springer.de>

© Springer-Verlag Berlin Heidelberg 2003
Printed in Germany

The use of general descriptive names, registered names, trademarks, etc. in this publication does not imply, even in the absence of a specific statement, that such names are exempt from the relevant protective laws and regulations and therefore free for general use.

Typesetting: Data conversion by the authors.
Final processing by PTP-Berlin Protago-TeX-Production GmbH, Berlin
Cover-Design: design & production GmbH, Heidelberg
Printed on acid-free paper 62/3020Yu - 5 4 3 2 1 0

Preface

Chaos control refers to purposefully manipulating chaotic dynamical behaviors of some complex nonlinear systems. As a new and young discipline, chaos control has in effect come into play with many traditional scientific and technological advances today. Automatic control theory and practice, on the other hand, is a traditional and long-lasting engineering discipline. It has recently rapidly evolved and expanded, to overlap with and sometimes completely encompass many new and emerging technical areas of developments, and chaos control is one of them.

This new technology of chaos control promises to have a major impact on many novel, perhaps not-so-traditional, time- and energy-critical engineering applications. Examples include such as data traffic congestion control in the Internet, encryption and secure communication at different levels of communications, high-performance circuits and devices (e.g., delta-sigma modulators and power converters), liquid mixing, chemical reactions, power systems collapse prediction and protection, oscillators design, biological systems modelling and analysis (e.g., the brain and the heart), crisis management (e.g., jet-engine surge and stall), nonlinear computing and information processing, and critical decision-making in political, economic as well as military events. In fact, this new and challenging research and development area has become an attractive scientific inter-discipline involving control and systems engineers, theoretical and experimental physicists, applied mathematicians, and physiologists alike.

There are many practical reasons for controlling or ordering chaos. In a system where chaotic response is undesired or harmful, it should be reduced as much as possible, or totally suppressed. Examples of this include avoiding fatal voltage collapse in power networks, eliminating deadly cardiac arrhythmias, guiding disordered circuit arrays (e.g., multi-coupled oscillators and cellular neural networks) to reach a certain level of desirable pattern formation, regulating dynamical responses of mechanical and electronic devices (e.g., diodes, laser machines, and machine tools), and organizing a multi-agency corporation to achieve optimal performance.

Ironically, recent research has shown that chaos can actually be quite useful under certain circumstances, and there is growing interest in utilizing the very nature of it, particularly in some novel time- and/or energy-critical applications. A salient observation about this possibility is that chaos enables a system to explore its every dynamical possibility due to its ergodicity. When chaos is controllable, it can provide the system designer with an exciting variety of properties, richness of flexibility, and a cornucopia of opportunities. Oftentimes, conventional engineering design tried to completely eliminate such “irregular” dynamical behaviors of a system. However, such over-design is usually accomplished at the high price of loss of flexibility in achieving opti-

mal performance near the stability boundaries, or at the expense of radically modifying the original system dynamics which in many cases is undesirable or unnecessary.

It has been shown that the sensitivity of chaotic systems to small perturbations can be used to rapidly direct system trajectories to a desired target using minimal control energy. This may be crucial, for example, in interplanetary space navigation. A suitable manipulation of chaotic dynamics, such as stability conversion or bifurcation delay can significantly extend the operational range of machine tools and aircraft engines, enhance the artificial intelligence of neural networks, and increase coding/decoding efficiency in signal and image encryption and communications.

It has been demonstrated that data traffic through the Internet is likely to be chaotic. Special chaos control strategies may help network designers in better congestion control, thereby further benefiting the rapidly evolving and expanding Internet, to handle the exponentially increasing demands from the industry and the commercial market.

Fluid mixing is another good example in which chaos is not only useful but actually very desirable. The objective here is to thoroughly mix together two or more fluids of different kinds, while minimizing the control energy required. For this purpose, fluid mixing turns out to be much simpler to achieve if the particle motion dynamics are strongly chaotic. Otherwise, it is difficult to obtain rigorous mixing properties due to the possibility of invariant two-tori in the flow. This has been one of the main subjects in fluid-mixing processing, known as *chaotic advection*. Chaotic mixing is also important in engineering applications involving heat transfer. One example is in plasma heating within a nuclear fusion reactor, where heat waves are injected into the reactor, for which the best result is obtained when the convection inside the reactor is chaotic.

Within the context of biological systems, chaos control seems to be a crucial mechanism employed by the human brain in carrying out many of its tasks such as learning, perception, memorization and particularly conceptualization. Additionally, some recent laboratory studies reveal that the complex dynamical variability in a variety of normal-functioning physiological systems demonstrates features reminiscent of chaos. Some medical evidence lends support to the idea that control of certain chaotic cardiac arrhythmias may soon lead to the design of a safe and highly effective intelligent pacemaker. In fact, chaos has become a public focal point in various research areas of life sciences, medicine research, and biomedical engineering.

Motivated by many potential real-world applications, current research on control and anti-control of chaos (chaotification) has proliferated in recent years. With respect to theoretical considerations, chaos control poses a substantial challenge to both system analysts and control engineers. This is due to the extreme complexity and sensitivity of chaotic dynamics, which in turn is associated with the reduction in long-term predictability and short-term

controllability of chaotic systems. A controlled chaotic system is inherently non-autonomous. In most cases, it cannot be converted to an autonomous system since the required time-dependent controller has yet to be designed and therefore cannot be defined as a new system state variable. Possible time-delay, noise, and coupling influences often make a controlled chaotic system Lyapunov-irregular and extremely complex topologically. As a result, many existing theories and methodologies for autonomous systems are no longer applicable to the analysis and control of many chaotic systems. On the other hand, chaos control poses new challenges to controllers designers and automation engineers. A successful controller implementation in a chaotic environment is generally difficult to achieve due to the extreme sensitivity of chaos to parameter variations and noise perturbations, and to the non-robustness of chaos with respect to the structural stability of the physical devices involved.

Notwithstanding many technical obstacles, both theoretical and practical developments in this area have experienced remarkable progress in the last decade. Surprisingly, however, there exist no control-theory-oriented books written by control engineers for control engineers available in the market that are devoted to the subject of Chaos Control and Anti-Control of Chaos. In particular, there has been no exposure of these very active research topics in the Lecture Notes Series in Control and Information Science.

This edited book aims at filling in the gap and presenting current achievements in this challenging field at the forefront of research, with emphasis on the engineering perspectives, methodologies, and potential applications of chaos and bifurcation controls. It is intended as a combination of overview, tutorial and technical reports, reflecting state-of-the-art research of significant problems in this field. The anticipated readership includes university professors, graduate students, laboratory researchers and industrial practitioners, as well as applied mathematicians and physicists in the areas of electrical, mechanical, physical, chemical, and biomedical engineering and sciences.

We received enthusiastic assistance from several individuals in the preparation of this book. In particular, we are very grateful to Noel Patson, who helped a great deal in taking care of many painful editorial tasks. We would also like to thank Prof. T. Thoma and Dr. T. Ditzinger, Editors of Springer-Verlag, for their continued support and kind cooperation. Finally, we wish to express our sincere thanks to all the authors whose significant scientific contributions have directly led to the publication of this timely treatise.

Guanrong Chen, Xinghuo Yu
Hong Kong and Melbourne, January, 2003

Contents

Chaos Control

| | |
|---------------|---|
| Preface | V |
|---------------|---|

Chaos Control

| | |
|--|---|
| Targeting Control of Chaotic Systems | 1 |
| <i>Erik M. Boltt</i> | |

| | |
|---|----|
| Chaotic Vibration of the Wave Equation with Nonlinear Feedback Boundary Control: Progress and Open Questions ... | 25 |
| <i>Goong Chen, Sze-Bi Hsu, Jianxin Zhou</i> | |

| | |
|---|----|
| Time-delayed Impulsive Stabilization of Unstable Periodic Orbits in Chaotic Hybrid Systems | 51 |
| <i>Yu-Ping Tian, Xinghuo Yu</i> | |

| | |
|---|----|
| Odd Number Limitation in Delayed Feedback Control | 71 |
| <i>Shigeru Yamamoto, Toshimitsu Ushio</i> | |

| | |
|--|----|
| Introduction to Some Methods of Chaos Analysis and Control for PDEs | 89 |
| <i>Yi Zhao</i> | |

Chaos Synchronization

| | |
|--|-----|
| Chaotic Systems Synchronization | 117 |
| <i>Johan Suykens, Mustak Yalçın, Joos Vandewalle</i> | |

| | |
|---|-----|
| Neural Network Design for Chaos Synchronization | 137 |
| <i>Edgar N. Sanchez, Jose P. Perez, Luis J. Ricalde</i> | |

Chaos Anti-Control

| | |
|--|-----|
| Chaotification via Feedback: The Discrete Case | 159 |
| <i>Guanrong Chen</i> | |

| | |
|---|-----|
| Generating Chaos in Continuous-Time Systems via Feedback Control | 179 |
| <i>Xiao Fan Wang</i> | |

Applications

| | |
|--|-----|
| Formation Mechanisms and Control Methods of Beam Halo-Chaos in High-Current Ion Linacs..... | 205 |
| <i>Jin-Qing Fang, Guanrong Chen, Xinghuo Yu</i> | |
| Chaos and Pseudo-Randomness..... | 247 |
| <i>Ljupco Kocarev, Goce Jakimoski, Zarko Tasev</i> | |
| Applying Ergodic Theory to Improve Noise Performance of Differential Chaos Shift Keying | 265 |
| <i>Henry Leung and Haiyang Yu</i> | |
| Control of Chaos Statistics for Optimization of DS-CDMA Systems | 295 |
| <i>Gianluca Setti, Riccardo Rovatti, Gianluca Mazzini</i> | |
| Calculation and Control of Unstable Periodic Orbits in Piecewise Smooth Dynamical Systems | 321 |
| <i>Tetsushi Ueta, Tohru Kawabe, Guanrong Chen, Hiroshi Kawakami</i> | |
| Control of Chaos Statistics for the Generation of Timing Signals with Improved EMC | 341 |
| <i>Gianluca Setti, Riccardo Rovatti, Sergio Callegari, Michele Balestra</i> | |

Targeting Control of Chaotic Systems

Erik M. Bollt

Department of Mathematics and Computer Science
Clarkson University, Potsdam, NY 13699, USA
bolltem@clarkson.edu

Abstract. Targeting control of chaos is concerned with taking advantage of sensitive dependence to initial conditions to coax a dynamical system to follow a desirable trajectory. In other words, it is taking advantage of the butterfly effect so that the rich spectrum of possible trajectories embedded within a chaotic attractor can be selected with extremely small energy input. We review historical and popular approaches which fall under this general area in an attempt to reveal these techniques in a useful manner for applied scientists.

1 Introduction: Is “Controlling Chaos” an Oxymoron?

Over many years, chaos has been shown to be an interesting and even common phenomenon in nature. Chaotic systems are characterized by two defining properties: 1) *Sensitive Dependence to Initial Conditions*, 2) *Transitivity*¹ [25, 26]. Chaos has been shown to exist in a wide variety of settings: in fluid dynamics such as Raleigh-Bernard convection, in chemistry such as the Belousov-Zhaobitinsky reaction, in nonlinear optics in certain lasers, in celestial mechanics, in electronics such as Chua’s circuit, in the flutter of an overdriven airplane wing, some models of population dynamics, and likely in meteorology, physiological oscillations such as certain heart rhythms as well as brain patterns. A complete list of natural systems which can potentially become chaotic would be too large to publish here. Nonetheless, chaos was not considered a desirable property in engineering control practice.

In 1990, Ott, Grebogi, and Yorke [2] (OGY) published a paper which most importantly, to this discussion, served as a case study which dispelled the paradigm that chaos is undesirable. The answer to, “Why Chaos,” is this: in [2], the authors showed that any unstable periodic orbit of the system can be stabilized with small energy feedback control, and since a chaotic attractor is expected to be dense with periodic orbits, there is an arbitrarily rich array of different dynamic behaviors to choose amongst, already built into such a system, all accessible via small energy inputs.

The OGY technique essentially stabilizes an unstable periodic orbit by a specialized version of the pole-placement technique [3] applied to the linearized system, when trajectories have already tracked closed to the to-be

¹ Transitivity is equivalent to the statement that there exists a dense orbit.

stabilized orbit. Ergodicity is relied upon to ensure that such close encounters will occur. Since waiting times to apply the feedback control can be very long,² the next obvious question is how does one shorten the waiting time. This leads to the targeting problem. In a sense, the OGY solution to the targeting problem is ergodicity plus time.

The initial surprise with the oxymoron of the phrase “controlling chaos” comes from the fact that while a chaotic system is impossible to predict in the long run, it still arises in a deterministic system, which is therefore predictable in the short run. The short term evolution is deterministic, predictable, and controllable. In Fig. 1, we see the evolution of two initially very close initial conditions. At first their evolutions are close and predictable, a consequence of the usual Lipschitz continuity result that output of such a differential equation is continuous with respect to initial conditions [4]. In the long run, we see that the two trajectories are quite different; this is the numerical experiment that lead E. Lorenz to the historically important observed problem of sensitive dependence to initial conditions when predicting the weather. Now, considering the exponential growth rate of such errors from an optimistic standpoint, a vanishingly small energy input has the potential to yield a wide range of outcomes. The problem of programming when and how much those perturbations should be applied is the targeting problem.

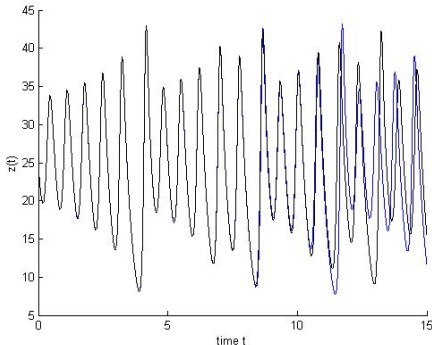


Fig. 1. Sensitive dependence to initial conditions in the famous Lorenz equations [1], $\dot{x} = 10(y - x)$, $\dot{y} = x(28 - z) - y$, $\dot{z} = xy - (8/3)z$. Shown is the evolution of the z -time series from two nearby initial conditions.

2 Statement of the Targeting Problem

We formulate the targeting problem in terms of a discrete-time system. Let,

$$\mathbf{z}_{n+1} = \mathbf{f}_\lambda(\mathbf{z}_n), \quad (1)$$

² See [2,3] for explicit formulation of the scaling of expected wait time as a function of perturbation energy, for the map formulation of the problem

where $\mathbf{z} \in \Re^m$ is the phase-space variable, and $\lambda \in \Re^p$ are adjustable control variables. Later in the chapter, we will discuss continuous-time systems in terms of Poincaré section, to generalize the following techniques.

Suppose at time zero the initial state $\mathbf{z}_0 = \mathbf{a}$, but we wish to bring the system to (near) $\mathbf{z}_i \approx \mathbf{b}$ as “quickly” as possible, and subject to small energy input. The point \mathbf{b} may for example be one iterate of a periodic orbit.

We have shown [29] that a general formulation of the targeting problem that can then be adapted for stabilization by feedback control in a differential equation is to find a “good” ϵ -chain orbit. See Fig. 12.

- **Define** an ϵ -chain from \mathbf{a} to \mathbf{b} as a set of points $\{\mathbf{z}_i\}_{i=0}^m$ such that,

$$\mathbf{z}_{i+1} = \mathbf{f}_\lambda(\mathbf{z}_i) + \epsilon_i, \quad (2)$$

where

$$|\epsilon_i| < \epsilon, \quad (3)$$

are the sequence of (small) errors, $\mathbf{z}_0 = \mathbf{a}$, and $\mathbf{z}_m \in N_\epsilon(\mathbf{b})$.

Here the notation $N_\epsilon(\mathbf{b}) = \{\mathbf{y} : |\mathbf{b} - \mathbf{y}| < \epsilon\}$ denotes an ϵ -neighborhood of \mathbf{b} .

The reason for this formulation is that an ϵ -chain can be stabilized as a sequence of two-point boundary value problems which are expected to be computably solvable when ϵ is small; see Chapter 5 for more discussion on this point. Whereas, the full two-point boundary value problem of a fast-transporting true orbit ($\epsilon = 0$) would be hard for long time, we will effectively break the problem into a sequence of short and easy such problems.

Note that without an objective function to qualify the word “good”, we might choose any transporting orbit. The transitivity part of the definition of chaos implies infinitely many n such that $\mathbf{a} \in \mathbf{f}^{-n}(N_\epsilon(\mathbf{b}))$, but n is usually large if ϵ is small.

Objective: fast and small energy A reasonable objective function should balance short time, with low energy. Omitting either yields trivial extremes: if $\epsilon \sim O(1)$ then one can hit any target in one step, while if short time is not required then we generally need to do nothing since the orbit of \mathbf{a} will wander near \mathbf{b} eventually and indeed that is the original OGY solution to targeting [2].

We state our favorite objective functions:

- Minimum iterate, constrained energy,

$$F(\{\mathbf{z}_i\}_{i=0}^m) = m, \quad (4)$$

subject to $\{\mathbf{z}_i\}_{i=0}^m$ is an ϵ -chain such that $\epsilon < \epsilon_{max}$.

Other reasonable cost functions [5] might be continuous time, which will be different in general than number of iterates when time-of-flight between Poincaré surfaces is nonuniform, or perhaps fuel required in designing a space flight mission design, or reaction rate in a chemical reaction for example.

As far as we know, solving any such problem as an optimal control problem is in general an open problem. Nonetheless, it is important to have a good objective function to have a basis to compare quality between various candidate solutions. Surprisingly, there is still almost no mention of objective or cost in the now relatively large literature on targeting.

3 Targeting: A Simple and Instructive One-Dimensional Example

We present here a concrete example of targeting, which while limited in scope in that it only works for one-dimensional maps, it serves as a “cartoon” of how sensitive dependence can be leveraged and useful. The following was inspired by [6, 7], but was explicitly developed in [8] as a undergraduate student project.

Consider the logistic map,

$$x_{n+1} = f_r(x_n) = rx_n(1 - x_n), \quad (5)$$

and given the initial condition $a = x_0 = 0.4$ for example, suppose we wish to hit the target $b = 0.8$ in as few iterates as possible subject to small parameter variations. Let $r_0 = 3.9$ be the nominal parameter value, and constrain,

$$3.8 \leq r_0 + \delta r \leq 4.0, \quad (6)$$

for the example.

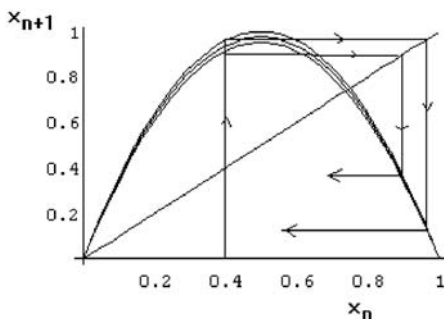


Fig. 2. Parametric variations in the logistic map yields an initially small interval of possible outcomes, which then grows exponentially under sensitive dependence to initial conditions.

Iterating the initial condition under the entire family of maps, corresponding to the parameter interval, we get (See Fig. 2),

$$x_1 \in f_{[3.8,4.0]}(0.4) = [0.91, 0.96]. \quad (7)$$

Then returning the parameter to $r = r_0$, for simplicity of the example, we get,

$$\begin{aligned} x_2 &\in f_{3.9}([0.91, 0.96]) = [0.14976, 0.312998], \\ x_3 &\in f_{3.9}([0.14976, 0.312998]) = [0.496595, 0.838618]. \end{aligned} \quad (8)$$

At this point we see that the target is bracketed, and since f_r is continuous with respect to r , the intermediate value theorem implies a root of the equation,

$$f_{3.9} \circ f_{3.9} \circ f_r(0.4) = 0.8, \quad (9)$$

for the unknown control parameter r . Bisection yields, $r = 3.831890\dots$

The lesson we learn from this example is that a small and *deliberate* perturbation quickly grows to fill the compact phase space, and hence sensitive dependence to initial conditions can be helpful to design a responsive control system.

In fact, this simple technique can be adapted to experimental systems [9, 10]. However, the specific details of this algorithm requires a one-dimensional map. One-dimensional maps are however surprisingly common in nature, since strong dissipation often creates surprisingly low-dimensional attractors. For example, plotting successive maxima of the $z(t)$ time-series seen in Fig. 1 of the Lorenz system is known [1] to yield a one-humped map.

3.1 The higher-dimensional generalization

The direct generalization of the above algorithm is to iterate a neighborhood $N_\epsilon(\mathbf{a})$ forwards under f , and perhaps iterate $N_\epsilon(\mathbf{b})$ backwards under f^{-1} if the inverse exists. This is the idea behind the work by Shinbrot, Ott, Grebogi and Yorke, [11] sometimes called SOGY. The idea is to resolve (the boundary of) $N_\epsilon(\mathbf{a})$ and $N_\epsilon(\mathbf{b})$ into a fine enough grid so that iterating under f and f^{-1} if it exists allows us to solve for an m and n which solve,

$$f^m(N_\epsilon(\mathbf{a})) \cap f^{-n}(N_\epsilon(\mathbf{b})) \neq \emptyset, \quad (10)$$

Deciding the intersection of two regions defined by grid points on their boundaries reduces to a problem of computational geometry: deciding crossings of pairs of vectors from successive grid points of from each boundary. One simple solution in terms of the cross product can be found in, [12].

This method works adequately well when there exist a small $p = m + n$ solution of Eq. (10). Simple low-dimensional attractors, such as the Henon

attractor lend themselves well to this technique, [11, 12]. However, if the minimal solution $p = m+n$ to Eq. (10) is not small, then the problem becomes computationally impossible. Since a grid of r points, spread uniformly around $N_\epsilon(\mathbf{a})$, is expected to spread approximately by factors of λ_u , where $\lambda_u > 1$ is the largest Lyapunov number, then those points which were initially $2\pi\epsilon/r$ apart are expected to be approximately $2\pi\epsilon/r\lambda_u^m$ apart for large m . Quickly, no initial grid is fine enough that $2\pi\epsilon/r\lambda_u^m$ is still small for large m . Likewise, if $\lambda_s < 1$ is the smallest Lyapunov number, the s initial points around $N_\epsilon(\mathbf{b})$ gets spread too thinly according to, $2\pi\epsilon/s\lambda_u^{-n}$. Leaving the simple details to those interested, it is clear that sensitive dependence works against us here: it is computationally impossible to resolve intersections such as those depicted in Fig. 3 for large p by the brute force of iterating grids.

Specifically, transport is too slow to directly solve Eq. (10) in many systems, such as for example, in higher dimensions [16], or in Hamiltonian systems with resonance layers, [12–15].

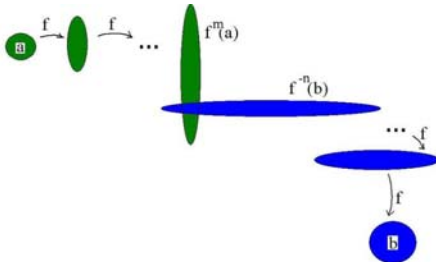


Fig. 3. The SOGY [11] is a constructive targeting method. A forward iterate of a neighborhood of a which is found to intersect an inverse iteration of a neighborhood b implies, by continuity, existence of fast trajectory. The difficulty is that representing $N_\epsilon(\mathbf{a})$ and $N_\epsilon(\mathbf{b})$ with a fine enough grid so that $f^m(N_\epsilon(\mathbf{a}))$ and $f^{-n}(N_\epsilon(\mathbf{b}))$ can still be resolved accurately enough at time of intersection, for large $p = m + n$ is exponentially memory consuming.

3.2 A web approach to higher-dimensional targeting

The exponential growth of $N_\epsilon(\mathbf{a})$ upon iteration is equivalent to growth of possibilities of outcomes, and this idea is essentially related to the entropy of the system. The first technique to address growth of possibilities used a tree structure as designed by E. Kostelich *et. al.*, [16]. See also, [17, 18].

The idea of the Kostelich technique is to find a tree of paths leading to a target point b . For example, if a free-running trajectory leads to $N_\epsilon(\mathbf{b})$ in say 30 iterates, then keep that last 30 iterates, and call them the primary trunk of the tree and label them $\{\mathbf{z}_i^1\}_{i=1}^{30}$. Then continuing to iterate, one

expects a recurrence to one of the points $\{\mathbf{z}_i^1\}_{i=1}^{30}$. Record those, say 30, previous iterates and call them, $\{\mathbf{z}_i^{2,1}\}_{i=1}^{30}$, and these are a primary branch. By construction, $\mathbf{z}_{30}^{2,1} \in N_\epsilon(\mathbf{z}_i^1)$ for some i . Likewise collect several ($j = 1, 2, \dots$) more primary branches, by simple iteration, and collecting primary trunk intersections, $\{\mathbf{z}_i^{2,j}\}_{i=1}^{30}$. Similarly by recurrence and iteration construct secondary branches of paths which lead to primary branches, etc. See Fig. 4. When we are done, we have constructed a tree of paths, which hopefully covers a significant measure of the attractor, and more specifically every possible initial condition is no more than a few iterates from one of the members of the tree. In [16], the authors showed this technique to be successful in the four-dimensional double-rotor map [19].

In a sense, this technique is a generalization of the OGY technique. In the OGY technique, there is an essentially random transient time while one waits for the orbit to wander into the capture window around a periodic orbit. With the Kostelich tree, one also has a transient time of waiting while the orbit wanders into a now extended set of neighborhoods of point, and active feedback control is launched as soon as any one of those pre-recorded points is approached.

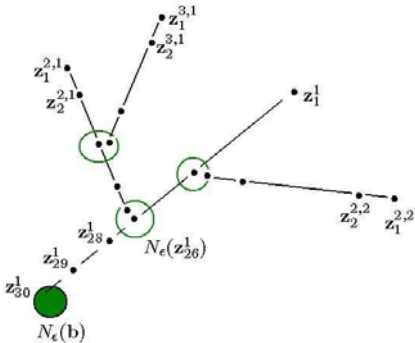


Fig. 4. Caricature of a typical tree of ϵ -chain paths leading to a target point \mathbf{b} , as in [16].

3.3 Targeting through recurrence through resonance layers and to the moon

Uncontrolled transport in one and a half degree of freedom Hamiltonian systems with resonance layers is particularly slow, [20, 21] and the above described techniques do not work well, [12–15]. Consider for example the Chirikov Standard map,

$$\mathbf{z}' = \begin{pmatrix} y' \\ x' \end{pmatrix} = T(\mathbf{z}) \equiv \begin{pmatrix} y - \frac{k}{2\pi} \sin(2\pi kx) \\ y - \frac{k}{2\pi} \sin(2\pi kx) + x \end{pmatrix}, \quad (11)$$

often used as the prototypical example of an area-preserving twist map. Specifically, we expect KAM circles which become “cantori” as k increases, but which still serve as partial barriers inhibiting transport. This is responsible for the sticky islands-around-islands effect. Chaotic transport mechanisms provides that a fast orbit must pass through the “turnstiles” [21] via “lobe dynamics” [66] corresponding to intermediate barriers. It follows that a fast orbit should pass through these localized regions exactly once [12, 14]. The constructive approach is to compute the turnstiles, and perhaps find short orbit segments between them, such as was tried in [12, 14] and also [27], but a problem with this approach is the fact that there are infinitely many resonances which layer the phase space with a great deal of resonance overlap, and it is not obvious which are most important. We have found the explicit approach to be unnecessary by the following technique which provides that a slow orbit goes through all of the intermediate obstacles and more, and thus signals the fast way, needing only some shortening.

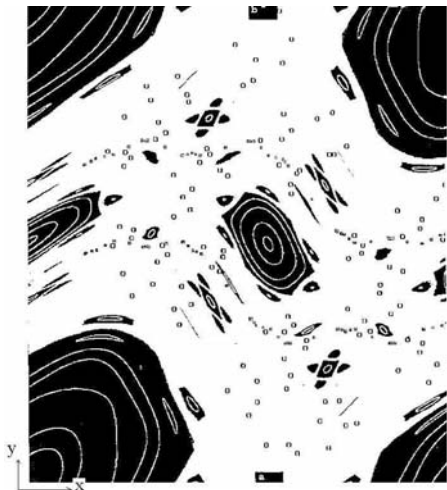


Fig. 5. A fast orbit of the standard map, (the “o”’s) from near $\mathbf{a} = (x_a, y_a) = (0.5, 0.0)$, to near $\mathbf{b} = (x_b, y_b) = (0.5, 1.0)$. Here, $k = 1.25 > k_c$, and a slow test orbit wanders in the “chaotic sea” (the large white region) from near \mathbf{a} = to near \mathbf{b} . The test orbit which may wander near the remaining resonance islands remains for a long sojourn before again escaping to continue towards the target. A 80307 test orbit has been used to find a nearby 131 fast orbit.

As a concrete example, we investigate transport from a neighborhood of the $(0, 1)$ hyperbolic point to a neighborhood of the $(1, 1)$ resonance. The notation (p, q) denotes the frequency of an orbit, i.e. q iterations of the map results in exactly p wraps around the cylinder: $T^q(\mathbf{z}) = \mathbf{z} + p$. The starting

point $(0, 1)$ **a** is located at $(x_a, y_a) = (0.5, 0.0)$, and $(1, 1)$, our target point **b**, at $(x_b, y_b) = (0.5, 1.0)$.

Such an orbit does not exist if $k < k_c \approx 0.97163540631\dots$ [21]; k_c is the parameter value at which the last invariant curve dividing phase space between $(0, 1)$ and $(1, 1)$ becomes a cantorus. The most robust curves between $(0, 1)$ and $(1, 1)$ are the circles with rotation frequencies $\frac{1}{\gamma}$ and $\frac{1}{\gamma^2}$, where $\gamma = \frac{1+\sqrt{5}}{2}$ is the golden mean. If $k > k_c$, there are no invariant curves separating vertical transport of the cylinder, and therefore according to Mather's theorem [22], there exists a heteroclinic connection between the $(0, 1)$ and $(1, 1)$ orbits for which we will search.

For $k > k_c$, the golden mean invariant curves become cantori. They have the smallest lobe areas, and hence, represent the most difficult barriers to transport. An arbitrary orbit will typically pass through these lobes many times before finally reaching the target point **b**. This effect also occurs when an orbit is trapped near an island, and near islands around islands, and so on. This phenomenon has been successfully modelled using Markov trees [23, 24]. It was found that a point initially "near" a KAM surface has a survival probability $F(t)$ is asymptotic to $t^{-\alpha}$ and that the orbit will still be near the surface at large time t with small constant α [24]. Therefore in the presence of KAM surfaces, we find long correlations and, hence, roughly power law decay. However the important point is that, without knowing where the lobes are located, recurrence is a way of locally detecting globally inefficient orbits.

The idea of cutting recurrent loops is as follows:

- All orbits go through intermediate barriers, which for area preserving maps are the turnstiles. Distinguishing fast from slow is that fast transporting orbits go through necessary pseudo-barriers (turnstiles) exactly once, and do not go through unnecessary barriers (drawing closer to islands) at all. Slow transporting orbits go through necessary pseudo-barriers (turnstiles) some odd number of times greater than once, and go through turnstiles leading to islands some even number of times. See caricature in Fig. 6.
- Unnecessary or slowing transport is signaled by recurrence in the turnstiles.
- A slow transporting orbit may be used as a test orbit, and the long recurrent loops can be removed if the error can be forced to be small by the hyperbolicity method described below in Eq. (12). We define a recurrence as unnecessary when a solution to Eq. (12) is found.

Once a recurrence has been identified between \mathbf{z}_i and \mathbf{z}_{i+s} , to find an ϵ -chain which skips the s -step recurrent loop, we must solve the following two-point boundary valued problem. See Fig. 7. We require that a point on the unstable direction f_u at \mathbf{z}_{i-m} lands on the stable direction f_s at \mathbf{z}_{i+s+m} . Thus we must find ξ which solves [15],

$$[T^{2m}(\mathbf{z}_{i-m} + \xi f_u) - \mathbf{z}_{i+s+m}] \times f_s = 0. \quad (12)$$

To find the stable and unstable foliations [14, 67], recall that the Jacobian matrix rotates a vector in the tangent space towards the unstable direction, and the Jacobian matrix of the inverse map T^{-1} rotates a vector towards the stable direction (if they exist!). Therefore, in practice, we choose an arbitrary unit vector \mathbf{u} and forward multiply, starting at \mathbf{z}_{-n} , the Jacobian matrices along the orbit to \mathbf{z} , normalizing the vector at each step:

$$DT^n|_{z_{-n}} \cdot \mathbf{u} \equiv DT|_{z_{-1}} \cdot DT|_{z_{-2}} \cdot \dots \cdot DT|_{z_{-n}} \cdot \mathbf{u} \rightarrow f_u(\mathbf{z}) \text{ as } n \rightarrow \infty. \quad (13)$$

Likewise, the stable direction is formed from the inverse Jacobian starting at $T^n(\mathbf{z})$.

$$DT^{-n}|_{z_n} \cdot \mathbf{u} \equiv DT^{-1}|_{z_1} \cdot DT^{-1}|_{z_2} \cdot \dots \cdot DT^{-1}|_{z_n} \cdot \mathbf{u} \rightarrow f_s(\mathbf{z}) \text{ as } n \rightarrow \infty. \quad (14)$$

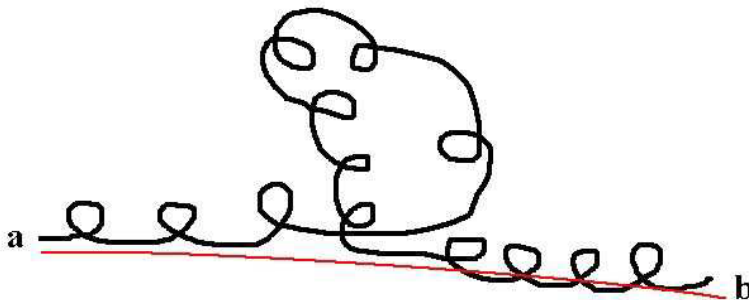


Fig. 6. Caricature of a slow transporting orbit, which recurs with itself many times during its flight to **b**. The fast orbit in red does not suffer unnecessary recurrence.

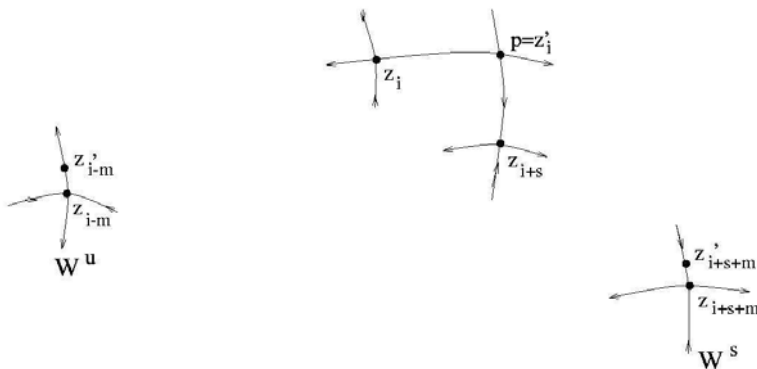


Fig. 7. Hyperbolicity is used to diminish a recurrence error, and to remove the recurrent loop.

Considering the specific standard map $k = 1.25$, with **a** and **b** shown in Fig. 5. The first recurrence that we can successfully remove from one representative 80307 step orbit is between \mathbf{z}_{16} and \mathbf{z}_{78704} which recurs to a distance of $\delta = 0.08$. In this example, we construct an orbit patch $\{\mathbf{z}'_1, \dots, \mathbf{z}'_{31}\}$ such that the error to perturb on to the orbit patch is only $\|\mathbf{z}'_1 - \mathbf{z}_1\| = 0.002$, and the error to perturb back off of the orbit patch is $\|\mathbf{z}'_{31} - \mathbf{z}_{78720}\| = 0.002$. With this single patch, we have already demonstrated a 1619 step epsilon chain orbit near our original orbit. By finding every recurrence within a threshold $\delta = 0.1$ and cutting those that can be patched within the error $\epsilon = 0.005$ we eventually construct a 131 step epsilon chain orbit including 13 overlapping patches. The largest error found in this example was $\|T(\mathbf{z}_{92}) - \mathbf{z}_{93}\| = 0.003$, but there were several others of the same order.

As an example of the utility of targeting in area-preserving maps, consider the circular, Restricted-Three-Body Problem (RTBP), defined by the Hamiltonian [28],

$$H = \frac{(p_x + y)^2 + (p_y - x)^2 + p_z^2}{2} - \Omega(x, y, z), \quad (15)$$

where,

$$\Omega(x, y, z) = \frac{x^2 + y^2}{2} + \frac{1 - \mu}{r_1} + \frac{\mu}{r_2} + \frac{\mu(1 - \mu)}{2}, \quad (16)$$

and,

$$r_1 = \sqrt{(x + \mu)^2 + y^2 + z^2}, r_2 = \sqrt{(x - 1 + \mu)^2 + y^2 + z^2}. \quad (17)$$

The resulting equations of motion,

$$\begin{aligned} \dot{x} &= \frac{\partial H}{\partial p_x} = p_x + y, \quad \dot{p}_x = -\frac{\partial H}{\partial x} = p_y - x + \Omega_x, \\ \dot{y} &= \frac{\partial H}{\partial p_y} = p_y - x, \quad \dot{p}_y = -\frac{\partial H}{\partial y} = -p_x - y + \Omega_y. \end{aligned} \quad (18)$$

evolve as a flow in \mathbb{R}^4 , but there is the Jacobi integral, which is constant along the flow,

$$J(x, y, z, \dot{x}, \dot{y}, \dot{z}) = (\dot{x}^2 + \dot{y}^2 + \dot{z}^2) - 2\Omega(x, y, z), \quad (19)$$

whose existence implies that the flow occupies a 3-dimensional submanifold. Thus a Poincaré mapping, of x versus \dot{x} for each point when the flow transverse $y = 0$ with $\dot{y} > 0$ yields an area preserving map. See Fig. 8.

The RTBP is considered a good initial model of the Earth-Moon system, in which a third small particle, such as a spaceship is too small to essentially alter the integrable Kepler motion of the primaries. Choosing realistic relative masses, $m_1/m_2 = 0.0123$, there is insufficient energy in the system for an Earth-Moon escape for Jacobi-integral $J < -3.1883$. We choose

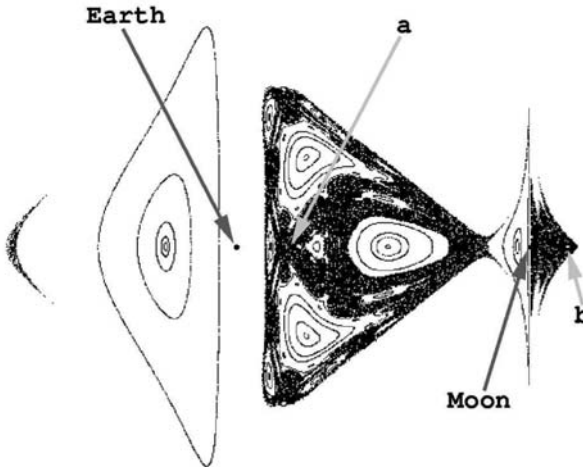


Fig. 8. Circular Restricted-Three Body Problem, as the Poincaré mapping, (x, \dot{x}) for each transverse point when $y = 0$ with $\dot{y} > 0$.

$J = -3.17948$, just after transport is possible, and well below the $J = -2.761$ energy required for the pictured Hohmann transfer. Our technique reduced a “Chaotic test orbit” (See Fig. 8) from 10710 iterates to 58 iterates on Poincaré section, or down to 2.05 years. Whereas the Hohmann transfer (Apollo-type mission) shown takes 6.61 days and a 1219.8m/s impulse budget, the chaotic transfer requires 2.05 years and only 749.6m/s of impulse, most of it to boost from the same circular orbit around the Earth to the $J = -3.17948$ transferring parameter. Since rockets expel most of their weight as ejected fuel, this translates to 83% more payload with a constant sized booster. Thus the theme of targeting in chaos: *we can trade time for energy*.

4 Combinatorial Targeting and Symbolic Dynamics

The tree description of the growing possible orbits, such as that depicted in Fig. 4 is suggestive of the combinatorial explosion in possible outcomes, which is essentially a discrete approximation of the notion of sensitive dependence to initial conditions. In [5, 29], we posed the targeting control problem in terms of approximating the action of a dynamical system on its phase space as a directed graph between vertices which label a rectangular covering of the phase space. In fact, a map on a topology of open sets can be considered as a directed graph between the sigma algebra of open sets; such an abstract description is simplified by a generating partition, from which follows the symbolic dynamics [30–32]. We and others have shown that combinatorial [5, 29, 33] and symbolic methods [10, 34–37], and [56] are a complete and efficient descriptions of all possible orbits of a dynamical system. Within

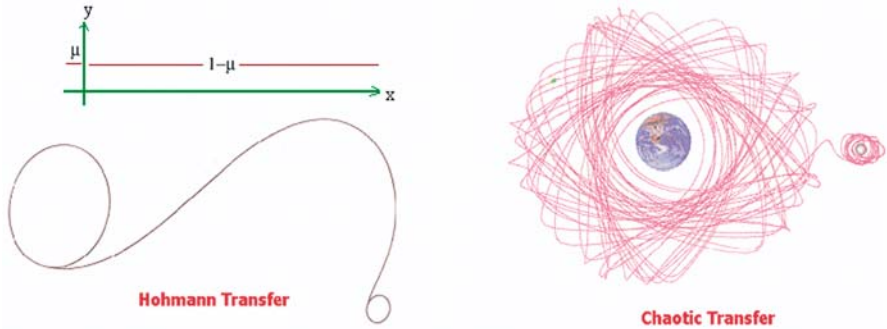


Fig. 9. Left: A “Hohmann transfer” in the Circular Restricted-Three Body Problem; this is essentially skeet shooting in a $1/r^2$ potential well and it is the sort of trajectory the Apollo astronauts flew. Right: A chaotic transfer. The Homann transfer takes less time but substantially more fuel than the chaotic transfer.

such a description, targeting is reduced to the simpler and well-understood discrete problem of path searching in graph theory. For example, the shortest path through an unweighted directed graph is found by the breadth-first-search algorithm and through a positively weighted graph by the Dijkstra algorithm [38, 39].

For these reasons, we will briefly review the role of symbolic dynamics in dynamical systems, first for one-dimensional mappings, followed by diffeomorphisms of the plane. Then following, we review application of symbolic dynamics to targeting control.

4.1 One-dimensional maps with a single critical point

First consider a one-humped interval map, such as the logistic map Eq. (5) or Lorenz’s successive maxima map, which follows by plotting just the local maxima of the $z(t)$ time-series from the Lorenz differential equations [1] in Fig. 1 and similarly for many other systems.

$$f : [a, b] \rightarrow [a, b]. \quad (20)$$

Such a map “has” symbolic dynamics [40, 41] relative to a partition at the critical point x_c . Choosing a two symbol partition, labelled $\mathcal{I}=\{0, 1\}$, names iterates of an initial condition x_0 dynamically,

$$\sigma_i(x_0) = \begin{cases} 0 & \text{if } f^i(x_0) < x_c \\ 1 & \text{if } f^i(x_0) > x_c \end{cases}. \quad (21)$$

The function h labels each initial condition x_0 and corresponding orbit $\{x_0, x_1, x_2, \dots\}$ by an infinite symbol sequence,

$$h(x_0) \equiv \sigma(x_0) = \sigma_0(x_0).\sigma_1(x_0)\sigma_2(x_0)\dots \quad (22)$$

Defining the “fullshift” $\Sigma_2 = \{\sigma = \sigma_0.\sigma_1\sigma_2\dots \text{ where } \sigma_0 = 0 \text{ or } 1\}$ to be the set of all possible infinite symbolic strings of 0’s and 1’s, any given infinite symbolic sequence is a singleton (a point) in the fullshift space, $\sigma \in \Sigma_2$. The usual topology of open sets in the shift space Σ_2 follows the metric,

$$d_{\Sigma_2}(\sigma, \bar{\sigma}) = \sum_{i=0}^{\infty} \frac{|\sigma_i - \bar{\sigma}_i|}{2^i}, \quad (23)$$

which defines two symbol sequences to be close if they agree in the first several bits. Eq. (21) is a good “change of coordinates,” or more precisely a homeomorphism,³

$$h : [a, b] - \cup_{i=0}^{\infty} f^{-i}(x_c) \rightarrow \Sigma'_2, \quad (24)$$

under conditions on f , such as piecewise $|f'| > 1$.⁴ The Bernoulli shift map moves the decimal point in Eq. (22) to the right, and “eliminates” the leading symbol,

$$s(\sigma_i) = \sigma_{i+1}. \quad (25)$$

All of those itineraries from the map f , Eq. (1) by Eq. (21), correspond to the Bernoulli shift map restricted to a subshift,⁵ $s : \Sigma'_2 \rightarrow \Sigma'_2$. Furthermore, the change of coordinates h is a conjugacy⁶.

In summary, the previous paragraph simply says that corresponding to the orbit of each initial condition of the map Eq. (20), there is an infinite itinerary of 0’s and 1’s, describing each iterate’s position relative the partition in a natural way which acts like a change of coordinates such that the dynamical description is equivalent. For our purposes, controlling orbits of the map f in phase space which is an interval corresponds also to controlling itineraries in symbol space. The control over x composed with the change of coordinates h can essentially be considered to be a coding algorithm.

³ A *homeomorphism* between two topological spaces A and B is a one-one and onto continuous function $h : A \rightarrow B$, which may be described loosely as topological equivalence.

⁴ Note that pre-images of the critical point are removed from $[a, b]$ for the homeomorphism. This leaves a Cantor subset of the interval $[a, b]$. This is necessary since a shift space is also closed and perfect, whereas the real line is a continuum. This is an often over-looked technicality, which is actually similar to the well known problem when constructing the real line in the decimal system (the ten-shift Σ_{10}) which requires identifying repeating decimal expansions of repeating 9’s such as for example $1/5 = 0.\overline{199} \equiv 0.2$. The corresponding operation to the shift maps [25] is to identify the repeating binary expressions $\sigma_0.\sigma_1..\sigma_n0\overline{11} \equiv \sigma_0.\sigma_1..\sigma_n1\overline{11}$, thus “closing the holes” of the shift space Cantor set.

⁵ A *subshift* Σ'_2 is a closed and Bernoulli shift map invariant subset of the fullshift, $\Sigma'_2 \subset \Sigma_2$.

⁶ A *conjugacy* is a homeomorphism h between topological spaces A and B , which commutes maps on those two spaces, $\alpha : A \rightarrow A$, $\beta : B \rightarrow B$, then $h \circ \alpha = \beta \circ h$.

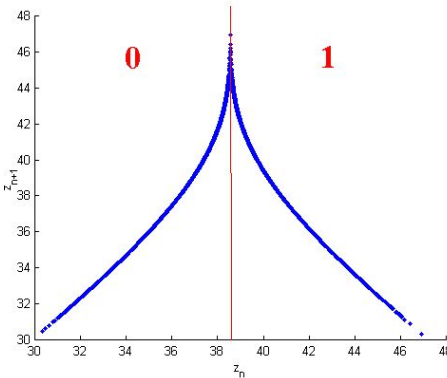


Fig. 10. Successive maxima map of the $z(t)$ variable, of the Lorenz flow $(x(t), y(t), z(t))$ from Fig. 1.

4.2 Higher-dimensional systems and symbolic dynamics of diffeomorphisms

Diffeomorphisms arise naturally by Poincaré mapping of a flow. In general, a diffeomorphism $f : M \rightarrow M$ is expected for an $N - 1$ manifold M which is transverse to a flow in \mathbf{R}^N .

Symbolic dynamics of higher dimensional systems is still a highly active research area and details here are necessarily slight. In particular, we refer the reader to see [44–46]. The fundamental difference of dimensionality is that invertible maps and hence diffeomorphisms are necessarily simple in the interval, whereas in more than one dimension, there may be chaos. In the interval, only a many-to-one map allows for the folding property which is an ingredient of chaos. However, S. Smale [48] showed that the folding mechanism of a horseshoe allows for chaos in a planar diffeomorphism.

In the development in the previous subsections, the one-sided shifts reflect the noninvertible nature of the corresponding interval maps Eq. (1). The generalization of symbolic dynamics for invertible maps requires bi-infinite symbol sequences,

$$\Sigma_2 = \{\sigma = \dots \sigma_{-2} \sigma_{-1} \sigma_0. \sigma_1 \sigma_2 \dots \text{ where } \sigma_0 = 0 \text{ or } 1\}. \quad (26)$$

The main technical difficulty of symbolic dynamics for a map with a more than one-dimensional domain is well defining a partition. A notion of Markov partitions is well defined⁷ for Axiom A diffeomorphisms [49, 50], but

⁷ R. Bowen [49, 51], defined conditions for a partition of “rectangles” to be Markov.

A topological partition $\{Q_i\}$ of open rectangles is Markov if, $\{Q_i\}$ have nonoverlapping interiors, such that when $f(Q_i) \cap Q_j \neq \emptyset$, then $f(Q_i)$ stretches across Q_j , in that stretching directions are mapped to stretching directions and contracting directions are mapped to contracting directions. Said more carefully, we require that $W^u(f_n(z), Q_i) \subset f_n(W^u(z, Q_i))$ and $f_n(W^s(z, Q_i)) \subset W^s(f_n(z), Q_i)$.

such maps are not expected to be generic. The more general notion of a generating partition [30] is also well defined,⁸ but particularly in the case of a nonuniformly hyperbolic dynamical system construction of the generating partition is an open problem for most maps. A well regarded conjecture for planar diffeomorphisms, such as the Hénon map [44–46], is that the generating partition should be a curve that connects all “primary” homoclinic tangencies. See also [47, 52–55].

4.3 Learning the grammar in practice

In a physical experiment, corresponding to the one-dimensional map such as Eq. (1), it is possible to approximately deduce the grammar of the corresponding symbolic dynamics by systematic recording of the measured variables relative either to a reasonable approximation of the generating partition, or a fine grid. First note that any real measurement of an experiment consists of a necessarily finite data set. Therefore, in practice, it can be argued that there is no such thing as a grammar of infinite type in the laboratory. So without loss of generality, we may consider only grammars of finite type for our purposes. Such a subshift is a special case of a sofic shift [42, 43]. In other words, there exists a finite digraph which completely describes the grammar. All allowed words of the subshift, Σ' corresponding to itineraries of orbits of the map correspond to some walk through the graph.

For example, the Hénon map,

$$(x_{n+1}, y_{n+1}) = f(x_n, y_n) = (1.8 - x_n^2 + b y_n, x_n), \quad (27)$$

has a symbolic dynamics as represented in Fig. 11. For this picture, for the illustration, we have explicitly calculated the generating partition in terms of homoclinic tangencies discussed above, [44–47]. Iterates and pre-iterates of the critical curve finely partitions the phase space, but most importantly, it finely partitions the attractor. We see that since the attractor fails to cover all 2^4 labelled permutations of the 4-bit symbols, there are missing words, in this relatively coarse (for sake of artistic Caricature) approximation. In the directed graph approximation of the corresponding transitions on the

⁸ Given a dynamical system $f : M \rightarrow M$, a *finite* collection of disjoint open sets, $\{B_k\}_{k=1}^K$, $B_k \cap B_j = \emptyset$ ($k \neq j$), is defined to be a topological partition if the union of their closures exactly covers M : $M = \bigcup_{k=1}^K \overline{B_k}$, [Lind & Marcus, 1995]. The set of intersection of the images and pre-images of these elements $\cap_{i=-n}^n f^{(-i)}(B_{x_i})$ is in general open. For a faithful symbolic representation of the dynamics, the limit $\cap_{n=0}^{\infty} \cap_{i=-n}^n f^{(-i)}(B_{x_i})$ should be a single point if nonempty. Given a dynamical system $f : \mathcal{M} \rightarrow \mathcal{M}$ on a measure space (\mathcal{M}, F, μ) , a finite partition $P = \{B_k\}_{k=1}^K$ is generating if the union of all images and preimages of P gives the set of all μ -measurable sets F . In other words, the “natural” tree of partitions: $\vee_{i=-\infty}^{\infty} f^i(P)$, always generates some sub- σ -algebra, but if it gives the full σ -algebra of all measurable sets F , then P is called *generating* [30].

attractor, observe that paths through the graph correspond to trajectories on the attractor, and cycles correspond to periodic orbits (or at least to ϵ -chain pseudo-orbits).

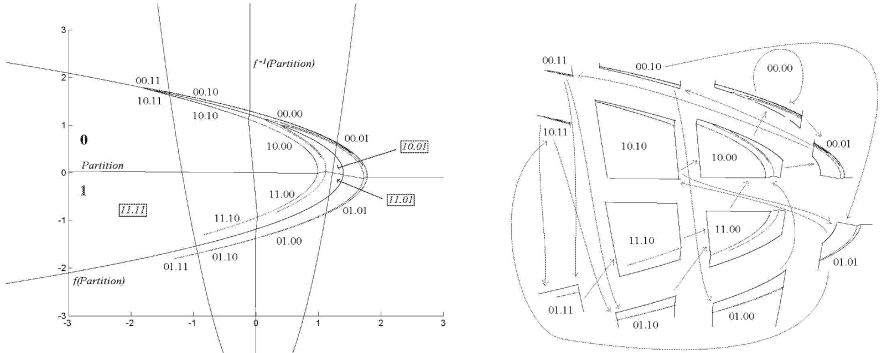


Fig. 11. Left, the Hénon attractor has a symbol dynamics generated by the w-shaped partition, which allows us to color the attractor Blue for current state is '0' above the curve, or Red for '1'. It is believed that iterates and pre-iterates of the curve generates the topology of opens sets. Right, using our coarse 4-bit approximation, we see all 4-bit transitions on the attractor, and hence all pseudo orbits are walks through the graph and cycles are pseudo-periodic orbits. This graph generates the symbolic dynamics Σ'_2 on the attractor.

Forcing the symbolic dynamics, via forcing paths through the corresponding graphic descriptions is all that is necessary now to create ϵ -chain pseudo-orbits of the dynamical system. In the next section, we discuss making these into real orbits of a differential equations. We close by mentioning that we are actually controlling the information production of the dynamical system, which can either be viewed as a control strategy over orbits as we are interested here, or alternatively as a communication via chaos scheme as we [10, 34, 35] and others [36, 37] have researched extensively elsewhere. As a technical note of practical importance, we have found link-lists to be the most efficient method to record a directed graph together with its allowed transitions.

5 Forcing the Path: Feedback Control

We have seen in the previous section that combinatorial and symbolic description of trajectories are efficient for designing trajectories of the dynamical system as ϵ -chain pseudo-orbits. What remains to be discussed is how to force the orbit of a randomly chosen initial condition to follow the above designed pseudo-orbit “plans,” in the case of a differential equation which is the necessary step to argue physical relevance of the above described techniques.

We will mention three main techniques: 1) Parametric feedback control which reduces to a sequence of two-point-boundary-valued-problems (TPBVP), 2) adaptive targeting, and 3) limiter control.

5.1 Parametric feedback control

By construction, the ϵ -chain pseudo-orbits are designed with small ϵ , and thus parametric control may be used [16, 29]. We refer the reader to Fig. 12 for what we hope is a clear pictorial description of this basic idea.

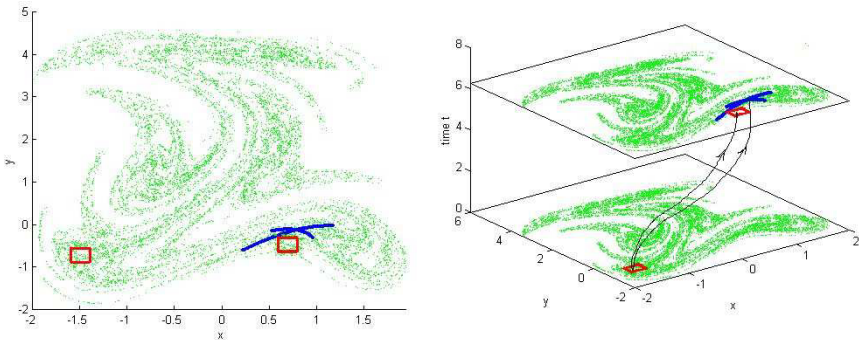


Fig. 12. Observed next responses due to parameter variations of the Duffing oscillator: $x'' + ax' + x^3 - x = b \sin(t)$, where $\lambda_0 = (a_0, b_0) = (0.02, 3)$. Left) Dots show $N = 10,000$ iterates of 2π -stroboscopic map. Bold squares show “from” and “to” nodes, in this (overly-large caricature) grid. Bold crossed curves show observed next responses due to maximal variations $|\delta\lambda| = (|\delta a|, |\delta b|) \leq (0.02, 0.25)$, where either δa or δb is varied separately, while the other is held fixed. Right) Caricature of flow between the piercings on the Poincaré section of the uncontrolled and controlled differential equation, and the target box.

Feedback control of a chaotic trajectory may be realized by small parameter variations. For example, given a flow of $\mathbf{z}(t) \in \mathbf{R}^N$ where we explicitly write the parameter dependence $\mathbf{p} \in \mathbf{R}^n$,

$$\dot{\mathbf{z}} = \mathbf{F}(\mathbf{z}, \mathbf{p}), \quad (28)$$

one can hope to effect the trajectory in a predictable manner in the short run. In particular, if the desired short-term response is small, a Lipschitz continuous right hand side F provides that small parameter variations should suffice. Furthermore for small enough desired short term responses, the required parameter variation can be usefully and easily found by directly solving the (TP-BVP). More specifically, suppose that on surface of section M , the initial condition $\mathbf{z}_0 \in M$ flows forward under Eq. (28) to $\mathbf{z}_1 \in M$, $\mathbf{z}_1 = \mathbf{f}(\mathbf{z}_0) = \Phi_t(\mathbf{z}_0)$ (t is the time of flight of the mapping, which is generally not uniform with

respect to \mathbf{z} , and this is not a concern to us here) at next Poincaré surface piercing, under a nominal/uncontrolled parameter value \mathbf{p}_0 . The Poincaré mapping we now denote,

$$\mathbf{f}(\mathbf{z}, \mathbf{p}) : M \rightarrow M, \quad (29)$$

to emphasize a family of mappings parameterized by adjustable parameter \mathbf{p} . If we prefer the next iterate to be $\mathbf{z}_{\text{desired}}$, then the next controlled response, is a solution to the equation,

$$\mathbf{z}_{\text{desired}} = \mathbf{f}(\mathbf{z}_0, \mathbf{p}_1) \quad (30)$$

whose solution is formally a TPBVP of the flow Eq. (28), where \mathbf{p}_1 is the unknown in the equation to be found, usually by shooting [58]. For long time of flight, the general TPBVP is expect to be numerically unreasonable to solve. However, since we have constructed

$$\|\mathbf{z}_{\text{desired}} - \mathbf{z}_0\|_2 < \epsilon, \quad (31)$$

for a small $\epsilon > 0$, and continuity of the flow with respect to parameter and spacial variations, we expect that $\|\mathbf{p}_1 - \mathbf{p}_0\|_2$ will likewise be small. In such case, a standard shooting algorithm, based on Newton's method generally works well [29], choosing $\mathbf{p} = \mathbf{p}_0$ as the initial seed. A solution exists for small enough $\epsilon > 0$, and nonsingular Jacobian derivative, by continuation of the trivial solution

$$\mathbf{z}_1 = \mathbf{f}(\mathbf{z}_0, \mathbf{p}_0), \quad (32)$$

along a parameterized solution manifold, $\delta\mathbf{p}(\mathbf{z})$, and $\mathbf{z} = f(\mathbf{z}_0, \mathbf{p}_0 + \delta\mathbf{p}(\mathbf{z}))$, which is an application of the implicit function theorem. In fact, the linearized equations of variation,

$$\dot{\delta}\mathbf{z} = \frac{\partial \mathbf{F}}{\partial \mathbf{z}}(\mathbf{z}, \mathbf{p}) \cdot \delta\mathbf{z} + \frac{\partial \mathbf{F}}{\partial \mathbf{p}}(\mathbf{z}, \mathbf{p}) \cdot \delta\mathbf{p}, \quad (33)$$

can be used to approximately solve for \mathbf{p}_1 , where $\frac{\partial \mathbf{F}}{\partial \mathbf{z}}$ and $\frac{\partial \mathbf{F}}{\partial \mathbf{p}}$ are respectively the Jacobian matrices of \mathbf{z} and \mathbf{p} variations. We mention that it is possible to model the necessary derivatives using only measured data by appropriately perturbing and observing responses of a physical system [9, 10].

5.2 Time-delayed feedback control

Time-delayed feedback control was first introduced (but not then so-called) by Pyragas [59] who added to Eq. (28) a feedback control perturbation,

$$U(t) = K(x_i(t - T) - x_i(t)), \quad (34)$$

where $x_i(t)$ is one of the component observed variables of $\mathbf{z}(t)$, K is a carefully chosen weighting variable, and the delay T in the control rule was shown to be useful in tuning to the period of a specific UPO; it is easy to see that the amplitude of this control law automatically decreases as the UPO is approached. This method has been generalized and improved by control [60] and “adaptive recognition” [61]. In brief [62], at time t_n , measuring the difference $\delta(t_n)$ between the observed variable $x_i(t_n)$ dynamics, and the goal dynamics $g_i(t_n)$, $\delta(t) = x_i(t_n) - g_i(t_n)$, the local variation rate,

$$\lambda(t_n) = \log \left| \frac{\delta(t_n)}{\delta(t_{n-1})} \right|, \quad (35)$$

measures exponential growth rate between actual and desired dynamics. The additive control rule to the observed variable is chosen,

$$U(t_n) = K(t_n)[g_i(t_n) - x_i(t_n)], \quad (36)$$

where,

$$\frac{1}{K(t_n)} = \frac{1}{K_0}(1 - \tanh(\sigma\lambda(t_n))), \sigma > 0, K_0 > 0, \quad (37)$$

This method adapts the strength of the control to the local dynamics, tending to push the actual evolution towards the goal, via a strength adapting to the local instabilities and the error. Notice that choosing $\sigma = 0$ specializes to the Pyragras method. This general set-up allows for the necessary targeting [63] to close the ϵ -chains constructed in previous sections, by choosing the goal dynamics to correspond to successive steps in the designed orbits.

5.3 Dynamic limiting

A particularly simple, and yet extremely effective new technique for stabilizing desired orbits is called “dynamic limiting,” by Corron and Pethel [64]. It has been successfully demonstrated experimentally, in a chaotic driven pendulum using a weight, and in a chaotic double scroll circuit using a diode, emphasizing the potential of this passive control strategy [65]. For both experiments, multiple unstable periodic orbits are selectively controlled using minimal perturbations and promises as the authors state that chaos control may apply to a much wider array of important problems.

We describe here dynamic limiting in the following language, using a simple state dependent but otherwise constant addition to the unperturbed dynamical system Eq. (28),

$$\dot{\mathbf{z}} = \mathbf{F}(\mathbf{z}, \mathbf{p}) + \mathbf{G}(\mathbf{z}, t), \quad (38)$$

and,

$$\mathbf{G}(\mathbf{z}, t) = \sum_{n=0}^{\infty} \sum_{i=1}^N d_{n,i} \chi_{t_n}(t) \chi_{A_i}(\mathbf{z}) \mathbf{k}_i. \quad (39)$$

For each fixed i , \mathbf{k}_i is a constant vector addition to the vectorfield whose influence tends to push trajectories in the general direction of \mathbf{k}_i which should be chosen appropriately pointing towards the goal. Each of the constant vector perturbations $\{\mathbf{k}_i\}_{i=1}^N$ turns on individually due to entering trigger regions of phase space $\{A_i\}_{i=1}^N$, since $\chi_{A_i}(\mathbf{z}) = 1$ if $\mathbf{z} \in A_i$, 0 else, is the usual characteristic function or Heaviside function in the scalar case. Likewise, $\chi_{t_n}(t)$ serves as a switch in time, which turns on if $t_{n-1} < t < t_n$, and if the corresponding decision to do so is on, $d_{n,i} = 1$, as opposed to off, $d_{n,i} = 0$. The degree of pushing depends on the amount of time spent in A_i , and hence accumulated total push, under the influence of the constant perturbation. Notice that this perturbation is only turned-on if the trajectory enters A_i . In practice this is quite simple to implement, in circuit hardware for example as a diode, or in a mechanical system as a weight [65]. For $N > 1$, a panel of diodes allows selection of relative influences. By carefully choosing A_i regions to actuate the influences \mathbf{k}_i , for example A_i having a desired periodic orbit on its boundary, relatively complex motions are effectively stabilized in experiment. In fact, in [64], Corron and Pethel used dynamic limiting to control the symbolic dynamics of a Rossler-like attractor LC oscillator.

References

1. Lorenz, E. N. (1963) Deterministic nonperiodic flow. *J. Atmos. Sci.*, **20**:130-141
2. Ott, E., Grebogi, C., Yorke, J. A. (1990) Controlling chaos. *Phys. Rev. Lett.*, **64**:1196–1199
3. Romerias, F., Grebogi, C., Ott, E., Dayawansa, W. (1992) Controlling chaotic dynamical systems. *Physica D*, **58**(1002):165–192
4. Hirsch, M., Smale, S. (1974) Differential Equations, Dynamical Systems and Linear Algebra. New York: Academic Press
5. Bollt, E., Kostelich, E., (1998) Optimal targeting of chaos. *Phys. Lett. A*, **245**(5):399–406
6. Shinbrot, T., Ott, E., Grebogi, C., Yorke, J. A. (1992) Using chaos to direct orbits to targets in systems describable by a one-dimensional map. *Phys. Rev. A*, **45**:4165-4168
7. Shinbrot, T., Grebogi, C., Ott, E., Yorke, J. A. (1993) Using small perturbations to control chaos. *Nature*, **363**:411–417
8. Bollt, E. (1997) Controlling the chaotic logistic map. *PRIMUS (Problems Resources, and Issues in Mathematics Undergraduate Studies)*, **VII**(1):1–18
9. Shinbrot, T., Ditto, W., Grebogi, C., Ott, E., Spano, M. L., Yorke, J. A. (1992) Using the sensitive dependence of chaos to direct orbits to targets in an experimental chaotic systems. *Phys. Rev. Lett.*, **68**:2863-2866
10. Dolnik, M., Bollt, E. (1998) Communication with chemical chaos in the presence of noise. *Chaos*, **8**(3):702–710, Bollt, E., Dolnik, M. (1997) Encoding information in chemical chaos by controlling symbolic dynamics. *Phys. Rev. E*, **55**: 6404-6413
11. Shinbrot, T., Ott, E., Grebogi, C., Yorke, J. A. (1990) Using chaos to direct trajectories to targets. *Phys. Rev. Lett.*, **65**:3215-3218
12. Bollt, E. (1995) Controlling Chaos, Targeting, and Transport. Ph.D thesis, U. Colorado, Boulder

13. Lai, Y. C., Ding, M., Grebogi, C. (1993) Controlling Hamiltonian chaos. *Phys. Rev. E*, **47**:86-92
14. Boltt, E., Meiss, J. D. (1995) Targeting chaotic orbits to the moon through recurrence. *Phys. Lett. A*, **204**:373–378
15. Boltt, E., Meiss, J. D. (1995) Controlling chaos through recurrence. *Physica D*, **81**:280–294
16. Kostelich, E. J., Grebogi, C., Ott, E., Yorke, J. A. (1993) Higher dimensional targeting. *Phys. Rev. E*, **47**:305-310
17. Barreto, E., Kostelich, E. J., Grebogi, C., Ott, E., Yorke, J. A. (1995) Efficient switching between controlled unstable periodic orbits in higher dimensional chaotic systems. *Phys. Rev. E*, **51**:4169-4172
18. Kostelich, E. J., Barreto, E. (1997) Targeting and control of chaos. In *Control and Chaos*, ed. by Judd, K., Mees, A., Teo, K. L., Vincent, T. L. Boston: Birkhäuser, 158–169
19. Kostelich, E., Yorke, J. A. (1987) Lorenz cross sections of the chaotic attractor of the double rotor. *Physica D*, **24**:263-278
20. Arrowsmith, D. K., Place, C. H. (1990) *Introduction to Dynamical Systems*. London: Cambridge Univ. Press
21. Meiss, J. D. (1992) Symplectic maps, variational principles, and transport. *Reviews of Modern Physics*, **64**:795–848
22. Mather, J. N. (1991) Variational construction of orbits of twist diffeomorphisms. *J. Am. Math. Soc.*, **4**:207–263
23. Hanson, J., Cary, J., Meiss, J. (1985) ‘Algebraic decay in self-similiar Markov chains. *J. Stat. Phys.*, **39**(3/4):327-345
24. Meiss, J. D., Ott, E. (1987) Markov tree model of transport in area preserving maps. *Physica D*, **20**:387–402
25. Devaney, R. L. (1989) *An Introduction to Chaotic Dynamical Systems*. 2nd ed. Redwood City, CA: Addison Wesley
26. Martelli, M., Dong, M., Seph, T. (1998) Defining chaos. *Mathematics Magazine*, **71**(2):112–122
27. Schroer, C. G., Ott, E. (1997) argeting in Hamiltonian systems that have mixed regular/chaotic phase spaces. *Chaos. Focus Issue: Control and Synchronization of Chaos*, **7**(4):512–519
28. Szebehely, V. (1967) *Theory of Orbits the Restricted Problem of Three Bodies*. New York: Academic Press
29. Boltt, E. (2001) Combinatorial control of global dynamics in a chaotic differential equation. *Int. J. Bifur. Chaos*, **11**(8):2145–2162
30. Rudolph, D. J. (1990) *Fundamentals of Measurable Dynamics, Ergodic Theory on Lebesgue Spaces*. Oxford: Clarendon Press
31. Boltt, E., Stanford, T., Lai, Y. -C., Zyczkowski, K. (2001) What symbolic dynamics do we get with a misplaced partition? on the validity of threshold crossings analysis of chaotic time-series. *Physica D*, **154**(3/4):259–286
32. Boltt, E., Stanford, T., Lai, Y. -C., Zyczkowski, K. (2000) Validity of threshold-crossing analysis of symbolic dynamics from chaotic time series. *Phys. Rev. Lett.* **85**(16):3524–3527
33. Boltt, E. (2003) Review of chaos communication by feedback control of symbolic dynamics. *Int. J. Bifur. Chaos*, to appear
34. Dolnik, M., Boltt, E. (1998) Communication with chemical chaos in the presence of noise. *Chaos*, **8**(3):702–710

35. Boltt, E., Lai, Y. -C., Grebogi, C. (1997) Analysis of the topological entropy versus noise resistance trade-off when communicating with chaos. *Phys. Rev. Lett.*, **79**(19):3787–3790
36. Hayes, S., Grebogi, C., Ott, E., Mark, A. (1994) Experimental control of chaos for communication. *Phys. Rev. Lett.*, **73**:1781–1784
37. Hayes, S., Grebogi, C., Ott, E. (1993) Communicating with chaos. *Phys. Rev. Lett.*, **70**:3031–3034
38. Gould, R. (1988) Graph Theory. Menlo Park, CA: Benjamin/Cummings Publishing
39. Bondy, J. A., Murty, U. S. R. (1976), Graph Theory with Applications. New York: American Elsevier
40. de Melo, W., van Strien, S. (1992) One-Dimensional Dynamics. New York: Springer-Verlag
41. Milnor, J., Thurston, W. (1997) On Iterated Maps of the Interval: I and II. Princeton: Princeton Univ. Press
42. Kitchens, B. P. (1998) Symbolic Dynamics, One-sided, Two-sided and Countable State Markov Shifts. New York: Springer-Verlag
43. Lind, D., Marcus, B. (1995) An Introduction to Symbolic Dynamics and Coding. New York: Cambridge Univ. Press
44. Cvitanovic, P., Gunaratne, G., Procaccia, I. (1988) Topological and metric properties of Hénon-type attractors. *Phys. Rev. A*, **38**:1503–1520
45. Cvitanovic, P. (1991) Periodic orbits as the skeleton of classical and quantum chaos. *Physica D*, **51**:138–151
46. Cvitanovic, P. (1995) Dynamical averaging in terms of periodic orbits. *Physica D*, **83**:109–123
47. Grassberger, P., Kantz, H., Moenig, U. (1989) On the symbolic dynamics of the Henon map. *J. Phys. A*, **22**:5217–5230
48. Smale, S. (1967) Differentiable dynamical systems. *Bull AMS*, **73**:747–817
49. Bowen, R. (1970) Markov partitions for axiom A diffeomorphisms. *Am. J. Math.*, **92**:725–747
50. Bowen, R. (1975) Equilibrium States and the Ergodic Theory of Anosov Diffeomorphisms. Berlin: Springer-Verlag
51. Bowen, R. (1975) Equilibrium States and the Ergodic Theory of Anosov Diffeomorphisms. Berlin: Springer-Verlag
52. Christiansen, F., Politi, A. (1996) Symbolic encoding in symplectic maps. *Nonlinearity*, **9**:1623–1640
53. Christiansen F., Politi A. (1997) Guidelines for the construction of a generating partition in the standard map. *Physica D*, **109**:32–41
54. Hansen, K. (1992) Pruning of orbits in four-disk and hyperbola billiards. *Chaos*, **2**:71–75
55. Hansen, K. (1993) Symbolic dynamics. I. Finite dispersive billiards. *Nonlinearity*, **6**:753–769
56. Place, C. M., Arrowsmith ,D. K. (2000) Control of transient chaos in tent maps near crisis. I: Fixed points. *Phys. Rev. E*, **61**(2):1357–1368; II: Periodic orbits. 1369–1381
57. Neter, J., Kutner, M. H., Nachtsheim, C. J., Wasserman, W. (1996) Applied Linear Regression Models. 3rd ed. Chicago: IRWIN
58. Press, W., Flannery, B., Teukolsky, S., Vetterling, W. (1988) Numerical Recipes in C: The Art of Scientific Computing. New York: Cambridge Univ. Press

59. Pyragas, K. (1992) Continuous control of chaos by self-controlling feedback. *Phys. Lett. A*, **170**:421–428
60. Boccaletti, S., Arecchi, F. T. (1996) Adaptive recognition and control of chaos. *Physica D*, **96**:9-16
61. Arecchi, F. T., Bsti, G., Boccaletti, S., Perrone, A. L. (1994) Adaptive recognition of a chaotic dynamics. *Europhys. Lett.*, **26**:327-332
62. Boccaletti, S., Grebogi, C., Lai, Y. -C., Mancini, H., Maza, D. (2000) The control of chaos: theory and applications. *Phys. Rep.*, **329**:103–197
63. Boccaletti, S., Fairimi, A., Kostelich, E. J., Arecchi, F. T. (1997) Adaptive targeting of chaos. *Phys. Rev. E*, **55**:R4845-R4848
64. Corron, N., Pethel, S. (2002) Control of long periodic orbits and arbitrary trajectories in chaotic systems using dynamic limiting. *Chaos* **12**(1):1–7
65. Corron, N. J., Pethel, S. D., Hopper, B. A. (2000) Controlling chaos with simple limiters. *Phys. Rev. Lett.*, **84**:3835–3838
66. Wiggins, S. (1992) Chaotic Transport in Dynamical Systems. New York: Springer-Verlag
67. Jaeger, L., Kantz, H. (1997) Homoclinic tangencies and non-normal Jacobians – effects of noise in non-hyperbolic systems. *Physica D*, **105**:79–96

Chaotic Vibration of the Wave Equation with Nonlinear Feedback Boundary Control: Progress and Open Questions

Goong Chen^{1,2}, Sze-Bi Hsu³, and Jianxin Zhou¹

¹ Department of Mathematics, Texas A&M University
College Station, TX 77843, USA

gchen@math.tamu.edu jzhou@math.tamu.edu

² Department of Mathematics and College of Science
National Tsing Hua University, Hsinchu 30043
Taiwan, R.O.C. sbhsu@math.nthu.edu.tw

Abstract. The study of chaotic phenomena in partial differential equations is a challenging subject. In this paper, we survey the recent progress in the study of chaotic vibration of the linear wave equation with nonlinear boundary feedback control law. We show that when there is linear energy injection at one end of the boundary and the self-regulating or van der Pol nonlinearity at the other end of the boundary, chaos occurs as a reconciliation between linear instability and nonlinear self-regulation when the parameters enter a certain regime. A list of open problems is also posed.

1 Introduction

The onset of chaotic phenomena in systems governed by nonlinear partial differential equations (PDEs) has fascinated scientists and mathematicians for many centuries. The most famous case in point is the Navier–Stokes equations and related models in fluid dynamics, where the occurrence of turbulence in fluids is well accepted as a chaotic phenomenon. Yet despite the diligence of numerous of the most brilliant minds of mankind, and the huge amount of new knowledge gained through the vastly improved computational and experimental methods and facilities, at present we still have not been able to rigorously prove that turbulence is indeed chaotic in a certain universal mathematical sense.

Nevertheless, rapid advances have been made in nonlinear science that now we do know much more about how and why nonlinear phenomena such as pattern formation, adaptation, self-organization, bifurcation and chaos, etc., happen in a variety of physical systems. So many new results are announced daily that there is no doubt that nonlinear science belongs to the frontiers of science and technology of the 21st Century, offering numerous challenges as well as exciting opportunities.

Look at the mathematics side. Three or four decades ago, the majority of the research publications in the area of nonlinear differential equations still

dealt with the existence and uniqueness issues. There seemed to be a mentality set during that period that these were the best qualities a nonlinear system (or any system) should possess, and no other qualities were more worthwhile. Gradually, we saw the shifts of emphases and interests. Bifurcation analysis have become popular, and new methods have been developed to prove *multiplicity* of solutions of genuinely nonlinear problems (where the linearization method would not lead anywhere). Nowadays, existence and uniqueness are treated mostly as “mundane” issues and few people are interested only in these issues.

Chaos may be viewed as an extreme form of the nonlinear dynamical phenomena. In general, it seems harder to prove the onset of chaos than, e.g., that of bifurcations. For systems of nonlinear ordinary differential equations (ODEs), pioneering work probing the chaotic behavior was done by Lorenz [18] for the Lorenz system and by Cartwright and Littlewood [1] for the forced van der Pol oscillator, among others. A useful mathematical technique to rigorously prove the occurrence of chaos was developed by Melnikov [20] using the Smale Horseshoe; see also [22].

Generalization of the Melnikov method to certain nonlinear PDEs has been made; see [12, 15–17], e.g. Those PDEs have a *Hamiltonian structure* available for exploitation. The PDEs (mostly) live on the entire space and, therefore, there are no boundary conditions to worry about.

When boundary conditions are present in a time-dependent nonlinear PDE, analysis becomes very complicated and, to our knowledge, not too much work is available in the literature. But for a special class of PDEs, namely, the wave equation, one can utilize wave reflection on the boundary to analyze or even “manipulate” chaotic behavior. This study actually complements the type of work mentioned in the preceding paragraph [12, 15–17] where, as we mentioned earlier, boundary conditions are for the most part either not included or not regarded as important in the models.

The historical background of our study came from the *boundary stabilization problem* of the linear wave equation. Let us describe it below. Let

$$\frac{1}{c^2} \frac{\partial^2 w(x, t)}{\partial t^2} - \frac{\partial w(x, t)}{\partial x^2} = 0, \quad 0 < x < 1, \quad t > 0, \quad (1)$$

denote the linear PDE modelling either acoustic wave propagation or a vibrating string on the unit interval $(0,1)$, where $c > 0$ denotes the speed of wave propagation. At the left-end $x = 0$, assume that the boundary condition is fixed:

$$w(0, t) = 0, \quad t > 0. \quad (2)$$

At the right-end $x = 1$, control is placed:

$$w_x(1, t) = u(1, t), \quad t > 0. \quad (3)$$

The initial conditions are

$$w(x, 0) = w_0(x), \quad w_t(x, 0) = w_1(x), \quad 0 < x < 1, \quad (4)$$

for two given functions w_0 and w_1 with sufficient smoothness, satisfying $w(0, t) = 0$ for all $t > 0$. The energy associated with vibration at time t is

$$E(t) = \frac{1}{2} \int_0^1 \left[w_x^2(x, t) + \frac{1}{c^2} w_t^2(x, t) \right] dx. \quad (5)$$

The objective of the stabilization problem is to find a feedback law for $u(t)$ in (3) such that

$$\lim_{t \rightarrow \infty} E(t) = 0. \quad (6)$$

A simple choice of the feedback law is the negative velocity feedback:

$$u(t) = -\alpha w_t(1, t), \quad t > 0, \quad \alpha > 0, \quad \alpha \neq 1/c, \quad (7)$$

under the assumption that the velocity $w_t(1, t)$ at $x = 1$ can be observed and be feedback. Substituting (7) into (3), we obtain the so-called *viscous damping boundary condition*

$$w_x(1, t) + \alpha w_t(1, t) = 0, \quad t > 0. \quad (8)$$

With this boundary condition, the energy of the system dissipates with time t :

$$\begin{aligned} \frac{d}{dt} E(t) &= \int_0^1 \left[w_x(x, t) w_{xt}(x, t) + \frac{1}{c^2} w_t(x, t) w_{tt}(x, t) \right] dx \\ &\quad (\text{integration by parts } \Rightarrow) \\ &= w_x(x, t) w_t(x, t) \Big|_{x=0}^{x=1} \\ &= -\alpha w_t^2(1, t) \leq 0. \end{aligned} \quad (9)$$

Using the method of characteristics (see Section 2), one can further show that the energy decays with an exponential rate:

$$E(t) \leq K e^{-\mu t} E(0), \quad \text{for some } K > 0 \text{ independent of } (w_0, w_t), \quad (10)$$

where the exponential rate $e^{-\mu t}$ with $\mu = -\frac{c}{2} \ln \left| \frac{1-\alpha c}{1+\alpha c} \right| > 0$ is *sharp*. Thus, (10) is actually a *uniform exponential stabilization* result, where by “uniform” we mean the decay rate is uniform with respect to any initial condition (w_0, w_1) given in (4). This uniform stabilization result is also useful in solving the *exact controllability problem*:

“For any given sufficiently smooth functions $z_0(x)$ and $z_1(x)$ on $[0, 1]$, satisfying $z_0(0) = 0$, find a controller $u(t)$ in (3) such that at the terminal time $T > 0$,

$$w(T, x) = z_0(x), \quad w_t(T, x) = z_1(x), \quad 0 < x < 1.$$

Using the “controllability via stabilizability” method of Russell [21] for time-reversible distributed parameter systems, one can prove that the exact controllability problem is solvable if $T > 0$ is sufficiently large. (The provision that T be sufficiently large cannot be weakened because the wave propagates with a finite speed and it takes a certain amount of time for the boundary control effect to be propagated to the entire interval.)

So the linear feedback boundary condition (8) is nice and useful. However, in the design of many *servomechanisms*, stabilizability or controllability are not issues of any concern. What is really of concern is the safe or robust operation of the servomechanism. One such example is the classical van der Pol equation

$$\ddot{x} - (\alpha - \beta\dot{x}^2)\dot{x} + kx = 0; \quad \alpha, \beta > 0, \quad (11)$$

where $x = x(t)$ is proportional to the electric current at time t on a circuit equipped with a van der Pol device. Then the energy at time t is $E(t) = \frac{1}{2}(\dot{x}^2 + kx^2)$ and

$$\frac{d}{dt}E(t) = \dot{x}(\ddot{x} + kx) = \dot{x}^2(\alpha - \beta\dot{x}^2),$$

so we have

$$E'(t) \begin{cases} \geq 0 & \text{if } |\dot{x}| \leq (\alpha/\beta)^{1/2}, \\ < 0 & \text{if } |\dot{x}| > (\alpha/\beta)^{1/2} \end{cases} \quad (12)$$

which is the desired *self-regulation effect*, i.e., energy will increase when $|\dot{x}|$ is small which is unfit for operation, and energy will decrease when $|\dot{x}|$ is large in order to prevent electric current surge which may destroy the circuit. (This self-regulating effect is also called *self-excitation*.) A second version of the van der Pol equation is

$$\ddot{x} - (\alpha - 3\beta x^2)\dot{x} + kx = 0, \quad (13)$$

which may be regarded as a differentiated version of (11), satisfying a regulation effect similar to (12). Neither (11) nor (13) has any chaotic behavior as the solutions tend to limit cycles according to the Poincaré–Bendixon Theorem. However, when a *forcing term* $A \cos(\omega t)$ is added to the right hand side of (11) or (13), solutions display chaotic behavior when the parameters A and ω enter a certain regime [12, 14].

What happens when we study the PDE analogue of (11) or (13) for the wave equation? This is one of the major motivations of our study to be delineated in Section 2. In Section 3, we provide what we regard as a set of interesting open questions for further research.

2 Linear Wave Equation with a van der Pol Boundary Condition

In this section, we survey four cases of chaos generation or *anticontrol* by nonlinear feedback boundary control. Consider (1), but set the wave speed $c = 1$ therein because c is not an essential parameter as far as the mathematical analysis of chaotic vibration is concerned. Thus, we consider

$$w_{tt}(x, t) - w_{xx}(x, t) = 0, \quad 0 < x < 1, \quad t > 0. \quad (14)$$

Repeat the two initial conditions in (4) here:

$$w(x, 0) = w_0(x), \quad w_t(x, 0) = w_1(x), \quad 0 < x < 1. \quad (15)$$

At the right-end $x = 1$, assume a nonlinear boundary condition

$$w_x(1, t) = \alpha w_t(1, t) - \beta w_t^3(1, t); \quad t > 0, \quad \alpha, \beta > 0. \quad (16)$$

At the left-end $x = 0$, we have options to choose several types of boundary conditions. Here, let us choose it to be

$$w_t(0, t) = -\eta w_x(0, t), \quad t > 0; \quad \eta > 0, \quad \eta \neq 1. \quad (17)$$

Remark 1 Equation (17) says that negative force is feedback to the velocity at $x = 0$. An alternate choice would be

$$w_x(0, t) = -\eta w_t(0, t), \quad t > 0; \quad \eta > 0, \quad \eta \neq 1,$$

which says negative velocity is feedback to force. \square

With (16) and (17), we have, by (9), (16) and (17),

$$\begin{aligned} \frac{d}{dt} E(t) &= \frac{d}{dt} \int_0^1 \left[\frac{1}{2} w_x^2(x, t) + w_t^2(x, t) \right] dt \\ &= \eta w_x^2(0, t) + w_t^2(1, t)[\alpha - \beta w_t^2(1, t)]. \end{aligned} \quad (18)$$

The contribution $\eta w_x^2(0, t)$ above, due to (17), is always nonnegative. Thus we see that the effect of (17) is to cause energy to increase. For this reason, the boundary condition (17) is said to be *energy-injecting* or *energy-pumping*. On the other hand, we have

$$w_t^2(1, t)[\alpha - \beta w_t^2(1, t)] \begin{cases} \geq 0 & \text{if } |w_t(1, t)| \leq (\alpha/\beta)^{1/2}, \\ < 0 & \text{if } |w_t(1, t)| > (\alpha/\beta)^{1/2}, \end{cases} \quad (19)$$

so the contribution of the boundary condition (16) to (18) is *self-regulating* because (19) works in exactly the same way as (12). Thus, we call (16) a *van der Pol, self-regulating*, or *self-excitation*, boundary condition. Intuitively

speaking, with the boundary condition (17) alone (and with the right-end boundary condition (16) replaced by a conservative boundary condition such as $w(1, t) = 0$ or $w_x(1, t) = 0$ for all $t > 0$) it causes the well-known *classical linear instability*, namely, the energy grows with an exponential rate:

$$E(t) = \mathcal{O}(e^{kt}), \quad k = \frac{1}{2} \ln \left(\left| \frac{1+\eta}{1-\eta} \right| \right) > 0. \quad (20)$$

However, the self-regulating boundary condition (16) can hold the instability (20) partly in check by its regulation effect, for a large class of *bounded initial states* with bounds depending on the parameters α, β and η . When α, β and η match in a certain regime, chaos happens, which could be viewed as a *reconciliation between linear instability and nonlinear self-regulation*. Overall, there is a richness of nonlinear phenomena, including: the existence of *asymptotically periodic solutions, hysteresis, instability* of the type of unbounded growth, and *fractal invariant sets*.

A basic approach for the problems under consideration in this section is the *method of characteristics*. Let u and v be the Riemann invariants of (14) defined by

$$\begin{aligned} u(x, t) &= \frac{1}{2}[w_x(x, t) + w_t(x, t)], \\ v(x, t) &= \frac{1}{2}[w_x(x, t) - w_t(x, t)]. \end{aligned} \quad (21)$$

Then u and v satisfy a diagonalized first order linear hyperbolic system

$$\frac{\partial}{\partial t} \begin{bmatrix} u(x, t) \\ v(x, t) \end{bmatrix} = \begin{bmatrix} 1 & 0 \\ 0 & -1 \end{bmatrix} \frac{\partial}{\partial x} \begin{bmatrix} u(x, t) \\ v(x, t) \end{bmatrix}, \quad 0 < x < 1, \quad t > 0, \quad (22)$$

with initial conditions

$$\left. \begin{aligned} u(x, 0) &= u_0(x) \equiv \frac{1}{2}[w'_0(x) + w_1(x)], \\ v(x, 0) &= v_0(x) \equiv \frac{1}{2}[w'_0(x) - w_1(x)], \end{aligned} \right\} \quad 0 < x < 1. \quad (23)$$

The boundary condition (16), after converting to u and v and simplifying, becomes

$$u(1, t) = F_{\alpha, \beta}(v(1, t)), \quad t > 0, \quad (24)$$

where the relation $u = F_{\alpha, \beta}(v)$ is defined implicitly by

$$\beta(u - v)^3 + (1 - \alpha)(u - v) + 2v = 0; \quad \alpha, \beta > 0. \quad (25)$$

Remark 2 For (25), we know that

- (i) when $0 < \alpha \leq 1$, for each $v \in \mathbb{R}$, there exists a unique $u \in \mathbb{R}$;

- (ii) when $\alpha > 1$, for each $v \in \mathbb{R}$, in general there may exist two or three distinct $u \in \mathbb{R}$ satisfying (25). Thus $u = F_{\alpha,\beta}(v)$ is not a function relation.

Case (i) will be treated in Subsection 2 while case (ii), containing hysteresis, will be treated in Subsection 2. \square

The boundary conditions (14), by (21), becomes

$$v(0, t) = G_\eta(u(0, t)) \equiv \frac{1+\eta}{1-\eta} u(0, t), \quad t > 0. \quad (26)$$

Equations (25) and (26) are, respectively, the wave-reflection relations at the right-end $x = 1$ and the left-end $x = 0$. The reflection of characteristics is depicted in Fig. 1.

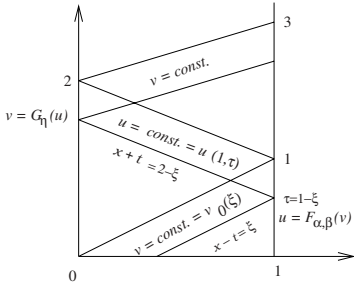


Fig. 1. Reflection of characteristics

Assume that $F_{\alpha,\beta}$ is well defined. Then a solution (u, v) of the system (22), (23), (24) and (26) can be expressed as follows:

For $0 \leq x \leq 1$ and $t = 2k + \tau$, with $k = 0, 1, 2, \dots$, and $0 \leq \tau < 2$,

$$u(x, t) = \begin{cases} (F \circ G)^k(u_0(x + \tau)), & \tau \leq 1 - x, \\ G^{-1} \circ (G \circ F)^{k+1}(v_0(2 - x - \tau)), & 1 - x < \tau \leq 2 - x, \\ (F \circ G)^{k+1}(u_0(\tau + x - 2)), & 2 - x < \tau \leq 2; \end{cases} \quad (27)$$

$$v(x, t) = \begin{cases} (G \circ F)^k(v_0(x - \tau)), & \tau \leq x, \\ G \circ (F \circ G)^k(u_0(\tau - x)), & x < \tau \leq 1 + x, \\ (G \circ F)^{k+1}(v_0(2 + x - \tau)), & 1 + x < \tau \leq 2, \end{cases}$$

where in the above, $F = F_{\alpha,\beta}$ and $G = G_\eta$, and $(G \circ F)^k$ represents the k -th iterate of the map $G \circ F$. From now on, we often abbreviate $F_{\alpha,\beta}$ and G_η , respectively, as F and G , in case no ambiguities will occur. We call the map $G_\eta \circ F_{\alpha,\beta}$, naturally, the *composite reflection relation*. This map $G_\eta \circ F_{\alpha,\beta}$ can be regarded as the *Poincaré section* of the PDE system because we can essentially construct the solution from $G_\eta \circ F_{\alpha,\beta}$ using (27).

From (27), it becomes quite apparent that the solutions $(u(x, t), v(x, t))$ will manifest chaotic behavior when the map $G \circ F$ is chaotic, in the sense

of Devaney [11, p. 50], for example. We proceed with the discussion in the following four subsections. The main sources for Subsections 2–2 are, in sequential order respectively, [4, 5, 7, 9].

Chaotic vibration of the classical solution: the case $0 < \alpha \leq 1$ As mentioned in Remark 1, when $0 < \alpha \leq 1$, for each $v \in \mathbb{R}$ there exists a unique $u \in \mathbb{R}$ such that $u = F_{\alpha,\beta}(v)$. Therefore, the solution (u, v) to (22), (23), (24) and (26) is unique. When the initial condition (u_0, v_0) is sufficiently smooth satisfying compatibility conditions with the boundary conditions, then (u, v) will also be C^1 -smooth on the spatiotemporal domain.

Let α and β be fixed, and let $\eta > 0$ be the only parameter that varies. To aid understanding, we include a sample graph of the map $G_\eta \circ F_{\alpha,\beta}$, with $\alpha = 1/2$, $\beta = 1$, and $\eta = 0.552$, in Fig. 2. We only need to establish that $G_\eta \circ F_{\alpha,\beta}$ is chaotic, because $F_{\alpha,\beta} \circ G_\eta$ is topologically conjugate to $G_\eta \circ F_{\alpha,\beta}$ through

$$F_{\alpha,\beta} \circ G_\eta = G_\eta^{-1} \circ (G_\eta \circ F_{\alpha,\beta}) \circ G_\eta$$

and, thus, the iterates $(F \circ G)^k$ or $(F \circ G)^{k+1}$ appearing in (27) do not need to be treated separately.

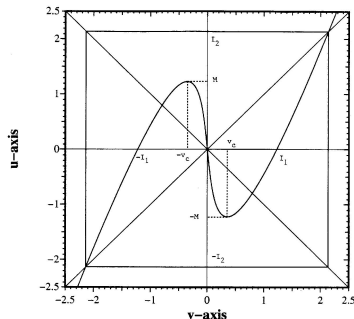


Fig. 2. The graph of $u = G_\eta \circ F_{\alpha,\beta}(v)$. (Here $\alpha = 0.5$, $\beta = 1$, $\eta = 0.552$ are used.) Note that

- $\pm I_1 = v$ -axis nonzero intercepts, $I_1 = [(1 + \alpha/\beta)^{1/2}]$;
- $\pm v_c$ = (local) critical points, $v_c = [(2 - \alpha)/3][(1 + \alpha)/(3\beta)]^{1/2}$;
- $\pm M$ = local extremum values, $M = \frac{1+\eta}{1-\eta} \frac{1+\alpha}{3} [(1 + \alpha/3\beta)^{1/2}]$;
- $\pm I_2 = v$ -values where the curve intersects with the line $u - v = 0$,
- and $[-I_2, I_2] \times [-I_2, I_2]$ is an invariant square when $M \leq I_2$.

We note the following bifurcations: For fixed α : $0 < \alpha \leq 1$ and $\beta > 0$, let $\eta \in (0, 1)$ be varying.

- (1) *Period-doubling bifurcation* [4, p. 431, Theorem 3.1]

Define

$$h(v, \eta) = -G_\eta \circ F(v)$$

and let

$$v_0(\eta) \equiv \eta[(1 + \eta)/2][(\alpha + \eta)/\beta]^{1/2}$$

which, for each η , represents a fixed point of h , i.e.,

$$h(v_0(\eta), \eta) = v_0(\eta).$$

Then the algebraic equation

$$\frac{1}{2} \left(\frac{1 + \alpha\eta}{3\beta\eta} \right)^{1/2} \left[\frac{1 + (3 - 2\alpha)\eta}{3\eta} \right] = \frac{1 + \eta}{2} \left(\frac{\alpha + \eta}{\beta} \right)^{1/2} \quad (28)$$

has a unique solution $\eta = \eta_0$: $0 < \eta_0 \leq \eta_H$, where

$$\eta_H \equiv \left(1 - \frac{1 + \alpha}{3\sqrt{3}} \right) / \left(1 + \frac{1 + \alpha}{3\sqrt{3}} \right) \quad (29)$$

satisfying

$$\frac{\partial}{\partial v} h_1(v, \eta) \Big|_{\substack{v=v_0(\eta_0) \\ \eta=\eta_0}} = -1 \quad (30)$$

which is the primary necessary condition for period-doubling bifurcation to happen, at $v = v_0(\eta_0)$, $\eta = \eta_0$. Furthermore, the other “accessory” conditions are also satisfied, and the bifurcated period-2 solutions are attracting.

Consequently, there is a period-doubling route to chaos, as illustrated in the orbit diagram in Fig. 3.

(2) *Homoclinic orbits* [4, pp. 436–437, Theorem 4.1]

Let η_H be given by (28). If

$$\eta_H \leq \eta < 1, \quad (31)$$

then $M \geq I_1$ (cf. Fig. 2) and, consequently, the repelling fixed point 0 of $G_\eta \circ F$ has homoclinic orbits. Furthermore, if $\eta = \eta_H$, then there are *degenerate homoclinic orbits* (and, thus, homoclinic bifurcations [11, p. 125]).

When $M > I_2$; cf. Fig. 2, then $[-I_2, I_2] \times [-I_2, I_2]$ is no longer an invariant square for the map $G \circ F$. What happens is exactly similar to the case of the quadratic map $f_\mu(x) = \mu x(1 - x)$, for $0 \leq x \leq 1$, when $\mu > 4$ because part of the graph of f_μ will protrude above the unit square. See Fig. 4. It is easy to see that now the map $G \circ F$ has a Cantor-like fractal invariant set A on the interval $[-I_2, I_2]$, where $A = \bigcap_{j=1}^{\infty} (G \circ F)^k([-I_2, I_2])$. All the other points outside A are eventually mapped to $\pm\infty$ as the number of iterations increases.

We furnish a PDE example below.

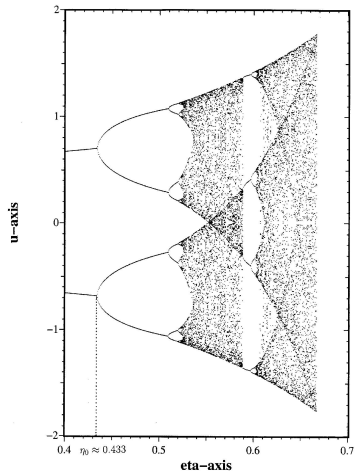


Fig. 3. The orbit diagram of $G_\eta \circ F_{\alpha,\beta}$, where $\alpha = 0.5$, $\beta = 1$, and η varies in $[0.4, 2/3]$. Note that the first period-doubling occurs near $\eta_0 \approx 0.433$, agreeing with the computational result of (1.30). (Reprinted from [4, p. 433, Fig. 3], courtesy of World Scientific, Singapore.)

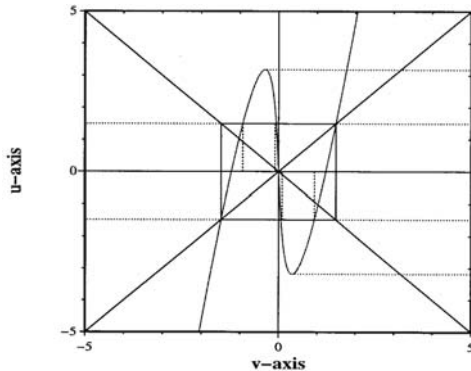


Fig. 4. The graph of $G_\eta \circ F_{\alpha,\beta}$ with $\alpha = 0.5$, $\beta = 1$ and $\eta = 0.8$. Note that here $M > I_2$ (cf. Fig. 2) and $[-I_2, I_2] \times [-I_2, I_2]$ is no longer an invariant square for $G_\eta \circ F_{\alpha,\beta}$. On $[-I_2, I_2]$, what $G_\eta \circ F_{\alpha,\beta}$ has is a Cantor-like fractal invariant set.

Example 1 [4, p. 435, Example 3.3] Consider (22), (23), (24) and (26), where we choose

$$\alpha = 0.5, \beta = 1, \eta = 0.525 \approx \eta_H, \text{ satisfying (31),}$$

$$w_0(x) = 0.2 \sin\left(\frac{\pi}{2}x\right), \quad w_1(x) = 0.2 \sin(\pi x), \quad x \in [0, 1].$$

Two spatiotemporal profiles of u and v are plotted, respectively, in Figs. 5 and 6. Their rugged outlooks manifest chaotic vibration. \square

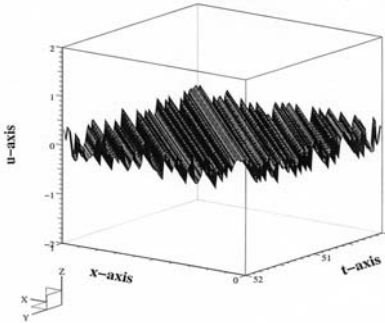


Fig. 5. The spatiotemporal profile of the u -component for Example 1.1, for $t \in [50, 52]$, $x \in [0, 1]$. (Reprinted from [4, p. 435, Fig. 7], courtesy of World Scientific, Singapore.)

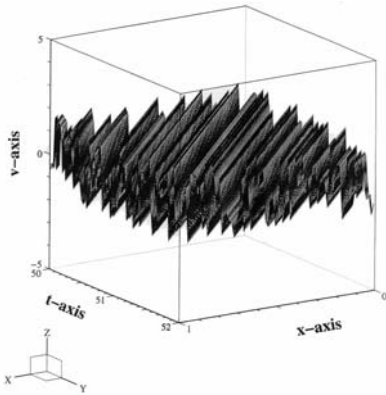


Fig. 6. The spatiotemporal profile of the v -component for Example 1.1, for $t \in [50, 52]$, $x \in [0, 1]$. (Reprinted from [4, p. 435, Fig. 8], courtesy of World Scientific, Singapore.)

Miscellaneous remarks

- (1) In this subsection, we have illustrated only the case $0 < \eta < 1$. When $\eta > 1$, the results are similar. See [4].

- (2) With the nonlinear boundary condition (16), we can only establish that u and v are chaotic. From this, we can then show that w_x and w_t , i.e., the gradient of w , are also chaotic by a natural topological conjugacy, see [3, Section 5]. However, w itself is not chaotic because w is the time integral of w_t , which smooths out the oscillatory behavior of w_t . In order to have chaotic vibration of w , one must use a differentiated boundary condition; see [4, Section 6]. This is actually an analog of (13).
- (3) When the initial data (u_0, v_0) takes values outside the invariant square $[-I_2, I_2] \times [I_2, I_2]$, then part of u and v will diverge to $\pm\infty$ as $t \rightarrow \infty$. This behavior belongs to classical unbounded instability.

Chaotic vibration when there is hysteresis: the case $\alpha > 1$ When $\alpha > 1$, the relation $u = F_{\alpha,\beta}(v)$ is no longer single-valued. (The notation $u \in F_{\alpha,\beta}(v)$ would be more appropriate.) For each value of $v \in \mathbb{R}$, there may exist up to three $u \in \mathbb{R}$ satisfying (25). We plot a graph of $u = G_\eta \circ F_{\alpha,\beta}(v)$ in Fig. 7. Throughout this subsection, we require $0 < \eta < 1$.

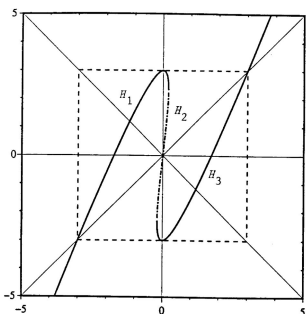


Fig. 7. The multi-valued relation $u = G_\eta \circ F_{\alpha,\beta}(v)$, with $\eta = 1/2$, $\alpha = 2$, and $\beta = 1$. The three branches H_1 , H_2 and H_3 are labelled from the left to right, respectively, as solid, dotted and solid curves.

The multi-valued relation $u = G_\eta \circ F_{\alpha,\beta}(v)$ consists of three piecewise single-valued branches, H_1 , H_2 and H_3 (where H stands for “hysteresis”), to be defined below. First, let $v^* \equiv \frac{\alpha-1}{3} \left[\frac{\alpha-1}{3\beta} \right]^{1/2}$. Note that if $v \notin [-v^*, v^*]$, then $F_{\alpha,\beta}$ is actually single-valued: it consists of a continuous branch $F_{\alpha,\beta}^{(1)}$, defined for $v < -v^*$ and a second branch $F_{\alpha,\beta}^{(3)}$ defined for $v > v^*$. Now, let $\tilde{F}_{\alpha,\beta}^{(1)}$ be the *maximal single-valued continuous extension* of the continuous function $F_{\alpha,\beta}^{(1)}$, and let $\tilde{F}_{\alpha,\beta}^{(3)}$ similarly be the maximal single-valued continuous

extension of the function $F_{\alpha,\beta}^{(3)}$ such that

$$F_{\alpha,\beta}^{(i)}(v) \in F_{\alpha,\beta}(v), \quad \text{for } i = 1 \text{ or } 3.$$

Then we see that $\tilde{F}_{\alpha,\beta}^{(1)}$ is defined for $v \in (-\infty, v^*]$, and $\tilde{F}_{\alpha,\beta}^{(3)}$ is defined for $[-v^*, \infty)$. We define $\tilde{F}_{\alpha,\beta}^{(2)}$ to be

$$\begin{aligned} u &= \tilde{F}_{\alpha,\beta}^{(2)}(v) \text{ if } v \in (-v^*, v^*) \text{ and } \tilde{F}_{\alpha,\beta}^{(2)}(v) \in F_{\alpha,\beta}(v) \\ &\text{but } \tilde{F}_{\alpha,\beta}^{(2)}(v) \neq \tilde{F}_{\alpha,\beta}^{(i)}(v) \text{ for } i = 1, 3. \end{aligned}$$

Now we define

$$\begin{aligned} u &= H_1(v) \equiv G_\eta \circ \tilde{F}_{\alpha,\beta}^{(1)}(v) \quad \text{if } v \in (-\infty, v^*], \\ u &= H_2(v) \equiv G_\eta \circ \tilde{F}_{\alpha,\beta}^{(2)}(v) \quad \text{if } v \in (-v^*, v^*), \\ u &= H_3(v) \equiv G_\eta \circ \tilde{F}_{\alpha,\beta}^{(3)}(v) \quad \text{if } v \in [-v^*, \infty). \end{aligned}$$

These three branches are also illustrated in Fig. 7. We know that when two branches have overlapping domains, such as H_1 and H_2 overlap over $(-\infty, v^*] \cap (-v^*, v^*)$, or H_2 and H_3 do over $(-v^*, v^*) \cap [-v^*, \infty)$, there is a *selection rule in favor of the branch with more stability*, in this case H_1 is selected over H_2 , and H_3 over H_2 as well, because the slopes on the H_1 and H_3 branches have smaller magnitude than the counterpart on H_2 . We now define the *hysteresis iterates* [5, p. 451, Def. 2.1] as follows: for $u_0 \in \mathbb{R}$, $u_k = H^k(u_0)$ is given inductively according to:

(i) For $k = 1$, $u_1 \equiv H(u_0)$, where

$$u_1 = \begin{cases} H_1(u_0), & \text{if } u_0 < -v^*, \\ H_2(u_0), & \text{if } u_0 \in [-v^*, v^*], \\ H_3(u_0), & \text{if } u_0 > v^*. \end{cases}$$

(ii) For $k = 2$, $u_2 \equiv H^2(u_0)$, where

$$u_2 = \begin{cases} H_1(u_1), & \text{if either } u_1 \leq -v^* \text{ or if } u_0 < -v^* \text{ and } u_1 \in [-v^*, v^*], \\ H_2(u_1), & \text{if } u_0 \in [-v^*, v^*], u_1 \in (-v^*, v^*), \\ H_3(u_1), & \text{if either } u_1 \geq v^* \text{ or if } u_0 > v^* \text{ and } u_1 \in [-v^*, v^*], \end{cases}$$

for $u_1 = H(u_0)$.

(iii) Assume that $u_j = H^j(u_0)$ are defined for $j = 1, 2, \dots, k, k \geq 2$. We define $u_{k+1} = H^{k+1}(u_0)$ by

$$u_{k+1} = \begin{cases} H_1(u_k), & \text{if either } u_k \leq -v^* \text{ or if } u_{k-1} < -v^* \text{ and } u_k \in [-v^*, v^*], \\ H_2(u_k), & \text{if } u_0 \in [-v^*, v^*], u_1, u_2, \dots, u_k \in (-v^*, v^*), \\ H_3(u_k), & \text{if either } u_k \geq v^* \text{ or if } u_{k-1} > v^* \text{ and } u_k \in [-v^*, v^*]. \end{cases}$$

When $\eta = 0$, i.e., no energy injection, then it is known that when α increases (with β held fixed), the hysteresis iteration $u = H^*(v)$ has periodic orbits with larger and larger periods, but *no chaos* [5, Section 3]. However, if $\eta > 0$, then under the following sufficient conditions, chaos occurs.

Theorem 1 [5, p. 467, Theorem 4.1]

Let $0 < \eta < 1, \alpha > 1$ and $\beta > 0$ such that

$$\tilde{m} \equiv \frac{1+\eta}{1-\eta} \frac{1+\alpha}{3} \left[\frac{1+\alpha}{3\beta} \right]^{1/2} \leq \frac{1+\eta}{2\eta} \left[\frac{1+\alpha\eta}{\beta\eta} \right]^{1/2}.$$

Define $\theta_0 = -v^* \equiv \frac{\alpha-1}{3} \left[\frac{\alpha-1}{3\beta} \right]^{1/2}$, and let

$$\theta_{j+1} = H_3^{-1}(\theta_j), \quad j = 0, 1, 2, \dots.$$

If for some $j \geq 1$, we have $\tilde{\theta}_{j-1} < v^*$, and $\tilde{\theta}_j, \tilde{\theta}_{j+1}, \tilde{\theta}_{j+2} \in [v^*, \tilde{m}]$, then the hysteresis map $u = H(v)$ is chaotic on the interval $[-\tilde{m}, \tilde{m}]$. \square

Remark 3 The proof of Theorem 1 basically shows that property (36) (see the next subsection) is true. The hysteresis map H in Theorem 1 is essentially a piecewise continuous map, though not single-valued. Thus, useful ideas from Keener [13] can be adopted as well as adapted for our purpose here, and elsewhere [3]. But now we can use a more unified approach based on the exponential growth of total variations as developed in [8, 10] by proving the property (36) instead. \square

Example 2 [5, p. 468, Example 4.1] Choose $\eta = 1/2, \alpha = 2, \beta = 1$, and

$$\begin{cases} u_0(x) = u_0(0) + x[u_0(1) - u_0(0)], \\ v_0(x) = u_0(x)^2 + bu_0(x) + c, \end{cases} \quad 0 \leq x \leq 1,$$

with $u_0(0) = 0.5, u_0(1) = H(v_0(1)), b = -0.32830, c = 1.4145$ and so, $v_0(0) = 1.5, v_0(1) = 1.5$. Then the initial data u_0 and v_0 satisfy the compatibility conditions, and

$$v^* = 0.1925, \theta_0 = -0.1925, \theta_1 = 1.6461, \theta_2 = 2.4408, \theta_3 = 2.7710,$$

$$\theta_4 = 2.9065, \dots, \lim_{j \rightarrow \infty} \theta_j = 3, \tilde{m} = 3,$$

and the conditions of Theorem 1 are satisfied. The solution (u, v) displays chaotic vibration, as can be seen in Fig. 8. \square

Memory effects when the displacement term is present in the nonlinear boundary condition Throughout this subsection, we assume that $0 < \alpha < 1$ and $\eta > 0, \eta \neq 1$.

The nonlinear boundary condition (16) does not contain the displacement term $w(1, t)$. However, such a term can naturally occur due to symmetry and reduction of dimensionality.

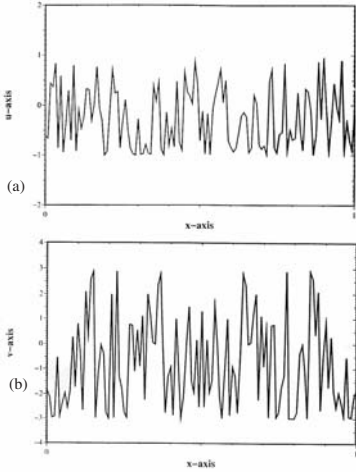


Fig. 8. Snapshots of the solution (a) $u(x, t)$ and (b) $v(x, t)$, $0 < x \leq 1$, for $t = 202$, for Example 1.2, where $\alpha = 2$, $\beta = 1$ and $\eta = 1/2$. (Reprinted from [5, p. 469, Fig. 18], courtesy of World Scientific, Singapore.)

Example 3 [9, pp. 966–967] *The wave equation in 3D*

$$\frac{\partial^2}{\partial x_1^2} W(\vec{x}, t) + \frac{\partial^2}{\partial x_2^2} W(\vec{x}, t) + \frac{\partial^2}{\partial x_3^2} W(\vec{x}, t) - \frac{1}{c^2} \frac{\partial^2 W(\vec{x}, t)}{\partial t^2} = 0, \quad t > 0,$$

where $\vec{x} = (x_1, x_2, x_3) \in \Omega = \{\vec{x} \in \mathbb{R}^3 \mid a < |\vec{x}| < b\}$, for some $a > 0$, $b > 0$, i.e., Ω is the 3D spherical-annular domain with radius a of the inner shell and radius b of the outer shell. The boundary conditions are

$$\begin{aligned} \frac{\partial W(\vec{x}, t)}{\partial n} &= \alpha W_t(\vec{x}, t) - \beta W_t^3(\vec{x}, t) - k_1 W(\vec{x}, t), \\ |\vec{x}| &= a, \quad t > 0; \quad k_1 \geq 0, \\ \frac{\partial W(\vec{x}, t)}{\partial n} &= \frac{1}{\eta} W_t(\vec{x}, t) - k_2 W(\vec{x}, t), \\ |\vec{x}| &= b, \quad t > 0; \quad \eta > 0, \quad k_2 \geq 0, \end{aligned}$$

where n is the unit outward normal at $\partial\Omega$, the boundary of Ω . Assume that the initial conditions are radially symmetric:

$$\left. \begin{aligned} W(\vec{x}, 0) &= W_0(|\vec{x}|), \\ W_t(\vec{x}, 0) &= W_1(|\vec{x}|) \end{aligned} \right\} \quad \vec{x} \in \Omega, \quad (32)$$

for some sufficiently smooth functions W_0 and W_1 defined on \mathbb{R} . We can utilize this radial symmetry to effect a reduction of dimensionality by setting

$$W(\vec{x}, t) = \frac{w(r, t)}{r}, \quad r = |\vec{x}|. \quad (33)$$

After some manipulation and simplifying assumptions, we obtain a 1D wave equation (14), along with (15) and (17). However, the boundary condition (16) now becomes

$$w_x(1, t) = \alpha w_t(1, t) - \beta w_t^3(1, t) - \gamma w(1, t), \quad t > 0, \quad (34)$$

for some $\gamma > 0$. Note that since $\gamma > 0$, the term $\gamma w(1, t)$ in (34) cannot be eliminated. \square

On the boundary $x = 1, t > 0$, we have

$$w(1, t) = \int_0^t w_t(1, \tau) d\tau - w(0, t).$$

Therefore, the wave-reflection condition (25) at the right-end $x = 1$ is now modified to be a nonlinear boundary integral equation:

“For given $v(\tau), 0 \leq \tau < 1$, and $a_0 \in \mathbb{R}$, find $u(\tau), 0 \leq \tau < t$ such that

$$\beta X^3(t) + (1 - \alpha)X(t) + \gamma \left[\int_0^t X(\tau) d\tau + a_0 \right] + 2v(t) = 0, \quad t > 0, \quad (35)$$

where $X(t) \equiv u(t) - v(t)$.”

It is not difficult to prove that the nonlinear integral equation (35) has a unique solution u when v is sufficiently smooth, say v is C^0 . But the difficulty here is that the integral term

$$\gamma \int_0^t v(\tau) d\tau, \text{ as part of } \gamma \int_0^t X(\tau) d\tau = \gamma \int_0^t [u(\tau) - v(\tau)] d\tau \text{ in (35)},$$

now has a *memory effect*. The Poincaré section of the PDE is no longer an interval map $G_\eta \circ F_{\alpha, \beta}$ which we relied so heavily in Subsections 2 and 2. The problem is no longer reducible to a 1-dimensional map. It is a genuine *infinite dimensional* problem.

For an infinite-dimensional problem, there is first the question of what we mean by chaos in such a system. Here we take an intuitive view that for a dynamical system

$$\begin{cases} \frac{d}{dt}x(t) = f(x(t)), t > 0, \\ x(0) = x_0 \in H, \end{cases} \quad (36)$$

where H is a certain function space over the spatial interval $I \subset \mathbb{R}$, we say that the solution $x(\cdot)$ of (36) is chaotic if

$$V_I(x(t)) \geq K e^{\mu t}, \text{ for some } K, \mu > 0, \text{ for all } t > 0, \quad (37)$$

where $V_I(f)$ is the total variation of f on the spatial interval I defined by

$$V_I(f) = \sup_{\mathcal{P}} \left\{ \sum_{j=0}^{n-1} |f(x_{j+1}) - f(x_j)| \mid \{x_0, x_1, \dots, x_n\} \in \mathcal{P}, \right. \\ \left. x_0 < x_1 < \dots < x_n, x_j \in I, j = 0, 1, \dots, n \right\} \quad (38)$$

and \mathcal{P} is the set of all partitions $\{x_0, x_1, \dots, x_n\}$ of the interval I . Thus, (37) says that the total variation in time of the solution $x(\cdot)$ grows exponentially. This view and approach is developed in [8, 10], motivated by the theorems in [10] that for interval maps, the exponential growth of iterates of total variations is equivalent to the fact that the interval map has a homoclinic orbit, and is thus chaotic.

A key idea in establishing the property (37) for our PDE system under study here in this subsection is to exploit the fact that the map $G_\eta \circ F_{\alpha, \beta}$ has, in addition to the invariant square $[-I_2, I_2] \times [-I_2, I_2]$ as indicated in Fig. 2, when $M < I_2$, also two smaller invariant rectangles contained within, such as Fig. 9 indicates visually. This leaves us with some *leeway* (called the *extra margin property* in [9]) to treat (35) as a (very) small perturbation term so that the solution stays within the large invariant square $[-I_2, I_2] \times [-I_2, I_2]$. But the restriction is that γ must be quite small. We have proved the following.

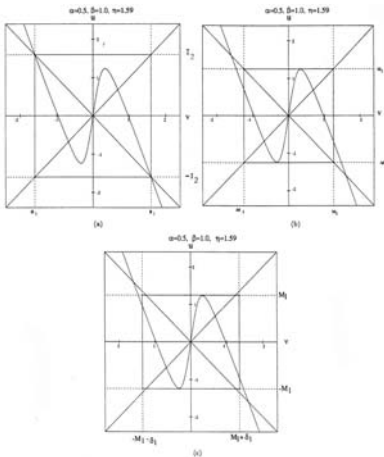


Fig. 9. The graph of $G_\eta \circ F_{\alpha, \beta}$, with $\alpha = 1/2$, $\beta = 1$ and $\eta = 1.59$. In (a), we see the big invariant square $[-I_2, I_2] \times [-I_2, I_2]$; in (b), the smaller invariant square is $[-M_1, M_1] \times [-M_1, M_1]$; and in (c), there is an invariant rectangle $[-M_1 - \delta_1, M_1 + \delta_1] \times [-M_1, M_1]$ for some $\delta_1 > 0$. The value of I_2 is given in the caption of Fig. 1, and that of M_1 is given in the statement of Theorem 1.2. (Reprinted from [9, p. 972, Fig. 1], courtesy of World Scientific, Singapore.)

Theorem 2 [9, pp. 978–979, Theorem 4.1] Consider (22), (23), (26) and (35). Let w_0 and w_1 in (23) be sufficiently smooth and be compatible with the boundary conditions (17) and (34) such that $u_0 = (1/2)(w'_0 + w_1)$ and $v_0 = (1/2)(w'_0 - w_1)$ satisfy

$$|v_0(x)| \leq M_1, \quad |u_0(x)| \leq M_2, \quad x \in [0, 1],$$

where

$M_1 \equiv$ local maximum of $G_\eta \circ F_{\alpha,\beta} = M$ (cf. caption of Fig. 2)

$$= \left| \frac{1+\eta}{1-\eta} \right| \frac{1+\alpha}{3} \sqrt{\frac{1+\alpha}{3\beta}},$$

$M_2 \equiv$ local maximum of $F_{\alpha,\beta} \circ G_\eta$

$$= \frac{1+\alpha}{3} \sqrt{\frac{1+\alpha}{3\beta}}.$$

Let η satisfy either

$$0 < \left(1 - \frac{1+\alpha}{3\sqrt{3}} \right) \left(1 + \frac{1+\alpha}{3\sqrt{3}} \right)^{-1} < \eta_0 < 1$$

or

$$1 < \bar{\eta}_0 < \eta < \left(1 - \frac{1+\alpha}{3\sqrt{3}} \right)^{-1} \left(1 + \frac{1+\alpha}{3\sqrt{3}} \right),$$

where η_0 : $0 < \eta_0 < 1$ and $\bar{\eta}_0$: $1 < \bar{\eta}_0 < \infty$ are the unique solution of, respectively, the following equations

$$\begin{aligned} \frac{1+\eta_0}{1-\eta_0} \frac{1+\alpha}{3} \left(\frac{1+\alpha}{3\beta} \right)^{1/2} &= \frac{1+\eta_0}{2\eta_0} \left(\frac{1+\alpha\eta_0}{\beta\eta_0} \right)^{1/2}, \\ \frac{\bar{\eta}_0+1}{\bar{\eta}_0-1} \frac{1+\alpha}{3} \left(\frac{1+\alpha}{3\beta} \right)^{1/2} &= \frac{1+\bar{\eta}_0}{2} \left(\frac{\alpha+\bar{\eta}_0}{\beta} \right)^{1/2}. \end{aligned}$$

Assume that $\gamma > 0$ is sufficiently small, and that

$$\text{Range } v_0 \supseteq [-\delta, M_1 - \delta], \quad \text{Range } u_0 \supseteq [-\delta, M_2 - \delta],$$

for some small $\delta > 0$ depending only on α, β, γ and η . Then we have

$$\left. \begin{aligned} V_{[0,1]}(u(\cdot, t)) &\geq K e^{\mu t} \rightarrow \infty, \\ V_{[0,1]}(v(\cdot, t)) &\geq K e^{\mu t} \rightarrow \infty, \end{aligned} \right\} \quad \text{as } t \rightarrow \infty,$$

for some $\mu > \ln 2$, where $V_{[0,1]}$ denotes the total variation on the x -interval $[0, 1]$. \square

Snapshots of u and v for some “generic” example are offered in Fig. 10.

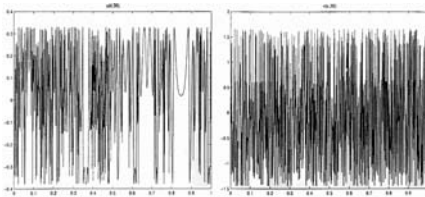


Fig. 10. Snapshots of (a) $u(\cdot, t)$ and (b) $v(\cdot, t)$ for $t = 30$ for some example given in [9]. (Reprinted from [9, p. 980, Fig. 2], courtesy of World Scientific, Singapore.)

Nonisotropic spatiotemporal chaotic vibration The chaotic vibrations studied in previous subsections are *isotropic* in space and time because the governing equation (14) is invariant with respect to the change of variables $x \leftrightarrow t$. (In addition, (14) is invariant under $x \leftrightarrow -t$.) A somewhat different equation, described by the PDE

$$w_{xx}(x, t) - \nu w_{xt}(x, t) - w_{tt}(x, t) = 0, \quad 0 < x < 1, \quad t > 0; \quad \nu > 0 \quad (39)$$

contains a special feature that the two families of characteristics propagate with different speeds and, thus, provide a simple model for the analysis of *nonisotropic* spatiotemporal chaotic vibration.

The time rate of change of energy corresponding to (39), subject to boundary conditions

$$w_x(0, t) = 0, \quad t > 0, \quad (40)$$

$$w_x(1, t) = \alpha w_t(1, t) - \beta w_t^3(1, t), \quad t > 0; \quad \alpha, \beta > 0, \quad (41)$$

is then found to be

$$\begin{aligned} \frac{d}{dt} E(t) &\equiv \frac{d}{dt} \left[\frac{1}{2} \int_0^1 (w_x^2 + w_t^2) dx \right] \\ &\text{(integration by parts } \Rightarrow) \\ &= T_1 + T_2, \end{aligned}$$

where

$$T_1 \equiv \frac{\nu}{2} w_t^2(0, t), \quad T_2 \equiv w_t^2(1, t) \left[\left(\alpha - \frac{\nu}{2} \right) - \beta w_t^2(1, t) \right]. \quad (42)$$

The positivity or negativity of T_1 and T_2 signifies the following:

- (i) $T_1 \geq 0$ if $\nu > 0$, i.e. there is *energy injection* into the system *indirectly through the term* $-\nu w_{xt}$ in (39). This T_1 term would have disappeared if the homogeneous Dirichlet condition $w(0, t) = 0$ were imposed at $x = 0$ in lieu of the Neumann condition (40).

(ii) T_2 is “regulating” if $\alpha - (\nu/2) > 0$, i.e.

$$\begin{aligned} T_2 \geq 0 \quad \text{if} \quad |w_t(1,t)| &\leq \sqrt{\frac{\alpha - \frac{\nu}{2}}{\beta}}; \\ T_2 < 0 \quad \text{if} \quad |w_t(1,t)| &> \sqrt{\frac{\alpha - \frac{\nu}{2}}{\beta}}. \end{aligned}$$

Thus energy is increasing if velocity is small, and decreasing if velocity is large.

(iii) T_2 is *dissipative*, i.e. $T_2 \leq 0$, if $\alpha - (\nu/2) \leq 0$.

Again, we hope that the imbalance between energy injection and the self-regulation effect may lead to chaos.

To study (39), we again use the method of characteristics by setting

$$\begin{aligned} u &= \frac{1}{\rho_1(\nu) + \rho_2(\nu)} [\rho_2(\nu)w_x + w_t], \\ v &= \frac{1}{\rho_1(\nu) + \rho_2(\nu)} [\rho_1(\nu)w_x - w_t], \end{aligned}$$

where

$$\rho_1(\nu) \equiv [-\nu + (4 + \nu^2)^{1/2}]/2, \quad \rho_2(\nu) = [\nu + (4 + \nu^2)^{1/2}]/2.$$

We obtain a diagonalized linear symmetric first order hyperbolic system

$$\frac{\partial}{\partial t} \begin{bmatrix} u(x,t) \\ v(x,t) \end{bmatrix} = \begin{bmatrix} \rho_1(\nu) & 0 \\ 0 & -\rho_2(\nu) \end{bmatrix} \frac{\partial}{\partial x} \begin{bmatrix} u(x,t) \\ v(x,t) \end{bmatrix}, \quad 0 < x < t, \quad t > 0. \quad (43)$$

Physically, the above says that one wave travels to the right with speed $1/\rho_1(\nu)$, while another wave travels to the left with speed $1/\rho_2(\nu)$. A complete cycle of vibration takes $\rho_1(\nu) + \rho_2(\nu)$ time units. The boundary condition (40) gives the reflection relation

$$v(0,t) = -u(0,t) \equiv G(u(0,t)), \quad t > 0, \quad (44)$$

at the left-end $x = 0$, while (41) gives

$$u + v = \alpha(\rho_1 u - \rho_1 v) - \beta(\rho_1 u - \rho_2 v)^3; \quad \rho_i = \rho_i(\nu) \text{ for } i = 1, 2,$$

or

$$\beta X^3 + (\rho_2 - \alpha)X + (\rho_2^2 + 1)v = 0; \quad X \equiv \rho_1 u - \rho_2 v. \quad (45)$$

In order to have a unique real solution u for a given v from the cubic equation, from now on we require that

$$\rho_2(\nu) - \alpha = \frac{\sqrt{4 + \nu^2} + \nu}{2} - \alpha \geq 0. \quad (46)$$

For each given v , then the real solution u of (45) is expressed as

$$u = F_\nu(v),$$

where $\nu > 0$ satisfying (46) is regarded as the varying parameter, while $\alpha, \beta > 0$ are assumed to be held fixed. The unique solution of (43)–(45), with initial conditions

$$u(x, 0) = u_0(x), \quad v(x, 0) = v_0(x), \quad 0 < x < 1,$$

can now be expressed explicitly as follows: for $0 < x < 1$ and for $t = k(\rho_1 + \rho_2) + \tau$, $k = 0, 1, 2, \dots, 0 \leq \tau < \rho_1 + \rho_2$,

$$u(x, t) = \begin{cases} (F_\nu \circ G)^k(u_0(x + \rho_1\tau)), & \tau \leq \rho_2(1 - x), \\ F_\nu \circ (G \circ F_\nu)^k(v_0(1 + \rho_2^2 - \rho_2^2(x + \rho_1\tau))), \\ \rho_2(1 - x) < \tau \leq \rho_2(1 + \rho_1^2 - x), \\ (F_\nu \circ G)^{k+1}(u_0(x + \rho_1\tau - 1 - \rho_1^2)), \\ \rho_2(1 + \rho_1^2 - x) < \tau < \rho_1 + \rho_2, \end{cases}$$

$$v(x, t) = \begin{cases} (G \circ F_\nu)^k(v_0(x - \rho_2\tau)), & \tau \leq \rho_1x \\ G \circ (F_\nu \circ G)^k(u_0(-\rho_1^2(x - \rho_2\tau))), & \rho_1x < \tau \leq \rho_1(x + \rho_2^2), \\ (F_\nu \circ G)^{k+1}(v_0(x - \rho_2\tau + 1 + \rho_2^2)), & \rho_1(x + \rho_2^2) < \tau < \rho_1 + \rho_2. \end{cases}$$

Again, as in (27), we see that $G \circ F_\nu$ forms a natural Poincaré section for the given PDE system. Chaotic vibration occurs if the map $G \circ F_\nu$ is chaotic.

One can analyze that as ν increases, the map $G \circ F_\nu$ has a period-doubling cascade similar to what we have in (28)–(30) in Subsection 2. Also, $G \circ F_\nu$ has homoclinic orbits and a Cantor-like fractal invariant set when ν enters a certain regime. For details, see [7].

To conclude, we provide the following example and graphics.

Example 4 [7, pp. 552–554, Example 6.2] Choose $\alpha = 0.5, \beta = 1$ and $\nu = 3.33$. For these parameters it is known [7] that the map $G \circ F_\nu$ is chaotic.

We have

$$\rho_1(\nu) = 0.277, \quad \rho_2(\nu) = 3.61.$$

A complete cycle of vibration takes $\rho_1 + \rho_2 \approx 3.88$ time units.

For initial conditions, we choose

$$v_0(x) \equiv 0, \quad 0 \leq x \leq 1,$$

and a C^2 -spline for u_0 :

$$u_0(x) = \frac{1}{12} \begin{cases} \frac{(x - x_1)^3}{h^3}, & x_1 \leq x \leq x_2, \\ 1 + \frac{3(x - x_2)}{h} + \frac{3(x - x_2)^2}{h^2} - \frac{3(x - x_2)^3}{h^3}, & x_2 \leq x \leq x_3, \\ 1 - \frac{3(x - x_4)}{h} + \frac{3(x - x_4)^2}{h^2} + \frac{3(x - x_4)^3}{h^3}, & x_3 \leq x \leq x_4, \\ \frac{(x_5 - x)^3}{h^3}, & x_4 \leq x \leq x_5, \\ 0, & elsewhere, \end{cases}$$

$$h = \frac{1}{6}, x_j = \frac{j}{6}, \quad j = 1, 2, 3, 4, 5.$$

The profiles of u and v , as well as the gradient w_x , w_t , are plotted in Figs. 11 and 12. The reader may observe sharp “randomness” in every direction of space and time. Thus, nonisotropic chaotic vibration shows strong mixing of waves. \square

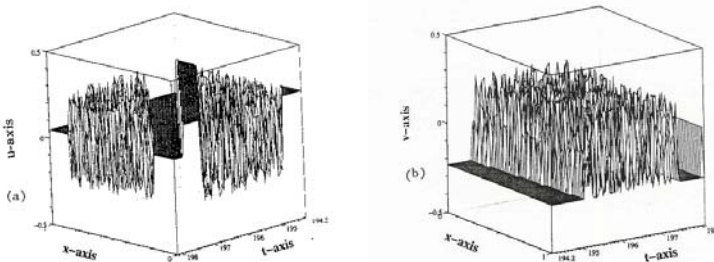


Fig. 11. The spatiotemporal-nonisotropic profile of (a) $u(x, t)$ and (b) $v(x, t)$, for $0 \leq x \leq 1$, $50 \cdot (3.88) \leq t \leq 50 \cdot (3.88)$, for Example 1.4. Note the sharp 2D randomness in the chaotic zone. (Reprinted from [7, p. 556, Figs. 14 and 15], courtesy of World Scientific, Singapore.)

3 Some Open Questions

We pose a few open questions relevant to the topics discussed in Section 2. In our opinion, these are “workable” problems whose resolution will significantly enhance our understanding of chaos in PDEs.

(Q1) Chaotic vibration in 3D

Example 3 in Subsection 2 shows a 3D problem whose solution has chaotic behavior in the radial variable, as we have successfully reduced the problem

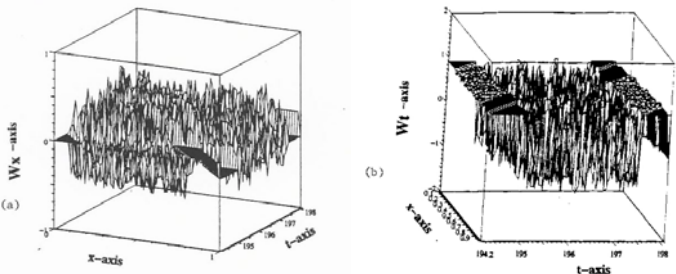


Fig. 12. The profile of (a) $w_x(x, t)$ and (b) $w_t(x, t)$, for $0 \leq x \leq 1$, $50 \cdot (3.88) \leq t \leq 51 \cdot (3.88)$, for Example 1.4. (Reprinted from [7, p. 557, Figs. 16 and 17], courtesy of World Scientific, Singapore.)

to 1D in terms of the variable $r = |x| = \sqrt{x_1^2 + x_2^2 + x_3^2}$ (which is rewritten as x in (14)). What if the initial conditions in (32) contain a small perturbation such as

$$W(\vec{x}, 0) = W_0(|\vec{x}|) + \varepsilon f(\vec{x}), \quad W_t(\vec{x}, 0) = W_1(|\vec{x}|),$$

where $f(\vec{x})$ is not a function of $|\vec{x}|$ only?

There is little trouble in believing that chaotic vibration will occur when α, β, γ and η satisfy the assumptions in Theorem 2. This will be *genuine 3D* chaotic vibration because $W(x, t)$ depends not only on $|\vec{x}|$ but also on the spherical angular variables θ and ϕ as well.

Can we establish a rigorous proof for this?

(Q2) Chaotic vibration of the wave equation on a 2D annular domain with radial symmetry

Consider Example 3 again, but in 2D, i.e.,

$$\Omega = \{\vec{x} \in \mathbb{R}^2 \mid a < |\vec{x}| < b\}.$$

Also assume (32), so we have radial symmetry. But the wave equation in 2D,

$$\frac{\partial^2 W(\vec{x}, t)}{\partial x_1^2} + \frac{\partial^2 W(\vec{x}, t)}{\partial x_2^2} - \frac{1}{c^2} \frac{\partial^2 W(\vec{x}, t)}{\partial t^2} = 0$$

is no longer reducible to the form (14) because the Huygen's principle does not apply to 2D. The reduced form we can reach is

$$\frac{\partial^2 w(r, t)}{\partial r^2} + \frac{1}{r} \frac{\partial w(r, t)}{\partial r} - \frac{1}{c^2} \frac{\partial^2 w(r, t)}{\partial t^2} = 0, \quad r = |\vec{x}|, \quad a < r < b.$$

For this equation, can we study its chaotic vibrations such as those discussed in Section 2?

(Q3) The 1D linear Klein–Gordon equation

The equation is

$$\frac{1}{c^2}w_{tt}(x, t) - w_{xx}(x, t) + k^2w(x, t) = 0, \quad 0 < x < 1, \quad t > 0, \quad k^2 > 0.$$

The *dispersion term* k^2w above causes significant technical difficulty in the analysis of its behavior when boundary conditions contain nonlinearities.

Can we develop effective methods and devise nonlinear feedback boundary conditions to determine if the system behaves chaotically?

(Q4) van der Pol nonlinearity distributed over the x -span

We have assumed the van der Pol nonlinearity to live on the boundary $x = 1$ such as (16). Instead, we may also consider the van der Pol nonlinearity to be distributed

$$w_{tt}(x, t) + [-\alpha w_t(x, t) + \beta w_t^3(x, t)] - w_{xx}(x, t) = 0, \\ 0 < x < 1, \quad t > 0, \quad \alpha, \beta > 0, \quad (47)$$

and set

$$w(1, t) = 0, \quad t > 0.$$

Then we have

$$\begin{aligned} \frac{d}{dt}E(t) &= \frac{d}{dt}\left[\frac{1}{2}\int_0^1(w_x^2 + w_t^2)dx\right] \\ &= \eta w_x^2(0, t) + \int_0^1w_t^2(\alpha - \beta w_t^2)dx. \end{aligned}$$

So again we see that the bracketed terms in (47) have a self-regulation effect.

Numerical experiments have shown that when η enters a certain regime (while α and β are held fixed), chaotic vibration occurs.

Can this be rigorously proved?

(Q5) Memory effect of the displacement term when $\gamma > 0$ in (34) is not small

The study in Subsection 2 was essentially carried out by a perturbation argument requiring that γ be small. There is never any doubt that even when γ is not small, the system will possess chaotic behavior. The memory effect of γw tends to cause a deformation of the invariant region, which we are unable to analyze so far.

We deem any successful study of the case when $\gamma > 0$ is not small very desirable.

(Q6) Coupled vibrating strings with a joint

This problem is of the type considered in [2, 6].

The composite reflection relation for such a coupled structure is a 2×2 nonlinear matrix relation instead of the scalar map $G_\eta \circ F_{\alpha,\beta}$ or $G \circ F_\nu$ surveyed in this paper. This type of 2×2 nonlinear relation is not invertible, preventing the applicability of the Smale Horseshoe method.

New analytical methods are desirable to enable the treatment of 2-dimensional nonlinear mappings in order to handle (Q6).

Acknowledgments.

G. Chen and J. Zhou were supported in part by a Texas A&M University Telecommunication Informatics Task Force (TITF) grant. S.-B. Hsu was supported in part by a research grant from the National Science Council of R.O.C.

References

1. Cartwright, M., Littlewood, J. (1945) On nonlinear differential equations of the second order: I. The equation $\ddot{y} - k(1 - y^2)\dot{y} + y = b\lambda k \cos(\lambda t + \alpha)$, *k*. J. London Math. Soc., **20**:180–189
2. Chen, G., Hsu, S. B., Zhou, J. (1996) Linear superposition of chaotic and orderly vibrations on two serially connected strings with a van der Pol joint. Int. J. Bifur. Chaos, **6**:1509–1527
3. Chen, G., Hsu, S. B., Zhou, J. (1998) Chaotic vibrations of the one-dimensional wave equation subject to a self-excitation boundary condition, Part I. Trans. Amer. Math. Soc., **350**:4265–4311
4. Chen, G., Hsu, S. B., Zhou, J. (1998) Ibid, Part II, Energy injection, period doubling and homoclinic orbits. Int. J. Bifur. Chaos, **8**:423–445
5. Chen, G., Hsu, S. B., Zhou, J. (1998) Ibid, Part III, Natural hysteresis memory effects. Int. J. Bifur. Chaos, **8**:447–470
6. Chen, G., Hsu, S. B., Zhou, J. (1998) Snapback repellers as a cause of chaotic vibration of the wave equation due to a van der Pol boundary condition and energy injection in the middle of the span. J. Math. Phys., **39**:6459–6489
7. Chen, G., Hsu, S. B., Zhou, J. (2002) Nonisotropic spatiotemporal chaotic vibration of the wave equation due to mixing energy transport and a van der Pol boundary condition. Int. J. Bifur. Chaos, **12**:535–559
8. Chen, G., Lasiecka, I., Zhou, J. (2001) Unbounded growth of total variations of snapshots of the 1D linear wave equation due to the chaotic behavior of iterates of composite nonlinear boundary reflection relations. In Advances in Control of Nonlinear Distributed Parameter Systems, ed. by Chen, G., Lasiecka, I., Zhou, J., New York: Marcel Dekker, 15–42
9. Chen, G., Hsu, S. B., Huang, T. W. (2002) Analyzing the displacement terms memory effect to prove the chaotic vibration of the wave equation. Int. J. Bifur. Chaos, **12**:965–981
10. Chen, G., Huang, T., Huang, Y. (2003) Chaotic behavior of interval maps and total variations of iterates. Int. J. Bifur. Chaos, to appear

11. Devaney, R. L. (1989) An Introduction to Chaotic Dynamical Systems. New York: Addison-Wesley
12. Guckenheimer, J., Holmes, P. (1983) Nonlinear Oscillations, Dynamical Systems, and Bifurcation of Vector Fields. New York: Springer-Verlag
13. Keener, J. P. (1980) Chaotic behavior in piecewise continuous difference equations. *Trans. Amer. Math. Soc.*, **261**:589–604
14. Levi, M. (1981) Qualitative analysis of the periodically forced relaxation oscillations. *Mem. Amer. Math. Soc.*, **214**:1–147
15. Li, C., McLaughlin, D. (1994) Morse and Melnikov functions for NLS Pde's. *Comm. Math. Phys.*, **162**:175–214
16. Li, C., McLaughlin, D., Shatah, J., Wiggins, S. (1996) Persistent homoclinic orbits for perturbed nonlinear Schrödinger equation. *Comm. Pure Appl. Math.*, **XLIX**:1175–1255
17. Li, C. (1999) Smale horseshoe and symbolic dynamics in perturbed nonlinear Schrödinger equations. *J. Nonlinear Sci.*, **9**:363–415
18. Lorenz, E. N. (1963) Deterministic non-periodic flow. *J. Atmos. Sci.*, **20**:130–141
19. Holmes, P., Marsden, J. (1981) A partial differential equation with infinitely many periodic orbits: chaotic oscillators of a forced beam. *Arch. Rat. Mech. Anal.*, **76**:135–165
20. Melnikov, V. K. (1963) On the stability of the center for time periodic perturbations. *Trans. Moscow Math. Soc.*, **12**:1–57
21. Russell, D. L. (1974) Exact boundary value controllability theorems for wave and heat processes in star-complemented regions. In Differential Games and Control Theory, ed. by Roxin, Liu, Sternberg, New York: Marcel Dekker
22. Wiggins, S. (1990) Introduction to Applied Nonlinear Dynamical Systems and Chaos. New York: Springer-Verlag

Time-delayed Impulsive Stabilization of Unstable Periodic Orbits in Chaotic Hybrid Systems

Yu-Ping Tian¹ and Xinghuo Yu²

¹ Department of Automatic Control
Southeast University, Nanjing, China
yptian@seu.edu.cn

² School of Electrical and Computer Engineering
Royal Melbourne Institute of Technology University
Melbourne, Australia x.yu@rmit.edu.au

Abstract. The chapter presents a time-delayed impulsive feedback approach for the stabilization of periodic orbits in hybrid chaotic systems. A rigorous stability analysis of the proposed method is given. By using the proposed time-delayed impulsive feedback method, we consider two special applications. One application is detecting periodic orbits in a special class of hybrid system, a switched arrival system, which is a prototype model of many manufacturing and computer systems where large amount of work is processed at a unit time. The other application considers the stabilization of periodic orbits of chaotic piecewise affine systems, in particular, Chua's circuit, which is another important class of chaotic hybrid systems. Simulations are presented to show the effectiveness of the approach proposed.

1 Introduction

Hybrid systems are systems which involve both continuous-time dynamics and discrete events. Hybrid behaviors arise in many situations both in man-made systems and in nature. Continuous-time systems, which have a phased operation, such as walking robots, nonlinear electronic circuits, biological cell growth, are well-suited to be modelled as hybrid systems, as are the continuous-time systems which are controlled by a discrete logic, for example, chemical plant controlled with valves and pumps, aircraft with a switching controller.

Because of the coupling and interaction of discrete and continuous-time phenomena, behaviors of hybrid systems can be extremely complex. Even relatively simple hybrid systems, such as piecewise linear systems, may exhibit very rich and typical nonlinear dynamics such as bifurcations and chaos. A well-known example of piecewise linear chaotic systems is the Chua's circuit and its extensions [5]. There are many other examples. For instance, Chua and Lin showed that chaos and fractal phenomena could occur in a second-order piecewise linear digital filter [6]. Ushio and Hsu, and Yu analyzed chaotic dynamics in switching control systems [29, 33]. Chase et al. analyzed chaotic

and periodic dynamics in a switched flow model which is an abstract model of many manufacturing systems and computer systems where large amount of work is processed at a unit time [3].

Stabilizing unstable periodic orbits (UPOs) embedded in chaotic dynamics has drawn much attention recently and become a very active multidisciplinary research area [4]. The first chaos control, known as the OGY method proposed by Ott, Grebogi and Yorke [15], stabilizes UPOs using small discontinuous parameter perturbations. Further extensions based on the OGY method and the concept of invariant manifolds have been reported [7,8,24,25]. Although methods of this kind are effective, they do require information about inherent UPOs which would be used as reference signals for control. However, due to the unstable nature of the inherent UPO, these signals are very difficult to derive by mathematical means or to implement by electronic circuits. Pyragas proposed a time-delayed feedback control method for stabilization of inherent UPO in chaotic systems [17, 18], that requires only a period constant instead of the exact information of the orbit to be stabilized. A dynamical version of the time-delayed feedback control using output information was presented in [27]. To overcome the so-called “odd number limitation” [30], various extensions of the method have been investigated [11, 19, 26, 28].

However, little attention has been paid to controlling chaos in hybrid systems so far. Those chaos control methods, which have been developed for continuous-time or discrete-time systems, may be difficult to apply to hybrid systems because both the system and the target orbit are non-differentiable at transition points. Even though some hybrid systems can formally be treated in the framework of continuous-time nonlinear control, specific features of these systems, such as inherent discontinuities, significantly aggravate both design and stability analysis, which are difficult even for pure continuous-time control systems [10, 13, 14]. Furthermore, treating hybrid systems as continuous-time systems neglects the discrete dynamics of chaotic systems which may have very important application potentials in communication and coding of digital signals [20, 21].

Recently, impulsive control method has been developed based on the theory of impulsive differential equations [2,12,32]. The method has been demonstrated to be applicable to solving the problem of stabilization and synchronization of chaotic systems [23]. This impulsive control method introduces state jumps in continuous-time systems at discrete time instants and is essentially a kind of hybrid control method. Therefore, hybrid system models and analysis tools can conveniently deal with a hybrid system controlled by an impulsive controller in a uniform framework.

In this chapter we propose an time-delayed impulsive feedback approach for stabilization of UPOs in hybrid chaotic systems. The rest of the chapter is organized as follows. In Section 2 we briefly describe models of hybrid systems and introduce the concept of hybrid periodic orbits of the systems. In Sec-

tion 3 a new time-delayed impulsive feedback control algorithm is proposed. Then we give some rigorous stability analysis of the proposed method. We also generalize the method to the multiple time-delayed feedback case and dynamical time-delayed feedback case. In Section 4, using the proposed time-delayed impulsive feedback method, we deal with the problem of detecting periodic orbits in a special class of hybrid systems, a switched arrival system, which is a prototype model of many manufacturing systems and computer systems where large amount of work is processed at a unit time. In Section 5 we focus on the stabilization of periodic orbits of chaotic piecewise linear systems, especially Chua's circuit, which is another important special class of hybrid systems. Concluding remarks are given in Section 6.

2 Hybrid Systems

Hybrid systems are dynamical systems that involve both continuous-time and discrete-event dynamics. These systems can be modelled by

$$\dot{x} = f(x(t), q(t)), \quad (1)$$

where $x \in X \subseteq R^n$ is the continuous state, and $q \in Q = \{q_1, q_2, \dots, q_m\}$ is the discrete state. We use $(q, x(t))$ to denote the hybrid state of the hybrid system. In the sequel, the equation $(q, x(t)) = (q', x'(t))$ will imply that $q = q'$ and $x(t) = x'(t)$. A transition map $R(q, x(t)) = (q', x'(t))$ is used in this chapter to denote that the system is switched from (q, x) to (q', x') at the time t . A guard of the hybrid system is the set of transition states at which the system state is switched from (q, x) to (q', x') , and can be therefore defined as

$$G(q, q') = \{x \in X_q \subseteq R^n : R(q, x) = (q', x'), q \in Q, q' \in Q, q \neq q'\}. \quad (2)$$

An important special class of hybrid systems is piecewise linear systems which can be written as

$$\dot{x} = A(q)x(t) + a(q), \quad (3)$$

where $A(q) \in R^{n \times n}$, $a(q) \in R^n$ are matrices depending on q , the location of the discrete state $q(t)$ is generally determined by some prescribed guards. Let $\{X_i\}_{i \in Q}$ be a partition of the continuous state space X into a number of closed (possibly unbounded) polyhedral with pairwise disjoint interiors. For piecewise linear systems, guards are often (but not necessarily) defined as the intersection of the boundaries of each two domains X_i and X_j , i.e.,

$$G(i, j) = \{x \in X_i : x \in \partial X_i \cap \partial X_j\}, \quad (4)$$

where ∂X_i denotes the boundary of X_i .

Let $x(t) \in \bigcup_{i \in Q} X_i$ be a continuous piecewise C^1 function on the time interval $[0, \infty)$. We say $x(t)$ is a trajectory of (1) (or, of (3) for the piecewise linear case) if derivative $\dot{x}(t)$ is well defined for any $t \geq 0$, the equation (1) (or (3) respectively) holds for all q with $x(t) \in X_q$. Let $s = \{s_1, s_2, \dots, s_i, \dots\}$ be the sequence of discrete states associated with the continuous trajectory $x(t)$. The sequence s actually defines the so-call symbolic dynamics of the system. The combination $w = (s, x(t))$ is usually referred to as a hybrid trajectory.

Now we introduce some definitions of periodic orbits of hybrid systems.

Definition 1: For any $t \geq 0$, if there exists some constant $T > 0$ such that $x(t) = x(t+T)$, then we say the system is travelling on a continuous period- T orbit.

Definition 2: For any integer $i > 0$, if there exists some integer constant $k > 0$ such that the symbolic sequence, s , has the property $s_i = s_{i+k}$, then we say the system is travelling on a discrete period- k orbit.

Note that in some hybrid control systems, the location of discrete state is used as a control variable. Different control policies may yield the same continuous trajectory. So a periodic continuous trajectory does not necessarily imply a periodic symbolic sequence. And vice versa, a periodic symbolic sequence dose not imply a periodic continuous trajectory either.

If trajectory of a hybrid system satisfies the conditions in both Definition 1 and Definition 2, then we say the system is travelling on a hybrid periodic orbit. Let $x(\tau_1), x(\tau_2), \dots, x(\tau_i), \dots$ be a sequence of the states at which the system trajectory visits the guard $G(q, q')$. Obviously, if the system is travelling on a hybrid periodic orbit, then there must exist an integer constant m such that $x(\tau_i) = x(\tau_{i+m})$ for $i = 1, 2, \dots$. For convenience of further discussion we give the following definition.

Definition 3: Let $x(\tau_1), x(\tau_2), \dots, x(\tau_i), \dots$ be a sequence of the states at which the system trajectory visits the guard $G(q, q')$. If there exists an integer constant m such that $x(\tau_i) = x(\tau_{i+m})$ for $i = 1, 2, \dots$, then we say the system is travelling on a period m orbit defined on $G(q, q')$.

In this chapter we will focus our attention on the hybrid systems where the system trajectory exhibits chaotic behavior. In this case, neither continuous trajectory nor the symbolic dynamics is periodic. However, as is well known, a chaotic attractor includes an infinite number of UPOs in general. Our objective is to stabilize a chaotic hybrid system at some desired hybrid periodic orbit.

3 Stabilization of UPOs in Hybrid Systems

3.1 Time-delayed impulsive feedback control

In this section we will consider the problem of stabilization of a periodic- m periodic orbit defined on the guard $G(q, q')$ using the impulsive control method.

Unlike conventional control methods, in the impulsive control framework, the system state is assumed to be “impulsively” changed at certain time instants denoted by τ_1, τ_2, \dots , such that

$$x(\tau_i^+) = x(\tau_i^-) + K(x), i = 1, 2, \dots$$

where $x(\tau_i^-)$ and $x(\tau_i^+)$ are the system states at $t = \tau_i$ before and after the impulsive action respectively. $K(x)$ is some feedback control law to be designed (see, e.g., [32] for details).

We denote the state at which the chaotic trajectory visits the guard $G(q, q')$ simply as $x(\tau_1), x(\tau_2), \dots$. Since we are interested in stabilizing an inherent period- m orbit, the instants of impulsive action are then chosen as $t = \tau_{km+1}, k = 1, 2, \dots$. The impulsive feedback law is designed as

$$x(\tau_{km+1}^+) = (I - K)x(\tau_{km+1}^-) + Kx(\tau_{(k-1)m+1}^+), \quad (5)$$

where K is a square gain matrix. Since a time-delayed state is used, we regard the feedback law (5) as a time-delayed impulsive feedback.

3.2 Generalization

The proposed time-delayed impulsive feedback control law can be generalized at least in the following directions.

A. Multiple time-delayed impulsive feedback. The essential of time-delayed feedback control for the UPO stabilization problem is using the time-delayed state as an estimation of the target. So we can use multiple delayed states to formulate the following impulsive control law:

$$x(\tau_{km+1}^+) = \sum_{i=1}^L \lambda_i (I - K_i)x(\tau_{(k-i+1)m+1}^-) + \sum_{i=1}^L \lambda_i K_i x(\tau_{(k-i)m+1}^+), \quad (6)$$

where L is an appropriate delay length, $\lambda_i, i = 1, \dots, L$, are some weight constants which satisfy

$$\sum_{i=1}^L \lambda_i = 1. \quad (7)$$

Obviously, when $L = 1$, the feedback control law (6) reduces to (5).

B. Dynamical time-delayed impulsive feedback. As it is well known, state feedback can be classified into two types: steady state feedback and dynamical state feedback. The feedback control (5) can be viewed as a steady time-delayed state feedback. In the spirit of conventional dynamical state feedback control, we can generalize it to a dynamical form. To this end, we rewrite (5) in the form

$$\Delta x(\tau_{km+1}) = -K(x(\tau_{km+1}^-) - x(\tau_{(k-1)m+1}^+)), \quad (8)$$

where $\Delta x(\tau_{km+1}) = x(\tau_{km+1}^+) - x(\tau_{km+1}^-)$. A dynamical generalization of (8) is

$$\Delta x(\tau_{km+1}) = F \Delta x(\tau_{(k-1)m+1}) - K(x(\tau_{km+1}^-) - x(\tau_{(k-1)m+1}^+)), \quad (9)$$

where $F \in R^{n \times n}$ is some constant matrix.

3.3 Convergence analysis

Now we analyze the convergence property of the proposed time-delayed impulsive feedback algorithm (5). The analysis for its extensions (6) and (9) can be carried out in a similar way with more complicated reasoning.

For the convenience of further discussion, we assume the period- m orbit to be detected by $\bar{x}(t)$. We define a Poincaré return mapping $\phi : G(q, q') \rightarrow G(q, q')$ such that

$$x(\tau_{(k+1)m+1}^-) = \phi(x(\tau_{km+1}^+)). \quad (10)$$

Then the target period- m orbit, denoted by $\bar{x}(t)$, is mapped onto a fixed point, denoted by \bar{x}_0 , on $G(q, q')$. If the impulsively controlled system is stable in the periodic orbit $\bar{x}(t)$, the following limiting equalities

$$\lim_{k \rightarrow \infty} (x(\tau_{km+1}^-) - \bar{x}_0) = 0, \quad (11)$$

$$\lim_{k \rightarrow \infty} (x(\tau_{km+1}^+) - x(\tau_{km+1}^-)) = 0 \quad (12)$$

should hold in a neighborhood of \bar{x}_0 . Equality (11) implies the trajectory of the detecting model converges to the target orbit while equality (12) implies that the impulsive “control” vanishes when $k \rightarrow \infty$, which in turn guarantees that the period- m orbit reached is the very inherent UPO of the original system. Obviously, (11) and (12) hold if and only if the following equalities hold

$$\lim_{k \rightarrow \infty} (x(\tau_{km+1}^+) - \bar{x}_0) = 0, \quad (13)$$

$$\lim_{k \rightarrow \infty} (x(\tau_{km+1}^+) - x(\tau_{km+1}^-)) = 0. \quad (14)$$

Now we try to find conditions on the gain matrix K in the control strategy (5) ensuring the equalities (13) and (14) hold. To this end, we rewrite the time-delayed impulsive feedback (5) as

$$\begin{aligned} x(\tau_{km+1}^+) &= (I - K)x(\tau_{km+1}^-) + Kx(\tau_{(k-1)m+1}^+) \\ &= (I - K)\phi(x(\tau_{(k-1)m+1}^+)) + Kx(\tau_{(k-1)m+1}^+). \end{aligned} \quad (15)$$

Since only right limits appear in the last equation of (15), we can simply rewrite it as

$$x_k = (I - K)\phi(x_{k-1}) + Kx_{k-1}, \quad (16)$$

where $x_k = x(\tau_{km+1}^+)$ and $x_{k-1} = x(\tau_{(k-1)m+1}^+)$. Let $\Delta x_k = x_k - \bar{x}_0$, Linearizing the equation (16) at \bar{x}_0 yields

$$\Delta x_k = (I - K)A\Delta x_{k-1} + K\Delta x_{k-1} \quad (17)$$

where $A = \frac{\partial \phi(x)}{\partial x}|_{x=\bar{x}_0}$. The equation (17) can be considered as a dynamical system with the characteristic equation as

$$\det(zI - (A - KA + K)) = 0, \quad (18)$$

where $z \in C$ is a complex variable.

Now we are in a position to prove the following theorem.

Theorem 1: If there exists a gain matrix K such that all the eigenvalues of both K and $A - K(A - I)$ are in the unit circle of the complex plane, then (13) and (14) hold in a neighborhood of \bar{x}_0 .

Proof. If all the eigenvalues of $A - K(A - I)$ are in the unit circle of the complex plane, the dynamical system (17) is asymptotically stable. Therefore, the limiting equality (13) holds. From (5) we have

$$\begin{aligned} &(K - I)(x(\tau_{km+1}^-) - x(\tau_{(k-1)m+1}^-)) \\ &= -x(\tau_{km+1}^+) + Kx(\tau_{(k-1)m+1}^+) - (-x(\tau_{(k-1)m+1}^+) + Kx(\tau_{(k-2)m+1}^+)) \\ &= -(x(\tau_{km+1}^+) - x(\tau_{(k-1)m+1}^+)) + K(x(\tau_{(k-1)m+1}^+) - x(\tau_{(k-2)m+1}^+)). \end{aligned}$$

From equation (13) it follows that the right-hand side of the above equation goes to zero when $k \rightarrow \infty$. Therefore, we get

$$\lim_{k \rightarrow \infty} x(\tau_{km+1}^-) - x(\tau_{(k-1)m+1}^-) = 0 \quad (19)$$

because $K - I$ is nonsingular under the assumption of the theorem. Now denote $\delta x_k = x(\tau_{km+1}^+) - x(\tau_{km+1}^-)$. Then using equation (5) again, we have

$$\begin{aligned} \delta x_k &= (I - K)x(\tau_{km+1}^-) + Kx(\tau_{(k-1)m+1}^+) - x(\tau_{km+1}^-) \\ &= -K(x(\tau_{km+1}^-) - x(\tau_{(k-1)m+1}^-)) + K\delta x_{k-1}. \end{aligned}$$

Taking into account equation (19) and the assumption that all the eigenvalues of K are in the unit circle of the complex plane, we can conclude that $\lim_{k \rightarrow \infty} \delta x_k = 0$ which is exactly the equality (14). The theorem is thus proved.

Remark 1: The convergence is established locally in a neighborhood of \bar{x}_0 . However, by virtue of ergodicity of chaotic attractors, a system trajectory starting from any initial state will visit, early or late, the neighborhood of \bar{x}_0 in which the convergence of the algorithm holds.

Remark 2: If $A - I$ is nonsingular, then by Hautus lemma (see, [22], pp.93) it is easy to verify that $(A, (A - I))$ is a controllable pair. Therefore, there must exist a K to assign all the eigenvalues of matrix $A - K(A - I)$ in the unit circle of the complex plane. However, by Theorem 1, one should choose a K such that $\|K\| < 1$ to assign the spectrum of matrix $A - K(A - I)$, where $\|\cdot\|$ denotes the spectrum norm of matrices.

4 Switched Arrival System

As a prototype of hybrid systems, switched flow models are very suitable for describing scheduling of many manufacturing systems and computer systems where large amount of work is processed at a unit time [3, 16]. These models can be also applied to some process control systems where logic control policies are adopted. Switched flow systems are classified into two types, namely switched arrival systems and switched server systems [3]. The dynamical behavior of such hybrid systems can be very complex. It was shown in [3] and [9] that switched arrival systems can be chaotic while switched server systems are eventually periodic.

Consider a switched arrival system of N buffers and one server. Each buffer corresponds to a machine processing work. Work is removed from buffer i at a fixed rate of $\rho_i > 0$ while the server delivers material to a selected buffer at a unit rate. The system is assumed to be closed so that $\sum_{i=1}^N \rho_i = 1$. Figure 1 shows a switched arrival system for $N = 3$ with the server in buffer 1.

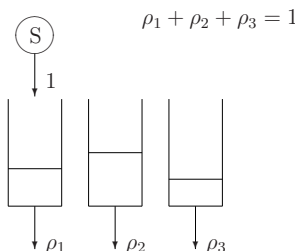


Fig. 1. Switched arrival system

Let $x_i(t)$ be the amount of work in buffer i at the time $t \geq 0$. We assume that the initial value of the total amount of work is 1, that is $\sum_{i=1}^N x_i(0) = 1$, which implies that $\sum_{i=1}^N x_i(t) = 1$ for any $t \geq 0$. The transition map $R(q, x(t)) = (q', x'(t))$ for this system denotes that the system is switched from (q, x) to (q', x') at the time t . Note that in the switched arrival system a switching action does not change the work distribution in buffers, i.e., $R(q, x) = (q', x)$.

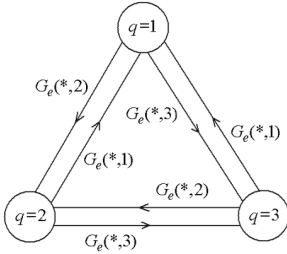


Fig. 2. Graph illustration of the switching process

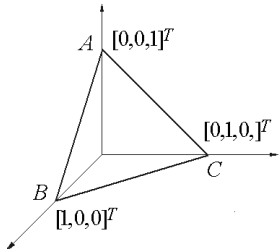


Fig. 3. Domain of system states

The location of the server is a control variable in the discussed system, and may be selected using a feedback policy. An *elementary control policy* considered in [3] is to define the guard as

$$G_e(i, j) = \{x \in X \subseteq R^N : x_j = 0\}, \quad (20)$$

which implies that the server switches buffers when some buffer becomes empty. Since $G_e(i, j)$ is independent of i , we will write it as $G_e(*, j)$. A graph illustration of the switching process of the system is shown in Fig. 2. Under the elementary control policy we have $x_i(t) \geq 0$ for all $i \in Q$ and all $t \geq 0$. So the system domain

$$X = \left\{ x : \sum_{i=1}^N x_i = 1, x_i \geq 0 \right\} \quad (21)$$

is a polytope in R^N . For $N = 3$ it is an equilateral triangle as shown in Fig. 3. And in this case, obviously, $G_e(*, j) \subset X, j = 1, 2, 3$ are three edges of the triangle.

Let $\{T_n\}$ be the sequence of the time when the server switches from one buffer to another. If the current system state is $(q_n, x(t))$, $t \in [T_n, T_{n+1})$, under the elementary control policy we have

$$T_{n+1} = T_n + \min_{i \neq q_n} x_i(T_n)/\rho_i. \quad (22)$$

The server keeps supplying work to buffer q_n for time interval $[T_n, T_{n+1})$, and each state $x_i(t)$ of buffer i in this time interval is described by the following equation:

$$x_i(t) = \begin{cases} x_i(T_n) - \rho_i(t - T_n), & i \neq q_n, \\ x_i(T_n) + (1 - \rho_i)(t - T_n), & i = q_n. \end{cases} \quad (23)$$

At the next transition time $t = T_{n+1}$ we have $R(q_n, x(T_{n+1})) = (q_{n+1}, x(T_{n+1}))$, where

$$q_{n+1} = \arg \min_{i \neq q_n} x_i(T_n)/\rho_i. \quad (24)$$

For simplicity we will focus on the system with $N = 3$, although our method is not restricted to such a special system. Without loss of generality, we assume that $\rho_1 < \rho_2 < \rho_3$.

It was shown in [3] that the switched arrival system is chaotic under the elementary control policy. A three-dimensional image of the chaotic behavior of the system is presented in Fig. 4.

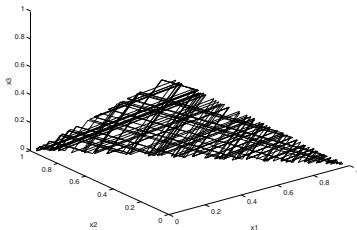


Fig. 4. Chaotic behavior of the switched arrival system

As it is well known, a chaotic attractor includes infinitely many unstable periodic orbits. In general, it is very difficult to analytically or even numerically give the exact position of unstable periodic orbits. For the switched arrival system, it was shown that period-one orbit can be determined by solving a system of algebraic equations [31]. But it may be difficult to apply the method to calculating the positions of other orbits longer than period-one because it is even not clear in what order they touch the edges. For example, depending

on values of ρ_1 , ρ_2 and ρ_3 , a period-two orbit may touch the edges in the order of $1 \rightarrow 2 \rightarrow 3 \rightarrow 1 \rightarrow 3 \rightarrow 1$ (shown in Fig. 5), or $1 \rightarrow 3 \rightarrow 2 \rightarrow 3 \rightarrow 2 \rightarrow 1$ (shown in Fig. 6), etc. Now we will use the time-delayed impulsive feedback method proposed in Section 3.1 to automatically detect unstable periodic orbits of the switched arrival system.

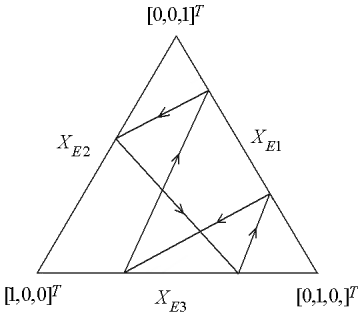


Fig. 5. Period-two orbit in the order of $1 \rightarrow 2 \rightarrow 3 \rightarrow 1 \rightarrow 3 \rightarrow 1$

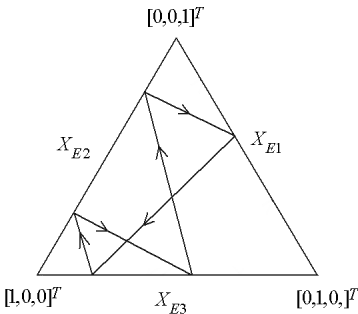


Fig. 6. Period-two orbit in the order of $1 \rightarrow 3 \rightarrow 2 \rightarrow 3 \rightarrow 2 \rightarrow 1$

Motivated by the impulsive feedback control approach we assume that the state of the switched arrival system can be instantly changed at the moment when the system trajectory touches an edge of X . There is no implementation problem of this kind of control since we are considering the problem of detecting UPOs, and all calculations are conducted on an off-line detecting model of the system.

Without loss of generality, we shall consider only unstable periodic orbits defined on the edge

$$X_{E3} = \{x \in X : x_3 = 0\}.$$

We denote the touch points of the trajectory with X_{E3} simply as $x(\tau_1)$, $x(\tau_2)$, \dots . Suppose that an inherent period- m orbit is to be detected. The instants

of impulsive action are then chosen as $t = \tau_{km+1}$, $k = 1, 2, \dots$. The impulsive feedback law is designed as

$$x(\tau_{km+1}^+) = (I - K)x(\tau_{km+1}^-) + Kx(\tau_{(k-1)m+1}^+),$$

where K is a square gain matrix satisfying the condition given by Theorem 1. Under this impulsive feedback, the trajectory of the system is re-initialized once per period at the time $t = \tau_{km+1}$, $k = 1, 2, \dots$.

Some simulations have been conducted to verify the proposed method. In simulations we set $\rho_1 = 0.1$, $\rho_2 = 0.3$, $\rho_3 = 0.6$. The impulsive feedback gain was selected as $K = \text{diag}[0.9, 0.9, 0.9]$. Figures 7 and 8 show that both the continuous trajectory and the sequence of selected buffers (discrete states) become periodic after several iterations. Figure 9 shows the impulsive action on the simulated model tends to zero, which guarantees that the reached periodic orbit is indeed the inherent unstable periodic orbit of the original system. Figure 10 presents the three-dimensional image of the obtained period-one orbit while Fig. 11 presents period-2 to period-5 orbits of the system obtained by applying the impulsive time-delayed feedback method.

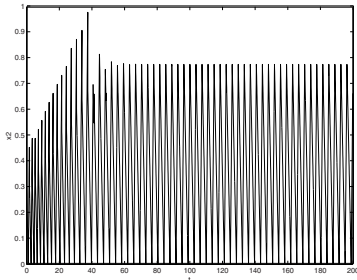


Fig. 7. State x_2 versus time

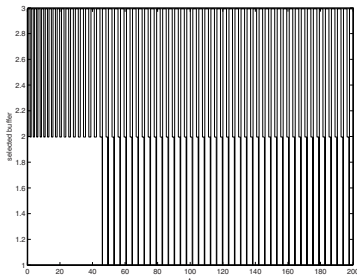


Fig. 8. Selected buffers versus time

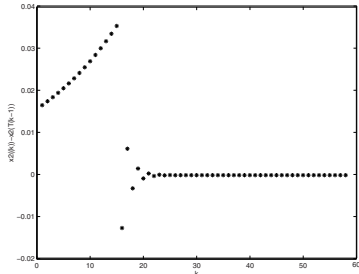


Fig. 9. Impulsive actions versus iteration

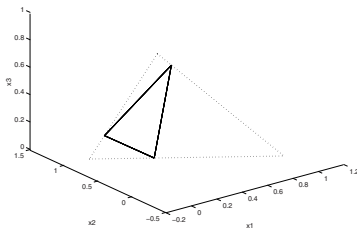


Fig. 10. Period-one orbit

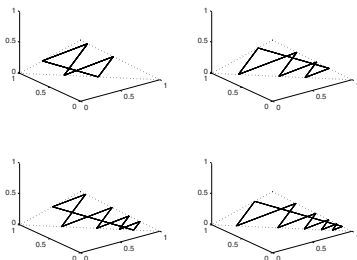


Fig. 11. Period-2 to period-5 orbits

5 Chua's Circuit

Chua's circuit is a very simple electronic system, which consists of only one inductor (L), two capacitors (C_1, C_2), one linear resister (G) and one piecewise-linear resister (g). However, as has been well known, it possesses very rich and typical nonlinear dynamics such as bifurcation and chaos [5].

The dynamic equation of Chua's circuit is given by

$$\begin{aligned} C_1 \dot{v}_{C_1} &= G(v_{C_2} - v_{C_1}) - g(v_{C_1}) \\ C_2 \dot{v}_{C_2} &= G(v_{C_1} - v_{C_2}) + i_L \\ L \dot{i}_L &= -v_{C_2} \end{aligned} \tag{25}$$

where i_L is the current through the inductor L , v_{C_1} and v_{C_2} the voltages across C_1 and C_2 , respectively, and

$$g(v_{C_1}) = m_0 v_{C_1} + \frac{1}{2}(m_1 - m_0)(|v_{C_1} + 1| - |v_{C_1} - 1|) \quad (26)$$

with $m_0 < 0$ and $m_1 < 0$ being some appropriately chosen constants.

For convenience we first reformulate the circuit equation (25) to be the following dynamically equivalent state equation

$$\begin{aligned} \dot{x}_1 &= p(-x_1 + x_2 - f(x_1)) \\ \dot{x}_2 &= x_1 - x_2 + x_3 \\ \dot{x}_3 &= -rx_2 \end{aligned} \quad (27)$$

where $p = C_2/C_1 > 0$ and $r = C_2/LG^2 > 0$ are the main bifurcation parameters of the circuit and the nonlinear term represented by a 3-segment piecewise-linear function

$$\begin{aligned} f(x_1) &= m'_0 x_1 + \frac{1}{2}(m'_1 - m'_0)(|x_1 + 1| - |x_1 - 1|) \\ &= \begin{cases} m'_0 x_1 + m'_1 - m'_0 & x_1 \geq 1 \\ m'_1 x_1 & |x_1| < 1 \\ m'_0 x_1 - m'_1 + m'_0 & x_1 \leq -1 \end{cases} \end{aligned}$$

where $m'_0 = m_0/G < 0$ and $m'_1 = m_1/G < 0$. We choose $p = 9$, $r = 14\frac{2}{7}$, $m'_0 = -57$ and $m'_1 = -87$ as in [5] and many other references on Chua's circuits, we observe a double scroll, which is shown in Fig. 12.

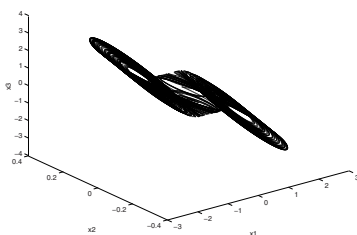


Fig. 12. Chaotic behavior of Chua's circuit

It is easy to model the Chua's circuit as a hybrid system as follows

$$\dot{x} = A(q)x + a(q)$$

where $q \in \{1, 2, 3\}$ is the discrete state which depends on the location of the continuous state of the system. Matrices of the three linear subsystems are

$$\begin{aligned} A(1) &= \begin{bmatrix} -p + m'_0 & p & 0 \\ 1 & -1 & 1 \\ 0 & -q & 0 \end{bmatrix}, \quad a(1) = \begin{bmatrix} -m'_1 + m'_0 \\ 0 \\ 0 \end{bmatrix}; \\ A(2) &= \begin{bmatrix} -p + m'_1 & p & 0 \\ 1 & -1 & 1 \\ 0 & -q & 0 \end{bmatrix}, \quad a(2) = \begin{bmatrix} 0 \\ 0 \\ 0 \end{bmatrix}; \\ A(3) &= \begin{bmatrix} -p + m'_0 & p & 0 \\ 1 & -1 & 1 \\ 0 & -q & 0 \end{bmatrix}, \quad a(3) = \begin{bmatrix} m'_1 - m'_0 \\ 0 \\ 0 \end{bmatrix}. \end{aligned}$$

The continuous state space is partitioned into three parts, i.e., $X = \bigcup_{i=1,2,3} X_i$, where

$$\begin{aligned} X_1 &= \{x \in R^3 : x_1 \leq -1\}, \\ X_2 &= \{x \in R^3 : |x_1| < 1\}, \\ X_3 &= \{x \in R^3 : x_1 \geq 1\}. \end{aligned}$$

If $x \in X_i$, then $q = i$. Therefore the guards of the system can be written as follows

$$\begin{aligned} G(1, 2) &= G(2, 1) = \{x \in R^3 : x_1 = -1\}, \\ G(2, 3) &= G(3, 2) = \{x \in R^3 : x_1 = 1\}. \end{aligned}$$

A graph illustration of the transition process of the system is given in Fig. 13.

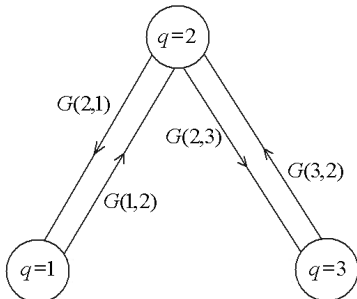


Fig. 13. Graph illustration of transition process

We now consider the stabilization of unstable periodic orbits defined on the guard $G(2, 3)$. We denote the states at which the trajectory visits $G(2, 3)$ as $x(\tau_1), x(\tau_2), \dots$. Suppose that an inherent period- m orbit is to be stabilized. The instants of impulsive actions are then chosen as $t = \tau_{km+1}$,

$k = 1, 2, \dots$. The impulsive feedback law is designed as

$$x(\tau_{km+1}^+) = (I - K)x(\tau_{km+1}^-) + Kx(\tau_{(k-1)m+1}^+),$$

where K is a square gain matrix satisfying the condition given by Theorem 1.

Some simulations have been conducted to verify the proposed method. In simulations we choose the impulsive feedback gain as $K = \text{diag}[0.7, 0.7, 0.7]$ for stabilization of period-1 orbit. Figures 14 and 15 show that both the continuous trajectory and the symbolic sequence become periodic after a few seconds. Figure 16 shows the impulsive action on the simulated model tends to zero, which guarantees that the reached periodic orbit is indeed the inherent unstable periodic orbit of the original system. Figure 17 presents the three-dimensional image of the obtained period-one to period-three orbits of the system obtained by applying the time-delayed impulsive feedback control method.

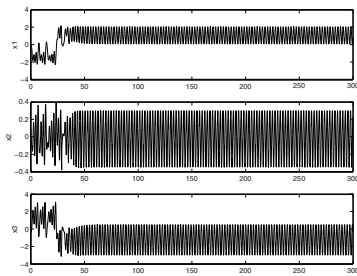


Fig. 14. State x_2 versus time

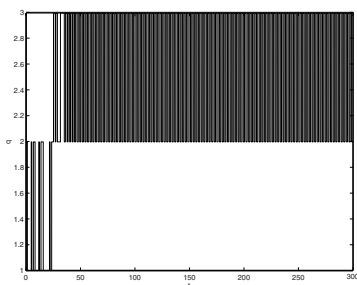


Fig. 15. Time history of discrete states

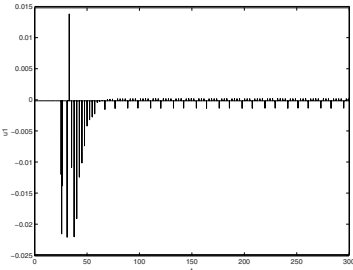


Fig. 16. Impulsive actions versus time

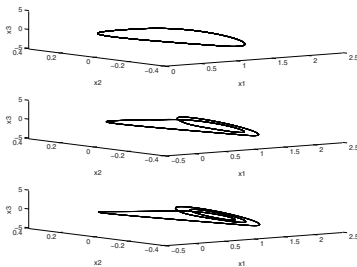


Fig. 17. Period-one to period-three orbits

6 Conclusions

Time-delayed feedback control, as a memory-based control method, has been considered as a promising control mechanism to achieve control tasks in the absence of full state information and without the use of asymptotic observers [1]. Meanwhile, due to the discontinuity feature, the impulsive control method is very suitable for digital communication systems [23]. In this chapter we show that these two promising control methods can be combined together to form a new chaos control method – a time delayed impulsive feedback control method. The method is very applicable, but not restricted, to stabilizing UPOs in chaotic hybrid systems. Compared to the conventional continuous time-delayed feedback control methods for the UPO stabilization problem, this method has the following advantages: (1) it does not need the period constant of the target UPO; (2) it allows rigorous stability analysis of the control system; (3) simulation results show that it can be used for stabilizing longer period UPOs of chaotic systems.

Acknowledgement.

This work was supported by National Natural Science Foundation of China and the Hwa Ying Culture and Education Foundation.

References

1. Atay, F. M. (2002) Delayed-feedback control of oscillation in non-linear planar systems. *Int. J. Control.*, **75**:297–304
2. Bainov, D. D., Simeonov, P. S. (1993) Impulsive Differential Equations: Periodic Solutions and Applications. London: Longman
3. Chase, C., Serrano, J., Ramadge, P. J. (1993) Periodicity and chaos from switched flow systems: contrasting examples of discretely controlled continuous systems. *IEEE Trans. Auto. Contr.*, **38**:70–83
4. Chen, G., Dong, X. (1998) From Chaos to Order: Perspectives, Methodologies, and Applications. Singapore: World Scientific
5. Chua, L. O., Komuro, M., Matsumoto, T. (1986) The double scroll family: I and II. *IEEE Trans. Circ. Syst.*, **33**:1072–1118
6. Chua, L. O., Lin, T. (1988) Chaos in digital filters. *IEEE Trans. Circ. Syst.*, **35**:648–652
7. Ditto, W. L., Spano, M. L., Lindner, J. F. (1995) Techniques for the control of chaos. *Physica D*, **86**:198–211
8. Grebogi, C., Lai, Y.-C. (1997) Controlling chaos in high dimensions. *IEEE Trans. Circ. Syst.-I*, **44**:971–975
9. Horn, C., Ramadge, P. J. (1993) Dynamics of switched arrival systems with thresholds. Proc. of the 32nd Conference on Decision and Control, 288–293
10. Just, W., Reckwerth, D., Mockel, J., Reibold, E., Benner, H. (1998) Delayed feedback control of periodic orbits in autonomous systems. *Phys. Rev. Lett.*, **81**:562–565
11. Konishi, K., Kokame, H. (1998) Observer-based delayed-feedback control for discrete-time chaotic systems. *Phys. Lett. A*, **248**:359–368
12. Lakshmikantham, V., Bainov, D. D., Simeonov, P. S. (1989) Theory of Impulsive Differential Equations. Singapore: World Scientific
13. Nakajima, H. (1997) On analytical properties of delayed feedback control of chaos. *Phys. Lett. A*, **232**:207–210
14. Nakajima, H., Ueda, Y. (1998) Limitation of generalized delayed feedback control. *Physica D*, **111**:143–150
15. Ott, E., Grebogi, C., Yorke, J. A. (1990) Controlling chaos. *Phys. Rev. Lett.*, **64**:1196–1199
16. Perkins, I. R., Kumar, P. R. (1989) Stable, distributed, real-time scheduling of flexible manufacturing/assembly/disassembly systems. *IEEE Trans. Auto. Contr.*, **34**:139–148
17. Pyragas, K. (1992) Continuous control of chaos by self-controlling feedback. *Phys. Lett. A*, **170**:421–428
18. Pyragas, K. (1995) Control of chaos via extended delay feedback, *Phys. Lett. A*, **206**:323–330
19. Pyragas, K. (2001) Control of chaos via an unstable delayed feedback controller. *Phys. Rev. Lett.*, **86**:2265–2268
20. Schweizer, J., Schimming, T. (2001) Symbolic dynamics for processing chaotic signals-I: noise reduction of chaotic sequence. *IEEE Trans. Circ. Syst.-I*, **48**:1269–1282
21. Schweizer, J., Schimming, T. (2001) Symbolic dynamics for processing chaotic signals-II: communication and coding. *IEEE Trans. Circ. Syst.-I*, **48**:1283–1295

22. Sontag, E. D. (1990) Mathematical Control Theory: Deterministic Finite Dimensional Systems. New York: Springer-Verlag
23. Suykens, J. A. K., Yang, T., Vandewalle, J., Chua, L. O. (2000) Impulsive control and synchronization of chaos. In Controlling Chaos and Bifurcations in Engineering Systems, ed. by Chen, G. Boca Raton: CRC Press, 275–297
24. Tian, Y.-P. (1999) Controlling chaos using invariant manifolds. *Int. J. Control.*, **72**:258–266
25. Tian, Y.-P., Yu, X. (2000) Adaptive control of chaotic dynamic systems using invariant manifold approach. *IEEE Trans. Circ. Syst.-I*, **47**:1537–1542
26. Tian, Y.-P., Yu, X. (2000) Stabilizing unstable periodic orbits of chaotic systems via an optimal principle. *J. Franklin Institute*, **337**:771–779
27. Tian, Y.-P., Chen, G. (2001) A separation principle for dynamical delayed output feedback control of chaos. *Phys. Lett. A*, **284**:31–42
28. Tian, Y.-P. (2002) An optimization approach to locating and stabilizing unstable periodic orbits in chaos. *Int. J. Bifur. Chaos*, **12**:1163–1172
29. Ushio, T., Hsu, C. S. (1987) Chaotic rounding error in digital control systems. *IEEE Trans. Circ. Syst.-I*, **34**:1333–1339
30. Ushio, T. (1996) Limitation of delayed feedback control in nonlinear discrete-time systems. *IEEE Trans. Circ. Syst.-I*, **43**:815–816
31. Ushio, T., Ueda, H., Hirai, K. (1995) Controlling chaos in a switched arrival system. *Sys. Contr. Lett.*, **26**:335–339
32. Yang, T. (2001) Impulsive Control Theory. Lecture Notes in Control and Information Sciences, **272**. Berlin: Springer-Verlag
33. Yu, X. (1995) Discretization chaos in the switching control systems with finite switching values. *Int. J. Bifur. Chaos*, **5**:1749–1755

Odd Number Limitation in Delayed Feedback Control

Shigeru Yamamoto and Toshimitsu Ushio

Graduate School of Engineering Science
Osaka University
Machikaneyama, Toyonaka, Osaka 560-8531, Japan
yamamoto@sys.es.osaka-u.ac.jp

Abstract. This chapter reviews the so-called odd number limitation in delayed feedback control (DFC) for chaotic systems. By the odd number limitation, the original DFC restricts the application to a special class of chaotic systems. So far, various methods have been developed to overcome the limitation. In this chapter, we show their key concepts to solve the problem.

1 Introduction

Delayed feedback control (DFC) is one of useful control methods for stabilizing unstable periodic orbits (UPOs) embedded in chaotic systems via a small control input. DFC does not make use of directly the unstable periodic orbit in feedback, but the difference between the current state and the delayed one. Hence, it is also called time-delayed feedback control or time-delayed auto-synchronization.

As an alternative control of chaos, the OGY method [2] is well-known. It is essentially state feedback based on the invariant manifold structure of UPOs. Although it is theoretically well understood, it requires the target UPO in advance. On the other hand, DFC possesses the ability to stabilize an uncertain UPO. In addition, it does not create a new periodic orbit, nor move the original UPO of the chaotic system to another one. DFC can affect the stability of the target UPO without changing the orbit. This comes from the fact that the delay element in DFC produces transmission zeros such that the control action vanishes at the fundamental frequency of the periodic orbit and at all multiple frequencies. As a result, all the harmonics remains unaltered. Hence, since Pyragas proposed the idea of DFC in 1992 [1], it has been applied to various systems (see Table 1).

DFC is not a panacea, because it cannot stabilize a class of periodic orbits due to the delay in the feedback loop. The class can be characterized by characteristic multipliers of the target UPO. More precisely speaking, DFC can not stabilize any unstable periodic orbit with an odd number real characteristic multipliers greater than unity. This restriction is called the odd number limitation [3, 4]. Since the limitation of the original DFC was revealed, several approach have been proposed to overcome the limitation. In this chapter, we review some of them.

Table 1. Practical applications of delayed feedback control

| |
|--|
| Diode Resonator Circuits [5] |
| Magneto-Elastic Ribbon [31] |
| Lasers [22, 32] |
| Coupled Map Lattice [33] |
| Traffic Flow Model [34] |
| Gravity-Gradient Satellite [35] |
| Atrioventricular Conduction Model [36] |
| Fitzhugh-Nagumo Model [37] |

2 Delayed Feedback Control

2.1 Stabilization of periodic orbits

We consider a parameter-dependent continuous-time chaotic dynamical system:

$$\dot{\mathbf{x}}(t) = f(\mathbf{x}(t), \mathbf{u}(t)) \quad (1)$$

where $\mathbf{x} \in \Re^n$ is the state vector; $f : \Re^n \times \Re^m \rightarrow \Re^n$ is a differentiable vector valued function; and $\mathbf{u} \in \Re^m$ is the control input. We assume that (1) evolves a chaotic trajectory, and it has an UPO $\mathbf{x}_T(t)$ with period T , when $\mathbf{u} \equiv 0$. That is, $\mathbf{x}_T(t) = \mathbf{x}_T(t - T)$ and $\dot{\mathbf{x}}_T(t) = f(\mathbf{x}_T(t), 0)$ for every t .

The control objective is to stabilize the UPO $\mathbf{x}_T(t)$ by feedback control with a small control input \mathbf{u} . In other words, our aim is to design a feedback controller producing a small control input $\mathbf{u}(t)$ making a chaotic trajectory $\mathbf{x}(t)$ of (1) converge to $\mathbf{x}_T(t)$.

When we *globally* use a state feedback control method, it is generally difficult to obtain a small control input. However, if the state trajectory $\mathbf{x}(t)$ of (1) is chaotic, then there exists a time instant when $\mathbf{x}(t)$ passes through the vicinity of $\mathbf{x}_T(t)$ because chaotic orbits are ergodic on the attractor. If we apply a control input to the system just at the moment, we can prevent it from increasing of the control input.

Ott et al. proposed the well-known OGY method [2]. The original OGY method makes use of discrete-time proportional state feedback. In continuous-time fashion, it is given by $\mathbf{u}(t) = K(\mathbf{x}(t) - \mathbf{x}_T(t))$. The feedback gain K is chosen based on the structure formed by both stable and unstable manifolds. In addition, it requires the target UPO $\mathbf{x}_T(t)$ to be known in advance. These preliminary computations are more complicated when we deal with higher-order chaotic systems. Hence, it is preferable that stabilization of $\mathbf{x}_T(t)$ can be achieved without using its precise value.

2.2 Continuous-time delayed feedback control

Delayed Feedback Control utilizes the state $\mathbf{x}(t - T)$ instead of $\mathbf{x}_T(t)$ as

$$\mathbf{u}(t) = K(\mathbf{x}(t) - \mathbf{x}(t - T)). \quad (2)$$

When the vector of measured signals $\mathbf{y} \in \Re^p$, which is given by

$$\mathbf{y}(t) = g(\mathbf{x}(t)), \quad (3)$$

is not the state vector, DFC is

$$\mathbf{u}(t) = K(\mathbf{y}(t) - \mathbf{y}(t - T)). \quad (4)$$

DFC has a feedback gain $K(1 - e^{-sT})$ that obviously includes the time-delay element e^{-sT} . Due to (2) or (4), if $\mathbf{x}(t) = \mathbf{x}_T(t)$, then $\mathbf{u}(t) = 0$. Moreover, in the frequency domain representation $U(j\omega) = K(1 - e^{-j\omega T})Y(j\omega)$, $U(j\omega) = 0$ whenever $\omega = 2\pi i/T (i = 0, 1, 2, \dots)$. It shows that the target periodic orbit is not affected by DFC. This enables us to stabilize the original periodic orbit $\mathbf{x}_T(t)$ of the chaotic system if the feedback gain can be appropriately chosen.

An expansion of Pyragas's DFC, which is called extended delayed feedback control (EDFC), was proposed in [5]. The control input is given by

$$\mathbf{u}(t) = K \left(\mathbf{y}(t) - (1 - r) \sum_{k=1}^{\infty} r^{k-1} \mathbf{y}(t - kT) \right), \quad (5)$$

where $r \in [0, 1]$. When $r = 0$, it is equivalent to the original DFC. Since $\mathbf{y}(t) = \mathbf{y}(t - kT)$ for any integer $k \geq 1$ when $\mathbf{y}(t)$ is T -periodic, we have $\mathbf{u}(t) = 0$.

2.3 Discrete-time delayed feedback control

Stabilization of periodic orbits in continuous-time systems can be formulated as a fixed point stabilization problem in discrete-time ones in terms of the Poincaré map. Any fixed point of the discrete-time systems is corresponding to a periodic orbit in the continuous-time systems. Hence, convergence of a sequence to a fixed point in the discrete-time systems implies stability of a periodic orbit of the continuous-time systems. Hence, hereafter we focus on the discrete-time systems. For simplicity, we use the same symbols for continuous and discrete-time systems.

$$\begin{aligned} \mathbf{x}(k+1) &= f(\mathbf{x}(k), \mathbf{u}(k)) \\ \mathbf{y}(k) &= g(\mathbf{x}(k)), \end{aligned} \quad (6)$$

where k is the discrete-time; $\mathbf{x} \in \Re^n$ is the state; $\mathbf{u} \in \Re^m$ is the input; $\mathbf{y} \in \Re^p$ is the measured output. Let \mathbf{x}_f be a fixed point of (6) when $\mathbf{u} \equiv 0$. It must satisfy $\mathbf{x}_f = f(\mathbf{x}_f, 0)$. We assume that f and g are differentiable. The purpose of control is to stabilize an unstable fixed point \mathbf{x}_f .

Then delayed feedback control is given by

$$\mathbf{u}(k) = K(\mathbf{x}(k) - \mathbf{x}(k-1)) \quad (7)$$

or

$$\mathbf{u}(k) = K(\mathbf{y}(k) - \mathbf{y}(k-1)) \quad (8)$$

where K is a gain matrix to be designed.

Extended delayed feedback control (EDFC) proposed by Socolar et al. [5] is given by

$$\mathbf{u}(k) = K \left(\mathbf{y}(k) - (1-r) \sum_{i=1}^{\infty} r^{i-1} \mathbf{y}(k-i) \right), \quad (9)$$

where $r \in [0, 1]$.

These control inputs are applied to the chaotic systems only when $\|\mathbf{y}(k) - \mathbf{y}(k-1)\|$ is sufficiently small to prevent it from affecting chaotic systems before stabilization. Stability of the closed-loop system can be checked in the vicinity of the fixed point. In addition, feedback gains K are designed simply for the linearized system around the fixed point.

3 The Odd Number Limitation

Delayed feedback control has a substantial limitation called the odd number limitation: *If a hyperbolic unstable fixed point suffers from the odd number limitation, then DFC cannot stabilize the unstable fixed point.* It was not for the continuous chaotic systems that the limitation was first pointed out, but the discrete-time systems [3]. A little later, the limitation for the continuous chaotic systems was derived [4]. There also exist similar limitations for extended delayed feedback control and generalized extended delayed feedback control [6, 7].

Table 2. Original and extended delayed feedback control

Original DFC

| | |
|-----------------|--|
| continuous-time | $\mathbf{u}(t) = K(\mathbf{x}(t) - \mathbf{x}(t-T))$ |
| discrete-time | $\mathbf{u}(k) = K(\mathbf{x}(k) - \mathbf{x}(k-1))$ |

Extended DFC

| | |
|-----------------|---|
| continuous-time | $\mathbf{u}(t) = K \left(\mathbf{y}(t) - (1-r) \sum_{k=1}^{\infty} r^{k-1} \mathbf{y}(t-kT) \right)$ |
| discrete-time | $\mathbf{u}(k) = K \left(\mathbf{y}(k) - (1-r) \sum_{i=1}^{\infty} r^{i-1} \mathbf{y}(k-i) \right)$ |

3.1 The odd number limitation via discrete-time DFC

The linearized system around the fixed point of the closed-loop system with DFC (8) can be described by

$$\begin{bmatrix} x(k+1) \\ x(k) \end{bmatrix} = \begin{bmatrix} A + BK - BKC & -BKC \\ I_n & 0 \end{bmatrix} \begin{bmatrix} x(k) \\ x(k-1) \end{bmatrix}, \quad (10)$$

where $x(k) = \mathbf{x}(k) - \mathbf{x}_f$, and

$$A = \frac{\partial}{\partial \mathbf{x}} f(\mathbf{x}_f, 0) \in \Re^{n \times n}, \quad B = \frac{\partial}{\partial u} f(\mathbf{x}_f, 0) \in \Re^{n \times m},$$

$$C = \frac{\partial}{\partial \mathbf{x}} g(\mathbf{x}_f) \in \Re^{p \times n}.$$

Defining

$$\mathcal{A} = \begin{bmatrix} A & 0 \\ I_n & 0 \end{bmatrix}, \quad \mathcal{B} = \begin{bmatrix} B \\ 0 \end{bmatrix}, \quad \mathcal{C} = [C \ -C], \quad \xi(k) = \begin{bmatrix} x(k) \\ x(k-1) \end{bmatrix},$$

we have

$$\xi(k+1) = (\mathcal{A} + \mathcal{B}K\mathcal{C})\xi(k). \quad (11)$$

Obviously, this is a stabilization problem via a constant output feedback. It is noted that even if the full state are available ($C = I_n$), it would not be a state feedback stabilization problem.

To investigate stability of the closed-loop system (10) and (11), we define $F(z) := \det(zI - \mathcal{A} - \mathcal{B}K\mathcal{C})$. When the closed-loop system (11) is asymptotically stable, the roots of $F(z) = 0$ lie within the unit circle $|z| < 1$. Hence, it is necessary for stability that $F(1) \neq 0$. Since $F(z)$ is continuous with respect to real $z > 0$ and $\lim_{z \rightarrow \infty} F(z) = +\infty$, $F(1) > 0$ is necessary. In fact, it follows from \mathcal{A} , \mathcal{B} and \mathcal{C} that

$$F(1) = \det(I_n - A).$$

Therefore, if the closed-loop system (11) is asymptotically stable, then

$$\det(I_n - A) > 0. \quad (12)$$

The above condition is independent of K . Hence, it also gives us a necessary condition for stabilizability. Moreover, it is noted that $\det(I_n - A) = \prod_{i=1}^n (1 - \lambda_i)$ where $\lambda_1, \dots, \lambda_n$ are eigenvalues of A . Hence, $\det(I_n - A) > 0$ implies that the number of real eigenvalue satisfying $1 - \lambda_i < 0$ is even or zero. Conversely, if there exist odd numbers of real eigenvalues satisfying $1 < \lambda_i$, then the necessary condition never be satisfied. Consequently, delayed feedback control (4) can never stabilize such any unstable fixed points. This is the so-called odd number limitation [3].

Theorem 1. *If there exists a delayed feedback controller (4) locally asymptotically stabilizing an unstable fixed point of (6), then the condition (12) holds.*

The odd number limitation is inherent in stabilization of unstable periodic orbits of a discrete-time chaotic system via delayed feedback control [8].

3.2 The odd number limitation in continuous-time DFC

For a continuous-time chaotic system, the odd number limitation is also infinite [4, 9].

A nonlinear system with delayed feedback control linearized around a periodic orbit with period T can be described as

$$\dot{x}(t) = A(t)x(t) + B(t)K(x(t) - x(t - T)). \quad (13)$$

This system is T -periodic. Then, we can conclude the following theorem from Floquet theory.

Theorem 2. *Suppose that (1) is T -periodic. If the number of real characteristic multipliers of a hyperbolic unstable periodic orbit greater than unity is odd, then DFC cannot stabilize the unstable periodic orbit.*

A similar result holds for autonomous systems [4]. An autonomous system with delayed feedback control linearized around a unstable equilibrium point can be described as

$$\dot{x}(t) = Ax(t) + BK(x(t) - x(t - T)). \quad (14)$$

Let the characteristic polynomial be $F(s) = \det(sI - A - (1 - e^{-sT})BK)$. For real $s > 0$, we have $\lim_{s \rightarrow \infty} F(s) = +\infty$. From continuity, $F(0) \leq 0$ implies that there exists at least one unstable eigenvalue. Hence, it is necessary for stability that $F(0) > 0$. This condition is independent of both K and T . On the other hand, due to $F(0) = \det(-A)$, asymptotic stability of the closed-loop system (14) requires

$$\det(-A) > 0. \quad (15)$$

Stability when EDFC (5) is used was investigated in [10–12]. Even in a generalized DFC of EDFC (5), it has been reported that the odd number limitation exists [6].

3.3 Overcoming the odd number limitation

Several improvements to DFC, for example, modified DFC [13–15], and dynamic DFC [16] have been attempted to overcome the odd number limitation. For discrete-time systems, dynamic DFC is effective. It contains observer-based DFC [17], DFC based on a Newton method [18], recursive DFC [19], and generalized DFC [20]. As shown below, they have different stabilizability conditions and the order of controllers. DFC using periodic gains is also effective [22–24]. However, a directly applying periodic DFC to continuous-time systems will lead to the odd number limitation, because it belongs to a class of generalized DFC [6].

For continuous-time systems, half-periodic DFC [25] and DFC based on a variable structure [26] have been proposed. Particularly, if the condition (15) holds for an unstable equilibrium point, then it is possible to stabilize it via DFC(2). This sufficient condition for stabilization is valid for all single-input controllable systems and almost all multi-input controllable systems, [27, 28].

4 Modified DFC

Modified DFC can be obtained by modifying the delayed term $\mathbf{x}(t - T)$ in continuous-time DFC(2) and $\mathbf{x}(k - 1)$ in discrete-time DFC(7). The modified DFC methods shown below are summarized in Table 3.

4.1 Half-periodic DFC

The Duffing equation is a two-dimensional nonautonomous differential equation with periodic external forcing. It is an oscillatory system with a sinusoidal periodic forcing of the period T . In what follows, we deal with 2π -periodic solutions.

The Duffing equation has a symmetric property. That is, when $\mathbf{x}(t)$ is its solution, so is $-\mathbf{x}(t - \pi)$. We call a solution satisfying $\mathbf{x}(t) = -\mathbf{x}(t - T/2)$ at every t a self-symmetric solution. The Lorenz equation that is a three-dimensional autonomous system has a more general symmetric property. It has a solution satisfying $\mathbf{x}(t) = -S\mathbf{x}(t - T/2)$ at every t for $S = \text{diag}\{-1, -1, 1\}$. This symmetry, $\mathbf{x}(t) = S\mathbf{x}(t - T/2)$, can be extended to n -dimensional systems $\dot{\mathbf{x}}(t) = f(\mathbf{x}(t), t)$ with a solution satisfying

$$f(S\mathbf{x}(t), t + T/2) = Sf(\mathbf{x}(t), t) \quad (16)$$

$$S^2 = I_n, \quad S \in \Re^{n \times n}. \quad (17)$$

To stabilize self-symmetric periodic orbits, half-periodic DFC has been proposed [25].

$$\mathbf{u}(t) = K(\mathbf{x}(t) - S\mathbf{x}(t - T/2)) \quad (18)$$

Although it has not been proved that an unstable periodic orbit with the odd number limitation can always be stabilized, its feasibility is confirmed by numerical experiments [25].

Table 3. Modified DFC (NC: necessary condition for stabilization, SC: sufficient condition for stabilization)

| | |
|----------------------|--|
| Half-Period DFC | $\mathbf{u}(t) = K(\mathbf{x}(t) - S\mathbf{x}(t - T/2))$ |
| | NC : a symmetric property |
| | SC : not available |
| Nonlinear estimation | $\mathbf{u}(k) = K\left(\mathbf{x}(k) - (I - A)^{-1}\hat{f}(\mathbf{x}(k - 1))\right)$ |
| | NC : $\det(I_n - A) \neq 0$ |
| State prediction | $\mathbf{u}(k) = K\left(\mathbf{x}(k) - f(\mathbf{x}(k), 0)\right)$ |
| | NC : $\det(I_n - A) \neq 0$ |
| | SC : $\det(I_n - A) \neq 0$ and (A, B) is stabilizable |

4.2 Nonlinear estimation

In [13], DFC is modified as

$$\mathbf{u}(k) = K \left(\mathbf{x}(k) - h(\mathbf{x}(k-1)) \right), \quad (19)$$

where h is given by $h(\mathbf{x}) = (I_n - A)^{-1} \hat{f}(\mathbf{x})$ under the assumption that $\det(I_n - A) \neq 0$, and $\hat{f}(\mathbf{x})$ represents the higher-order terms in the Taylor series expansion of $f(\mathbf{x}, 0) = A\mathbf{x} + \hat{f}(\mathbf{x})$. Since a fixed point \mathbf{x}_f satisfies $\mathbf{x}_f = A\mathbf{x}_f + \hat{f}(\mathbf{x}_f)$, (19) vanishes for \mathbf{x}_f . By using (19), \mathcal{C} in (11) is replaced with

$$\mathcal{C} = [I_n \ -G], \quad (20)$$

where $G = \frac{\partial}{\partial \mathbf{x}} h(\mathbf{x}_f) \in \Re^{n \times n}$. Consequently, we can overcome the odd number limitation.

4.3 State prediction

Another type of modification

$$\mathbf{u}(k) = K \left(\mathbf{x}(k) - f(\mathbf{x}(k), 0) \right) \quad (21)$$

is proposed in [14]. This utilizes a one-time ahead prediction $f(\mathbf{x}(k), 0)$ of the uncontrolled chaotic system. Hence, strictly speaking, this is not DFC. However, for the fixed point \mathbf{x}_f satisfying $\mathbf{x}_f = f(\mathbf{x}_f, 0)$, (21) vanishes. By using (21), the closed-loop system can be linearized as

$$x(k+1) = (A + BK(I - A))x(k) \quad (22)$$

in the vicinity of the fixed point. Hence, we can conclude that it can overcome the odd number limitation.

Theorem 3. *Suppose that (A, B) is stabilizable. Then, there exists K asymptotically stabilizing (24) if and only if $\det(I_n - A) \neq 0$.*

This result has been extended to continuous-time systems [15].

5 Dynamic DFC

Dynamic delayed feedback control [16] is given as an \hat{n} -dimensional dynamical controller

$$\begin{aligned} \hat{x}(k+1) &= \hat{A}\hat{x}(k) + \hat{B}\mathbf{e}(k) \\ \mathbf{u}(k) &= \hat{C}\hat{x}(k) + \hat{D}\mathbf{e}(k) \\ \mathbf{e}(k) &= \mathbf{y}(k) - \mathbf{y}(k-1) \end{aligned} \quad (23)$$

where $\hat{A} \in \Re^{\hat{n} \times \hat{n}}$, $\hat{B} \in \Re^{\hat{n} \times n}$, $\hat{C} \in \Re^{m \times \hat{n}}$, $\hat{D} \in \Re^{m \times n}$, and $\hat{x} \in \Re^{\hat{n}}$. The control input $\mathbf{u}(k)$ is applied to the chaotic system only when $\|\mathbf{e}(k)\|$ is sufficiently small. Otherwise, let $\mathbf{u}(k) = 0$ and $\hat{x}(k) = 0$. Similar to static DFC, in the vicinity of the fixed point \mathbf{x}_f , the linearized closed-loop system can be described by

$$x_c(k+1) = A_c x_c(k), \quad (24)$$

where

$$A_c = \begin{bmatrix} \mathcal{A} + \mathcal{B}\hat{D}\mathcal{C} & \mathcal{B}\hat{C} \\ \hat{B}\mathcal{C} & \hat{A} \end{bmatrix}, \quad x_c(k) = \begin{bmatrix} \xi(k) \\ \hat{x}(k) \end{bmatrix}. \quad (25)$$

Defining $F(z) := \det(zI - A_c)$, we have

$$F(1) = \det(I_n - A) \det(I_{\hat{n}} - \hat{A}).$$

It is noted that it is necessary for asymptotic stability of the closed-loop system (24) that $F(1) \neq 0$, equivalently $\det(I_n - A) \neq 0$. Hence, we can conclude the following theorem.

Theorem 4. *If there exists a dynamic delayed feedback controller (23) asymptotically stabilizing (24), then $\det(I_n - A) \neq 0$.*

This theorem suggests that the odd number limitation $\det(I_n - A) < 0$ can be relaxed by a dynamic controller with the odd number condition $\det(I_{\hat{n}} - \hat{A}) < 0$. It is also noted that any hyperbolic fixed point of chaotic systems satisfies the necessary condition $\det(I_n - A) \neq 0$ in Theorem 4.

In what follows, we see several cases where $\det(I_n - A) \neq 0$ gives us a necessary and sufficient condition for stabilization under some additional assumptions. They are summarized in Table 4.

5.1 Observer-based DFC

Now, we design output delayed feedback controllers based on a reduced-dimensional state estimator. Under the assumption that $\text{rank } C = p$, we can construct a $(2n-p)$ th order dynamic delayed feedback controller for a given n th order chaotic system, where p is the size of measurement output signal [29].

Rewriting the system to be stabilized via dynamic delayed feedback control (23) as

$$\begin{aligned} \xi(k+1) &= \mathcal{A}\xi(k) + \mathcal{B}u(k) \\ e(k) &= \mathcal{C}\xi(k), \end{aligned} \quad (26)$$

we obtain a minimal order observer for (26)

$$\begin{aligned} \hat{x}(k+1) &= \hat{F}\hat{x}(k) + \hat{R}e(k) + \hat{S}u(k) \\ \tilde{\xi}(k) &= \hat{H}\hat{x}(k) + \hat{J}e(k), \end{aligned} \quad (27)$$

where

$$\hat{W}\mathcal{A} - \hat{F}\hat{W} = \hat{R}\mathcal{C}, \quad \hat{S} = \hat{W}\mathcal{B}, \quad \hat{H}\hat{W} + \hat{J}\mathcal{C} = I_{2n}.$$

For asymptotic estimation, \hat{F} must be stable. If $(\mathcal{C}, \mathcal{A})$ is detectable, then such a stable \hat{F} always exists. Furthermore, when $I_n - A$ is nonsingular, detectability of (C, A) is equivalent to that of $(\mathcal{C}, \mathcal{A})$.

Now, linear feedback of the estimated state produced by the observer (27), $\mathbf{u}(k) = \hat{K}\tilde{\xi}(k)$, yields an output dynamic DFC (23) with coefficients

$$\hat{A} = \hat{F} + \hat{S}\hat{K}\hat{H}, \quad \hat{B} = \hat{R} + \hat{S}\hat{K}\hat{J}, \quad \hat{C} = \hat{K}\hat{H}, \quad \hat{D} = \hat{K}\hat{J}. \quad (28)$$

The observer-based controller structure leads to the well-known eigenvalue separation property, the closed-loop eigenvalues consist of those of the full-state regulator together with those of the estimator. That is, the characteristic polynomial of the closed-loop system is $\det(zI - \mathcal{A} - \mathcal{B}\hat{K}) \cdot \det(zI - \hat{F})$. Particularly, choosing $\hat{K} = [K \ 0]$ with K such that $A + BK$ is stable, we obtain stable eigenvalues of

$$\mathcal{A} + \mathcal{B}\hat{K} = \begin{bmatrix} A + BK & 0 \\ I_n & 0 \end{bmatrix}.$$

Hence, stabilization can be achieved.

Theorem 5. *Suppose that (A, B) is stabilizable and (C, A) is detectable. If $\det(I_n - A) \neq 0$, then there exists an output DFC (23) locally asymptotically stabilizing the closed-loop system (24).*

A delayed feedback control method using a 2nth order observer is proposed [17]. Nevertheless, it is not output feedback, but state feedback, because it requires the assumption that full-states are available for measurement.

5.2 State feedback

In this subsection, we consider the case where the full state vector is available for measurement ($C = I_n$). The following theorem gives us a condition for the existence of a dynamic DFC with the same order of the chaotic system ($n = \hat{n}$) [16].

Theorem 6. *Suppose that (A, B) is stabilizable. There exists a dynamic DFC (23) locally stabilizing a fixed point \mathbf{x}_f if and only if $I_n - A$ is nonsingular. Moreover, when the condition holds, one such dynamic DFC (23) is given by*

$$\begin{aligned} \hat{A} &= (I_n - A)^{-1}BK, \\ \hat{B} &= -(I_n - A)^{-1}BKA(I_n - A)^{-1}, \\ \hat{C} &= K, \\ \hat{D} &= -KA(I_n - A)^{-1}, \end{aligned} \quad (29)$$

where K is a gain such that $A + BK$ is stable.

Even if we consider the case where dynamic DFC has a lower order than that chaotic system has (that is, $\hat{n} < n$), $\det(I_n - A) \neq 0$ is still a necessary condition for the existence of stabilizing dynamic DFC. Conversely, a sufficient condition is obtained in terms of matrix inequalities [16]. It is also possible to derive a reduced-order dynamic DFC based on the matrix inequalities. However, it causes more computational efforts than that required by the methods in the following sections.

On the other hand, dynamic DFC with a higher order than that of the chaotic system ($\hat{n} > n$) also can be obtained based on a 2nth observer ($\hat{n} = 2n$) [17].

5.3 Extended DFC

Extended DFC (9) for discrete-time systems can be realized by a dynamic DFC. When $R = rI_p$, it has $\hat{A} = R$, $\hat{B} = I_p$, $\hat{C} = KR$ and $\hat{D} = K$. The odd number limitation of extended DFC is caused by $\det(I - R) > 0$ due to $r \in [0, 1)$ [7]. The constraint on r to be in $[0, 1)$ is to guarantee that the power series in (9) converges to $(1 - r)^{-1}$. On the other hand, if we use dynamic DFC, then we are allowed to use an unstable $r > 1$. Hence, the odd number limitation can be resolved by $\det(I - R) < 0$ [30].

Furthermore, we can choose R as a general matrix. In the case, an unstable R avoids the odd number limitation [20]. It is also pointed out that a comparable result in the fixed point stabilization problem for continuous-time systems.

Table 4. Dynamic delayed feedback control methods with the stabilizability condition $\det(I_n - A) \neq 0$ under the additional assumption that (A, B) is stabilizable. For output feedback, it is further required that (C, A) is detectable.

| method | controller | additional assumption |
|---|--|--|
| Observer-based DFC (Output feedback) | $\hat{x}(k+1) = \hat{A}\hat{x}(k) + \hat{B}\mathbf{e}(k)$ $\mathbf{u}(k) = \hat{C}\hat{x}(k) + \hat{D}\mathbf{e}(k)$ $\mathbf{e}(k) = \mathbf{y}(k) - \mathbf{y}(k-1)$ | (A, B) is stabilizable (C, A) is detectable |
| Dynamic DFC (State feedback) | $\hat{x}(k+1) = \hat{A}\hat{x}(k) + \hat{B}\mathbf{e}(k)$ $\mathbf{u}(k) = \hat{C}\hat{x}(k) + \hat{D}\mathbf{e}(k)$ $\mathbf{e}(k) = \mathbf{x}(k) - \mathbf{x}(k-1)$ | (A, B) is stabilizable |
| Generalized EDFC (State feedback) | $\mathbf{u}(k) = K(\mathbf{x}(k) -$ $(I - R) \sum_{i=1}^{\infty} R^{i-1} \mathbf{x}(k-i))$ | (A, B) is stabilizable |
| Recursive DFC (State feedback) | $\mathbf{u}(k) = K_e \mathbf{e}(k) +$ $(K_u + I_m) \mathbf{u}(k-1)$ $\mathbf{e}(k) = \mathbf{x}(k) - \mathbf{x}(k-1)$ | (A, B) is stabilizable |

6 Recursive DFC

Recursive delayed feedback [19] is given by

$$\mathbf{u}(k) = K_e \mathbf{e}(k) + (K_u + I_m) \mathbf{u}(k-1), \quad (30)$$

where K_e and K_u are constant gain matrices. This recursive DFC can be realized by an m th order dynamic DFC. For example,

$$\begin{aligned} \hat{x}(k+1) &= \hat{A}\hat{x}(k) + \hat{B}\mathbf{e}(k) \\ \mathbf{u}(k) &= \hat{C}\hat{x}(k) + \hat{D}\mathbf{e}(k), \end{aligned} \quad (31)$$

where $\hat{x}(k) = \mathbf{u}(k-1)$, $\hat{A} = \hat{C} = K_u + I_m$ and $\hat{B} = \hat{D} = K_e$. Hence, it is obviously shown that recursive DFC can overcome the odd number limitation. Furthermore, any hyperbolic fixed point with a stabilizable pair (A, B) can always be stabilized by recursive DFC.

Theorem 7. Suppose that (A, B) is stabilizable. There exists recursive DFC (30) locally stabilizing a fixed point \mathbf{x}_f if and only if $I_n - A$ is nonsingular.

Another advantage of recursive DFC enables us to design it to solve a constant state feedback problem. This comes from the fact that stability of the closed-loop system can be reduced to that of $\bar{A} + \bar{B}K$ where

$$\bar{A} = \begin{bmatrix} A & 0 \\ 0 & I_m \end{bmatrix}, \quad \bar{B} = \begin{bmatrix} B \\ I_m \end{bmatrix}, \quad K = [K_e \ K_u].$$

Hence, constant feedback gains K_e and K_u can be designed by K making $\bar{A} + \bar{B}K$ stable. Such a stabilizing gain K always exists if $I_n - A$ is nonsingular. This is ensured by the equivalence between stabilizability of (\bar{A}, \bar{B}) and (A, B) under nonsingularity of $I_n - A$.

It is convenient that gains of DFC can be designed by solving a constant state feedback problem because we can apply various techniques developed in control theory to it. For example, it is easy to adopt robust control theory such as quadratic stabilization to treat uncertainties in (A, B) [19].

A control method based on the Newton algorithm [18] can be realized by a recursive DFC. Under the assumption that B is of full column rank, it is given by

$$\begin{aligned} \mathbf{u}(k) &= -(B^T B)^{-1} B^T \left((A - I_n)^{-1} + I_n \right) \\ &\quad \times \left(A(\mathbf{x}(k) - \mathbf{x}(k-1)) - B\mathbf{u}(k-1) \right). \end{aligned} \quad (32)$$

To compare with (30), (32) can be realized by recursive DFC with

$$\begin{aligned} K_e &= -(B^T B)^{-1} B^T A (A - I_n)^{-1} A \\ K_u &= (B^T B)^{-1} B^T A (A - I_n)^{-1} B - I_m. \end{aligned} \quad (33)$$

When we use (32) (or recursive DFC with (33)),

$$\det(zI_{n+m} - (\bar{A} + \bar{B}K)) = z^m \det(zI_n - (I_n - B(B^T B)^{-1}B^T)A).$$

This implies that (32) can stabilize only unstable fixed point with the property that $(I_n - B(B^T B)^{-1}B^T)A$ is stable.

7 A Numerical Example

We have designed a dynamic delayed feedback controller and a recursive delayed feedback controller for the second-order discrete-time system [21]:

$$\begin{aligned} x_1(k+1) &= 1.9x_1(k) - x_1^3(k) + x_2(k) + u(k) \\ x_2(k+1) &= 0.5x_1(k). \end{aligned} \quad (34)$$

This system has three fixed points given by

$$x_{f1} = \begin{bmatrix} 0 \\ 0 \end{bmatrix}, \quad x_{f2} = \begin{bmatrix} \sqrt{1.4} \\ \sqrt{1.4}/2 \end{bmatrix}, \quad x_{f3} = -x_{f2}.$$

The linearized system around the unstable fixed point x_{f1} has a stabilizable pair

$$A = \begin{bmatrix} 1.9 & 1 \\ 0.5 & 0 \end{bmatrix}, \quad B = \begin{bmatrix} 1 \\ 0 \end{bmatrix}.$$

Since $\det(I - A) = -1.4 < 0$, x_{f1} cannot be stabilized by static DFC (7).

7.1 Second-order dynamic delayed feedback controller

Since (A, B) is controllable, we can determine K such that all eigenvalues of $A + BK$ are zero. Then, we obtain a dynamic controller with

$$\begin{aligned} \hat{A} &= \begin{bmatrix} 1.3571 & 0.7143 \\ 0.6786 & 0.3571 \end{bmatrix} \\ \hat{B} &= \begin{bmatrix} 2.5816 & 1.2245 \\ 1.2908 & 0.6122 \end{bmatrix} \\ \hat{C} &= [-1.9 \ -1] \\ \hat{D} &= [-3.6143 \ -1.7143]. \end{aligned}$$

Figure 1 shows a behavior of the controlled system starting from the initial state $[x_1(0), x_2(0)] = [0.7, -0.6]$ where $\varepsilon = 0.05$. The controller starts at $k = 144$ and the states converge to x_{f1} while the control action at $k = 115$ fails in the stabilization. The failure is caused by the fact that the state is not close to x_{f1} .

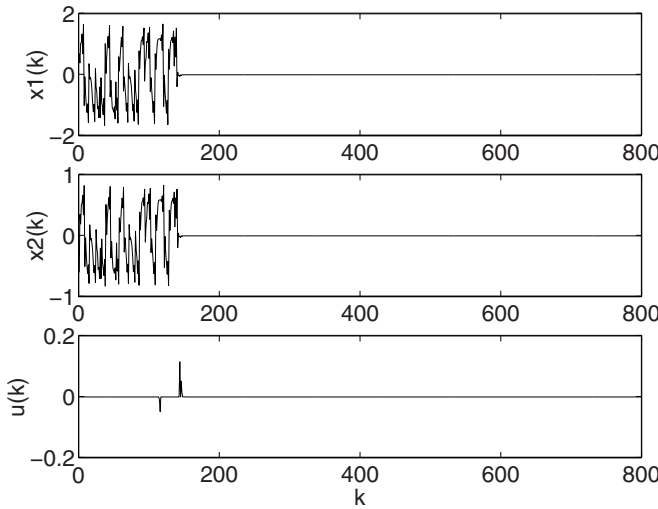


Fig. 1. Stabilization via dynamic delayed feedback control

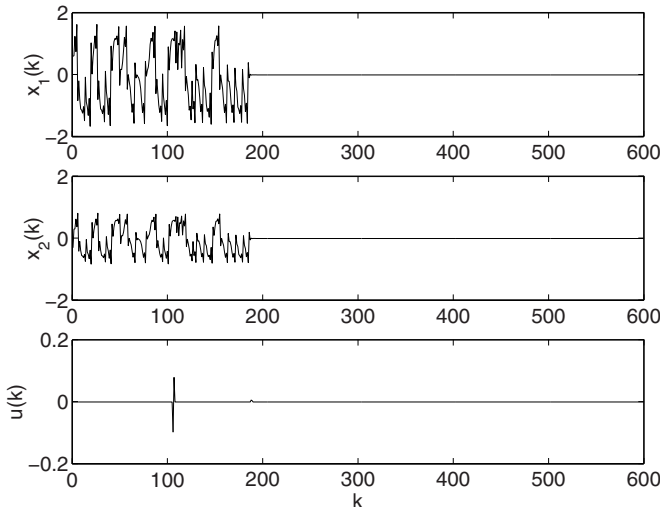


Fig. 2. Stabilization via recursive delayed feedback control

7.2 Recursive delayed feedback controller

One of the recursive delayed feedback controller is obtained by

$$K_e = [-3.6158 \quad -1.7149] \text{ and } K_u = 0.7149.$$

This RDFC assigns all eigenvalues of the linearized closed-loop system to the origin. By this recursive DFC, state trajectories of (34) starting from the initial state $[x_1(0), x_2(0)] = [0.6, -0.3]$ can be stabilized (Figure 2). Recursive DFC starts at $k = 188$ and the state converges to x_{f1} . The control action at $k = 106$ fails in the stabilization, since the state is not close to x_{f1} .

8 Conclusions

In this chapter, we discuss the odd number limitation in delayed feedback control which is an efficient controlling method for chaos. So far several methods have been developed to overcome the limitation, which maintain the advantage of the DFC mechanism.

References

1. Pyragas, K. (1992) Continuous control of chaos by self-controlling feedback. *Phys. Lett. A*, **170**:421–428
2. Ott, E., Grebogi, C., Yorke, J. A. (1990) Controlling chaos. *Phys. Rev. Lett.*, **64**(11):1196–1199
3. Ushio, T. (1996) Limitation of delayed feedback control in non-linear discrete-time systems. *IEEE Trans. Circ. Syst.-I*, **43**(9):815–816
4. Nakajima, H. (1997) On analytical properties of delayed feedback control of chaos. *Phys. Lett. A*, **232**:207–210
5. Socolar, J. E. S., Sukow, D. W., Gauthier, D. J. (1994) Stabilizing unstable periodic orbits in fast dynamical systems. *Phys. Rev. E*, **50**(2):3245–3248
6. Nakajima, H., Ueda, Y. (1998) Limitation of generalized delayed feedback control. *Physica D*, **111**:143–150
7. Konishi, K., Ishii, M., Kokame, H. (1999) Stability of extended delayed feedback control for discrete-time chaotic systems. *IEEE Trans. Circ. Syst.-I*, **46**(10):1285–1288
8. Hino, T., Yamamoto, S., Ushio, T. (2000) Stabilization of unstable periodic orbits of chaotic discrete-time systems using prediction-based feedback control. *Int. J. Bifur. Chaos*, **12**(2):439–446
9. Just, W., Bernard, T., Osthermer, M., Reibold, E., Benner, H. (1997) Mechanism of time-delayed feedback control. *Phys. Rev. Lett.*, **78**(2):203–206
10. Pyragas, K. (1995) Control of chaos via extended delay feedback. *Phys. Lett. A*, **206**:323–330
11. Bleich, M. E., Socolar, J. E. S. (1996) Stability of periodic orbits controlled by time-delay feedback. *Phys. Lett. A*, **210**:87–94
12. Just, W., Reibold, E., Benner, H., Kacperski, K., Fronczak, P., Holyst, J. (1999) Limits of time-delayed feedback control. *Phys. Lett. A*, **254**:158–164
13. Ushio, T., Yamamoto, S. (1998) Delayed feedback control with nonlinear estimation in chaotic discrete-time systems. *Phys. Lett. A*, **247**:112–118
14. Ushio, T., Yamamoto, S. (1999) Prediction-based control of chaos. *Phys. Lett. A*, **264**:30–35
15. Nakajima, H. (2002) Delayed feedback control with state predictor for continuous-time chaotic systems. *Int. J. Bifur. Chaos*, **12**(5):1067–1077

16. Yamamoto, S., Hino, T., Ushio, T. (2001) Dynamic delayed feedback controllers for chaotic discrete-time systems. *IEEE Trans. Circ. Syst.-I*, **48**(6):785–789
17. Konishi, K., Kokame, H. (1998) Observer-based delayed-feedback control for discrete-time chaotic systems. *Phys. Lett. A*, **248**:359–368
18. Xu, D., Bishop, S. R. (1996) Self-locating control of chaotic systems using Newton algorithm. *Phys. Lett. A*, **210**:273–278
19. Yamamoto, S., Hino, T., Ushio, T. (2001) Recursive delayed feedback control for chaotic discrete-time systems. In Proc. of the 40th IEEE Conference on Decision and Control, 2187–2192
20. Nakajima, H. (2000) A generalization of the extended delayed feedback control for chaotic systems. In Proc. of Int. Conference on Control of Oscillations and Chaos, **2**:209–212
21. Ushio, T. (1995) Chaotic synchronization and controlling chaos based on contraction mappings. *Phys. Lett. A*, **198**:14–22
22. Bielawski, S., Derozier, D., Glorieux, P. (1993) Experimental characterization of unstable periodic orbits by controlling chaos. *Phys. Rev. A*, **47**(2):2493–2495
23. Schuster, H. G., Stemmler, M. B. (1997) Control of chaos by oscillating feedback. *Phys. Rev. E*, **56**(6):6410–6417
24. Yamamoto, S., Ushio, T. (2002) Stabilization of discrete-time chaotic systems by periodic delayed feedback control. In Proc. of American Control Conference, **TA17-4**:2260–2261
25. Nakajima, H., Ueda, Y. (1998) Half-period delayed feedback control for dynamical systems with symmetries. *Phys. Rev. E*, **58**(2):1757–1763
26. Yu, X. (1999) Tracking inherent periodic orbits in chaotic dynamic systems via adaptive variable structure time-delayed self control. *IEEE Trans. Circ. Syst.-I*, **46**(11):1408–1411
27. Kokame, H., Hirata, K., Konishi, K., Mori, T. (2001) State difference feedback for stabilizing uncertain steady states of non-linear systems. *Int. J. Control.*, **74**(6):537–546
28. Kokame, H., Hirata, K., Konishi, K., Mori, T. (2001) Difference feedback can stabilize uncertain steady states. *IEEE Trans. Auto. Contr.*, **46**(12):1908–1913
29. Yamamoto, S., Hino, T., Ushio, T. (2002) Delayed feedback control with a minimal-order observer for stabilization of chaotic discrete-time systems. *Int. J. Bifur. Chaos*, **12**(5):1047–1055
30. Pyragas, K. (2001) Control of chaos via an unstable delayed feedback controller. *Phys. Rev. Lett.*, **86**(11):2265–2268
31. Hikihara, T., Kawagishi, K. (1996) An experimental study on stabilization of unstable periodic motion in magneto-elastic chaos. *Phys. Lett. A*, **211**(1):29–36
32. Bleich, M. E., Hochheiser, D., Moloney, J. V., Socolar, J. E. S. (1997) Controlling extended systems with spatially filtered, time-delayed feedback. *Phys. Rev. E*, **55**(3):2119–2126
33. Konishi, K., Hirai, M., Hirata, K. (1998) Decentralized delayed-feedback control of a coupled map model for open flow. *Phys. Rev. E*, **58**(3):3055–3059
34. Konishi, K., Kokame, H., Hirata, K. (1999) Coupled map car-following model and its delayed-feedback control. *Phys. Rev. E*, **60**(4):4000–4007
35. Fujii, H., Ichiki, W., Suda, S., Watanabe, T. R. (1999) Chaos analysis on librational control of gravity-gradient satellite in elliptic orbit. *J. Guidance, Contr. Dynamics*, **23**(1):145–146

36. Brandt, M. E., Chen, G. (2000) Time-delay feedback control of complex pathological rhythms in an atrioventricular conduction model. *Int. J. Bifur. Chaos*, **10**(12):2781–2784
37. Bleich, M. E., Socolar, J. E. S. (2000) Delayed feedback control of a paced excitable oscillator. *Int. J. Bifur. Chaos*, **10**(3):603–609

Introduction to Some Methods of Chaos Analysis and Control for PDEs

Yi Zhao

Department of Mathematics, Zhongshan University,
Guangzhou 510275, P. R. China
stszy@zsu.edu.cn

Abstract. Following the development of the research on chaos and controlling chaos for ODEs, some methods and results of that for PDEs were developed in last decade. In this chapter, in addition to give a summary account in part, we present some results on controlling chaos for a class of parabolic type PDEs by applying the invariant manifold and structure stability theory.

1 Some Typical Models of PDEs

In recent years the chaotic behavior of the systems described by some PDE models are often studied. The subject of this section is devoted to present mathematical setting of some of these models and brief in their physical background.

1.1 The generalized complex Ginzburg-Landau equation (CGLE)

$$u_t = \rho u + (1 + ic_1)\Delta u + (1 + ic_2)|u|^2u \quad (1)$$

that describes the evolution of a complex-valued $u = u(x, t)$. It has a long history in physics as a generic amplitude equation near the onset of instabilities that lead to chaotic dynamics in fluid mechanical systems, as well as in the theory of phase transitions and superconductivity. It is a particularly interesting model because it is important for the study of turbulent problems and spatiotemporal structure. So, the long time and finite dimensional behavior, such as the global attractor and approximate inertial manifolds (AIM), for CGLE are discussed in some papers. Especially, the turbulent behavior and control of spatiotemporal chaos as well as spatiotemporal patterns for CGLE are studied (see [1]- [3]). Moreover, the convergence of chaotic attractor with increased partial resolution is done for CGLE (see [4]).

1.2 The perturbed nonlinear Schrödinger equation (NSL)

$$iq_t = q_{xx} + 2[|q|^2 - w^2]q + i\varepsilon(aq - bq_{xx} + r), \quad (2)$$

where $q(x, t)$ is l -periodic and even in x , i.e., $q(x + l, t) = q(x, t)$, $q(x, t) = q(-x, t)$. Schrödinger equation is an important equation for the study of nonlinear optics and propagation of laser beams, the propagation of solitons and quantum mechanics. So, thousands of papers concerned them in different aspects. Especially, in recent years some papers have devoted to the study of the existence and persistence of homoclinic orbits for (2) which are closely related to chaos (see [5]- [7]) and chaotic behavior in the sense of Smale horseshoes is analyzed (see [8, 9]).

1.3 The Karamoto-Sivashivisky (K-S) equation

$$u_t + \gamma u_{xxxx} + u_{xx} + \frac{1}{2}(u_x)^2 = 0, \quad (3)$$

introduced for the study of phase turbulence in the Belousov-Zhabotinsky reactions and is also encountered as a model for the Bénard problem in an elongated box. An extension of this equation to space dimension 2 (or more) is introduced to study the propagation of a flame front in the case of mild combustion. Particularly, it is a well-known model that describes the spatiotemporal chaos. The chaotic behavior of a variant of (3) as follows:

$$\begin{aligned} & u_t + \varphi u + u_{xx} + u_{xxxx} + 2\psi u_x = 0, \\ & u(0) = u(L) = 0, \quad u_x(0) = u_x(L) = 0, \end{aligned} \quad (4)$$

is discussed by Lyapunov exponent (LE) method (see [10]).

1.4 The extended Fisher-Kolmogorov (F-K) equation

$$u_t = -ru_{xxxx} + u_{xx} - f(u), \quad r > 0, \quad (5)$$

where the function f will be specified below as a cubic-like piecewise linear one. When $f(u) = u^3 - u$ Eq. (5) was proposed as a generalization of the classical F-K equation:

$$u_t = u_{xx} + u - u^3. \quad (6)$$

Equation (6) has a bistable nonlinearity in the sense that the ODE $u_t = u - u^3$ has two stable stationary solutions $u = \pm 1$. It plays an important role in various areas of physics, chemistry and biology. The presence of a bistable nonlinearity in Eq. (5) is the cause for spatial chaos that is studied in [11].

1.5 Other models

One-dimensional conserved Zakharov equations (ZEs)

$$\begin{aligned} iE_t + E_{xx} &= nE, \\ n_{tt} - n_{xx} &= |E|_{xx}^2, \end{aligned} \tag{7}$$

where $E(x, t)$ is a slowly varying envelope of Langmuir electric field, and $n(x, t)$ is ion-sound density. So far the ZEs are extensively studied as a model describing strong plasma turbulence. The pattern dynamics and spatiotemporal chaos in ZKs are shown in [12].

The Sine-Gordon equation

$$u_{tt} + \alpha u_t - \Delta u + \beta \sin u = f, \tag{8}$$

which is used to model, for instance, the dynamics of a Josephson junction driven by a current source. The perturbed Sine-Gordon equation is also studied by quite many papers which is given by

$$u_{tt} - u_{xx} + \sin u = \varepsilon(-au_t + bu_{xx} + c \sin \omega t), \tag{9}$$

with periodic, even boundary conditions:

$$u(x, t) = u(x + l, t), \quad u(x, t) = u(-x, t),$$

with $0 < \varepsilon a \ll 1$, $0 < \varepsilon b \ll 1$, $w = 1 - \varepsilon \tilde{\omega}$ and l fixed where ε and $\tilde{\omega}$ are both positive.

2 Some Methods and Results of Chaos Analysis for PDE Models

2.1 The Lyapunov exponent method

The Lyapunov exponent has attracted considerable attention for many years because a widely accepted criterion for a trajectory to be chaotic is the existence of a positive Lyapunov exponent, and it is convenient and computable to show the temporal chaos for discrete and ODE systems. Also, the mean Lyapunov exponent and local Lyapunov exponent are introduced in order to characterize the chaos of the systems described by PDEs (see [10] and [13]). It is shown that the mean Lyapunov exponent expresses clearly how disordered the spatial patterns are, and the local Lyapunov exponent which is a finite time average of the mean Lyapunov exponent has close relation to spatiotemporal patterns.

In the following we cite the results and examples in [10] and [13] to illustrate. Let us consider the PDE system described by:

$$u_t = bu_{xx} + a(u - u^3), \quad (10)$$

with Dirichlet boundary condition:

$$u(0, t) = u(1, t) = 0. \quad (11)$$

We use the difference method in order to solve (10) and (11) by rewriting to:

$$\frac{\nu_j^{k+1} - \nu_j^k}{\Delta t} = b \frac{\nu_{j+1}^k - 2\nu_j^k + \nu_{j-1}^k}{(\Delta x)^2} + a(1 - \nu_j^k)\nu_j^k, \quad (12)$$

where $\nu_j^k = u(j\Delta x, k\Delta t)$, $k = 0, 1, \dots$ and $j = 1, 2, \dots, J$. The initial condition is set to be:

$$\nu_j^0 = \begin{cases} \frac{j-1}{J}, & j = 2, \dots, \frac{J+1}{2} \\ 1 - \frac{j-1}{J}, & j = \frac{J+1}{2} + 1, \dots, J \end{cases}$$

$$\nu_1^k = \nu_{J+1}^k = 0, \quad k = 0, 1, \dots$$

is made corresponding to (11).

It follows from (12) that

$$\nu_j^{k+1} = \nu_j^k + \frac{\Delta t \cdot d}{(\Delta x)^2} (\nu_{j+1}^k - 2\nu_j^k + \nu_{j-1}^k) + \Delta t \cdot a(1 - \nu_j^k)\nu_j^k. \quad (13)$$

After setting the values for $b, a, J = \frac{1}{\Delta x}$ and Δt , the Jacobi matrix for (13) can be deduced and denoted by

$$B_{k,J} = \left\{ \frac{\partial \nu_i^{k+1}}{\partial \nu_j^k} \right\}_{i,j=2,\dots,J}.$$

So, one can calculate the mean Lyapunov exponent

$$\lambda_k = \frac{1}{J-1} \log |B_{k,J}|$$

and the local Lyapunov exponent

$$\Lambda_T = \frac{1}{n} \sum_{j=0}^{n-1} \lambda_j,$$

where $T = n \cdot \Delta t$. As a concrete computational result, when we set at $a = 4.0, J = 33, \Delta t = 0.55$, one can get various spatiotemporal patterns as b is set at 0.000113, 0.000110, 0.000060, 0.000010, respectively. When the

mean Lyapunov exponent takes large values, the spatiotemporal patterns are disordered.

In order to characterize quantitatively the spatiotemporal patterns the probability distribution function of the local Lyapunov exponent was introduced as follows:

$$P(\Lambda, T) = \langle \delta(\Lambda - \Lambda_T) \rangle,$$

where $\delta(\cdot)$ is the Dirac's distribution and $\langle \dots \rangle$ is a long time average.

A similar analysis for K-S equation (4) was made in [10]. In this case, instead of (12) the finite-difference equation for (4) is as follows:

$$\begin{aligned} & \frac{\nu_j^{k+1} - \nu_j^k}{\Delta t} + \eta \frac{\nu_{j+1}^k + \nu_j^k - \nu_{j-1}^k}{3} + \frac{\nu_{j+1}^k - 2\nu_j^k - \nu_{j-1}^k}{(\Delta x)^2} \\ & + \frac{\nu_{j+2}^k - 4\nu_{j+1}^k + 6\nu_j^k - 4\nu_{j-1}^k + \nu_{j-2}^k}{(\Delta x)^4} + \frac{\nu_j^k(\nu_{j+1}^k - \nu_{j-1}^k)}{\Delta x} = 0 \end{aligned}$$

and

$$B_{k,N-1} = \left\{ \frac{\partial \nu_i^{k+1}}{\partial \nu_j^k} \right\}_{i,j=1,\dots,N-1}.$$

As an application of Lyapunov exponent for continuous dynamical systems a method combines the Lyapunov exponent with approximate inertial manifolds (AIMs) (see [15] Chapter X) was proposed in [4]. Consider a special version of (1) as follows:

$$u_t - r^2(c + i)u_{xx} - cu + (c - i)|u|^2u = 0,$$

$$u(x + 2\pi, t) = u(x, t), \quad u(x, t) = u(-x, t). \quad (14)$$

Denote by $H_{per}^d(0, 2\pi)$ the subspace of the complexified Sobolev space $H^d(0, 2\pi)$ consisting of complex-valued functions which along with their spatial derivatives up to order $d - 1$ are periodic with period 2π in x . Let

$$V = \{u \in H_{per}^1(0, 2\pi) : u(x, t) = u(-x, t)\},$$

$$A = -cI - r^2(c + i)\Delta, \quad D(A) = H_{per}^2(0, 2\pi) := H.$$

Equation (14) may now be expressed as a nonlinear evolutionary equation

$$u_t + Au + F(u) = 0, \quad u \in H, \quad (15)$$

where

$$F(u) = (c - i)|u|^2u.$$

The eigenvalue eigenfunction pairs of A are given by

$$\delta_k = -c + r^2 k^2(c + i), \quad \psi_k = \cos(kx), \quad k = 0, 1, 2, \dots$$

Let $P = P_m$ be the L_2 orthogonal projector from H onto $\text{span}\{\psi_0, \psi_1, \dots, \psi_m\}$ and $Q = Q_m = I - P$. Since P and Q commute with A one may split (15) as

$$\begin{aligned} P_t + Ap + PF(p + q) &= 0, \quad p \in Pu, \\ qt + Aq + QF(p + q) &= 0, \quad q \in Qu. \end{aligned} \quad (16)$$

Using nonlinear Galerkin method the sequence of AIMs of (16), which are the graphs of functions from PH to QH , is defined recursively by the following iteration algorithm:

$$\begin{aligned} \varphi_i(p) &= -A^{-1}QF(p + \varphi_{i-1}(p)), \quad p \in PH, \quad i = 1, 2, \dots \\ \varphi_0 &= 0. \end{aligned} \quad (17)$$

The j th AIM yields the approximate inertial form

$$p_t + Ap - PF(p + \varphi_j(p)) = 0. \quad (18)$$

The long time behavior of (14) can be described by that of (18) approximately and the approximate order can be defined by estimating the distance from the global attractor of (14) to the AIMs given by φ_j , $j = 1, 2, \dots$.

So, one can compute the Lyapunov exponent for (18) to characterize the chaotic behavior for (14) approximately. The method of computing Lyapunov exponent for continuous dynamical systems, such as (18), is given by [14] mainly with QR factorization.

Note that linear Galerkin method corresponds to the ‘flat’ AIM given by φ_0 . In this case (18) with $\varphi_j = \varphi_0$ is called the truncation system of (14) and so-called low-dimension chaos can be studied for it.

Since the Lyapunov exponents are the averages of the expansion or contraction rates for points on a trajectory, they do not indicate local variations which might distinguish one trajectory from another. A natural extension is to consider the expansion or contraction rates for each individual point on the attractor. This leads to refer to as instantaneous Lyapunov exponents and the QR factorization procedure directly provides us with these instantaneous expansion/contraction rates. One can refer to [4] for detail.

Lyapunov exponents themselves are closely relative to estimation of fractal dimension of the attractors for dynamical systems (see [15], Chapter V) and both the positive maximum Lyapunov exponent and fractal dimension are typical indicators that can be used to characterize the chaotic flow of a dynamical system. So, some results are presented to discuss the conditions that can possibly lead to chaotic motion for a simply supported large deflection rectangular plate of thermo-mechanical coupling by utilizing the criteria of both the fractal dimension and the Lyapunov exponent (see [16] and [17]). The corresponding governing PDE, say in [17], is as follows:

$$\begin{aligned} & D\nabla^4 w + phw_{tt} + \delta w_t - hL(f, w) + N_1 W_{xx} + N_2 w_{yy} + \alpha(1 + \nu)D\nabla^2 M_T \\ &= q \cos(wt), \end{aligned} \quad (19)$$

$$\nabla^4 F + E\alpha\nabla^2 N_T + \frac{E}{2}L(w, w) = 0, \quad (20)$$

where

$$\begin{aligned} L(F, w) &= \frac{\partial^2 F}{\partial x^4} \frac{\partial^2 w}{\partial y^2} + \frac{\partial^2 F}{\partial y^2} \frac{\partial^2 w}{\partial x^2} - 2 \frac{\partial^2 F}{\partial x \partial y} \frac{\partial^2 w}{\partial x \partial y}, \\ \nabla^4 &= \frac{\partial^4}{\partial x^4} + 2 \frac{\partial^4}{\partial x^2 \partial y^2} + \frac{\partial^4}{\partial y^4}, \\ D &= \frac{Eh^3}{12(1 - \nu^2)}, \quad \nabla^2 = \frac{\partial^2}{\partial x^2} + \frac{\partial^2}{\partial y^2}, \end{aligned}$$

where $w(x, y, t)$ is the deflection of neutral plane of the plate, $F(x, y, t)$ is the stress functions, δ is the damping coefficient, ρ is the material density of the plate, h is the thickness of the plate, and E is Young's modulus, α is the coefficient of linear thermal expansion, M_T is the additional membranous force caused by temperature. Define

$$w(x, y, t) = A(t)\psi(x, y), \quad M_T(x, y, t) = B(t)\psi(x, y),$$

$$N_T(x, y, t) = C(t)\psi(x, y),$$

where

$$\psi(x, y) = \sin\left(\frac{\pi x}{a}\right) \sin\left(\frac{\pi y}{b}\right),$$

and substitute them to (20) to solve for stress function F . The Galerkin method then is employed to derive and simplify Eqs. (19) and (20) to a set of three ordinary differential equations as follows:

$$A''(t) + a_5 A'(t) + a_6 q \cos wt + q_1 B(t) + a_2 A(t) + A_3 A(t)c(t) + a_4 A(t)^3 = 0,$$

$$B'(t) + b_1 A'(t) + b_2 B(t) = 0, \quad (21)$$

$$C'(t) + c_1 C(t) + c_2 A(t)A'(t) + c_3 = 0,$$

which can approximately characterize the dynamics of (19) and (20).

After nondimensionalized (21) the numerical method can be used to determine the fractal dimension of the system by plotting “ $\log C(r)$ ” against “ $\log r$,” where $C(r)$ is the correlation function and r is the radius of an n -dimensional hyper-sphere. The correlation dimension can then be determined by computing the slope of the plotted curve of $\log C(r)$ versus $\log r$ as

$$d_G = \lim_{r \rightarrow 0} \frac{\log C(r)}{\log r},$$

where

$$C(r) = \lim_{N \rightarrow \infty} \frac{1}{N^2} \sum_{i,j=1}^N H(r - |x_i - x_j|),$$

and H is the Heaviside step function, N is the number of data point.

Also, the Lyapunov exponent and several different features including power spectra, phase plot, Poincaré map and bifurcation diagram are then numerically computed in [17].

2.2 Measurement of chaos by entropy

As is well known, the topological entropy is a quantitative measurement of how chaotic the map is (see [18], Chapter IX). Recently, the spatial entropy is introduced and estimated to characterize the spatial chaos for F-K equation (5) with piecewise linear cubic like nonlinearity (see [11]):

$$f(u) = \begin{cases} u - 1, & u > 0, \\ u + 1, & u < 0, \\ 0, & u = 0. \end{cases} \quad (22)$$

The bounded stationary solutions were studied by solving the following equation:

$$ry^{(4)} - y'' + y = \text{sign}(y), \quad r > \frac{1}{4}, \quad (23)$$

and it is proved that if a bounded solution of (23) changes its sign in a neighborhood of each zero, then this solution is uniquely defined (up to the sign) by its zeros. Furthermore, let $y(x, \{x_k\})$ be a bounded solution of (23) with zeros $\{x_k\}$ increasingly ordered, the sequence of natural numbers $n_k = [(\frac{\beta}{\pi})(x_k - x_{k-1})] + 1$ was defined as a skeleton of the solution $y(x, \{x_k\})$ where $\beta = (\frac{1}{2\sqrt[3]{r}} - \frac{1}{4r})^{\frac{1}{2}}$. Let $y(x, \{x_k\})$ be a bounded solution of (23) with a finite number of zeros $\{x_k\}_{k=1}^m$, and $a_n = x_n - x_{n-1} \geq \frac{\pi}{\beta}$. Then it is proved that this solution is uniquely defined, up to the sign and translation in x , by its skeleton $\{n_k\}_{k=1}^m$. Based on this result, it was shown that (5) with (22) for $r > \frac{1}{4}$ gives rise to a spatial chaos, i.e., for any $\varepsilon > 0$ there exists $L(\varepsilon) > 0$ such that for any sequence of points $\{(x_n, \sigma_n)\}_{n=1}^N$ with $x_{n+1} - x_n > L(\varepsilon)$ and σ_n taking one of two stable values for every n ($\sigma_n = \pm 1$), (5) has a bounded stationary solution such that $|y(x_n) - \sigma_n| < \varepsilon$ $n = 1, \dots, N$. Moreover, for Eq. (23) the spatial entropy η , which is defined by

$$\eta = \lim_{L \rightarrow \infty} \frac{1}{L} \log S(L),$$

where $S(L)$ is the numbers of all bounded solutions of Eq. (23) such that zeros belong to the interval $[0, L]$ and that the point $x = 0$ is a zero of all

solutions, admits the following estimate

$$\eta > 0.14\beta > 0, \quad \text{for } r > \frac{1}{4}. \quad (24)$$

The positive values of φ signify the existence of spatial chaos in system (5), (22) under consideration (one can refer to [11] for detail).

2.3 Perturbation theory and the Melnikov method

As is well known, the existence of the chaos in the sense of Smale horseshoes is based on the existence of homoclinic orbits and their transversality, whereas these can be judged by perturbation theory and Melnikov method.

As a recent result chaos in discretized perturbed NLS systems was studied in [8]. The discussed NLS system is described by (2) and the corresponding N -particle ($2 < N < \infty$) finite-difference dynamical system is

$$\begin{aligned} i\dot{q}_n = & \frac{1}{u^2} [q_{n+1} - 2q_n + q_{n-1}] + |q_n|^2 (q_{n+1} + q_{n-1}) - 2w^2 q_n, \\ & + i\varepsilon [-aq_n + \frac{b}{u^2} (q_{n+1} - 2q_n + q_{n-1}) + r], \end{aligned} \quad (25)$$

where q_n s are complex variables and $q_{N+N} = q_n$ (periodic condition), $q_{N-n} = q_n$ (even condition). Therefore (25) is a $2(M+1)$ dimensional system where $M = \frac{N}{2}$ (for N even) or $M = \frac{(N-1)}{2}$ (for N odd) with $\mu = \frac{1}{N}$.

Denote the external parameter space by \sum_N ($N \geq 7$) where

$$\begin{aligned} \sigma_N = & \left\{ (w, a, b, r) : w \in \left(N \tan \frac{\pi}{N}, N \tan \frac{2\pi}{N} \right), \right. \\ & \left. r \in (0, 1), a \in (0, a_0), b \in (0, b_0) \right\}, \end{aligned}$$

where a_0 and b_0 are any positive numbers ($< \infty$). First the existence of homoclinic orbits for (25) was proved in [7] as a theorem given by the following statement: for any $N \in [7, \infty]$, there exists a positive number ε_0 such that for any $\varepsilon \in (0, \varepsilon_0)$, there exists a codimension 1 submanifold E_ε in \sum_N which is in an $O(\varepsilon^\nu)$ neighborhood of the hyperplane $b = ka$ where $k = k(w, N)$, $\nu = \frac{1}{2} - \delta_0$, $0 < \delta_0 \ll \frac{1}{2}$. For any (w, a, b, r) on E_ε , there exists a homoclinic orbit asymptotic to a fixed point. Consequently, in [8] it is shown that how Smale horseshoes can be constructed near these homoclinic orbits and most importantly, how the geometry associated with the horseshoes gives a mechanism for chaotic ‘center-wing jumping.’ The research steps for such purpose in [8] are as follows:

- (1) Set a general high dimensional $(2m+n)$ system as follows:

$$\begin{aligned}\dot{x}_j &= \varepsilon_j a_j x_j - b_j y_j + X_j(x, y, z) \\ \dot{y}_j &= b_j x_j + \varepsilon_j a_j y_j + Y_j(x, y, z), \quad j = 1, \dots, m, \\ \dot{z}_k &= \delta_k r_k z_k + Z_k(x, y, z), \quad k = 1, \dots, n,\end{aligned}\tag{26}$$

where

$$\varepsilon_j = \begin{cases} -1 & 1 \leq j \leq m_1 \\ 1 & m_1 < j \leq m \end{cases}, \quad \delta_k = \begin{cases} 1 & 1 \leq k \leq n_1 \\ -1 & n_1 < k \leq n \end{cases},$$

$$x = (x_1, \dots, x_m)^T, \quad y = (y_1, \dots, y_m)^T, \quad z = (z_1, \dots, z_n)^T,$$

$$X_j(0, 0, 0) = Y_j(0, 0, 0) = 0,$$

$$\text{grad } X_j(0, 0, 0) = \text{grad } Y_j(0, 0, 0) = 0, \quad j = 1, \dots, m,$$

$$Z_k(0, 0, 0) = \text{grad } Z_k(0, 0, 0) = 0, \quad k = 1, \dots, n.$$

Moreover, X_j , Y_j , and Z_k are C^∞ function in a neighborhood of $(0, 0, 0)$, and a_j , b_j , and r_k are positive constants. therefore $(0, 0, 0)$ is a saddle point.

The motivation for setting (26) is that the discrete NLS system (25) can be normalized into a special form of (26). According to the results in [7] as mentioned above one can assume that there is a homoclinic orbit h asymptotic to $(0, 0, 0)$, and there are smallest attracting rate a_1 and smallest repelling rate r_1 with $a_1 < r_1$ satisfying some properties.

(2) Define two Poincaré sections Σ_0 , Σ_1 in a small neighborhood of $(0, 0, 0)$ and Poincaré map $P : U \subset \Sigma_0 \rightarrow \Sigma_0$, $P = P_1^0 \cdot P_0^1$ for (26), where $P_0^1 : U_0 \subset \Sigma_0 \rightarrow \Sigma_1$, $P_1^0 : U_1 \subset \Sigma_1 \rightarrow \Sigma_0$, Σ_0 and Σ_1 sit in a tubular neighborhood of the homoclinic orbit h .

(3) Construct a certain compact invariant Cantor set $\Lambda(\subset \Sigma_0)$ on which the Poincaré map P is proved to be topologically conjugate to the shift automorphism on two symbols, 0 and 1 by applying the Conley-Morse conditions. This gives rise to deterministic chaos in the sense of Smale horseshoe. Meanwhile the fixed points of map P are computed and the definition of ‘slabs’ is presented.

(4) Apply the above results to discrete NLS systems. First, the fact that the discrete NLS systems possess a symmetric pair of homoclinic orbits is deduced. Then the Smale horseshoes and chaos created by the pair of homoclinic orbits are also studied using the general theory. Most importantly, as a consequence certain numerical experiments on the discrete NLS systems as “chaotic center-wing jumping” can be interpreted.

2.4 Some numerical and analytic methods

In chaos analysis many PDEs are firstly reduced to the ODEs by different modes, then the numerical method for the qualitative analysis of ODE systems are applied to obtain the fixed points and the periodic solutions, analyze the heteroclinic and a cascade of period doublings that lead eventually to chaos. Here we list the followings to indicate.

(1) In [19] it deals with an evolution equation for a growing epitaxial film

$$h_t = \lambda_1 h_x^2 + \nu_2 h_{xx} + \nu_3 (h_x^2)_{xx} + \nu_4 h_{xxxx} + F, \quad (27)$$

where h is the surface height (orthogonal to x), and F the incident molecular flux, i.e. the average growth rate. Eq. (27) represents a macroscopic picture of epitaxial crystal growth, where the discrete microscope structure is approximated by a continuous function describing the surface height. In view of mathematical model Eq. (27) is related to K-S equation (3).

After defining the new height variable $y(x, t) := h(x, t) - (F + \lambda_1 a^2)t - ax$ ($a := \tan\alpha$, α is an angle by which the initial configuration for the surfaces is slightly misoriented), and normalize the parameters to 1 in (27) except λ_3 , one has

$$y_t = (2a + y_x)y_x + y_{xx} + 2b(y_{xx}^2 + (a + y_x)y_{xxx}) + y_{xxxx}, \quad (28)$$

For looking for structures that remain invariant under the growth process one focuses on the travelling wave solutions of Eq. (28), i.e. solutions of the form $y(x, t) = y(x - ct)$. These solutions represent profiles that propagate with the constant speed c . With the substitution $z := x - ct$ and the abbreviations $y_1 = y_z$, $y_2 = y_{zz}$, $y_3 = y_{zzz}$, we finally arrive at a third order autonomous system of ODE:

$$\begin{aligned} y'_1 &= y_2, \\ y'_2 &= y_3, \\ y'_3 &= -(c + 2a + y_1) - y_2 - 2z(y_2^2 + (a + y_1)y_3), \end{aligned} \quad (29)$$

where the prime denotes differentiation with respect to z , Eq. (29) is the basic equation to parameter study.

For Eq. (29) the two equilibria, the periodic solutions and heteroclinic orbits are analyzed, and stability results are given. By numerical computation one finds almost periodic orbits that are called pretzel orbits because of their twisted shape. Also, the existence of period doubling and homoclinic bifurcations are shown and the computation of heteroclinic orbits was discussed in [19].

(2) The bifurcation phenomena for the incompressible Navier-Stokes equations in two space dimensions with periodic boundary conditions was studied in [20]. The nondimensional form of the equation is as follows:

$$\begin{aligned} v_t + (v \cdot \operatorname{grad} v) &= R^{-1} \Delta v - \operatorname{grad}(p) + f, \\ \operatorname{div} v &= 0, \end{aligned} \quad (30)$$

where v and p denote the dimensionless fluid velocity and thermal pressure, R the Reynolds numbers, and f a yet-unspecified body force. The system can

be considered on the torus $T^2 = [0, 2\pi] \times [0, 2\pi]$ by the periodic boundary conditions on a square region of side length 2π and assumed

$$\int_{T^2} vd^2x = 0, \quad \int_{T^2} fd^2x = 0.$$

Adopting the Fourier representations of v , p and f :

$$v(x) = \sum_{k \in Z^2, k \neq 0} v_k \exp(ik \cdot x), \quad p(x) = \sum_{k \in Z^2} p_k \exp(ik \cdot x),$$

$$f(x) = \sum_{k \in Z^2, k \neq 0} f_x \exp(ik \cdot x),$$

Equation (30) is transformed into an ODE system with some deduction. Taking R and the strength of forcing as the bifurcation parameters of the system, and applying the numerical methods to analyze the ODE system, the invariant sets and notably steady states was traced for varying R or strength of the imposed forcing respectively. For increasing strength of the forcing the system exhibits a rather complex sequence of bifurcations of steady states, travelling waves, periodic solutions and solutions on two-dimensional tori leading to chaos. The appearance of a chaotic attractor was verified by calculating the Lyapunov exponents, of which just one becomes positive. The results seem to confirm the Ruelle-Takens scenario for the transition to turbulence.

(3) The nonlinear axisymmetric mean-field dynamos in accretion disks was investigated in [21]. The evolution of a mean magnetic field B can be described by the $\alpha\Omega$ -dynamo equations:

$$B_t = \nabla_x(u \times B + \alpha B - \varphi_t u_0 J), \quad \nabla \cdot B = 0, \quad (31)$$

where u is the mean velocity, α describes the generation of the mean magnetic field through helical (cyclonic) turbulence, φ_t is the turbulent magnetic diffusivity u_0 the magnetic permeability of free space, and $J = \frac{\nabla \times B}{u_0}$ the mean electric current. Equation (31) is solved numerically in spherical polar coordinates so that the bifurcation sequences is found and the route to chaotic solutions is obtained in certain parameter regimes. The results show that the route to chaos is: *torus* T^2 (\rightarrow *torus* T^3) \rightarrow *chaos* $\rightarrow T^2 \rightarrow$ *chaos*. The Physical significance of these results was discussed.

(4) An excitable reaction-diffusion model describing the oxidation of CO on a $P_t(110)$ surface in one spatial dimension was studied in [22], and is reduced to FitzHugh-Nagumo type of equations as follows:

$$u_t = -\frac{1}{\varepsilon}u(u-1)\left(u - \frac{b+v}{a}\right) + u_{xx},$$

$$v_t = f(u) - v, \quad (32)$$

$$f(u) = \begin{cases} 0, & 0 \leq u < \frac{1}{3}, \\ 1 - 6.75u(u-1)^2, & \frac{1}{3} \leq u \leq 1, \\ 1, & 1 < u, \end{cases}$$

where u is the CO adsorbate coverage, and v the fraction of surface in the reconstructed 1-phase. The parameter in the system are $0 < a < 1, b > 0$, and $\varepsilon > 0$.

Similar to the discussion in [9] as mentioned in (1), with the substitution $z = x - ct$ the PDE (32) reduces to a dynamical system in R^3 , the travelling-wave ODE, with an additional parameter c (corresponding to the velocity).

$$u' = w,$$

$$w' = -cw + \frac{1}{\varepsilon}u(u-1)(u-u_{th}), \quad (33)$$

$$v' = \left(v - \frac{f(u)}{c} \right),$$

with $u_{th} = \frac{(b+v)}{c}$ and the prime denotes differentiation with respect to z . Because of the relationship between the solution of (32) and the solution of (33), and (33) is easily amenable to a systematic bifurcation study, a combination of analytical and numerical methods is applied to expose the dynamics of the system under some parameter conditions. The three equilibria of Eq. (33) (corresponding to the homogeneous fixed points of the Eq. (32)), and the limit cycles in Eq. (33) (corresponding to wavetrains in (32)) are driven. The homoclinic connections to the equilibria of Eq. (33) are found and hetroclinic cycle between the equilibria of Eq. (33) is formed. Two branches of homoclinic orbits in Eq. (33) (corresponding to solitary pulse solutions in Eq. (32)) originate from a codimension-Z global bifurcation. This bifurcation mediates a change in the dynamics of the excitable medium from a regime dominated by stable pulses and wavetrains travelling with constant shape and speed to spatiotemporally chaotic dynamics. Also, the spatial signature of a found branch of hetroclinic orbits in Eq. (33) (corresponding to fronts in Eq. (32)) is frequently observed locally as part of the spatiotemporally chaotic profiles obtained by direct numerical simulation.

A similar result is also given in [23].

Sometimes the numerical method is directly applied to PDEs to show the spatiotemporal chaos for the system, for example see [24].

2.5 Use decay mutual information to characterize spatiotemporal chaotic dynamics.

As stated in [25], as dealing with the damped NLS equation

$$i\psi_t + \psi_{xx} + 2|\psi|^2\psi = -i\alpha\psi + \Gamma e^{i(wt+r)}, \quad (34)$$

the working definition for spatiotemporal chaos is as follows: A wave $\psi(x, t)$ is spatiotemporal chaotic if

(1) $\psi(x, t)$ is a temporally chaotic orbit;

(2) the mutual information between two spatial points, $I(xy)$, decays exponentially in space as $|x - y| \rightarrow \infty$;

where

$$I(x, y) = \int dudv P_{xy}(u, v) \log \frac{P_{x,y}(u, v)}{P_x(u)P_y(v)},$$

in which the distributions $P_{x,y}(u, v)$, $P_x(u)$, and $P_y(v)$ are generated through time series $\{\psi(x, t), \forall t\}$ and $\{\psi(y, t), \forall t\}$.

After modifying the dispersion of the NLS equation to obtain a model system for which the number of unstable modes remains fixed while the domain size increases, it is shown in [25] that spatiotemporal chaos arises in the presence of only two unstable modes and characterized by chaotic dynamics in time and by an exponential decay in space of mutual information with the decay rate becoming system-size independent in the large system size limit.

Remark 1: The above discussion mostly concerns the discretization of PDEs that can be obtained in different methods and in various sense, such as “truncation,” “projection,” “along the special solution.” Despite which one is employed, a crucial problem to be solved is the topological equivalence between the flow on the global attractor of PDE and that of its discretization. In next section we are going to give some results on this problem in the discussion of controlling control for a kind of PDE motivated by [26].

3 Controlling chaos to a class of PDEs by applying invariant manifold and structure stability theory

Controlling chaos includes dual implications: control of chaos and anti-control of chaos (or called chaotification). The former means that the control is applying to eliminating chaos from a complex dynamical system when chaos is harmful and unwanted, the later means that the control is applying to generate or excite chaos which permits a system to explore its every dynamical possibility and provides the designer with an exciting variety of properties and richness of flexibility. In such case the new target state can be selected and take the place of old (undesirable) one which may be a stable state in original system. So, the later attracts much more interesting and attention recently.

For control of chaos there are quite systematical results (see [2] and [27]) for which many conventional control methods are adopted and effective. Especially, some of them are concerned with PDE systems. For examples:

(1) the control of chaos industry plasmas was discussed in [29] for the Alfvén systems. By means of Poincaré map analysis, it is shown that a small fraction of these charged dust grains can eliminate the chaos in the systems which are chaotic in the absence of dust particles.

(2) The synchronization of spatiotemporal chemical chaos for two uncoupled F-N type equations as given by (32) was studied using random signals in [30]. The synchronization is achieved not only for identical systems, but also for systems operating under unequal parameter values, exhibiting a different dynamical behavior.

(3) For conserved ZEs the spatiotemporal chaos that is caused by collisions and fusions among patterns with strong ion-sound emission was discussed in [31]. It may switch on the onset of weak turbulence in plasma.

(4) In [32] several mechanisms had been proposed to control the spatiotemporal chaos for CGLE. It is shown that how a nonlinear diffraction term stabilizes unstable polarized standing waves and linearly polarized travelling waves in a chaotic scenery. The similar subject are discussed in [2].

For anti-control of chaos, some significant results for discrete systems are presented in recent years (see [33] and references there in). But, it turns out that the continuous-time case is much more difficult and challenging, especially the PDE case.

Nevertheless, there have been some promising progress in the development of chaos anti-control for ODEs (see [34]- [36]).

In the following we are going to deal with a control systems by a kind of PDEs and present a method and procedure to reduce the PDE into ODEs motivated by [26] and [37], so that the PDE system may possess the expect dynamics given by the ODEs system. What we want to emphasis lies in the topological equivalence between the flow on the global attractor of PDE and that of ODEs by such method.

In such way the dynamical behavior of PDE under control, including bifurcation and chaos, can be exposed and redesigned via doing the same thing for ODEs provided the topological equivalence in the above sense is guaranteed.

Consider the following one dimensional scalar parabolic type control system:

$$\begin{aligned} u_t &= u_{xx} + f(u) + Bg, \quad 0 < x < 1, \quad t > 0, \\ u(0, x) &= u_0(x), \end{aligned} \tag{35}$$

with boundary condition

$$u_x(0) = u_x(1) = 0, \tag{36}$$

and observation equation

$$y(t) = Cu(t) = (u(\tilde{x}_j))_{j=1,\dots,l}, \tag{37}$$

where C is observation operator, and controller form

$$Bg = \sum_{i=1}^r g_i \psi_i(x), \quad (38)$$

where $g = (g_1, \dots, g_r)^T$ is control vector and B is control operator.

Let $X = L^2(0, 1)$ with the norm $\|\cdot\|$. It is well known that $-A$ is a sectorial operator, so we can define $|A^{\frac{1}{2}}u| = |Du| := \|u\|$ and $F : D(A^{\frac{1}{2}}) \subset X \rightarrow X$ by $F(\varphi)(x) = f(\varphi(x))$, and

$$A : D(A) \subset L^2(0, 1) \rightarrow L^2(0, 1),$$

$$D(A) = H_N^2(0, 1) = \{\varphi \in H^2(0, 1) : \varphi'(0) = \varphi'(1) = 0\},$$

$$A\varphi = -\varphi_{xx}.$$

The observation space and control space are set to be $Y \cong R^l$ and $G \cong R^r$ respectively, so operator C is a map from X to Y and operator B a map from G to X . The control is taken the output feedback form $g(y)$ which is determined by the purpose of design for the system, Of course, it can be written in state feedback form $\bar{g}(u) = g(Cu)$.

In such way we rewrite (35) as an evolution equation as follows:

$$\begin{aligned} u_t + Au &= F(u) + B\bar{g}(u) := \bar{F}(u) \\ u(0) &= u_0. \end{aligned} \quad (39)$$

Remark 2: The selection of operator C and B as (37) and (38) is adaptive to real-world applications. It is meant by (37) that the observation is taken at finite points in the interval $[0, 1]$ and easy to realize. The controller can be easy to construct by choosing the family of functions $\{\psi_i(x)\}$ which are so called switching pulse generator.

As the spatial discretization of (35) we consider the points

$$x_j = \frac{j - \frac{1}{2}}{m}, \quad j = 1, \dots, m, \quad (40)$$

and denote $u_j(t) = u(x_j, t)$. Then we have ODEs as follows:

$$\begin{aligned} \dot{u}_1 &= m^2(u_2 - u_1) + f(u_1) + B\bar{g}(u)(x_1), \\ \dot{u}_j &= m^2(u_{j-1} - 2u_j + u_{j+1}) + f(u_j) + B\bar{g}(u)(x_j), \\ \dot{u}_m &= m^2(u_{m-1} - u_m) + f(u_m) + B\bar{g}(u)(x_m). \end{aligned} \quad (41)$$

Note that the boundary conditions (36) have changed to $u_1 = u_0$ $u_{m+1} = u_m$ and have been incorporated with the linear operator L as follows.

Setting $U = (u, \dots, u_m)^T$ Eqs. (41) can be rewritten in a matrix form:

$$\dot{U} = -LU + \bar{f}(U), \quad (42)$$

where L is a $m \times m$ matrix given by

$$L = m^2 \begin{bmatrix} 1 & -1 & 0 & \dots & 0 & 0 & 0 \\ -1 & 2 & -1 & \dots & 0 & 0 & 0 \\ 0 & -1 & 2 & \dots & 0 & 0 & 0 \\ \vdots & \vdots & \vdots & \ddots & \vdots & \vdots & \vdots \\ \vdots & \vdots & \vdots & \ddots & \vdots & \vdots & \vdots \\ 0 & 0 & 0 & \dots & 2 & -1 & 0 \\ 0 & 0 & 0 & \dots & -1 & 2 & -1 \\ 0 & 0 & 0 & \dots & 0 & -1 & 1 \end{bmatrix},$$

which is symmetrical, and

$$\bar{f}(U) = (f(u_1) + B\bar{g}(u)(x_1), \dots, f(u_m) + B\bar{g}(u)(x_m))^T.$$

Assume that $f : R \rightarrow R$ is a C^2 function and

$$(f(u) + B\bar{g}(u))u < 0, \quad |u| > \xi, \quad (43)$$

for some constant ξ . Let $\lambda_0 < \lambda_1 < \lambda_2 \dots$ be the sequence of eigenvalues of A , where $\lambda_k = (k\pi)^2$ and $\varphi_0, \varphi_1, \dots$ a corresponding sequence of normalized eigenfunctions $\varphi_k(x) = \sqrt{2} \cos(k\pi x)$.

Now consider the following decomposition of $X = W \oplus W^\perp$ where

$$W = \text{span}[\varphi_0, \varphi_1, \dots, \varphi_{n-1}] := P_n x,$$

$$W^\perp = \{\varphi \in X : \langle \varphi, w \rangle = 0, \forall w \in W\} := Q_n x,$$

where $\langle \cdot, \cdot \rangle$ is the inner product of X .

Then $u \in X$ can be written as

$$u = \sum_{i=1}^n v_i \varphi_{i-1} + \bar{w},$$

where

$$v_i = \langle u, \varphi_{i-1} \rangle = \int_0^1 u(x) \varphi_{i-1}(x) dx, \quad i = 1, \dots, n.$$

Let u be a solution of (39), then for each t we can write

$$u(x, t) = \sum_{i=1}^n v_i(t) \varphi_{i-1}(x) + \bar{w}(x, t) := \bar{v}(x, t) + \bar{w}(x, t)$$

and

$$\dot{v}_i = -\lambda_{i-1} v_i + \langle \bar{F}(u), \varphi_{i-1} \rangle,$$

$$\bar{w}_t + A_w \bar{w} = \bar{F}(u) - \sum_{i=0}^{n-1} \langle \bar{F}(u), \varphi_i \rangle \varphi_i,$$

where A_W denotes $A|_{D(A) \cap W^\perp}$.

Writing $v = (v_1, v_2, \dots, v_n)$, $w = (w_{n+1}, w_{n+2}, \dots)$ where $w_i = \langle \bar{w}, \varphi_{i-1} \rangle$, $i = n+1, \dots$, $u = (v, w)$ and B_n a $n \times n$ diagonal matrix $B_n = \text{diag}(\lambda_0, \lambda_1, \dots, \lambda_{n-1})$ and $A_n = \text{diag}(\lambda_{n+1}, \lambda_{n+2}, \dots)$, we obtain the following system:

$$\begin{aligned} \dot{v} + B_n v &= h_n(v, w) \\ w_t + A_n w &= f_n(v, w), \end{aligned} \tag{44}$$

where $h_n(v, w) = (\langle \bar{F}(\bar{v}, \bar{w}), \varphi_0 \rangle, \dots, \langle \bar{F}(\bar{v}, \bar{w}), \varphi_{n-1} \rangle)^T$ and $f_n(v, w) = (\langle \bar{F}(\bar{v}, \bar{w}), \varphi_n \rangle, \langle \bar{F}(\bar{v}, \bar{w}), \varphi_{n+1} \rangle, \dots)$.

Similarly (see [26]), the eigenvalues of L are given by $\lambda_k^m = 4m^2 \sin^2 \frac{k\pi}{2m}$ and associated eigenvectors are $w_k^m = (\cos k\pi x_1, \dots, \cos k\pi x_m)$ for $k = 0, \dots, m-1$. We define in R^m the inner product: $\langle x, y \rangle = \frac{1}{m} \sum_{i=1}^m x_i y_i$ for $x = (x_1, \dots, x_m)^T$, $y = (y_1, \dots, y_m)^T$ which is referred as discretized L^2 inner product. Normalizing w_k^m according to this inner product we obtain

$$\bar{e}_k^m = \frac{w_k^m}{\|w_k^m\|} = \frac{(\cos k\pi x_1, \dots, \cos k\pi x_m)}{\sqrt{\frac{1}{m} \sum_{i=1}^m \cos^2 k\pi x_i}}. \tag{45}$$

Set

$$\bar{e}_k^m(x) = \frac{\sum_{i=1}^m \cos k\pi x_i \cdot \chi_{I_i}(x)}{\sqrt{\frac{1}{m} \sum_{i=1}^m \cos^2 k\pi x_i}},$$

where $I_i = [\frac{i-1}{m}, \frac{i}{m}]$ we obtain that $\bar{e}_k^m \in L^\infty(0, 1)$ and

$$\|\bar{e}_k^m(x) - \sqrt{2} \cos k\pi x\|_\infty \rightarrow 0, \quad \text{as } m \rightarrow \infty. \tag{46}$$

Instead of usual basis $\{e_k^m\}_{k=0, \dots, m-1}$ we take $\{\bar{e}_k^m\}_{k=0, \dots, m-1}$ as the new coordinates. Denote the K -th coordinate of \bar{e}_j^m by \bar{e}_{jk}^m and the transform matrix between $\{e_k^m\}_{k=0, \dots, m-1}$ and $\{\bar{e}_k^m\}_{k=0, \dots, m-1}$ by $Z = \{z_{kj}\}$. We have $z_{kj} = \bar{e}_{j-1,k}^m$ and $Z^{-1} = \frac{1}{m} Z^T$. In this new coordinates (42) becomes

$$\dot{v} = -\tilde{L}v + Q(v), \tag{47}$$

where $v = (v_1, \dots, v_m)$ and $v_i = (v, \bar{e}_{i-1}^m)$ $i = 1, \dots, m$, and \tilde{L} is the $m \times m$ matrix given by $\tilde{L} = \text{disag}(\lambda_0^m, \dots, \lambda_{m-1}^m)$, and $Q(v) = (Q_1(v), \dots, Q_m(v))^T$ with each $Q_j(v)$ given by

$$Q_j(v) = \langle \bar{f}(U), \bar{e}_{j-1}^m \rangle = \sum_{k=1}^m \frac{1}{m} \bar{e}_{j-1,k}^m \bar{f} \left(\sum_{i=0}^{m-1} \bar{e}_{i,k}^m v_{i+1} \right),$$

since $U = Z^T v$.

Similarly, consider the following decomposition of $R^m = R^n \oplus R^{n^3-n}$ with $m = n^3$, where

$$R_n = \text{span}[\bar{e}_0^{n^3}, \dots, \bar{e}_{n-1}^{n^3}],$$

$$R^{n^3-n} = \text{span}[\bar{e}_n^{n^3}, \dots, \bar{e}_{n^3-1}^{n^3}],$$

with this decomposition we obtain the following weakly coupled system

$$\begin{aligned} \dot{v}_n + \tilde{B}_n v_n &= \tilde{h}_n(v_n, w_n) \\ \dot{w}_n + \tilde{A}_n w_n &= \tilde{f}_n(v_n, w_n), \end{aligned} \quad (48)$$

where $\tilde{B}_n = \text{diag}(\lambda_0^{n^3}, \dots, \lambda_{n-1}^{n^3})$, $\tilde{A}_n = \text{diag}(\lambda_n^{n^3}, \dots, \lambda_{n^3-1}^{n^3})$, $\tilde{h}_n(v_n, w_n) = (Q_1(v_n, w_n), \dots, Q_n(v_n, w_n))^T$, and $\tilde{f}_n(v_n, w_n) = (Q_{n+1}(v_n, w_n), \dots, Q_{n^3}(v_n, w_n))^T$.

To obtain the topological equivalence between the flow on the global attractor of infinite dimensional system (44) (i.e., (39)) and that of finite dimensional system (48) (i.e., (42)), we have to give the form of $g(y)$ which is associated with the operators B and C . So, we firstly discuss the properties of B and C .

Let $r = n^2$ and $\psi_i(x)$ is given by

$$\psi_i(x) = \begin{cases} (x - \bar{x}_{i-1})/\bar{h}, & x \in [\bar{x}_{i-1}, \bar{x}_i) \\ (\bar{x}_{i+1} - x)/\bar{h}, & x \in [\bar{x}_i, \bar{x}_{i+1}) \\ 0 & i = 1, \dots, r, \end{cases} \quad (49)$$

with $0 = \bar{x}_0 < \bar{x}_1 < \dots < \bar{x}_i < \dots < \bar{x}_r < \bar{x}_{r+1} = 1$ where $\bar{h} = \frac{1}{n^2+1} = \bar{x}_i - \bar{x}_{i-1}$, $i = 1, \dots, r+1$. Similarly, let $l = n^4$, $0 = \tilde{x}_0 < \tilde{x}_1 < \dots < \tilde{x}_i < \dots < \tilde{x}_l < \tilde{x}_{l+1} = 1$ and $\tilde{h} = \frac{1}{n^4+1} = \tilde{x}_i - \tilde{x}_{i-1}$, $i = 1, \dots, l+1$.

We endow G and Y with the norms given by

$$\|g\|_G^2 = \sum_{i=1}^r \frac{|g_i - g_{i-1}|^2}{\bar{h}}, \quad \forall g \in G,$$

with $g_0 = g_{r+1} = 0$, and

$$\|y\|_Y^2 = \sum_{i=1}^l \frac{|y_i - y_{i-1}|^2}{\tilde{h}}, \quad \forall y \in Y,$$

with $y_0 = y_{l+1} = 0$.

Let $D(A^{\frac{1}{2}}) = E$, $P_n E = P_n X \cap D(A^{\frac{1}{2}})$. By the results in [37] we have

$$\|B\|_{L(G, E)} = 1, \quad \|C\|_{L(E, X)} = 1, \quad (50)$$

and

$$\|(CP_m)^{-1}\|_{L(Y,E)} \leq \sqrt{\frac{2}{1 - 2\tilde{h}^2\lambda_m}} \leq \sqrt{\frac{2}{1 - \frac{2\pi^2}{n^2}}}, \quad (51)$$

where $CP_m : P_m E \rightarrow CP_m E \subset Y$ and $(CP_m)^{-1} : Y \rightarrow P_m E \subset E$, and

$$\|(P_n B)^{-1}\|_{L(P_n E, G)} \leq \sqrt{\frac{1}{1 - 2\bar{h}^2\lambda_n}} \leq \sqrt{\frac{1}{1 - \frac{2\pi^2}{n^2}}}, \quad (52)$$

where $P_n B : G \rightarrow P_n E$ and $(P_n B)^{-1} : P_n E \rightarrow G$.

Let $N : P_n E \rightarrow P_n E$ and function N defined by $N(\varphi(x)) = N(\varphi)(x) \forall \varphi \in P_n E$. Assume that $N : R \rightarrow R$ is a C^2 function. By this assumption N is Lipschitz continuous in bounded subset of $P_n E$, i.e.,

$$|N(u) - N(v)| \leq L_N \|u - v\|, \quad \forall u, v \in P_n E, \quad (53)$$

where $L_N (> 0)$ is the local Lipschitz constant. Similarly, by the conditions imposed on f , we have

$$|F(u) - F(v)| \leq L_F \|u - v\|, \quad \forall u, v \in E, \quad (54)$$

where $L_F (> 0)$ is the local Lipschitz constant.

Now define $g : Y \rightarrow G$ by

$$g(y) = (P_n B)^{-1} N(P_n (CP_m)^{-1} y), \quad (55)$$

and one can see that g is Lipschitz continuous with

$$Lip(g) \leq 4L_N \quad (56)$$

by (51)-(53).

Assume that N is chosen such that the dissipativeness condition (43) holds.

Hence systems (39) and (42) have absorbing set E_η and R_η^m , and global attractor \mathcal{A}_n and \mathcal{A} respectively (see the relative results in [15]):

$$\begin{aligned} E_\eta &= \{u \in E : \|u\| \leq \eta\}, \\ R_\eta^m &= \{v \in R^m : |v_i| \leq \eta, 1 \leq i \leq m\}, \\ \mathcal{A}_n &\subset R_\eta^m, \quad \mathcal{A} \subset E_\eta, \end{aligned} \quad (57)$$

which implies

$$\sup_{u \in A} \sup_{x \in [0,1]} |u(x)| \leq \xi, \quad (58)$$

for some constant ξ .

The above bound allow as to discuss the problem restricted in R_η^m and E_η and to cut the nonlinearity f and N in such way that L_N and L_F become global Lipschitz constants, and

$$\begin{aligned} \|DF(u) - DF(v)\|_{L(E)} &\leq M\|u - v\|^2, \quad \forall u, v \in E \\ |DN(u) - DN(v)|_{L(E)} &\leq M'\|u - v\|^\nu, \quad \forall u, v \in P_n E, \end{aligned} \tag{59}$$

where $0 < \nu \leq 1$, and

$$\|F(u)\| \leq M_F, \quad \forall u \in E, \quad \|N(u)\| \leq M_N, \quad \forall u \in P_n E. \tag{60}$$

Sine f and N possess bounded first and second derivative. Also we can set $M_F = \|f\|_\infty$, $M_N = \|N\|_\infty$. Note that

$$\begin{aligned} \lambda_n^{n^3} - \lambda_{n-1}^{n^3} &= 2n + 1, \quad \text{for (9.3.14)} \\ \lambda_n - \lambda_{n-1} &= (2n + 1)\pi^2, \quad \text{for (9.3.10).} \end{aligned} \tag{61}$$

We can apply the lemma given in Appendix to (48) and (44) with $L_f = L_g = L_F$, $N_f = N_g = M_F$, $\beta_n = \lambda_n^{n^3}$ (or λ_n), and $\rho_n = \lambda_{n-1}^{n^3}$ (or λ_{n-1}) to obtain that for n sufficiently large we have

(1) system (48) possesses a invariant manifold

$$M_n = \{(v_n, w_n) \in R^{n^3} : w_n = \tilde{\sigma}(v_n)\},$$

which is exponentially attracting where $\tilde{\sigma}_n : R^n \rightarrow R^{n^3-n}$ is smooth function with the properties presented in the lemma. The flux on M_n is given by $v(t) = v_n(t) + \tilde{\sigma}_n(v_n(t))$ where $v_n(t)$ is the solution of

$$\dot{v}_n + \tilde{B}v_n = \tilde{h}_n(v_n, \tilde{\sigma}_n(v_n)). \tag{62}$$

In fact, M_n is a C^1 inertial manifold.

(2) system (44) possesses C^1 inertial manifold S_n . The flux on S_n is given by $(v(t), \sigma_n(v(t)))$ where v is the solution of

$$\dot{v} + B_nv = h_n(v, \sigma_n(v)), \tag{63}$$

where $\sigma_n(v)$ satisfies the properties given in the lemma.

As a matter of fact it follows from (54)-(56) and (61) that the spectral gap condition can be verified so that system (39) possesses a C^1 manifold with the smoothness of nonlinear term taken into account (see the relative results in [15]). The manifold can be described by a graph of C^1 function $\Phi : P_n E \rightarrow Q_n E : p \rightarrow \Phi(p)$. As compared with (63) we have

$$p = \sum_{i=1}^n v_i \varphi_{i-1}, \quad \sigma_n(v) = (\langle \Phi(p), \varphi_n \rangle, \langle \Phi(p), \varphi_{n+1} \rangle, \dots). \tag{64}$$

So, the inertial form of system (39) is as follows:

$$p_t + Ap = P_n F(p + \Phi(p)) + P_n Bg(CP + \Phi(p)), \quad (65)$$

which corresponding to (63).

To obtain the expression of the system (39) under the output feedback control $Bg(y)$ we shall also consider the following m -dimensional auxiliary equation:

$$z_t + Az = P_m F(P_m z) + P_m Bg(CP_m z). \quad (66)$$

Denote the inertial manifold of system (56) by the graph of C^1 function $\psi : P_n E \rightarrow Q_n E$, and let the corresponding inertial form be as follows:

$$\rho_t + A\rho = P_n F(P_m(\rho + \psi(p))) + P_n Bg(CP_m(\rho + \psi(p))). \quad (67)$$

Substituting $g(y)$ given by (55) into (67) we have

$$\rho_t + A\rho = P_n F(P_m(\rho + \psi(\rho))) + N(\rho). \quad (68)$$

Concerning the (65) we can write it as

$$p_t + Ap = P_n F(p + \Phi(p)) + N(p) + E(p), \quad (69)$$

where

$$\begin{aligned} E(p) &= P_n F(p + \Phi(p)) + P_n Bg(C(p + \Phi(p))) \\ &\quad - P_n F(p + P_m \psi(p)) - B_n Bg(C(p + P_m \psi(p))) \end{aligned} \quad (70)$$

and it is estimated in [15] as given by

$$\|E(\rho)\| \leq \frac{1}{m\pi} (\alpha_1 + \alpha_2 \|p\|), \quad \forall p \in P_n E, \quad (71)$$

$$\|DE(\rho)\|_{L(P_n E)} \leq \frac{\alpha_3}{m\pi} + \frac{\alpha_4}{m^\nu \pi^\nu}, \quad \forall p \in P_n E, \quad (72)$$

where α_i ($i = 1, 2, 3, 4$) are constants, α_i ($i = 1, 2, 3$) depend on n, L_M, L_N, M_0, M'_0 , and α_4 depends on $n, L_M, L_N, M, M', M_0, M'_0$ where $M_0 = \|F(0)\|$, $M'_0 = \|N(0)\|$. According to (70) E is Lipschitz and $\|E\|_\infty$ makes sense.

To prove the flow of (39) on the attractor \mathcal{A} and the flow of (42) on \mathcal{A}_n are topologically equivalent we have to show that

(1) $\lambda_K^{n^3}$ and λ_K ($K = 0, \dots, n-1$), and $h_n(v, \sigma(v))$ and $\tilde{h}_n(v, \tilde{\sigma}_n(v))$ are C^1 close where $v = (v_1, v_2, \dots, v_n)$;

(2) the flow on \mathcal{A} is structurally stable;

First of all, we have [26]

$$|\lambda_K^{n^3} - \lambda_K| \leq (n\pi)^2 \left| \frac{2}{3!} \left(\frac{\pi}{2n^2} \right)^2 + o\left(\left(\frac{1}{n^2} \right)^3 \right) \right| = o\left(\frac{1}{n} \right), \quad K = 0, \dots, n-1,$$

so $|\lambda_K^{n^3} - \lambda_K| \rightarrow o$ for all $K = 0, \dots, n-1$ uniformly as $n \rightarrow \infty$. For $x \in [\frac{j-1}{n^3}, \frac{j}{n^3}]$ we have that

$$|\cos(K\pi x) - \cos(K\pi x_j)| \leq \frac{K\pi}{2n^3}, \quad K = 0, \dots, n-1,$$

so that

$$|\cos(K\pi x) - \cos(K\pi x_j)| \leq \frac{\pi}{2n^2},$$

for all $K = 0, \dots, n-1$ and $j = 1, \dots, n^3$. Hence,

$$\|\nu_K^{n^3}(x) - \sqrt{2}\cos(K\pi x)\|_\infty \leq \frac{c}{n^2}. \quad (73)$$

Note that

$$\begin{aligned} \|h_n(v, \sigma_n(v)) - \tilde{h}_n(v, \tilde{\sigma}_n(v))\| &\leq \|h_n(v, \sigma_n(v)) - h_n(v, o)\| \\ &+ \|h_n(v, o) - \tilde{h}_n(v, o)\| + \|\tilde{h}_n(v, o) - \tilde{h}_n(v, \tilde{\sigma}_n(v))\|, \end{aligned} \quad (74)$$

and denote by \tilde{h}_n^j and h_n^j the j th coordinate function of \tilde{h}_n and h_n respectively.

In the presence we have

$$\begin{aligned} \tilde{h}_n^j(v, o) &= \sum_{k=1}^{n^3} \frac{1}{n^3} \bar{e}_{g-1, K}^{n^3} \left[f \left(\sum_{l=1}^n \bar{e}_{l-1, K}^{n^3} v_l \right) \right. \\ &+ N \left(\frac{1}{n^3} \sum_{l=1}^n \bar{e}_{l-1, K}^{n^3} \left(\sum_{r=1}^m \bar{e}_{l, r-1}^{n^3} \sum_{i=1}^n v_i \sqrt{2} \cos \pi(i-1)x_r \right) \right) \left. \right] \\ &+ E \left(\frac{1}{n^3} \sum_{l=1}^n \bar{e}_{l-1, K}^{n^3} \left(\sum_{r=1}^m \bar{e}_{l, r-1}^{n^3} \sum_{i=1}^n v_i \sqrt{2} \cos \pi(i-1)x_r \right) \right) \\ h_n^j(v, o) &= \int_0^1 \left[f \left(\sum_{l=1}^n v_l \sqrt{2} \cos(l-1)\pi x \right) + N \left(\sum_{l=1}^n v_l \sqrt{2} \cos(l-1)\pi x \right) \right. \\ &+ E \left(\sum_{l=1}^n v_l \sqrt{2} \cos(l-1)\pi x \right) \left. \right] \sqrt{2} \cos(j-1)\pi x dx. \end{aligned}$$

Note that

$$\sum_{k=1}^{n^3} \bigcirc - \int_0^1 \Delta dx = \sum_{k=1}^{n^3} \int_{\frac{(k-1)}{n^3}}^{\frac{k}{n^3}} (\bigcirc - \Delta) dx.$$

So, it is not difficult to show that

$$|h_n^j(v, o) - \tilde{h}_n^j(v, o)| \leq C_1(M_F + M_N) \frac{C}{n^3} + (L_f + L_N + L_E) \frac{C_2 \sqrt{2}}{n^2} \sum_{l=1}^n |v_l|$$

by (73) and preceding results in this section. Therefore by (74) we have

$$\begin{aligned} \|h_n(v, \sigma_n(v)) - \tilde{h}_n(v, \tilde{\sigma}_n(v))\| &\leq (L_f + L_N + L_E)(\|\sigma_n(v)\| + \|\tilde{\sigma}_n(v)\|) \\ &+ \frac{1}{\sqrt{n}} \left[C_1(M_F + M_N) \frac{C}{n} + (L_f + L_N + L_E)\eta C \sqrt{2} \right], \end{aligned}$$

where η is as in (57). Since by lemma in Appendix $\|\sigma_n\| \rightarrow 0$ and $\|\tilde{\sigma}_n\| \rightarrow 0$ as $n \rightarrow \infty$ then

$$\|h_n(v, \sigma_n(v)) - \tilde{h}_n(v, \tilde{\sigma}_n(v))\| \rightarrow 0 \quad \text{as } n \rightarrow \infty.$$

Similarly using the fact that f' , N' and E' are globally Lipschitz, $\|D\sigma_n\| \rightarrow 0$ and $\|D\tilde{\sigma}_n\| \rightarrow 0$ as $n \rightarrow \infty$. So we have shown the functions $h_n(v, \sigma_n(v))$ and $\tilde{h}_n(v, \tilde{\sigma}_n(v))$ are C^1 closed, i.e., ((44),(39)) is a C^1 small perturbation of ((48),(42)).

As concerns structurally stable on \mathcal{A} we note that (39) is generically Morse-Smale under our assumptions and so the structural stability on \mathcal{A} can be deduced to the class of maps f and N under consideration (see [38] and [39]) with (71) and (72) taken account.

Summarize the above results we obtain a theorem as follows:

Theorem: Let $f, N \in C^2(R, R)$ and the output feedback control as given by (37), (38), (49) and (55), such that (43) holds. Then for n (so is m, l, r) large enough the flow of (39) on the attractor \mathcal{A} and the flow of (42) on \mathcal{A}_n are topologically equivalent.

Remark 3: The theorem means that the dynamics on \mathcal{A} is completely described by the dynamics on \mathcal{A}_n provided the restricted conditions on f and N given in the theorem are satisfied and n, m, l, r are large enough. In this case if N is chosen such that system (42) possesses a chaotic attractor A_n then so is \mathcal{A} for (39).

Remark 4: The word “ n, m, l, r are large enough” has quantitative description: n is chosen such that the spectral gap condition holds, and $m = n^3$, $l = n^4$, $r = n^2$ determined in this section. They give the number of partition points on $[0,1]$, observation points, and switching pulse generators respectively in the real-world applications. Of course, they can be more accurately estimated.

Remark 6: Sometimes for the dissipativeness condition to be held f, N has to be strong dissipative with the dissipative constant satisfying some conditions relative to the constants in (71) and (72).

Remark 7: Equation (42) as the spatial discretization of Eq. (35) is different from the discretization of Eq. (39) by Galerkin method. The former is more suitable for analysis and computation because it is “really” a ODE systems and it is not necessary to know the explicit expression of inertial manifold of PDE. So, something may be easier to do, say for the computation of Lyapunov exponents.

Appendix

Lemma [26] Let X_n and Y_n be a sequence Banach spaces, $A_n : D(A_n) \subset X_n \rightarrow X_n$ be a sequence of sectorial operators and $B_n : D(B_n) \subset Y_n \rightarrow Y_n$ be a sequence of generators of C^0 groups of bounded linear operators. Suppose that $f_n : X_n^\alpha \times Y_n^\alpha \rightarrow X_n$ and $g_n : X_n^\alpha \times Y_n^\alpha \rightarrow Y_n$ are a sequence of functions satisfying:

$$\|f_n(x, y) - f_n(z, w)\|_{X_n} \leq L_f(\|x - z\|_{X_n^\alpha} + \|y - w\|_{Y_n^\alpha}),$$

$$\|f_n(x, y)\|_{X_n} \leq N_f,$$

for every $(x, y), (z, w)$ in $X_n^\alpha \times Y_n^\alpha$ and

$$\|g_n(x, y) - g_n(z, w)\|_{Y_n} \leq L_g(\|x - z\|_{X_n^2} + \|y - w\|_{Y_n^2}),$$

$$\|g_n(x, y)\|_{Y_n} \leq N_g,$$

for every $(x, y), (z, w)$ in $X_n^\alpha \times Y_n^\alpha$ and

$$\|e^{-A_n t} w\|_{X_n^2} \leq M_a e^{-\beta(n)t} \|w\|_{X_n^\alpha}, \quad t \geq 0,$$

$$\|e^{-A_n t} w\|_{X_n^2} \leq M_a t^{-\alpha} e^{-\beta(n)t} \|w\|_{X_n}, \quad t > 0,$$

$$\|e^{-B_n t} z\|_{Y_n^2} = \|e^{B_n(-t)} z\|_{Y_n^2} \leq M_b e^{-\rho(n)t} \|z\|_{Y_n^\alpha}, \quad t \geq 0,$$

$$\|e^{-B_n t} z\| \leq M_b (-t)^{-\alpha} e^{-\rho(n)t} \|z\|_{Y_n}, \quad t < 0$$

for any $w \in X_n^\alpha$ and $z \in Y_n$, where $\beta(n) - \rho(n) \rightarrow +\infty$ as $n \rightarrow \infty$. Consider the weakly coupled system:

$$\begin{cases} \dot{x} = -A_n x + f_n(x, y), \\ \dot{y} = -B_n y + g_n(x, y). \end{cases} \quad (75)$$

Then for n large enough, there is an exponentially attracting invariant manifold for (75):

$$S = \{(x, y) : x = \sigma_n(y), y \in Y_n^\alpha\},$$

where $\sigma_n : Y_n^\alpha \rightarrow X_n^\alpha$ satisfies

$$s(n) = \sup_{\{y \in Y_n^\alpha\}} \|\sigma_n(y)\|_{X_n^\alpha},$$

$$\|\sigma_n(y) - \sigma_n(z)\|_{X_n^\alpha} \leq l(n) \|y - z\|_{X_n^\alpha},$$

with $s(n), l(n) \rightarrow 0$ when $n \rightarrow \infty$. If f_n, g_n are smooth, then, σ_n is smooth and its derivative $D\sigma_n$ satisfy

$$\sup_{y \in Y_n} \|D\sigma_n(y)\|_{L(Y_n^\alpha, X_n^\alpha)} \leq l(n).$$

Acknowledgement.

This project was partly supported by the Foundation of Zhongshan University Advanced Research Centre and the National Science Foundation of China and Guangdong Province of China (021765).

References

1. Bartuccelli, M., Constantin, P., Doering, C., Ginibon, J. D., Gissel-fält, M. (1990) On the possibility of soft and hard turbulence in the complex Ginzburg-Landau equation. *Physica D*, **44**:421–444
2. Hu, G., Xiao, J., Zheng, Z. (2000) Chaos Control. (in Chinese) Advanced Series in Nonlinear Science, Shanghai Scientific and Technological Education Publishing House, Shanghai, China
3. Kahan, S., Montagne, R. (2001) Controlling spatio-temporal chaos. *Physica A*, **290**:87–91
4. Jolly, M.S., Témam, R., Xiong, C. (1995) Convergence of a chaotic attractors with increased spatial resolution of Ginzburg-Landau equation. *Chaos, Solitons & Fractals*, **10**(5):1833–1845
5. Li, Y., McLaughlin, D. W., Shatah, J., Wiggins, S. (1996) Persistent homoclinic orbits for a perturbed nonlinear Schrödinger equation. *Comm. Pure Appl. Math*, **XLIX**:1175–1255
6. Zeng, C. (2000) Homoclinic orbits for perturbed nonlinear Schrödinger equation. *Comm. Pure Appl. Math*, **LIII**:1222–1283
7. Li, Y., McLaughlin, D. W. (1997) Homoclinic orbits and chaos in discretized perturbed NLS system: Part I. Homoclinic orbits. *J. Nonlinear Sci.*, **7**:211–269
8. Li, Y., Wiggins, S. (1997) Homoclinic orbits and chaos in discretized perturbed NLS system: Part II. Symbolic dynamics. *J. Nonlinear Sci.*, **7**:315–370
9. McLaughlin, D. W., Overman, E. A., Wiggins, S., Xiong, C. (1996) Homoclinic orbits in a four dimensional model of a perturbed NLS equation: A geometric singular perturbation study. In *Dynamics Reported*, **5**, Berlin: Springer, 190–287
10. Shibata, H. (1999) Lyapunov exponent of partial differential equation. *Physica A*, **264**:226–233
11. Albeverio, S., Nizhnik, I. L. (2001) Spatial chaos in a fourth-order nonlinear parabolic equation. *Phys. Lett. A*, **288**:299–304
12. He, X. T., Zheng, C. Y., Zhu, S. P. (2000) Pattern dynamics and spatiotemporal chaos in the conserved Zakharov equations. *Physica A*, **288**:338–343
13. Shibata, H. (1998) Quantitative characterization of spatiotemporal patterns II. *Physica A*, **260**:374–380
14. Dieci, L., Russell, R. D., Van Vleck, E. S. (1997) On the computation of Lyapunov exponents for continuous dynamical systems. *SIAM J. Numer. Anal.*, **34**(1):402–423
15. Témam, R. (1997) Infinte Simensional Dynamical Systems in Mechanics and Physics, Applied Mathematical Sciences, **68**, 2nd ed. New York: Springer-Verlag
16. Lai, H. Y., Chen, C. K., Yeh, Y. L. (2002) Double-mode modeling of chaotic and bifurcation dynamics for a simply supported rectangular plate in large deflection. *Int. J. Non-linear Mechanics*, **37**:331–343

17. Yeh, Y. L., Chen, C. K., Lai, H. Y. (2002) Chaotic and bifurcation dynamics for a simply supported rectangular plate of thermo-mechanical coupling in large deflection. *Chaos, Solitons & Fractals*, **13**:1493–1506
18. Robinsion, C. (1998) *Dynamical Systems – Stability, Symbolic Dynamics, and Chaos*. 2nd ed. Boca Raton, FL: CRC Press
19. Menke, C. (2000) A parameter study of epitaxial crystal growth. *Chaos, Solitons & Fractals*, **11**:841–852
20. Feudel, F., Seehafer, N. (1995) On the bifurcation phenomena in truncations of the 2D Navier-Stokes equations. *Chaos, Solitons & Fractals*, **5**(10):1805–1816
21. Torkelsson, U., Brandenburg, A. (1995) Chaos in accretion disk dynamos? *Chaos, Solitons & Fractals*, **5**(10):1975–1984
22. Zimmermann, M.G., et al. (1997) Pulse bifurcation and transition to spatiotemporal chaos in an excitable reaction-diffusion model. *Physica D*, **110**:92–104
23. Krishnan, J., et al. (1999) Numerical bifurcation and stability analysis of solitary pulses in an excitable reaction-diffusion medium. *Computer Methods in Applied Mechanics and Engineering*, **170**:253–275
24. Ito, H., Ueda, Y. (2001) Emergence of a multi domain regime and spatiotemporal chaos in Gunn diodes under impact ionization conditions. *Phys. Lett. A*, **280**:312–317
25. Cai, D., McLaughlin, D. W., Shatah, J. (2001) Spatiotemporal chaos in spatially extended systems. *Mathematics and Computers in Simulation*, **55**:329–340
26. Bruschi, S. M., Carvalho, A. N., Ruasfilho, J. G. (2000) The dynamics of a one-dimensional parabolic problem versus the dynamics of its discretization, *J. Diff. Eqs.*, **168**:67–92
27. Lakshmanan, M., Murali, K. (1996) *Chaos in Nonlinear Oscillators – Controlling and Synchronization*. Singapore: World Scientific
28. Chen, G. (ed.) (1999) *Controlling Chaos and Bifurcations in Engineering Systems*. Boca Raton, FL: CRC Press
29. Buti, B. (1997) Control of chaos in dusty plasmas. *Phys. Lett. A*, **235**:241–247
30. Parmananda, P., Jiang, Y. (1998) Synchronization of spatiotemporal chemical chaos using random signals. *Phys. Lett. A*, **241**:173–178
31. He, X. T., Zheng, C. Y., Zhu, S. P. (2000) Pattern dynamics and spatiotemporal chaos in the conserved Zakharov equations. *Physica A*, **288**:338–343
32. Kahan, S., Montagne, R. (2001) Controlling spatio-temporal chaos. *Physica A*, **290**:87–91
33. Wang, X. F., Chen, G. (2000) Chaotification via arbitrarily small feedback controls. *Int. J. Bifur. Chaos*, **10**:549–570
34. Tang, K. S., Man, K. F., Zhong, G. Q., Chen, G. (2001) Generating chaos via $x|x|$. *IEEE Trans. Circ. Syst.-I*, **48**:636–641
35. Zhong, G. Q., Man, K. F., Chen, G. (2001) Generating chaos via a dynamical controller. *Int. J. Bifur. Chaos*, **11**:865–869
36. Yang, L. B., Yang, T. (2000) Sampled-data feedback control for Chen's chaotic system. (in Chinese) *ACTA Physica Sinica*, **49**:1039–1042
37. Rosa, R., Témam, R. (1997) Finite-dimensional feedback control of a scalar reaction-diffusion equation via inertial manifold theory. In *Foundations of Computational Mathematics* (Rio de Janerio, 1997), Berlin: Springer, 382–291
38. Henry, D. B. (1985) Some infinite-dimensional Morse-Smale systems defined by parabolic partial differential equations. *J. Diff. Eqs.*, **59**:165–205
39. Lu, K. (1994) Structural stability for scalar parabolic equations. *J. Diff. Eqs.*, **114**:253–271

Chaotic Systems Synchronization

Johan Suykens, Mustak Yalçın, and Joos Vandewalle

Katholieke Universiteit Leuven

Department of Electrical Engineering (ESAT), SCD-SISTA

Kasteelpark Arenberg 10, B-3001, Heverlee (Leuven), Belgium

{johan.suykens, mey, joos.vandewalle}@esat.kuleuven.ac.be

Abstract. In this chapter a systematic overview is given of methods for chaotic systems synchronization in the case of Lur'e systems. For autonomous schemes the link with absolute stability theory is emphasized and robust synchronization is discussed. For non-autonomous schemes nonlinear H_∞ synchronization is explained. Criteria for schemes with time delay are given which can be either delay-independent or delay-dependent. Impulsive synchronization is discussed for state and dynamic measurement feedback. Sufficient conditions for global synchronization are expressed in terms of matrix inequalities and are illustrated on a number of examples.

1 Introduction

Synchronization of chaotic systems [25] has received a lot of attention in recent years since the early work by Pecora and Carroll [24] on synchronization phenomena of chaotic systems and its application to secure communications. Over the last decade, several synchronization schemes have been proposed, but often in an ad hoc way. In the early stage, several specific systems were investigated such as Lorenz attractor and Chua's circuit. Later, methods for analysis and design of synchronization schemes became developed in a more systematic way and for classes of nonlinear systems. The link was made between synchronization and absolute stability theory of Lur'e systems [27, 28] and with observer design in [20, 23]. Synchronization theory was brought to the attention of the systems and control community for example in [1, 13, 22].

In this chapter we discuss chaotic systems synchronization methods for the class of Lur'e systems. Lur'e systems consist of a linear dynamical system interconnected by feedback to a nonlinearity that satisfies a sector condition [14, 16, 21, 38]. Several chaotic and hyperchaotic systems including Chua circuit [6, 7], n -scroll circuits [29], coupled Chua circuits [12] and others are representable in Lur'e form. Families of chaotic and hyperchaotic Lur'e systems have been described in [34]. Synchronization of master-slave systems without external input (autonomous case) is discussed by analyzing global asymptotic stability of the error system. Especially for the class of Lur'e system, the synchronization problem is explicitly linked to the absolute stability problem of Lur'e systems.

The study of absolute stability dates back from classical nonlinear control theory with fundamental contributions such as the circle criterion and the Popov criterion, corresponding to a quadratic and Lur'e-Postnikov Lyapunov function, respectively. The criteria can be either expressed in terms of matrix inequalities or frequency domain criteria by applying the well-known Kalman-Yacubovich-Popov (KYP) Lemma. The striking similarities between the absolute stability problem known in control theory and stability analysis of synchronization schemes containing these chaotic systems, motivates the study of synchronization criteria for the class of Lur'e systems. Synchronization has been studied mainly for identical master-slave systems, but also non-identical systems [28, 40]. Such issues of robustness are important because non-robust schemes may cause loss of synchronization.

For the robustness criteria derived in [28] it is illustrated that even for a large parameter mismatch between Lur'e systems synchronization can be achieved up to a small synchronization error. Furthermore, time delay or propagation delay between master and slave system is another effect which may destroy the synchronization. This problem has been considered in [44] with delay-independent and delay-dependent criteria for synchronization, where the latter provide sharper results. For schemes with external inputs, methods of nonlinear H_∞ synchronization have been proposed [30–32]. In this approach a tracking error concept is used and the synchronization scheme is represented in standard plant form. By employing a quadratic storage function and supply rate with finite L_2 -gain, H_∞ synchronization for Lur'e systems is characterized in the term of matrix inequalities.

Furthermore, impulsive synchronization methods have been studied for Lur'e systems, both for full state feedback and dynamic measurement feedback [35–37, 47, 49] which have been applied to CDMA systems [48].

This chapter is organized as follows. In Section 2 we discuss autonomous synchronization schemes and its link to absolute stability theory both for full state and dynamic feedback, and robust synchronization. In Section 3 nonlinear H_∞ synchronization is explained. In Section 4 we present results on impulsive synchronization and finally in Section 5 a number of illustrations are given.

2 Master-Slave Synchronization: Autonomous Case

Synchronization of chaotic systems is often studied for schemes of the form [5, 40]

$$\begin{cases} \dot{x} = f(x) + M(x - z) \\ \dot{z} = g(z) + N(x - z) \end{cases} \quad (1)$$

with $f(\cdot) : \mathbb{R}^n \rightarrow \mathbb{R}^n$, $g(\cdot) : \mathbb{R}^n \rightarrow \mathbb{R}^n$, state vectors $x, z \in \mathbb{R}^n$ and coupling matrices $M, N \in \mathbb{R}^{n \times n}$. In this scheme one has mutual coupling.

For master-slave synchronization of identical Lur'e systems one has the scheme

$$\begin{cases} \mathcal{M} : \dot{x} = Ax + B\sigma(Cx) \\ \mathcal{S} : \dot{z} = Az + B\sigma(Cz) + K(x - z) \end{cases} \quad (2)$$

with master system \mathcal{M} and slave system \mathcal{S} . The master and slave system are identical Lur'e systems with state vectors $x, z \in \mathbb{R}^n$ and matrices $A \in \mathbb{R}^{n \times n}$, $B \in \mathbb{R}^{n \times n_h}$, $C \in \mathbb{R}^{n_h \times n}$ and feedback matrix $K \in \mathbb{R}^{n \times n}$ where n_h may be considered as a number of hidden units by interpreting the Lur'e form as a recurrent neural network with one hidden layer [33]. The static nonlinearity $\sigma(\cdot) : \mathbb{R}^{n_h} \rightarrow \mathbb{R}^{n_h}$ is assumed to be diagonal and to satisfy a sector $[0, k]$ condition.

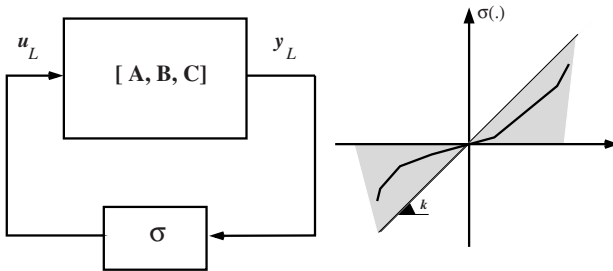


Fig. 1. Lur'e system consisting of a linear dynamical system interconnected by feedback to a static nonlinearity σ in sector $[0, k]$.

By state synchronization one usually means that $\|x - z\|_2 \rightarrow 0$ as $t \rightarrow \infty$. Many results on synchronization in the literature are about local synchronization. However, for Lur'e systems it is straightforward to derive conditions for global synchronization in the sense that the synchronization property holds for all initial conditions $x(0), z(0)$.

Investigating synchronization of the schemes is done by stability analysis of the error system

$$\dot{e} = (A - K)e + B\eta(Ce; z) \quad (3)$$

where $\eta(Ce; z) = \sigma(Ce + Cz) - \sigma(Cz)$ and $e = x - z$. One assumes that the nonlinearity $\eta(Ce, z)$ belongs to sector $[0, k]$ [8]:

$$0 \leq \frac{\eta_i(c_i^T e; z)}{c_i^T e} = \frac{\sigma_i(c_i^T e + c_i^T z) - \sigma_i(c_i^T z)}{c_i^T e} \leq k, \quad \forall e, z; i = 1, 2, \dots, n_h. \quad (4)$$

The following inequality holds then [3, 14, 38]:

$$\eta_i(c_i^T e; z)[\eta_i(c_i^T e; z) - kc_i^T e] \leq 0, \quad \forall e, z; i = 1, 2, \dots, n_h. \quad (5)$$

Therefore the error system is also a Lur'e system. Hence, the problem of synchronization of Lur'e systems can be reduced to the problem of absolute stability of the error system [14, 38].

2.1 Absolute stability of Lur'e system

Studying global synchronization of Lur'e systems involves the analysis of global asymptotic stability of the error system. The sector nonlinearity is satisfied globally. For the given sector condition the circle criterion is used as synchronization criterion, which can be derived from a quadratic Lyapunov function [8]. The criteria can be expressed in terms of matrix inequalities [3] and are sufficient conditions for global synchronization. Although they are not necessary, for many practical systems such Chua's circuit and other chaotic and hyperchaotic systems which can be represented in Lur'e form, they are sufficiently sharp.

Lemma 1 Master-slave synchronization *The master and slave system (3) synchronize if there exist matrices $0 < P = P^T \in \mathbb{R}^{n \times n}$, $\Lambda = \text{diag}(\lambda_i)$ with $\lambda_i \geq 0$ for $i = 1, \dots, n_h$ and*

$$Z = \begin{bmatrix} (A - K)^T P + P(A - K) & PB + kC^T \Lambda \\ B^T P + k\Lambda C & -2\Lambda \end{bmatrix} < 0. \quad (6)$$

Proof [8]: Consider the following quadratic Lyapunov function

$$V(e) = e^T Pe, \quad P = P^T > 0. \quad (7)$$

After applying the \mathcal{S} -procedure [3] by using the inequalities (5) from the sector conditions, one has

$$\dot{V}(e) - 2\eta^T \Lambda[\eta - kCe] \leq [e^T \eta^T] Z[e; \eta].$$

The rhs is strictly negative for all values of e, η (except the origin), provided Z is negative definite. \square

2.2 Master-slave synchronization using dynamic output feedback

In the scheme (2) it is assumed that the full state vectors x, z can be measured. An alternative scheme with linear dynamic output feedback \mathcal{C} (Fig. 4) has been proposed in [27]:

$$\begin{aligned} \mathcal{M} : & \begin{cases} \dot{x} = Ax + B\sigma(Cx) \\ p = Hx \end{cases} \\ \mathcal{S} : & \begin{cases} \dot{z} = Az + B\sigma(Cz) + Du \\ q = Hz \end{cases} \\ \mathcal{C} : & \begin{cases} \dot{\rho} = E\rho + G(p - q) \\ u = M\rho + N(p - q) \end{cases} \end{aligned} \quad (8)$$

with $\rho \in \mathbb{R}^{n_c}$, control input $u \in \mathbb{R}^m$ and outputs $p, q \in \mathbb{R}^l$ where $l, m \leq n$. Note that $p - q$ is taken here as input to the linear dynamic controller. The error system becomes

$$\begin{bmatrix} \dot{e} \\ \dot{\rho} \end{bmatrix} = \begin{bmatrix} A - DNH & -DM \\ GH & E \end{bmatrix} \begin{bmatrix} e \\ \rho \end{bmatrix} + \begin{bmatrix} B \\ 0 \end{bmatrix} \eta(Ce; z). \quad (9)$$

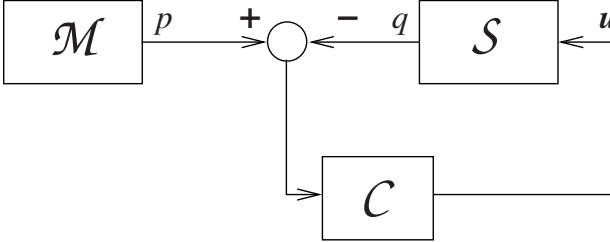


Fig. 2. Master-slave synchronization scheme with dynamic measurement feedback

Lemma 2 Synchronization using dynamic output feedback *The master and slave system (8) synchronize if there exist matrices $0 < P = P^T \in \mathbb{R}^{n \times n}$ and $\Lambda = \text{diag}(\lambda_i)$ with $\lambda_i \geq 0$ for $i = 1, \dots, n_h$ and*

$$Y = Y^T = \begin{bmatrix} Y_{11} & Y_{12} & Y_{13} \\ . & Y_{22} & P_{21}B \\ . & . & -2\Lambda \end{bmatrix} < 0 \quad (10)$$

with $Y_{11} = (A - DNH)^T P_{11} + P_{11}(A - DNH) + H^T G^T P_{21} + P_{12}GH$, $Y_{12} = (A - DNH)^T P_{12} + H^T G^T P_{22} - P_{11}DM + P_{12}E$, $Y_{13} = P_{11}B + kC^T \Lambda$, $Y_{22} = E^T P_{22} + P_{22}E - M^T D^T P_{12} - P_{21}DM$.

Proof [27]: similar to the previous theorem. □

2.3 Robust synchronization

For the schemes (2)(8) the given Lur'e systems are identical. The case of non-identical Lur'e systems is described by

$$\begin{cases} \mathcal{M} : \dot{x} = A_1x + B_1\sigma(C_1x) \\ \mathcal{S} : \dot{z} = A_2z + B_2\sigma(C_2z) + K(z - x) \end{cases} \quad (11)$$

The error system can be decomposed into two terms, according to [40]:

$$\dot{e} = \{(A_2 - K)e + B_2\eta(C_2e; z)\} + \{\Delta Ax + B_1\sigma(C_1x) - B_2\sigma(C_2x)\} \quad (12)$$

where $\Delta = A_1 - A_2$. One can show then

Lemma 3 Robust master-slave synchronization Suppose that there exists $0 < P = P^T \in \mathbb{R}^{n \times n}$, $\Lambda = \text{diag}(\lambda_i)$ with $\lambda_i \geq 0$ for $i = 1, \dots, n_h$ and

$$Y = Y^T = \begin{bmatrix} (A_2 - K)^T P + P(A_2 - K) + \alpha I & PB_2 + kC_2^T \Lambda \\ B_2^T P + k\Lambda C & -2\Lambda \end{bmatrix} < 0.$$

Define $\gamma = 2\beta\delta\sigma_{\max}(P)$, where β and δ are defined

$$\begin{aligned} \|x(t; x_0)\|_2 &\leq \delta, & \forall t \geq T \\ \|\Delta Ax + B_1\sigma(C_1x) - B_2\sigma(C_2x)\|_2 &\leq \beta\|x\|_2, \quad \forall x \in \mathbb{R}^n \end{aligned} \quad (13)$$

and $\sigma_{\max}(P)$ denotes the maximal singular value of P . Then the synchronization scheme (11) is uniformly synchronizing with error bound $\sqrt{c_2}$, if there exist positive real constant c and c_2 such that

$$\mathcal{B}_1^s = \{e | e^T e \geq \frac{\gamma^2}{\alpha^2}\} \subset \mathcal{E}^s = \{e | e^T e \geq c\} \subset \mathcal{B}_2^s = \{e | e^T e \geq c_2\}.$$

Proof [28]: □

The robust synthesis of dynamic output error feedback for master-slave synchronization of Lur'e system is also presented in [28].

2.4 Synchronization with time delay

Consider the following master-slave synchronization scheme with static error feedback and time-delay τ :

$$\begin{aligned} \mathcal{M} : & \begin{cases} \dot{x}(t) = Ax(t) + B\sigma(Cx(t)) \\ p(t) = Hx(t) \end{cases} \\ \mathcal{S} : & \begin{cases} \dot{y}(t) = Ay(t) + B\sigma(Cy(t)) + u(t) \\ q(t) = Hy(t) \end{cases} \\ \mathcal{C} : & \{ u(t) = G(p(t - \tau) - q(t - \tau)) \end{aligned} \quad (14)$$

with master system \mathcal{M} , slave system \mathcal{S} and controller \mathcal{C} . One obtains the error system \mathcal{E} :

$$\mathcal{E} : \dot{e} = Ae + B\eta(Ce; y) + Fe(t - \tau) \quad (15)$$

with $e = e(t)$, $F = -GH$.

Lemma 4 Delay independent synchronization criterion Let $\Lambda = \text{diag}\{\lambda_i\}$ be a diagonal matrix with $\lambda_i \geq 0$ for $i = 1, 2, \dots, n_h$, $0 < P = P^T \in \mathbb{R}^{n \times n}$ and $0 < Q = Q^T \in \mathbb{R}^{n \times n}$ then a sufficient condition for synchronization of the master-slave system (14) is given by the matrix inequality

$$Y = \begin{bmatrix} A^T P + PA + Q & PB + kC^T \Lambda & PF \\ B^T P + k\Lambda^T C & -2\Lambda & 0 \\ F^T P & 0 & -Q \end{bmatrix} < 0. \quad (16)$$

Proof [44]: By taking the Lyapunov-Krasovskii function

$$V(e) = e^T P e + \int_{-\tau}^0 e(t+s)^T Q e(t+s) ds, \quad P = P^T > 0, \quad Q = Q^T > 0$$

it is straightforward to find the above condition using a similar procedure as in the previous proofs and imposing $\dot{V} \leq [e^T \eta^T e(t-\tau)^T] Y[e; \eta; e(t-\tau)] < 0$.

□

Lemma 5 Delay dependent synchronization criterion *Let $\Lambda = \text{diag}\{\lambda_i\}$ be a diagonal matrix with $\lambda_i \geq 0$ for $i = 1, 2, \dots, n_h$, $0 < P = P^T \in \mathbb{R}^{n \times n}$, $0 < Q = Q^T \in \mathbb{R}^{n \times n}$ and $r_1 > 0$, $r_2 > 0$, $r_3 > 0$, $\tau^* > 0$ be a scalar, then a sufficient condition for synchronization of the master-slave system (14) for any constant time-delay τ satisfying $0 \leq \tau \leq \tau^*$ is given by the matrix inequality:*

$$Y = \begin{bmatrix} Z & PB + kCA \\ B^T P + k\Lambda C^T & r_3\tau B^T B - 2\Lambda \end{bmatrix} < 0 \quad (17)$$

where $Z = P(A + F) + (A + F)^T P + r_1\tau A^T A + r_2\tau F^T F + (\frac{1}{r_1} + \frac{1}{r_2} + \frac{1}{r_3})\tau PFF^T P$.

Proof [44]: In order to find a delay-dependent synchronization condition, the classical Lyapunov-Krasovskii function for delay-dependent stability is modified into

$$\begin{aligned} V(e) = & e^T P e + r_1 \int_{t-\tau}^t \int_{t+\theta}^t [e^T(s) A^T A e(s)] ds d\theta \\ & + r_2 \int_{t-\tau}^t \int_{t+\theta-\tau}^t [e^T(s) F^T F e(s)] ds d\theta \\ & + r_3 \int_{t-\tau}^t \int_{t+\theta}^t [\eta^T(Ce(s); y(s)) B^T B \eta(Ce(s); y(s))] ds d\theta \end{aligned} \quad (18)$$

where $P = P^T > 0$ and $r_1, r_2, r_3 > 0$.

□

3 Nonlinear H_∞ Synchronization

In view of the nonlinear H_∞ synchronization method introduced in [30–32] the following scheme is considered

$$\begin{aligned} \mathcal{R} : & \begin{cases} \dot{m} = Rm + Sr \\ d = Tm + Ur \end{cases} \\ \mathcal{M} : & \begin{cases} \dot{x} = Ax + B\sigma(Cx) + Dd \\ p = Hx \end{cases} \\ \mathcal{S} : & \begin{cases} \dot{z} = Az + B\sigma(Cz) + Fu \\ q = Hz \end{cases} \\ \mathcal{C} : & \begin{cases} \dot{\rho} = E\rho + G(p + \epsilon - q) \\ u = M\rho + N(p + \epsilon - q). \end{cases} \end{aligned} \quad (19)$$

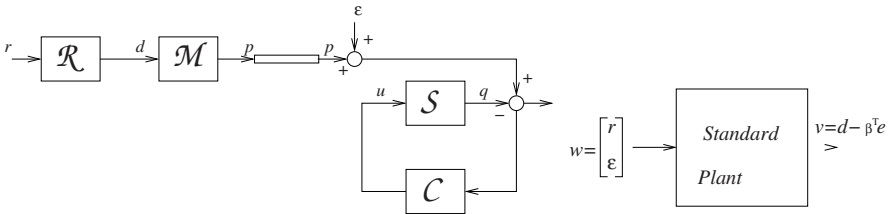


Fig. 3. Nonlinear H_∞ synchronization scheme and standard plant representation.

The message signal $r \in \mathbb{R}$, which is assumed to be binary valued is low pass filtered by \mathcal{R} . The filtered message signal $d \in \mathbb{R}$ is modulating the master system. The signal $p \in \mathbb{R}^l$ is transmitted through the channel, which is corrupted by the noise signal $\epsilon \in \mathbb{R}^l$. Instead of the dynamic controller one could also consider a static controller $u = K(p + \epsilon - q)$, e.g. in the case of Chua's circuit. The system is visualized in Fig. 3. This basic scheme could be refined in terms of additional channel and noise models. An error system in the sense of the autonomous case (3) can never be globally asymptotically stable for (19) because it is driven by the message r . Therefore another error signal concept has been proposed in [30–32] by defining as tracking error signal

$$\nu = d - \beta^T e \quad (20)$$

where $\beta = [1; 0; 0; \dots; 0]$ selects the first component of $e = x - z$. The synchronization scheme is represented then in standard plant form [2, 17] with as regulated output the tracking error ν and exogenous input $w = [r; \epsilon]$. The

equations for the standard plant form related to (19) are given by

$$\left\{ \begin{array}{l} \begin{bmatrix} \dot{e} \\ \dot{\rho} \\ \dot{\mu} \end{bmatrix} = \begin{bmatrix} A_* & -F_* & D_* \\ G_* & E & 0 \\ 0 & 0 & R \end{bmatrix} \begin{bmatrix} e \\ \rho \\ \mu \end{bmatrix} + \begin{bmatrix} B \\ 0 \\ 0 \end{bmatrix} \eta(Ce; z) + \begin{bmatrix} DU & -FN \\ 0 & G \\ S & 0 \end{bmatrix} \begin{bmatrix} r \\ \epsilon \end{bmatrix} \\ \nu = [-\beta^T \ 0 \ T] \begin{bmatrix} e \\ \rho \\ \mu \end{bmatrix} + [U \ 0] \begin{bmatrix} r \\ \epsilon \end{bmatrix} \end{array} \right. \quad (21)$$

with $A_* = A - FNH$, $F_* = FM$, $D_* = DT$ and $G_* = GH$.

Lemma 6 Nonlinear H_∞ synchronization *Let $\Lambda = \text{diag } \{\lambda_i\}$ be a diagonal matrix with $\lambda_i \geq 0$ for $i = 1, 2, \dots, n_h$ and $0 < P = P^T \in \mathbb{R}^{n \times n}$. Then a sufficient condition for dissipativity of the synchronization scheme (21) with respect to the quadratic storage function $\phi(\xi) = \xi^T P \xi$ and supply rate $s(w, \nu) = \gamma^2 w^T w - \nu^T \nu$ with finite L_2 -gain γ is given by matrix inequality*

$$Z = Z^T = \begin{bmatrix} Z_{11} & Z_{12} & Z_{13} & Z_{14} & Z_{15} & Z_{16} \\ . & Z_{22} & Z_{23} & Z_{24} & Z_{25} & Z_{26} \\ . & . & Z_{33} & Z_{34} & Z_{25} & Z_{36} \\ . & . & . & Z_{44} & 0 & 0 \\ . & . & . & . & Z_{55} & 0 \\ . & . & . & . & . & Z_{66} \end{bmatrix} < 0$$

with

$$\begin{aligned} Z_{11} &= A_* P_{11} + P_{11} A_* + G_*^T P_{21} + P_{12} G_* + \beta \beta^T & Z_{24} &= P_{21} B \\ Z_{12} &= A_*^T P_{12} + G_*^T P_{22} - P_{11} F + P_{12} E & Z_{25} &= P_{21} D U + P_{23} S \\ Z_{13} &= A_*^T P_{13} + G_*^T P_{23} - P_{11} D_* + P_{13} R - \beta T & Z_{26} &= P_{22} G - P_{21} F N \\ Z_{14} &= P_{11} B + k C^T \Lambda & Z_{55} &= -\gamma^2 I + U^T U \\ Z_{15} &= P_{11} D U + P_{13} S - \beta U & Z_{34} &= P_{31} B \\ Z_{16} &= P_{12} G - P_{11} F N & Z_{35} &= P_{31} D U + P_{33} S + T^T U \\ Z_{22} &= E^T P_{22} + P_{22} E - F_*^T P_{12} - P_{21} F_* & Z_{36} &= P_{32} G - P_{31} F N \\ Z_{23} &= E^T P_{23} - F_*^T P_{13} + P_{21} D_* + P_{23} R & Z_{44} &= -2 \Lambda \\ Z_{33} &= R^T P_{33} + P_{33} R + D_*^T P_{13} + P_{31} D_* + T^T T & Z_{66} &= -\alpha^2 \gamma^2 I. \end{aligned}$$

Proof [31]: For a given quadratic storage function and a supply rate, dissipativity is checked by

$$\dot{\phi}(\xi) \leq s(w, \nu), \quad \forall v, w.$$

Expressing $\dot{\phi}(\xi) - s(w, \nu)$, exploiting the sector condition on η and imposing that $\dot{\phi} - s(w, \nu) - 2\eta^T \Lambda[\eta - kCe] = \varphi^T Z \varphi < 0$ where $\varphi = [e; \rho; \mu; \eta; r; \epsilon]$, the matrix inequality $Z < 0$ is giving a sufficient condition for dissipativity with finite L_2 -gain γ . \square

Robust nonlinear H_∞ synchronization of Lur'e systems with full static state error feedback and linear dynamic output error feedback are presented in [32]. These schemes also take into account parameter mismatch between the master and the slave scheme. While in the autonomous case a quite large mismatch can be tolerated by applying the robust synchronization criteria, this is no longer the case for the nonlinear H_∞ synchronization method where mismatch can also be tolerated but a much smaller amount. These aspects are relevant with respect to a robustness-security trade-off towards secure communications applications.

4 Impulsive Synchronization

In [47] a theory of impulsive differential equations [15] has been applied to chaos control and synchronization of Chua's circuit. For Lur'e systems certain extensions have been presented in [35–37]. In impulsive control the control signal is applied at discrete time instants, which are allowed to be non-equidistant in time. The method of impulsive synchronization has been applied to CDMA systems [48].

4.1 Impulsive synchronization: state feedback case

Here we illustrate the main ideas by hand of the synchronization scheme

$$\begin{cases} \mathcal{M} : \dot{x} = Ax + B\sigma(Cx) \\ \mathcal{S} : \dot{z} = Az + B\sigma(Cz), \quad t \neq \tau_i \\ \mathcal{C} : \Delta z = K(x - z), \quad t = \tau_i. \end{cases} \quad (22)$$

For the impulsive control law \mathcal{C} , a set of discrete time instants τ_i are considered where $0 < \tau_1 < \tau_2 < \dots < \tau_i < \tau_{i+1} < \dots$. At the time instants τ_i , instantaneous jumps in the state variable z are imposed: $\Delta z|_{t=\tau_i} = z(\tau_i^+) - z(\tau_i^-)$. One has the error system

$$\begin{cases} \dot{e} = Ae + B\eta(ce; z), & t \neq \tau_i \\ \Delta e = -K(x - z), & t = \tau_i \end{cases} \quad (23)$$

with $\Delta e = \Delta x - \Delta z$ with $\Delta x = 0$ for the master system.

Lemma 7 Impulsive synchronization: state feedback *Let $\Lambda = \text{diag}\{\lambda_i\}$ be a diagonal matrix with $\lambda_i \geq 0$ for $i = 1, 2, \dots, n_h$, $0 < P = P^T \in \mathbb{R}^{n \times n}$ and α, β scalars. Then a sufficient condition for impulsive synchronization of the master slave system (22) is given by following set of inequalities*

$$\begin{aligned} & \left[\begin{array}{cc} A^T P + PA - \alpha P PB + C^T \Lambda & \\ B^T P + \Lambda C & -2\Lambda \end{array} \right] \leq 0 \\ & (I - K)^T P (I - K) < \beta P \\ & (I - K)^T (I - K) < I \\ & \alpha (\tau_{i+1} - \tau_i) + \log \beta < 0. \end{aligned}$$

Proof [36]: By employing the Lyapunov function $V(e) = e^T P e$ ($P = P^T > 0$). According to [15, 47] it is sufficient then to prove that

$$\begin{cases} \dot{V} \leq \alpha V, & \alpha > 0, \quad t \neq \tau_i \\ V(\zeta + \Delta\zeta) < \beta V, & \beta > 0, \quad t = \tau_i \\ \|\zeta + \Delta\zeta\|_2 < \|\zeta\|_2, & t = \tau_i \\ \alpha(\tau_{i+1} - \tau_i) + \log \beta < 0. \end{cases} \quad (24)$$

After exploiting the sector condition on η the set of inequalities is derived as a sufficient condition for synchronization. \square

4.2 Impulsive synchronization: measurement feedback case

We consider the following master-slave synchronization scheme

$$\begin{aligned} \mathcal{M} : & \begin{cases} \dot{x} = Ax + B\sigma(Cx) \\ p = Lx \end{cases} \\ \mathcal{S} : & \begin{cases} \dot{z} = Az + B\sigma(Cz) \\ q = Lz \end{cases} \\ \mathcal{C} : & \begin{cases} \dot{\xi} = E\xi + F(p - q) + W_F\sigma(V_{F_1}\xi + V_{F_2}(p - q)) & \tau \neq \tau_k \\ \Delta z = D_1 u, & \tau = \tau_k \\ \Delta\xi = D_2 v, & \tau \neq \tau_k \\ u = G_1\xi + H_1(p - q) \\ v = G_2\xi + H_2(p - q) \end{cases} \end{aligned} \quad (25)$$

which consists of a master \mathcal{M} , a slave system \mathcal{S} and a controller \mathcal{C} . \mathcal{M} and \mathcal{S} are identical Lur'e systems. The output or measurement vectors of \mathcal{M} and \mathcal{S} are $p, q \in \mathbb{R}^l$ with $l \leq n$ and $L \in \mathbb{R}^{l \times n}$. For the sake of generality, a nonlinear dynamic output feedback controller of the Lur'e form is taken for the state equation with state vector $\xi \in \mathbb{R}^{n_\xi}$. By the means of the matrices D_1 and D_2 it is decided on which state equations the impulsive controls $u \in \mathbb{R}^{m_z}$ and $v \in \mathbb{R}^{m_\xi}$ are applied. The output difference $p - q$ is taken as input of the controller \mathcal{C} . The matrices of the controller are of dimension $E \in \mathbb{R}^{n_\xi \times n_\xi}$, $F \in \mathbb{R}^{n_\xi \times l}$, $W_F \in \mathbb{R}^{n_\xi \times n_{h_\xi}}$, $V_{F_1} \in \mathbb{R}^{n_{h_\xi} \times n_\xi}$, $V_{F_2} \in \mathbb{R}^{n_{h_\xi} \times l}$, $D_1 \in \mathbb{R}^{n_z \times m_z}$, $D_2 \in \mathbb{R}^{n_\xi \times m_\xi}$, $G_1 \in \mathbb{R}^{m_z \times n_\xi}$, $G_2 \in \mathbb{R}^{m_\xi \times n_\xi}$, $H_1 \in \mathbb{R}^{m_z \times l}$, $H_2 \in \mathbb{R}^{m_\xi \times l}$ where n_{h_ξ} is the number of hidden units in the Lur'e system of \mathcal{C} . The output error system for e_L becomes

$$\mathcal{E} : \begin{cases} \dot{e}_L = LAe + LB\eta(Ce; z), & \tau \neq \tau_k \\ \dot{\xi} = E\xi + F(p - q) + W_F\sigma(V_{F_1}\xi + V_{F_2}(p - q)), & \tau \neq \tau_k \\ \Delta e_L = -LD_1 u, & \tau = \tau_k \\ \Delta\xi = D_2 v, & \tau = \tau_k \\ u = G_1\xi + H_1(p - q) \\ v = G_2\xi + H_2(p - q) \end{cases} \quad (26)$$

where the synchronization error is defined as $e = x - z$ for the state vectors and $e_L = p - q = Le$ for the outputs and also $\Delta_L = -L\Delta z$.

Lemma 8 Impulsive synchronization: measurement feedback *Let Λ and Γ be diagonal matrices with positive diagonal elements, $\alpha > 0$ and β are scalars and $P = Q^T Q > 0$. Then a sufficient condition for impulsive synchronization of the master slave system (26) with measurement feedback is given by following set of inequalities*

$$\begin{aligned} Z &\leq 0 \\ M^T P M &< \beta P \\ M^T M &< I \\ \alpha(\tau_{k+1} - \tau_k) + \log \beta &< 0 \end{aligned}$$

where $Z = Z^T$ and matrix blocks

$$\begin{aligned} Z_{11} &= AP_{11} + L^T P_{11} A + L^T P_{21} F L + L^T F^T P_{21} L - \alpha_* L^T P_{11} L & Z_{33} &= -2\Lambda \\ Z_{12} &= A^T P_{12} + L^T P_{12} E + L^T F^T P_{22} - \alpha_* L^T P_{12} & Z_{44} &= -2\Gamma \\ Z_{13} &= L^T P_{11} LB + C^T \Lambda & Z_{23} &= P_{21} LB \\ Z_{14} &= L^T P_{12} W_F + L^T V_{F_2}^T \Gamma & Z_{24} &= P_{22} W_F + V_{F_1}^T \end{aligned}$$

$$Z_{34} = 0 \text{ and } M = \begin{bmatrix} I - LD_1 H_1 & -LD_1 G_1 \\ D_2 H_2 & I + D_2 G_2 \end{bmatrix}.$$

Proof [35, 37]: In order to derive a sufficient condition for global asymptotic stability of the error system \mathcal{E} , the Lyapunov function

$$V(e_L, \xi) = [e_L^T \ \xi^T] \begin{bmatrix} P_{11} & P_{12} \\ P_{21} & P_{22} \end{bmatrix} \begin{bmatrix} e_L^T \\ \xi \end{bmatrix} \quad (27)$$

is taken. According to [15, 47] it is sufficient then to prove (24). After exploiting the sector condition on η the first condition which is $Z \leq 0$, can be formulated as given in the Lemma. In the order to express the other conditions in (24) as a matrix inequality, one writes

$$\zeta + \Delta\zeta = \begin{bmatrix} e_L^T \\ \xi \end{bmatrix} + \begin{bmatrix} \Delta e_L^T \\ \Delta \xi \end{bmatrix} = M \begin{bmatrix} e_L^T \\ \xi \end{bmatrix}. \quad (28)$$

This yields the matrix inequality $M^T P M < \beta P$ and $M^T M < I$. \square

5 Examples

Many of the schemes discussed in this chapter have been verified on many examples both in simulation and for real electronic circuit implementations, such as for Chua's circuit [6, 7], n -scroll attractors from generalized Chua's circuit [29,34] and hyperchaotic systems which consist of two unidirectionally coupled Chua's circuits [12].

In dimensionless form Chua's circuit is given by

$$\begin{cases} \dot{x} = \alpha[y - h(x)] \\ \dot{y} = x - y - z \\ \dot{z} = -\beta y \end{cases} \quad (29)$$

where $f(x)$ is the piecewise-linear characteristic of Chua's diode [6], which is given by

$$h(x) = m_1 x + \frac{1}{2}(m_0 - m_1)(|x + 1| - |x - 1|)$$

and parameters $\alpha = 9$, $\beta = 14.28$, $m_0 = -\frac{1}{7}$, $m_1 = \frac{2}{7}$ in order to obtain the double scroll (Fig. 4 (a)) attractor [7]. The nonlinearity $\sigma(x) = \frac{1}{2}(|x + 1| - |x - 1|)$ belongs to sector $[0, 1]$. A Lur'e representation $\dot{x} = Ax + B\sigma(Cx)$ of Chua's circuit is given by

$$A = \begin{bmatrix} -\alpha m_1 & \alpha & 0 \\ -1 & -1 & -1 \\ 0 & -\beta & 0 \end{bmatrix}, B = \begin{bmatrix} -\alpha(m_0 - m_1) \\ 0 \\ 0 \end{bmatrix}, C = [1 \ 0 \ 0].$$

Master-slave synchronization has been experimentally confirmed by observations done on a hardware realization for Chua's Circuit [41]. The circuit realization is based on the realization of Chua's circuit by a voltage controlled voltage sources [46].

Figure 4.b shows a (V_{C1}, \hat{V}_{C1}) plot, which corresponds to x state variable for the master and slave system in (29), when the master and slave systems are not connected. In order to find a feedback matrix K , matrices P and Λ such that Lemma 1 holds, the following constrained nonlinear optimization problem has been solved

$$\min_{P, K, \Lambda} \lambda_{\max}(Z_1) \text{ such that } \|K\|_2 < c$$

where $\lambda_{\max}(\cdot)$ denotes the maximum eigenvalue. The constraint $\|K\|_2 < c$ is bounding the norm of the feedback matrix. In matlab, the above optimization problem was solved by means of sequential quadratic programming for Chua circuit and a feedback matrix has been obtained. This was done by representing $P = R^T R$ and taking R as unknown instead of P . This parametrization ensures that P is positive definite. Alternatively, one may prefer to solve convex subproblems for the LMIs. The result of master slave synchronization is shown (V_{C1}, \hat{V}_{C1}) plot in Fig. 4 (c) for the obtained feedback matrix.

The nonlinear H_∞ synchronization scheme has been confirmed in [41] and [42] for Chua's circuit and 5-scroll attractors, respectively.

Like master-slave synchronization, in order to design a controller \mathcal{C} in (19) such that Lemma 6 holds, the nonlinear H_∞ synchronization problem is formulated as

$$\min_{P, F, \Lambda, \gamma} \gamma \text{ such that } Z(P, F, \Lambda, \gamma) < 0.$$

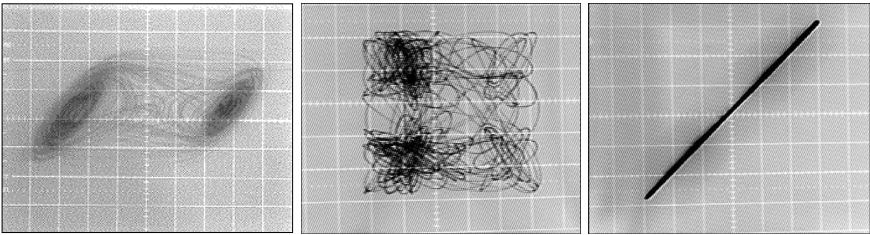


Fig. 4. Scope pictures for master-slave synchronization using Chua's circuit implementations: (a) $(V_{C1}(t), V_{C2}(t))$ for master system ($0.1V/div - 50mV/div$); $(V_{C1}(t), \hat{V}_{C2}(t))$ (b) ($0.2V/div - 50mV/div$) (c).

The (V_{C1}, V_{C2}) plot for master system driven by a square wave with $f = 11kHz$ and $(\hat{V}_{C1}, \hat{V}_{C2})$ plot for slave system are given in Fig. 5 (a) and (b), respectively. The application to a square wave with $f = 11kHz$ reference input is shown on Fig. 5 (c) with recovery of the message Fig. 5 (c).

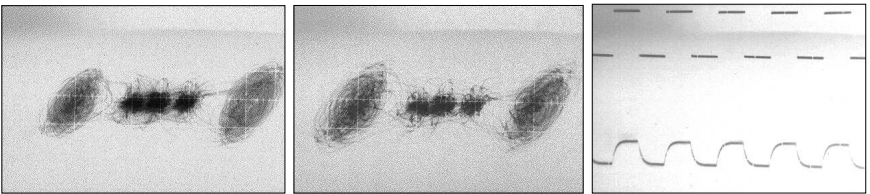


Fig. 5. Scope pictures for nonlinear H_∞ synchronization using 5-scroll attractors implementations: (a) $(V_{C1}(t), V_{C2}(t))$ for master system ($0.1V/div - 50mV/div$); (b) $(\hat{V}_{C1}(t), \hat{V}_{C2}(t))$ for slave system ($0.2V/div - 50mV/div$). (c) $s(t)$ (above) and $V_{C1}(t) - \hat{V}_{C1}(t)$ (below) ($20mV/div - 50\mu s/div$ and $20mV/div - 50\mu s/div$)

For schemes with delay, Chua's circuit, 5-scroll attractors and hyperchaotic attractors have been tested for delay-independent synchronization which can be formulated as

$$\min_{P, Q, F, A} \lambda_{\max}(Z_1) \text{ such that } \|F\|_2 < c$$

such that Lemma 5 holds. One obtains that Lemma 5 is useless for these examples. Instead, delay-dependent master-slave synchronization criteria are applied and controllers are designed by solving the constrained nonlinear optimization problem

$$\min_{P, F, A, r_1, r_2, r_3} \lambda_{\max}(Y) \text{ such that } \begin{cases} P = P^T \\ A \geq 0 \\ r_1, r_2, r_3 > 0. \end{cases}$$

This optimization problem was also solved by means of sequential quadratic programming in Matlab for chaotic and hyperchaotic systems. In the exam-

ple, for $\tau > 0.038$ no feasible points were found such that Lemma 4 holds. Figure 6.(a)-(c) and (d)-(f) shows the master system, slave system and the error signal with respect to time when $\tau = 0.038$ and $\tau = 0.18$, respectively.

In Fig. 7 an example on impulsive synchronization of hyperchaotic systems by dynamic measurement feedback is shown. The hyperchaotic master and slave systems consist of two coupled chaotic Chua's circuit cells. Successful global synchronization has been achieved for the defined outputs.

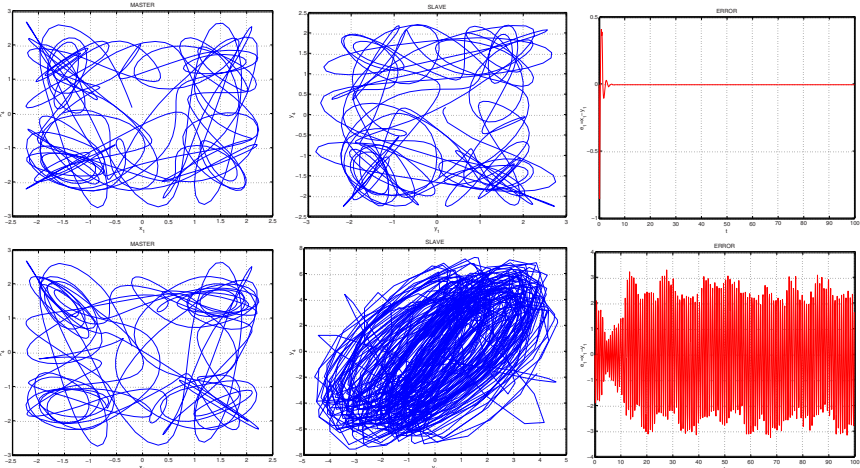


Fig. 6. Simulation result for master-slave synchronization of two identical hyperchaotic system. The master system is coupled to slave system with first and fourth state variable with delay $\tau = 0.038$ and $\tau = 0.18$: (a),(d) Double-double scroll attractor generated at the master system (projection onto the $x_1 - x_4$ plane) (b),(e) and slave system (projection onto the $y_1 - y_4$ plane) (c),(f) Error signal ($x_1(t) - y_1(t)$) with respect to time, respectively.

6 Conclusions

In this chapter an overview has been given on several methods for chaotic systems synchronization for the class of Lur'e systems, including full static state feedback, measurement feedback schemes, robust synchronization methods, autonomous and non-autonomous schemes, synchronization schemes with time delays and impulsive synchronization methods.

While in the past many of such schemes were investigated in a rather ad hoc fashion, presently several systems and control theoretical interpretations have been given to synchronization methods. A considerable advantage for the class of Lur'e systems is that it is straightforward to derive sufficient conditions for global synchronization which can be expressed in terms of matrix

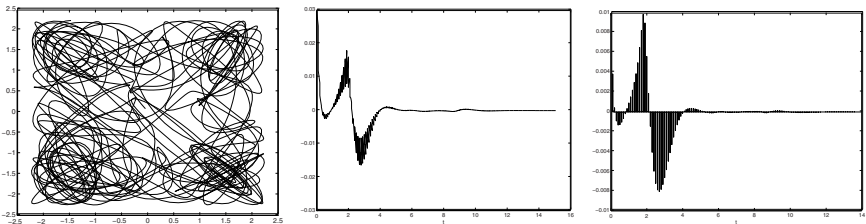


Fig. 7. Impulsive synchronization of two identical hyperchaotic systems (coupled Chua's circuits) by linear dynamic output feedback with two outputs and two control inputs: (a) hyperchaotic attractor, where the first state variable is shown with respect to the fourth for a system with 2 coupled cells and six state variables in total; (b) output synchronization error for one of the outputs; (c) one of the impulsive control signals applied to the slave system.

inequality. Many circuits and systems of practical interest such as Chua's circuit and generalized chaotic and hyperchaotic versions, can be represented in this Lur'e form.

Acknowledgments.

This research work was carried out at the ESAT laboratory and the Interdisciplinary Center of Neural Networks (ICNN) of the KULeuven, in the framework of the Belgian Programme on Interuniversity Poles of Attraction, initiated by the Belgian State, Prime Minister's Office for Science, Technology and Culture (IUAP P4-02) and the Concerted Action Project MEFISTO of the Flemish Community, ESPRIT IV 27077 (DICTAM) and FWO project G.0080.01. JS is a postdoctoral researcher with the Fund for Scientific Research FWO-Flanders.

References

1. Angeli, D. (2002) A Lyapunov approach to incremental stability properties. *IEEE Trans. Auto. Contr.*, **47**(3):410–421
2. Boyd, S., Barratt, C. (1991) *Linear Controller Design, Limits of Performance*. Englewood Cliffs, NJ: Prentice-Hall
3. Boyd, S., El Ghaoui, L., Feron, E., Balakrishnan, V. (1994) *Linear Matrix Inequalities in System and Control Theory*. Studies in Applied Mathematics, **15**, Philadelphia, MA: SIMA
4. Blekhman, I. I., Fradkov, A. L., Nijmeijer, H., Pogromsky, A. Yu. (1997) On self-synchronization and controlled synchronization. *Sys. Contr. Lett.*, **31**(5):299 – 305
5. Chen, G., Dong, X. (1998) *From Chaos to Order - Perspectives, Methodologies, and Applications*. Singapore: World Scientific

6. Chua, L. O. (1994) Chua's circuit 10 years later. *Int. J. Circ. Theory Appl.*, **22**:279–305
7. Chua, L. O., Komuro, M., Matsumoto, T. (1986) The double scroll family. *IEEE Trans. Circ. Syst.-I*, **33**(11):1072–1118
8. Curran, P. F., Chua, L. O. (1997) Absolute stability theory and synchronization problem. *Int. J. Bifur. Chaos*, **7**(6):1375–1382
9. Fletcher, R. (1987) *Practical Methods of Optimization*. New York: Wiley
10. Hill, D. J., Moylan, P. J. (1976) The stability of nonlinear dissipative systems. *IEEE Trans. Auto. Contr.*, **21**:708–711
11. Isidori, A., Astolfi, A. (1992) Disturbance attenuation and H_∞ control via measurement feedback in nonlinear systems. *IEEE Trans. Auto. Contr.*, **37**:1283–1293
12. Kapitaniak, T., Chua, L. O. (1994) Hyperchaotic attractors of unidirectionally-coupled Chua's circuits. *Int. J. Bifur. Chaos*, **4**(2):477–482
13. Kennedy, M. P., Ogorzalek, M. J. (eds.) (1997) Special Issue on Chaos Synchronization, Control and Applications. *IEEE Trans. Circ. Syst.-I*, **44**(10)
14. Khalil, H. K. (1992) *Nonlinear Systems*. New York: Macmillan
15. Lakshmikantham, V., Bainov, D. D., Simeonov, P. S. (1989) *Theory of Impulsive Differential Equations*. Singapore: World Scientific
16. Lur'e, A. I., Postnikov, V. N. (1944) On the theory of stability of control systems. *Prikl. Mat. i Mehk.*, **8**(3)
17. Maciejowski, J. M. (1989) *Multivariable Feedback Design*. New York: Addison-Wesley
18. Madan, R. N. (ed.) (1993) *Chua's Circuit: A Paradigm for Chaos*. Singapore: World Scientific
19. Mahmoud M. S. (2000) *Robust Control and Filtering for Time-Delay Systems*. Marcel Dekker, Boston
20. Morgul, O., Solak, E. (1996) On the observer based synchronization of chaotic systems. *Phys. Rev. E*, **54**(5):4803–4811
21. Narendra, K. S., Taylor, J. H. (1973) *Frequency Domain Criteria for Absolute Stability*. New York: Academic Press
22. Nijmeijer, H. (ed.) (1997) Special Issue on Control of Chaos and Synchronization. *Sys. Contr. Lett.*, **31**(5)
23. Nijmeijer, H., Mareels, M. Y. (1997) An observer looks at synchronization. *IEEE Trans. Circ. Syst.-I*, **44**(10):882–890
24. Pecora, L. M., Carroll, T. L. (1991) Synchronization in chaotic Systems. *Phys. Rev. Lett.*, **64**(8):821–824
25. Pikovsky, A., Rosenblum, M., Kurths, J. (2001) *Synchronization: A Universal Concept in Nonlinear Science*. Cambnridge: Cambridge Univ. Prssss
26. Short, K. M. (1994) Steps toward unmasking secure communications. *Int. J. Bifur. Chaos*, **4**:957–977
27. Suykens, J. A. K., Curran, P. F., Chua, L. O. (1997) Master-slave synchronization using dynamic output feedback. *Int. J. Bifur. Chaos*, **7**(3):671–679
28. Suykens, J. A. K., Curran, P. F., Chua, L. O. (1999) Robust synthesis for master-slave synchronization of Lur'e systems. *IEEE Trans. Circ. Syst.-I*, **46**(7):841–850
29. Suykens, J. A. K., Huang, A., Chua, L. O. (1997) A family of n-scroll attractors from a generalized Chua's circuit. *Archiv fur Elektronik und Ubertragungstechnik*, **51**(3):131–138

30. Suykens, J. A. K., Vandewalle, J., Chua, L. O. (1997) Nonlinear H_∞ synchronization of chaotic Lur'e systems *Int. J. Bifur. Chaos*, **7**(6):1323–1335
31. Suykens, J. A. K., Curran, P. F., Yang, T., Vandewalle, J., Chua, L. O. (1997) Nonlinear H_∞ synchronization of Lur'e systems: dynamic output feedback case. *IEEE Trans. Circ. Syst.-I*, **44**(11):1089–1092
32. Suykens, J. A. K., Curran, P. F., Vandewalle, J., Chua, L. O. (1997) Robust nonlinear H_∞ synchronization of chaotic Lur'e systems. *IEEE Trans. Circ. Syst.-I*, **44**(10):891–904
33. Suykens, J. A. K., Vandewalle, J., De Moor, B. L. R. (1996) Artificial Neural Networks for Modelling and Control of Non-Linear Systems. Boston: Kluwer
34. Suykens, J. A. K., Yalçın, M. E., Vandewalle, J. (2002) A generic class of chaotic and hyperchaotic circuits with synchronization methods. In *Chaos in Circuits and Systems*, ed. by Chen, G., Ueta, T. Singapore: World Scientific, 151–170
35. Suykens, J. A. K., Yang, T., Chua, L. O. (1998) Impulsive synchronization of chaotic Lur'e systems by measurement feedback. *Int. J. Bifur. Chaos*, **8**(6):1371–1381
36. Suykens, J. A. K., Yang, T., Vandewalle, J., Chua, L. O. (1998) Impulsive synchronization of Lur'e systems: state feedback case. In Proc. of the IEEE Conference on Decision and Control, Tampa, Florida, 1963–1966
37. Suykens, J. A. K., Yang, T., Vandewalle, J., Chua, L. O. (1999) Impulsive control and synchronization of chaos. In *Controlling Chaos and Bifurcations in Engineering Systems*, ed. by Chen, G. Boca Raton, FL: CRC Press, 275–298
38. Vidyasagar, M. (1993) Nonlinear Systems Analysis. Englewood Cliffs, NJ: Prentice-Hall
39. Willems, J. C. (1972) Dissipative dynamical systems I: General theory. II: Linear systems with quadratic supply rates. *Archive for Rational Mechanics and Analysis*, **45**:321–343
40. Wu, C. W., Chua, L. O. (1994) A unified framework for synchronization and control of dynamical systems. *Int. J. Bifur. Chaos*, **4**(4):979–989
41. Yalçın, M. E., Suykens, J. A. K., Vandewalle, J. (1999) Experimental confirmation of nonlinear H_∞ synchronization for Chua's circuit. In Proc. of the European Conference on Circuit Theory and Design, Stresa, Italy, 177–180
42. Yalçın, M. E., Suykens, J. A. K., Vandewalle, J. (1999) Experimental confirmation of a nonlinear H_∞ synchronization scheme with 5-scroll attractors. In Proc. of the International Workshop on Nonlinear Dynamics of Electronic Systems, Ronne, Denmark, 257–260
43. Yalçın, M. E., Ozoguz, S., Suykens, J. A. K., Vandewalle, J. (2002) Families of scroll grid attractors. *Int. J. Bifur. Chaos*, **12**(1):23–41
44. Yalçın, M. E., Suykens, J. A. K., Vandewalle, J. (2001) Master-slave synchronization of Lur'e systems with time-delay. *Int. J. Bifur. Chaos*, **11**(6):1707–1721
45. Yalçın, M. E., Suykens, J. A. K., Vandewalle, J. (2000) Mutual synchronization of Lur'e systems with time delay. In Proc. of the 2000 International Symposium on Nonlinear Theory and Its Applications, Dresden, Germany, 241–244.
46. Yalçın, M. E., Savaci, F. A. (1999) Realization of Chua's circuit by using voltage controlled voltage source (VCVS) and its harmonic balance analysis. ARI (ITU-Springer Verlag), **51**(3):169–174
47. Yang, T., Chua, L. O. (1997) Impulsive stabilization for control and synchronization of chaotic systems: Theory and application to secure communication. *IEEE Trans. Circ. Syst.-I*, **44**(10):976–988

48. Yang, T., Chua, L. O. (1998) Applications of chaotic digital code-division multiple access (CDMA) to cable communication systems. *Int. J. Bifur. Chaos*, **8**(8):1657–1669
49. Yang, T. (2001) Impulsive Control Theory. New York: Springer-Verlag

Neural Network Design for Chaos Synchronization

Edgar N. Sanchez¹, Jose P. Perez², and Luis J. Ricalde¹

¹ CINVESTAV, Unidad Guadalajara
Apartado Postal 31-438, Plaza La Luna
Guadalajara, Jalisco C. P. 45091, Mexico
e-mail: sanchez@gdl.cinvestav.mx

² CINVESTAV, Unidad Guadalajara, and
School of Physics and Mathematics
Universidad Autonoma de Nuevo Leon (UANL)
Monterrey, Mexico

Abstract. This chapter presents an application of neural networks to chaos synchronization. The two main methodologies, on which the approach is based, are recurrent neural networks and inverse optimal control for nonlinear systems. On the basis of the last technique, chaos is first produced by a stable recurrent neural network; an adaptive recurrent neural controller is then developed for chaos synchronization.

1 Introduction

Chaotic behavior, as a characteristic of a dynamical system, could be desirable or undesirable, depending of the current application. In mixing substances process a chaotic behavior might improve the efficiency of the system, while in process which involves vibrations chaos could produce critical structural failures. As a consequence, it is important to be able to manipulate the chaotic nature of the systems, driving a stable system to be chaotic or otherwise stabilize a chaotic system. In many applications, it is also important to change the chaotic nature of a system without losing the chaotic behavior.

Controlling and synchronizing chaotic dynamical systems has recently attracted a great deal of attention within the engineering society, in which different techniques have been proposed. For instance, linear state space feedback [3], Lyapunov function methods [18], adaptive control [29], and bang-bang control [27], among many others [5].

On the other hand, control methods of general nonlinear systems have been extensively developed since the early 1980's, for example based on differential geometry theory [15]. Recently, the passivity approach has generated increasing interest for synthesizing control laws for nonlinear systems [2,9,16]. An important problem in this field is how to achieve robust nonlinear control in the presence of unmodelled dynamics and external disturbances; along the same line there is the so-called H_∞ nonlinear control [1,12]. One major difficulty with this approach, alongside its possible system structural instability

issue, seems to be caused by the requirement of solving some associated PDE equations. In order to alleviate this computational problem, the so-called inverse optimal control technique was recently introduced to nonlinear systems [25], and further extended to obtain robust nonlinear control systems in [14].

After their rebirth in the mid-1980's, artificial neural networks have become a working technology, which has been applied in many disciplines such as physics, computer science, and engineering. They find applications in such diverse fields as modelling, time series analysis, signal processing and control systems due to their ability to learn from experimental data. For a comprehensive foundation, see [8].

In this chapter, on the basis of recurrent neural networks, we develop two different schemes for chaos synchronization. After briefly reviewing the basic concepts of inverse optimal control, chaos is first produced by a stable recurrent neural networks, and then an adaptive recurrent neural controller is developed for chaos synchronization.

2 Inverse Optimal Control

This section closely follows [14] and [25]. As stated in [25], optimal stabilization guarantees several desirable properties for closed-loop systems, including stability margins. In a direct approach we would have to solve the so-called Hamilton-Jacobi-Bellman (HJB) equation, which is not an easy task. Besides, the robustness achieved is largely independent of the particular choice of two functions, denoted $l(x) > 0$ and $R(x) > 0$. This motivated to pursue the development of design methods that solve the inverse problem of optimal stabilization. In the inverse approach, a stabilizing feedback is designed first and then shown to optimize a cost functional of the form

$$J = \int_0^\infty (l(x) + u^T R(x)u) dt.$$

The problem is inverse because the functions $l(x)$ and $R(x)$ are *a posteriori* determined by the stabilizing feedback, rather than *a priori* chosen by the designer.

A stabilizing control law $u(x)$ solves an inverse optimal problem for the system

$$\dot{x} = f(x) + g(x)u,$$

if it can be expressed as

$$u = -k(x) = -\frac{1}{2}R^{-1}(x)(L_g V(x))^\top, \quad R(x) = R^\top(x) > 0,$$

where $V(x)$ is a positive semi-definite function, such that the negative semi-definiteness of \dot{V} is achieved with the control $u = -\frac{1}{2}k(x)$. That is,

$$\dot{V} = L_f V(x) - \frac{1}{2}L_g V(x)k(x) \leq 0.$$

When the function $l(x)$ is set to be the right hand side of

$$l(x) = -L_f V(x) + \frac{1}{2}L_g V(x)k(x) \geq 0,$$

then $V(x)$ is a solution of the HJB equation

$$l(x) + L_f V(x) - \frac{1}{4}(L_g V(x))R^{-1}(x)(L_g V(x))^T = 0.$$

Based on this inverse optimal control approach, disturbance attenuation is considered in [14]. Two types of disturbance attenuation are considered: a) input-to-state stabilization, and b) differential games. They are demonstrated to be equivalent. These results can be seen as the solution of a nonlinear H_∞ problem without requiring the Hamilton-Jacobi-Isaacs (HJI) partial differential equation to be solved.

In order to solve the disturbance attenuation problem, the following non-linear system is considered:

$$\dot{x} = f(x, t) + g_1(x)d, \quad (1)$$

where $x \in \Re^n$ is the state, $d \in \Re^r$ is the disturbance and $f(0, t) = 0$.

In this section, from this point, all concepts follow [14].

Definition 2.1. System (1) is said to be input-to-state stable (ISS), if there exist a class- KL function [11] β and a class- K function [11] χ , such that for any $x(t_0)$ and any d continuous on $[0, \infty)$, the solution exist for all $t \geq 0$ and satisfies

$$|x(t)| \leq \beta(|x(t_0)|, t - t_0) + \chi \left(\sup_{0 \leq t_0 \leq t} |d(t)| \right)$$

for all t_0 and t such that $0 \leq t_0 \leq t$.

Consider the system which, in addition to the disturbance d , also has a control input u :

$$\dot{x} = f(x) + g_1(x)d + g_2(x)u, \quad (2)$$

where $u \in \Re^m$. The time dependence from f and g_1 are omitted for simplicity.

Definition 2.2. System (2) is input-to-state stabilizable, if there exist a control law $u = \alpha(x)$ continuous everywhere with $\alpha(0) = 0$ (small control property) such that the closed loop system is ISS with respect to d .

Definition 2.3. A smooth positive defined radially unbounded function [11] $V : \mathbb{R}^n \rightarrow \mathbb{R}$ is called an ISS-control Lyapunov function (iss-clf) for (2), if there exist a class- K_∞ [11] function ρ such that the following implication holds for all $x \neq 0$ and all $d \in \mathbb{R}^r$:

$$|x| > \rho(|d|) \Rightarrow \inf_{u \in \mathbb{R}^m} \{L_f V + L_{g_1} V + L_{g_2} V u\} < 0,$$

where $L_f V + L_{g_1} V + L_{g_2} V u$ stand for the respective Lie derivatives.

Theorem 2.1. System (2) is input-to-state stabilizable, if and only if there exists an iss-clf with the small control property.

Definition 2.4. The inverse optimal control gain assignment problem for system (2) is solvable if there exist a class- K_∞ function γ , whose derivative is also a class- K_∞ function, a matrix-valued function $R_2(x) = R_2^\top(x) > 0$ for all $x \neq 0$, positive definite and radially unbounded functions $l(x)$ and $T(x)$, and a feedback law $u = \alpha(x)$, continuous everywhere with $\alpha(0) = 0$, which minimizes the cost functional

$$J(u) = \sup_{d \in D} \left\{ \lim_{t \rightarrow \infty} \left[T(x(t)) + \int_0^t (l(x) + u^\top R_2(x) u - \gamma(|d|)) d\tau \right] \right\},$$

where D is a set of bounded functions of x .

A typical choice of the Lyapunov function is the following:

$$V = \frac{1}{2} (x^2 + y^2 + z^2). \quad (3)$$

3 Chaos Production by Recurrent Neural Networks

It is now known that a neural network, if appropriately designed, can reproduce chaos after intensive learning [4] or via small-amplitude perturbations [28]. And yet how to achieve this goal by using some traditional feedback control strategies is still open for investigation. This section addresses this issue and completes a conventional controller design for this purpose.

In this section, a new approach is developed for reproducing chaos by a dynamic neural network from an inverse optimal control approach. As an example for demonstration, Chen's chaotic system is studied. The control law is derived to force the neural network to reproduce Chen's chaotic attractor. Computer simulation is included to show the success of the design.

3.1 Mathematical description

Consider the following dynamic neural network:

$$\dot{x} = Ax + Wf(x) + u, \quad x, u \in \mathbb{R}^n, \quad A, W \in \mathbb{R}^{n \times n}, \quad (4)$$

where x is the state, u is the input, $A = -\lambda I$, with λ being a positive constant, is the state-feedback matrix, $f(\cdot)$ is a bounded sector function [11] such that $f(x) = 0$ only at $x = 0$ and that $\lim_{x \rightarrow \infty} (f(x))^\top x = +\infty$, and W is the weight matrix.

A common selection for the basic element of $f(\cdot)$ is the sector function $\sigma(\cdot) = \tanh(\cdot)$. There exist positive constants k_1 and k_2 such that $k_1 \|x\|_2^2 \leq (f(x))^\top x \leq k_2 \|x\|_2^2$. Also, (4) can be expressed as $\dot{x} = \tilde{f}(x) + g(x)u$, with $\tilde{f}(x) = Ax + Wf(x)$ and $g(x) = I$. It is clear that $x = 0$ is an equilibrium point of this system, when $u = 0$.

Let the model system (for the neural network to track) be

$$\dot{x}_r = f(x_r) + g(x_r)u_r, \quad x_r, u_r \in \mathbb{R}^n, \quad f(\cdot) \in \mathbb{R}^n, \quad g(\cdot) \in \mathbb{R}^{nxn}, \quad (5)$$

where x_r is the state, u_r is the input, and $f(\cdot)$ and $g(\cdot)$ are smooth nonlinear functions of appropriate dimensions.

As is clear, this setup is very general, and the model (5) can be a complex such as a chaotic nonlinear system.

3.2 Model-following as a stabilization problem

Define the model following error to be

$$e = x - x_r, \quad (6)$$

and then substitute (4) and (5) into (6), with the use of $f(\cdot) = \sigma(\cdot) = \tanh(\cdot)$, to obtain

$$\dot{e} = Ae + W\sigma(e + x_r) + u - f(x_r) - g(x_r)u_r + Ax_r. \quad (7)$$

Adding and subtracting to (7) the terms $W\sigma(x_r)$ and $\alpha(t)$ gives

$$\begin{aligned} \dot{e} &= Ae + W(\sigma(e + x_r) - \sigma(x_r)) + Ax_r + W\sigma(x_r) + \alpha(t) \\ &\quad - (f(x_r) + g(x_r)u_r) + (u - \alpha(t)), \end{aligned} \quad (8)$$

where $\alpha(\cdot)$ is a function to be determined.

For system (4) to follow model (5), the following solvability assumption is needed, as discussed in [14]:

Assumption 1. There exist functions $\rho(t)$ and $\alpha(t)$ such that

$$\begin{aligned} \frac{d\rho(t)}{dt} &= A\rho(t) + W\sigma(\rho(t)) + \alpha(t) \\ \rho(t) &= x_r(t). \end{aligned} \quad (9)$$

It follows from (9) and (5) that

$$Ax_r + W\sigma(x_r) + \alpha(t) = f(x_r) + g(x_r)u_r, \quad (10)$$

so that (8) becomes

$$\dot{e} = Ae + W(\sigma(e + x_r) - \sigma(x_r)) + (u - \alpha(t)). \quad (11)$$

Now, by introducing the following functions:

$$\begin{aligned}\phi(e, x_r) &= \sigma(e + x_r) - \sigma(x_r) \\ \tilde{u} &= (u - \alpha(t)),\end{aligned}$$

we can rewrite (11) as

$$\dot{e} = Ae + W\phi(e, x_r) + \tilde{u}, \quad (12)$$

where x_r can be viewed as an external disturbance. It is obvious that $e = 0$ is an equilibrium point of (12), when $\tilde{u} = 0$.

Consider the function $\phi(e, x_r) = \sigma(e + x_r) - \sigma(x_r)$. Clearly, if $e = 0$ then $\phi(e, x_r) = 0$. Moreover, for each component, $e_i > 0$ implies $e_i + x_{ri} > x_{ri}$ for all x_{ri} . Since σ is monotonically increasing, $\sigma(e + x_r) > \sigma(x_r)$ and $\phi(e, x_r)^\top e = (\sigma(e + x_r) - \sigma(x_r))^\top e > 0$. Similarly, $e_i < 0$ implies $e_i + x_{ri} < x_{ri}$ for all x_{ri} . Since σ is monotonically increasing, $\sigma(e + x_r) < \sigma(x_r)$ and $\phi(e, x_r)^\top e = (\sigma(e + x_r) - \sigma(x_r))^\top e > 0$. Therefore, $\phi(e, x_r)$ is a sector function and is Lipschitz with respect to e .

At this point, the model-following problem can be restated as a global asymptotical stabilization problem for system (12).

3.3 Inverse optimal control

To globally asymptotically stabilize system (12), we proceed along the line of the inverse optimal control approach [14].

We first find a candidate function as an input-to-state control Lyapunov function, which is essential for the design of a globally asymptotically stabilizing control law in this approach. Consider

$$V(e) = \sum_{i=1}^n \int_0^{e_i} \phi(\eta, x_r) d\eta. \quad (13)$$

Since $\phi(e, x_r)$ is a sector function with respect to e , $V(e)$ is radially unbounded, i.e., $V(e) > 0$ for all $e \neq 0$ and $V(e) \rightarrow +\infty$ as $e \rightarrow \infty$. Its time-derivative is

$$\begin{aligned}\dot{V}(e) &= \phi(e, x_r)^\top (Ae + W\phi(e, x_r) + \tilde{u}) \\ &= \phi(e, x_r)^\top Ae + \phi(e, x_r)^\top W\phi(e, x_r) + \phi(e, x_r)^\top \tilde{u} \\ &= -\lambda \phi(e, x_r)^\top e + \phi(e, x_r)^\top W\phi(e, x_r) + \phi(e, x_r)^\top \tilde{u} \\ &:= L_f V + (L_g V) \tilde{u},\end{aligned} \quad (14)$$

where $L_f V = -\lambda \phi(e, x_r)^\top e + \phi(e, x_r)^\top W\phi(e, x_r)$ and $L_g V = \phi(e, x_r)^\top$.

Next, consider the following inequality, proved in [21]:

$$X^\top Y + Y^\top X \leq X^\top \Lambda X + Y^\top \Lambda^{-1} Y, \quad (15)$$

which holds for all matrices $X, Y \in \mathbb{R}^{n \times k}$ and $\Lambda \in \mathbb{R}^{n \times n}$ with $\Lambda = \Lambda^\top > 0$.

Applying (15) with $\Lambda = I$ to $\phi(e, x_r)^\top W \phi(e, x_r)$, we obtain

$$\begin{aligned} \dot{V}(e) &\leq -\lambda \phi(e, x_r)^\top e + \frac{1}{2} \phi(e, x_r)^\top \phi(e, x_r) \\ &\quad + \frac{1}{2} \phi(e, x_r)^\top W^\top W \phi(e, x_r) + \phi(e, x_r)^\top \tilde{u}. \end{aligned} \quad (16)$$

Again, since $\phi(e, x_r)$ is a sector function with respect to e , there exist positive constants k_1 and k_2 such that $k_1 \|e\|_2^2 \leq \phi(e, x_r)^\top e \leq k_2 \|e\|_2^2$. Also, since $\phi(e, x_r)$ is Lipschitz with respect to e , there exists a positive constant L_ϕ such that $\phi(e, x_r)^\top \phi(e, x_r) \leq L_\phi^2 \|e\|_2^2$. Henceforth (16) can be rewritten as

$$\dot{V} \leq -\left(\lambda k_1 - \frac{1}{2} L_\phi^2\right) \|e\|_2^2 + \frac{1}{2} \phi(e, x_r)^\top W^\top W \phi(e, x_r) + \phi(e, x_r)^\top \tilde{u}. \quad (17)$$

Now, we suggest to use the following control law:

$$\tilde{u} = -\left(W^\top W + I\right) \phi(e, x_r) := -\beta (R(e))^{-1} (L_g V)^\top, \quad (18)$$

where β is a positive constant and $(R(e))^{-1}$ is a function of e in general but here it is chosen to be

$$(R(e))^{-1} = \frac{1}{\beta} (W^\top W + I). \quad (19)$$

The motivation for this choice of the control law will be seen from the optimization discussed below.

Substituting (18) into (17), we obtain

$$\begin{aligned} \dot{V}(e) &\leq -\left(\lambda k_1 - \frac{1}{2} L_\phi^2\right) \|e\|_2^2 - \frac{1}{2} \|W^\top W\| L_\phi^2 \|e\|_2^2 - L_\phi^2 \|e\|_2^2 \\ &\leq -\left(\lambda k_1 - \frac{1}{2} L_\phi^2 + \frac{1}{2} \|W^\top W\| L_\phi^2 + L_\phi^2\right) \|e\|_2^2 \end{aligned} \quad (20)$$

If $\lambda k_1 - \frac{1}{2} L_\phi^2 + \frac{1}{2} \|W^\top W\| L_\phi^2 + L_\phi^2 > 0$, or equivalently,

$$\|W^\top W\| > 2 \left(-\lambda k_1 - \frac{1}{2} L_\phi^2\right) / L_\phi^2,$$

which can always be satisfied, then $\dot{V}(e) < 0$ for all $e \neq 0$. This means that the proposed control law (18) can globally asymptotically stabilize the system (12) and so ensures the model-following of (5) by (4).

Note that system (12) is input-to-state stabilizable, because its control Lyapunov function satisfies the small control property [14]. Besides, the inverse optimal control problem, defined below, is solvable.

For the purpose of assigning the control gain, following [14], we consider the control law (18) and define a cost functional as follows:

$$J(\tilde{u}) = \lim_{t \rightarrow \infty} \left\{ 2\beta V(e) + \int_0^t \left(l(e) + \tilde{u}^\top R(e) \tilde{u} \right) d\tau \right\}, \quad (21)$$

where

$$\begin{aligned} l(e) &= -2\beta L_f V + 2\beta (L_g V) (R(e))^{-1} (L_g V)^\top \\ &\quad + \beta(\beta - 2) (L_g V) (R(e))^{-1} (L_g V)^\top \\ &= -2\beta L_f V + \beta (L_g V) \left(\beta (R(e))^{-1} \right) (L_g V)^\top. \end{aligned}$$

According to the basic idea of the inverse optimal control theory, it is required that $l(e)$ be radially unbounded, i.e., $l(e) > 0$ for all $e \neq 0$ and $l(e) \rightarrow +\infty$ as $e \rightarrow \infty$. In order to prove this property, we first specify the term $\beta (R(e))^{-1} (L_g V)^\top$ in the expression of $l(e)$ to be $(W^\top W + I) \phi(e, x_r)$ (see (19)). We also specify the terms $L_g V$ and $L_f V$ by their definitions. We thus obtain

$$\begin{aligned} l(e) &= 2\beta \lambda \phi(e, x_r)^\top e - 2\beta \phi(e, x_r)^\top W \phi(e, x_r) \\ &\quad + \beta \phi(e, x_r)^\top (W^\top W + I) \phi(e, x_r). \end{aligned} \quad (22)$$

Next, by applying inequality (15) to the second term of the right-hand side of (22) we obtain

$$\begin{aligned} l(e) &\geq 2\beta \lambda \phi(e, x_r)^\top e - \beta \phi(e, x_r)^\top \phi(e, x_r) - \beta \phi(e, x_r)^\top W^\top W \phi(e, x_r) \\ &\quad + \beta \phi(e, x_r)^\top (W^\top W + I) \phi(e, x_r) \\ &\geq 2\beta \lambda \phi(e, x_r)^\top e. \end{aligned}$$

Because $\phi(e, x_r)^\top$ is a sector function with respect to e ,

$$l(e) \geq 2\beta \lambda \phi(e, x_r)^\top e \geq 0$$

and $\lim_{e \rightarrow \infty} l(e) = +\infty$, which satisfies the radially unbounded condition.

Substituting \tilde{u} defined by (18) into (14), we obtain

$$\dot{V} = L_f V + (L_g V) (-\beta (R(e))^{-1}) (L_g V)^\top.$$

Then, multiplying it by -2β , we obtain

$$-2\beta \dot{V} = -2\beta L_f V + 2\beta^2 (L_g V) (R(e))^{-1} (L_g V)^\top.$$

Finally, taking into account of (18), which implies

$$\tilde{u}^\top R(e) \tilde{u} = \beta^2 (L_g V)(R(e))^{-1} (L_g V)^\top,$$

we arrive at

$$l(e) + \tilde{u}^\top R(e) \tilde{u} = -2\beta \dot{V}. \quad (23)$$

To this end, substituting (23) into (21), we have

$$\begin{aligned} J(\tilde{u}) &= \lim_{t \rightarrow \infty} \left\{ 2\beta V(e(t)) + \int_0^t -2\beta \dot{V} d\tau \right\} \\ &= \lim_{t \rightarrow \infty} \{ 2\beta V(e(t)) - 2\beta V(e(t)) + 2\beta V(e(0)) \} \\ &= 2\beta V(e(0)). \end{aligned}$$

Thus, the minimum of the cost functional is $J(\tilde{u}) = 2\beta V(e(0))$, for the optimal control law (18).

In summary, the optimal and stabilizing control law, which guarantees the model-following requirement of (5) by (4), is given by

$$\tilde{u}^* = - (W^T W + I) \phi(e, x_r)$$

In order to obtain the final controller u precisely, as input to the neural network (4), we take into account the equalities $u = \tilde{u}^* + \alpha(t)$ and $\alpha(t) = f(x_r) + g(x_r)u_r - Ax_r - W\sigma(x_r)$. This leads to

$$u = -W^T W \phi(e, x_r) - \phi(e, x_r) + f(x_r) + g(x_r)u_r - Ax_r - W\sigma(x_r). \quad (24)$$

Substituting (24) into (4) then gives

$$\begin{aligned} \dot{x} &= Ax + W\sigma(x) - W^T W \phi(e, x_r) - \phi(e, x_r) + f(x_r) + g(x_r)u_r \\ &\quad - Ax_r - W\sigma(x_r) \\ &= -\lambda e + W(\sigma(e + x_r) - \sigma(x_r)) - W^T W \phi(e, x_r) + I\phi(e, x_r) \\ &\quad + f(x_r) + g(x_r)u_r \\ &= -\lambda e + (W - W^T W + I)(\sigma(e + x_r) - \sigma(x_r)) + f(x_r) \\ &\quad + g(x_r)u_r. \end{aligned} \quad (25)$$

It follows from the last equation of (25) that, as $e \rightarrow 0$, the desired model-following goal is achieved.

3.4 Chaos reproduction

To demonstrate the applicability of the proposed approach, consider the case of a chaos reproduction problem. Chaos has been shown to be quite useful in many engineering applications, and there is a strong and increasing demand for generating chaos at will [5]. In this new research direction, chaos reproduction is one important task, particularly using neural networks [4, 5].

To show that the model-following controller designed in this chapter can also accomplish this chaos-reproduction task, we apply the developed methodology to Chen's system, recently discovered [6]. This system is described by

$$\begin{aligned}\dot{x} &= a(y - x) \\ \dot{y} &= (c - a)x - xz + cy \\ \dot{z} &= xy - bz,\end{aligned}\tag{26}$$

which has a chaotic attractor as shown in Fig. 1 when $a = 35, b = 3, c = 28$. It has been experienced that this chaotic system is relatively difficult to control as compared to the Lorenz and Chua's system due to the prominent three-dimensional and some complex features of its attractor.

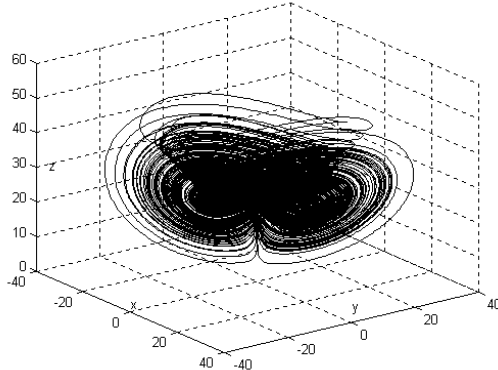


Fig. 1. Attractor of Chen's chaotic system

To follow the chaotic attractor of system (26), we select the following controlled neural network:

$$\begin{aligned}\begin{pmatrix} \dot{x} \\ \dot{y} \\ \dot{z} \end{pmatrix} &= \begin{pmatrix} -2 & 0 & 0 \\ 0 & -2 & 0 \\ 0 & 0 & -2 \end{pmatrix} \begin{pmatrix} x \\ y \\ z \end{pmatrix} \\ &\quad + \begin{pmatrix} 0.3 & 0.8 & 0 \\ 0.4 & 0.3 & 0 \\ 0 & 0 & 1 \end{pmatrix} \begin{pmatrix} \tanh(x) \\ \tanh(y) \\ \tanh(z) \end{pmatrix} + \begin{pmatrix} u_1 \\ u_2 \\ u_3 \end{pmatrix}.\end{aligned}\tag{27}$$

It can be easily verified that network (27) satisfies the condition to be input-to-state stable, which was derived in [21].

3.5 Simulation results

For the network (27) to follow the chaotic system (26), we implement the control law (24). In our simulation, the following initial conditions were used:

$$\begin{pmatrix} x_r(0) \\ y_r(0) \\ z_r(0) \end{pmatrix} = \begin{pmatrix} -10 \\ 0 \\ 37 \end{pmatrix}, \quad \begin{pmatrix} x(0) \\ y(0) \\ z(0) \end{pmatrix} = \begin{pmatrix} 50 \\ 70 \\ 90 \end{pmatrix}.$$

Our simulation produced a 3-dimensional Chen's attractor that is visually indistinguishable from that shown in Fig. 1. Therefore, to reveal more insights of the reproduced attractor, Figure 2 shows the resulting orbit for the first state variable, while those corresponding to the second and the third state variables are displayed in Fig. 3 and Fig. 4, respectively.

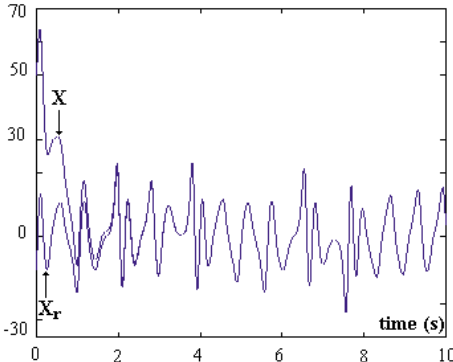


Fig. 2. First state variable in reproduction

4 Chaos Synchronization via Adaptive Recurrent Neural Control

Since the seminal publication [17], there has been increasing interest for applying neural networks to identification and control of nonlinear systems. Most of these applications uses feedforward structures [7, 10]. Lately, the use of dynamic neural networks is increasing, which allows more efficient modelling of dynamic systems [19]. Two recent books [20, 26] have reviewed the application of dynamic neural networks for nonlinear system identification and control. In [26], off-line learning is used, and [20] analyzes adaptive identification and control by means of on-line learning, where stability of the closed loop is established based on the Lyapunov function method. In [20]

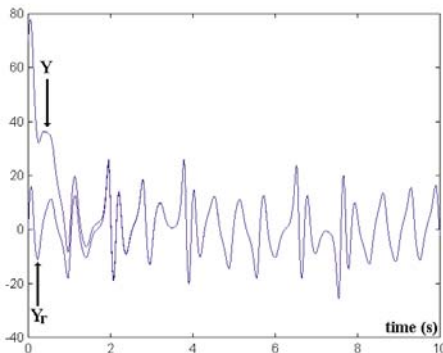


Fig. 3. Second state variable in reproduction

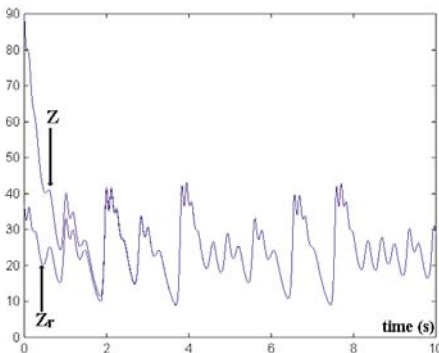


Fig. 4. Third state variable in reproduction

the tracking problem is reduced to a linear model following and the main application focuses on DC electric motors.

Using the inverse optimal control approach, a control law, which allows to reproduce chaos on a dynamic neural network, was discussed in [22]. In this section, we further extend these results to the adaptive case for non-linear system trajectory tracking. The proposed new scheme is composed of a dynamic neural identifier, which builds an on-line model for the unknown plant, and a control law, which ensures that the unknown plant tracks the reference trajectory. The applicability of the approach is illustrated by one example: chaos synchronization. An early publication of the section results is [24].

In the following, we first briefly describe the dynamic neural network to be used.

4.1 Recurrent high-order neural network

In [13], recurrent high order neural network (RHONN) are defined as

$$\dot{x}_i = -a_i x_i + \sum_{k=1}^L w_{ik} \prod_{j \in I_k} y_j^{d_j(k)}, \quad i = 1, \dots, n, \quad (28)$$

where x_i is i -th neuron state, L is number of high-order connections, $\{I_1, I_2, \dots, I_L\}$ is a collection of non-ordered subsets of $\{1, 2, \dots, m+n\}$, $a_i > 0$, w_{ik} are the adjustable weights of the neural network, $d_j(k)$ are nonnegative integers, and y is a vector defined as: $y = [y_1, \dots, y_n, y_{n+1}, \dots, y_{n+m}]^\top = [S(x_1), \dots, S(x_n), S(u_1), \dots, S(u_m)]^\top$, with $u = [u_1, u_2, \dots, u_m]^\top$ the input to the neural networks, and $S(\cdot)$ a smooth sigmoid function formulated by $S(x) = \frac{1}{1+\exp(-\beta x)} + \varepsilon$. For the sigmoid, β is a positive constant and ε is a small positive real number. Hence $S(x) \in [\varepsilon, \varepsilon + 1]$.

As can be seen, (28) allows the inclusion of high-order terms.

Defining the vector

$$z(x, u) = [z_1(x, u), \dots, z_L(x, u)]^\top = \left[\prod_{j \in I_1} y_j^{d_j(1)}, \dots, \prod_{j \in I_L} y_j^{d_j(L)} \right]^\top,$$

then (28) can be rewritten as

$$\dot{x}_i = -a_i x_i + \sum_{k=1}^L w_{ik} z_k(x, u), \quad i = 1, \dots, n,$$

or

$$\dot{x}_i = -a_i x_i + w_i^\top z_i(x, u), \quad i = 1, \dots, n, \quad (29)$$

where $w_i = [w_{i,1} \dots w_{i,L}]^\top$.

In this chapter, we consider such terms as

$$y = [y_1, \dots, y_n, y_{n+1}, \dots, y_{n+m}]^\top = [S(x_1), \dots, S(x_n), u_1, \dots, u_n]^\top,$$

which means that we are assuming the same number of inputs and states. We also assume that the input to the neural network enters directly. Hence (28) can be rewritten as

$$\dot{x}_i = -a_i x_i + w_i^\top z_i(x) + u_i, \quad i = 1, \dots, n. \quad (30)$$

Reformulating (29) in matrix form yields

$$\dot{x} = Ax + Wz(x) + u \quad (31)$$

where $x \in \mathbb{R}^n$, $W^* \in \mathbb{R}^{n \times L}$, $z(x) \in \mathbb{R}^L$, $u \in \mathbb{R}^n$, and $A = -\lambda I$, $\lambda > 0$.

In this chapter, we use a slight modification of RHONN as follows

$$\dot{x} = Ax + W\Gamma z(x) + u,$$

where $\Gamma \in \Re^{L \times L}$ is a diagonal matrix defined as

$$\Gamma = \begin{pmatrix} \gamma_1 & 0 & \cdots & \cdot & 0 \\ 0 & \gamma_2 & \cdots & \cdot & 0 \\ \cdot & \cdot & \cdots & \cdot & \cdot \\ \cdot & \cdot & \cdots & \cdot & \cdot \\ \cdot & \cdot & \cdots & \gamma_{L-1} & 0 \\ 0 & 0 & \cdots & 0 & \gamma_L \end{pmatrix}$$

$$\gamma_i > 0, \quad i = 1 \dots L.$$

These γ parameters play the role of the step for the gradient-descent algorithm defined below.

4.2 Plant modelling

The unknown nonlinear plant is modelled as

$$\dot{x}_p = F_p(x_p, u) \triangleq f_p(x_p) + g_p(x_p)u \quad (32)$$

where $x_p, f_p \in \Re^n$, $g_p \in \Re^{n \times n}$, $u \in \Re^n$.

Taking into account that both f_p and g_p are unknown, we propose to model (32) by a neural networks in the form (31). Henceforth the plant model becomes

$$\dot{x}_p = \dot{x} + w_{per} = Ax + W^* \Gamma z(x) + w_{per} + u, \quad (33)$$

where the term w_{per} represents the modelling error, and W^* are the unknown values of the neural network weights which minimize the modelling error. In this chapter, we define $w_{per} = x - x_p$.

4.3 Tracking analysis

We proceed to analyze the tracking error between the unknown plant modelled as (33) and a reference trajectory defined by

$$\dot{x}_r = f_r(x_r, u_r), \quad x_r \in \Re^n. \quad (34)$$

For this purpose, we define the tracking error by

$$e = x_p - x_r, \quad (35)$$

whose time derivative is

$$\begin{aligned} \dot{e} &= \dot{x}_p - \dot{x}_r \\ &= Ax + W^* \Gamma z(x) + w_{per} + u - f_r(x_r, u_r). \end{aligned} \quad (36)$$

Now, by adding and subtracting, to the right hand side of (36) the terms $\hat{W}\Gamma z(x_r)$, $\alpha_r(t, \hat{W})$, and Ae , and by taking into account $w_{per} = x - x_p$, then

$$\begin{aligned}\dot{e} &= Ax + W^*z(x) + x - x_p + u - f_r(x_r, u_r) \pm \hat{W}\Gamma z(x_r) \pm \alpha_r(t, \hat{W}) \pm Ae \\ &= Ae + W^*\Gamma z(x) + u - \hat{W}\Gamma z(x_r) - \alpha_r(t, \hat{W}) \\ &\quad + \left(-f_r(x_r, u_r) + \hat{W}\Gamma z(x_r) + x - x_p + Ax - Ae + \alpha_r(t, \hat{W}) \right),\end{aligned}\quad (37)$$

where \hat{W} is an estimation of W^* .

At this stage, the terms Ax_r and x_r are added and subtracted to (37) to obtain

$$\begin{aligned}\dot{e} &= Ae + W^*\Gamma z(x) + u \\ &\quad + \left(-f_r(x_r, u_r) + Ax_r + \hat{W}\Gamma z(x_r) + x_r - x_p + \alpha_r(t, \hat{W}) \right) \\ &\quad - Ae - \hat{W}\Gamma z(x_r) - \alpha_r(t, \hat{W}) - Ax_r - x_r + x + Ax.\end{aligned}\quad (38)$$

Assumption 2. Following [14], the following equality is assumed:

$$Ax_r + \hat{W}\Gamma z(x_r) + x_r - x_p + \alpha_r(t, \hat{W}) = f_r(x_r, u_r). \quad (39)$$

Then, (38) is reduced to

$$\dot{e} = Ae + W^*\Gamma z(x) - \hat{W}\Gamma z(x_r) - Ae + (A + I)(x - x_r) + u - \alpha_r(t, \hat{W}). \quad (40)$$

Adding and subtracting to (40) the term $\hat{W}\Gamma z(x)$ gives

$$\begin{aligned}\dot{e} &= Ae + \left(W^* - \hat{W} \right) \Gamma z(x) + \hat{W}\Gamma (z(x) - z(x_r)) \\ &\quad + (A + I)(x - x_r) - Ae + u - \alpha_r(t, \hat{W}).\end{aligned}\quad (41)$$

Then, defining

$$\tilde{W} = W^* - \hat{W}, \quad \tilde{u} = u - \alpha_r(t, \hat{W}), \quad (42)$$

and substituting (42) in (41), we obtain

$$\begin{aligned}\dot{e} &= Ae + \tilde{W}\Gamma z(x) + \hat{W}\Gamma (z(x) - z(x_r)) + (A + I)(x - x_r) - Ae + \tilde{u} \\ &= Ae + \tilde{W}\Gamma z(x) + \hat{W}\Gamma (z(x) - z(x_p) + z(x_p) - z(x_r)) \\ &\quad + (A + I)(x - x_p + x_p - x_r) - Ae + \tilde{u}.\end{aligned}\quad (43)$$

In order to continue the analysis, we define

$$\tilde{u} = u_1 + u_2 \quad (44)$$

with

$$u_1 = -\hat{W}\Gamma(z(x) - z(x_p)) - (A + I)(x - x_p). \quad (45)$$

Then (43) is reduced to

$$\dot{e} = Ae + \tilde{W}\Gamma z(x) + \hat{W}\Gamma (z(x_p) - z(x_r)) + (A + I)(x_p - x_r) - Ae + u_2. \quad (46)$$

Considering $e = x_p - x_r$, (46) can be rewritten as

$$\dot{e} = (A + I)e + \tilde{W}\Gamma z(x) + \hat{W}\Gamma (z(x_p) - z(x_r)) + u_2. \quad (47)$$

4.4 Tracking error stabilization

Once (47) obtained, we proceed to its stabilization. Notice that $e = 0$, $\tilde{W} = 0$, is an equilibrium point for the undisturbed autonomous system. In order to perform the stability analysis, we define the candidate Lyapunov function

$$V = \frac{1}{2}\|e\|^2 + \frac{1}{2}\text{tr}\left\{\tilde{W}^\top \tilde{W}\right\}, \quad (48)$$

whose time derivative, along the trajectories of (47), is

$$\begin{aligned} \dot{V} &= e^\top (A + I)e + e^\top \tilde{W}\Gamma z(x) + e^\top \hat{W}\Gamma(z(x_p) - z(x_r)) \\ &\quad + e^\top u_2 + \text{tr}\left\{\dot{\tilde{W}}^\top \tilde{W}\right\}. \end{aligned} \quad (49)$$

As in [20], we propose the following learning law:

$$\text{tr}\left\{\dot{\tilde{W}}^\top \tilde{W}\right\} = -e^\top \tilde{W}\Gamma z(x), \quad (50)$$

which can be written, element by element, as

$$\dot{\hat{w}}_{i,j} = e_i(\gamma_j z(x_j)), i = 1, 2, \dots, n, \quad j = 1, 2, \dots, L. \quad (51)$$

Replacing (50) in (49) yields

$$\begin{aligned} \dot{V} &= -(\lambda - 1)e^\top e + e^\top \hat{W}\Gamma(z(x_p) - z(x_r)) + e^\top u_2 \\ L_f V &= -(\lambda - 1)e^\top e + e^\top \hat{W}\Gamma(z(x_p) - z(x_r)) \\ L_g V &= e^\top. \end{aligned} \quad (52)$$

Next, consider the following inequality, proved in [21]:

$$X^\top Y + Y^\top X \leq X^\top \Lambda X + Y^\top \Lambda^{-1} Y, \quad (53)$$

which holds for all matrices $X, Y \in \Re^{n \times k}$ and $\Lambda \in \Re^{n \times n}$ with $\Lambda = \Lambda^\top > 0$, and applying it to the second term of (52) on the right, we obtain

$$\begin{aligned} \dot{V} &\leq -(\lambda - 1)e^\top e + \frac{1}{2}e^\top e \\ &\quad + \frac{1}{2}(z(x_p) - z(x_r))^\top \Gamma(\hat{W}^\top \hat{W}) \Gamma(z(x_p) - z(x_r)) + e^\top u_2 \\ \dot{V} &\leq -(\lambda - 1)e^\top e + \frac{1}{2}e^\top e + \frac{1}{2}\|\hat{W}\|^2 \|\Gamma\|^2 \|z(x_p) - z(x_r)\|^2 + e^\top u_2, \end{aligned}$$

where $\|\hat{W}\|$, $\|\Gamma\|$ are any matrix norms for \hat{W} and Γ .

Considering $x_p = e + x_r$ and defining $\phi_z = z(x_p) - z(x_r) = z(e + x_r) - z(x_r)$, then

$$\dot{V} \leq -(\lambda - 1)e^\top e + \frac{1}{2}e^\top e + \frac{1}{2}L_{\phi_z}^2 \|\hat{W}\|^2 \|\Gamma\|^2 \|e\|^2 + e^\top u_2 \quad (54)$$

$$\dot{V} \leq -(\lambda - 1)e^\top e + e^\top \left(\frac{1}{2} + \frac{1}{2}L_{\phi_z}^2 \|\hat{W}\|^2 \|\Gamma\|^2\right) e + e^\top u_2,$$

where $L_{\phi_z}^2$ is the Lipschitz constant of ϕ_z .

To this end, we define the following control law

$$\begin{aligned} u_2 &= -2 \left(\frac{1}{2} + \frac{1}{2} L_{\phi_z}^2 \|\hat{W}\|^2 \|\Gamma\|^2 \right) e \\ &\triangleq -\beta \left(R(e, \hat{W}) \right)^{-1} (L_g V)^\top, \quad \beta \left(R(e, \hat{W}) \right)^{-1} \\ &= 2 \left(\frac{1}{2} + \frac{1}{2} L_{\phi_z}^2 \|\hat{W}\|^2 \|\Gamma\|^2 \right) \end{aligned} \quad (55)$$

with the scalar $R(e, \hat{W}) > 0, \beta > 0$.

Substituting (55) in (54), we obtain

$$\dot{V} = -(\lambda - 1)e^\top e - e^\top \left(\frac{1}{2} + \frac{1}{2} L_{\phi_z}^2 \|\hat{W}\|^2 \|\Gamma\|^2 \right) e < 0, \forall e, \hat{W} \neq 0. \quad (56)$$

Hence $\lim_{t \rightarrow \infty} e(t) \rightarrow 0$.

Remark 1. From (56), we have

$$\dot{V} \leq -(\lambda - 1)\|e\|^2 - e^\top \left(\frac{1}{2} + \frac{1}{2} L_{\phi_z}^2 \|\hat{W}\|^2 \|\Gamma\|^2 \right) e < 0, \forall e \neq 0, \forall \hat{W},$$

where V is decreasing and bounded from below by $V(0)$, and since

$$V = \frac{1}{2}\|e\|^2 + \frac{1}{2} \operatorname{tr} \{ \tilde{W}^\top \tilde{W} \},$$

we conclude that $e, \hat{w} \in L_1$; this mean that both of them are bounded.

4.5 Inverse optimal control

Once the tracking error stabilized, according to [14], it is required to demonstrate that the same stabilizing control law (55) minimizes a meaningful cost functional, defined as

$$J(\tilde{u}) = \lim_{t \rightarrow \infty} \left\{ 2\beta V + \int_0^t \left(l(e, \hat{W}) + u_2^\top R(e, \hat{W}) u_2 \right) d\tau \right\}, \quad (57)$$

where the Lyapunov function solves the Hamilton-Jacobi-Bellman family of partial derivative equations parameterized with $\beta > 0$ as follows:

$$l(e, \hat{W}) + 2\beta L_f V - \beta^2 L_g V R(e, \hat{W})^{-1} L_g V^\top = 0, \quad (58)$$

Note that $2\beta V$ in (57) is bounded when $t \rightarrow \infty$, since by (56) V is decreasing and bounded from below by $V(0)$. Therefore, $\lim_{t \rightarrow \infty} V(t)$ exists and is finite.

In [14] we need $l(e, \hat{W})$ to be positive definite and radially unbounded with respect to e . Here, from (58) we have

$$l(e, \hat{W}) = -2\beta L_f V + \beta^2 L_g V R(e, \hat{W})^{-1} L_g V^\top.$$

Substituting (52) into (58) and then applying (53) to the second term on the right side of $L_f V$, we have

$$l(e, \hat{W}) \geq (\lambda - 1)\|e\|^2.$$

Since we select $\lambda > 1$, we know that $l(e, \hat{W})$ satisfies the condition of being positive definite and radially unbounded. Hence, (57) is a cost functional.

It is easy to verify that, in (57),

$$l(e, \hat{W}, \hat{W}_1) + \tilde{u}^\top R(e, \hat{W}, \hat{W}_1) \tilde{u} = -2\beta \dot{V},$$

with optimal value $J^* = 2\beta V(0)$. This is achieved by the control law (55).

Finally, the control law, which affects the plant and the neural network, can be obtained from (39), (42), (44), (45) and (55).

$$\begin{aligned} u &= \tilde{u} + \alpha_r(t, \hat{W}) \\ &= u_1 + u_2 + \alpha_r(t, \hat{W}) \\ &= -\hat{W}\Gamma(z(x) - z(x_p)) - (A + I)(x - x_p) \\ &\quad - 2\left(\frac{1}{2} + \frac{1}{2}L_{\phi_z}^2\|\hat{W}\|^2\|\Gamma\|^2\right)e + \alpha_r(t, \hat{W}). \end{aligned}$$

The control law is given by

$$\begin{aligned} u &= -\hat{W}\Gamma(z(x) - z(x_p)) - (A + I)(x - x_p) - 2\left(\frac{1}{2} + \frac{1}{2}L_{\phi_z}^2\|\hat{W}\|^2\|\Gamma\|^2\right)e \\ &\quad + f_r(x_r, u_r) - Ax_r - \hat{W}\Gamma z(x_r) - x_r + x_p. \end{aligned} \tag{59}$$

4.6 Chaos synchronization

In order to test the applicability of the proposed adaptive control scheme, we include the following example.

Synchronization of the Chen's system by the Chua's system

In this example, the unknown plant considered is Chua's chaotic attractor generated by

$$\begin{aligned} \dot{x} &= p(-x + y - \Phi(x)) \\ \dot{y} &= x - y + z \\ \dot{z} &= -qy, \end{aligned} \tag{60}$$

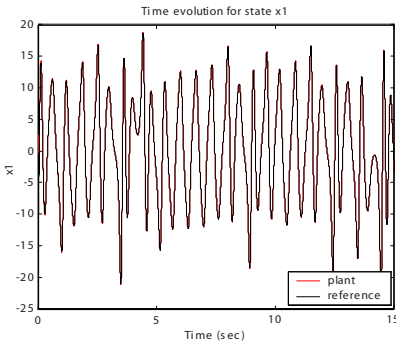


Fig. 5. x_1 Time evolution.

where

$$\Phi(x) = \begin{cases} m_0x - m_1 & si \quad x \leq -1 \\ m_1x & si \quad |x| < 1 \\ m_0x + m_1 & si \quad x \geq 1. \end{cases} \quad (61)$$

In this case, $p = 10, q = 14.87, m_0 = -0.68, m_1 = -1.27$.

The goal is to force the chaotic Chua's attractor to synchronize the chaotic Chen's attractor, described in a previous section.

In the simulations, the following dynamic neural network was used:

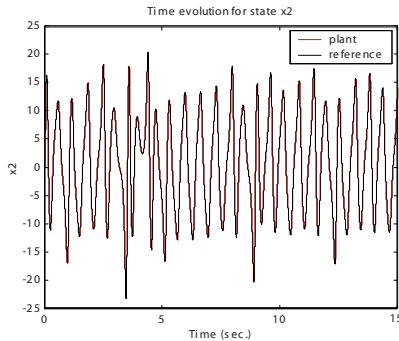
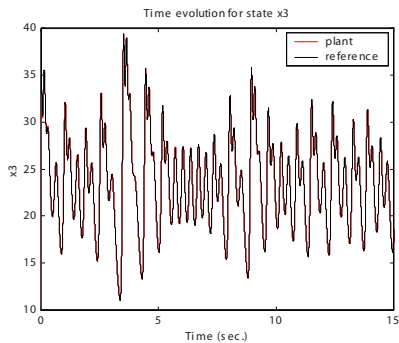
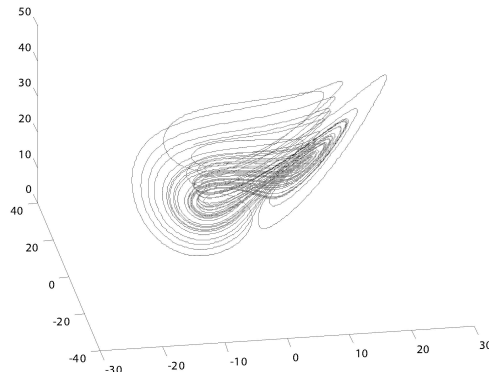
$$\dot{x} = Ax + W^* \Gamma z(x) + u, \quad (62)$$

with

$$A = \begin{pmatrix} -5 & 0 & 0 \\ 0 & -5 & 0 \\ 0 & 0 & -5 \end{pmatrix}, \quad \Gamma = \begin{pmatrix} 15 & 0 & 0 \\ 0 & 15 & 0 \\ 0 & 0 & 15 \end{pmatrix}$$

$$z(x) = \begin{pmatrix} \tanh(\beta x_1) \\ \tanh(\beta x_2) \\ \tanh(\beta x_3) \end{pmatrix}, \quad \beta = 0.45.$$

The simulation results are shown in Figures 5 to 9, where the time evolution of the states and phase portraits are presented.

**Fig. 6.** x_2 Time evolution.**Fig. 7.** x_3 Time evolution**Fig. 8.** Reference phase portrait

5 Conclusions

In this chapter, we have discussed neural network design for chaos control. The two main methodologies we used are: recurrent neural networks and in-

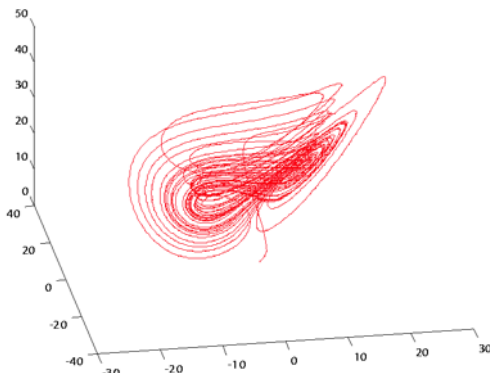


Fig. 9. Plant phase portrait

verse optimal control. On the basis of the last methodology, first chaos was reproduced by a stable recurrent neural network; then, synchronization of two chaotic system was performed by means of an adaptive recurrent neural controller. Simulations result illustrate the applicability of the proposed schemes.

Acknowledgments.

The authors thank the support of CONACYT, Mexico, on Project 32059A. The second author also thanks the support of UANL Mathematics and Physics School.

References

1. Basar, T., Bernhard, P. (1995) H_∞ Optimal Control and Related Minimax Design Problems. Boston: Birkhäuser
2. Byrnes, C. I., Isidori, A., Willems, J. C. (1991) Passivity, feedback equivalence, and the global stabilization of minimum phase nonlinear systems. IEEE Trans. Auto. Contr., **36**:1228-1240
3. Chen, G., Dong, X. (1993) On feedback control of chaotic continuous-time systems. IEEE Trans. Circ. Syst.-I, **40**:591-601
4. Chen, G., Chen, Y., Olgmen, H. (1997) Identifying chaotic systems via a Wiener-type cascade model. IEEE Control Systems Magazine, **17**:29-36
5. Chen, G., Dong, X. (1998) From Chaos to Order: Methodologies, Perspectives, and Applications. Singapore: World Scientific
6. Chen, G., Ueta, T. (1999) Yet another chaotic attractor. Int. J. Bifur. Chaos, **9**:1465-1466
7. Gupta, M. M., Rao, D. H. (eds.) (1994) Neuro-Control Systems, Theory and Applications. Piscataway, NJ: IEEE Press

8. Haykin, S. (1999) Neural Networks. 2nd ed. Upper Saddle River, NJ: Prentice-Hall
9. Hill, D. J., Moylan, P. (1996) The stability of nonlinear dissipative systems. *IEEE Trans. Auto. Contr.*, **21**:708-711
10. Hunt, K., Irwin, G., Warwick, K. (eds.) (1995) Neural Networks Engineering in Dynamic Control Systems. New York: Springer-Verlag
11. Khalil H. (1996) Nonlinear System Analysis. 2nd ed. Upper Saddle River, NJ: Prentice-Hall
12. Knobloch, H. W., Isidori, A., Flockerzi, D. (1993) Topics in Control Theory. Boston: Birkhäuser
13. Kosmatopoulos, E.B., et al. (1997) Dynamical neural networks that ensure exponential identification error convergence. *Neural Networks*, **1**(2):299-314
14. Krstic, M., Deng, H. (1998) Stabilization of Nonlinear Uncertain Systems. New York: Springer-Verlag
15. Isidori, A. (1995) Nonlinear Control Systems. 3rd ed. New York: Springer-Verlag
16. Lin, W. (1995) Feedback stabilization of general nonlinear control systems: a passive system approach. *Sys. Contr. Lett.*, **25**:41-52
17. Narendra, K. S., Parthasarathy, K. (1990) Identification and control of dynamical systems using neural networks. *IEEE Trans. Neural Networks*, **1**(1):4-27
18. Nijmeijer, H., Berghuis, H. (1995) On Lyapunov control of Duffing equation. *IEEE Trans. Circ. Syst.-I*, **42**:473-477
19. Poznyak, A. S., Yu, W., Sanchez, E. N., Perez, J. P. (1999) Nonlinear adaptive trajectory tracking using dynamic neural networks. *IEEE Trans. Neural Networks*, **10**:402-1411
20. Rovitahkis, G. A., Christodoulou, M. A. (2000) Adaptive Control with Recurrent High-Order Neural Networks. New York: Springer-Verlag
21. Sanchez, E. N., Perez, J. P. (1999) Input-to-state stability analysis for dynamic neural networks. *IEEE Trans. Circ. Syst.-I*, **46**:1395-1398
22. Sanchez, E. N., Perez, J. P., Chen, G. (2001) Using dynamic neural control to generate chaos: An inverse optimal control approach. *Int. J. Bifur. Chaos*, **11**:857-863
23. Sanchez, E. N., Perez, J. P., Ricalde, L. J., Chen, G. (2001) Trajectory tracking via adaptive neural control. Proc. of IEEE Int. Symposium on Intelligent Control, Mexico City, 286-289
24. Sanchez, E. N., Perez, J. P., Ricalde, L. J., Chen, G. (2001) Chaos production and synchronization via adaptive neural control. Proc. of IEEE Conf. on Decision and Control, Orlando, FL, USA
25. Sepulchre, R., Jankovic, M., Kokotovic, P. (1997) Constructive Nonlinear Control. London: Springer-Verlag
26. Suykens, K., Vandewalle, J., de Moor, R. (1996) Artificial Neural Networks for Modelling and Control of Nonlinear Systems. Boston: Kluwer
27. Vincent, T. L., Yu, J. (1991) Control of a chaotic system. *Dynamic and Control*, **1**:35-52
28. Wang, X., Chen, G. (2000) Chaotification via arbitrarily small feedback controls: Theory, method, and applications. *Int. J. Bifur. Chaos*, **10**:549-570
29. Zeng, Y., Singh, S. N. (1997) Adaptive control of chaos in Lorenz system. *Dynamic and Control*, **7**:143-154

Chaotification via Feedback: The Discrete Case

Guanrong Chen

Centre for Chaos Control and Synchronization
Faculty of Science and Engineering
City University of Hong Kong, P.R. China
gchen@ee.cityu.edu.hk

Abstract. This chapter introduces the notion of chaotification (or, anticontrol of chaos), which means to make an originally non-chaotic dynamical system chaotic, or to enhance the existing chaos of a chaotic system, via feedback control techniques. Only the discrete case is discussed in detail. A basic and yet “universal” approach to discrete chaotification is described, with a simple example worked out in a step-by-step fashion for illustration.

1 Introduction

Research on the emerging subjects of chaos control and chaos synchronization has seen a very rapid development in the last decade (see, e.g., [7], and many references cited therein). In particular, the concept of chaotification (or, sometimes, called “anticontrol of chaos”) by means of making an originally non-chaotic dynamical system chaotic, or enhancing the existing chaos of a chaotic system, has attracted increasing attention in recent years (see, e.g., [5, 6] and the references therein). This interest seems to be continuously increasing, mainly due to the great potentials of chaos in some non-traditional applications such as those found within the context of electronic, informatic, mechanical, optical, and especially biological and medical systems [5–7].

This chapter focuses on the topic of discrete chaotification. Discrete maps (discrete dynamical systems) with chaotic and bifurcating behaviors have been studied from a feedback control point of view [1], and have been found very useful in some real-world applications, particularly in encryption [21], digital communications [22], and human brain [37] as well as heart pathology and analysis [17], to name just a few representative examples. These provide a strong motivation for the current research on chaotification of various dynamical systems. In these endeavors, for the discrete case, the reader is referred to [10, 11, 25, 28, 30, 31, 47–49, 55–57], and for the continuous case, [12–14, 18, 20, 33, 34, 38, 40, 41, 43, 45, 50–54, 58].

In the pursuit of chaotifying discrete maps, a simple yet mathematically rigorous chaotification method was first developed by Chen and Lai [9–11] from the engineering state feedback control approach, which yields chaos in the sense of Devaney [16]. Afterwards, Wang and Chen [47, 48] further showed

that the Chen-Lai algorithm for chaotification leads to chaos not only in the sense of Devaney but also in the sense of Li-Yorke [27]. Lately, Li and Chen further relaxed the condition for chaotification [25], showing that the Wang-Chen chaotification theorems established in [48] can be somewhat generalized and that the Chen-Lai scheme is indeed a “universal” chaotification algorithm for discrete systems. More recently, the state feedback chaotification scheme of Chen-Lai-Wang was improved to be an output feedback anti-control algorithm by Zhang and Chen [55], and meanwhile be simplified to a new design with a single state variable feedback in each dimension, by Zheng et al. [56, 57] where, again, the generated chaos was shown to be in the sense of both Devaney and Li-Yorke.

In the effort of showing that the generated chaos indeed is chaos in a rigorous mathematical sense, the celebrated Li-Yorke theorem (for the 1-D case [27]) and the Marotto theorem (for the n -D case [35]) were usually employed. Historically, Li and Yorke introduced the first precise definition of discrete chaos and established a very simple criterion of chaos for one-dimensional iterative maps [27], that is, “period three implies chaos” for brevity. After three years, Marotto generalized this result to n -dimensional maps, showing that the existence of a snap-back repeller implies chaos in the sense of Li-Yorke. This theorem is up to now the best one for predicting and analyzing discrete chaos in higher-dimensional difference equations. Yet, it is well known that there exists an error in the condition of the original Marotto theorem, and several authors had tried to correct it in different ways [8, 32]. As a result, a corrected and improved version of the Marotto theorem was derived very recently by Li and Chen [26].

It should be mentioned that possibilities of using other definitions of chaos for chaotification are being explored, which however is beyond the scope of the present brief introduction to the subject.

This chapter is organized as follows. In Sec. 2, a necessary and detailed mathematical preliminary on chaos in the sense of Devaney and of Li-Yorke is provided. The central problem of chaotification is formulated and described in Sec. 3, where the state-of-the-art achievement and progress in this research area are summarized and commented. To give more insights to the concerned issue of how a mathematically rigorous chaotification can be done via engineering state feedback control, a simple illustrative example is worked out on a step-by-step basis in Sec. 4, where graphical illustrations are used to visualize some concepts and reasoning and as well to eliminate some trivial but tedious mathematical manipulations. Section 5 highlights the chaotification problem for the continuous case, which is beyond the scope of this chapter, therefore only some key references are provided therein for the reader’s further reading. The last section then concludes the chapter with some very brief discussions.

2 Preliminary: Chaos in the Sense of Devaney and Li-Yorke

In this section, a necessary mathematical preliminary on the concept of discrete chaos is first provided. Two important criteria in the sense of Devaney and of Li-Yorke are given, which supply some rigorous guidelines for chaosification to be further discussed in the following sections.

2.1 Chaos in the sense of Devaney

The following is a typical textbook definition of discrete chaos given by Devaney [16], although it has some redundancy and can be further simplified (see, e.g., [42]):

Let S be a set in a topological space (typically, \mathbb{R}), and let f^m be the m th-order iteration of a map $f: S \rightarrow S$, namely, $f^m := f(f^{m-1})$, $m = 1, 2, \dots$ with $f^0 = \text{identity}$.

Definitions A point $x^* \in S$ is called a *period point with period m* (or m -*period point*) if $x^* = f^m(x^*)$ but $x^* \neq f^k(x^*)$ for $1 \leq k < m$. If $m = 1$, that is $f(x^*) = x^*$, then x^* is called a *fixed point*. The point x^* is called *periodic*, or is named a *period point*, if it is an m -periodic point for some $m \geq 1$.

Devaney Definition A map $f: S \rightarrow S$ is *chaotic* if

- (i) the map f has sensitive dependence on initial conditions, in the sense that for any $x \in S$ and any neighborhood \mathcal{N} of x in S , there exists a $\delta > 0$ such that $|f^m(x) - f^m(y)| > \delta$ for some $y \in \mathcal{N}$ and some $m \geq 0$;
- (ii) the map f is topologically transitive, in the sense that for any pair of nonempty open subsets $U, V \subset S$, there exists an integer $m > 0$ such that $f^m(U) \cap V \neq \emptyset$;
- (iii) the periodic points of the map f are dense in S .

2.2 Chaos in the sense of Li-Yorke

Considered a one-dimensional discrete map, written in the following form as a dynamical system:

$$x_{k+1} = f(x_k), \quad x_k \in I \subset \mathbb{R}, \quad k = 0, 1, 2, \dots . \quad (1)$$

Li and Yorke [27] introduced the first mathematical definition of chaos and established a very simple criterion for it – “period three implying chaos” for short. This criterion plays an important role in predicting and analyzing one-dimensional chaotic dynamical systems, which is described as follows.

Li-Yorke Theorem [27] Let I be an interval in \mathbb{R} and $f: I \rightarrow I$ be a continuous map. Assume that there is one point $a \in I$, for which the points $b = f(a)$, $c = f^2(a)$ and $d = f^3(a)$ satisfy

$$d \leq a < b < c \quad (\text{or } d \geq a > b > c).$$

Then:

- (i) for every $k = 1, 2, \dots$, there is a k -periodic point in I ;
- (ii) there is an uncountable set $S \subset I$, containing no periodic points, which satisfies the following conditions:
 - (ii₁) for every $p_S, q_S \in S$ with $p_S \neq q_S$,

$$\lim_{n \rightarrow \infty} \sup |f^n(p_S) - f^n(q_S)| > 0$$

and

$$\lim_{n \rightarrow \infty} \inf |f^n(p_S) - f^n(q_S)| = 0;$$

- (ii₂) for every $p_S \in S$ and periodic points $q_{\text{per}} \in I$, with $p_S \neq q_{\text{per}}$,

$$\lim_{n \rightarrow \infty} \sup |f^n(p_S) - f^n(q_{\text{per}})| > 0.$$

Li-Yorke Remark [27] The above theorem can be slightly generalized by assuming that $f: I \rightarrow R$ without assuming that $f(I) \subset I$ but, of course, one should ensure that $f(I) \cap I \neq \emptyset$ so that it contains the well-defined points a, b, c .

Motivated by Li-Yorke's work, Marotto [35] further generalized this elegant result to the higher-dimensional setting.

Considered the following n -dimensional dynamical system:

$$x_{k+1} = F(x_k), \quad x_k \in R^n, \quad k = 0, 1, 2, \dots, \quad (2)$$

where the map $F: R^n \rightarrow R^n$ is continuous. Denote by $B_r(x)$ the closed ball in R^n of radius r centered at a point $x \in R^n$, and by $B_r^0(x)$ its interior.

Marotto Definitions [35]

- (i) Let F be differentiable in $B_r(x)$. The point $x \in R^n$ is an *expanding fixed point* of F in $B_r(x)$ if $F(x) = x$ and all eigenvalues of $DF(y)$ exceed 1 in absolute value for all $y \in B_r(x)$.
- (ii) Assume that x is an expanding fixed point of F in $B_r(x)$ for some $r > 0$. Then x is said to be a *snap-back repeller* of F if there exists a point $x_0 \in B_r(x)$ with $x_0 \neq x$, such that $F^m(x_0) = x$ and the determinant $|DF^m(x_0)| \neq 0$ for an integer $m > 0$.

In the following theorem, $\|x\|$ denotes the usual Euclidean norm of $x \in R^n$.

Marotto Theorem [35] If F possesses a snap-back repeller, then system (2) is chaotic in the sense of Li-Yorke:

- (i) There is a positive integer N such that for each integer $p \geq N$, F has a point of period p .

- (ii) There is a “scrambled set” of F , namely, an uncountable set S containing no periodic points of F , such that
 (ii₁) $F(S) \subset S$,
 (ii₂) for every $x_S, y_S \in S$ with $x_S \neq y_S$,

$$\lim_{k \rightarrow \infty} \sup ||F^k(x_S) - F^k(y_S)|| > 0,$$

(ii₃) for every $x_S \in S$ and any periodic point y_{per} of F ,

$$\lim_{k \rightarrow \infty} \sup ||F^k(x_S) - F^k(y_{\text{per}})|| > 0;$$

(iii) there is an uncountable subset S_0 of S such that for every $x_{S_0}, y_{S_0} \in S_0$:

$$\lim_{k \rightarrow \infty} \inf ||F^k(x_{S_0}) - F^k(y_{S_0})|| = 0.$$

For the one-dimensional case, the existence of a snap-back repeller of f is equivalent to the existence of a point of period-3 for the map f^n for some positive integer n , as pointed out in Remark 3.1 of Marotto’s paper [35].

As mentioned in the Introduction section, to verify that the generated chaos indeed is chaos in a rigorous mathematical sense, the celebrated Li-Yorke theorem for the 1-D case and the Marotto theorem for the n -D case were usually employed. The Marotto theorem is the best one in predicting and analyzing discrete chaos in higher-dimensional difference equations to date. Although it has been known that there exists an error in the condition of the original Marotto theorem, and a corrected and improved version of this theorem has been derived very recently by Li and Chen [26], the original version of the theorem is still used here in this chapter for the purpose of easier illustration.

3 Chaosification: Problem Formulation

Now, consider a general finite-dimensional discrete-time dynamical system, originally need not be chaotic or complex, nor be ill-behaved or unstable, in the form of

$$x_{k+1} = f_k(x_k), \quad x_0 \in R^n \text{ is given,} \quad (3)$$

where, at the moment, $f_k(\cdot)$ is only assumed to be continuously differentiable, at least locally in a region of interest. This means that the given system (3) can be linear or nonlinear, time-invariant or time-varying, and stable or unstable.

The objective, then, is to design a control input sequence, $\{u_k\}$, such that the output (state vector sequence) of the controlled system

$$x_{k+1} = f_k(x_k) + u_k \quad (4)$$

behaves chaotically, in the sense of some commonly used mathematical criteria for chaos such as those defined by Devaney and Li-Yorke.

At this point, a very important remark is in order. A practical design of a meaningful controller should come out with a simple structure, as simple as possible and at least it should be simpler than the given system, such that the goal of control (here, chaotification) can be achieved. The main reason is that, although many things can be done mathematically, a designed controller should be simple, cheap, and implementable in engineering applications; therefore it practically does not make sense to come out with a controller that is more complex and expensive than the given system to be controlled. The discussion below tries to follow this basic engineering principle, thereby designing some very simple and implementable chaotifiers (anti-controllers).

Chaosification problem description

Consider a simple nonlinear state-feedback controller of the form

$$u_k = a_k \varphi(\sigma_k x_k) \mathbf{1}, \quad (5)$$

where $\mathbf{1} = [1, \dots, 1]^\top$ is an all-one vector, $\{a_k\}$ and $\{\sigma_k\}$ are two sequences of real constants to be determined, and $\varphi(\cdot)$ is a simple unimodal function such as the piecewise-linear sawtooth function [10, 11] as shown in Fig. 1, or the standard sine function [47, 48], which can both be easily implemented by commercial circuits. Note that actually even this simple anti-controller can be further simplified, as will be discussed below by the end of this section.

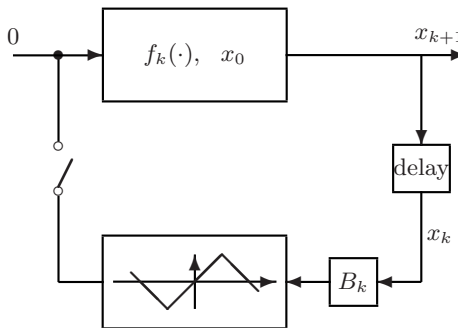


Fig. 1. The state-feedback anti-control configuration

Using this controller, without tuning any of the system parameters, the controlled system

$$x_{k+1} = f_k(x_k) + a_k \varphi(\sigma_k x_k) \mathbf{1} \quad (6)$$

is expected to become chaotic, regardless of the functional form of the given system $f_k(\cdot)$.

When the sawtooth function is used in (5), the controlled system is equivalent to the following, within the context of chaotification [47]:

$$x_{k+1} = f_k(x_k) + B_k x_k \pmod{1}, \quad (7)$$

where $\{B_k\}$ is a sequence of constant matrices and $(\text{mod } 1)$ is the modulo-one operation, which maps $[0,1]$ onto itself. Here, in operation $(\text{mod } 1)$, the magnitude 1 can be equivalently replaced by any positive real number such as 2π when the sine function is used in (5) [11, 47].

The controlled system (7) rather than (6) is discussed here for notational simplicity.

To describe the problem more precisely, some new notation is first introduced. Let

$$J_j(z) = f'_j(z) + B_j \quad (8)$$

be the Jacobian of the controlled system (7), evaluated at z , $j = 0, 1, \dots$, and let

$$T_j = T_j(x_0, \dots, x_j) := J_j(x_j) \cdots J_0(x_0).$$

Moreover, let $\mu_i^j = \mu_i^j(T_j^\top T_j)$ be the i th eigenvalue of the j th product matrix $[T_j^\top T_j]$, $i = 1, \dots, n$, $j = 0, 1, \dots$, and recall from standard textbooks that the i th Lyapunov exponent of the orbit $\{x_k\}$ of the controlled system, starting from x_0 , is defined by

$$\lambda_i(x_0) = \lim_{k \rightarrow \infty} \frac{1}{2k} \ln |\mu_i [T_j^\top T_j]|, \quad i = 1, \dots, n. \quad (9)$$

The approach suggested in [11, 48] is divided into two steps:

First, design the constant matrices $\{B_k\}$ such that the Lyapunov exponents of the controlled system orbit are arbitrarily assigned, which turns out that this is possible [9]. Since the notion of Lyapunov exponents defined in (9) for nonlinear systems is a generalization of the concept of eigenvalues for linear systems, the determination of the linear feedback control gains $\{B_k\}$, such that the Lyapunov exponents of the controlled system orbit can be arbitrarily assigned, is a generalization of the well-known ‘‘pole assignment’’ technique for discrete-time linear systems. A statistical analysis of this technique can be found in [24]. Here, for the purpose of anti-control of chaos, a very simple and convenient choice (although not necessary) is to determine the gain matrices such that all the Lyapunov exponents become finite and strictly positive:

$$0 < c \leq \lambda_i < \infty, \quad i = 1, \dots, n, \quad (10)$$

where c is a pre-desired constant. To be practical in achieving this goal, namely, for implementation purpose, it is also required here that the constant gain sequence $\{B_k\}$ be uniformly bounded for all $k = 0, 1, \dots$. It turns out that this objective can be achieved by a very simple constant feedback gain $B_k \equiv \sigma I_n$ with some $\sigma > 0$ for all $k = 0, 1, \dots$.

Second, take the (mod 1) operation, so as to force the diverging system orbits back into a bounded region, thereby generating chaos as desired.

It has been shown [11] that the above-described task of chaotification is always possible under one (and only one) natural condition that all Jacobians $J_k(x_k)$ of the given system are uniformly bounded:

$$\|f'_k(x_k)\| \leq M < \infty, \quad \forall k = 0, 1, \dots, \quad (11)$$

where suitable matrix norm such as the spectral norm is used. This restriction simply avoids that the system orbits diverge too quickly before the controller takes effective actions. Note that this condition is not too restrictive, since many systems such as all the linear time-invariant systems satisfy it. Of course, slightly relaxing this condition is still possible [25].

A generic chaotification algorithm [10,11]

Start with the initial controlled system $x_1 = f_0(x_0) + B_0 x_0$, where x_0 is initially given. Calculate its Jacobian $J_0(x_0) = f'_0(x_0) + B_0$ and then let $T_0 = J_0(x_0)$. Design a positive feedback control gain, $B_0 = \sigma_0 I$, by choosing a constant $\sigma_0 > 0$ such that the matrix $T_0 T_0^\top$ is finite and diagonally dominant.

For $k = 0, 1, 2, \dots$, start with the controlled system $x_{k+1} = f_k(x_k) + B_k x_k$, where both B_k and x_k have been obtained from the previous step. Perform the following steps iteratively:

Step 1. Compute the Jacobian $J_k(x_k) = f'_k(x_k) + \sigma_k I$ and then let $T_k = J_k T_{k-1}$.

Step 2. Design a positive feedback controller by choosing a constant $\sigma_k > 0$ such that the matrix $[T_k T_k^\top - e^{2kc} I]$ is finite and diagonally dominant, where the constant $c > 0$ is the one specified in (10).

Step 3. Apply the (mod 1) operation to the controlled system, as shown in (7), or apply a unimodal function (e.g., the piecewise-linear sawtooth function shown in Fig. 2) to the controller, as formulated in (6).

To this end, it can be rigorously proved [11,48] that the controlled system so designed is guaranteed to be chaotic in the sense of Devaney and also of Li-Yorke.

A few remarks are in order. First, a simple choice for $\{\sigma_k\}$ is to use the constant $\sigma = M + e^c$, where c is given in (10) and M is given in (11), which

works well for all $k = 0, 1, \dots$ [11]. Second, in Step 3 above, if the sawtooth function is used, its magnitude can be a constant, $a_k = a$ for all $k = 0, 1, \dots$, and this constant can be arbitrarily small [48], which means that “small control” is possible; but in this case, σ should be large, i.e., the frequency should be high. Third, some other unimodal functions such as the simple sine function can also be used at Step 3 for the controller. Finally, this algorithm is “universal,” as discussed in [25].

It is particularly important to emphasize that this chaosification scheme is fairly general because the given system (3) can be quite arbitrary: it can be linear or nonlinear, time-invariant or time-varying, stable or unstable, of any finite dimension, provided that the system Jacobians are uniformly bounded in the sense of (11).

It is easily noticed that the above chaosification algorithm utilizes a full state feedback, which often is not desirable in engineering applications because full state information is not always feasible to obtain, usually via sensors, in practice. For engineering control systems, it is more preferable to use output feedback instead of state feedback, which means that only part of the state vector is measured and used for feedback control. Therefore, it is natural to ask if the above-described chaosification can be further modified or improved, so as to use output feedback instead of full state feedback to achieve rigorous chaosification. In this regard, very recently two approaches have been successful, which are briefly introduced in the following.

Modification and improvement of the basic algorithm [55–57]

Recall the anti-controller (5) discussed above, namely,

$$u_k = a_k \varphi(\sigma_k x_k) \mathbf{1}, \quad (12)$$

where $\mathbf{1} = [1, \dots, 1]^\top$ is an all-one vector, $\{a_k\}$ and $\{\sigma_k\}$ are two sequences of real constants to be determined, and $\varphi(\cdot)$ is a simple unimodal function such as the piecewise-linear sawtooth function or the sine function. This is a full state feedback controller, since complete information about the entire state vector x_k are needed for all $k = 0, 1, 2, \dots$; therefore, it is not the most economic one to use in engineering applications.

In [55], this controller is modified to be the following:

$$u_k = b \varphi(x_k) = -b \sin(h x_k), \quad (13)$$

where b is an $n \times 1$ constant vector and h is a $1 \times n$ constant vector, both are to be determined. It was proved [57] that if the originally given system is a linear time-invariant one in the controllable form, then such a constant vector h exists with a simple $h = [0, 0, \dots, 0, 1]^\top$, such that the controlled system (4) with this controller is chaotic in the rigorous mathematical sense of Li-Yorke.

In [56], the anti-controller (5) is improved to be the following:

$$u_k = a\varphi(x_k) = a [\sin x_k^1, \sin x_k^2, \dots, \sin x_k^n]^\top, \quad (14)$$

where a is a constant to be determined, and $x_k = [x_k^1, x_k^2, \dots, x_k^n]^\top$ is the state vector. It is proved [56] that, as long as the control gain a is large enough, the controlled system (4) with this controller is chaotic in the sense of Devaney, which turns out to be a simple Bernoulli shift.

Another approach is to slightly change the above anti-controller to be

$$u_k = a\phi(cx_k) = a [\sin cx_k^1, \sin cx_k^2, \dots, \sin cx_k^n]^\top, \quad (15)$$

where a and c are constants to be determined, and $x_k = [x_k^1, x_k^2, \dots, x_k^n]^\top$ is the state vector as above. It was proved [57] that the corresponding controlled system (4) using this anti-controller is chaotic in the sense of Devaney, as well as in the sense of Li-Yorke, for some different given systems.

4 An Illustrative Example

To illustrate how the aforementioned simple state feedback controllers can chaotify a given non-chaotic system, and how the generated chaos can be proven to be chaos satisfying a mathematical definition, a very simple example is given in this section via a step-by-step explanation. In order to avoid some obvious but tedious mathematical arguments and manipulations, thereby making the illustration more transparent, some steps in the following derivation are depicted graphically.

Consider, therefore, the following one-dimensional linear control system:

$$x_{k+1} = ax_k + bu_k, \quad k = 0, 1, 2, \dots, \quad (16)$$

where a and b are constants to be determined. Without loss of generality, it is assumed that the constant $a > 0$; otherwise, a variable transform $x \rightarrow -x$ and $u \rightarrow -u$ suffices to support the assumption. Let the controller be

$$u_k = u_k(x_k) = \begin{cases} < 0 & \text{if } x_k < 0 \\ = 0 & \text{if } x_k = 0 \\ > 0 & \text{if } 0 < x_k < M \\ = 0 & \text{if } x_k = M \\ < 0 & \text{if } x_k > M \end{cases} \quad (17)$$

for a positive constant $M < \infty$, in which the case of a unimodal function $u_k(\cdot)$, as shown by Fig. 2, is first discussed. Typical examples of such unimodal functions that can be used for chaotification include the sawtooth function [47] and the sine function [48], as shown in Fig. 3.

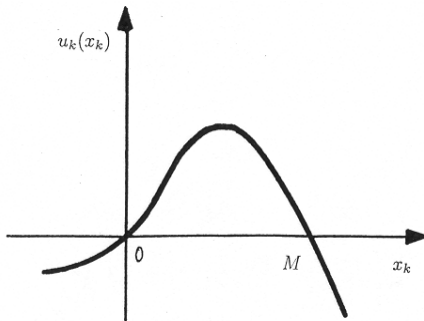


Fig. 2. A unimodal function in discussion

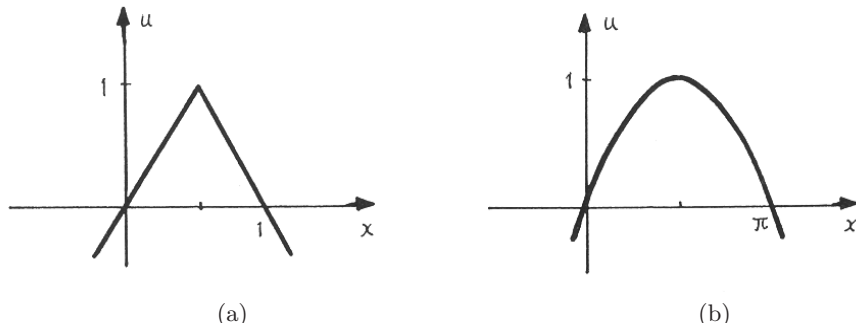


Fig. 3. Two typical functions: (a) The sawtooth function (b) the sine function

Proposition 1. There are two positive constants, $0 < c_1 < c_2 < \infty$, such that if the control gain b satisfies $c_1 \leq b \leq c_2$ then the controlled system (16)–(17) will be chaotic in the sense of Li-Yorke for any initial condition $x_0 \in [0, M]$.

Proof. Let

$$f(x) = ax + bu(x). \quad (18)$$

Then, $f: R \rightarrow R$ is continuous. By using a large enough value of $b > c_1 > 0$, one can guarantee that there exist two points, $w \in [0, M)$ and $v \in [M, \infty)$, such that

$$w < f(w), \quad f(v) < v,$$

as visualized by Fig. 4.

Therefore, according to the fixed point theorem, there exists a point, $h \in (w, v)$, such that

$$f(h) = h.$$

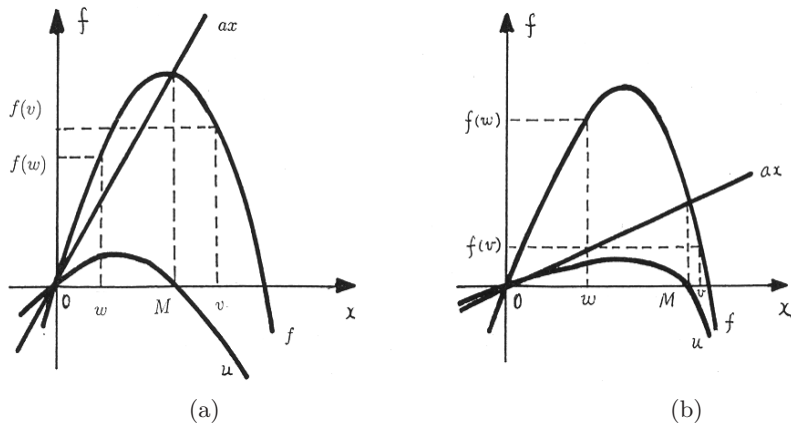


Fig. 4. Illustration of Proposition 1. Two cases: (a) $a \geq 1$ (b) $a \leq 1$

This means that for a large enough value of $b \geq c_1 > 0$, the function $u = f(x)$ is a unimodal map, as shown in Fig. 5. Also, there is a constant, c_2 , such that when $b = c_2$ the rectangle shown in Fig. 5 will become a square, $I \times I$, and this implies that $f : I \rightarrow I$ is an invariant unimodal map. Hence, for any $b \in [c_1, c_2]$, the map f is chaotic in the sense of Li-Yorke, as proved by Theorems 11.2 and 11.3 in the book [19].

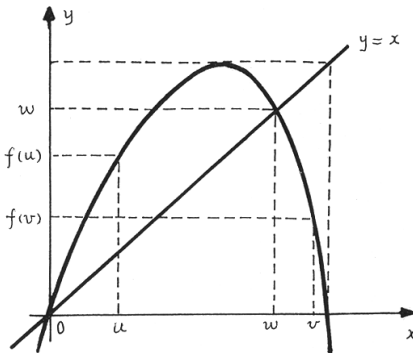


Fig. 5. $u = f(x)$ is a unimodal function

Remark. This explains why the anti-controller designed suggested in [48], namely,

$$u = a \sin(cx),$$

with an arbitrarily small $a > 0$ and a large enough $c > 0$, can generate rigorous chaos (see Fig. 6 and compare it with Fig. 5).

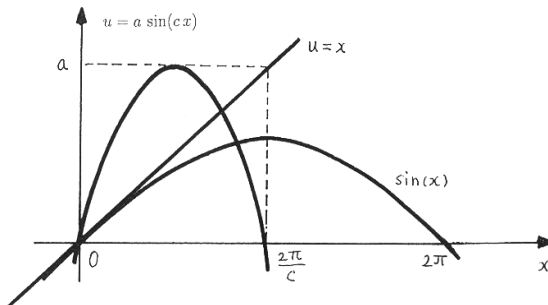


Fig. 6. Illustration for the chaos generation principle

Next, consider a more general case where u is only continuous but not necessarily strictly unimodal in a sense to be further described below.

The first observation is that similar to the case of the unimodal function discussed above, on the interval $(0, M)$ over which $u > 0$, as $b \rightarrow \infty$ the function f is increasing while the first zero z of the function f is decreasing (see Fig. 7). Thus, when b is large enough such that $b \geq c_1$, one has $F \geq z$, where $z = z(b)$ is the first zero of the function $f = f(x; b)$ and

$$F = F(b) := \max_{0 \leq x \leq M} f(x; b).$$

This observation, illustrated by Fig. 7, leads to the following conclusion.

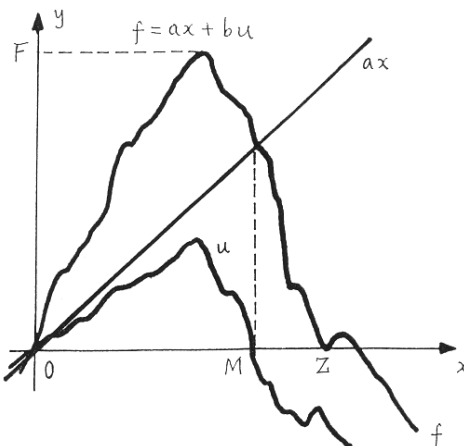


Fig. 7. Illustration of the first zero of the continuous function f

Lemma. There is a constant, $c_1 > 0$, such that

$$z(b) \leq F(b), \quad \text{for all } b \geq c_1.$$

Proof. First, notice the definition of the function $F(\cdot)$, namely,

$$F(b) = \max_{0 \leq x \leq M} f(x; b) = \max_{0 \leq x \leq M} \{ ax + bu(x) \}.$$

It can be seen that $F(\cdot)$ has the following properties:

- (a.1) $F(0) = \max_{0 \leq x \leq M} \{ ax \} = aM$;
- (a.2) $F(\infty) = \infty$;
- (a.3) $F(b)$ is continuous in b ;
- (a.4) $F(b)$ is monotonically increasing.

Second, notice the definition of z , namely, the first zero of f satisfying

$$z(b) = \max_{M \leq x < \infty} \{ f(x; b) \} = \{ x \mid x \geq M \text{ and } f(x; b) > 0 \}.$$

It can be seen that $z(\cdot)$ has the following properties:

- (b.1) $z(0) = \infty$;
- (b.2) $z(\infty) = M$;
- (b.3) $z(b)$ is continuous in b ;
- (b.4) $z(b)$ is monotonically decreasing.

The above properties of $F(\cdot)$ and $z(\cdot)$ together imply that there exists a constant, $c_1 > 0$, such that $z(b) \leq F(b)$ for all $b \geq c_1$.

Proposition 2. There exist a point, $x^* \in [0, M]$, and two constants, $0 < c_1 < c_2 < \infty$, such that

$$0 < f^3(x^*; b) < x^* < f(x^*; b) < f^2(x^*; b) < \infty \tag{19}$$

for all $c_1 \leq b \leq c_2$. Consequently, the controlled system (16)–(17) is chaotic on $[0, \infty)$ in the sense of Li-Yorke.

Proof. A proof can be carried out based on the continuity of the function $f(\cdot)$, by using the mean-value theorem and the fixed point theorem. Figure 8 best illustrates the arguments. This proof can be completed by following similar arguments of Theorems 11.2 and 11.3 in the book [19] and then using the Li-Yorke Remark reviewed in Sec. 2.2 above.

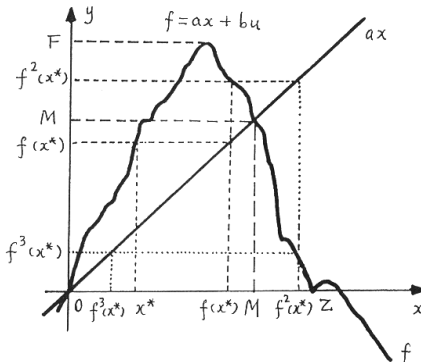


Fig. 8. Illustration of inequalities (19)

5 Some Remarks on the Continuous-Time Case

The discrete-time case of chaotification has been discussed in some detail above. It turns out that the continuous-time case is much more difficult and challenging, as can be easily imaged, because even a unified definition of chaos for continuous-time systems has not yet been formally established in the scientific as well as mathematical literatures. As simple an issue as it is, even the existence of the well-known Lorenz attractor, discovered nearly 40 years ago, has just been mathematically proved very recently [39].

Nevertheless, there have been some promising progress in the development of chaotification for the continuous-time case: chaos can indeed be generated as desired by several different methods, such as those referred at the beginning of the Introduction section. In particular, a few approaches that are seemingly more closely related to the discussion of the present chapter include such methodologies as using time-delay feedback [2, 52], or applying active control [15], by modifying the Chen-Lai scheme [23], or employing a special $x|x|$ function [40, 41], employing a neural network [28, 36], or via an observer-type of controller [58], through reshaping periodic excitations [4], or modifying some fuzzy systems [31], etc. As a byproduct, these endeavors have led to the recent discovery of a new chaotic attractor, Chen's attractor, which is generated by a dual system to the Lorenz system in a canonical form [3, 12, 44], as shown in Fig. 9.

Due to the intrinsic difficulty of defining chaos for general continuous-time systems, the pursuit for chaotification in this setting is believed to be a long-lasting and challenging scientific research subject, which nevertheless is very stimulating and exciting not only for anti-control but also for nonlinear dynamical systems analysis. For more details about this topic, the reader is referred to [46].

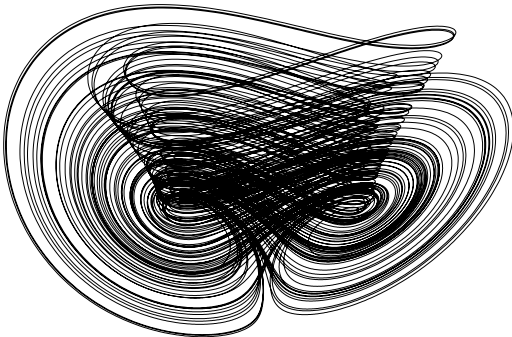


Fig. 9. Chen's chaotic attractor

6 Concluding Remarks

The emerging field of chaos control and anti-control (chaotification) is very stimulating and full of promise; it is expected to have far-reaching impacts with enormous opportunities in academic, medical, industrial, and commercial applications. New theories for dynamics analysis, new methodologies for controls, and new design for circuit implementation altogether are calling for new efforts and endeavors from the communities of nonlinear dynamics, circuits and systems, biological and social sciences, and, above all, control systems and applied mathematics. Control theorists and engineers should not miss this golden opportunity, especially those who have expertise in both nonlinear dynamics and nonlinear control systems. One has many good reasons to believe that the new century will be a glory era for great success of the beautiful nonlinear science, nonlinear mathematics, and their engineering technologies.

Acknowledgments.

The author thanks Goong Chen, Marius-F. Danca, Mingzhou Ding, Jin-Qing Fang, Dejian Lai, Chang-Pin Li, Xiang Li, Zhong Li, Wen Bo Liu, Zengrong Liu, Jinghu Lü, Kim F. Man, Edgard N. Sanchez, Ira Schwartz, Wallace K. S. Tang, Tetsushi Ueta, Xiao Fan Wang, Ling Yang, Xinghuo Yu, Huaizhou Zhang, Yi Zhao, Yongai Zheng, and Guo-Qun Zhong, among others, for their long-term cooperation in the joint endeavor of chaotification (anti-control of chaos) for both discrete and continuous dynamical systems.

The underlying research was supported by the Hong Kong Research Grants Council under the CERG Grants CityU 1098/00E (2000-02), CityU 1018/01E (2001-03), and CityU 1004/02E (2002-04).

References

1. Baillieul, J., Brockett, R. W., Washburn, R. B. (1980) Chaotic motion in non-linear feedback systems. *IEEE Trans. Auto. Control*, **27**:990–997
2. Bondarenko, V. E. (2002) Control and ‘anticontrol’ of chaos in an analog neural network with time delay. *Chaos, Solitons & Fractals*, **13**:139–154
3. Celikovsky, S., Chen, G. (2002) On a generalized Lorenz canonical form of chaotic systems. *Int. J. Bifur. Chaos*, **12**:1789–1812
4. Chacón, R., García-Hoz, A. M. (2002) Route to chaos via strang non-chaotic attractors by reshaping periodic excitations. *Europhysics Letters*, **57**:7–13
5. Chen, G. (1998) Chaos: control and anticontrol. *IEEE Circuits and Systems Society Newsletter*, March Issue, 1–5
6. Chen, G. (2001) What does chaos have to do with systems and control engineering? *J. Sys. Sci. Complex.*, **14**(1):32–39
7. Chen, G., Dong, X. (1998) *From Chaos to Order: Methodologies, Perspectives and Applications*. Singapore: World Scientific
8. Chen, G., Hsu, S., Zhou, J. (1998) Snap-back repellers as a cause of chaotic vibration of the wave equation with a an der Pol boundary condition and energy injection at the middle of the span. *J. Math. Phys.*, **39**(12):6459–6489
9. Chen, G., Lai, D. (1996) Feedback control of Lyapunov exponents for discrete-time dynamical systems. *Int. J. Bifur. Chaos*, **6**, 1341–1349
10. Chen, G., Lai, D. (1997) Anticontrol of chaos via feedback. In Proc. of IEEE Confence on Decision and Control, San Diego, CA, 367–372
11. Chen, G., Lai, D. (1998) Feedback anticontrol of chaos. *Int. J. Bifur. Chaos*, **8**:1585–1590
12. Chen, G., Ueta, T. (1999) Yet another chaotic attractor. *Int. J. Bifur. Chaos*, **9**:1465–1466
13. Chen, G., Yang, L. (2003) Chaotifying a continuous-time system near a stable limit cycle. *Chaos, Solitons & Fractals*, **15**:245–254
14. Chen, G., Yang, L., Liu, Z. R. (2001) Anticontrol of chaos for continuous-time systems. *IEICE Transactions: Fundamentals*, **E85-A**:1333–1335
15. Cordreanu, S. (2002) Desynchronization and chaotification of nonlinear dynamical systems. *Chaos, Solitons & Fractals*, **13**:839–843
16. Devaney, R. L. (1987) *An Introduction to Chaotic Dynamical Systems*. New York: Addison-Wesley
17. Ditto, W. L., Spano, M. L., In, V., Neff, J., Meadows, B., Langberg, J. J., Bolmann, A., McTeague, K. (2000) Control of human atrial fibrillation. *Int. J. Bifur. Chaos*, **10**:593–602
18. Elwikal, A. S., Ozoguz, S., Kennedy, M. P. (2002) Creation of a complex butterfly attractor using a novel Lorenz-type system. *IEEE Trans. Circ. Syst.-I*, **49**:527–530
19. Glendinning, P. (1994) *Stability, Instability and Chaos*, Cambridge: Cambridge Univ. Press
20. In, V., Mahan, S. E., Ditto, W. L., Spano, M. L. (1995) Experimental maintenance of chaos. *Phys. Rev. Lett.*, **74**:4420–4423
21. Jakimoski, G., Kocarev, L. (2001) Chaos and cryptography: Block encryption ciphers based on chaotic maps. *IEEE Trans. Circ. Syst.-I*, **48**:163–169
22. Kocarev, L., Maggio, G. M., Ogorzalek, M., Pecora, L., Yao, K. (2001) Special Issue on Applications of Chaos in Modern Communication Systems, *IEEE Trans. Circ. Syst.-I*, **48**:1385–1527

23. Konishi, K. (2001) Making chaotic behavior in a damped linear harmonic oscillator. *Phys. Lett. A*, **284**:85–90
24. Lai, D. and Chen, G. (2000) Distribution of controlled Lyapunov exponents: A statistical simulation study. *Comput. Stat. Data Anal.*, **33**:69–77
25. Li, C. P., Chen, G. (2003a) On a universal chaotification scheme. *J. Sys. Sci. Complex.*, to appear
26. Li, C. P., Chen, G. (2003b) An improved version of the Marotto theorem. *Chaos, Solitons & Fractals*, to appear
27. Li, T. Y., Yorke, J. A. (1975) Period three implies chaos. *Amer. Math. Monthly*, **82**:481–485
28. Li, X., Chen, G., Chen, Z., Yuan, Z. (2002) Chaotifying linear Elman networks. *IEEE Trans. Neural Networks*, **13**:1193–1199
29. Li, X., Chen, Z., Yuan, Z., Chen, G. (2001) Generating chaos by an Elman network. *IEEE Trans. Circ. Syst.-I*, **48**:1126–1131
30. Li, Z., Park, J. B., Joo, Y. H., Choi, Y. H., Chen, G. (2002) Anticontrol of chaos for discrete TS fuzzy systems. *IEEE Trans. Circ. Syst.-I*, **49**:249–253
31. Li, Z., Park, J. B., Chen, G., Joo, Y. H. (2002) Generating chaos via feedback control from a stable TS fuzzy system through a sinusoidal nonlinearity. *Int. J. Bifur. Chaos*, **12**:2283–2291
32. Lin, W., Ruan, J., Zhou, W. (2002) On the mathematical clarification of the snapback repeller in high-dimensional systems and chaos in a discrete neural network model. *Int. J. Bifur. Chaos*, **12**(5):1129–1139
33. Lü, J., Chen, G. (2002) A new chaotic attractor coined. *Int. J. Bifur. Chaos*, **12**:659–661
34. Lü, J., Zhou, T. S., Chen, G., Yang, X. S. (2002) Generating chaos with a switching piecewise-linear controller. *Chaos*, **12**(2):344–349
35. Marotto, F. R. (1978) Snap-back repellers imply chaos in R^n . *J. Math. Anal. Appl.*, **3**:199–223
36. Sanchez, E. N., Perez, J. P., Chen, G. (2001) Using dynamic neural networks to generate chaos: An inverse optimal control approach. *Int. J. Bifur. Chaos*, **11**:857–863
37. Schiff, S. J., Jerger, K., Duong, D. H., Chang, T., Spano, M. L., Ditto, W. L. (1994) Controlling chaos in the brain. *Nature*, **370**:615–620
38. Schwartz, I. B., Triandaf, I., Meucci, R., Carr, T. W. (2002) Open-loop sustained chaos and control: A manifold approach. *Phys. Rev. E*, **66**026213: 1–7
39. Stewart, I. (2000) The Lorenz attractor exists. *Nature*, **406**:948–949
40. Tang, K. S., Man, K. F., Zhong, G.-Q., Chen, G. (2001) Generating chaos via $|x|$. *IEEE Trans. Circ. Syst.-I*, **48**:636–641
41. Tang, K. S., Zhong, G.-Q., Chen, G., Man, K. F. (2001) Generation of n-scroll attractors via sine function. *IEEE Trans. Circ. Syst.-I*, **48**:1369–1372
42. Touhey, P. (1997) Yet another definition of chaos. *Amer. Math. Monthly*, May Issue, 411–414
43. Triandaf, I., Schwartz, I. B. (2000) Tracking sustained chaos: A segmentation method. *Phys. Rev. E*, **62**:3529–2534.
44. Ueta, T., Chen, G. (2000) Bifurcation analysis of Chen's equation. *Int. J. Bifur. Chaos*, **10**:1917–1931
45. Vaneeck, A., Celikovsky, S. (1996) Control Systems: From Linear Analysis to Synthesis of Chaos, London: Prentice-Hall
46. Wang, X. F. (2003) Generating chaos in continuous-time systems via feedback control. In this book: 179–204

47. Wang, X. F., Chen, G. (1999) On feedback anticontrol of discrete chaos. *Int. J. Bifur. Chaos*, **9**:1435–1441
48. Wang, X. F., Chen, G. (2000) Chaotification via arbitrarily small feedback controls. *Int. J. Bifur. Chaos*, **10**:549–570
49. Wang, X. F., Chen, G. (2000) Chaotifying a stable map via smooth small-amplitude high-frequency feedback control. *Int. J. Circ. Theory Appl.*, **28**:305–312
50. Wang, X. F., Chen, G. (2000) Chaotifying a stable LTI system by tiny feedback control. *IEEE Trans. Circ. Syst.-I*, **47**:410–415
51. Wang, X. F., Chen, G., Man, K. F. (2001) Making a continuous-time minimum-phase system chaotic by using time-delay feedback. *IEEE Trans. Circ. Syst.-I*, **48**:641–645
52. Wang, X. F., Chen, G., Yu, X. (2000) Anticontrol of continuous-time systems by time-delay feedback. *Chaos*, **10**:771–779
53. Yang, L., Liu, Z., Chen, G. (2002) Chaotifying a continuous-time system via impulsive input. *Int. J. Bifur. Chaos*, **12**:1121–1128
54. Yang, W., Ding, M., Mandell, A. J., Ott, E. (1995) Preserving chaos: control strategies to preserve complex dynamics with potential relevance to biological disorders. *Phys. Rev. E*, **51**:102–110
55. Zhang, H. Z., Chen, G. (2002) Single-input multi-output state-feedback chaotification of general discrete systems. *Int. J. Bifur. Chaos*, to appear
56. Zheng, Y., Chen, G., Liu, Z. (2002) On chaotification of discrete systems. *Int. J. Bifur. Chaos*, to appear
57. Zheng, Y., Chen, G. (2002) Single state-feedback chaotification of discrete dynamical systems. *Int. J. Bifur. Chaos*, to appear
58. Zhong, G.-Q., Man, K. F., Chen, G. (2001) Generating chaos via a dynamical controller. *Int. J. Bifur. Chaos*, **11**:865–869

Generating Chaos in Continuous-Time Systems via Feedback Control

Xiao Fan Wang

Department of Automation,
Shanghai Jiaotong University,
Shanghai 200030, P. R. China
xfwang@sjtu.edu.cn

Abstract. This chapter studies the anticontrol problem of making a continuous-time system chaotic by using feedback control. A time-delay feedback approach to generating chaos in finite-dimensional continuous-time systems, a state feedback control approach and a impulsive control approach to generating chaos in n -dimensional ($n \geq 3$) continuous-time systems are described in detail.

1 Introduction

In recent years, as opposed to the mainstream of controlling or eliminating chaos in dynamical systems[1-2], anticontrol of chaos (sometimes called chao-tification), which means creating chaos when it is beneficial, has also attracted some growing interests[3-12]. This is due to some desirable features of chaos in some time-and/or energy-critical applications where chaos can provide a system designer with a variety of special properties, richness of flexibility, and a cornucopia of opportunities. Typical examples include liquid mixing [13], human brain [14], resonance prevention in mechanical systems [15], and secure communications [16]. It is expected that chaos research in engineering will eventually reach the point where it will lead to improved and refined design procedures, enabling a designer to design a system to be either chaotic or nonchaotic at will.

In this chapter, we will introduce some feedback control techniques for generating chaos in continuous-time systems. A system with time-delay feedback is inherently infinite dimensional, so it is known to be able to produce complicated dynamics such as bifurcation and chaos, even in a very simple first-order system [17-20]. In Section 2, we describe a general approach to generating chaos in continuous-time systems via time-delay feedback [7-9]. According to the Poincaré-Bendixson theorem [21], a necessary condition for an n -dimensional continuous vector field to be chaotic is $n \geq 3$. In Section 3, we introduce a state feedback approach to generating chaos in n -dimensional continuous-time affine control systems, with $n \geq 3$. Finally, in Section 4, an impulsive control approach to generating chaos in n -dimensional ($n \geq 3$) continuous-time systems is described.

2 Generating Chaos in Continuous-Time Systems via Time-Delay Feedback

2.1 Generating chaos in a linear differential equation

We first consider an n th-order single-input single-output (SISO) linear time-invariant (LTI) system described by the following differential equation:

$$y^{(n)}(t) + \alpha_{n-1}y^{(n-1)}(t) + \cdots + \alpha_1\dot{y}(t) + \alpha_0y(t) = \beta_0u(t), \quad (1)$$

where $u(t)$ and $y(t)$ are the input and output of the system, respectively. $\{\alpha_i\}_{i=0}^{n-1}$ and β_0 are constants with $\alpha_0\beta_0 \neq 0$. $s^n + \alpha_{n-1}s^{n-1} + \cdots + \alpha_1s + \alpha_0$ is a Hurwitz stable polynomial with all of its roots having sufficiently negative real parts. Therefore, the uncontrolled system (i.e., $u(t) \equiv 0$) is stable in the sense that $\mathbf{z}(t) \rightarrow \mathbf{0}$ as $t \rightarrow \infty$, where $\mathbf{z}(t) = [z_1, z_2, \dots, z_n]^T = [y, \dot{y}, \dots, y^{n-1}]^T$. We want to design a time-delay feedback of the form

$$u(t) = w(y(t - \tau)), \quad (2)$$

where w is a continuous function and $\tau > 0$ is the delay time, satisfying

$$|u(t)| \leq \varepsilon, \quad \forall t \geq 0, \quad (3)$$

for a pre-specified amplitude $\varepsilon > 0$, such that the output $y(t)$ of the system is chaotic.

We can recast Eq. (1) in the following n -dimensional state-space form

$$\dot{\mathbf{z}} = A_c\mathbf{z} + \beta_0\mathbf{b}_c u, \quad (4)$$

where A_c and \mathbf{b}_c are in controllable companion form, i.e.,

$$A_c = \begin{bmatrix} 0 & 1 & 0 & \cdots & 0 \\ 0 & 0 & 1 & \cdots & 0 \\ \vdots & \vdots & \ddots & \ddots & \vdots \\ 0 & 0 & 0 & \cdots & 1 \\ -\alpha_0 & -\alpha_1 & -\alpha_2 & \cdots & -\alpha_{n-1} \end{bmatrix}, \quad \mathbf{b}_c = \begin{bmatrix} 0 \\ 0 \\ \vdots \\ 0 \\ 1 \end{bmatrix}. \quad (5)$$

Since A_c is a Hurwitz stable matrix and $u(t)$ is uniformly bounded, the solution of Eq. (4) is bounded for any bounded initial condition and can be computed iteratively on each τ -time interval $(m\tau, (m+1)\tau)$ for $m = 0, 1, \dots$.

Denote

$$\mathbf{z}(t) = \mathbf{z}(m\tau + \hat{t}) = \mathbf{z}(m, \hat{t}), \quad \text{for } t = m\tau + \hat{t}, \hat{t} \in (0, \tau].$$

It follows that

$$\mathbf{z}(t) = \mathbf{z}(m\tau + \hat{t}) = e^{A_c\hat{t}}\mathbf{z}(m-1, \tau) + \int_0^{\hat{t}} \beta_0 e^{A_c(\hat{t}-t')} \mathbf{b}_c w(y(m-1, t')) dt'. \quad (6)$$

Lemma 1 [7]: Let $\delta(t-t_0)$ be the scalar valued Dirac distribution centered at $t_0 \geq 0$, and let $d\xi(t, t_0) = e^{A_c(t_0-t)}dt$ be a matrix valued measure defined on $[0, \tau]$. If it is imposed that $d\xi(t, t_0) = B(t, t_0)\delta(t - t_0)dt$, then

$$B(t, t_0) \approx -A_c^{-1}e^{A_c(t_0-t)}$$

for a sufficiently large $\tau > 0$. Moreover, $B(t, t_0) \rightarrow -A_c^{-1}$, as $t \rightarrow t_0$.

Lemma 2 [7]: Denote $y(m, \hat{t}) = y(m\tau + \hat{t})$. For a sufficiently large τ and a large $\hat{t} : t_0 < \hat{t} < \tau$,

$$y(m, \hat{t}) \approx \frac{\beta_0}{\alpha_0}w(y(m-1, \hat{t})), \quad y^{(k)}(m, \hat{t}) \approx 0 \quad (7)$$

for $m = 0, 1, \dots$ and $k = 1, 2, \dots, n-1$.

Lemma 2 establishes an asymptotically approximate relationship between the time-delay equation (1) and the difference equation (7). Although there is difference between the dynamics of a time-delay equation and that of its associated difference equation, it is reasonable to expect that the output $y(t)$ of the time-delay equation (1) is chaotic if $\frac{\beta_0}{\alpha_0}w(\cdot)$ is a chaotic map and the delay time is sufficiently large.

The functional form for the map w is not unique. One simple choice is

$$u(t) = w(y(t-\tau)) = \varepsilon \sin(\delta y(t-\tau)). \quad (8)$$

In this case, if the map

$$y_{k+1} = \frac{\beta_0}{\alpha_0}w(y_k) = \varepsilon_0 \sin(\delta y_k) \quad (9)$$

is chaotic, then we may expect that the time-delay feedback law (8) can make the output $y(t)$ of system (1) chaotic provided that the delay time τ is sufficiently large, where $\varepsilon_0 = \varepsilon \beta_0 / \alpha_0$.

A benefit of this choice of w is that the map (9) can be chaotic for any given nonzero values of ε_0 , which can be arbitrarily small, as long as δ is chosen to be sufficiently large. In other words, small amplitude is compensated by high oscillation.

Now let us take a closer look at the dynamics of the map (9). For any fixed nonzero value of ε_0 , the origin is a globally asymptotically stable fixed point of this map, if $0 < \sigma < \varepsilon_0$. As σ passes through ε_0 , the map (9) has a pair of nonzero conjugate, locally asymptotically stable fixed points $y^+ > 0$ and $y^- = -y^+ < 0$. As σ continues to increase, each nonzero fixed point undergoes a cascade of period-doubling bifurcation leading to a chaotic attractor. With a further increases in the

bifurcation parameter σ , each chaotic attractor increases in size. Finally, at a critical value $\bar{\sigma} = \pi/\varepsilon_0$, the two chaotic attractors merge into one, still chaotic but with an almost unchanged size proportional to ε_0 . Mathematically, we can show that the map (9) is indeed chaotic in the sense of Li-Yorke.

2.2 Generating chaos in a general stable linear system

Consider a general n -dimensional single-input LTI system in the state-space form

$$\dot{\mathbf{x}} = A\mathbf{x} + \mathbf{b}u, \quad (10)$$

where $u \in \mathbb{R}$ and $\mathbf{x} \in \mathbb{R}^n$ are the input and state of the system, respectively. $A \in \mathbb{R}^{n \times n}$ is a Hurwitz stable matrix. Therefore, the uncontrolled system (with $u(t) \equiv 0$) is stable in the sense that $\mathbf{x}(t) \rightarrow \mathbf{0}$ as $t \rightarrow \infty$ for any bounded initial condition.

Suppose that system (10) is controllable which implies that the rank of the $n \times n$ controllability matrix

$$P_c = [\mathbf{b} \ A\mathbf{b} \ \cdots \ A^{n-1}\mathbf{b}]$$

is n . Let \mathbf{q}_1^T be the n -th row of P_c^{-1} . According to linear system theory [22], we can construct an $n \times n$ nonsingular matrix

$$Q = \begin{bmatrix} \mathbf{q}_1^T \\ \mathbf{q}_1^T A \\ \vdots \\ \mathbf{q}_1^T A^{n-1} \end{bmatrix}$$

such that system (10) can be reduced via the transformation $\mathbf{z} = Q\mathbf{x}$ to an equivalent controllable companion form; that is

$$\dot{\mathbf{z}} = A_c\mathbf{z} + \mathbf{b}_c u, \quad (11)$$

where A_c and \mathbf{b}_c are defined as in (5). Denote $y(t) = z_1(t) = \mathbf{q}_1^T \mathbf{x}(t)$, equation (11) is equivalent to

$$y^{(n)}(t) + \alpha_{n-1}y^{(n-1)}(t) + \cdots + \alpha_1\dot{y}(t) + \alpha_0y(t) = u(t). \quad (12)$$

Thus, we can take the time-delay feedback law

$$u(t) = \varepsilon \sin(\sigma y(t - \tau)) = \varepsilon \sin(\sigma \mathbf{q}_1^T \mathbf{x}(t - \tau)), \quad (13)$$

to drive system (10) chaotic.

2.3 Generating chaos in feedback linearizable systems

Consider an n -dimensional single-input affine nonlinear system of the form

$$\dot{\mathbf{x}} = \mathbf{f}(\mathbf{x}, u) = \mathbf{f}(\mathbf{x}) + \mathbf{g}(\mathbf{x})u, \quad (14)$$

where $\mathbf{x} \in \Re^n$ is the state of the system and $u \in \Re$ is control input. $\mathbf{f}(\mathbf{x})$ and $\mathbf{g}(\mathbf{x})$ are smooth vector fields on \Re^n . System (14) is said to be *feedback linearizable* on a neighborhood U of a given point \mathbf{x}^* if there exists a feedback

$$u = p(\mathbf{x}) + q(\mathbf{x})v, \quad (15)$$

defined on U , and a coordinate transformation,

$$\mathbf{z} = \Phi(\mathbf{x}), \quad (16)$$

also defined on U , such that the closed-loop system (14) can be transformed into the following linear control system:

$$\dot{\mathbf{z}} = A_c \mathbf{z} + b_c v, \quad (17)$$

where A_c and b_c are defined as in (5).

Assume that the origin is an equilibrium point of the uncontrolled system, namely, $\mathbf{f}(0) = 0$. The problem under investigation here is to design a feedback law $u(t)$ such that the controlled system is chaotic. We first recall some concepts and notation from the differential geometry control theory [23]. The *Lie derivative* of a scalar smooth function $h(\mathbf{x})$ with respect to a vector field $\mathbf{f}(\mathbf{x})$ is defined recursively by

$$L_{\mathbf{f}} h(\mathbf{x}) = \left(\frac{\partial h}{\partial \mathbf{x}} \right)^T \mathbf{f}(\mathbf{x}),$$

$$L_{\mathbf{f}}^i h(\mathbf{x}) = L_{\mathbf{f}}(L_{\mathbf{f}}^{i-1} h(\mathbf{x})) = \left(\frac{\partial(L_{\mathbf{f}}^{i-1} h)}{\partial \mathbf{x}} \right)^T \mathbf{f}(\mathbf{x}), \quad i > 1.$$

The Lie bracket is an operation on two smooth vector fields (e.g., $\mathbf{f}(\mathbf{x})$ and $\mathbf{g}(\mathbf{x})$) which generates a new, smooth vector field and is defined recursively by

$$ad_{\mathbf{f}} \mathbf{g}(\mathbf{x}) = \frac{\partial \mathbf{g}}{\partial \mathbf{x}} \mathbf{f}(\mathbf{x}) - \frac{\partial \mathbf{f}}{\partial \mathbf{x}} \mathbf{g}(\mathbf{x}),$$

$$ad_{\mathbf{f}}^i \mathbf{g}(\mathbf{x}) = ad_{\mathbf{f}}(ad_{\mathbf{f}}^{i-1} \mathbf{g}) = \frac{\partial(ad_{\mathbf{f}}^{i-1} \mathbf{g})}{\partial \mathbf{x}} \mathbf{f}(\mathbf{x}) - \frac{\partial \mathbf{f}}{\partial \mathbf{x}} (ad_{\mathbf{f}}^{i-1} \mathbf{g}(\mathbf{x})), \quad i > 1.$$

Lemma 3 [23]: Control system (14) is feedback linearizable on a neighborhood of a point \mathbf{x}^* if and only if there exists a smooth function $h(\mathbf{x})$ such that the SISO system

$$\begin{cases} \dot{\mathbf{x}} = \mathbf{f}(\mathbf{x}) + \mathbf{g}(\mathbf{x})u \\ y = h(\mathbf{x}) \end{cases} \quad (18)$$

has relative degree n at \mathbf{x}^* , in the sense that

- (i) $L_{\mathbf{g}} L_{\mathbf{f}}^k h(\mathbf{x}) = 0, \quad 0 \leq k < n - 1;$
- (ii) $L_{\mathbf{g}} L_{\mathbf{f}}^{n-1} h(\mathbf{x}) \neq 0, \quad \text{for all } \mathbf{x} \in D.$

Lemma 4 [23]: Control system (14) is feedback linearizable on a neighborhood U of a point \mathbf{x}^* if and only if

- (i) the matrix $(\mathbf{g}(\mathbf{x}) \ ad_f \mathbf{g}(\mathbf{x}) \ \cdots \ ad_f^{n-1} \mathbf{g}(\mathbf{x}))$ has rank n at \mathbf{x}^* .
- (ii) the distribution $D = \text{span}\{\mathbf{g} \ ad_f \mathbf{g} \ \cdots \ ad_f^{n-2} \mathbf{g}\}$ is involutive on U , in the sense that the Lie bracket of any pair of vector fields belonging to D is also a vector field in D .

In this case, the output $y = h(\mathbf{x})$ is a solution of the partial differential equations

$$\frac{\partial h(\mathbf{x})}{\partial \mathbf{x}} [\mathbf{g}(\mathbf{x}), ad_f \mathbf{g}(\mathbf{x}), \cdots, ad_f^{n-2} \mathbf{g}(\mathbf{x})] = 0. \quad (19)$$

Then, we have a diffeomorphism

$$\mathbf{z} = \Phi(\mathbf{x}) = \left[h(\mathbf{x}), \quad L_{\mathbf{f}} h(\mathbf{x}), \quad \cdots, \quad L_{\mathbf{f}}^{(n-1)} h(\mathbf{x}) \right]^T, \quad (20)$$

where $\mathbf{z} = [z_1, z_2, \cdots, z_n]^T = [y, \dot{y}, \cdots, y^{n-1}]^T$. Moreover, it is easy to show that

$$y^{(n)} = \alpha(\mathbf{x}) + \beta(\mathbf{x})u, \quad (21)$$

where

$$\alpha(\mathbf{x}) = L_{\mathbf{f}}^n h(\mathbf{x}), \quad \beta(\mathbf{x}) = L_{\mathbf{g}} L_{\mathbf{f}}^{n-1} h(\mathbf{x}) \neq 0, \quad \text{for all } \mathbf{x} \in D.$$

Let $\{\gamma_i\}_{i=0}^{n-1}$ be n constants with $\gamma_0 \neq 0$ such that

$$s^n + \gamma_{n-1}s^{n-1} + \cdots + \gamma_1s + \gamma_0$$

is a Hurwitz stable polynomial. If we take

$$u = \frac{1}{\beta(\mathbf{x})} (-\alpha(\mathbf{x}) - \gamma_{n-1}L_{\mathbf{f}}^{n-1}h(\mathbf{x}) - \cdots - \gamma_1L_{\mathbf{f}}h(\mathbf{x}) - \gamma_0h(\mathbf{x}) + v(t)) \quad (22)$$

then Eq. (21) becomes

$$y^{(n)} + \gamma_{n-1}y^{(n-1)} + \cdots + \gamma_1y' + \gamma_0y = v(t), \quad (23)$$

which is in the same form as linear control system (1). Therefore, controller (22) with

$$v(t) = \varepsilon \sin(\sigma y(t - \tau))$$

can make system (14) chaotic.

Clearly, controller (22) actually cancels the nonlinearity of the original system and renders it linear. Such a complex controller is physically impractical in many cases.

Suppose that \mathbf{x}^* is an asymptotically stable equilibrium point of the uncontrolled system (14) with $u \equiv 0$. Let us rewrite the Eq. (21) as

$$\begin{cases} \dot{z}_1 = z_2, & \dot{z}_2 = z_3, \dots, \dot{z}_{n-1} = z_n \\ \dot{z}_n = \alpha(\mathbf{x}) + \beta(\mathbf{x})u = \bar{\alpha}(\mathbf{z}) + \bar{\beta}(\mathbf{z})u, \end{cases} \quad (24)$$

where

$$\bar{\alpha}(\mathbf{z}) = \alpha(\Phi^{-1}(\mathbf{z})), \quad \bar{\beta}(\mathbf{z}) = \beta(\Phi^{-1}(\mathbf{z})).$$

Clearly, $\mathbf{z}^* = \Phi(\mathbf{x}^*) = \mathbf{0}$ is an asymptotically stable equilibrium point of the system (24) with $u(t) \equiv 0$. To make the system chaotic, we now take

$$u(t) = w(t - \tau) = \varepsilon \sin(\sigma y(t - \tau)) = \varepsilon \sin(\sigma h(\mathbf{x}(t - \tau))), \quad (25)$$

where ε represents the control amplitude, τ is the time-delay and σ is a sufficiently large constant. Clearly,

$$|u(t)| \leq \varepsilon, \quad \text{for all } t \geq 0.$$

It is known in nonlinear system theory that for sufficiently small ε , there exists a sufficiently small neighborhood Ω of $\mathbf{z}^* = \mathbf{0}$ such that if the initial states of the system (24) are in Ω , then the states of the system (24) will stay in Ω forever.

In the small neighborhood Ω , the Eq. (24) can be represented by its linearization at $\mathbf{z}^* = \mathbf{0}$,

$$\begin{cases} \dot{z}_1 = z_2, & \dot{z}_2 = z_3, \dots, \dot{z}_{n-1} = z_n \\ \dot{z}_n = \alpha_{n-1}z_n + \alpha_{n-2}z_{(n-1)} + \dots + \alpha_0z_1 + \bar{\beta}(\mathbf{0})w(z_1(t - \tau)), \end{cases} \quad (26)$$

or equivalently,

$$y^{(n)} = \alpha_{n-1}y^{n-1} + \alpha_{n-2}y^{(n-2)} + \dots + \alpha_0y + \bar{\beta}(\mathbf{0})w(y(t - \tau)), \quad (27)$$

where

$$\alpha_i = \left. \frac{\partial \bar{\alpha}(\mathbf{z})}{\partial y^{(i)}} \right|_{z=0}, \quad i = 0, 1, \dots, n-1.$$

To conclude, if \mathbf{x}^* is an asymptotically stable equilibrium point of the uncontrolled system (14) with $u \equiv 0$, then the small-amplitude time-delay feedback law (25) would make the controlled system chaotic, if σ and τ are large enough. The proposed approach can also be generalized to make a continuous-time minimum-phase system chaotic [8].

Example 1: Consider the well-known Lorenz system

$$\begin{pmatrix} \dot{x}_1(t) \\ \dot{x}_2(t) \\ \dot{x}_3(t) \end{pmatrix} = \begin{pmatrix} \sigma(x_2 - x_1) \\ rx_1 - x_2 - x_1x_3 \\ x_1x_2 - bx_3 \end{pmatrix}, \quad (28)$$

where we fixed $a = 10$ and $b = 8/3$. For $0 < r < 1$, the origin is a globally exponentially stable equilibrium point. For $1 < r < r_H \approx 24.74$, the Lorenz system has two locally exponentially stable equilibria: $A_+ = (\sqrt{b(r-1)}, \sqrt{b(r-1)}, r-1)$ and $A_- = (-\sqrt{b(r-1)}, -\sqrt{b(r-1)}, r-1)$. The Lorenz system is chaotic only if $r > r_H$.

In our simulations, we take $r = 5 < r_H$. In this setting, the uncontrolled Lorenz system is not chaotic and has two stable equilibria: $A_+ = (3.27, 3.27, 4)$ and $A_- = (-3.27, -3.27, 4)$. We use r as the control parameter. Denote $\mathbf{x} = [x_1, x_2, x_3]^T$ and $r(t) = r + \delta r(t)$. The controlled Lorenz system becomes

$$\dot{\mathbf{x}} = f(\mathbf{x}) + g(\mathbf{x})\delta r(t)$$

where

$$f(\mathbf{x}) = \begin{pmatrix} a(x_2 - x_1) \\ rx_1 - x_2 - x_1x_3 \\ x_1x_2 - bx_3 \end{pmatrix}, \quad g(\mathbf{x}) = \begin{pmatrix} 0 \\ x_1 \\ 0 \end{pmatrix},$$

Now we show that chaos can be created in the controlled Lorenz system with $0 < \delta r(t) < r_H - r \approx 19.74$. It can be verified that the controlled Lorenz system is feedback linearizable for all $\mathbf{x} \neq 0$. From the partial differential equations

$$\frac{\partial h(\mathbf{x})}{\partial \mathbf{x}} [\mathbf{g}(\mathbf{x}), ad_{\mathbf{f}}\mathbf{g}(\mathbf{x})] = 0,$$

we have

$$\frac{\partial h(\mathbf{x})}{\partial x_2} = 0, \quad a \frac{\partial h(\mathbf{x})}{\partial x_1} + \frac{\partial h(\mathbf{x})}{\partial x_3} x_1^2 = 0. \quad (29)$$

A solution of (29) is given by

$$y = h(\mathbf{x}) = 0.5x_1^2 - ax_3$$

Therefore, we may take

$$\delta r(t) = \varepsilon \sin(\sigma(0.5x_1^2(t-\tau) - ax_3(t-\tau))).$$

In simulation, we fixed $\tau = 1$. Fig. 1 shows one of the two separate chaotic attractors of the controlled Lorenz system with $\varepsilon = 1$ and $\sigma = 30$. Fig. 2 shows a single chaotic attractor of the controlled system with $\varepsilon = 10$ and $\sigma = 20$.

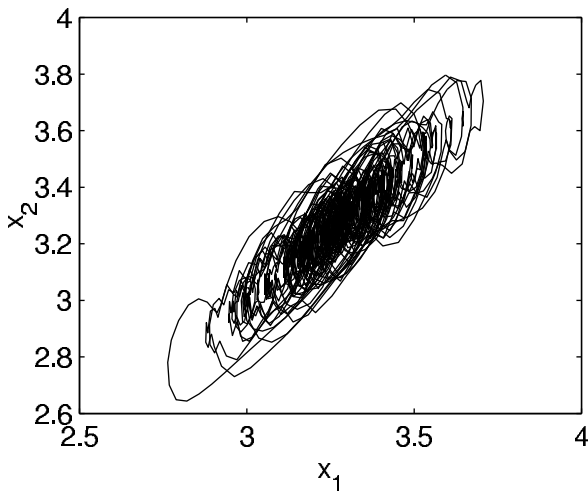


Fig. 1. One of the two separate chaotic attractors of the controlled Lorenz system with $\varepsilon = 1$ and $\sigma = 30$

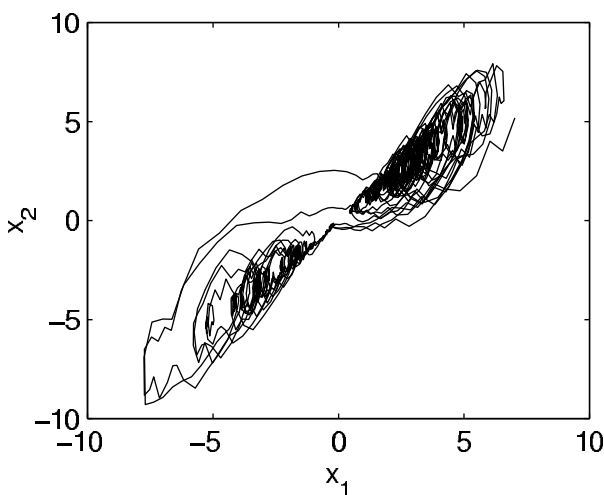


Fig. 2. A single chaotic attractor of the controlled Lorenz system with $\varepsilon = 10$ and $\sigma = 20$

3 Generating Topologically Conjugate Chaotic Systems via Feedback Control

3.1 Normal form of chaotic systems

Consider an n -dimensional continuous-time chaotic systems of the form

$$\dot{\mathbf{x}}_c = f_c(\mathbf{x}_c). \quad (30)$$

The Poincaré-Bendixson theorem implies that if f_c is continuous, then a necessary condition for system (30) to be chaotic is $n \geq 3$ [21]. For a smooth dynamical system (30) and a smooth scalar output function $y = \phi(\mathbf{x})$, the Takens reconstruction theorem states that [24], generically, one can reconstruct the chaotic attractor of (30) using its output samples

$$Y = [y \ \dot{y} \ \cdots \ y^{(m-1)}]^T, \quad (31)$$

provided that $m > 2n$. Here, we assume that, for the given chaotic system (30), there exists a scalar smooth function

$$y_c = \phi_{c1}(\mathbf{x}_c), \quad (32)$$

such that

$$z_c = [y \ \dot{y} \ \cdots \ y^{(n-1)}]^T = \Phi_c(\mathbf{x}_c), \quad (33)$$

is a diffeomorphism on a set $\Omega_c \subseteq \Re^n$, which contains the chaotic attractor of system (30). Under the coordinates transformation (33), system (30) can be recast into the following normal form

$$\dot{\mathbf{z}}_c = A_c \mathbf{z}_c + b_c G_c(\mathbf{z}_c), \quad (34)$$

where $G_c(\mathbf{z}_c)$ is a nonlinear function of $\mathbf{z}_c \in \Re^n$,

$$A_c = \begin{bmatrix} 0 & 1 & 0 & \cdots & 0 \\ 0 & 0 & 1 & \cdots & 0 \\ \vdots & \vdots & \ddots & \ddots & \vdots \\ 0 & 0 & 0 & \cdots & 1 \\ 0 & 0 & 0 & \cdots & 0 \end{bmatrix}, \quad \mathbf{b}_c = \begin{bmatrix} 0 \\ 0 \\ \vdots \\ 0 \\ 1 \end{bmatrix}. \quad (35)$$

Clearly, y_c satisfies the n th-order scalar differential equation

$$y_c^{(n)} = G_c(y_c, y'_c, \dots, y_c^{(n-1)}). \quad (36)$$

In mechanical systems, the 3rd derivative represents the rate of change of the acceleration and is sometimes called the *jerk*. Therefore, for $n = 3$, Eq. (36) is called the jerk equation and G_c is called the jerk function [25].

It is well known that if the Jacobian matrix of Φ_c is nonsingular at a point \mathbf{x}^0 , then $\Phi_c(\mathbf{x})$ defines a local diffeomorphism on a neighborhood of \mathbf{x}^0 . The following theorem shows that a large class of chaotic systems can be transformed into the normal form (34) via global diffeomorphisms on \Re^n .

Theorem 1: Consider an n -dimensional dynamical system of the form

$$\dot{\mathbf{x}}_c = A\mathbf{x}_c + \mathbf{b}_c g(\mathbf{x}_c) , \quad (37)$$

where \mathbf{b}_c is defined as in (35), g is an real-valued function, and A is a constant matrix of the form

$$A = \begin{bmatrix} a_{11} & a_{12} & 0 & \cdots & 0 \\ a_{21} & a_{22} & a_{23} & \cdots & 0 \\ \vdots & \vdots & \ddots & \ddots & \vdots \\ a_{n-1,1} & a_{n-1,2} & a_{n-1,2} & \cdots & a_{n-1,n} \\ a_{n1} & a_{n2} & a_{n3} & \cdots & a_{nn} \end{bmatrix}$$

with

$$a_{i,i+1} \neq 0 , \quad i = 1, 2, \dots, n-1 . \quad (38)$$

Let $\mathbf{z}_c = [x_{c1} \ \dot{x}_{c1} \ \dots \ x_{c1}^{(n-1)}]^T$. Then there exists a global linear co-ordinates transformation,

$$\mathbf{z}_c = Q_c \mathbf{x}_c , \quad (39)$$

where Q_c is a nonsingular matrix, such that system (37) can be recast in the normal form (34).

Example 2 (Rössler's toroidal chaos): Rössler found a simple system that exhibits toroidal chaos. The system is described by [26]

$$\begin{pmatrix} \dot{x}_1(t) \\ \dot{x}_2(t) \\ \dot{x}_3(t) \end{pmatrix} = \begin{pmatrix} -x_2 - x_3 \\ x_1 \\ \alpha(x_2 - x_2^2) - \beta x_3 \end{pmatrix} , \quad (40)$$

where α and β are real parameters. Figure 3 shows the chaotic attractor of system (40), with $\alpha = 0.386$ and $\beta = 0.2$.

If we take

$$\mathbf{x}_c = [x_{c1} \ x_{c2} \ x_{c3}]^T = [x_2 \ x_1 \ x_3]^T ,$$

then system (40) will be in the form (37). The following global diffeomorphism

$$\mathbf{z} = [x_2 \ \dot{x}_2 \ \ddot{x}_2]^T = [x_2 \ x_1 \ -x_2 - x_3]^T ,$$

reformulates the system into the normal form (34), with the corresponding jerk function

$$G_c(\mathbf{z}) = -\beta z_3^2 - z_2 - (\alpha + \beta)z_1 + \alpha z_1^2 . \quad (41)$$

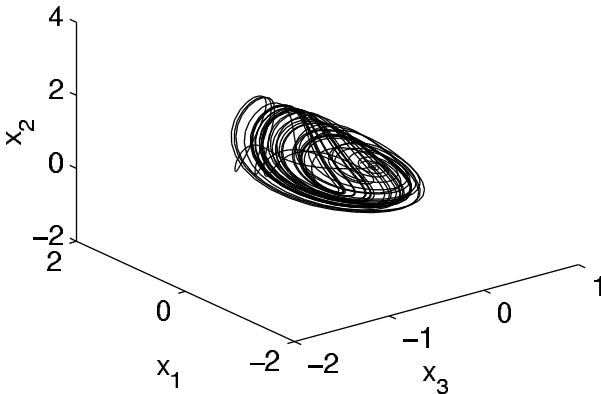


Fig. 3. A chaotic attractor of the Rössler system (40)

Example 3 (Chua's oscillator): Chua's oscillator is a physical system for which the presence of chaos in the sense of Shil'nikov has been established experimentally, confirmed numerically, and proven mathematically. The state equations of Chua's oscillator in the dimensionless form are given by [27]

$$\begin{pmatrix} \dot{x}_1(t) \\ \dot{x}_2(t) \\ \dot{x}_3(t) \end{pmatrix} = \begin{pmatrix} \alpha(-x_2 - x_1 + f(x_1)) \\ x_1 - x_2 + x_3 \\ -\beta x_2 - \gamma x_3 \end{pmatrix}, \quad (42)$$

where $f(\cdot)$ is a piecewise linear function,

$$f(x_1) = \begin{cases} -bx_1 - a + b & x_1 > 1 \\ -ax_1 & |x_1| \leq 1 \\ -bx_1 + a - b & x_1 < -1, \end{cases} \quad (43)$$

where $\alpha > 0$, $\beta > 0$, $\gamma > 0$ and $a < b < 0$. With

$$\alpha = 10.0000, \beta = 15.0000, \gamma = 0.0385, a = -1.2700, b = -0.6800,$$

Chua's oscillator (42) generates a chaotic attractor as shown in Fig. 4.

If we take

$$\mathbf{x}_c = [x_{c1} \ x_{c2} \ x_{c3}]^T = [x_3 \ x_2 \ x_1]^T,$$

then system (42) will be in the form (37). One may take the global diffeomorphism

$$\mathbf{z} = \begin{pmatrix} x_3 \\ \dot{x}_3 \\ \ddot{x}_3 \end{pmatrix} = \begin{pmatrix} -x_3 \\ -\beta x_2 - \gamma x_3 \\ -\beta x_1 + \beta(\gamma + 1)x_2 + (\gamma^2 - \beta)x_3 \end{pmatrix}, \quad (44)$$

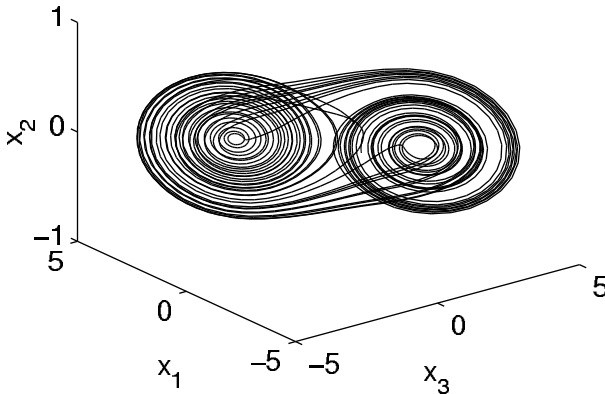


Fig. 4. A chaotic attractor of the Chua's oscillator (42)

to recast the system (42) into the normal form (34), where the corresponding jerk function is

$$G_c(\mathbf{z}) = -\alpha\beta z_1 + (\alpha\gamma + \gamma - \beta)z_2 - (\alpha + \gamma + 1)z_3 + \alpha\beta f(\beta^{-1}(-(\beta + \gamma)z_1 + (\gamma + 1)z_2 - z_3)). \quad (45)$$

It has been shown that Chua's oscillator is topologically conjugate to many three-dimensional systems that are defined by a 3-segmented odd-symmetric piecewise-linear continuous vector field.

In addition, Eichhorn *et al.* showed that [28], all the 19 simple 3-dimensional chaotic systems found by Sprott in 1994 [29] can be transformed into jerk equations. Sprott also performed an extensive search for chaos in various jerk equations and found that a variety of very simple jerk equations can indeed produce chaos [30-32]. The simplest such equation is with quadratic nonlinearity, given by

$$\ddot{x} = -x \pm \dot{x}^2 - a\ddot{x}, \quad (46)$$

which, with $a = 2.017$, can generate chaos. The simplest chaotic jerk equation with piecewise linear nonlinearity is

$$\ddot{x} = -1 + |x| - b\dot{x} - a\ddot{x}, \quad (47)$$

which exhibits chaos for $a = 0.6$ and $b = 1$. All these jerky systems can be directly transformed into the normal form.

Transforming the fourth- and higher-dimensional dynamical systems to the normal form does not pose a conceptual problem. As an example, consider the transformation of a 4-dimensional hyperchaotic system in the following.

Example 4 (TNC's hyperchaotic oscillator): The state equations of the TNC's oscillator are [33]:

$$\begin{pmatrix} \dot{x}_1(t) \\ \dot{x}_2(t) \\ \dot{x}_3(t) \\ \dot{x}_4(t) \end{pmatrix} = \begin{pmatrix} ax_1 - x_2 - x_3 \\ x_1 - bx_2 \\ \mu^{-1}(x_1 - cx_3 - x_4) \\ \varepsilon^{-1}(x_3 - d(x_4 - 1)H(x_4 - 1)) \end{pmatrix}, \quad (48)$$

where

$$H(x_4 - 1) = \begin{cases} 0 & x_4 < 1 \\ 1 & x_4 \geq 1. \end{cases} \quad (49)$$

System (48) can be transformed to the normal form (34) via the global co-ordinates transformation

$$\mathbf{z} = \begin{pmatrix} 0 & 1 & 0 & 0 \\ 1 & -b & 0 & 0 \\ a - b & b^2 - 1 & -1 & 0 \\ a(a - b) + \frac{1}{b} - 1 - \frac{1}{\mu} & 2b - a - b^3 & b - a + \frac{c}{\mu} & \frac{1}{\mu} \end{pmatrix} \mathbf{x}. \quad (50)$$

3.2 Generating chaos in linear controllable systems

Consider a general n -dimensional single-input linear control system of the form

$$\dot{\mathbf{x}} = A\mathbf{x} + bu. \quad (51)$$

Suppose that system (51) is controllable. Then system (51) can be reduced, via linear transformation $\mathbf{z} = Q\mathbf{x}$, to an equivalent form,

$$\dot{\mathbf{z}} = A_c\mathbf{z} + b_c(u - \alpha^T \mathbf{z}), \quad (52)$$

where A_c and b_c are defined in (35), and α is a constant vector.

If the control law in (52) is taken as

$$u = \alpha^T \mathbf{z} + G_c(\mathbf{z}), \quad (53)$$

then the closed-loop system (52) is in the normal form (34). This means that, if the control law in (51) is taken as

$$u = \alpha^T Q\mathbf{x} + G_c(Q\mathbf{x}), \quad (54)$$

then the closed-loop system (51) is topologically conjugate to the chaotic system (30), and therefore, is also chaotic.

Example 4: Consider a 3-dimensional linear control system given by

$$\dot{\mathbf{x}} = \begin{pmatrix} -1 & -1 & 0 \\ 1 & -1 & 1 \\ 2 & 0 & -1 \end{pmatrix} \mathbf{x} + \begin{pmatrix} 1 \\ 0 \\ 0 \end{pmatrix} u . \quad (55)$$

Under the linear transformation $\mathbf{z} = Q\mathbf{x}$ with

$$Q = \begin{pmatrix} 0 & 0.5 & -0.25 \\ 0 & -0.5 & 0.75 \\ 1 & 0.5 & -1.25 \end{pmatrix} ,$$

system (55) is transformed into the following control canonical form

$$\dot{\mathbf{z}} = \begin{pmatrix} 0 & 1 & 0 \\ 0 & 0 & 1 \\ -4 & -4 & -3 \end{pmatrix} \mathbf{z} + \begin{pmatrix} 1 \\ 0 \\ 0 \end{pmatrix} u .$$

Therefore, if the control law is taken as

$$u = [-4 \ -4 \ -3]^T Q\mathbf{x} + G_c(Q\mathbf{x}) , \quad (56)$$

then the closed-loop system (55)-(56) is topologically conjugate to the chaotic system (30), so becomes chaotic.

Figures 5-6 show two chaotic attractors of the controlled system (55) and (56) with G_c being the jerk functions of the Rössler system and the Chua's oscillator, respectively.

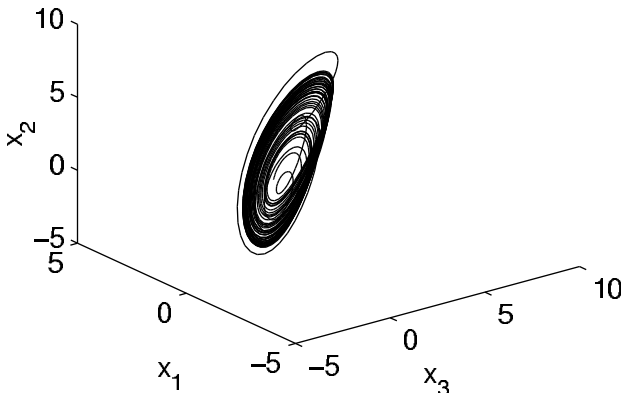


Fig. 5. A chaotic attractor of the controlled system (55) and (56), with G_c being the jerk functions of the Rössler system

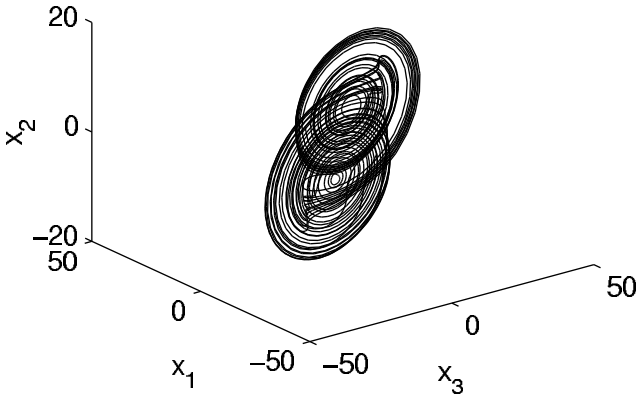


Fig. 6. A chaotic attractor of the controlled system (55) and (56), with G_c being the jerk functions of the Chua's oscillator

3.3 Generating chaos in feedback linearizable systems

Consider an n -dimensional single-input nonlinear control system of the form

$$\dot{\mathbf{x}} = f(\mathbf{x}) + g(\mathbf{x})u . \quad (57)$$

Suppose that system (57) is feedback linearizable on a neighborhood U of a given point \mathbf{x}^0 . Then there exists a feedback

$$u = \alpha(\mathbf{x}) + \beta(\mathbf{x})v , \quad (58)$$

defined on U , and a coordinate transformation,

$$\mathbf{z} = \Phi(\mathbf{x}) , \quad (59)$$

also defined on U , such that the closed-loop system can be transformed into the following linear control system:

$$\dot{\mathbf{z}} = A_c \mathbf{z} + b_c v , \quad (60)$$

where A_c and b_c are defined as in (5). Control system (57) is feedback linearizable on a set $\Omega \subseteq \Re^n$ if it is feedback linearizable at each point $\mathbf{x}^0 \in \Omega$. If $\Omega \supseteq \Phi^{-1}(\Phi_c(\Omega_c))$ and the control law in (57) is taken as

$$u = \alpha(\mathbf{x}) + \beta(\mathbf{x})G_c(\Phi(\mathbf{x})) , \quad (61)$$

then the closed-loop system is topologically conjugate to the chaotic system (30) on Ω_c , which contains the chaotic attractor of (30). Therefore, the closed-loop system (57) is also chaotic.

Based on Lemma 3 and 4, the procedure for constructing the control law (61) can be formulated as the following steps:

- Check the feedback linearization conditions (i) and (ii) in Lemma 3.
- If both conditions are satisfied, solve the partial differential equation for $\lambda(\mathbf{x})$:

$$L_g \lambda(\mathbf{x}) = L_{ad_f g} \lambda(\mathbf{x}) = \cdots = L_{ad_f^{n-2} g} \lambda(\mathbf{x}) = 0 . \quad (62)$$

- Set

$$\alpha(\mathbf{x}) = \frac{-L_f^n \lambda(\mathbf{x})}{L_g L_f^{(n-1)} \lambda(\mathbf{x})} , \quad \beta(\mathbf{x}) = \frac{1}{L_g L_f^{(n-1)} \lambda(\mathbf{x})} . \quad (63)$$

- Set

$$\Phi(\mathbf{x}) = [\lambda(\mathbf{x}) \ L_f \lambda(\mathbf{x}) \ \cdots \ L_f^{n-1} \lambda(\mathbf{x})]^T . \quad (64)$$

- Choose the jerk function G_c of a desired chaotic system and use it in the control law (61).

Example 5: Consider a given nonlinear control system of the form

$$\dot{\mathbf{x}} = \mathbf{f}(\mathbf{x}) + \mathbf{g}(\mathbf{x})u = \begin{pmatrix} x_2 - x_1 \\ x_1 - x_2 \\ x_2 - x_3^2 \end{pmatrix} + \begin{pmatrix} 1 \\ 0 \\ 0 \end{pmatrix} u . \quad (65)$$

Since

$$ad_f \mathbf{g} = [1 \ -1 \ 0]^T , \quad ad_f^2 \mathbf{g} = [2 \ -2 \ 1]^T ,$$

the feedback linearization conditions are satisfied on \Re^3 . A solution of the equations

$$L_g \lambda(\mathbf{x}) = L_{ad_f \mathbf{g}} \lambda(\mathbf{x}) = 0$$

is

$$\lambda(\mathbf{x}) = x_3 .$$

So we have

$$\alpha(\mathbf{x}) = \frac{-L_f^3 \lambda(\mathbf{x})}{L_g L_f^2 \lambda(\mathbf{x})} = -2[(1+x_3)(x_2-x_1) + (x_2-x_3^2)(3x_3^2-x_2)] ,$$

$$\beta(\mathbf{x}) = \frac{1}{L_g L_f^2 \lambda(\mathbf{x})} = 1 .$$

The global coordinates transformation is

$$\Phi(\mathbf{x}) = \begin{pmatrix} x_3 \\ \dot{x}_3 \\ \ddot{x}_3 \end{pmatrix} = \begin{pmatrix} x_3 \\ x_2 - x_3^2 \\ x_1 - x_2 - 2x_3(x_2 - x_3^2) \end{pmatrix} .$$

If G_c is the jerk function of a chaotic system, then the feedback control law

$$u(\mathbf{x}) = -2[(1 + x_3)(x_2 - x_1) + (x_2 - x_3^2)(3x_3^2 - x_2)] + G_c(\Phi(\mathbf{x})) \quad (66)$$

will drive the given system chaotic.

Figures 7-8 show two chaotic attractors of the controlled system (65) and (66), with G_c being the jerk functions of the Rössler system and Chua's oscillator, respectively.

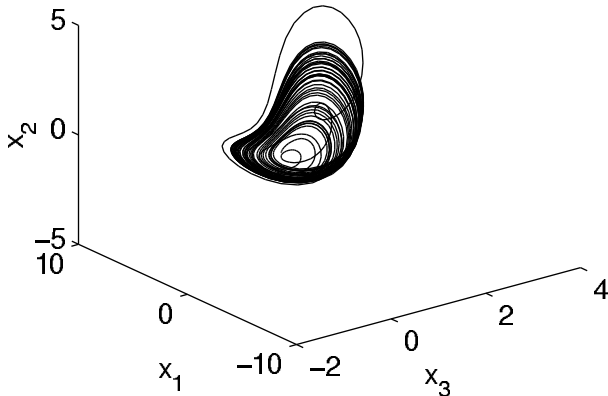


Fig. 7. A chaotic attractor of the controlled system (65) and (66), with G_c being the jerk functions of the Rössler system

3.4 Generating chaos in feedback unlinearizable systems

Now we consider a m -dimensional feedback unlinearizable single-input control system of the form

$$\dot{\mathbf{x}} = f(\mathbf{x}) + g(\mathbf{x})u. \quad (67)$$

Assume that there exists a scalar output function,

$$y = h(\mathbf{x}), \quad (68)$$

such that the SISO system (67)-(68) has a uniform relative degree n on \mathbb{R}^m , with $3 \leq n < m$. Without loss of generality, assume that $f(0) = 0$ and $h(0) = 0$. Set

$$\xi = \begin{pmatrix} z_1 \\ z_2 \\ \vdots \\ z_n \end{pmatrix} = \begin{pmatrix} \phi_1(\mathbf{x}) \\ \phi_2(\mathbf{x}) \\ \vdots \\ \phi_n(\mathbf{x}) \end{pmatrix} = \begin{pmatrix} h(\mathbf{x}) \\ L_f h(\mathbf{x}) \\ \vdots \\ L_f^{n-1} h(\mathbf{x}) \end{pmatrix}. \quad (69)$$

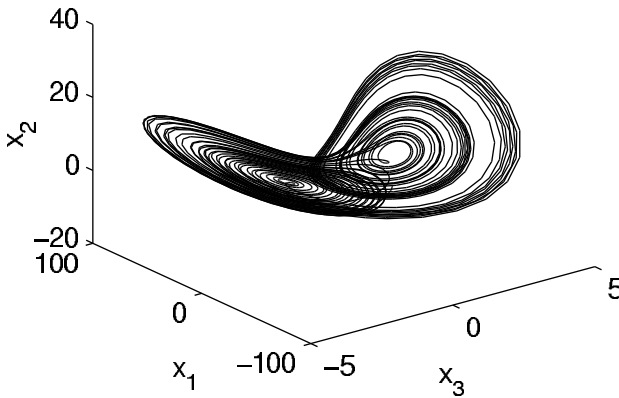


Fig. 8. A chaotic attractor of the controlled system (65) and (66), with G_c being the jerk functions of the Chua's oscillator

According to the differential geometry control theory, it is possible to find $m - n$ more functions,

$$\eta = \begin{pmatrix} z_{n+1} \\ z_{n+2} \\ \vdots \\ z_m \end{pmatrix} = \begin{pmatrix} \phi_{n+1}(\mathbf{x}) \\ \phi_{n+2}(\mathbf{x}) \\ \vdots \\ \phi_m(\mathbf{x}) \end{pmatrix}, \quad (70)$$

in such a way that

$$L_g \phi_i(\mathbf{x}) = 0 \quad (71)$$

for all $n + 1 \leq i \leq m$ and $\mathbf{x} \in \Re^m$, and such that

$$\mathbf{z} = \begin{pmatrix} \phi \\ \eta \end{pmatrix} = \Phi(\mathbf{x}) \quad (72)$$

is a non-singular coordinates transformation.

The state space description of system (67) in the new coordinates becomes

$$\begin{cases} \dot{z}_1 = z_2 \\ \dot{z}_2 = z_3 \\ \dots \\ \dot{z}_{n-1} = z_n \\ \dot{z}_n = b(\mathbf{z}) + a(\mathbf{z})u \\ \dot{\eta} = q(\xi, \eta), \end{cases} \quad (73)$$

where

$$a(\mathbf{z}) = L_g L_f^{n-1} h(\Phi^{-1}(\mathbf{z})) \neq 0, \quad b(\mathbf{z}) = L_f^n h(\Phi^{-1}(\mathbf{z})). \quad (74)$$

The dynamics of the η -subsystem,

$$\dot{\eta} = q(\xi, \eta), \quad (75)$$

correspond to the dynamics describing the *internal* behavior of the system. Here, assume that (75), when being viewed as a system with input $\xi(t)$ and state $\eta(t)$, is *input-to-state stable* [34], in the sense that there exists a class-KL function $\beta(\cdot, \cdot)$ and a class-K function $\gamma(\cdot)$ such that, for any bounded function $\xi(t)$ and any initial state $\eta(0) = \eta^0$, the solution $\eta(t)$ of (75) satisfies

$$\|\eta(t)\| \leq \beta(\|\eta^0\|, t) + \gamma(\|\xi(t)\|_\infty) \quad (76)$$

for all $t \geq 0$.

Here, a continuous function $\alpha : [0, \alpha) \rightarrow [0, \infty)$ is said to belong to *class-K* if it is strictly increasing starting from $\alpha(0) = 0$. If $a = \infty$ and $\lim_{r \rightarrow \infty} \alpha(r) = \infty$, the function is said to belong to *class- K_∞* . A continuous function $\beta : [0, a] \times [0, \infty) \rightarrow [0, \infty)$ is said to belong to *class-KL* if, for each fixed s , the function $\beta(r, s)$ belongs to class-K and, for each fixed r , the function $\beta(r, s)$ is decreasing with $\lim_{s \rightarrow \infty} \beta(r, s) = 0$.

Lemma 5 [34] : The η -subsystem (75), when being viewed as a system with input $\xi(t)$ and state $\eta(t)$, is input-to-state stable if and only if there exists an ISS-Lyapunov function V for this system.

Here, a C^1 -function V is called an ISS-Lyapunov function for system (75) if there exist class K_∞ functions $\alpha_1(\cdot), \alpha_2(\cdot), \alpha(\cdot)$, and a class-K function $\sigma(\cdot)$ such that

$$\alpha_1(\|\eta\|) \leq V(\eta) \leq \alpha_2(\|\eta\|) \quad (77)$$

for all $\eta \in \Re^{m-n}$, and

$$\frac{\partial V}{\partial \eta} q(\xi, \eta) \leq -\alpha(\|\eta\|) + \sigma(\|\xi\|) \quad (78)$$

for all $\xi \in \Re^n$ and $\eta \in \Re^{m-n}$. If one takes

$$u = \frac{G_c(\xi) - b(\mathbf{z})}{a(\mathbf{z})}, \quad (79)$$

then

$$\dot{\xi} = A_c \xi + b_c G_c(\xi), \quad (80)$$

Notice that this is in the normal form (34), and it means that the n -dimensional ξ -subsystem of the closed-loop system (73) is topologically conjugate to the chaotic system (30), so is itself chaotic.

Thus, in summary, if the m -dimensional SISO system (67)-(68) has a uniform relative degree n , $3 \leq n < m$, and the corresponding η -subsystem is input-to-state stable, then the feedback control law

$$u = \frac{G_c(\Phi_\xi(\mathbf{x})) - L_f^n h(\mathbf{x})}{L_g L_f^{n-1} h(\mathbf{x})} \quad (81)$$

can drive the given m -dimensional system chaotic.

Example 6: Consider a given SISO nonlinear control system of the form

$$\dot{\mathbf{x}} = f(\mathbf{x}) + g(\mathbf{x})u = \begin{pmatrix} x_2 - x_1 \\ x_1 - x_2 + x_3 \\ x_1 x_4 + x_3 \\ x_1 x_3 - 2x_4 \end{pmatrix} + \begin{pmatrix} 0 \\ 0 \\ 1 \\ 0 \end{pmatrix} u, \quad y = x_1. \quad (82)$$

It can be easily verified that this system has a uniform relative degree 3. Denote

$$\xi = \begin{pmatrix} z_1 \\ z_2 \\ z_3 \end{pmatrix} = \begin{pmatrix} x_1 \\ x_2 - x_1 \\ 2x_1 - 2x_2 + x_3 \end{pmatrix} = \Phi_\xi(\mathbf{x})$$

and take

$$\eta = z_4 = x_4.$$

We have

$$\begin{cases} \dot{z}_1 = z_2 \\ \dot{z}_2 = z_3 \\ \dot{z}_3 = 2z_2 - z_3 + z_1 z_4 + u, \end{cases} \quad (83)$$

$$\dot{z}_4 = z_1(2z_2 + z_3) - 2z_4. \quad (84)$$

Clearly, system (84), when being viewed as a system with input $\xi = [z_1 \ z_2 \ z_3]^T$ and state z_4 , is input-to-state stable. It can be verified by computation that

$$L_f^3 h(\mathbf{x}) = 4(x_2 - x_1) - x_3 + x_1 x_4, \quad L_g L_f^2 h(\mathbf{x}) = 1.$$

Therefore, if G_c is the jerk function of a selected chaotic system, then the feedback control law

$$u = \frac{G_c(\Phi_\xi(\mathbf{x})) - L_f^3 h(\mathbf{x})}{L_g L_f^2 h(\mathbf{x})} = G_c(\Phi_\xi(\mathbf{x})) + 4(x_1 - x_2) + x_3 - x_1 x_4 \quad (85)$$

can drive the given system (82) chaotic.

Figures 9-10 show two chaotic attractors of the controlled system (82) and (85), with G_c being the jerk functions of the Rössler system and Chua's oscillator, respectively.

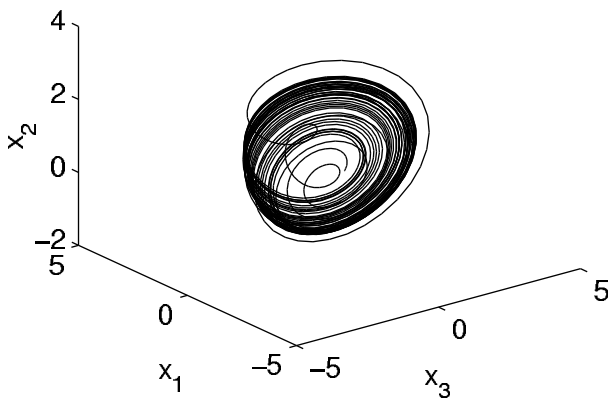


Fig. 9. A chaotic attractor of the controlled system (82) and (85), with G_c being the jerk functions of the Rössler system

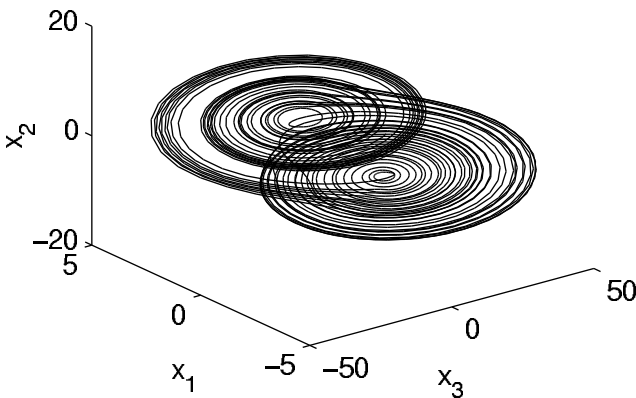


Fig. 10. A chaotic attractor of the controlled system (82) and (85), with G_c being the jerk functions of the Chua's oscillator

4 Generating Chaos in Continuous-Time Systems Using Impulsive Control

Consider an n -dimensional ($n \geq 3$) continuous-time system of the form

$$\dot{\mathbf{x}} = f(\mathbf{x}) \quad (86)$$

where f is a continuous vector field. Assume that system (86) has a stable limit cycle γ : $P(t)$, of period $T > 0$.

Suppose that an impulsive controller is added to the system (86) as following:

$$\dot{\mathbf{x}} = f(\mathbf{x}) + \sum_{k=1}^{\infty} g_k \delta(t - kT) \quad (87)$$

where $\delta(t)$ is the Dirac delta function, and $g_k \in \Re^n$. The impulsive controller only fires at those instants $t = T, \dots, kT, \dots$. The problem is to design g_k such that the local linearized Poincaré map of the controlled system (87) is identical to a chaotic map [10].

To find a suitable chaotic map for the controlled Poincaré map to match, the following $(n - 1)$ -dimensional chaotic map is applied:

$$q_{k+1} = Bq_k + u_k, \quad q_k, u_k \in \Re^{n-1}, \quad (88)$$

with

$$u_k = (N + e^c)q_k \bmod(r), \quad (89)$$

where B is a constant matrix, $N \geq \|B\|$, and c and r are pre-chosen positive constants. One can verify that all Lyapunov exponents of the controlled map (88) are strictly positive but the controlled orbit is uniformly bounded.

Let γ be a periodic orbit $\phi_t \in \Re^n$ of system (86). Take a local $(n - 1)$ -dimensional cross section $\Pi \subset \Re^n$. Denote by p the first point at which γ intersects Π , and let $U \subseteq \Pi$ be a neighborhood of p . Then, the first return Poincaré map, $P_m : U \rightarrow \Pi$, is defined for the point $q \in U$: $P_m(q) = \phi_r(q)$, where $\tau = \tau(q)$ is the time that the orbit $\phi_\tau(q)$ needs to return to Π for the first time. Clearly, p is a fixed point of the map P_m , and the stability of p reflects the stability of γ for flow ϕ .

To design the controller, one may choose a point $p = P(0) \in \gamma$, and uses its normal plane Π as the Poincaré section. Assume that the initial value \mathbf{x}_0 is near p and $\mathbf{x}_0 \in \Pi$. Denote by \mathbf{k} the unit tangent vector of γ at point p , and let $\mathbf{I}_1, \dots, \mathbf{I}_{n-1}$ be some orthogonal basis vectors in Π . Then an $(n - 1)$ -dimensional local coordinate system in Π can be established as follows: Let P_l be the origin and $\mathbf{I}_1, \dots, \mathbf{I}_{n-1}$ be the basis coordinate vectors, respectively. The Poincaré map $P_m : U \rightarrow \Pi$ is formulated as follows: Let P_l be the local linearized map of P_m defined by

$$q_{k+1} = Aq_k, \quad q_k \in U. \quad (90)$$

It can be proved that A is invertible under some mild continuity conditions on the map.

Now denote the point $\mathbf{x}_k = \phi_{kT}(\mathbf{x}_0)$, which arises from system (87), based at \mathbf{x}_0 after time kT . Let $q_k = [\mathbf{I}_1, \dots, \mathbf{I}_{n-1}]^T(\mathbf{x}_k - p)$ be the projection of

\mathbf{x}_k on Π . Also, let $\bar{\mathbf{x}}_k$ be the point resulted after an impulse $g_k \delta(t - kT)$ is applied at time kT , and let $\bar{q}_k = [\mathbf{I}_1, \dots, \mathbf{I}_{n-1}]^T(\bar{\mathbf{x}}_k - p)$.

Notice that on the time interval $(kT, (k+1)T)$, system (87) is the same as system (86), and that the local linearized Poincaré map of system (86) satisfies (90). Therefore, equation $q_{k+1} = A\bar{q}_k$ is satisfied approximately. To achieve the desired chaotification, q_{k+1} should satisfy the pre-chosen chaotic map (88). This leads to

$$A\bar{q}_k = q_{k+1} = Bq_k + u_k \quad (91)$$

so that $\bar{q}_k = A^{-1}(Bq_k + u_k)$, where u_k is given by (89). Thus the expression of g_k can be written as

$$g_k = [\mathbf{I}_1, \dots, \mathbf{I}_{n-1}](\bar{q}_k - q_k) - (\mathbf{k} \cdot (\mathbf{x}_k - p))\mathbf{k} \quad (92)$$

As an illustrative example, consider the following system

$$\begin{cases} \dot{x} = x - 10y - x(x^2 + y^2) \\ \dot{y} = 10x + y - y(x^2 + y^2) \\ \dot{z} = -z \end{cases} \quad (93)$$

which has a stable limit cycle γ : $P(t) = (\cos(10t), \sin(10t), 0)^T$ with period $T = 0.2\pi$. Let $p = P(0) = (1, 0, 0)^T$, $\mathbf{I}_1 = (1, 0, 0)$, $\mathbf{I}_2 = (0, 0, 1)$ and $\mathbf{k} = (0, 1, 0)$. Then

$$A = \begin{pmatrix} e^{-0.4\pi} & 0 \\ 0 & e^{-0.2\pi} \end{pmatrix}.$$

For the controller, $B = A$, $N = e^{-0.2\pi}$, $c = 1$, $r = 0.2$, and

$$\begin{aligned} g_k = & \begin{pmatrix} e^{0.4\pi} & 0 \\ 0 & e^{0.2\pi} \\ 0 & 0 \end{pmatrix} [(e^{-0.2\pi} + e^1) \\ & \begin{pmatrix} 1 & 0 & 0 \\ 0 & 1 & 0 \end{pmatrix} (\mathbf{x}(kT) - (1 0 0)^T) \bmod(0.2)] \\ & - (0 0 1)^T (\mathbf{x}(kT) - (1 0 0)^T) (0 0 1)^T. \end{aligned} \quad (94)$$

5 Conclusions

In this chapter, we have introduced three general feedback approaches to generating chaos in continuous-time systems. First, a general time-delay feedback approach is described which can drive a finite-dimensional continuous-time system chaotic. Then, a state feedback control approach and a impulsive control approach to generating chaos in n -dimensional ($n \geq 3$) continuous-time systems are described.

Acknowledgments.

This work was supported by the National Science Fund for Distinguished Young Scholars of China, the National Natural Science Foundation of China through the grant number 60174005 and 70271072.

References

1. Chen, G., Dong, X. (1998) From Chaos to Order: Methodologies, Perspectives and Applications. Singapore: World Scientific
2. Chen, G. (1999) Controlling Chaos and Bifurcations in Engineering Systems. Boca Raton, FL: CRC Press
3. Chen, G., Lai, D. (1998) Feedback anticontrol of discrete chaos. *Int. J. Bifur. Chaos* **8**:1585–1590
4. Wang, X. F., Chen, G. (2000) Chaotification via arbitrarily small feedback controls: theory, method, and applications. *Int. J. Bifur. Chaos*. **10**:549–570
5. Wang, X. F., Chen, G. (2000) Chaotifying a stable LTI system by tiny feedback control. *IEEE Trans. Circ. Syst.-I*, **47**:410–415
6. Wang, X. F., Chen, G. (2000) Chaotifying a stable map via smooth small-amplitude high-frequency feedback control. *Int. J. Circ. Theory Appl.*, **28**:305–312
7. Wang, X. F., Chen, G., Yu, X. (2000) Anticontrol of continuous-time systems by time-delay feedback. *Chaos*, **10**:771–779
8. Wang, X. F., Chen, G., Man, K. F. (2001) Making a continuous-time minimum-phase system chaotic by using time-delay feedback. *IEEE Trans. Circ. Syst.-I*, **48**:641–646
9. Wang, X. F., Zhong, G. Q., Tang, K. S., Man, K. F., Liu, Z. (2001) Generating chaos in Chua's circuit via time-delay feedback. *IEEE Trans. Circ. Syst.-I* **48**:1151–1156
10. Chen, G., Yang, L., Liu, Z. (2002) Anticontrol of chaos for continuous-time systems. *IEICE Trans. Fundamentals*, **E85-A**:1333–1335
11. Lü, J., Zhou, T., Chen, G., Yang, X. (2002) Generating chaos with a switching piecewise-linear controller. *Chaos*, **12**:344–349
12. Wang, X. F., Chen, G. (2003) Generating topologically conjugate chaotic systems via feedback control. *IEEE Trans. Circ. Syst.-I*, to appear
13. Ottino, M., et al. (1992) Chaos, symmetry, and self-similarity: Exploiting order and disorder in mixing processes. *Science*, **257**:754–760
14. Schiff, S. J., Jerger, K., Duong, D. H., Chang, T., Spano, M. L., Ditto, W. L. (1994) Controlling chaos in the brain. *Nature*, **370**:615–620
15. Georgiou, I. T., Schwartz, I. B. (1999) Dynamics of large scale coupled structural/mechanical systems: A singular perturbation/proper orthogonal decomposition approach. *SIAM J. Appl. Math.*, **59**:1178–1207.
16. Kennedy, M. P., Kolumban, G., Kis, G. (2000) Chaotic modulation for robust digital communications over multipath channels. *Int. J. Bifur. Chaos*, **10**:695–718
17. Mackey, M. C., Glass, L. (1977) Oscillation and chaos in physiological control systems. *Science*, **197**:287–289

18. Farmer, J. D. (1982) Chaotic attractors of an infinite-dimensional dynamical system. *Physica D*, **4**:366–393
19. Ikeda, K., Matsumoto, K. (1987) High-dimensional chaotic behavior in systems with time-delay feedback. *Physica D*, **29**:223–235
20. Celka, P. (1997) Delay-differential equations versus 1D-map: Application to chaos control. *Physica D*, **104**:127–147
21. Hirsch, M. W., Smale, S. (1974) *Differential Equations, Dynamical Systems and Linear Algebra*. New York: Academic Press
22. Kailath, T. (1980) *Linear Systems*. Englewood Cliffs, NJ: Prentice-Hall
23. Isidori, A. (1995) *Nonlinear Control Systems*, 3rd ed. Berlin: Springer-Verlag
24. Takens, F. (1981) Detecting strange attractors in turbulence. *Lecture Notes in Mathematics* **898**, Berlin: Springer, 366–381
25. Sprott, J. C. (1997) Some simple chaotic jerk functions. *Amer. J. Phys.*, **65**:537–543
26. Rössler, O. E. (1979) Continuous chaos-four prototype equations. *Ann. (N.Y.) Acad. Sci.*, **315**:376–392
27. Chua, L. O., Wu, C. W., Huang, A., Zhong, G. Q. (1993) A universal circuit for studying and generating chaos, Part I+II. *IEEE Trans. Circ. Syst.-I*, **40**:732–761
28. Eichhorn, R., Linz, S. J., Hanggi, P. (1998) Transformations of nonlinear dynamical systems to jerky motion and its application to minimal chaotic flows. *Phys. Rev. E*, **58**:7151–7164
29. Sprott, J. C. (1994) Some simple chaotic flows. *Phys. Rev. E*, **50**:R647–R650
30. Sprott, J. C. (1997) Simplest dissipative chaotic flow. *Phys. Lett. A*, **228**:271–274
31. Linz, S. J., Sprott, J. C. (1999) Elementary chaotic flow. *Phys. Lett. A*, **259**:240–245
32. Sprott, J. C. (2000) A new class of chaotic circuit. *Phys. Lett. A*, **266**:19–23
33. Tamasevicius, A., Namajunas, A., Cenys, A. (1996) Simple 4D chaotic oscillators. *Electr. Lett.*, **32**:957–958
34. Isidori, A. (1999) *Nonlinear Control Systems*, 2nd ed. Berlin: Springer-Verlag

Chaos and Pseudo-Randomness

Ljupco Kocarev¹, Goce Jakimoski², and Zarko Tasev¹

¹ Institute for Nonlinear Science
University of California, San Diego
La Jolla, CA 92093-0402, USA
lkocarev@ucsd.edu

² Computer Science Department
Florida State University
Tallahassee, FL 32306-4530, USA

Abstract. We discuss the effect on finite machine implementation of chaotic system on randomness. We show that the most significant bit even for fully developed chaotic systems implemented with high precision (using 1000-bit arithmetics) is not random. We propose chaos-based pseudo-random bit generators and discuss their efficient software implementation.

1 Introduction

Pseudo-random number generators (PRNG) are useful in every scientific area which uses Monte Carlo methods and also in cryptography [1]. PRNGs are algorithms implemented on finite-state machines and are capable of generating sequences of numbers which appear random-like from many aspects. Though they are necessarily periodic (“Anyone who considers arithmetical methods of producing random digits is, of course, in a state of sin”, John von Neumann), their periods are very long, they pass many statistical tests and can be easily implemented with simple and fast software routines.

Chaotic systems may be used to generate pseudo-random numbers. For example, in a series of papers [2], the authors proposed a chaos derived pseudo-random number generator. They numerically observed that the average cycle and transient lengths grow exponentially with the precision of implementation, and from this fact deduced that using high-precision arithmetic one can obtain PRNGs which are still of cryptographic interest. The usual statistical tests applied to PRNGs for use in Monte Carlo simulations are generally simple; for cryptographic applications, PRNGs must pass next-bit test, Section 2. However, the authors did not discuss this question.

Statistical properties of binary sequences generated by class of ergodic maps with some symmetrical properties are discussed in [3]. The authors derived a sufficient condition for this class of maps to produce a sequence of independent and identically distributed binary random variables. However, the authors did not discuss the implementation of these maps on finite-state machines and the consequence this implementation may have on the randomness of the generated sequences.

In this chapter we discuss relations between chaos and randomness, and propose a class of chaos-based pseudo-random bit generators. This is the outline of the chapter. Section 2 introduces basic concepts of pseudo-random number generators and briefly discusses a class of such generators, so called congruential generators.

In Section 3 we survey an approach to randomness based on algorithmic complexity. In this approach, the word *random* is linked to incompressibility of information: a string of numbers is termed random when the shortest program that generates it has (essentially) the same size as the string itself. Section 4 outlines another approach to randomness based on computational complexity. In this approach, a probability distribution is considered “pseudo-random” if no “efficient procedure” can distinguish it from the uniform probability distribution. Assuming the existence of one-way 1-to-1 and onto functions, there exist probability distributions, which are not uniform and are not even statistically close to a uniform distribution, that, nevertheless, are indistinguishable from a uniform distribution. Note that, in this approach, pseudo-randomness and computationally difficulty play dual roles. In this section, the notion of cryptographically secure pseudo-random number generator is introduced and several examples of such generators are given.

Section 5 deals with determinism, chaos and randomness. Determinism of a dynamical system implies existence and uniqueness of its solutions, chaos implies random trajectories (at macroscopic level of description), while randomness means algorithmic complexity and/or computational complexity. For chaotic processes neighboring trajectories diverge exponentially from each other. While a noisy trajectory diverges rapidly from the true trajectory with the same initial conditions, there might exist a different true trajectory with slightly different initial conditions which stays near the noisy trajectory for a long time. This question is related to shadowing process and it is discussed in Section 6. In Section 7 we discuss the effect on finite machine implementation of chaotic system on randomness (or pseudo-randomness). We show, contrary to common believe, that even fully developed chaotic systems when implemented with high precision (using 1000-bit arithmetics) have non random bits. We propose chaos-based pseudo-random number generators and discuss their efficient software implementation.

2 Pseudo-Random Number Generators

In this section we introduce basic concepts of pseudo-random number (bit) generations; we follow [1], see also [4].

Definition 1. A (truly) random bit generator is a device which outputs a sequence of statistically independent and unbiased binary digits.

A random bit generator can be used to generate random numbers. For a chaos-based generator of truly random bits see [5].

Definition 2. A *pseudo-random bit generator* (PRBG) is a deterministic algorithm which, given a truly random binary sequence of length k , outputs a binary sequence of length $l \gg k$ which “appears” to be random. The input of the PRBG is called the *seed*, while the output of the PRBG is called a *pseudo-random bit sequence*.

Definition 3. A pseudo-random bit generator is said to pass all polynomial-time statistical tests if no polynomial-time algorithm can correctly distinguish between an output sequence of the generator and a truly random sequence of the same length with probability significantly greater than $1/2$.

Definition 4. A pseudo-random bit generator is said to pass the next-bit test if there is no polynomial-time algorithm which, on input of the first l bits of an output sequence s , can predict the $(l+1)$ st bit of s with probability significantly greater than $1/2$.

We say also, in this case, that a PRBG is unpredictable.

Theorem 1. *A pseudo-random bit generator passes the next-bit test if and only if it passes all polynomial-time statistical tests.*

All above definitions and the theorem are informal. For a formal definition of statistical test, see section 4 and/or Yao [6]. The notion of cryptographically secure pseudo-random bit generator was introduced by Blum and Micali [7]. The theorem 1 (universality of the next-bit test) is due to Yao [6].

A *linear congruential generator* produces a pseudo-random sequence of numbers x_1, x_2, \dots according to the linear recurrence

$$x_n = ax_{n-1} + b \pmod{m}, \quad n \geq 1.$$

Integers a , b and m are parameters which characterize the generator, while x_0 is the seed. Generators of this form are widely used in Monte Carlo methods, taking x_i/m to simulate uniform draws on $[0, 1]$.

For a study of linear congruential generators, see Knuth [8]. Plumstead [9] and Boyar [10] showed how to predict the output sequence of a linear congruential generator given only a few elements of the output sequence, and when the parameters a , b , and m of the generator are unknown. Boyar [10] extended her methods and showed that linear multivariate congruential generators,

$$x_n = a_1x_{n-1} + a_2x_{n-2} + \dots + a_lx_{n-l} \pmod{m},$$

and quadratic congruential generators,

$$x_n = ax_{n-1}^2 + bx_{n-1} + c \pmod{m},$$

are cryptographically insecure. Krawczyk [11] showed how the output of any multivariate polynomial generator can be efficiently predicted. A truncated linear congruential generator is one where a fraction of the least significant

bits of x_i are discarded. Frieze et al. [12] showed that these generators can be efficiently predicted if the parameters a, b , and m are known. Stern [13] extended this method to the case where only m is known. Boyar [14] presented an efficient algorithm for predicting linear congruential generators when $O(\log \log m)$ bits are discarded, and the parameters are unknown. No efficient prediction algorithms are known for truncated multivariate polynomial congruential generators.

3 Algorithmic Complexity and Randomness

In this section we survey an approach to randomness based on algorithmic complexity. In this approach, the word *random* is linked to incompressibility of information: a string of numbers is termed random when the shortest program that generates it has (essentially) the same size as the string itself.

Consider a Turing machine U operating on three tapes: the first contains the program in the form of a finite binary string which is read sequentially from left to right, the second is a work tape, and the third is reserved for output. A string π , with finite length $l(\pi)$, is a *program* if it lets the Turing machine halt after reading all of its $l(\pi)$ input symbols. Let $U(\pi)$ be the output of the machine U when instructed by the program π .

Definition 5. *Algorithmic complexity* $K_U(S)$ of a finite string S with respect to a universal Turing machine U is the length $l(\pi)$ of the smallest computer program π which computes it, that is,

$$K_U(S) = \min_{\pi: U(\pi)=S} l(\pi),$$

where minimum is taken over all programs π that yield S and halt when processed by U .

Throughout this section we use complexity as a short for algorithmic complexity. It is proved by Kolmogorov that the complexity with respect to any other Turing machine A is related to $K_U(S)$ via $K_U(S) \leq K_A(S) + C_A$, where C_A is a constant which depends on U and A , but not on S . Therefore, the subscript U defining the particular Turing machine can be omitted.

A finite sequence is called random if its complexity is approximately equal to its size. For a random sequence S , the shortest computer program is “Print S ”, that is, we can not find a more compact presentation of S than itself. Algorithmic complexity definition of randomness agrees with the intuitive expectation of the concept of randomness as being equal to unpredictability and incompressibility (a sequence is random if it is not compressible by any possible compression algorithms).

Definition 6. For each constant c we say a sting x is *c-incompressible* if $K(x) \geq l(x) - c$.

Strings that are incompressible (say, c -incompressible with small c) are unpredictable and do not display patterns. Intuitively, we think of such sequences as being random and called them *algorithmically random*. How many strings of length n are c -incompressible? For each n there are 2^n binary string of length n , but only $\sum_{i=0}^n 2^i = 2^n - 1$ possible shorter descriptions. Therefore, there is at least one 0-incompressible string of length n . By the same counting argument we find that the number of strings of length n that are c -incompressible is at least $2^n - 2^{n-c} + 1$. Hence, at least one-half of all strings of length n are 1-incompressible, at least three-fourths of all strings of length n are 2-incompressible, and so on. This means that for each constant $c > 1$ the majority of all strings of length n with $n > c$ is c -incompressible. Nevertheless, no particular string, except finitely many, can be proved to be algorithmically random.

4 Computational Complexity and Randomness

In this section we survey an approach to randomness based on computational complexity. A string is algorithmic random if, roughly speaking, its length equals the length of the shortest program producing it. A finite string S of length $l(S)$ is algorithmic random if the length of the shortest input to a Turing machine, which halts and outputs S , is of length $\geq l(S)$. Therefore, this notion of randomness is that of *computationally incompressibility*. Unfortunately, it is an undecidable problem to decide whether a given string S is algorithmic random.

Another, weaker notion of randomness is based on computational complexity. In this approach, a probability distribution is considered “pseudo-random” if no “efficient procedure” can distinguish it from the uniform probability distribution. Assuming the existence of one-way 1-to-1 and onto functions, there exist probability distributions, which are not uniform and are not even statistically close to a uniform distribution, that, nevertheless, are indistinguishable from a uniform distribution. Thus, pseudo-randomness is defined in terms of an observer (a Turing machine) and is subjective to the abilities of the observer. We note that, in this approach, pseudo-randomness and computationally difficulty play dual roles.

We start with the definition of one-way function.

Definition 7. A function $f : \{0, 1\}^* \rightarrow \{0, 1\}^*$ is called one-way if the following two conditions hold:

1. There exists a deterministic polynomial-time Turing machine that on input x outputs $f(x)$.
2. For any probabilistic polynomial-time Turing machine M , any constant $c > 0$, and sufficiently large n

$$\text{Prob}(M(f(x), 1^n) \in f^{-1}(f(x))) < \frac{1}{n^c},$$

where the probability is taken over all x 's of length n and the internal coin tosses of M with uniform probability distribution.

Therefore, a probabilistic machine M trying to invert the function f will succeed only on a “negligible” fraction of inputs. Thus, the events which occur with negligible probability as a function of the input length are ignored, since they are unlikely to occur when repeating the experiment polynomially many times. The role of 1^n in the above definition is to allow machine M to run in time polynomial in the length of the preimage it is supposed to find.

The following three number theoretical 1-to-1 and onto functions are widely believed to be one-way.

Example 1. Modular Exponential: Let p be a prime and g be a primitive element of Z_p^* (the multiplicative group modulo p). Define $ME(p, g, x) = (p, g, y)$, where $y \equiv g^x \pmod{p}$. Inverting ME is known as discrete logarithm problem, which is an apparently hard number-theoretical problem.

Example 2. RSA: Let p and q be primes, $N = p \cdot q$ and e be relative prime to $\phi(N) = (p - 1) \cdot (q - 1)$. Define $RSA(N, e, x) = (N, e, y)$, where $y \equiv x^e \pmod{N}$.

Example 3. Modular Squaring: Let p and q be primes both congruent to $3 \pmod{4}$, and $N = p \cdot q$. Define $MS(N, x) = (N, y)$, where $y \equiv x^2 \pmod{N}$. To make this function 1-to-1, restrict x to be a quadratic residue modulo N . Inverting MS is computationally equivalent to factoring N .

Definition 8. A probability distribution is a function π from strings to non-negative real numbers such that $\sum_{\alpha \in \{0,1\}^*} \pi(\alpha) = 1$. A probability ensemble indexed by I is a sequence, $\Pi = \{\pi_i\}_{i \in I}$, of probability distribution.

Through this section, we adopt the convention that the probability distributions in an ensemble assign nonzero probability only to strings of length polynomial in the length of the index of the distribution. Two probability distributions π_1 and π_2 are equal if they assign identical probability mass to the same string, i.e., for all $\alpha \in \{0,1\}^*$, $\pi_1(\alpha) = \pi_2(\alpha)$. Two distributions are *statistically close* if they assign “about the same” mass to the same subsets of strings, i.e., for all $S \subseteq \{0,1\}^*$, the absolute difference between the sums $\sum_{\alpha \in S} \pi_1(\alpha)$ and $\sum_{\alpha \in S} \pi_2(\alpha)$ is negligible. Roughly speaking, two distributions are *polynomial indistinguishable* if they assign “about the same” probability mass to any efficiently recognizable set of strings.

Definition 9. Let $\Pi_1 = \{\pi_{1,i}\}_{i \in I}$ and $\Pi_2 = \{\pi_{2,i}\}_{i \in I}$ be two probability ensembles each indexed by elements of I . Let T be a probabilistic polynomial-time Turing machine (hereafter called a test). The test gets two inputs: an index i and a string α . Denote by $p_1^T(i)$ the probability that, on input index i and a string α chosen according to the distribution $\pi_{1,i}$, the test T outputs 1. Similarly, $p_2^T(i)$ denotes the probability that, on input index i and a string

α chosen according to the distribution $\pi_{2,i}$, the test T outputs 1. We say that Π_1 and Π_2 are polynomially indistinguishable if for all probabilistic polynomial-time tests T , all constants $c > 0$ and all sufficiently large $i \in I$,

$$| p_1^T(i) - p_2^T(i) | < [l(i)]^{-c}.$$

An important special case of indistinguishable ensembles is that of probability ensembles which are polynomially indistinguishable from a uniform probability ensemble.

Definition 10. Let $l : \{0,1\}^* \rightarrow N$ be a (length) function, $\pi_{0,i}^l$ denote the uniform probability distribution on the set $\{0,1\}^{l(i)}$, and $\Pi_0^l = \{\pi_{0,i}^l\}_{i \in I}$. Let $\Pi_1 = \{\pi_{1,i}\}_{i \in I}$ be a probability ensemble indexed by I . We say that Π_1 is pseudo-random if it is polynomially indistinguishable from Π_0^l for some function l .

Having defined pseudo-random ensembles it is natural to ask whether ensembles, which are not uniform, and furthermore are not statistically close to uniform, do exist.

Definition 11. Let $\Pi_1 = \{\pi_{1,i}\}_{i \in I}$ be a probability ensemble indexed by I . Let M be a probabilistic polynomial-time Turing machine that on inputs i and y , outputs a single bit (called the *guess*). Let $bit(\alpha, r)$ denote r -th bit of the string α , and $pref(\alpha, r)$ denote the prefix of the first r bits of the string α (i.e., $pref(\alpha, r) = bit(\alpha, 1) \ bit(\alpha, 2) \dots bit(\alpha, r)$). We say that the machine M predicts the next bit of Π_1 if for some $c > 0$ and infinity many i 's,

$$\text{Prob}(M(i, pref(\alpha, r)) = bit(\alpha, r + 1)) \geq \frac{1}{2} + [l(i)]^{-c},$$

where the probability space is that of the string α chosen according to $\pi_{1,i}$, the integer r chosen at random with uniform distribution in $\{0, 1, \dots, l(\alpha)-1\}$ and the internal coin tosses of M . We say that Π_1 is *unpredictable* if there exists no probabilistic polynomial-time machine M which predicts the next bit of Π_1 .

Theorem 2. Let Π_1 be a probability ensemble. Then Π_1 is pseudo-random if and only if Π_1 is unpredictable.

We now give a precise definition of pseudo-random bit generator. To achieve insensitivity to the computational model, this definition is asymptotic.

Definition 12. Let $\mathcal{G} = \{G_n, n \geq 1\}$ be an ensemble of generators, with $G_n : \{0,1\}^n \rightarrow \{0,1\}^{p(n)}$, where $p(\cdot)$ is a polynomial satisfying $n + 1 \leq p(n) \leq n^c + c$ for some fixed integer c . We say that \mathcal{G} is a pseudo-number generator if

1. There is a deterministic polynomial-time Turing machine that on input of any n -bit string outputs a string of length $p(n)$.
2. Two probability ensembles $\Pi_1 = G_n(\Pi_0^n)$ and $\Pi_0^{p(n)}$ are polynomially indistinguishable for sufficiently large n .

Theorem 3. *If there exists an cryptographically secure PRBG with $p(n) = n + 1$, then there exists an cryptographically secure PRNG with $p(n) = n^c + c$ for each $c \geq 2$.*

The notion of cryptographically secure pseudo-random bit generator was introduced by Blum and Micali [7]. The theorem 2 is due to Yao [6]. The theorem 3 is due to Goldreich and Micali (unpublished); a proof appears in [15].

The last definitions above are given in complexity-theoretic terms and are asymptotic in nature because the notion of “polynomial-time” is meaningful for asymptotically large inputs only. Therefore, the security results for a particular family of PRBGs are only an indirect indication about the security of individual members.

Blum and Micali [7] presented the following construction of cryptographically secure PRBG. Let D be a finite set, and let $f : D \rightarrow D$ be a permutation that can be efficiently computed. Let $B : D \rightarrow \{0, 1\}$ be a Boolean predicate with the property that $B(x)$ is hard to compute given only $x \in D$, however, $B(x)$ can be efficiently computed given $y = f^{-1}(x)$. The output sequence z_1, z_2, \dots, z_l corresponding to the seed $x_0 \in D$ is obtained by computing $x_i = f(x_{i-1}), z_i = B(x_i)$, for $1 \leq i \leq l$.

Blum and Micali [7] proposed the first concrete instance of cryptographically secure PRBG. Let p be a large prime, and α a generator of Z_p^* . Define $D = Z_p^* = \{1, 2, \dots, p - 1\}$. The function $f : D \rightarrow D$ is defined by $f(x) = \alpha^x \text{mod} p$. The function $B : D \rightarrow \{0, 1\}$ is defined by $B(x) = 1$ if $0 \leq \log_\alpha x \leq (p - 1)/2$ and $B(x) = 0$ if $\log_\alpha x \geq (p - 1)/2$. Assuming the intractability of the discrete logarithm problem in Z_p^* , the Blum-Micali generator was proven to satisfy the next-bit test. Other examples of cryptographically secure PRBGs are RSA generator [16] and Blum-Blum-Shub generator [17].

5 Determinism, Chaos and Randomness

We consider *deterministic chaotic* discrete time dynamical systems

$$\mathbf{x}_{n+1} = \mathbf{f}(\mathbf{x}_n); \mathbf{x} \in \mathcal{S} \subseteq \mathcal{R}^N, \quad (1)$$

whose defining maps $\mathbf{f} : \mathcal{S} \rightarrow \mathcal{S}$ contain no random terms of any nature (noisy perturbations of the system’s state, random variations of the parameter values, etc.). Unless otherwise stated, for sake of simplicity we assume that Eq. (1) has a single attractor which is chaotic. This implies no loss of

generalization since \mathcal{S} can always be restricted to the basin of attraction of the chaotic attractor.

We examine only dynamical systems whose evolution is determined by the defining vector field and the initial condition \mathbf{x}_1 . However, to completely specify an initial condition an infinite amount of information and a measuring system with an infinite precision are required, which are both intractable. What are the effects of a measuring system's finite precision? Measuring an initial (and future) state is equivalent to partitioning the state space into a finite number of regions, and observing the evolution in this macroscopic world. Any set of m disjoint regions $\beta = \{\mathcal{C}_1, \dots, \mathcal{C}_m\}$ which covers the state space \mathcal{S} of Eq. (1) is called a partition of Eq. (1), that is,

$$\beta = \{\mathcal{C}_1, \dots, \mathcal{C}_m\}; \bigcup_{i=1}^{i=m} \mathcal{C}_i = \mathcal{S}; \mathcal{C}_i \cap \mathcal{C}_j = \emptyset \text{ for } i \neq j.$$

The partition with $m = 1$ is called trivial partition. For a partition β we denote the union of boundaries between regions of β as $\mathcal{B}(\beta)$. If we allow for the regions of β to overlap, then the set β is called open cover of \mathcal{S} .

A unique symbol $i = \sigma(\mathcal{C}_i), i \in M = \{1, 2, \dots, m\}$ is assigned to every region $\mathcal{C}_i \in \beta$. The process of partitioning the state space, assigning symbols to every region from the partition, and the resulting macroscopic dynamics are called symbolic dynamics. Denote with $\Psi = \prod_{j=1}^{\infty} M$ the space of all sequences $X_1^\infty = X_1 X_2 \dots X_j \dots$ with infinite length, where $X_j \in M$. This way we obtain a map $\mu_\beta : \mathcal{S} \rightarrow \Psi$ defined as

$$\begin{aligned} \mu_\beta(\mathbf{x}_1) = X_1^\infty &\Leftrightarrow \mathbf{f}^{j-1}(\mathbf{x}_1) \in \mathcal{C}_{X_j} \Leftrightarrow \\ \mathbf{x}_1 &\in \bigcap_j \mathbf{f}^{-j+1}(\mathcal{C}_{X_j}) \text{ for } j \geq 1, \end{aligned}$$

which assigns a sequence $X_1^\infty \in \Psi$ to every point $\mathbf{x}_1 \in \mathcal{S}$, and X_j is the symbol generated at time j . Since (1) is chaotic, $\mathbf{f}^j(\mathcal{C}_i), j > 1$, may expand over several regions for some $\mathcal{C}_i \in \beta$. Different initial states belonging to a same region \mathcal{C}_{X_1} will produce different observations at some later time $j > 1$. From the viewpoint of our measuring system, identical macroscopic initial states evolve differently. A loss of determinism occurred, and transitions between the regions of β can only be specified by means of probabilities. Partitioning of the state space turns the deterministic chaotic system (1) into an ergodic information source which can be analyzed in terms of information theory. Ergodicity of the source follows from the assumption that Eq. (1) has a single chaotic attractor, that is, from the ergodicity of its invariant measure [18]. The source tends to become stationary for mixing maps, in which case every initial measure leads to the ergodic invariant measure. For the newly obtained information source one can compute entropies

$$H_n^\beta = - \sum_{X_1^n} P(X_1^n) \log P(X_1^n),$$

with $P(X_1^n)$ being probability of occurrence of trajectory subsequence (word) X_1^n . H_n^β quantifies the average uncertainty when predicting words of length n . Throughout the paper we use logarithms with base 2 and the amount of information will be expressed in bits. The conditional entropy of the $(n+1)$ -th symbol in the macroscopic trajectory when the previous n symbols are known is equal to

$$h_n^\beta = H_{n+1|n}^\beta = \begin{cases} H_{n+1}^\beta - H_n^\beta & \text{for } n \geq 1 \\ H_1^\beta & \text{for } n = 0. \end{cases}$$

Source entropy of Eq. (1) for a partition β is defined by

$$h^\beta = \lim_{n \rightarrow \infty} h_n^\beta = \lim_{n \rightarrow \infty} \frac{1}{n} H_n^\beta.$$

Kolmogorov-Sinai (KS) entropy of Eq. (1) is the supremum of the source entropy over all possible partitions

$$h_{KS} = \sup_{\beta} h^\beta.$$

If $h^\beta = h_{KS}$, then β is a generating partition. An interesting property of a generating partition β is that the corresponding map μ_β is injective, that is, $\mathbf{x}' \neq \mathbf{x}'' \Rightarrow \mu_\beta(\mathbf{x}') \neq \mu_\beta(\mathbf{x}'')$.

A dynamical system (1) is chaotic if $h^\beta > 0$ for every partition β different than the trivial partition. If $h^\beta = 0$ for every partition β , then the dynamical system is called regular. In other words, if from the viewpoint of any measuring device, the dynamical system produces unpredictable sequences, then the dynamical system is called chaotic. While the motion of the dynamical system (1) in the continuous (microscopic) state space is deterministic, its motion in the partitioned (macroscopic) space is stochastic and the trajectories are sequences of symbols [18, 19]. On the basis of the knowledge of the past coarse-grained trajectory of Eq. (1) we can predict its future macroscopic states only in probabilistic terms. From the viewpoint of the h^β value, chaotic systems are similar to stochastic systems since in both cases predictability is bounded by an always present uncertainty $h^\beta > 0$.

Observing a chaotic system in a coarse-grained space gives information about the initial state. In other words, a chaotic system encodes the information contained in the initial state into its trajectory. In case of a generating partition β , μ_β is injective, and the corresponding observer can successfully decode the initial state. Almost all of the initial states are irrational numbers whose complexity is positive, and so are the complexities of the infinite coarse grained trajectories. More precise mathematical formulation to this intuitively drawn conclusion is provided in [20], and is sketched here. First, we define complexity of the trajectory of a point \mathbf{x}_1 with respect to an open cover β of \mathcal{S} as

$$\mathcal{K}(\mathbf{x}_1, \mathbf{f}|\beta) = \limsup_{n \rightarrow \infty} \frac{1}{n} \min_{X_1^n \in [\psi(x)]^n} K(X_1^n),$$

where $[\psi(x)]^n = \{X_1^n | f^{j-1}(\mathbf{x}_1) \in \mathcal{C}_{X_j}\}$ may contain more than one element since the regions of β may overlap. Then, *complexity of the trajectory* of a point \mathbf{x}_1 is defined as

$$\mathcal{K}(\mathbf{x}_1, \mathbf{f}) = \sup_{\beta} \mathcal{K}(\mathbf{x}_1, \mathbf{f} | \beta).$$

The trajectory of a point \mathbf{x}_1 is called algorithmic random if its complexity is positive. Following theorem is of essential significance in this case:

Theorem 4. [20] *The trajectories of almost all state points $\mathbf{x} \in \mathcal{S}$ are algorithmic random and their complexity is equal to h_{KS} .*

The way a chaotic system can be used as a pseudo-random number generator is obvious: find a chaotic system with positive KS entropy and let β be a binary generic partition of its phase space. Amongst the simplest chaotic maps which satisfy the above requirements are logistic map $x_{n+1} = rx_n(1 - x_n)$ with fully developed chaos $r = 4$, and its homeomorphically conjugate maps such as Bernoulli shift, tent map etc. Following binary generating partition $\beta = \{\beta_1, \beta_2\}$, where $\beta_1 = [0, \frac{1}{2})$ and $\beta_2 = [\frac{1}{2}, 1)$ produces a bit $z_n = 0$ if $x_n \in \beta_1$, otherwise $z_n = 1$. Then $\{z_n : n \geq 1\}$ are pseudo-random bits generated from the seed x_0 . However, one can not implement this pseudo-random generator on a finite-state machine (computer).

6 Shadowing

For chaotic processes neighboring trajectories diverge exponentially from each other. While a noisy trajectory diverges rapidly from the true trajectory with the same initial conditions, there might exist a different true trajectory with slightly different initial conditions which stays near the noisy trajectory for a long time. In [21] the authors devised a rigorous procedure to prove whether there exists a true trajectory which stays near or shadows the noisy trajectory for a long time. When this is the case, the noisy trajectory is an excellent approximation of the true dynamics of the actual chaotic process.

Definition 13. $\{p_n\}_0^N$ is a δ -pseudo-trajectory for f if $|p_{n+1} - f(p_n)| < \delta$ for all $n = 0, 1, \dots, N$.

Definition 14. A true trajectory $\{x_n\}_0^N$ satisfies $x_{n+1} = f(x_n)$.

Definition 15. The true trajectory x_n ε -shadows p_n on $0 \leq n \leq N$ if $|x_n - p_n| < \varepsilon$ for $n = 0, 1, \dots, N$.

A true orbit stays near the pseudo-orbit is said to *shadow* the pseudo-orbit. Anosov and Bowen proved shadowing results for hyperbolic maps on a differential manifold. The conclusion of Anosov [22] for a hyperbolic map says that, given any prescribed shadowing distance ε (between the pseudo-orbit and the true orbit) there exists a δ so that any δ -pseudo-orbit can be

ε -shadowed by a true orbit. Bowen [23] showed that the same result holds if the map is required only to be hyperbolic on a basic set containing the orbit.

Let $f : R^m \rightarrow R^m$ be a C^2 -diffeomorphism. A compact set Λ is called hyperbolic if there is a continuous splitting of the tangent space $T_x R^m = E_x^s \oplus E_x^u$, for $x \in \Lambda$, and positive constants $\lambda < 1$, $C > 0$ such that

1. $Df(x)(E_x^s) = E_{f(x)}^s$,
2. $Df(x)(E_x^u) = E_{f(x)}^u$,
3. $\|Df^n(x)(v)\| \leq C\lambda^{-n}|v|$, for $v \in E_x^s$,
4. $\|Df^{-n}(x)(v)\| \leq C\lambda^{-n}|v|$, for $v \in E_x^u$,

for all $x \in \Lambda$ and for all $n \geq 0$.

Theorem 5. *Assume Λ is a hyperbolic set for f . For every $\varepsilon > 0$ there is a $\delta > 0$ so that every δ -pseudo-orbit in Λ can be ε -shadowed.*

There are two factors that make use of the above theorem impractical [21]. First, the δ that is produced can be orders of magnitude smaller than the machine epsilon of existing digital computers. Second, most interesting dynamical systems currently being studied are not hyperbolic. The approach of Anosov and Bowen was generalized in [21].

Theorem 6. —— *For typical systems under certain conditions and given δ there is a true orbit for which the pseudo orbit is within a distance $\varepsilon \approx \delta^{0.5}$ of the true orbit for $N \approx \delta^{-0.5}$.*

Theorem 6 does not assume that the system is hyperbolic. In [21] several examples of shadowed dynamical systems were presented. For Hénon map, a computer-generated δ -pseudo-orbit with initial condition $(0, 0)$ and $\delta = 10^{-14}$ was found to have a true orbit within 10^{-7} for over one million iterates.

The way a shadowed chaotic system can be used as a pseudo-random number generator is obvious: find a chaotic system with positive KS entropy and shadow this map with smallest possible δ . Since, for chaotic systems, the trajectories of almost all initial conditions are algorithmic random and their complexity is equal to KS entropy, we expect that for $N \approx \delta^{-0.5}$ iterates, the complexity of the pseudo orbit is large enough (proportional to $\log N$, so that the pseudo orbit is random and unpredictable. The way how this generator can be implemented in the digital computer is presented in the next section.

7 Chaos-Based Pseudo-Random Number Generators

Let $f : \mathcal{X} \rightarrow \mathcal{X}$ be a chaotic map. For simplicity let us assume that $\mathcal{X} = I = [0, 1]$. It is convenient to consider the set of *one-way infinite* sequences \mathcal{B}^∞ . If ω is an element of \mathcal{B}^∞ , then $\omega = \omega_1\omega_2\dots$ and $\omega_{1:n} = \omega_1\omega_2\dots\omega_n$. Let

$\mathcal{B} = \{0, 1\}$. It is well known that if r is a real number from the unit interval $[0, 1]$, then there exists a sequence $\omega_1 \omega_2 \dots$ of elements $\omega_n \in \{0, 1\}$ such that

$$r = \sum_n \frac{\omega_n}{2^n},$$

and this sequence is unique except when r is of the form $q/2^n$, in which case there exist exactly two such sequences, one of which has infinitely many 0's. This sequence is called binary expansion of r . In the following we identify a real number r with its binary expansion (if there are two binary expansions, then we identify r with the expansion with infinitely many 0's).

Let x be a number from the unit interval. Assume that x is an initial position of a chaotic map shadowed with n -bit precision. Then, there is a true orbit for which the pseudo orbit is within a distance $2^{-n/2} \approx 10^{-n/6.64}$ of the true orbit for $2^{n/2}$ iterates.

Let $x = 0.a_1 \dots a_n \dots$ be the binary expansion of $x \in I = [0, 1]$. We define a set,

$$I^{(n)} = \{x | x = (0.a_1 \dots a_n)\},$$

as a set of truncated real numbers in I . Let $\text{trun}_n : I \rightarrow I^{(n)}$ and $H : I^{(n)} \rightarrow \{0, 1\}$ be two functions defined as follows:

$$\text{trun}_n(x) = (0.a_1 \dots a_n),$$

and

$$H_j(x) = a_{j-7} \oplus a_{j-6} \oplus \dots \oplus a_j,$$

where $j = 8, \dots, n$.

The seed of the generator is the string of 0s and 1s of length n , which we write in the form $x_0 = 0.a_1 \dots a_n$. The output of the generator is a sequence of bits X_1, X_2, \dots produced as follows:

$$x_{i+1} = \text{trun}_n[f(x_i)],$$

$$X_{i+1} = H_j(x_{i+1}).$$

By defining n , j , and the chaotic function f a particular pseudo-random number generator can be constructed. We now present two examples.

Example 4. For this example, we use the well-known logistic map:

$$x_{i+1} = \text{trun}_n[4x_i(1 - x_i)],$$

$$X_{i+1} = H_j(x_{i+1}),$$

which, as we know from previous sections, using the binary generating partition $\beta = \{\beta_1, \beta_2\}$, where $\beta_1 = [0, \frac{1}{2})$ and $\beta_2 = [\frac{1}{2}, 1)$, produces truly random bits.

Table 1. Logistic map as a PRNG: dependance on n

| | $n = 64$ $j = 64$ | $n = 96$ $j = 96$ | $n = 128$ $j = 128$ |
|------------------------------------|----------------------|----------------------|------------------------|
| Birthday Spacings | pass | pass | pass |
| Overlapping 5-permutation | FAIL | pass | pass |
| Binary rank for 31x31 matrices | FAIL | pass | pass |
| Binary rank for 32x32 matrices | FAIL | pass | pass |
| Binary rank for 6x8 matrices | pass | pass | pass |
| Bitstream | FAIL | pass | pass |
| OPSO | FAIL | pass | pass |
| OQSO | FAIL | pass | pass |
| DNA | FAIL | pass | pass |
| Count-the-1's on a stream of bytes | FAIL | pass | pass |
| Count-the-1's for specific bytes | pass | pass | pass |
| Parking lot | pass | pass | pass |
| Minimum distance | FAIL | pass | pass |
| 3DSpheres | pass | pass | pass |
| Squeeze | FAIL | pass | pass |
| Overlapping sums | pass | pass | pass |
| Runs | pass | pass | pass |
| Craps | FAIL | pass | pass |

What is the effect on randomness when one implements this generator on the finite machine? To answer this question, we use statistical tests. Statistical tests can not prove that a sequence is random, tests can only show that a sequence is not random. In other words, tests help only to detect certain kinds of weaknesses a generator may have. If a sequence passes a finite number of statistical tests, there is no guarantee that the sequence was indeed generated by a (truly) random number generator. Five standard tests, commonly used for determining whether a binary sequence possesses some properties that a truly random sequence would be likely to exhibit, are [1]: frequency test, serial test, poker test, runs test and autocorrelation test. Linear congruential generators pass standard tests. Additional package of tests, called DIEHARD, was proposed in [24], for which standard random number generators (congruential, shift-register and lagged-Fibonacci generators) give poor results. We have performed all these tests to the generator based on the logistic map and the results are summarized in the following tables.

Table 1 shows that using 64-bit arithmetic, logistic-map-based PRNG gives pure results, and the sequences of bits which are produced by this generator are, in fact, not random. Pseudo-random bit generator based on logistic map with $n = 96$ and $j = 96$ passes all statistical tests from DIEHARD. The theory outlined in Section 5, implies that the first bit of the logistic map is random. However, implementation of this map on a finite machine even with 64-bit precision, destroys the randomness of the bits, not only the first, but

even the last (64th bit) is still not random. Using 96-bit precision gives better results; main message from the Table 2 is: *for pseudo-random bit generators based on chaotic maps do not use significant bits*. Similar results were obtain for other maps with fully developed chaos (for example: $x_{n+1} = 3x_n \bmod 1$). Increasing the machine precision (we have tried with 1000-bit precision arithmetic) does not help: XOR of the first 8 bits is always not random.

Example 5. For this example, we use the following shift map:

$$x_{i+1} = \text{trun}_n[1.25x_i \bmod 1],$$

$$X_{i+1} = H_j(x_{i+1}),$$

and again perform similar statistical tests as in the previous example. Thus, for example, with 96-bit arithmetic 16th bit is still not random, although the generator with $n = j = 64$ passes all statistical tests from DIEHARD. Note that this generator can be efficiently implement in software: 1.25 can be written as $1 + 1/4$, and therefore, multiplication by 1.25 can be implement with two binary operations: addition and shift to the right for 2 bits.

Table 2. Logistic map as a PRNG: dependance on j

| | $n = 96$ $j = 8$ | $n = 96$ $j = 16$ | $n = 96$ $j = 24$ |
|------------------------------------|---------------------|----------------------|----------------------|
| Birthday Spacings | pass | pass | pass |
| Overlapping 5-permutation | FAIL | FAIL | pass |
| Binary rank for 31x31 matrices | pass | pass | pass |
| Binary rank for 32x32 matrices | pass | pass | pass |
| Binary rank for 6x8 matrices | FAIL | FAIL | pass |
| Bitstream | FAIL | FAIL | pass |
| OPSO | FAIL | FAIL | pass |
| OQSO | FAIL | FAIL | pass |
| DNA | FAIL | FAIL | pass |
| Count-the-1's on a stream of bytes | FAIL | FAIL | pass |
| Count-the-1's for specific bytes | FAIL | FAIL | pass |
| Parking lot | FAIL | pass | pass |
| Minimum distance | pass | pass | pass |
| 3DSpheres | pass | pass | pass |
| Squeeze | FAIL | pass | pass |
| Overlapping sums | pass | pass | pass |
| Runs | pass | pass | pass |
| Craps | FAIL | pass | pass |

8 Conclusions

Pseudo-random ensembles are unpredictable by probabilistic polynomial-time machines associated with feasible computations, but may be predictable by infinite powerful machines. On the other hand, theorem 4 asserts that chaotic systems are unpredictable by infinite powerful machines, but does not say anything about their predictability when they are implemented on finite-state machines. Therefore, finite-state implementation of chaotic systems may or may not be predictable by probabilistic polynomial-time machines. *Whether and under what conditions finite-state version of a chaotic system is unpredictable by probabilistic polynomial-time machines is a central problem of chaos-based cryptography.* The future impact of chaos-based cryptography may have on conventional cryptography depends strongly on the successful solution of this problem.

In this chapter, we have shown using statistical tests that the most significant bit of the finite-state implementation of a chaotic system, even with high precision implementation, is not random. This is true not only for general chaotic systems, but also for systems with fully developed chaos, which are equivalent (when defined on real numbers) to random processes. However, the least significant bit is random (in the sense that it passes statistical tests from DIEHARD), and therefore, one can use such chaotic systems as pseudo-random bit generators.

Acknowledgment.

This work was supported in part by the ARO (grant DAAG55-98-1-0269, MURI Project “Digital Communication Devices based on Nonlinear Dynamics and Chaos”) and by the STMicroelectronics.

References

1. Menezes, A., Oorschot, van P., Vanstone, S. (1997) *Handbook of Applied Cryptography*. Boca Raton, FL: CRC Press
2. Matthews, R. A. J (1989) On the derivation of a ‘chaotic’ encryption algorithm. *Cryptologia*, **13**:29–42; Wheeler, D. D. (1989) Problems with chaotic cryptosystems. *Cryptologia*, **13**:243–250; Wheeler, D. D., Matthews, R. A. J. (1991) Supercomputer investigations of a chaotic encryption algorithm. *Cryptologia*, **15**:140–152
3. Kohda, T., Tsuneda, A. (1997) Statistics of chaotic binary sequences. *IEEE Trans. Infor. Theory*, **43**:104–112
4. Goldreich, O. (1998) *Modern Cryptography, Probabilistic Proofs and Pseudo-randomness*. New York: Springer-Verlag
5. Stojanovski, T., Kocarev, L. (2001) Chaos based random number generators Part I: Analysis. *IEEE Trans. Circ. Syst.-I*, **43**(3):281–288; Stojanovski, T., Pihl, J., Kocarev, L. (2001) Chaos based random number generators, Part II: Practical realization. *IEEE Trans. Circ. Syst.-I*, **43**(3):382–385

6. Yao, A. (1982) Theory and applications of trapdoor functions. In Proc. of IEEE 23rd Symposium on Foundations of Computer Science, 80–91
7. Blum, M., Micali, S. (1982) How to generate cryptographically strong sequences of pseudorandom bits. In Proc. of IEEE 23rd Symposium on Foundations of Computer Science, 112–117
8. Knuth, D. E. (1981) The Art of Computer Programming - Seminumerical Algorithms. vol. 2. Reading, MA: Addison-Wesley
9. Plumstead, J. B. (1982) Inferring a sequence generated by a linear congruence. In Proc. of IEEE 23rd Symposium on Foundations of Computer Science, 153–159
10. Boyar, J. (1989) Inferring sequences produced by pseudo-random number generators. J. Association of Computing Machinery, **36**:129–142
11. Krawczyk, H. (1992) How to predict congruential generators. J. Algorithms, **13**:527–545
12. Frieze, A. M., Hastad, J., Kannan, R., Lagarias, J. C., Shamir, S. (1988) Reconstructing truncated integer variables satisfying linear congruences. SIAM J. Computing, **17**:262–280
13. Stern, J. (1987) Secret linear congruential generators are not cryptographically secure. In Proc. of IEEE 28th Symposium on Foundations of Computer Science, 421–426
14. Boyar, J. (1989) Inferring sequences produced by a linear congruential generator missing low-order bits. J. Cryptology, **1**:177–184
15. Boppana, J., Hirschfeld, R. (1989) Pseudorandom generators and complexity classes. In Randomness and Complexity, ed. by Micali, S. Advances in Computing Research, vol. 5. Connecticut: JAI Press
16. Alexi, W., Chor, B., Goldreich, O., Schnorr, C. P. (1987) RSA/Rabin bits are $\frac{1}{2} + \frac{1}{\text{poly}(\log n)}$ secure. In Proc. of IEEE 25th Symposium on Foundations of Computer Science, 449–457
17. Blum, L., Blum, M., Shub, M. (1986) A simple unpredictable pseudo-random number generator. SIAM J. Computing, **15**:364–383
18. Eckmann, J. P., Ruelle, D. (1985) Ergodic theory of chaos and strange attractors. Rev. Modern Physics, **57**:617–656
19. Alekseev, V. M., Yakobson, M. V. (1981) Symbolic dynamics and hyperbolic dynamic systems. Phys. Rep., **75**:287–325
20. Brudno, A. A. (1976) The complexity of the trajectories of a dynamical system. Russian Math. Surveys, **33**:197–198
21. Sauer, T., Yorke, J. (1991) Rigorous verification of trajectories for the computer simulation of dynamical systems. Nonlinearity, **4**:961–979
22. Anosov, D. V. (1967) Geodesic flows and closed Riemannian manifolds with negative curvature. Proc. Steklov Inst. Math, **90**
23. Bowen, R. (1975) ω -limit set for Axiom A diffeomorphisms. J. Diff. Eq., **18**:333–339
24. <http://stat.fsu.edu/~geo/diehard.html>

Applying Ergodic Theory to Improve the Noise Performance of Differential Chaos Shift Keying

Henry Leung and Haiyang Yu

Dept of Electrical and Computer Engineering
University of Calgary
Calgary AB T2N 1N4, Canada
leungh@enel.ucalgary.ca

Abstract. This chapter provides an overview of the state of the art of current chaos communication schemes and introduces the use of signal processing to improve the communication performances. Popular communication schemes in the literature, including chaotic spreading sequence (CSS), chaotic carrier (CC), chaos masking (CM), chaos shift keying (CSK), differential chaos shift keying (DCSK) and chaotic parameter modulation (CPM), are discussed here and they are classified into three main categories according to the way how chaos is applied, that is, the use of chaotic signal, basis function and chaotic parameters. Their architecture and operations are addressed. Compared to the conventional digital communication systems, all these schemes are found to have inferior noise performance. We propose here by exploiting the ergodic property of chaotic signals, the noise performance of chaos communication can be enhanced. Using the most popular DCSK for demonstration, it is shown here that the ergodic DCSK (E-DCSK) has an improved noise performance. The theoretical noise performance, bit error rate (BER), of the proposed E-DCSK is derived, and is compared to those of other chaos communication schemes. The performance of E-DCSK in different noise channels is also investigated.

1 Introduction

In a conventional spread spectrum (SS) digital communication system, the spreading signals used to transmit digital information are distinguished by their wideband, flat spectrum, and pseudo-randomness. The expanding bandwidth of the signal could overcome the severe levels of interference and its pseudo-randomness could make the signal less detectable [1,2]. These advantages make SS become widely used in many communication fields [3].

Recently, chaos has been applied to communications. Chaos communication has drawn a great deal of interest because it has a similar wideband nature as a SS system. A chaotic system is a nonlinear deterministic dynamical system whose states change with time in a deterministic way [4,5]. For a discrete time chaotic system, the state equation can be expressed as:

$$x(t) = f(\mathbf{X}(t-1), \theta), \quad (1)$$

where $\mathbf{X}(t-1) = [x(t-1), x(t-2), \dots, x(t-d)]^T$ is the d -dimensional state vector at time $t-1$, f is the nonlinear state function, and θ is the bifurcating parameter lying in the chaotic regime $[\theta_{min}, \theta_{max}]$. Application of chaos to communications has been found to offer many advantages to the conventional SS system including security, hardware implementation, synchronization and potential for performance enhancement [6].

In general, a chaos communication system can be structured as shown in Fig. 1. The chaos modulation takes the functionality of modulating the information signal with the chaos system and spreading the narrowband information signal to a relatively wide bandwidth for transmission. At the receiver, a demodulator is used to retrieve the information signal from the received signal. Note that the received signal is wideband transmitted signal, and the despreading process is carried out in the demodulation process.

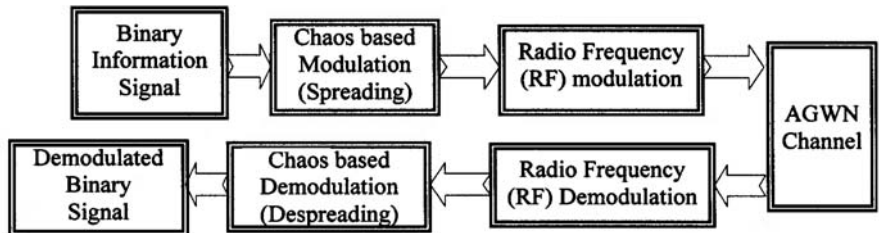


Fig. 1. A basic block diagram of the chaos based spread spectrum communication system

Various chaos communication schemes have been proposed in the literature [7-37]. These approaches exploit different characteristics of a chaotic system to achieve wideband communication. Based on the different ways of modulating the digital information, we classify the major chaos communication schemes in the literature into three major categories as shown in Table 1. From (1), there are three intuitive variables: the chaotic state $x(t)$, the nonlinear map f , and the bifurcating parameter θ . These three variables can be used to classify the different chaos communication schemes. For the first category, digital information is modulated by using the chaotic signal waveform $x(t)$. It means that the chaotic signal generated by a chaos system is used as a modulation carrier directly. $x(t)$ can be used directly to mask the information signal or used to generate binary spreading codes for direct sequence SS (DSSS). Chaos communication schemes including chaotic spread sequence (CSS) [10-12], chaotic carrier (CC) [13,14], and chaotic masking (CM) [15,16] all belong to this category. Second, the digital information is modulated into the chaotic system by using the chaotic map f . For instance, in a chaos shift keying (CSK) system, different chaotic maps are used to represent different digital states. Demodulating the digital information is then

equivalent to determining which chaotic map is used to generate the transmitted chaotic signal [17-19]. The most popular frequency-modulated differential chaos shift keying (FM-DCSK) [20-22] is also categorized into this group even though FM-DCSK only applies one chaotic map. For the last category, digital information is modulated by emerging it into the chaotic parameter θ . By controlling the parameter θ in an appropriate chaotic regime, the output of the chaotic system is therefore wideband for transmission. At the receiver, demodulation is basically a parameter estimation process, and this scheme is called chaotic parameter modulation (CPM) [23,24].

Table 1. Categorization of chaos communication schemes

| | Category I: Chaotic states $x(t)$ | Category II: Chaotic map f | Category III: Bifurcating parameter θ |
|---------------------|--|---|--|
| Modulation method | Modulating with the chaotic signal | Controlling the state function | Controlling the parameter |
| Demodulation method | Retrieve the digital information out from the chaotic signal | Determination of the state function used for the transmitted chaotic signal | Tracking the parameter used for the transmitted chaotic signal |
| Schemes | CSS, CC, CM | CSK, FM-DCSK | CPM |

Although chaos communication offers many potential benefits to the conventional digital SS system, to the best of our knowledge, it has not been used in any real communication system. The main reason is that most of these schemes suffer from poor performance in noisy environments. Various techniques have been proposed to improve the noise performances of chaos communications, but their noise performance are still much worse than the conventional communication system. In this chapter, we propose applying the ergodic theory of dynamic systems to handle this problem. Based on a recent discovery that the mean values of many chaotic maps have a monotone relationship with their system parameters, the channel noise can be effectively removed from the received signal for demodulation in a chaos communication system.

In this chapter, we first give a brief overview of the popular chaos communication schemes according to the above categorization. The idea of applying ergodic theory to chaos communication to improve the performance in noise is then given. In general, the ergodic concept can be applied to different chaos communication schemes. In this chapter, we use the most popular scheme, DCSK, for illustration. We call this proposed method Ergodic Differential

Chaos Shift Keying (E-DCSK). To have a good understanding of this new scheme, we derive the theoretical BER performance of E-DCSK and perform a comprehensive comparison with other chaos communication schemes. The capacity for high data rate transmission is also investigated.

This chapter is organized as follows. Section 2 gives a brief overview of various chaos communication schemes listed in Table 1. Section 3 introduces an ergodic property of chaos systems that can be applied to the demodulation process of DCSK. The operation of this E-DCSK scheme is analyzed and its theoretical BER performance is derived. A comparative evaluation among several chaos communication schemes is presented in Section 4 based on their theoretical BER performances and computer simulations. Concluding remarks are given in Section 5.

2 Overview of Chaos Based Spread Spectrum Digital Communication Systems

In this section, various chaos communication systems are briefly overviewed. The readers are referred to the references for the details of these methods. The following symbols are used in our presentation. $x(t)$ denotes the chaotic signal generated from a chaos system with the nonlinear mapping f as shown in (1); θ denotes the system parameter; $x'(t)$ represents the modulated signal; $n(t)$ denotes the channel noise; $d(n)$ represents the binary information data; T_b is the bit duration and $m(n)$ denotes the sampled output of a demodulator

2.1 Category I: Modulation based on the chaotic signals

- Chaotic spreading sequences

In a direct sequence SS (DSSS) communication system, binary pseudo-random (PN) sequences with good auto-correlation and cross-correlation properties, such as Gold sequences and Kasami sequences are used as spreading codes to spread the message signal via a wide bandwidth for transmission [1]. The noise-like behavior of a PN sequence stimulates the use of chaotic signal as spreading sequences [26,27]. Given a chaotic system as shown in (1), a symbolic chaotic sequence $b(k)$ can be generated from the chaotic signal $x(t)$ by some transformation such as:

$$b(k) = g(x(t) - E[x(t)])_{t=kT_c}, \quad (2)$$

where $g(x)=1$ for $x \geq 0$ and $g(x) = 0$ for $x < 0$, $E[x(t)]$ is the expectation of $x(t)$, and T_c is the discrete sampling duration of $x(t)$. In a DSSS system, T_c can be viewed as the chip duration. At the receiver side, an identical synchronized chaos system is employed to generate the chaotic spreading signal. A coherent correlator is usually employed to demodulate the transmitted signal.

This chaotic communication approach is basically the same as the conventional DSSS system except that the spreading code is generated by a chaotic system. The difference in the performance of the CSS scheme therefore mainly comes from the difference in the correlation of the spreading code. The block diagram of CSS system is shown in Fig. 2. As we can see, the structure of the CSS is very similar to that of conventional DSSS system.

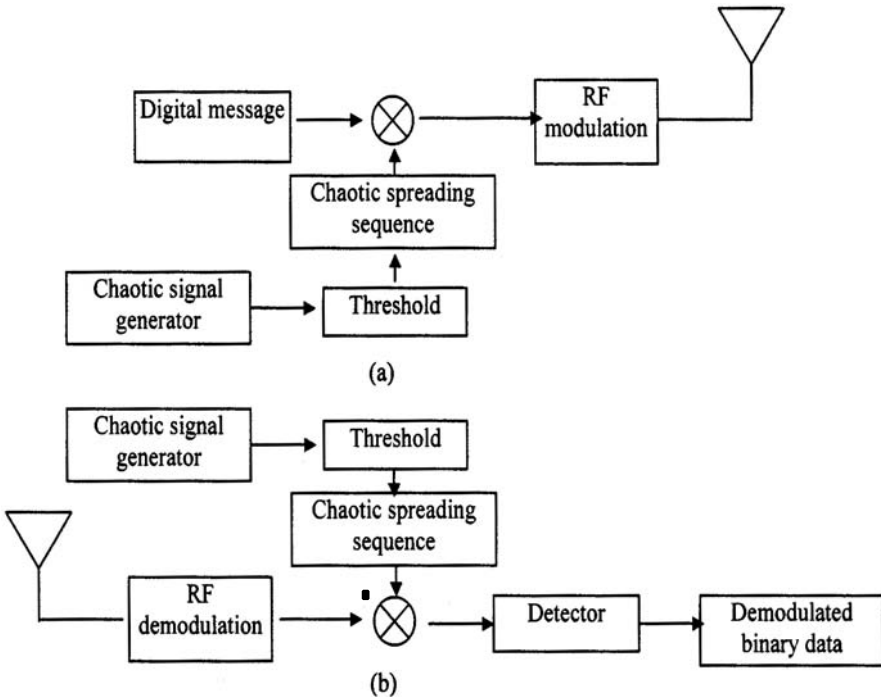


Fig. 2. Block diagram of chaotic spreading sequence (CSS) system. (a) Transmitter; (b) Receiver

• Chaotic carrier

Chaotic carrier (CC) is another direct application of chaotic signals to SS communications by using a chaotic signal as the carrier directly [13, 14]. The suggested chaotic carrier $x'(t)$ is given by [13]

$$x'(t) = \sum_{i=1}^N x_i(t) \cos(\omega_c t + \phi_i) \quad N \in [1, \infty), \quad (3)$$

where ω_c is the central frequency of the transmission carrier, ϕ_i is a random variable uniformly distributed on $(-\pi, \pi]$. The chaotic carrier can be a chaotic

signal generated from only one chaotic system ($N = 1$), or the combination of signals generated from multiple chaotic systems ($N > 1$). According to (3), the chaotic carrier can be generated unlimited and non-periodically.

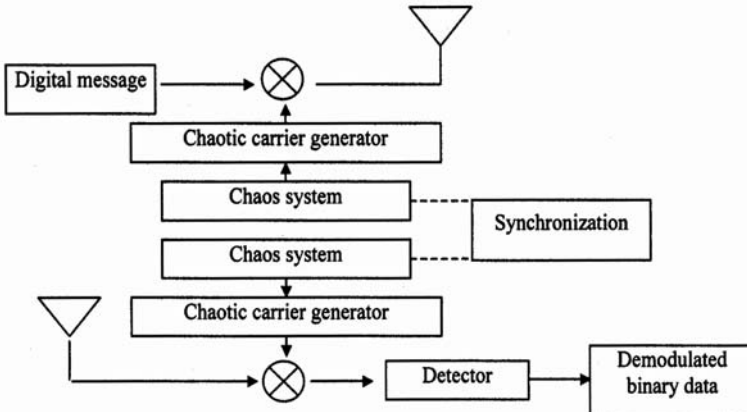


Fig. 3. Block diagram of chaotic carrier (CC) system

A simple system block diagram of CC is shown in Fig. 3. The system structure is similar to that of CSS and DSSS. However, for CC modulation, the digital message is modulated by an analog chaotic carrier rather than a binary sequence as in the CSS. Because a chaotic signal has an auto-correlation close to a delta function, at the receiver side, the transmitted binary information of this CC scheme can be easily retrieved by applying a correlator and a threshold detector.

• Chaotic masking

Chaotic masking (CM) is originally proposed for transmitting analog signals. The analog information is masked by a wide-band chaotic signal for transmission [15,16]. Based on the capability of chaotic synchronization [18, 19, 28], the chaotically masked signal is used at the receiving end to drive the chaotic synchronization system. By subtracting the reconstructed chaotic signal $x_\gamma(t)$ from the received signal, the transmitted information signal can then be determined. Such an operation of CM modulation and demodulation is shown in Fig. 4.

Practically, the CM scheme can be applied to both analog and digital communications. If a digital signal $d(n)$ is being transmitted, then it will be masked by a chaotic signal directly, that is,

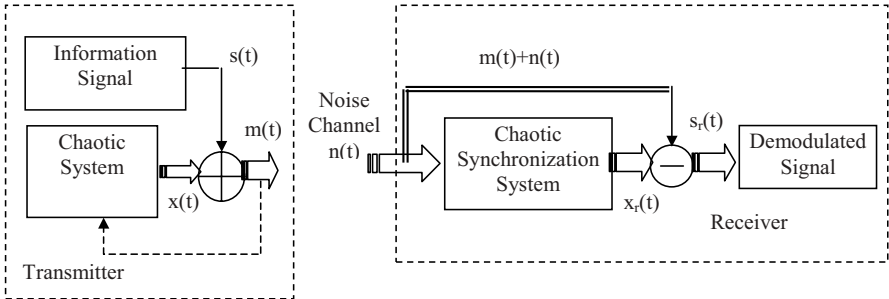


Fig. 4. Block diagram of chaotic masking (CM) system

$$x'(t) = \begin{cases} x(t) + A, & \text{if } d(n) = 1 \\ x(t) - A, & \text{if } d(n) = 0, \end{cases} \quad (4)$$

where A is a positive constant indicating the message information level. The demodulation process is therefore required to remove the channel noise as well as the masking chaotic signal. A widely used demodulator for a digital CM scheme is given by:

$$\begin{aligned} m(n) &= \frac{1}{T_b} \int_0^{T_b} [x'(t) + n(t) - x_r(t)] dt \\ &= \frac{1}{T_b} \int_0^{T_b} [x(t) \pm A + n(t) - x_r(t)] dt. \end{aligned} \quad (5)$$

When chaotic synchronization is performed, the reconstructed chaotic signal $x_r(t)$ is theoretically identical to the transmitted chaotic signal, $x_r(t) \approx x(t)$. Thus the masked chaotic signal can be removed. Noted that $\frac{1}{T_b} \int_0^{T_b} n(t) dt \approx 0$ if $n(t)$ is AWGN process. A decision can be made by setting a zero threshold level as shown below:

$$\hat{d}(t) = \begin{cases} 1 & m(n) \geq 0 \\ 0 & m(n) < 0. \end{cases} \quad (6)$$

2.2 Category II: Modulation based on chaotic state functions

- **Chaos shift keying**

Chaos shift keying (CSK) uses the state equations of chaotic systems to represent the different information symbols for transmission [8,17,18]. For binary communications, the symbols “0” and “1” are assigned to different chaotic maps f_i , $i = 0, 1$ by the following rules:

$$x'(t) = \begin{cases} x_0(t) & \text{for } d(n) = 0 \text{ where } x_0(t) = x(t), x(t) = f_0(x(t-1)) \\ x_1(t) & \text{for } d(n) = 1 \text{ where } x_1(t) = x(t), x(t) = f_1(x(t-1)). \end{cases} \quad (7)$$

The demodulator is therefore to decide, on the basis of a noisy received signal, which map is more likely to have been used in producing the received waveform. One method to demodulate the information is the non-coherent CSK (NCSK). It uses the transmitted chaotic signal itself as the reference signal to perform correlation. The output of the demodulator is given by:

$$\begin{aligned} m(n) &= \int_{T_b} (x'(t) + n(t))(x'(t) + n(t))dt \\ &= \int_{T_b} x'(t)^2 dt + 2 \int_{T_b} x'(t)n(t)dt + \int_{T_b} n(t)^2 dt. \end{aligned} \quad (8)$$

Final decision is based on the property that the bit energies of chaotic signals from different chaotic maps are different, i.e. $\int_{T_b} x_0(t)^2 dt \neq \int_{T_b} x_1(t)^2 dt$. By applying a threshold to the detector, the transmitted binary data can then be determined by:

$$\hat{d}(t) = \begin{cases} 0 & m(n) \leq \text{Threshold} \\ 1 & m(n) \geq \text{Threshold}, \end{cases} \quad (9)$$

where the threshold can be set as $\frac{1}{2}[\int_{T_b} x_0(t)^2 dt + \int_{T_b} x_1(t)^2 dt]$ by assuming $\int_{T_b} x_0(t)^2 dt \leq \int_{T_b} x_1(t)^2 dt$.

However, this method may not be practical since the bit energies of the chaotic signal varies from time to time and may not be stable enough for a satisfactory performance. Another popular demodulation method is the coherent CSK (CCSK). It uses chaotic synchronization to reproduce the reference signal used for correlation, more precisely, two chaotic synchronization systems are installed at the receiver corresponding to the two chaotic maps f_i , $i = 0, 1$ used in the transmitter. The received signal is used as a driving signal to both synchronization systems. The reconstructed signals from both synchronization systems are then correlated with the received signal. That is,

$$\begin{cases} m_0(n) = \int_{T_b} (x'(t) + n(t))x_{r0}(t)dt \\ \quad = \int_{T_b} x'(t)x_{r0}(t)dt + \int_{T_b} x_{r0}(t)n(t)dt \\ m_1(n) = \int_{T_b} (x'(t) + n(t))x_{r1}(t)dt \\ \quad = \int_{T_b} x'(t)x_{r1}(t)dt + \int_{T_b} x_{r1}(t)n(t)dt, \end{cases} \quad (10)$$

where $x_{ri}(t)$ is the reconstructed signal of the chaotic map f_i for $i = 1, 0$. Ideally, the two chaotic signals x_{r0} and x_{r1} are completely orthogonal. Assuming that the chaotic synchronization can reproduce the exactly identical transmitted signal. Comparing the outputs of the two correlators, the larger one is selected and it is used to determine which binary symbol is transmitted. That is,

$$\hat{d}(t) = \begin{cases} 0 & m_0 > m_1 \\ 1 & m_1 \geq m_0. \end{cases} \quad (11)$$

Noted that only the correct synchronization can generate an identical signal to the transmitted chaotic signal. The signal generated from the other unmatched synchronization will be uncorrelated with the transmitted chaotic signal. Figure 5 gives a general system structure of the CSK, including the modulator, the NCSK and the coherent demodulator.

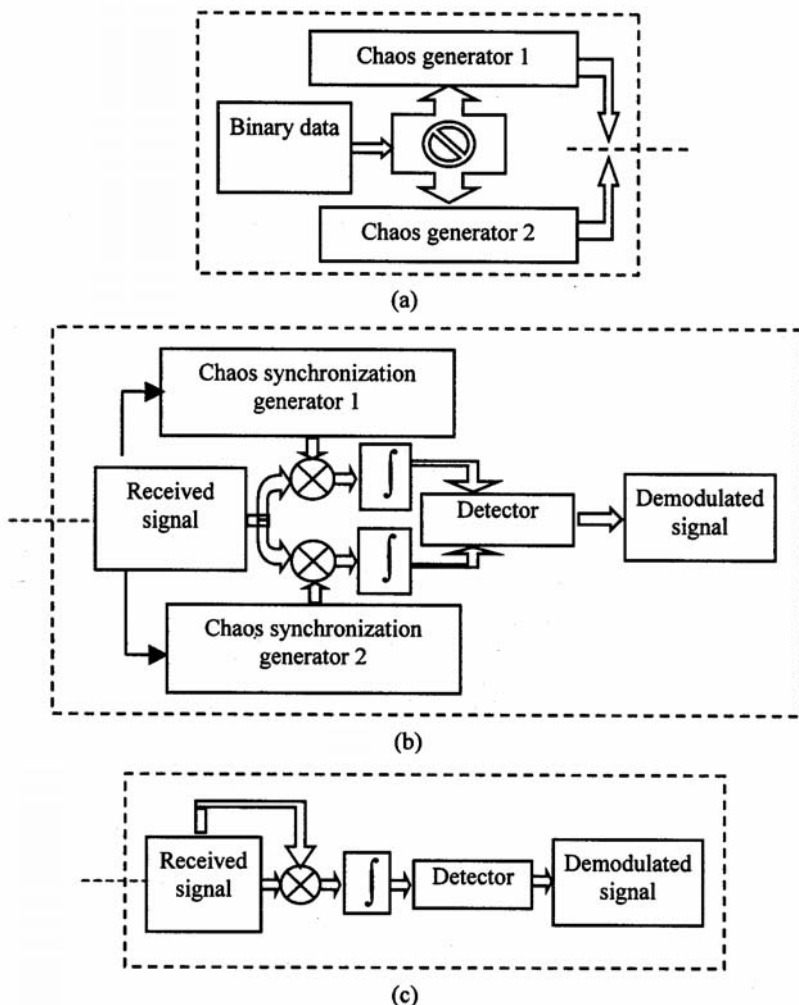


Fig. 5. General system structure of chaotic shift keying (CSK) modulation scheme
(a) Modulator of CSK; (b) Coherent demodulator of CSK; (c) Non-coherent de-modulator of CSK

- Frequency-modulated differential chaos shift keying

An improved implementation of DCSK is the popular frequency-modulated differential chaos shift keying (FM-DCSK) technique [20-22]. The basic concept of FM-DCSK is that every binary information bit $d(n)$ is mapped to two chaotic sample functions. While the first function is used as a reference, the second one represents the information to be transmitted as shown in Fig. 6 (a). When the symbol “0” is to be transmitted, the reference signal $x(t)$ generated from the chaotic system is transmitted within the first half bit duration $[0, T_b/2]$. And the chaotic signal $x(t)$ is used for transmission in the second half bit duration $[T_b/2, T_b]$. When the symbol “1” is to be transmitted, $x(t)$ is transmitted in the first half bit duration but its negative waveform is used instead in the second half bit duration. That is,

$$x'(t) = \begin{cases} \begin{cases} x(t), & 0 \leq t < T_b/2 \\ x(t - T_b/2), & T_b/2 \leq t < T_b; \end{cases} & d(n) = 0, \\ \begin{cases} x(t), & 0 \leq t < T_b/2 \\ -x(t - T_b/2), & T_b/2 \leq t < T_b; \end{cases} & d(n) = 1. \end{cases} \quad (12)$$

At the receiver side, a self-synchronized correlator is employed where the received signal within the time period of $[0, T_b/2]$ is multiplied with the signal within time period of $[T_b/2, T_b]$, as shown in Fig. 6(b). The sampled output

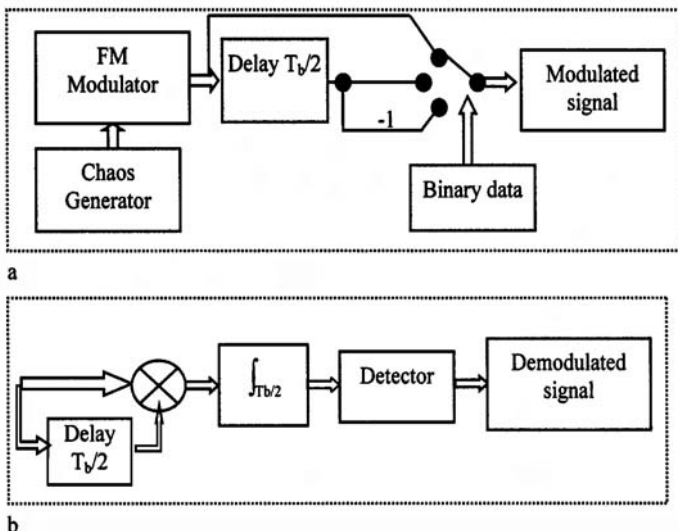


Fig. 6. Block diagram of frequency modulated differential chaos shift keying (FM-DCSK) modulation scheme (a) Modulator; (b) Demodulator

of the correlator can be expressed as:

$$m(n) = \int_{\frac{T_b}{2}} [x'(t) + n(t)] \left[x' \left(t - \frac{T_b}{2} \right) + n \left(t - \frac{T_b}{2} \right) \right] dt. \quad (13)$$

According to the differential modulation rule, a positive correlation between the signals within the first half bit duration and the second half bit duration indicates that a “0” is received. On the other hand, when a negative correlation is found, it means the reception of the data “1”. The decision is made by a simple level comparator, which has a constant, zero threshold level, as shown below:

$$\hat{d}(t) = \begin{cases} 0 & m(n) \geq 0 \\ 1 & m(n) < 0. \end{cases} \quad (14)$$

2.3 Category III: Modulation based on the system parameters

- Chaotic parameter modulation

Chaotic parameter modulation (CPM) modulates the message signal into the parameters of a chaotic system to achieve the goal of wideband transmission [23,24]. The message signal can be in either analog or digital format. For digital communication, CPM is basically a special case of CSK where the two chaotic waveforms are generated by a single map with two different parameters. More precisely, it can be expressed as

$$x'(t) = \begin{cases} x(t) = f[x(t-1), \theta_0], & \text{if } d(n) = 0 \\ x(t) = f[x(t-1), \theta_1], & \text{if } d(n) = 1, \end{cases} \quad (15)$$

where $d(n)$ is the binary data, and θ_0 and θ_1 are different bifurcating parameter values. Demodulation is therefore equivalent to estimation of the bifurcating parameter from the noisy received signal. Assuming that $\hat{\theta}$ is the estimated system parameter, the decision process for the transmitted symbol can be carried out by:

$$\hat{d}(n) = \begin{cases} 0, & \text{if } \hat{\theta} \text{ is closer to } \theta_0 \\ 1, & \text{if } \hat{\theta} \text{ is closer to } \theta_1. \end{cases} \quad (16)$$

One of the most efficient ways to estimate the chaotic parameter from the received signal is achieved by applying adaptive filtering algorithms to track the parameters [24,25]. The basic idea of using an adaptive filter as demodulator in CPM is to minimize some error function such as the mean square error between the estimated and measured states by searching for an optimal system parameter. For example, the least mean square (LMS), recursive least square (RLS), and extended Kalman filter (EKF) have all been investigated for this application. Their tracking and estimation abilities

make them suitable for demodulating the transmitted binary information in a real time communication system. The system block diagram of CPM with an adaptive filtering as demodulator is shown in Fig. 7. Assuming that the modulated signal is corrupted by an AWGN channel, i.e. $r(t) = x'(t) + n(t)$, the adaptive filtering demodulator based on the gradient search method [26,27] can be expressed as

$$\hat{\theta}_k = \hat{\theta}_{k-1} - \mu[r_k - f(r_{k-1}, \hat{\theta}_{k-1})] \frac{df(r, \lambda)}{dr} \Big|_{r=r_{k-1}, \theta=\theta_{k-1}}. \quad (17)$$

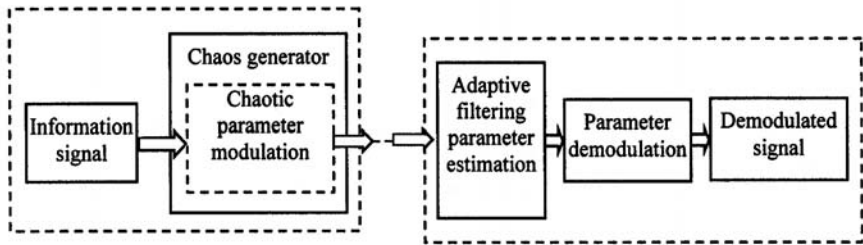


Fig. 7. Block diagram of chaotic parameter modulation (CPM) scheme with adaptive filter as demodulator

3 The Ergodic Differential Chaos Shift Keying Scheme

Ergodic property is an important characteristic of chaos systems [4-6,34]. This property has recently been exploited for chaos communications[30,31]. In this chapter, we propose to improve the noise performance of DCSK by offering an ergodic approach. This novel scheme combines the merits of both DCSK and the efficiency of ergodic theory, and is called: the Ergodic Differential Chaos Shift Keying (E-DCSK).

3.1 An ergodic approach to chaos communication

From the ergodic theory for dynamic system, it is well known that for each $\theta \in [\theta_{min}, \theta_{max}]$, the dynamic system f_θ has a unique invariant ergodic measure μ_θ . According to the Birkhoff ergodic theorem [4], the limit

$$\lim_{N \rightarrow \infty} \frac{1}{N} \sum_{t=1}^N x(t)$$

exists and is equal to the constant $\int x d\mu_\theta(x)$. This limit depends only on the parameter θ and is called the mean value function $M(\theta)$ of the chaotic

map f_θ . It is found recently that for many chaotic maps, their mean value functions are in fact monotone over their parameter range [28]. The parameter values can then be determined based on this one-to-one relationship, and this estimation technique is shown to be very effective even at low signal to noise ratio (SNR) level [28].

Applying this ergodic property to design an efficient demodulator for chaos communications, the demodulation approach is modified to demodulate the transmitted information data according to the mean value of the received chaotic signal. More precisely, assume that $s(t)$ is the message signal, the chaotic modulation method uses a chaos system to modulate $s(t)$ by setting $\theta = g(s(t))$, i.e. a function of $s(t)$. By keeping θ in the chaotic regime, the output signal $x(t)$ is therefore chaotic and hence has a wide bandwidth for transmission. For digital communications, the message signal $s(t)$ takes on only two values within each bit duration, that is, “0” or “1” at $t \in [0, T_b]$. Therefore, in the modulation process, only two parameter values are needed to represent the message. That is,

$$\theta = \begin{cases} \theta_0 & \text{if } s(t) = 0 \\ \theta_1 & \text{if } s(t) = 1. \end{cases} \quad (18)$$

The demodulation process therefore does not require estimation of a wide range of parameters but only two pre-selected values θ_0 and θ_1 . To apply the mean value estimation to demodulation, a necessary condition is that θ_0 and θ_1 should not have the same mean value, that is, $M(\theta_0) \neq M(\theta_1)$. Without loss of generality, we can choose θ_0 and θ_1 such that $M(\theta_0) < M(\theta_1)$, and $\Delta M = |M(\theta_0) - M(\theta_1)|$ is defined as the mean value distance.

The modulated chaotic signal is converted up to the radio frequency (RF), and after the RF demodulation, the received baseband signal can be expressed as $r(t) = x(t) + n(t)$, where $n(t)$ is an AWGN process. The received baseband signal is passed to the demodulator which includes a mean value estimator and a threshold detector. The mean value estimator is used to estimate the mean value of $r(t)$ using the ensemble average. The output is sampled with frequency f_b and $f_b = 1/T_b$. The sampled output of the k_{th} transmitted bit can then be expressed as:

$$\begin{aligned} m_k &= \frac{1}{T_b} \int_{kT_b}^{(k+1)T_b} r(t) dt \\ &= \frac{1}{T_b} \int_{kT_b}^{(k+1)T_b} x(t) dt + \frac{1}{T_b} \int_{kT_b}^{(k+1)T_b} n(t) dt. \end{aligned} \quad (19)$$

Since the expectation of an AWGN process is zero, if $T(b)$ is large enough, we have $\frac{1}{T_b} \int_{kT_b}^{(k+1)T_b} n(t) dt \approx 0$. As described above, the mean value of the chaotic signal is a constant for different parameters, that is $\frac{1}{T_b} \int_{kT_b}^{(k+1)T_b} x(t) dt \approx M(\theta_i)$. The estimator output therefore approaches $M(\theta_i)$, that is $m_k \approx M(\theta_i)$.

Theoretically, since $M(\theta_0) \neq M(\theta_1)$, the information bit can be retrieved by applying a threshold, μ_m , to a binary decision process. That is,

$$\hat{s}(t) = \begin{cases} 1 & \text{if } m_k > \mu_m \\ 0 & \text{if } m_k \leq \mu_m. \end{cases} \quad (20)$$

In this study, we take the threshold μ_m as the midpoint between $M(\theta_0)$ and $M(\theta_1)$, that is, $\mu_m = \frac{M(\theta_0)+M(\theta_1)}{2}$.

3.2 System model of E-DCSK

The ergodic approach described above is now applied to DCSK and its system structure is shown in Fig. 8.

In the presented E-DCSK system, we set the chaos system with the fixed parameter θ_0 , and it generates chaotic signals that have a non-zero mean value $M(\theta_0)$. A good choice for θ_0 is the one that can maximize the mean value within its chaotic regime to increase the signal separability. The modulation

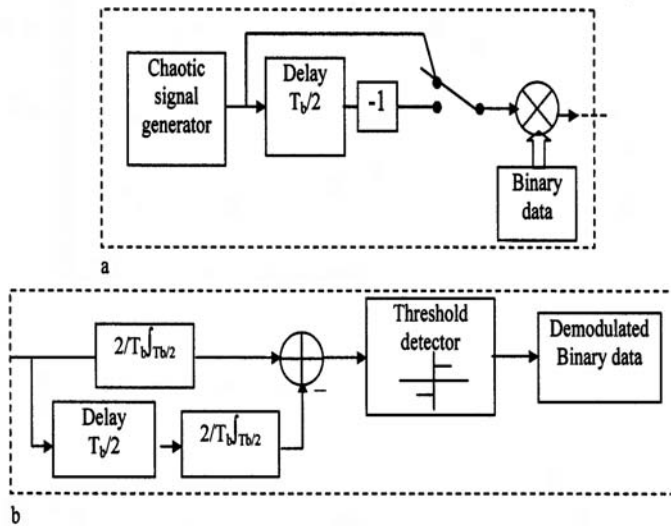


Fig. 8. Block diagram of ergodic differential chaos shift keying (E-DCSK) scheme
(a) E-DCSK modulator; (b) Non-coherent differential demodulator

in the E-DCSK system is basically similar as that of the DCSK as given in (12). Let x_t denotes the signal from the chaos generator and T_b denotes the bit duration. The reference signal provided by the chaos generator is transmitted within the first half bit duration $[0, T_b/2]$, and the same reference signal is repeated but reversed within the second half bit duration $[T_b/2, T_b]$. The chaotic signal used for modulation can be expressed as follows:

$$x'_t = \begin{cases} x_t & 0 \leq t < \frac{T_b}{2} \\ -x_{t-\frac{T_b}{2}} & \frac{T_b}{2} \leq t < T_b, \end{cases} \quad (21)$$

where x'_t is the chaotic signal waveform used for modulation. It is then modulated with the binary digital signal as shown below:

$$s_t = x'_t \text{data}(n) = \begin{cases} \begin{cases} x_t, & 0 \leq t < T_b/2 \\ -x_{t-T_b/2}, & T_b/2 \leq t < T_b; \end{cases} & \text{data}(n) = 1, \\ \begin{cases} -x_t, & 0 \leq t < T_b/2 \\ x_{t-T_b/2}, & T_b/2 \leq t < T_b; \end{cases} & \text{data}(n) = 0. \end{cases} \quad (22)$$

Without losing the generality, the symbol “0” is converted to “-1” in the application for multiplication. At the receiver, a self-synchronized differential mean value estimator is employed, where the estimated mean value of the chaotic signal within the time period of $[0, T_b/2]$ is added with the negative estimated mean value of the chaotic signal within the time period of $[T_b/2, T_b]$. The sampled output of the demodulator can be expressed as:

$$\begin{aligned} m_k &= \frac{1}{T_b/2} \int_{T_b/2} (s_t + n_t) dt - \frac{1}{T_b/2} \int_{T_b/2} (s_{t-T_b/2} + n_{t-T_b/2}) dt \\ &= \frac{1}{T_b/2} \int_{T_b/2} (s_t - s_{t-T_b/2}) dt + \frac{1}{T_b/2} \int_{T_b/2} (n_t - n_{t-T_b/2}) dt \\ &\approx \pm 2M(\theta_0) + \frac{1}{T_b/2} \int_{T_b/2} (n_t - n_{t-T_b/2}) dt. \end{aligned} \quad (23)$$

According to the differential modulation rule, a positive summation between the signal within the first half bit duration and the negative signal within the second half bit duration shows that the symbol “1” is received while a negative value indicates the reception of the symbol “0”. The decision is made by the following simple comparison assuming $M(\theta_0) \geq 0$:

$$\hat{d}(k) = \begin{cases} 1 & m_k \geq 0 \\ 0 & m_k < 0. \end{cases} \quad (24)$$

3.3 BER of E-DCSK

In order to evaluate the performance of the proposed E-DCSK scheme, its BER performance in an AWGN channel is investigated in this subsection. To derive its theoretical BER performance, the output of the E-DCSK demod-

ulator is rewritten in the discrete format as

$$\begin{aligned}
 m_k &= \frac{1}{T_b/2} \sum_{t=1}^{T_b/2} y_t - \frac{1}{T_b/2} \sum_{t=T_b/2+1}^{T_b} y_t \\
 &= \frac{1}{T_b/2} \sum_{t=1}^{T_b/2} (s_t + n_t) - \frac{1}{T_b/2} \sum_{t=T_b/2+1}^{T_b} (s_t + n_t) \\
 &= x_{T_b} + n_{T_b},
 \end{aligned} \tag{25}$$

where

$$\begin{aligned}
 y_t &= s_t + n_t, \\
 x_{T_b} &= \frac{1}{T_b/2} \sum_{t=1}^{T_b/2} s_t - \frac{1}{T_b/2} \sum_{t=T_b/2+1}^{T_b} s_t = \pm 2 \frac{1}{T_b/2} \sum_{t=1}^{T_b/2} x_t, \\
 n_{T_b} &= \frac{1}{T_b/2} \left[\sum_{t=1}^{T_b/2} n_t - \sum_{t=T_b/2+1}^{T_b} n_t \right].
 \end{aligned}$$

Suppose that the mean and variance of the chaotic signal x_t are m_0 and $N_0/2$, respectively when symbol “0” is transmitted, and the mean and variance of the noise n_t are 0 and $N_n/2$ respectively. Therefore, there are two equally probable outcomes $x_{T_b} = \pm 2m_0$ with variance of

$$2 \frac{1}{T_b/2} \frac{N_0}{2} = \frac{2N_0}{T_b}.$$

The decision is made by setting the threshold of the detector to be zero.

According to the Central Limit Theorem, the conditional probability of density function (pdf) of the random variable x_{T_b} , given that symbol “0” is transmitted, can be approximated by

$$f_{x_{T_b}}(x_{T_b}|0) = \frac{\sqrt{T_b}}{\sqrt{4\pi N_0}} e^{\frac{T_b(x_{T_b}+2m_0)^2}{4N_0}}. \tag{26}$$

Since the random variables x_{T_b} and n_{T_b} are independent, the conditional pdf of the variable m_k , given that symbol “0” is transmitted, can be given by

$$f_{m_k}(m_k|0) = \frac{\sqrt{T_b}}{\sqrt{4\pi(N_0 + N_n)}} e^{\frac{T_b(x_{T_b}+2m_0)^2}{4N_0+4N_n}}. \tag{27}$$

The conditional probability of the E-DCSK receiver in favor of symbol “1”, given that symbol “0” is transmitted, is therefore

$$\begin{aligned} p_{10} &= \int_0^\infty f_{m_k}(m_k|0) dm_k \\ &= \int_0^\infty \frac{\sqrt{T_b}}{\sqrt{4\pi(N_0 + N_n)}} e^{\frac{T_b(x_{T_b} + 2m_0)^2}{4N_0 + 4N_n}} dm_k. \end{aligned} \quad (28)$$

Putting

$$z = \frac{\sqrt{T_b}(x_{T_b} + 2m_0)}{\sqrt{4\pi(N_0 + N_n)}}$$

and changing the variable of integration from m_k to z , we may rewrite (28) in the compact form:

$$\begin{aligned} p_{10} &= \int_{-\frac{m_0\sqrt{T_b}}{\sqrt{N_0 + N_n}}}^\infty \frac{1}{\sqrt{\pi}} e^{-z^2} dz \\ &= \frac{1}{2} \operatorname{erfc}\left(\frac{m_0\sqrt{T_b}}{\sqrt{N_0 + N_n}}\right) \end{aligned} \quad (29)$$

where $\operatorname{erfc}(.)$ is the complementary error function.

Similarly, the conditional pdf of the random variable m_k , given that symbol “1” is transmitted, can be given by

$$f_{m_k}(m_k|1) = \frac{\sqrt{T_b}}{\sqrt{4\pi(N_0 + N_n)}} e^{\frac{T_b(x_{T_b} + 2m_0)^2}{4N_0 + 4N_n}} \quad (30)$$

The conditional probability of the receiver in favor of symbol “0”, given that symbol “1” is transmitted, is therefore

$$\begin{aligned} p_{01} &= \int_{-\infty}^0 f_{m_k}(m_k|1) dm_k \\ &= \int_{-\infty}^0 \frac{\sqrt{T_b}}{\sqrt{4\pi(N_0 + N_n)}} e^{\frac{T_b(x_{T_b} + 2m_0)^2}{4N_0 + 4N_n}} dm_k. \end{aligned} \quad (31)$$

Putting

$$z = \frac{\sqrt{T_b}(x_{T_b} + 2m_0)}{\sqrt{4\pi(N_0 + N_n)}}$$

and changing the variable of integration from m_k to z , we may rewrite (31) in the compact form:

$$\begin{aligned} p_{01} &= \int_{-\infty}^{\frac{m_0\sqrt{T_b}}{\sqrt{N_0 + N_n}}} \frac{1}{\sqrt{\pi}} e^{-z^2} dz \\ &= \int_{-\frac{m_0\sqrt{T_b}}{\sqrt{N_0 + N_n}}}^\infty \frac{1}{\sqrt{\pi}} e^{-z^2} dz \\ &= \frac{1}{2} \operatorname{erfc}\left(\frac{m_0\sqrt{T_b}}{\sqrt{N_0 + N_n}}\right). \end{aligned} \quad (32)$$

Thus, taking the average of the conditional error probabilities p_{10} and p_{01} , we have the bit error rate (BER) for E-DCSK receiver:

$$\begin{aligned} p_e &= p_0 p_{10} + p_1 p_{01} \\ &= \frac{1}{2} \operatorname{erfc} \left(\frac{m_0 \sqrt{T_b}}{\sqrt{N_0 + N_n}} \right). \end{aligned} \quad (33)$$

where p_0 and p_1 are the probabilities of the symbol “0” or “1”. In practical digital communications, the transmitted binary symbols are the equiprobable symbols, that is $p_0 = p_1 = 1/2$. Let E_b denote the transmitted signal energy per bit and

$$E_b = \frac{(2m_0^2 + N_0)T_b}{2} \quad (34)$$

The BER performance can be expressed in terms of the signal to noise ratio, E_b/N_n , which in fact is the ratio of the signal energy per bit to the noise power spectrum density. That is,

$$\begin{aligned} p_e &= \frac{1}{2} \operatorname{erfc} \left(\frac{m_0 \sqrt{T_b}}{\sqrt{N_0 + \frac{(2m_0^2 + N_0)T_b}{2E_b/N_n}}} \right) \\ &= \frac{1}{2} \operatorname{erfc} \left(\frac{m_0 \sqrt{2T_b E_b / N_n}}{\sqrt{2N_0 E_b / N_n + T_b (2m_0^2 + N_0)}} \right) \end{aligned} \quad (35)$$

4 Performance Evaluation of Chaos Communications

One standard measure of a communication system is its performance in a noisy channel. The noise performance of a digital communication scheme is usually determined by the probability distribution of the observation variable at the output of its demodulator. The error probability performance, i.e. BER, of a modulation scheme is determined by the pdf of the observation, which depends on the signal space diagram and the type of various demodulations. For many schemes, the observations of the demodulator can be expressed as a sum of terms, which depend on the received noisy signal. The shape of the pdf is hence determined by these constituent terms, which are also random variables.

4.1 Noise performance in an AWGN channel

The most popular channel model for wireless communications is probably AWGN channel. The basic model of the received signal is usually expressed by $r(t) = x'(t) + n(t)$, where $x'(t)$ is the modulated signal and $n(t)$ is an AWGN process with uniform power spectral density $\phi_{nn}(f) = \delta_n^2 = N_n/2W/\text{Hz}$. To characterize the communication performance, the BER as a function of the

ratio of the signal energy per bit E_b to the noise spectral density $N_n(E_b/N_n)$, is used here as the measure criterion. In terms of RF transmission, the signal to noise ratio (SNR) and E_b/N_n are basically related. Note that the total spread bandwidth of the RF channel is B_w and the bit duration of the binary data is T_b , the SNR at the input of the demodulator can be described as a function of E_bNR by the following:

$$SNR = \frac{P_{signal}}{P_{noise}} = \frac{E_b}{N_n} \frac{1}{B_w T_b} = \frac{E_b}{N_n G}. \quad (36)$$

For discrete chaotic system, let the step size between two adjacent states be T_c , then at most cases, the transmitted bandwidth B_w can be expressed as $B_w = 1/T_c$. The ratio of the bit duration, T_b , to the chaos generation step size, T_c , is called the processing gain. That is,

$$G = \frac{T_b}{T_c} = T_b|_{T_c=1}. \quad (37)$$

In our discussion, T_c is assumed to be equal to unity. Thus T_b will represent the processing gain. In other words, it represents the number of signal samples used to transmit one data symbol. Achieving processing gain, the property of SS systems to suppress interference due to application of a wider bandwidth, is the key point in the design of chaos communication systems. Clearly, this can only be done if the bandwidth of chaotic carrier is wider than that of the information signal. However, it is not a sufficient condition. For example, the chaotic masking (CM) scheme and the adaptive filter based chaotic parameter modulation (CPM) scheme do not yield any processing gain for their noise performance. Therefore they have no advantages with respect to standard modulation techniques according to the noise performance.

For several of the proposed chaos communication systems, theoretical analysis exists on the achievable bit error probability [35-38]. For example, the theoretical BER performances of DS based BPSK scheme (CSS and CC), coherent CSK, DCSK, and E-DCSK, have all been derived. A comparison of BER performances of these chaos based communication schemes is given in Table 2. Detailed explanations are given after the table. Numerical simulation is also carried out for further analysis [39].

Both CSS and CC are basically the conventional DSSS system except that the PN sequence is replaced by a chaotic sequence (or signal). The basic spread and despread operations remain the same as that for the conventional DSSS system, and hence their BERs are also the same. Sometimes, these two schemes are not considered as chaotic modulation schemes. Their performances are also included here mainly for reference.

The coherent CSK has the same BER performance as that of the binary orthogonal signals. Compared with the binary antipodal signals (CC and CSS), we find it requires a factor of two increase in energy to achieve the same error probability as CC and CSS. Since $10 \log_{10}(2) = 3$, the coherent

Table 2. Comparison of theoretical BER performances of various chaos-based communication systems

| Schemes | Theoretical BER performance | Notes |
|----------------------|---|--|
| DS-BPSK (CC, CSS) | $BER = \frac{1}{2} \operatorname{erfc} \left(\sqrt{\frac{E_b}{N_n}} \right)$ | The same as conventional DS-BPSK, only related to $\frac{E_b}{N_n}$ |
| Coherent CSK | $BER = \frac{1}{2} \operatorname{erfc} \left(\sqrt{\frac{E_b}{2N_n}} \right)$ | The same as binary orthogonal signals, only related to $\frac{E_b}{N_n}$ |
| DCSK | $BER = \frac{1}{2^{T_b}} \exp \left(-\frac{E_b}{2N_n} \right) \\ \times \sum_{t=0}^{T_b-1} \frac{\left(\frac{E_b}{2N_n} \right)^i}{i!} \sum_{j=1}^{T_b-1} \frac{1}{2^j} \binom{j + T_b - 1}{j - i}$ | Related to T_b , if $T_b = 1$, it is equal to that of non-coherent binary FSK. For some specific chaos system, the BER can be simplified. |
| E-DCSK | $BER = \frac{1}{2} \operatorname{erfc} \left(\frac{m_0 \sqrt{2T_b E_b / N_n}}{\sqrt{2N_0 E_b / N_n + T_b (2m_0^2 + N_0)}} \right)$ | m_0 and $\frac{N_0}{2}$ are the mean value and variance of the chaotic signal. Related to T_b |

CSK is about 3dB worse than CC and CSS. This performance is under the assumption that the chaotic synchronization process can completely recover the transmitted chaotic signal. However, to the best of our knowledge, the coherent CSK scheme has not yet been demonstrated in practice or by computer simulation to achieve this upper-bound performance. The main reason is that finding a chaotic synchronization scheme which can recover the chaotic basis functions with an acceptable error is still an open problem.

Clearly, the only difference is that the basis functions in DCSK are generated directly from the chaotic signal, and in FM-DCSK the source of the basis functions is the output of the FM modulator, we will not distinguish between DCSK and FM-DCSK. From the operation discussed in the previous sections, we know that half of E_b , that is, half of the bit duration signals, is not used to carry any information; it only provides the reference for the demodulator. In this sense, half of the transmitted energy per bit is lost in order to avoid periodicity in the DCSK signal. Note that, as seen from its theoretical BER performance, the noise performance of DCSK depends on both E_b/N_n and

processing gain T_b . If $T_b = 1$, $BER = \frac{1}{2} \exp(-\frac{E_b}{2N_b})$, the noise performance of DCSK is equivalent to that of the non-coherent binary FSK [36]. In fact, under this condition, the DCSK signal is no longer wide-band but becomes narrow-band instead. It should also be noted that for some specific chaotic systems, the BER performance of their DCSK implementations can be approximated to have a simple form. For example, for the symmetric tent map: $x_{t+1} = 1 - 2|x_t|$, the distribution of x_t is uniform, and, the BER of DCSK can be approximately simplified as

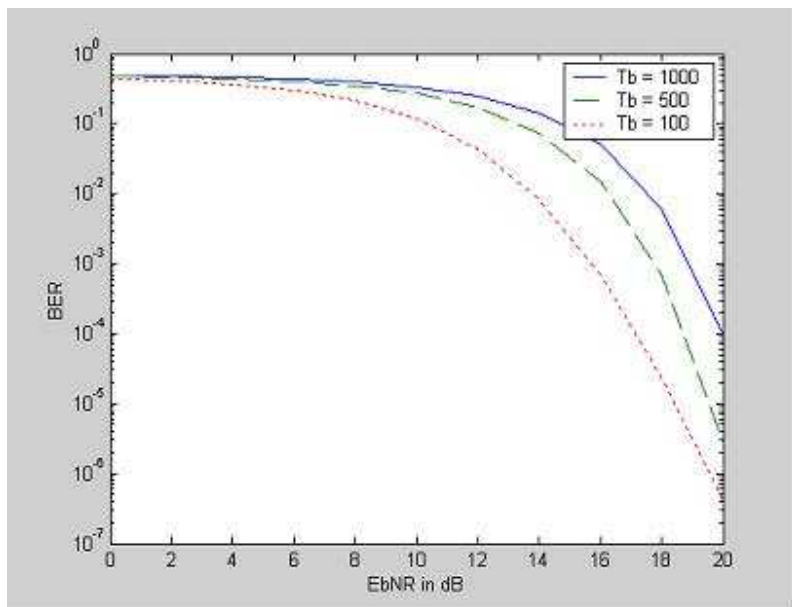
$$BER = \frac{1}{2} \operatorname{erfc} \left(\sqrt{\frac{E_b}{4N_n} \left(1 + \frac{4}{5T_b N_n} + \frac{N_n}{4E_b} T_b \right)^{-1}} \right). \quad (38)$$

Based on (38), we plot the theoretical BER performance with various values of T_b in Fig. 9(a). It can be seen that at large T_b , the noise performance of DCSK degrades with an increasing T_b , which is confirmed by the simulation results too. As T_b gets small, the approximate given in (38) is not really close to the theoretical value. The numerical simulation shown in Fig. 9(b) also confirms that the BER performance degrades with increasing T_b . This is due to the increasing impact of cross correlation noise term at the demodulator output.

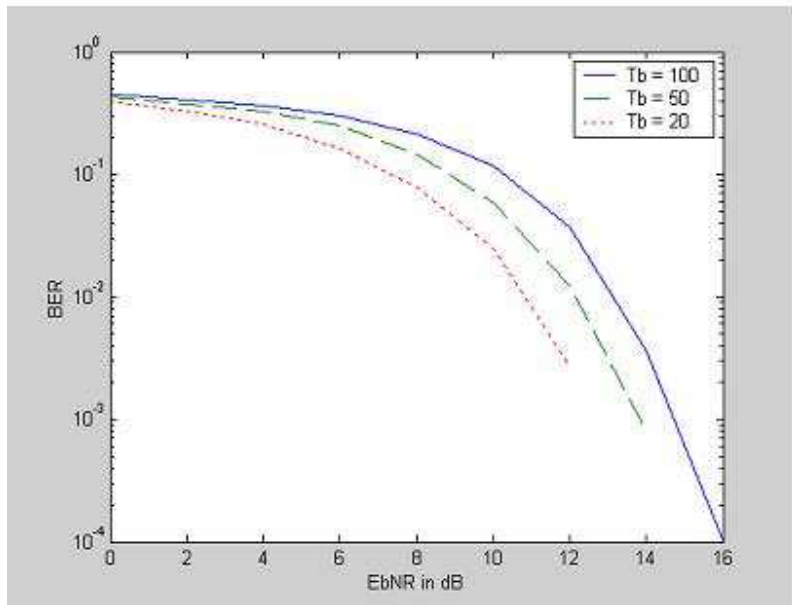
According to (33) and (35), the BER performance of E-DCSK is dependent of the mean value m_0 and variance N_0 of the chaotic signal. Obviously, for a larger value of m_0 , the E-DCSK scheme will have better BER performance. To design an efficient E-DCSK system, one has to pick a signal with a large mean value from a chaotic map for signal transmission. In [28,29], it is reported that the Chebyshev map can achieve a significant large mean value distance, and hence is used in this study. The one dimension popular Chebyshev map [33,34] is given by: $x_t = \cos(\theta \cos^{-1}(x_{t-1}))$, where $\theta \in [1.3, 2]$. It is observed that the mean value of chaotic signal generated with $\theta_0 = 1.3$ is -0.85; and 0 with $\theta_1 = 2$. For different parameters within the chaotic regime, the chaotic signal generated from Chebyshev map has different mean values and variance as shown in Table 3.

Figure 10 depicts the theoretical BER of E-DCSK based on Chebyshev map with various parameters. The noise performance of E-DCSK varies with the mean values. As the absolute value of the mean values increases, the BER performance of E-DCSK also improves. The simulation shows a good agreement with the analytical prediction. In our system, we choose $\theta_0 = 1.3$ and its BER performance of E-DCSK is pretty well. It only requires an $E_b NR$ of 10 dB to achieve a BER performance of 10^{-5} .

Another factor that affects the BER performance is T_b . The BER performances of E-DCSK with various T_b values are plotted in Figs. 11(a) and (b). $\theta_0 = 1.3$ is used for the E-DCSK system in Figs. 11(a) and (b) is plotted using $\theta_0 = 1.7$. From Fig. 11(a), we can see that the value of T_b does not have a strong impact on the BER performance of E-DCSK with $\theta_0 = 1.3$. However, Fig. 11(b) shows that the BER performance of E-DCSK with pa-



(a)



(b)

Fig. 9. BER performance of DCSK with various values of T_b . (a) Theoretical performance with large T_b ; (b) Simulation performance with small T_b

Table 3. Various mean values and variance for chaotic signal generated from Chebyshev map with different parameters

| Parameter θ_i | Mean values m_i | Variance $N_0/2$ |
|----------------------|-------------------|------------------|
| $\theta_0 = 2.0$ | 0.0169 | 0.5091 |
| $\theta_0 = 1.9$ | -0.1824 | 0.4092 |
| $\theta_0 = 1.7$ | -0.4474 | 0.2373 |
| $\theta_0 = 1.5$ | -0.6978 | 0.0812 |
| $\theta_0 = 1.3$ | -0.8478 | 0.0232 |

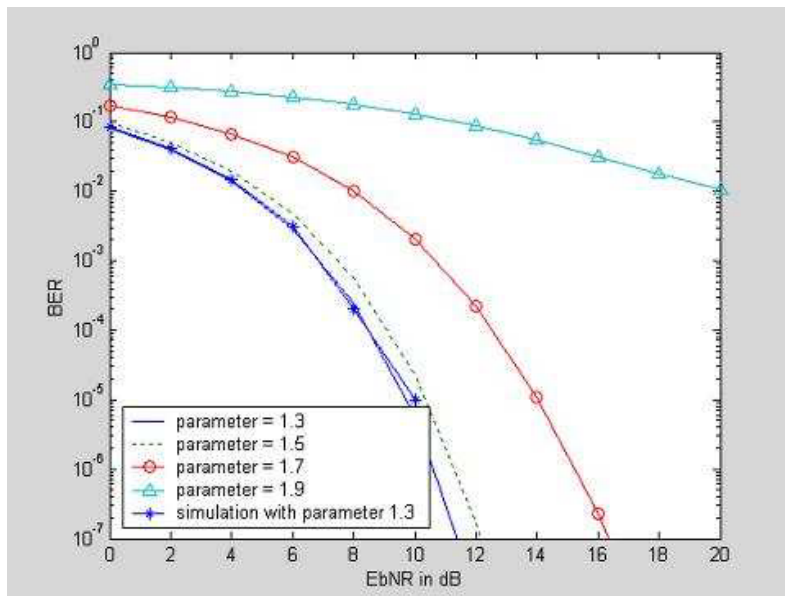
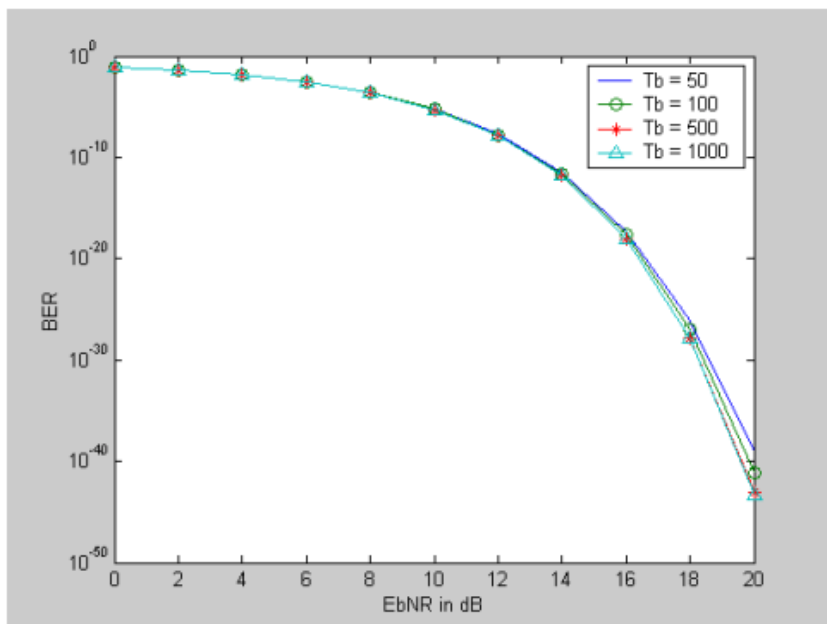
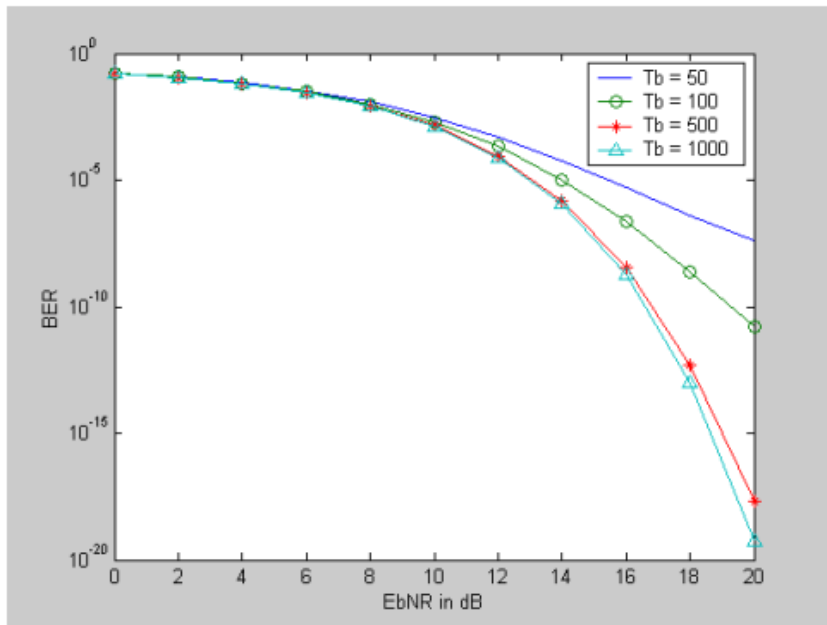


Fig. 10. BER performance of E-DCSK scheme based on Chebyshev map with various chaotic parameters, where $T_b = 100$

parameter $\theta_0 = 1.7$ degrades when T_b decreases. Compared to the system with $\theta_0 = 1.3$, it has a smaller mean value but a larger variance. In the E-DCSK system, we have $E_b = \frac{2m_0^2 + N_0}{2} T_b$. By fixing T_b and E_b , it implies that an increasing m_0 will result in a decreasing N_0 . If N_0 is very small, say $N_0 \rightarrow 0$, then $N_0 \frac{E_b}{N_n} \rightarrow 0$ and $E_b \approx m_0^2 T_b$. It implies that the impact of T_b on the BER performance with a smaller value of N_0 is less sever than that with a greater value of N_0 . In fact, using the approximation $E_b \approx m_0^2 T_b$, the factor T_b in the BER equation can be removed and the BER performance of E-DCSK can be



(a)



(b)

Fig. 11. BER performance of E-DCSK with various values of T_b with application of Chebyshev map (a) parameter $\theta_0 = 1.3$ is used; (b) parameter $\theta_0 = 1.7$ is used.

simplified to:

$$BER \approx \frac{1}{2} \operatorname{erfc} \left(\frac{m_0 \sqrt{2T_b \frac{E_b}{N_n}}}{\sqrt{2T_b m_0^2}} \right) \approx \frac{1}{2} \operatorname{erfc} \left(\sqrt{\frac{E_b}{N_n}} \right) \quad (39)$$

which is equivalent to the BER performance of binary antipodal signals (DS BPSK, CC and CSS).

In the last numerical analysis, we perform a complete BER comparison of the various chaos communication schemes, including DS-SS based scheme (CSS and CC), coherent CSK, DCSK, and E-DCSK, and the result is given in Fig. 12. $T_b = 100$ and $T_b = 20$ are considered respectively in Figs. 12(a) and (b). From the comparison, we observe that the E-DCSK can achieve a very closed BER performance to the conventional DS-SS system. However, most systems work well for $T_b = 20$, which indicates the suitability for higher data transmission rate, except for E-DCSK whose performance degrades for small T_b .

4.2 BER performance of E-DCSK under special noise environment

One advantage of the proposed E-DCSK scheme is that if the mean value of channel noise is stable or can be estimated, the mean value of the distortion can then be subtracted from the demodulation process. Considering the item

$$n_{Tb} = \frac{1}{T_b/2} \left[\sum_{t=1}^{T_b/2} n_t - \sum_{t=T_b/2+1}^{T_b} n_t \right]$$

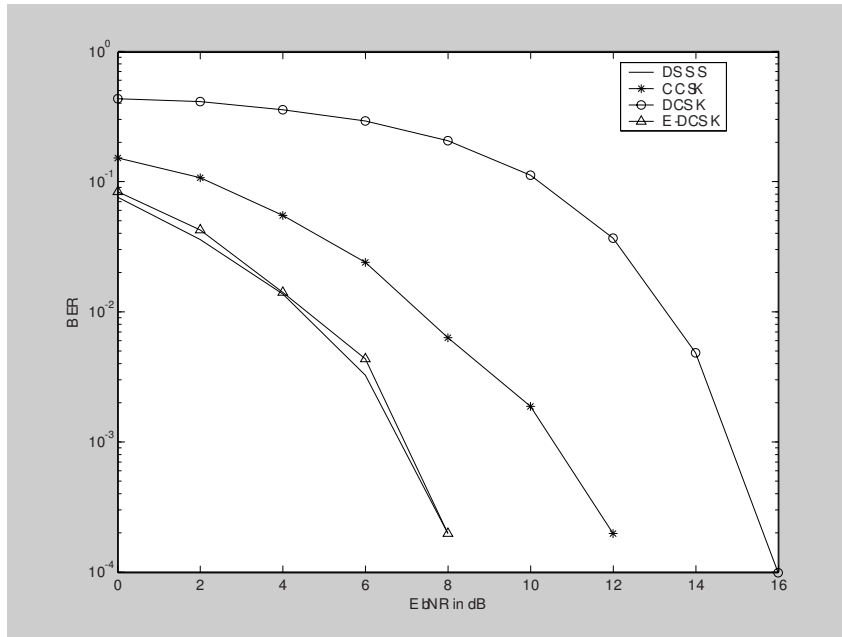
in (25), if the mean value of the noise is stable, which means

$$\sum_{t=1}^{T_b/2} n_t = \sum_{t=T_b/2+1}^{T_b} n_t,$$

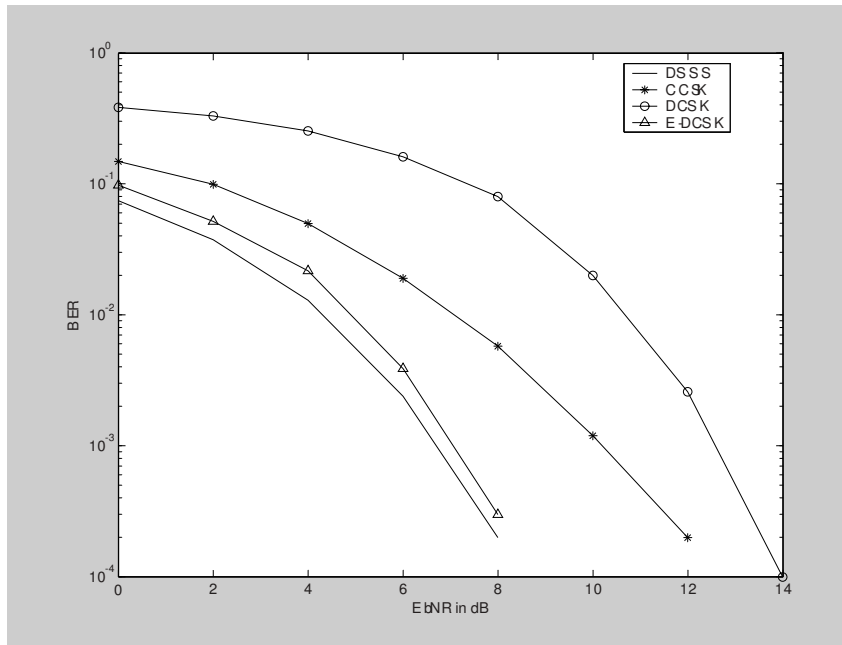
then we have $n_{Tb} = 0$. The output of the demodulator of E-DCSK can be simplified to be

$$m_k = x_{Tb} = 2 \frac{1}{T_b/2} \sum_{t=1}^{T_b/2} x_t.$$

Note that the channel noise now has little influence on the demodulation performance of E-DCSK. This situation can be found in different environments including very stable AWGN channel, digital water-marking [40], noise generated from AR model and channels where the mean value of noise is predictable.



(a)



(b)

Fig. 12. Comparative BER performance of various chaos communication schemes
(a) $T_b = 100$; **(b)** $T_b = 20$.

In this case, the conditional pdf of the random variable m_k , given that the symbol “0” is transmitted, can be given by

$$f_{m_k}(m_k|0) = \frac{\sqrt{T_b}}{\sqrt{4\pi N_0}} e^{\frac{T_b(x_{T_b}+2m_0)^2}{4N_0}}. \quad (40)$$

The conditional probability p_{10} is therefore

$$\begin{aligned} p_{10} &= \int_0^\infty f_{m_k}(m_k|0) dm_k \\ &= \int_0^\infty \frac{\sqrt{T_b}}{\sqrt{4\pi(N_0 + N_n)}} e^{\frac{T_b(x_{T_b}+2m_0)^2}{4N_0+4N_n}} dm_k \\ &= \int_{-\frac{m_0\sqrt{T_b}}{\sqrt{N_0}}}^\infty \frac{1}{\sqrt{\pi}} e^{-z^2} dz \\ &= \frac{1}{2} \operatorname{erfc}\left(-\frac{m_0\sqrt{T_b}}{\sqrt{N_0}}\right). \end{aligned} \quad (41)$$

Similarly, the conditional pdf of the random variable m_k , given that symbol “1” is transmitted, is given by

$$f_{m_k}(m_k|1) = \frac{\sqrt{T_b}}{\sqrt{4\pi N_0}} e^{-\frac{T_b(x_{T_b}-2m_0)^2}{4N_0}}, \quad (42)$$

and the conditional probability p_{01} is therefore

$$\begin{aligned} p_{01} &= \int_{-\infty}^0 f_{m_k}(m_k|1) dm_k \\ &= \int_{-\infty}^0 \frac{\sqrt{T_b}}{\sqrt{4\pi(N_0 + N_n)}} e^{-\frac{T_b(x_{T_b}+2m_0)^2}{4N_0+4N_n}} dm_k \\ &= \int_{-\frac{m_0\sqrt{T_b}}{\sqrt{N_0}}}^\infty \frac{1}{\sqrt{\pi}} e^{-z^2} dz \\ &= \frac{1}{2} \operatorname{erfc}\left(\frac{m_0\sqrt{T_b}}{\sqrt{N_0}}\right). \end{aligned} \quad (43)$$

Thus the average probability of symbol error, or equivalently the BER for the E-DCSK with a known noise mean is given by

$$p_e = \frac{1}{2} \operatorname{erfc}\left(-\frac{m_0\sqrt{T_b}}{\sqrt{N_0}}\right). \quad (44)$$

Its theoretical BER performance versus T_b is shown in Fig. 13, where Chebyshev map with various parameters is applied. Their mean values m_0 and variance $N_0/2$ are given in Table 3. We can see the BER performance of E-DCSK is extremely good under this situation. For the E-DCSK system with parameter of $\theta_0 = 1.3$, the communication is almost errorless where other communication systems can not achieve this performance at all in these environments.

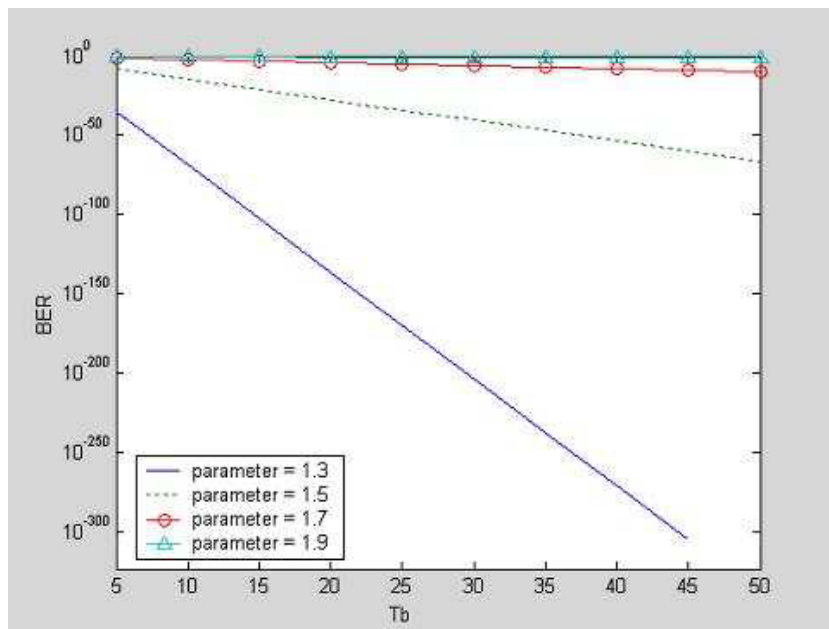


Fig. 13. BER performance of E-DCSK with no affection of channel noise.

5 Conclusions

In this chapter, we provide an overview of most of the popular chaos based communication schemes in the literature to-date. Although these chaos communication schemes share the common advantages of infinite sequences, aperiodicity and high security, most of them suffer from poor noise performance. To improve the noise performance of chaos communications, the ergodic theory is applied here. A novel chaos communication scheme called E-DCSK is proposed, and its theoretical BER performance is also derived. Based on the comparative study, both theoretical and numerical analysis confirm that by applying the ergodic theory to DCSK, the noise performance can be greatly improved. In fact, the E-DCSK system could achieve a noise performance closed to that of the conventional DS-SS system. Furthermore, in the situation that the mean value of channel noise is very stable or predictable, the E-DCSK shows superior immunity to the channel noise and outperforms the conventional optimum communication systems.

References

1. Proakis, J. G. (1998) Digital Communications,. 3rd ed. New York: McGraw-Hill
2. Cooper, G. R., McGillem, C. D. (1986) Modern Communications and Spread Spectrum. New York: McGraw-Hill

3. Dixon, R. C. (1994) Spread Spectrum Systems with Commercial Applications. 3rd Edition. New York: Wiley
4. Boyarsky, A., Gora, P. (1997) Laws of Chaos: Invariant Measures and Dynamical Systems in One Dimension. Boston: Birkhäuser
5. Parker, T. S, Chua, L. O. (1989) Practical Numerical Algorithms for Chaotic Systems. New York: Springer-Verlag
6. Kennedy, M.P., Rovatti, R., Setti, G. (2000) Chaotic Electronics in Telecommunications. Boca Raton, FL: CRC Press
7. Itoh, M. (1999) Spread spectrum communication via chaos. *Int. J. Bifur. Chaos*, **9**(1):155–213
8. Kennedy, M. P., Kolumban, G. (2000) Digital communications using chaos. *Signal Processing*, **80**:1307–1320
9. Yu, H., Leung, H. (2001) A comparative study of different chaos based spread spectrum communication systems. In Proc. of IEEE ISCAS, vol. III, Sydney, Australia 213–216
10. Umeno, K., Kitayama, K. (1999) Spreading sequences using periodic orbits of chaos for CDMA. *Electr. Lett.*, **35**(7):545–546
11. Mazzini, G., Setti, G., Povatti, R. (1997) Chaotic complex spreading sequences for asynchronous DS-CDMA, Part I: System modeling and results. *IEEE Trans. Circ. Syst.-I*, **44**(10):937–947
12. Heidari-Bateni, G., McGillem, C. D. (1994) A chaotic direct-sequence spread spectrum communication system. *IEEE Trans. Communications*, **42**(2):1524–1527
13. Yang, T., Chua, L. O.(1997) Chaotic digital code division multiple access (CDMA) communication systems. *Int. J. Bifur. Chaos*, **7**(12):2789–2805
14. Yang, T., Chua, L. O.(1998) Applications of chaotic digital code-division multiple access (CDMA) to cable communication systems. *Int. J. Bifur. Chaos*, **8**(8):1657–1669
15. Elmirghani, J. M. H., Cryan, R. A.(1994) Communication using chaotic masking. *IEE Colloquium on Exploiting Chaos in Signal Processing*, 12/1–12/6
16. Chen, Y.-Y.(1996) Masking messages in chaos. *Europhys. Lett.*, **34**:245–250
17. Kennedy, M. P., Dedieu, H., Hasler, M. (1993) Chaos shift keying: modulation and demodulation of a chaotic carrier using self-synchronizing Chua's circuits. *IEEE Trans. Circ. Syst.-II*, **40**(10):634–642
18. Kolumban, G., Kennedy, M. P., Chua, L. O. (1998) The role of synchronization in digital communications using chaos, Part II: Chaotic modulation and chaotic synchronization. *IEEE Trans. Circ. Syst.-I*, **45**(11):1129–1139
19. Kocarev, L., Halle, K. S., Eckert, K., Chua, L. O., Parlitz, U. (1992) Experimental demonstration of secure communications via chaotic synchronization. *Int. J. Bifur. Chaos*, **2**(3):709–713
20. Kolumban, G., Kis, G., Jako, Z., Kennedy, M. P. (1998) FM-DCSK: a robust modulation scheme for chaotic communications. *IEICE Trans. Fundamentals of Electr., Comm. Comput. Sci.*, **E81-A**(9):1798–1802
21. Kennedy, M. P., Kis, G. (2000) Elaboration of system specification for a WLAN FM-DCSK telecommunications system. In Proc. of NDES, 160–164
22. Kennedy, M. P., Kolumban, G., Kis, G., Jako, Z. (2000) Performance evaluation of FM-DCSK modulation in multipath environments. *IEEE Trans. Circ. Syst.-I*, **47**(12):1702–1711

23. Muller, A., Elmirghani, J. M. H. (2002) A novel approach to signal transaction based on chaotic signals and artificial neural networks. *IEEE Trans. Communications*, **50**(3):383–390
24. Leung, H., Lam, J. (1997) Design of demodulator for the chaotic modulation communication system. *IEEE Trans. Circ. Syst.-I*, **44**(3):262–267
25. Zhu, Z., Leung, H. (2000) Adaptive identification of nonlinear systems with application to chaotic communications. *IEEE Trans. Circ. Syst.-I*, **47**(7):1072–1080
26. Haykin, S. (1991) *Adaptive Filter Theory*. 2nd ed. Englewood Cliffs, NJ: Prentice-Hall
27. Ueberhuber, C. W. (1997) *Numerical Computation 2: Methods, Software and Analysis*. Berlin: Springer-Verlag
28. Leung, H., Yu, H. (2001) A novel method for chaotic signal parameter estimation. In Proc. of IEEE ISPACS, Tennessee, 113–117
29. Yu, H., Leung, H. (2002) A simple chaotic spread spectrum scheme for data broadcasting in intelligent transportation systems. In Proc. of VTC2002
30. Hasler, M. (2001) Ergodic chaos shift keying. In Proc. of ISCAS, Sydney, Australia
31. Chen, C., Yao, K., Umeno, K., Bilieri, E. (2001) Design of spread-spectrum sequences using chaotic dynamical systems and ergodic theory. *IEEE Trans. Circ. Syst.-I*, **48**(9):1110–1114
32. Kohda, T., Tsuueda, A. (1997) Statistics of chaotic binary sequence. *IEEE Trans. Infor. Theory*, **43**(1):104–112
33. Kohda, T., Tsuueda, A., Lawrence, A. J. (2000) Correlational properties of Chebyshev chaotic sequences. *J. Time Series Analysis*, **21**(2):181–192
34. Ott, E., Saucer, T., Yorke, J. A. (1994) *Coping with Chaos: Analysis of Chaotic Data and the Exploitation of Chaotic Systems*. New York: Wiley
35. Abel, A., Schwarz, W., Gotz, M. (2000) Noise performance of chaotic communication systems. *IEEE Trans. Circ. Syst.-I*, **47**(12):1726–1732
36. Kolumban, G. (2000) Theoretical noise performance of correlator-based chaotic communication schemes. *IEEE Trans. Circ. Syst.-I*, **47**(12):1692–1701
37. Chen, C., Yao, K. (2000) Numerical evaluation of error probabilities of self-synchronizing chaotic communications. *IEEE Comm. Lett.*, **4**(2):37–39
38. Hasler, M., Schimming, T. (2000) Chaos communication over noisy channel. *Int. J. Bifur. Chaos*, **10**:719–736
39. Jeruchim, M. C., Balaban, P., Shanmugan, K. S. (1992) *Simulation of Communication Systems*. New York: Plenum Press
40. Chen, S., Leung, H. (2002) Chaotic parameter modulation with application to digital watermarking. In Proc. of IEEE ICFS, Tokyo, Japan

Control of Chaos Statistics for Optimization of DS-CDMA Systems

Gianluca Setti^{1,3}, Riccardo Rovatti^{2,3}, and Gianluca Mazzini^{1,3}

¹ DI University of Ferrara
via Saragat 1, 44100 Ferrara, Italy
(gsetti,gmazzini)@ing.unife.it

² DEIS University of Bologna
viale Risorgimento 2
40136 Bologna, Italy
rrovatti@deis.unibo.it

³ ARCES, University of Bologna
via Toffano 2
40100 Bologna, Italy

Abstract. Results of recent theoretical investigations highlighted that the use of chaos in DS-CDMA systems may lead to non-negligible improvements in communication quality for several scenarios. We here briefly review the main steps in this derivation and report the corresponding theoretical prediction. In particular we show that the use of the so-called statistical approach to the study of a chaotic dynamical system allows to characterize and control the statistical features of the processes generated by it. By using such an approach, we highlight the path leading to the generation of chaos-based spreading sequences outperforming classical pseudo-random sequences in two important cases. Over non-selective channels, the ability of chaos-based spreading of minimizing multiple-access interference leads to an average improvement of 60% in P_{err} with respect to classical spreading. Over selective channels, the possibility of jointly optimizing chaos-based spreading and rake receiver profiles leads to improvements of up to 22% in P_{err} with respect to systems with either conventional spreading or conventional rake policies.

1 Introduction

Within the past decade, several research efforts have directly addressed the use the potential of chaotic dynamics for performances improvements in several fields of Electrical and Information Engineering. The main reason for such an event is surely linked to the awareness that chaotic systems possesses a nature at the borderline between deterministic and stochastic, and to the consequent adoption of tools from statistical dynamical systems theory for their analysis [1–4].

The use of these statistical methodologies helps clarifying that the application fields which are most likely to benefit from chaos-based techniques are those where the *statistical properties* of the signals are the dominant factor. Additionally, the same tools are also the key factor in developing the

quantitative models needed to control the statistical features of the processes generated by discrete-time chaotic systems.

Applications of such chaos-related techniques in the field of information processing range from chaos-based cryptography [5] audio and video watermarking [6], network traffic modelling [4, 7], noise generation [8] or suppression [9], electromagnetic interference control [10–12], and telecommunication, which has been so far the most fruitful area for applying chaos-related methodologies (see [13] for a fairly complete survey).

Beside the appreciable importance of the results achieved for the above applications, the existence of a plethora of different tasks to which the chaos-based approach (and the statistical techniques in particular) has been successfully applied, highlight the existence of a general scheme, which can in principle be applied to design a dynamical systems able to optimize the performance for the considered application. Such a procedure follows two phases. As a first step a model of the target application must be developed to link specifications (performance and constraints) with the statistical features of the signals entailed in the considered task. In the second phase, link will be exploited to deepen the comprehension of what improvements are achievable by the design and use, in the chosen applications framework, of a chaotic system with controllable statistical features.

Within the engineering problems that benefit from this design ability, the application of chaotic dynamics to the code-level optimization of a DS-CDMA systems is surely one of the most developed. The idea dates back to [14, 15] where a first model of the performance of a chaos-based DS-CDMA system is reported leading to encouraging analytical and numerical results. The exploitation of chaos-based techniques in this field have been further developed in [16–18] where the impact of the adoption of chaos-based sequences in a standard asynchronous DS-CDMA systems is studied when Additive White Gaussian Noise (AWGN) channels are considered and Multi-User Interference (MAI) is the dominant cause of nonideality. For such an environment, theoretical performance bounds have been obtained which show that significant improvement can be achieved by employing a properly designed family of chaotic systems generating real trajectories that are then quantized and periodically repeated to yield the users signatures. This result has been further strengthened in [19] where it is shown that chaos-based spreading allows to practically reach the absolute minimum of MAI and that such a lower bound is approximately 15% lower than the average interference achievable by classical pseudo-random sequences.

Few steps have also been taken in the direction of analyzing the synchronization between the transmitter and the receiver for the same user, which must be guaranteed before a reliable communication link can be established. In particular, in [20] it is found that, even if synchronization can always be ensured independently of the choice of the spreading sequences, their correlation properties affect the speed and the reliability of the mechanism employed

for achieving synchronization, so that chaos-based spreading may, again, offer advantages over classical ones.

Some dispersive channels, i.e. channels in which reflection, refraction and diffraction phenomena are non-negligible, have also been considered in connection with normal integrate-and-dump receivers [21, 22]. Furthermore, the case of the more complex rake receiver has been investigated. In this setting a FIR filter is put before a classical receiver, whose taps can be adapted on-line to follow the channel dispersion characteristics which are identified in parallel. A general method has been devised to adapt both sequences and receivers and optimize performance. Though in dispersive channels this method is approximate, theory predicts that it still results in better performance with respect to the conventional matched-filter policy usually adopted for rake-receivers [23]. Preliminary results on even more sophisticated architectures like parallel cancellers can be found in [26].

Beyond theoretical results, the performance improvement exploiting chaos-based techniques have been validated on field by measurement performed using an experimental set-up using low cost DSP boards. The results reported in [25] show that over non-selective channels, the ability of chaos-based spreading of minimizing MAI leads to an average improvement of 60% in P_{err} with respect to truncated m - and Gold sequences. Over selective channels, the possibility of jointly optimizing chaos-based spreading and rake receiver profiles leads to improvements of up to 22% in P_{err} with respect to systems with either conventional spreading or conventional rake policies.

Aim of this contribution is to review necessary steps to understand the methodology followed to achieve the previously mentioned results and to give a significative example of application of a procedure for controlling chaos statistics to a practical task.

The remaining of this chapter is organized as follows. In Section 2 we introduce the essential tools for computing statistical features from quantized trajectories generated by one-dimensional Piecewise Affine Markov (PWAM) chaotic maps. The section contains a simple and tutorially oriented bottom-up revisit of the concepts fully formalized in [21]: a suitable generalization of the widely employed Perron-Frobenius operator is here introduced and employed to find a way to compute high-order expectations of quantized chaotic trajectories. In Section 3, the channel and receiver models are illustrated to obtain a separate expression of all the components of the correlate-and-dump output before the hard decision block. These components are random variables whose sum is matched against a zero threshold to reconstruct the symbol. Their distribution affects the bit error probability, as considered in Section 4. Following an established path the Standard Gaussian Approximation (SGA) is adopted to tackle the cross- and self-interference terms, and, with some cautions, to the useful component. By exploiting this approximation, it is possible to simply express system performance as a function of the channel parameters, of the spreading sequence statistical features and of the

receiver FIR taps. In Section 5, such an expression is employed to state a simple constrained optimization problem in terms of the maximization of a cost function which combines multi-index quantities depending on the previous parameters. Such a problem is analytically solved to link the two design parameters (i.e. the spreading sequences and receiver FIR taps) to the channel characteristics. As a particular, but important case, it is shown that, when the channel is non-dispersive, such an optimization procedure yields the same result presented in [19] for the spreading sequences allowing the minimization of MAI.

In Section 6, the problem of designing chaotic maps able to generate spreading sequences with different correlation behaviors, and thus with different impact on the FIR optimization, is addressed. We show that, by properly choosing the structure of the chaotic map, we are able to generate optimal sequences when MAI is the unique cause of nonideality, and to jointly optimize sequences statistics and receiver FIR taps in case of selective channel. This result is the quantitative aspect of the general procedure that the ability of controlling the statistical features of signals benefits the mechanisms that process them.

In Section 7 details on a low-cost DSP-based DS-CDMA system implementation are shown, along with the measured bit error probability when classical m - and Gold and chaos-based sequences are employed for spectrum-spreading. Measured performance results to be in good agreement with the theoretical analysis. Finally, Section 8 reports some conclusive remarks.

2 Some Tools for Computing Expectations of Quantized Chaotic Trajectories

Sensitive dependence on initial conditions, probably the widest known characteristic of a chaotic system, makes it impossible to extract globally valid information from the study of single trajectories. On the contrary, considering the evolution of a non-vanishing set of points allows to track the complex dynamical mechanism causing the loss of information and to characterize it quantitatively [1, 2].

To follow this approach, consider a map $M : X = [0, 1] \mapsto X$ and indicate with M^k its k -th iterate. Let $\mathbb{D}(X)$ be the set of probability densities defined on X and assume that the initial condition x_0 is randomly drawn according to $\rho_0 \in \mathbb{D}(X)$. Then, the probability density regulating the distribution of the random point $x_k = M(x_{k-1}) = M^k(x_0)$ is $\rho_k = \mathbf{P}\rho_{k-1} = \mathbf{P}^k\rho_0$, where \mathbf{P} is the Perron-Frobenius operator [1, chap. 4]. Assume from now on that M is mixing, i.e. that a (natural) probability measure $\bar{\mu}$ exists such that $\bar{\mu}(A \cap M^{-k}(B)) \mapsto \bar{\mu}(A)\bar{\mu}(B)$ as $k \mapsto \infty$ for any set $A, B \subset X$, which roughly means that for large k the two events $\{x \in A\}$ and $\{M^k(x) \in B\}$ become statistically independent. For mixing maps, a unique invariant probability

density $\bar{\rho}$ exists such that $\mathbf{P}\bar{\rho} = \bar{\rho}$, and the natural measure can be expressed as $\bar{\mu}(A) = \int_A \bar{\rho}$.

Commonly, the study of this loss of statistical dependence is carried out by considering the quantity

$$\mathbf{E}[f(x_k)g(x_{k+q})] = \int_X f(x)g(M^q(x))d\bar{\mu}(x) \quad (1)$$

where $f, g : X \mapsto \mathbb{R}$ are two smooth functions. If one thinks of these function as *physical observable* of the system, then (1) quantifies the correlation between observing f at time k and g at time $k + p$.

For generic mixing maps, it is very difficult to compute $\mathbf{E}[f(x_k)g(x_{k+q})]$ and one is usually restricted to determine the rate $0 < r_{\text{mix}} < 1$ of geometric convergence of (1) to its limit value when $q \rightarrow \infty$, which is often referred to as the *rate of mixing* [2]. More formally, it can be shown that a constant $\alpha > 0$ exists such that

$$\left| \mathbf{E}[f(x_k)g(x_{k+q})] - \int_X f(x)d\bar{\mu}(x) \int_X g(x)d\bar{\mu}(x) \right| \leq \alpha \sup |f| \sup |g| r_{\text{mix}}^k \quad (2)$$

which highlights that the rate of mixing provides information on how quickly the system settles into a statistically regular behavior, and thus how quickly physical observables become uncorrelated.

Nevertheless, from an engineering point of view, the mere knowledge of r_{mix} and α cannot be considered as satisfactory. In fact, using (2) in the equations expressing the merit figure of a specific signal processing task as a function of statistical features of the chaotic sequences would simply yield to a (hopefully tight) *performance bound* (see e.g., [16, 18]).

On the contrary, the ability of computing the exact values of (1) would allow to analytically express the same merit figure as a function of the characteristics of M , which is surely the necessary starting point for any performance optimization procedure.

To follow this path, and to introduce the tools we need, we have to restrict the class of chaotic systems we are interested into. Consider a mixing map M , and let us assume that a Markov partition of X exists, namely that X can be divided into n intervals X_1, \dots, X_n such that, for any pair of indexes j_1 and j_2 either $X_{j_1} \subseteq M(X_{j_2})$ or $X_{j_1} \cap M(X_{j_2}) = \emptyset$. Then M is said to be a PWAM map if it is affine in each of the intervals X_{j_i} of a Markov partition. An example of piecewise map is shown in Fig. 1 (a).

For this kind of map, it is possible to give a simple matrix representation of \mathbf{P} . To this aim, let us introduce the so-called *kneading matrix* [2] which is defined componentwise as

$$\mathcal{K}_{j_1 j_2} = \frac{\mu(X_{j_1} \cap M^{-1}(X_{j_2}))}{\mu(X_{j_1})}$$

where μ is the usual interval measure, and whose entry in the j_1 -th row and j_2 -th column records the fraction of X_{j_1} that is mapped into X_{j_2} . From this

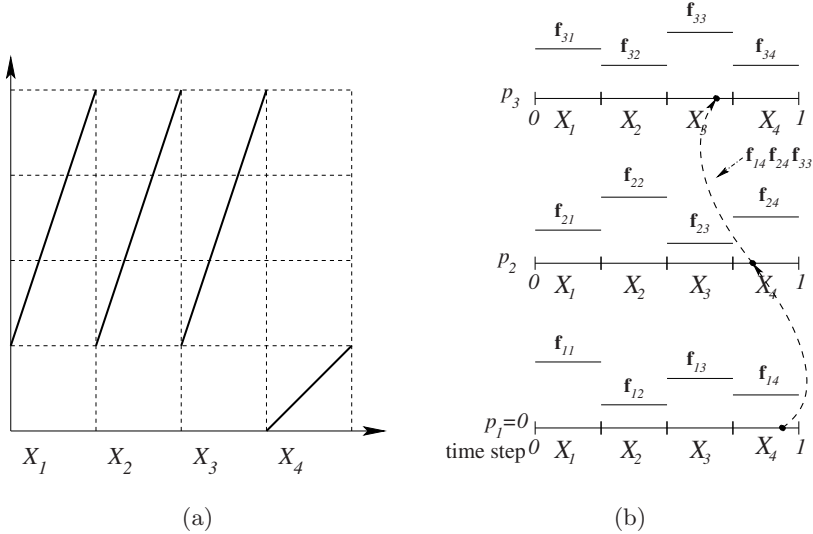


Fig. 1. (a) Sketch of a Piecewise Affine Markov map, and (b) Quantization of the state space at three different time steps along with two possible trajectories and the values associated to each of them

it easily follows that the sum of the row entries of any kneading matrix is always 1. It can be proved that \mathcal{K} is the restriction of the Perron-Frobenius operator to the space of functions which are constant in each X_{j_i} . As $\bar{\rho}$ for PWAM maps belong to that space it can be expressed as $\bar{\rho} = \sum_{i=1}^n e_i \chi_{X_i}$ where the vector $e = (e_1, \dots, e_n)$ is the (normalized) unique eigenvector of \mathcal{K} corresponding to a unit eigenvalue, i.e. $e = e\mathcal{K}$, and where χ_{X_i} is the characteristic function of X_i . Obviously such a simple representation of the Perron-Frobenius operator allow to devise a straightforward procedure to design a map with a prescribed piecewise-constant invariant probability density.

To give a closed form representation also to quantities such as (1), we need to introduce a suitable quantization of the chaotic map state space. Let us consider observables f_i which quantize the state at a given time step p_i , i.e let us assume that the function $f_i : [0, 1] \mapsto \mathbb{C}$ is constant in each of n intervals of the Markov partition. Define also the n -dimensional vector $f_i = (f_{i1}, \dots, f_{in})$ so that $f_i(X_j) = \{f_{ij}\}$; as an example, Fig. 1 (b) shows the functions f_1, f_2 and f_3 constant on each of the four interval of a partition of the state space. A different quantization is adopted at different time steps and different trajectories are associated to different values depending on which intervals they visit.

From now on, we will also assume that $\bar{\rho} = 1$, so that one easily gets that $e_i = 1$ and also the sum of the row entries of \mathcal{K} is always 1, i.e. \mathcal{K} is a doubly stochastic matrix. With this we are able to compute second-order expectation of quantized chaotic trajectories of the kind (1). More formally we have

Property 1. Consider a PWAM map with $\bar{\rho} = 1$ and where $\mu(X_j) = 1/n$ for $j = 1, \dots, n$. Then, for trajectories generated with $\rho_0 = \bar{\rho}$ one has

$$\mathbf{E}[f_1(x_{k+p_1})f_2(x_{k+p_2})] = \frac{1}{n} \langle \mathbf{f}_1 \otimes \mathbf{f}_2, \mathcal{K}^{p_2-p_1} \rangle = \mathbf{f}_1 \mathcal{K}^{p_2-p_1} \mathbf{f}_2^T$$

where $.^T$ indicates matrix transposition, and $\langle \cdot, \cdot \rangle$ and \otimes denotes the usual inner and outer product among vectors.

To show this, consider first that if $\rho_0 = \bar{\rho}$ it is very easy to show that the (quantized) chaotic sequences generated by M are second-order stationary, i.e. $\mathbf{E}[f_1(x_{k+p_1})f_2(x_{k+p_2})] = \mathbf{E}[f_1(x_0)f_2(x_q)]$, where $q = p_2 - p_1$. By its very definition one then has

$$\begin{aligned} \mathbf{E}[f_1(x_0)f_2(x_q)] &= \int_X f_1(\xi_1)f_2(M^q(\xi_1))\bar{\rho}(\xi_1)d\xi_1 \\ &= \int_{X \times X} f_1(\xi_1)f_2((\xi_2))\delta(\xi_2 - M^q(\xi_1))\bar{\rho}(\xi_1)d\xi_1d\xi_2 \end{aligned}$$

where the last equation holds thanks to the causality of the system and implicitly defines a two-steps Perron-Frobenius operator $\mathbf{P}^{0,q} = \bar{\mathbf{P}}^q : \mathbb{D}(X) \mapsto \mathbb{D}(X^2)$ such as $\bar{\mathbf{P}}^q[\bar{\rho}](\xi) = \bar{\rho}(\xi_1)\delta(\xi_2 - M^q(\xi_1))$, where $\xi = (\xi_1, \xi_2)$. This operator can be applied to the probability density $\bar{\rho}$ regulating the distribution of the points x_0 to obtain the probability density $\bar{\mathbf{P}}^q[\bar{\rho}]$ of the random vector (x_0, x_q) . By exploiting the particular choice of the observables, the previous expression can be recast as

$$= \sum_{j_1=1}^n \sum_{j_2=1}^n \mathbf{f}_{1j_1} \mathbf{f}_{2j_2} \int_{X_{j_1} \times X_{j_2}} \bar{\mathbf{P}}^q[\bar{\rho}](\xi) d\xi_1 d\xi_2$$

in which the integral term is nothing but the probability that a trajectory starting in X_{j_1} falls in X_{j_2} at time step q . Since $\bar{\rho} = 1$, the previous term can be further expressed as $\int_{X_{j_1} \cap M^{-q}(X_{j_2})} \bar{\rho}(\xi_1) d\xi_1 = \mu(X_{j_1} \cap M^{-q}(X_{j_2}))$. With this, and considering that [17] $\mu(X_{j_1} \cap M^{-p}(X_{j_2})) / \mu(X_{j_1}) = (\mathcal{K}^p)_{j_1 j_2}$, we have

$$= \sum_{j_1=1}^n \sum_{j_2=1}^n \mathbf{f}_{1j_1} \mathbf{f}_{2j_2} \mathcal{K}_{j_1 j_2}^q \mu(X_{j_1})$$

from which, since $\mu(X_j) = 1/n$ and collecting the values of the quantization at the different time steps in the matrix $\mathbf{f}_1 \otimes \mathbf{f}_2$, we finally obtain the thesis.

As it is formally proven in [21] and further exemplified in [24], the previous result can be further generalized obtaining a closed form expression

for computing the higher-order statistics of quantized chaotic processes. To this aim we have to introduce multi-index quantities that we will call *tensors* that generalize vectors and matrixes. Several kind of *products* can be defined among tensors and we may now define those that will be of use in the following discussion.

Given two m -order tensors \mathcal{A} and \mathcal{B} with identical index ranges, their *inner product* is a scalar defined as

$$\langle \mathcal{A}, \mathcal{B} \rangle = \sum_{j_1, \dots, j_m} \mathcal{A}_{j_1, \dots, j_m} \mathcal{B}_{j_1, \dots, j_m}$$

where every index sweeps all its range. The inner product is a commutative bilinear operator.

Given an m' -order tensor \mathcal{A} and an m'' -order tensor \mathcal{B} , their *outer product* is an $(m' + m'')$ -order tensor $\mathcal{C} = \mathcal{A} \otimes \mathcal{B}$ such that

$$\mathcal{C}_{j_1, \dots, j_{m'+m''}} = \mathcal{A}_{j_1, \dots, j_{m'}} \mathcal{B}_{j_{m'+1}, \dots, j_{m'+m''}}$$

where every index sweeps all its range. The outer product is a non-commutative, associative and bilinear operator.

Given the m' -order tensor \mathcal{A} and the m'' -order tensor \mathcal{B} such that the range of the last index of \mathcal{A} is the same of the first index of \mathcal{B} , their *chain product* is an $(m' + m'' - 1)$ -order tensor $\mathcal{C} = \mathcal{A} \circ \mathcal{B}$ such that

$$\mathcal{C}_{j_1, \dots, j_{m'+m''-1}} = \mathcal{A}_{j_1, \dots, j_{m'}} \mathcal{B}_{j_{m'+1}, \dots, j_{m'+m''-1}}$$

The chain product is a non-commutative associative bilinear operator.

The tensor products defined above enjoy few *distributive* properties which are recalled without proof in the following

Property 2. For any four tensors \mathcal{A} , \mathcal{B} , \mathcal{C} and \mathcal{D} whose index ranges make the equalities below well defined, we have

$$\begin{aligned} \mathcal{A} \otimes (\mathcal{B} \circ \mathcal{C}) &= (\mathcal{A} \otimes \mathcal{B}) \circ \mathcal{C} \\ \mathcal{A} \circ (\mathcal{B} \otimes \mathcal{C}) &= (\mathcal{A} \circ \mathcal{B}) \otimes \mathcal{C} \\ \langle \mathcal{A} \otimes \mathcal{B}, \mathcal{C} \otimes \mathcal{D} \rangle &= \langle \mathcal{A}, \mathcal{C} \rangle \langle \mathcal{B}, \mathcal{D} \rangle \end{aligned}$$

The adoption of the tensor-formalism allows to generalize the result of Property 1 to the computation of m -th order expectations of the quantized trajectories [21]. In fact, we may assume $p_1 = 0 < p_2 < \dots < p_m$ and indicate with $\bar{\mathbf{P}}^{p_2, \dots, p_m} : \mathbb{D}([0, 1]) \mapsto \mathbb{D}([0, 1]^m)$ an operator that is formally expressed for any $m - 1$ integers $p_2 < \dots < p_m$ as

$$\bar{\mathbf{P}}^{p_2, \dots, p_m} [\bar{\rho}] (\boldsymbol{\xi}) = \bar{\rho}(\boldsymbol{\xi}_1) \prod_{i=2}^m \delta(\boldsymbol{\xi}_i - M^{p_i - p_1}(\boldsymbol{\xi}_1))$$

and which represents the joint probability density of the random vector $(x_0, x_{p_2}, \dots, x_{p_m})$.

With this we obtain

$$\begin{aligned}\mathbf{E} \left[\prod_{i=1}^m f_i(x_{p_i}) \right] &= \int_{[0,1]^m} \prod_{i=1}^m f_i(\boldsymbol{\xi}_i) \bar{\mathbf{P}}^{p_2, \dots, p_m} [\bar{\rho}] (\boldsymbol{\xi}) d\boldsymbol{\xi} \\ &= \sum_{j_1=1}^n \cdots \sum_{j_m=1}^n \left[\prod_{i=1}^m f_{ij_i} \int_{X_{j_1} \times \cdots \times X_{j_m}} \bar{\mathbf{P}}^{p_2, \dots, p_m} [\bar{\rho}] (\boldsymbol{\xi}) d\boldsymbol{\xi} \right]\end{aligned}$$

where the integral term, which represents the probability that a trajectory starting in X_{j_1} pass through X_{j_2} at time step p_2 , through X_{j_3} at time step p_3 , etc, can be collected in a m -order tensor $\mathcal{H}^{p_2, \dots, p_m}$

$$\mathcal{H}_{j_1, \dots, j_m}^{p_2, \dots, p_m} = \int_{X_{j_1} \times \cdots \times X_{j_m}} \bar{\mathbf{P}}^{p_2, \dots, p_m} [\bar{\rho}] (\boldsymbol{\xi}) d\boldsymbol{\xi} \quad (3)$$

which will be indicated as the *symbolic dynamic tracking tensor* (SDTT).

Note now that the terms $\prod_{i=1}^m f_{ij_i}$ for j_1, \dots, j_m spanning the range $1, \dots, m$, can be also compounded in the m -order tensor $\mathcal{F} = \mathbf{f}_1 \otimes \cdots \otimes \mathbf{f}_m$, so that the expression of the m -th order moment is

$$\mathbf{E} \left[\prod_{i=1}^m f_i(x_{p_i}) \right] = \langle \mathcal{F}, \mathcal{H}^{p_2, \dots, p_m} \rangle \quad (4)$$

It can be proved that [21, 22], since we adopt piecewise-affine Markov maps, and as long $\bar{\rho} = 1$ and all the intervals X_j are equal, the SDTT can be factorized into smaller pieces by exploiting Property 2 so that (4) becomes

$$\mathbf{E} \left[\prod_{i=1}^m f_i(x_{p_i}) \right] = \frac{1}{n} \langle \mathcal{F}, \bigcirc_{i=2}^m \mathcal{K}^{p_i - p_{i-1}} \rangle \quad (5)$$

where \mathcal{K} is the kneading matrix defined above and the symbols \bigcirc represents the iterative application of the chain-product that is associative.

Under the assumption that let the factorization of the SDTT hold, we also know that [21, 22] if \mathcal{K} is primitive (i.e. a power of \mathcal{K} exists in which no entry is null), a family of matrixes $\mathcal{A}(p)$ exists such that

$$\mathcal{K}^p = \mathfrak{I} + \mathcal{A}(p)$$

with $\mathcal{A}(p)$ exponentially vanishing as $p \rightarrow \infty$ and $\mathfrak{I} = (1/n)\mathbf{1} \otimes \mathbf{1}$ with $\mathbf{1} = (1, \dots, 1)$.

With this and few tensor algebra manipulations exploiting the distributivity of the tensor products we may easily derive that any inner product of the kind $\langle \mathcal{F}, \mathcal{H}^{p_2, \dots, p_m} \rangle$ can be expressed as a weighted sum of terms of the kind $\langle \mathcal{F}, \mathcal{A}' \circ \mathcal{A}'' \circ \dots \rangle$. For example if $\sum_{j=1}^n f_{ij} = 0$ for $i = 1, \dots, m$ then we

may express the generic higher-order expectation term (5) as

$$\begin{aligned}
 \mathbf{E} \left[f_1(x_0) \prod_{i=2}^m f_i(x_{p_i}) \right] &= \frac{1}{n} \left\langle \bigotimes_{j=1}^m \mathbf{f}_j, \bigcirc_{j=2}^m \mathcal{A}(p_j - p_{j-1}) \right\rangle + \\
 \frac{1}{n^2} \sum_{k'}^{m-1} \left\langle \bigotimes_{j=1}^{k'} \mathbf{f}_j, \bigcirc_{j=2}^{k'} \mathcal{A}(p_j - p_{j-1}) \right\rangle &\left\langle \bigotimes_{j=k'+1}^m \mathbf{f}_j, \bigcirc_{j=k'+2}^m \mathcal{A}(p_j - p_{j-1}) \right\rangle + \\
 \frac{1}{n^3} \sum_{k'}^{m-2} \sum_{k''+1}^{m-1} \left\langle \bigotimes_{j=1}^{k'} \mathbf{f}_j, \bigcirc_{j=2}^{k'} \mathcal{A}(p_j - p_{j-1}) \right\rangle &\times \\
 \left\langle \bigotimes_{j=k'+1}^{k''} \mathbf{f}_j, \bigcirc_{j=k'+2}^{k''} \mathcal{A}(p_j - p_{j-1}) \right\rangle &\left\langle \bigotimes_{j=k''+1}^m \mathbf{f}_j, \bigcirc_{j=k''+2}^m \mathcal{A}(p_j - p_{j-1}) \right\rangle + \\
 \vdots &\quad \vdots \quad \vdots \quad (6)
 \end{aligned}$$

3 Asynchronous DS-CDMA Systems Model

Figure 2 reports the simplified baseband equivalent scheme of an asynchronous DS-CDMA system in which the carrier is common, U users are supposed, and t^u and θ^u indicate respectively the absolute delay and carrier phase of the u -th user signal. To model the transmission from mobile terminals to a fixed base-station, we will assume that the latter quantities are independent and uniformly distributed random variables. Additionally, we will assume the v -th user as the useful one.

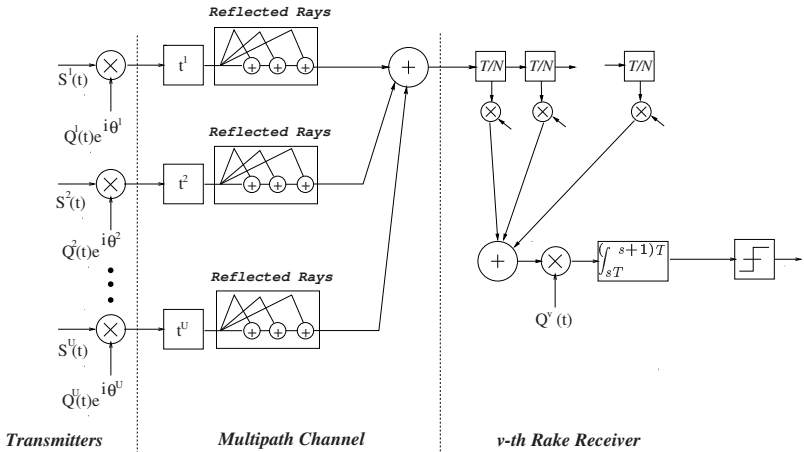


Fig. 2. Simplified baseband equivalent of a DS-CDMA system with a multipath channel

As far as transmitted signals are concerned, the u -th user information signal is $S^u(t) = \sum_{s=-\infty}^{\infty} S_s^u g_T(t - sT)$, where $g_T(t)$ is the rectangular pulse which is 1 within $[0, T]$ and vanishes otherwise. We will also assume that the bipolar information symbols S_s^u are independent and produced by perfectly uncorrelated sources.

The spreading signal depends on sequences of symbols x_s^u from the alphabet X which are mapped into $\{-1, +1\}$ by the function Q , and combined to form the signal $Q^u(t) = \sum_{s=-\infty}^{\infty} Q(x_s^u) g_{T/N}(t - sT/N)$. The signal $Q^u(t)$ is then multiplied by $S^u(t)$ and transmitted along the (equivalent) channel together with the spread-spectrum signals from the other users. Each user adopts a different spreading code, assigned at the connection start-up. Following the approach in [27, 28] we will assume that spreading sequences are periodic of a period equal to the spreading factor N .

We will model the selective fading communication channel as a linear time-varying propagation medium, where the multipath effect is due to the simultaneous presence of $\Lambda+1$ rays for each transmitted signal. For the generic u -th user the channel is described by the the following low-pass impulse response

$$h_c^u(t) = \beta_{-1}\delta(t) + \sum_{\tau=0}^{\Lambda} \beta_{\tau} a_{\tau}^u \delta\left(t - \tau \frac{T}{N}\right)$$

where $\delta(t)$ is the Dirac's generalized function, β_{-1}^2 is the direct ray power attenuation, $\beta_{\tau}^2 |a_{\tau}^u|^2$ is the instantaneous random power attenuation of the τ -th ray whose delay is $\tau T/N$. As thoroughly discussed in [29], considering ray delays multiple of the chip time leads to no loss of generality.

The random nature of the first and secondary rays, assumed independent from each others, is modelled by the complex random variables a_{τ}^u whose real and imaginary part are independent and Gaussian with zero mean and variance $1/2$.

This channel model is the same already used in [22] (with the exception of the truncation to Λ rays) and in [23] since, although not the most general possible setting, it allows to ease analytical computations and to better focus the impact of the adoption of chaos-based spreading.

We indicate with K the Rice factor, i.e. the ratio between the power of the first ray and the remaining rays, such that $\beta_{-1}^2 + \beta_0^2 = K \sum_{\tau=1}^{\Lambda} \beta_{\tau}^2$ with $(\beta_{-1}^2 + \beta_0^2)(K+1)/K = 1$. Furthermore, to consider what fraction of the main ray power is associated to random component we refer to a second similar quantity $\alpha = \beta_{-1}^2/\beta_0^2$. The channel adds up the contributions of all the users so that the baseband receiver is presented with a signal which is the sum of the convolutions of the signal transmitted by each user and the corresponding channel impulse response. Additionally, all the random variables describing the channel contributions will be considered independent.

To cope with the selective fading effect due to the multipath propagating channel it is common practice to employ a rake filter with the aim of collect-

ing time-scattered power before the signal undergoes common despreading operation. More specifically, consider the v -th users rake receiver shown on the right part of Fig. 2. The presence of a further FIR filter of coefficients $\gamma_{-1}, \gamma_0, \dots, \gamma_A$, implies that the channel is cascaded with a further linear system whose impulse response is

$$h_r^v(t) = \gamma_{-1} \delta\left(t - \Lambda \frac{T}{N}\right) + \sum_{\tau=0}^A \gamma_\tau (a_\tau^v)^* \delta\left(t - (\Lambda - \tau) \frac{T}{N}\right)$$

where \cdot^* stands for complex conjugation.

With this, the equivalent channel from the u -th transmitter to the v -th receiver has the impulse response

$$[h_c^u * h_r^v](t) = \delta\left(t - \Lambda \frac{T}{N}\right) * \sum_{\tau=-\Lambda}^A A_\tau^{uv} \delta\left(t - \tau \frac{T}{N}\right)$$

where the coefficients A_τ^{uv} identify an equivalent channel model between the u -th transmitter and the v -th receiver, whose expression can be derived by direct computation of the above convolution (see e.g. [23]). In such a model, the main ray has amplitude A_0^{uv} , and secondary rays are delayed by $\tau T/N$ for $\tau = \pm 1, \pm 2, \dots, \pm \Lambda$. In the following we will refer to this equivalent channel model and drop convolution with the term $\delta(t - \Lambda T/N)$ which accounts for the total transmission and filtering delay.

The joint effect of the channel and of the rake receiver on the final performance is obviously compounded in the statistics of the coefficients A_τ^{uv} . In particular, since the features of all the random variables a_τ^v and a_τ^u are known, it is possible to compute $\mathbf{E}[A_{\tau_1}^{uv} A_{\tau_2}^{uv}]$ and $\mathbf{E}[A_{\tau_1}^{uv} (A_{\tau_2}^{uv})^*]$ with respect to all these channel parameters, and to express them in terms of the parameters $\beta_{-1}, \beta_\tau, \gamma_{-1}, \gamma_\tau$ [23].

The output of the rake filter is fed into a multiplier which combines it with a synchronized replica of the spreading sequence of the v -th user and of an integrate-and-dump stage in charge of recovering the information symbol by correlation. Even if the unavoidable influence of thermal noise can be neglected, symbol extraction is corrupted by the presence of the delayed version of the useful signal and by the current and delayed signals transmitted by the other users, who acts as interferers for the useful one.

The key to estimate the performance of such a communication system is the knowledge of how much the non-useful signals affect the receiver output, i.e. of how much they are correlated with the spreading sequence of the useful user.

As correlation with a fixed sequence is a linear operation, error causes add at the receiver output Υ_s^v before the hard decision block of the useful v -th user, so that it can be decomposed into three main terms

$$\Upsilon_s^v = \Omega_s^v + \Xi_s^v + \Psi_s^v$$

where Ω_s^v is the main equivalent ray carrying the information to be retrieved, Ξ_s^v represents the disturbance due to the secondary equivalent rays carrying the previous symbols of the useful user, and Ψ_s^v is the disturbance due to the primary and secondary equivalent rays carrying the information transmitted by the other users.

To compute a closed form expression for the previous quantities, one needs to consider the contribution to the correlation with the spreading sequence of the v -th user of a complex signal with envelope ϵ coming from the u -th user with relative delay Δt . Such a contribution $\Theta_s^{uv}(\epsilon, \Delta t)$ can be expressed depending on the two symbols from the u -th transmitter that are overlapping with the generic s -th symbol from the v -th one, and whose choice is linked with the integer and fractional part of $\Delta t/T$ [16].

With this we may derive [23]

$$\begin{aligned}\Omega_s^v &= \frac{1}{2} \Theta_s^{vv}(A_0^{vv}, 0) = \frac{1}{2} S_s^v A_0^{vv} \\ \Xi_s^v &= \frac{1}{2} \sum_{\substack{\tau=-\Lambda \\ \tau \neq 0}}^{\Lambda} \Theta_s^{vv} \left(A_\tau^{vv}, -\tau \frac{T}{N} \right) \\ \Psi_s^v &= \frac{1}{2} \sum_{u \neq v} \sum_{\tau=-\Lambda}^{\Lambda} \Theta_s^{uv} \left(A_\tau^{uv} e^{i\theta^{uv}}, t^{uv} - \tau \frac{T}{N} \right)\end{aligned}\quad (7)$$

where i indicates the imaginary unit, θ^{uv} is the relative phase between the u -th and v -th users after demodulation and t^{uv} is the relative delay [16]. Assuming that the receiver is synchronized with the signal it is supposed to decode, we also have $\theta^{vv} = 0$ and $t^{vv} = 0$.

4 System Performance Merit Figure

In our investigations we assume that the speed of variation of the channel parameters is of the same order of the speed of variation of the transmitted signal. With this, expectations on both channel-related (i.e. delays and phases) and transmission-related (i.e. information symbols) random variables can be considered at the same time. These are the conditions under which the error probability P_{err} is the most sensible merit figure. Considering the threshold mechanism at the end of the receiver, we can express it as $P_{\text{err}}^v = \Pr\{\Upsilon_s^v < 0 | S_s^v = +1\}$.

A careful consideration of the nature of the interfering signals [23] reveals that Ξ_s^v is uncorrelated with Ω_s^v and that Ω_s^v and Ψ_s^{uv} are also uncorrelated, so that the computation of the previous quantity rely on the possibility to compute of the probability distribution of each of the three random variable composing Υ_s^v . To this aim, we mainly resort on the SGA, i.e. we assume that sums of independent random contributions are considered to be Gaussian random variables, characterized only by means of their average and variance.

The cross-interference term Ψ_s^v is made of contributions which are independent each of the other and of the useful one. Hence, we may consider it as a compound zero-mean Gaussian random variable characterized by its variance $(\sigma_\Psi^v)^2 = \mathbf{E}[|\Psi_s^v|^2]$. Hence, we may use SGA again to average over all the possible pairs of users, and obtain a unique σ_Ψ^2 (accounting for the average contribution to the error of the users interfering with the generic receiver) by simple multiplication by $U - 1$ [22]. With this we come up with

$$\begin{aligned} \sigma_\Psi^2 &= \frac{U-1}{24N^3} \left(\beta_{-1}^2 + \sum_{\tau=0}^A \beta_\tau^2 \right) \left(\gamma_{-1}^2 + \sum_{\tau=0}^A \gamma_\tau^2 \right) \times \\ &\quad \sum_{\tau=1-N}^{N-1} \mathbf{E}_{\underline{x}^u, \underline{x}^v}^{u \neq v} \left[\Gamma_{N,\tau}^2(\underline{x}^u, \underline{x}^v) + \operatorname{Re}[\Gamma_{N,\tau}(\underline{x}^u, \underline{x}^v) \Gamma_{N,\tau+1}^*(\underline{x}^u, \underline{x}^v)] \right] = \\ &\quad \frac{(U-1)c'}{4} \left(\beta_{-1}^2 + \sum_{\tau=0}^A \beta_\tau^2 \right) \left(\gamma_{-1}^2 + \sum_{\tau=0}^A \gamma_\tau^2 \right) \end{aligned}$$

where the quantity c' is implicitly defined by the last equality and Γ is the usual partial autocorrelation function $\Gamma_{N,\tau}(\underline{x}^u, \underline{x}^v) = \Gamma_{N,-\tau}(\underline{x}^v, \underline{x}^u) = \sum_{k=0}^{N-\tau-1} Q(x_k^u)Q(x_{k+\tau}^v)$ for $\tau = 0, 1, \dots, N-1$ and 0 otherwise.

What we obtain for σ_Ψ^2 is nothing but the term already considered in [16] and [17] to take co-channel interference into account which is here multiplied by the power gain of the actual channel and of an independent rake FIR.

To characterize the self interference term we need to follow a similar path first computing $(\sigma_\Xi^v)^2 = \mathbf{E}[|\Xi_s^v|^2]$ and then using again SGA to define a unique σ_Ξ^2 accounting for the average contribution of self-interference to the error on the generic receiver. By doing this, we are able to get [23]

$$\begin{aligned} \sigma_\Xi^2 &= \frac{1}{4} \sum_{\tau=1}^A \left[c''_\tau \left(\beta_{-1}^2 \gamma_\tau^2 + \beta_\tau^2 \gamma_{-1}^2 + \sum_{j=0}^{\Lambda-\tau} \beta_j^2 \gamma_{j+\tau}^2 + \beta_{j+\tau}^2 \gamma_j^2 \right) + \right. \\ &\quad \left. 2c'''_\tau \left(\beta_{-1} \beta_\tau \gamma_{-1} \gamma_\tau + \sum_{j=0}^{\Lambda-\tau} \beta_j \beta_{j+\tau} \gamma_j \gamma_{j+\tau} \right) \right] \end{aligned}$$

where $c''_\tau = (\mathbf{E}_{\underline{x}^v}[\Gamma_{N,N-\tau}^2(\underline{x}^v, \underline{x}^v)] + \mathbf{E}_{\underline{x}^v}[\Gamma_{N,\tau}^2(\underline{x}^v, \underline{x}^v)])/(2N^2)$ for $\tau > 0$ and $c''_0 = 1$ for $\tau = 0$ and $c'''_\tau = (\mathbf{E}_{\underline{x}^v}[\Gamma_{N,\tau}^2(\underline{x}^v, \underline{x}^v)])/(2N^2)$.

The treatment of the useful component Ω_s^v requires additional considerations and its approximation as a Gaussian random variable must be considered with care. A discussion of this kind of approximation can be found in [23]. We here exploit it to its ultimate consequences to derive that, if also the last variable can be considered Gaussian with variance σ_Ω^2 , then the bit error probability can be surely given an expression of the kind

$$P_{\text{err}} = \frac{1}{2} \operatorname{erfc} \sqrt{\rho} \tag{8}$$

for a signal-to-interference ratio (SIR) ρ defined as

$$\rho = \frac{\mathbf{E}[\Omega_s | S_s = +1]^2}{2(\sigma_{\Omega}^2 + \sigma_{\Psi}^2 + \sigma_{\Xi}^2)} \quad (9)$$

5 Performance Optimization in Dispersive and Non-Dispersive Channels

To optimize the final performance we may consider the expressions for $\mathbf{E}[\Omega_s | S_s = +1]^2$, σ_{Ω}^2 , σ_{Ψ}^2 and σ_{Ξ}^2 and define the vectors $\beta = (\beta_1, \dots, \beta_{A+2}) = (\beta_{-1}, \beta_0, \dots, \beta_A)$ and $\gamma = (\gamma_1, \dots, \gamma_{A+2}) = (\gamma_{-1}, \gamma_0, \dots, \gamma_A)$. Then, it is convenient to define the $(A+1) \times (A+1)$ square matrix \mathcal{A} as

$$\mathcal{A}_{j_1, j_2} = \begin{cases} \sum_{l=-1}^A \left[(U-1)c' + (1 - \delta_{l,1}\delta_{j_1,1})c''_{|l-j_1|} \right] (\beta_l)^2 & \text{if } j_1 = j_2 = -1, \dots, A \\ 2c'''_{|j_1-j_2|} \beta_{j_1} \beta_{j_2} & \text{if } j_1 \neq j_2 \end{cases}$$

where $\delta_{.,.}$ is the usual Kronecker's symbol, and obtain

$$\rho = \frac{1}{2} \frac{(\beta^T \gamma)^2}{\gamma^T \mathcal{A} \gamma} \quad (10)$$

It is worthwhile to notice that in (10) we have expressed $\rho = \rho(\mathcal{A}(\beta), \beta, \gamma)$ identifying the three factors affecting the performance, i.e. the statistics of the spreading sequences (\mathcal{A}), the channel power profile (β) and the rake power profile (γ).

Note also that, according to the physical intuition behind this dependence, $\rho(\mathcal{A}(\xi'\beta), \xi'\beta, \xi''\gamma) = \rho(\mathcal{A}(\beta), \beta, \gamma)$ for any $\xi', \xi'' \neq 0$, since channel and receiver gain cannot affect the SIR.

The maximization of ρ can be now simplified exploiting this double scale-invariance of ρ and setting, without any loss of generality, $\beta^T \beta = 1$ and $\beta^T \gamma = 1$. With this the numerator in the expression of ρ is fixed and we may maximize it solving the minimization problem

$$\min_{\gamma} \quad \gamma^T \mathcal{A} \gamma \quad \text{s.t.} \quad \beta^T \gamma = 1$$

whose solution gives the optimal receiver FIR taps $\hat{\gamma}$ [30]

$$\hat{\gamma} = \frac{\mathcal{A}^{-1} \beta}{\beta^T \mathcal{A} \beta} \quad (11)$$

Note that the above solution relies on the possibility of extracting averages of the incoming signal and thus of estimating the transfer function of the channel. Methods for this do exist, are commonly assumed available in the

classical rake receiver Literature, and we assume that the resulting estimation is reliable.

Note that such an optimization depends on \mathcal{A} and thus on the statistical properties of the spreading sequences and this offer room for further optimization if one may design sequences generators with prescribed statistical features, as it is possible in the chaos-based setting described in the next section. Additionally such a remark allow us to comment about the significance of (11) in some particular but important settings.

When information about the correlation of the spreading sequences is not available, one may assume that all the disturbances are white and thus proceed by maximization of the magnitude of the useful component in (9) $\mathbf{E}[\Omega_s^v | S_s^v = +1] = (1/2)\boldsymbol{\beta}^T \boldsymbol{\gamma}$ only. As, under these assumptions, the power gain of the receiver acts both on the useful component and on the white disturbance, maximization can be performed for a unit power gain receiver as in

$$\max_{\boldsymbol{\gamma}} \quad \boldsymbol{\beta}^T \boldsymbol{\gamma} \quad \text{s.t.} \quad \boldsymbol{\beta}^T \boldsymbol{\gamma} = 1$$

which, when $\boldsymbol{\beta}^T \boldsymbol{\beta} = 1$, has the trivial solution $\hat{\boldsymbol{\gamma}} = \boldsymbol{\beta}$, as it would happen in a conventional rake receiver.

Consider now the much simpler case of a non-dispersive channels, where $\beta_\tau = 0$ for $\tau \geq 0$ and $\beta_{-1} = 1$. Hence the constraint $\boldsymbol{\beta}^T \boldsymbol{\gamma} = 1$ sets $\gamma_\tau = 0$ for $\tau \geq 0$ and $\gamma_{-1} = 1$ to avoid resorting to rake-receivers for a non-dispersive channel. With this (10) is greatly simplified and ρ is maximized when the single quantity $\mathcal{A}_{-1,-1} = (U - 1)c'$ is minimized.

Details of such a minimization in the more general context of complex spreading sequences can be found in [19] and [22]. It is here enough to recall that if all the sequences can be thought as independent and if they satisfy a mild form of second-order stationarity, namely $\mathbf{E}_{\underline{x}^u}[Q(x_m^u)Q^*(x_n^u)] = \mathbf{E}_{\underline{x}^u}[Q(x_0^u)Q^*(x_{|n-m|}^u)]$ then, setting $h = 2 - \sqrt{3}$ the previous expression reaches a minimum given by

$$(U - 1) \frac{\sqrt{3}}{3N} \frac{h^{-2N} - h^{2N}}{h^{-2N} + h^{2N} - 2} \quad (12)$$

when the sequence are characterized by a real, almost-exponential, sign-alternating autocorrelation profile given by

$$\mathbf{E}_{\underline{x}^u}[Q(x_0^u)Q^*(x_\tau^u)]^{\text{opt}} = (-1)^\tau \frac{N}{N - \tau} \frac{h^{\tau - N} - h^{N - \tau}}{h^{-N} - h^N} \stackrel{N \text{ large}}{\simeq} (-h)^\tau \quad (13)$$

It is also important to notice that, since non-dispersive channels attach no randomness to the useful component (7) results $\Omega_s^v = 1/2S_s^v$, and the approximation that consider it as a Gaussian random variable is unnecessary. Hence, under the only assumption of Gaussian interference, we are able to identify the absolute optimum choice for spreading sequences. Since for any

practical N (12) is approximately $(U - 1)\sqrt{3}/(3N)$, i.e. 15% less than $2(U - 1)/(3N)$ (the classical merit figure for ideal random sequences), a definite improvement is demonstrated.

6 Chaos-Based Generation of Optimized Spreading Sequences

For generating spreading sequences with chaotic maps, let us set $X = [0, 1]$ and consider a one-dimensional chaotic system (map) $x_{k+1} = M(x_k)$ which is iterated $N - 1$ times starting from an initial condition x_0^u which is randomly and independently drawn for each users according to a uniform probability density. The trajectory is quantized by a function $Q : [0, 1] \mapsto \{-1, +1\}$.

Here, we assume that such a quantization is such that n is an even integer and that all the points in the intervals $X_j = [(j - 1)/n, j/n]$ with $j = 1, \dots, n/2$ or $j = n/2, \dots, n$ are mapped by Q to the same symbol.

We also refer to a particular family of maps which has been thoroughly characterized in [18], [21], [22], namely the so called (n, t) -tailed shifts defined as

$$M(x) = \begin{cases} (n - t)x \pmod{\frac{n-t}{n}} + \frac{t}{n} & \text{if } 0 \leq x < \frac{n-t}{n} \\ t(x - \frac{n-t}{n}) \pmod{\frac{t}{n}} & \text{otherwise} \end{cases}$$

for $t < n/2$. The family of (n, t) -tailed shifts includes some of the maps already analyzed in the chaos-based DS-CDMA framework [16] like the n -way Bernoulli shift (which is a $(n, 0)$ -tailed shift) and the n -way tailed shift (which is a $(n, 1)$ -tailed shift). Figure 1 (a) show the graphics of a $(4, 1)$ -tailed shift.

We are here interested in computing the entries of the matrix \mathcal{A} , i.e. the three quantities c' , c''_τ and c'''_τ that depend on the expectations $\mathbf{E}_{\underline{x}^v}[\Gamma_{N,\tau}^2(\underline{x}^v, \underline{x}^v)]$ and $\mathbf{E}_{\underline{x}^u, \underline{x}^v}[\Gamma_{N,\tau}(x^u, x^v)\Gamma_{N,\tau+l}(x^u, x^v)]$ for $l = 0$ and $l = 1$. To compute such expressions we may substitute the definition of $\Gamma_{N,\tau}(x^u, x^v)$ and perform a simple but lengthy algebraic expansion to obtain multiple sums of terms of the kind $\mathbf{E}_{\underline{x}^v}[Q(x_0^v)Q(x_{\tau_1}^v)]$ and $\mathbf{E}_{\underline{x}^v, \underline{x}^u}[Q(x_0^v)Q(x_{\tau_1}^v)Q(x_{\tau_2}^v)Q(x_{\tau_3}^v)]$.

As Q may assume only 2 different values, these expectations can be rewritten as a sum of the values associated to any possible product of Q multiplied by their probability which is the joint probability that the evolution of the map state belongs to certain intervals at certain time instants.

To compute these probabilities we may exploit the detailed analysis of the statistical features of (n, t) -tailed shifts carried out in [3, 18, 24] and based on the tensor approach recalled in Section 2 and on the expression (6) in particular. The key property used in those works is that (n, t) -tailed shifts are piecewise-affine Markov maps, i.e. that the statistical features of their trajectories can be studied referring to an “equivalent” Markov chain with n states (one for each interval X_j).

When $n > 2t$, straightforward but lengthy manipulations developed in [3, 18, 24] we are able to compute

$$\mathbf{E}_{\underline{x}^v} [\Gamma_{N,\tau}^2(\underline{x}^v, \underline{x}^v)] = (N - \tau) + [(N - \tau)^2 - (N - \tau)]r^{2\tau}$$

and, for $l = 0$ and $l = 1$,

$$\begin{aligned} \mathbf{E}_{\underline{x}^u, \underline{x}^v}^{u \neq v} [\Gamma_{N,\tau}(\underline{x}^u, \underline{x}^v)\Gamma_{N,\tau+l}(\underline{x}^u, \underline{x}^v)] &= (l+1)(N - \tau - l)r^l + \\ &2 \frac{r^{2+l}}{(1-r^2)^2} \left[(1-r^2)(N - \tau - l) + r^{2(N-\tau-l)} - 1 \right] \end{aligned}$$

where the number $r = -t/(n-t)$ is a map design parameter.

Note that, as needed, these expressions are the link between n and t and the quantities c' , c''_τ and c'''_τ that are assumed known in the optimization of the receiver FIR in the previous sections.

In fact, for each r (and thus for each sequence generation mechanism) the optimization procedure sketched in Section 5 gives us the best receiving filter and thus the lowest achievable P_{err} . This information can be used to iteratively search for that r whose corresponding optimum filter results in the minimum P_{err} thus simultaneously optimizing sequence generation and receiver taps. We will call this system OCOR, i.e. Optimal Chaos with Optimal Rake. Among the other possible option to test, we restrict ourselves to test the most interesting ones in a multipath propagation channel, namely OCCR (Optimal Chaos with Conventional Rake) and NCOR (No Chaos with Optimal Rake) as well as NCCR (No Chaos with Conventional Rake) where non-chaotic sequences are assumed to be a good approximation of the purely random case as, for example, m - or Gold codes (see e.g. [16] and references therein).

Performance of the different systems is reported in Fig. 3 for two different channel configurations, i.e. $\beta_k \propto e^{-k}$, $K = 1$, and α spanning $[0.1, 10]$ for the first case while $\alpha = 1$, and K spanning $[0.1, 10]$ for the second one. As can be easily seen, even if gains depend on the channel configuration, the relative ranking is always the same, namely $P_{\text{err}}^{\text{NCCR}} > P_{\text{err}}^{\text{OCCR}} > P_{\text{err}}^{\text{NCOR}} > P_{\text{err}}^{\text{OCOR}}$. We may therefore conclude that the adoption of chaos always benefits the overall performance even though the largest improvement is due to the availability of an optimization of the rake receiver taps.

In non-dispersive channels, no rake receiver is needed and (n, t) -tailed shift allow the absolute optimization of performance. In fact, for any given n , we may chose t as the integer closest to $nh/(1+h)$ so that $r \simeq -h$, the accuracy being obviously improved as $n \rightarrow \infty$. With this, the autocorrelation profile of the generated sequences matches (13) with a negligible error in practically any operation conditions. This is exemplified in Fig. 4 (a) which shows the trend of $\sigma_\psi^2/(U-1)$ as a function of r ; trivial visual inspection is sufficient to verify the match between the theoretical prediction and the actual data proving that the optimal profile (13), corresponding to the minimum of $\sigma_\psi^2/(U-1)$, can be practically achieved by sequences generated by an $(10, 2)$ -tailed shift. The

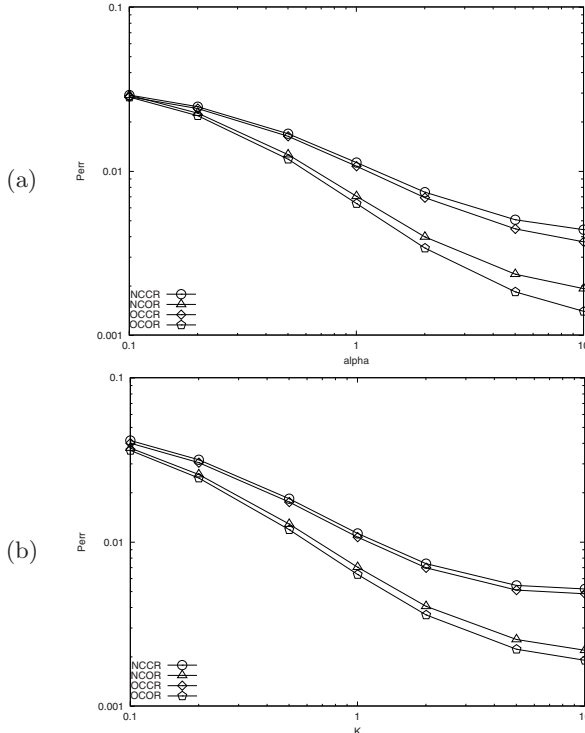


Fig. 3. Performance of different systems for different channel configurations and different systems with $\beta_k \propto e^{-k}$ (a) $K = 1$, $\alpha \in [0.1, 10]$, (b) $\alpha = 1$, $K \in [0.1, 10]$; NCCR=pseudo-random with classical rake, NCOR=pseudo-random with optimized rake, OCCR=optimized chaotic with classical rake, OCOR=optimized chaotic with optimized rake.

achievable advantage of chaos-based spreading is further highlighted in Fig. 4 (b) which shows P_{err} computed using (8), (9) as a function of the number of users U . As can be seen, employing chaos-based sequences generated allows, for any fixed quality of the communication link (e.g., $P_{\text{err}} = 10^{-3}$), to increase the number of users that can be allocated in the system (e.g., from 18 to 21) with respect to the case of conventional m - (and Gold) sequences.

7 Chaos-Based DS-CDMA System Prototype and Measurement Results

With the aim of obtaining a first and effective confirmation of the theoretical results reported in the previous Sections, we realized a low-cost prototype of the communication system using TMS320C542 DSP boards. A picture of the whole system is reported in Fig. 5 (a).

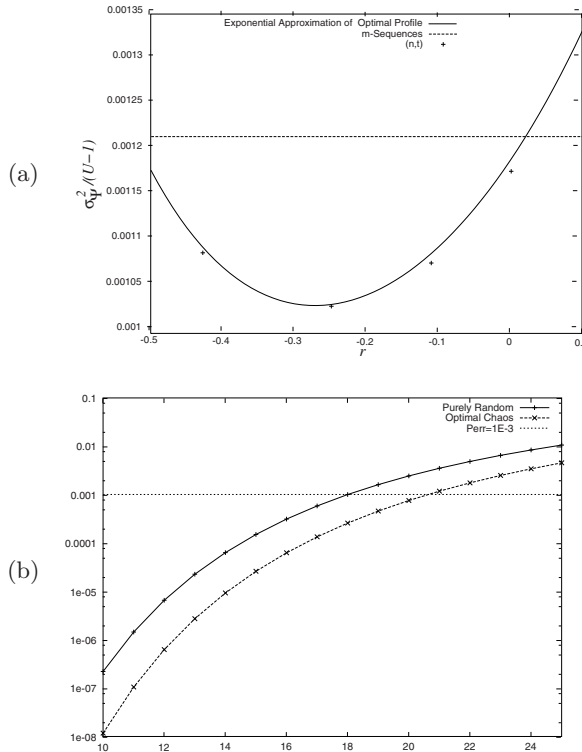


Fig. 4. (a) Plot of $\sigma_y^2/(U-1)$ as a function of r for the exponential approximation of (13), the classical m -sequences and chaos-based ones obtained by using $(10, 0)$ -, $(10, 1)$ -, $(10, 2)$ -, and $(10, 3)$ -tailed shifts; (b) Comparison of the P_{err} when classical m -sequences or the optimal ones (generated by $(10, 2)$ -tailed shifts) are adopted for spreading, as a function of the number of user U

Transmitter boards are in charge of generating baseband signals, of their BPSK modulation and of the simulation of the channel. No external RF circuit has been included in this low-cost realization. One board is devoted to the implementation of the useful transmitter, one board is devoted to the implementation of the corresponding receiver and of the estimator of the bit error rate while all the other boards can be used to account for multiple access interference.

Spreading sequences are generated off-line and stored in the transmitters. A copy of the useful sequences is also stored in the receiver. At symbol rate, information bits are locally generated. They are multiplied by the spreading sequence thus generating data at chip rate that are fed into a quadrature implementation of the five-taps ($A = 4$) complex FIR simulating the channel.

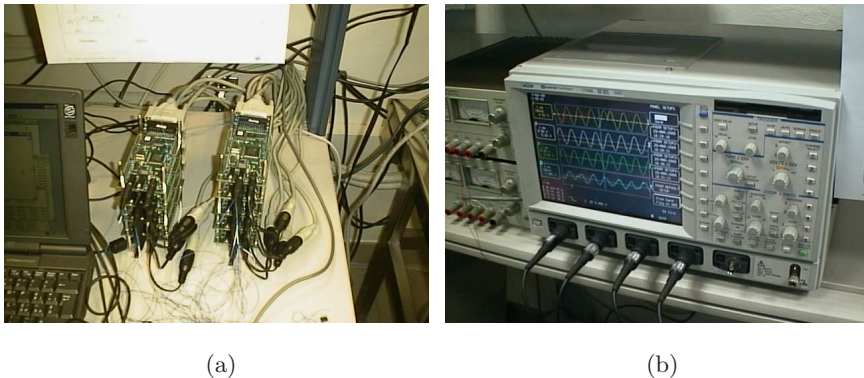


Fig. 5. (a) Experimental set-up of the DS-CDMA communication system prototype and its schematic representation and (b) oscilloscope waveforms of (top to bottom) the BPSK transmitted signal of 3 different users (transmitter and 2 interferes) and of the received signal

The two baseband components are then multiplied by stored samples of *sin* and *cos* to generate the passband signals that are added and converted into the analog output of the transmitter. The offsets in the *sin* and *cos* table can be adjusted to account for different time-varying delays and carrier phases in the interfering transmitters, they are kept constant in the useful transmitter.

The same structure is replicated for the interfering transmitters in which a randomly variable delay and a random carrier phase are also introduced to account for the asynchronous environment. The delay and carrier phase is obtained in the digital chain by means of the adjustable offsets in the *sin* and *cos* table. In the transmitters, digitally generated pseudo-random variables are used to generate information bits, generate and update real and imaginary parts of the channel FIR taps once every u_c bits, as well as to possibly generate and update interferer delays and carrier phases once every u_i bits.

The signal arriving at the receiver is converted into digital and fed into a quadrature demodulator relying again on *cos* and *sin* tables and on accumulators. This produces two streams of samples at chip-rate which are separately processed by a quadrature implementation of the rake FIR and finally summed. The output of the rake is then fed into the correlation-based despreader and in the decision block.

To ensure correct operation of the receiver, it must be synchronized with the transmitter and the channel taps have to be perfectly identified. In addition, to ascertain if the received bit is identical to the transmitted one the information stream generated at the transmitter must be also available. In fact, the two bit streams must be compared to compute the bit error rate.

As far as all the quantities depending on digital pseudo-random variables are concerned, we use a suitable digital generator addressing the trade-off between randomness and fixed-point computation whose seed is common to both the transmitter and receiver.

As far as the time-synchronization is concerned, the D/A converter of the useful transmitter and the A/D converter of the receiver share the same timing signals. In addition, at startup, a simple handshake is initiated relying on two more wires carrying interrupt signals from one board to the other.

7.1 Performance over non-dispersive channel

The prototype system has been first exploited to test performance of chaos-based DS-CDMA systems when no multipath is present. In this case $\Lambda = 1$, $K = \alpha = \infty$.

Figure 5 (b) shows, from top to bottom, the signal at the output of the transmitter, of two different interferes and at the input of the receiver. Table 1 compares the measured bit error rate when the prototype system is operated for 2×10^6 bits for $U = 6$, $N = 15$ and $N = 20$, and $u_i = 10$. For every configuration performance is averaged over 100 sequence sets and considering the average P_{err} experienced by every user.

Table 1. Theoretical and measured P_{err} with non-dispersive channel

| | N | $P_{\text{err}} \times 10^3$ | |
|--------------------------------------|-----|------------------------------|---------|
| | | Theory | Measure |
| Conventional Purely Random Sequences | 15 | 13.5 | 16.2 |
| Optimal Chaos-based Sequences | 15 | 6.33 | 6.52 |
| Conventional Purely Random Sequences | 20 | 2.66 | 3.81 |
| Optimal Chaos-based Sequences | 20 | 0.98 | 1.46 |

Results confirm the fact that chaos-based DS-CDMA outperform classical DS-CDMA of approximately 60%. Also quantitative theoretical predictions are in good agreement with experimental results.

7.2 Performance over exponential channel

To test performance over a dispersive channel we choose an exponential power profile characterized by $K = 1$, $\alpha = 10$, $\Lambda = 4$ and $\beta_k \propto e^{-k}$.

We used all the available interfering boards for a total of $U = 8$. We also have $N = 15$, and $u_c = u_i = 3$. The number of transmitted bits per configuration was 2×10^6 . For every configuration performance is averaged over 100 sequence sets. For every sequence set the average P_{err} experienced by all the user is considered.

Table 2. Theoretical and simulated P_{err} over a dispersive channel with exponential power profile

| Optimal r | $P_{\text{err}} \times 10^2$ | |
|-------------|------------------------------|---------|
| | Theory | Measure |
| OCOR | -0.217 | 2.22 |
| NCOR | na | 2.65 |
| OCCR | -0.192 | 3.02 |
| NCCR | na | 3.42 |
| | | 3.77 |

Again, results confirm the fact that chaos-based DS-CDMA outperforms classical DS-CDMA up to 22% and that the adoption of non-conventional and carefully designed receiver filters also contributes non-negligibly to the quality of the communication.

8 Conclusions

The main goal of the chapter is to apply the possibility to control the statistical features of quantized sequences generated by a chaotic map to the performance optimization in asynchronous DS-CDMA systems. To this aim we first report the formalization of a set of tools allowing the explicit computation of high-order expectations of quantized trajectories generated by chaotic maps. To do so, a suitable generalization of the Perron-Frobenius operator is introduced whose quantization reveals the tensor structure of the expectations.

As an example application, the cross- and self-interference terms appearing in the performance evaluation of a chaos-based DS-CDMA system affected by multipath are given closed analytical forms and employed to estimate the average bit error probability as a function of the characteristics of the channel, of the chaos-based spreading sequences and of the receiver FIR filter.

The knowledge of the previous expression as well as the possibility to control of statistics of the generated sequences allowed also to show that performances can be optimized by means of careful joint design of the spreading sequences and of the adaptation policy of the rake receiver.

A prototype asynchronous DS-CDMA system was built compounding commercially available DSP boards. Their programmability gives the flexibility needed to try different spreading sequences as well as different scenarios. The prototype system was first used to assess the real-world applicability of optimal spreading sequences whose existence is predicted by the theory when MAI is the dominant cause of transmission errors. Then we tested the more sophisticated case in which a non-conventional adaptation policy is applied to a rake receiver in charge of countering multipath effects.

In all tested cases, chaos-based spreading and related methodologies offered non-negligible improvement to any combination of classical solutions.

References

1. Lasota, A., Mackey, M. C., (1994) Chaos, Fractals, and Noise. New York: Springer-Verlag
2. Baladi, V. (2000), Positive Transfer Operator and Decay of Correlations. Singapore: World Scientific
3. Setti, G., Mazzini, G., Rovatti, R., Callegari, S. (2002) Statistical modeling of discrete-time chaotic processes: Basic finite-dimensional tools and applications. Proceedings of the IEEE, 662–690
4. Rovatti, R., Mazzini, G., Setti, G., Giovanardi, A. (2002) Statistical modeling of discrete-time chaotic processes: Advanced finite-dimensional tools and applications, Proceedings of the IEEE, 820–841
5. Götz, M., Kelber, K., Schwarz, W. (1997) Discrete-time chaotic encryption systems - Part I: Statistical design approach. IEEE Trans. Circ. Syst.-I, **44**:963–970
6. Nikolaidis, N., Tsekereidou, S., Nikolaidis, A., Tefas, A., Solachidis, V., Pitas, I. (2000) Applications of chaotic signal processing techniques to multimedia watermarking, In Proc. of NDES2000, Catania, 1–7
7. Erramilli, E., Slingh, P. (1995) An application of deterministic chaotic maps to model packet traffic. Queuing Systems, **20**:171–206
8. Kohda, T., Tsuneda, A. (1997) Statistics of chaotic binary sequences. IEEE Trans. Infor. Theory, **43**:104–112
9. Schimming, T., Dedieu, H., Hasler, M., Ogorzalek, M. (2000) Noise filtering in chaos-based communication. In Chaotic Electronics for Telecommunications, ed. by Kennedy, M. P., Rovatti, R., Setti, G. Boca Raton, FL: CRC Press, Chap 8
10. Setti, G., Balestra, M., Rovatti R. (2000) Experimental verification of enhanced electromagnetic compatibility in chaotic FM clock signals. In Proc. of ISCAS, Geneva, vol. III, 229–232
11. Deane, J. H. B., Hamill, D. C. (1996) Improvement of power supply EMC by chaos. Electr. Lett., **32**:1045
12. Baranowski, A. L., Mögel, A., Schwarz, W., Woywode, O. (2000) Statistical analysis of a dc-dc converter. In Proc. of ISCAS, Geneva, vol. II, 108–111
13. Kennedy, M. P., Rovatti, R., Setti, G. (eds.) (2000) Chaotic Electronics in Telecommunications. Boca Raton, FL: CRC Press
14. Kohda, T., Tsuneda, A., Sakae, T. (1992) Chaotic binary sequences by Chebyshev maps and their correlation properties. In Proc. of IEEE 2nd Int. Symposium on Spread Spectrum Techniques and Applications, 63–66
15. Kohda, T., Tsuneda, A. (1994), Explicit evaluations of correlation functions of Chebyshev binary and bit sequences based on Perron-Frobenius operator. IEICE Trans. Fundamentals, **E77-A**:1794–1800
16. Mazzini, G., Setti, G., Rovatti, R. (1997), Chaotic complex spreading sequences for asynchronous CDMA - Part I: System modeling and results. IEEE Trans. Circ. Syst.-I, **44**(10):937–947
17. Rovatti, R., Setti, G., Mazzini, G. (1998) Chaotic complex spreading sequences for asynchronous CDMA - Part II: Some theoretical performance bounds. IEEE Trans. Circ. Syst.-I, **45**(4):496–506
18. Rovatti, R., Mazzini, G., Setti, G. (2000) Interference bounds for DS-CDMA systems based on chaotic piecewise-affine Markov maps. IEEE Trans. Circ. Syst.-I, **47**:885–896

19. Mazzini, G., Rovatti, R., Setti, G. (1999) Interference minimization by autocorrelation shaping in asynchronous DS-CDMA systems: Chaos-based spreading is nearly optimal. *Electr. Lett.*, **35**:1054–1055
20. Setti, G., Mazzini, G., Rovatti, R. (1999) Chaos-based spreading sequence optimization for DS-CDMA synchronization. *IEICE Trans. Fundamentals*, **E82-A**(9):1737–1746
21. Rovatti, R., Mazzini, G., Setti, G. (2000) A tensor approach to higher-order expectations of quantized chaotic trajectories - Part I: General theory and specialization to piecewise affine Markov systems. *IEEE Trans. Circ. Syst.-I*, **47**:1571–1583
22. Mazzini, G., Rovatti, R., Setti, G. (2000) A tensor approach to higher-order expectations of quantized chaotic trajectories - Part II: Application to chaos-based DS-CDMA in multipath environments. *IEEE Trans. Circ. Syst.-I*, **47**:1584–1597
23. Rovatti, R., Mazzini, G., Setti, G. (2001) Enhanced rake receivers for chaos-based DS-CDMA. *IEEE Trans. Circ. Syst.I*, **48**:818–829
24. Setti, G., Rovatti, R., Mazzini, G. (2001) Tensor-based theory for quantized piecewise-affine Markov systems: Analysis of some map families. *IEICE Trans. Fundamentals*, **84**(9):2090–2100
25. Mazzini, G., Rovatti, R., Setti, G. (2001) Chaos-based asynchronous DS-CDMA systems and enhanced rake receivers: Measuring the improvements. *IEEE Trans. Circ. Syst.-I*, **48**:1445–1453
26. Mazzini, G., Rovatti, R., Setti, G. (2000) The impact of chaos-based spreading on parallel DS-CDMA cancellers. In Proc. of NOLTA, Dresden
27. Pursley, M. B. (1977) Performance evaluation for phase-coded spread-spectrum multiple-access communication - Part I: System analysis. *IEEE Trans. Communications*, **25**:795–799
28. Mazzini, G., Tralli, V. (1998) Performance evaluation of DS-CDMA systems on multipath propagation channels with multilevel spreading sequences and rake receivers. *IEEE Trans. Communications* **46**:244–257
29. Ochsner, H. (1987) Direct sequence spread-spectrum receiver for communication on frequency selective fading channels. In Proc. of IEEE JSAC, **5**:188–193
30. Eiselt, H. A., Pederzoli, G., Sandblom, C. L. (1987) Continuous Optimization Models. Berlin: de Gruyter

Calculation and Control of Unstable Periodic Orbits in Piecewise Smooth Dynamical Systems

Tetsushi Ueta¹, Tohru Kawabe², Guanrong Chen³, and Hiroshi Kawakami¹

¹ Tokushima University, Tokushima 770-8506, Japan
tetsushi@risa.is.tokushima-u.ac.jp

² University of Tsukuba, Tsukuba 305-8573, Japan

³ City University of Hong Kong, Kowloon, P. R. China

Abstract. This chapter describes a simple method for calculating unstable periodic orbits (UPOs) and their control in piecewise smooth autonomous systems. The algorithm can be used to obtain any desired UPO embedded in a chaotic attractor, and the UPO can be stabilized by a simple state feedback control. Some illustrative examples are shown for demonstration.

1 Introduction

Systems including switching motions are usually described as piecewise smooth systems [1]. Even piecewise affine/linear systems frequently exhibit chaotic behavior regardless of their exact solutions obtained piecewisely. Such systems attract much attentions from control engineering communities since they can be classified as *hybrid dynamical systems*.

It is well known that some simple electric circuits behave chaotically, such as Chua's circuit [2], hysteresis circuits [3], the Colpitts oscillator [4], the buck converter [5], and so on. In these systems, there exist some switching elements, so the overall system equation can be described by piecewise linear functions. It is noteworthy that these dynamical systems are regarded as some classes of hybrid dynamical systems.

While, in 1990, Otto, Grebogi, and Yorke developed a control method for stabilize an unstable periodic orbit (UPO) embedded in a chaotic attractor, Pyragas proposed two types of control schemes [6]: external force control (EFC) and the delayed feedback control. This work has also stimulated control engineering activities since the underlying systems are based on state feedback control. The delayed feedback control does not require any information of the UPO, however, we cannot stabilize a specific UPO. On the other hand, although EFC needs full UPO data, specific UPOs can be stabilized with guaranteed stability under some circumstances. However, the EFC scheme has serious problems; though infinitely many UPOs are embedded in a specified chaotic attractor, there exists no general method to obtain unstable periodic orbits for a given chaotic attractor except for some special systems.

In this chapter, we try to control UPOs embedded in a chaotic attractor of piecewise smooth systems by using an EFC. Firstly we review some recent

topics on piecewise affine system, which is one kind of subclass of piecewise smooth system, in the view point of controlling hybrid systems. Secondly we formulate piecewise smooth systems and propose a systematic calculation method of UPOs, and discuss some related problems on controlling chaos with EFC.

2 Piecewise Affine Systems

A powerful modelling framework for nonlinear systems is the class of piecewise affine systems [7–11]. In recent years, such systems have received increasing attention because they arise naturally in many applications of physical processes, such as systems with static nonlinearities, for example in switching elements of Chua’s circuit [2]. The dependence of the switching sequence is common in real systems, since it could be caused by saturation effects or limitations on the input signals. Piecewise affine models can approximate the switching elements as well as nonlinear dynamics with arbitrary accuracy via multiple linearizations at different operating points. They are therefore capable of modelling linear hybrid dynamical systems, hybrid automata, some class of discrete-event systems, and so on. Piecewise affine models have important advantage that they can permit introducing thresholds and discontinuities in a natural way that is not available in other algebraic approaches to nonlinear systems. This was pointed out in [8], which highlights the equivalence between discrete-time piecewise affine systems and interconnections of linear systems with finite automata [13].

Various useful “closed-form” representations for piecewise affine maps have been introduced in [7] and [9, 10], motivated by the network theoretic applications developed by Chua [12]. Standard continuous-time piecewise affine models are described by the state-space equations

$$\begin{cases} \dot{x} = A_i x + B_i u + \alpha_i \\ y = C_i x + D_i u + \beta_i \end{cases} \quad \text{for } \begin{bmatrix} x \\ u \end{bmatrix} \in \chi_i, \quad (1)$$

where $x \in \mathbb{R}^n$ is the state, $u \in \mathbb{R}^m$ is the control input, and $\{\chi_i\}_{i \in I}$ is a partition of the state+input space into a number of closed polyhedral cells. The index set of the cells is denoted I . $\alpha_i \in \mathbb{R}^n$, $\beta_i \in \mathbb{R}^m$ are suitable constant vectors.

Let $x(t)$ be a continuous piecewise function on the time interval $[t_0, t_1]$. $x(t)$ is called a trajectory of system (1), if for every $t \in [t_0, t_1]$ such that the derivative $\dot{x}(t)$ is well defined, the equation

$$\dot{x}(t) = A_i x(t) + B_i u(t) + \alpha_i, \quad \text{for } \begin{bmatrix} x \\ u \end{bmatrix} \in \chi_i \quad (2)$$

holds for all i , $i = 1, 2, \dots, n$. Notice that the trajectory cannot stay on the boundary $\chi_i \cap \chi_j$ unless it satisfies the differential equation for both i and j simultaneously.

If α_i and β_i are zero, system (1) is referred to as a piecewise linear system. From a complexity point of view, piecewise linear and piecewise affine systems are equivalent, since α_i and β_i could be thought of as being generated by integrator with no inputs.

Despite of the fact that piecewise affine systems are just a composition of linear time invariant dynamical systems, their structural properties such as stability and controllability are complex like typical nonlinear systems. One of the reason of this complexity is due to a significant feature of that the state-update map can be discontinuous along the boundary of the defined region. For instance, these discontinuities can arise from the representation of switching conditions. Therefore, the stability analysis or control synthesis problem for piecewise affine systems is computationally rather difficult. In fact, it was considered intractable before.

The computational complexity of the controllability and observability of piecewise affine systems was analyzed in [13] following the idea from [14, 15]. Recently, the NP-hardness of the stability of autonomous piecewise affine systems, even if it's constructed by using simple two-component subsystems, has been discussed in [16]. This means the stability of piecewise affine systems can not be assessed in finite time by means of a finite algorithm. Moreover, some global properties, global convergence, asymptotic stability of piecewise affine systems are undecidable [17]. Hence, there exists little research for developing analysis and synthesis tools on piecewise affine systems.

One of the earlier work was given in [18]. The method was based on backward solutions of Riccati differential equations. In [19, 20], a particular class of continuous-time piecewise affine systems was considered and an approach was proposed for stability analysis and control synthesis based on the piecewise quadratic Lyapunov functions that can be computed using convex optimization. Discrete-time case was addressed by using the dissipativity theory for nonlinear systems in [21]. In the discrete-time case, with respect to the continuous-time case, it is no need to guarantee the continuity of the Lyapunov function over the whole state space. This advantage can reduce the conservativeness of the stability result [21]. Construction of Lyapunov functions for switched systems has been proposed in [22]. An extension of the Lyapunov criterion based on multiple Lyapunov functions for general class of switched systems was addressed in [23].

Nevertheless, at the present stage, the existing methods for piecewise affine systems have not yet become practical and still remain conceptual. There is a large room for further investigation on the subject.

3 Piecewise Smooth Systems

Consider a system of m autonomous differential equations:

$$\frac{d\mathbf{x}}{dt} = \mathbf{f}_k(\mathbf{x}) \quad k = 0, 1, 2, \dots, m-1, \quad (3)$$

where $t \in \mathbb{R}$ is the time variable, $\mathbf{x} \in \mathbb{R}^n$ is the state vector. Assume that \mathbf{f}_k is C^∞ in all variables and parameters and that each equation in (3) has a unique solution for any finite initial value of $\mathbf{x}_k(0)$ such that

$$\mathbf{x}_k(t) = \varphi_k(t, \mathbf{x}_k(0)), \quad \mathbf{x}_k \equiv \mathbf{x}_k(0) = \varphi_k(0, \mathbf{x}_k(0)). \quad (4)$$

Assume also that the function changes from \mathbf{f}_k to \mathbf{f}_{k+1} when a solution orbit φ_k starting from $\mathbf{x}_k(0)$ reaches a section Π_{k+1} with $t = \tau_k$, where

$$\Pi_{k+1} = \{\mathbf{x}_{k+1} \in \mathbb{R}^n \mid q_{k+1}(\mathbf{x}_{k+1}) = 0\}. \quad (5)$$

These sections are called *break points*. Suppose that a solution of (3) is written as follows:

$$\mathbf{x}_{k+1}(t) = \varphi_{k+1}(t, \mathbf{x}_{k+1}), \quad \mathbf{x}_{k+1} = \varphi_{k+1}(0, \mathbf{x}_{k+1}) = \varphi_k(\tau_k, \mathbf{x}_k). \quad (6)$$

Then we call this system a piecewise smooth system [1]. Especially if all \mathbf{f}_k are linear, we call the system a piecewise linear system.

Clearly, a periodic orbit passing from Π_0 to Π_{m-1} satisfies

$$\mathbf{x}_0 = \mathbf{x}_m = \varphi_{m-1}(\tau_{m-1}, \mathbf{x}_{m-1}). \quad (7)$$

Note that a solution of (3), given in the form of (6) and (7), is continuous but not differentiable on Π_k .

For piecewise smooth systems, since the exact solutions are obtained as piecewise time functions, many analytic issues such as the stability of attractors, bifurcation, and existence of chaos can be discussed in a rigorous way. In 1960s, Andronov studied the stability of the limit cycle observed from the piecewise linear model of a vacuum-tube oscillator and it can be regarded as the first example of a hybrid dynamical system. This work is introduced in [24], where the differential equation includes a step-wise (binary level) function which is approximated by some continuous saturation characteristics. Because this model is a second-order autonomous system, the stability of its limit cycle can be studied analytically. However, this particular piecewise smooth system is probably one of the very few examples whose dynamical properties can be obtained in an analytical way. The key point in this analysis is that the switching time, at which the system equation changes nonsmoothly, can be exactly evaluated. Unfortunately, calculating a periodic orbit and analyzing its stability are difficult because the conditions on the switching time cannot be derived analytically, especially for higher-order systems even though the system is written in third-order differential equation [2].

We can always use numerical methods to analyze the dynamical behavior, even for higher-order systems. And yet, even if an efficient method is available for calculating periodic orbits, a large number of UPOs embedded within a chaos attractor are not able to calculate in general. An attempt was made by [25] to develop a systematic computational scheme for UPOs embedded

in a chaotic attractor. Other efficient techniques to obtain UPOs have also been proposed [26, 27].

In the following, we present a simple method to calculate UPOs. This method utilizes the ergodic property of chaos and the characteristic of a wide basin of attraction of the Newton numerical method. More precisely, we first describe a simple numerical method for calculating periodic orbits (points) in piecewise affine systems, then use Newton's method to provide numerical solutions for variational equations [28, 29]. This method requires no normal forms or approximations by continuous functions. To that end, we discuss an efficient algorithm for finding UPOs embedded within a specific chaotic attractor. This algorithm utilizes the ergodicity of chaos in addition to Newton's numerical method. Finally, we study a simple control technique that can stabilize these UPOs by using state feedback [30, 31]. Several examples of stabilizing UPOs are demonstrated, and a brief stability analysis is provided for completeness of the presentation.

4 Calculating Periodic Orbits of a Piecewise Smooth System

4.1 Formulation

To investigate the characteristics of periodic solutions of the piecewise smooth system of (3) ~ (7), we define the following local mappings:

$$\begin{aligned} T_0 : \quad \Pi_0 &\rightarrow \Pi_1 \\ \boldsymbol{x}_0 &\mapsto \boldsymbol{x}_1 = \varphi_0(\tau_0, \boldsymbol{x}_0), \\ T_1 : \quad \Pi_1 &\rightarrow \Pi_2 \\ \boldsymbol{x}_1 &\mapsto \boldsymbol{x}_2 = \varphi_1(\tau_1, \boldsymbol{x}_1), \\ &\dots \\ T_{m-1} : \quad \Pi_{m-1} &\rightarrow \Pi_0 \\ \boldsymbol{x}_{m-1} &\mapsto \boldsymbol{x}_0 = \varphi_{m-1}(\tau_{m-1}, \boldsymbol{x}_{m-1}). \end{aligned} \tag{8}$$

The Poincaré map is then defined as a differentiable map described by

$$T = T_0 \circ T_1 \circ \dots \circ T_{m-1}. \tag{9}$$

Thus, the period τ of a limit cycle is given as

$$\tau = \sum_{k=0}^{m-1} \tau_k. \tag{10}$$

The derivative of the Poincaré map with respect to the initial state is calculated by a product of the Jacobian matrices obtained at each break point [28]:

$$\left. \frac{\partial T}{\partial \boldsymbol{x}_0} \right|_{t=\tau} = \prod_{k=0}^{m-1} \left. \frac{\partial T_k}{\partial \boldsymbol{x}_k} \right|_{t=\tau_k}, \tag{11}$$

where each Jacobian matrix can be written as

$$\frac{\partial T_k}{\partial \mathbf{x}_k} \Big|_{t=\tau_k} = \frac{\partial \boldsymbol{\varphi}_k}{\partial \mathbf{x}_k} + \frac{\partial \boldsymbol{\varphi}_k}{\partial t} \frac{\partial \tau_k}{\partial \mathbf{x}_k} = \frac{\partial \boldsymbol{\varphi}_k}{\partial \mathbf{x}_k} + \mathbf{f}_k \frac{\partial \tau_k}{\partial \mathbf{x}_k}. \quad (12)$$

The scalar function q_k defining a section Π_k is assumed as a function of τ_k and \mathbf{x}_k :

$$q_k(\mathbf{x}_k) = q_k(\boldsymbol{\varphi}_k(\tau_k, \mathbf{x}_k)) = 0. \quad (13)$$

Derivative of q_k can be obtained as

$$\frac{\partial q_k}{\partial \mathbf{x}_k} \left(\frac{\partial \boldsymbol{\varphi}_k}{\partial \mathbf{x}_k} + \mathbf{f}_k \frac{\partial \tau_k}{\partial \mathbf{x}_k} \right) = \mathbf{0}, \quad (14)$$

where $q_m = q_0$. By substituting (14) into (12), we have

$$\frac{\partial T_k}{\partial \mathbf{x}_k} = \left(\mathbf{I}_n - \frac{1}{\frac{\partial q_k}{\partial \mathbf{x}_k} \cdot \mathbf{f}_k} \mathbf{f}_k \cdot \frac{\partial q_k}{\partial \mathbf{x}_k} \right) \frac{\partial \boldsymbol{\varphi}_k}{\partial \mathbf{x}_k}, \quad (15)$$

where \mathbf{I}_n is the $n \times n$ identity matrix, and $\partial \boldsymbol{\varphi}_k / \partial \mathbf{x}_k$ is the fundamental matrix of the following variational equations:

$$\begin{aligned} \frac{d}{dt} \left(\frac{\partial \boldsymbol{\varphi}_k}{\partial \mathbf{x}_k} \right) &= \frac{\partial \mathbf{f}_k}{\partial \mathbf{x}} \left(\frac{\partial \boldsymbol{\varphi}_k}{\partial \mathbf{x}_k} \right) \\ \frac{\partial \boldsymbol{\varphi}_k}{\partial \mathbf{x}_k} \Big|_{t=0} &= \mathbf{I}_n, \quad k = 0, 1, 2, \dots, m-1. \end{aligned} \quad (16)$$

Note that this equation should be solved from $t = 0$ to $t = \tau_i$, where τ_i is the time at which the orbit reaches the next section. Since the system is autonomous, we can reset t to 0 at every section in the computing process. More precise mathematical treatments of these sections can be found in [28].

Next, we define a local coordinate, $\mathbf{u} \in \Sigma_0 \subset \mathbb{R}^{n-1}$ corresponding to Π_0 , by using a projection p along with the associated embedding map p^{-1} :

$$p^{-1} : \Sigma \rightarrow \Pi, \quad p : \Pi \rightarrow \Sigma. \quad (17)$$

Accordingly, the Poincaré map in this local coordinate becomes

$$\begin{aligned} \mathcal{T} : \Sigma &\rightarrow \Sigma \\ \mathbf{u} &\mapsto p \circ T \circ p^{-1}(\mathbf{u}). \end{aligned} \quad (18)$$

A fixed point of the Poincaré map is then obtained by solving the following equation:

$$\mathcal{T}(\mathbf{u}) - \mathbf{u} = \mathbf{0}. \quad (19)$$

Its Jacobian matrix, which is needed in Newton's method to be discussed below, is given by

$$DT(\mathbf{u}_k) = \frac{\partial p}{\partial \mathbf{x}} \frac{\partial T}{\partial \mathbf{x}_0} \frac{\partial p^{-1}}{\partial \mathbf{u}} \quad (20)$$

$$= \prod_{k=0}^{m-1} \left(\frac{\partial p}{\partial \mathbf{x}} \frac{\partial T_k}{\partial \mathbf{x}_k} \frac{\partial p^{-1}}{\partial \mathbf{u}} \right) \quad (21)$$

$$= \prod_{k=0}^{m-1} \left(\frac{\partial p}{\partial \mathbf{x}} \left(\mathbf{I}_n - \frac{1}{\frac{\partial q_k}{\partial \mathbf{x}_k} \cdot \mathbf{f}_k} \mathbf{f}_k \cdot \frac{\partial q_k}{\partial \mathbf{x}_k} \right) \frac{\partial \varphi_k}{\partial \mathbf{x}_k} \frac{\partial p^{-1}}{\partial \mathbf{u}} \right). \quad (22)$$

Finally, the fixed point is computed by using Newton's method with the initial condition $\mathbf{u}^{(0)} = p(\mathbf{x}^{(0)})$. The recurrence formula is written as follows:

$$\begin{cases} D\mathbf{F}(\mathbf{u}^{(i)}) \cdot \boldsymbol{\eta}^{(i)} = -\mathbf{F}(\mathbf{u}^{(i)}) \\ \mathbf{u}^{(i+1)} = \mathbf{u}^{(i)} + \boldsymbol{\eta}^{(i)}, \end{cases} \quad i = 0, 1, 2, \dots, \quad (23)$$

where

$$\mathbf{F}(\mathbf{u}) = T(\mathbf{u}) - \mathbf{u} = \mathbf{0}, \quad (24)$$

$$D\mathbf{F}(\mathbf{u}) = DT(\mathbf{u}) - \mathbf{I}_{n-1}, \quad (25)$$

and, as usual, $\boldsymbol{\eta}^{(i)}$ is solved at every iteration. When $\|\boldsymbol{\eta}^{(i)}\|_\infty < \epsilon$ for a predesired $\epsilon > 0$, the Newton's method is terminated.

The multipliers of the fixed point are calculated by solving the following characteristic equation:

$$\left| \prod_{k=0}^{m-1} \frac{\partial \varphi_k}{\partial \mathbf{x}_k} \Big|_{t=\tau_k} - \mu \mathbf{I}_n \right| = 0. \quad (26)$$

The Runge-Kutta integration method is employed for solving the above variational equations as well as the original system (3) of differential equations. The initial step $\mathbf{u}^{(0)}$ from (3) is obtained by combining the Runge-Kutta scheme and the bisection method on the corresponding local section (break point) [28].

We should emphasize that taking local coordinate \mathbf{u} is mandatory. If we take $\mathbf{F}(\mathbf{x}) = T(\mathbf{x}) - \mathbf{x} = 0$ instead of Eq. (24), the variable \mathbf{x} will lie on the section by the condition of the Poincaré section $q_0(\mathbf{x}_0) = 0$. This means \mathbf{x} is not independent, and this fact affects the convergence of Newton's method.

4.2 Repetitive calculation of UPOs embedded in a chaotic attractor

If one has a good approximation of the periodic point on the local section, the recurrence formula Eq. (23) will converge and the accurate location of

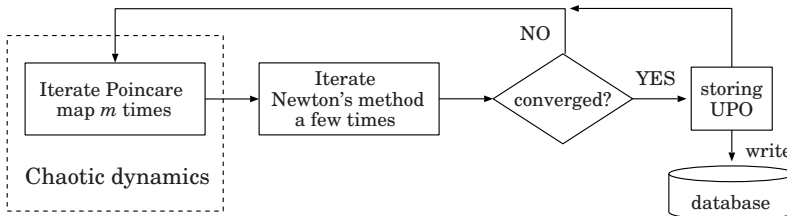


Fig. 1. Schematic diagram of computation.

the periodic point is identified. It is well known in numerical simulations on chaotic systems, however, that one can only visualize stable solutions such as stable periodic orbits, while unstable orbits such as saddle points are difficult to display or exactly calculated. Thus, to compute an UPO using the above algorithm, we have to resort to utilizing the information about the unstable orbits of the system. The main problem is how to provide the first-guess for the recurrence formula. We suggest to utilize the ergodicity of the chaotic dynamics, which are generally disregarded in numerical computation. In so doing, we gain quite a lot of first guess information for using the recurrence formula.

The algorithm is summarized as follows:

Step 1 Choose the parameters in which the system behaves chaotically, and set an appropriate initial condition. Select a number m defined in Eq. (7), where m indicates how many times the orbit hits different points on the sections.

Step 2 Calculate the orbit by solving Eq. (3) with the Runge-Kutta scheme. The Poincaré mapping point should be calculated by using the bisection method, and using the map n times.

Step 3 Iterate the recurrence formula Eq. (23) (then Eqs. (3) and (16) are solved simultaneously). If the formula converges, print the periodic point u_0 ; if the formula is not convergent within a few iterations, stop the iteration of the formula and, regardless of success or failure of the formula, go to Step 2.

The calculated points must be unstable and the whole family of UPOs may be produced by the Runge-Kutta method started from these points.

Compared to the method of [25], our method is simpler and convenient to use, which utilizes the ergodicity of chaos, i.e., it is possible for its orbit to visit the neighborhood of every UPO. Note that the main advantage is that the stability issue of the orbit is by-passed, which usually is quite troublesome. Moreover, Newton's method has quadratic convergence, so that we can expect a wide basin of attraction for the computation in general.

4.3 Calculation of UPOs in a piecewise smooth system

Here, we show an example of obtaining an UPO embedded within the chaotic attractor of a piecewise smooth system. We choose Chua's circuit, which contains a nonlinear conductor approximated by piecewise linear functions. The system is described by the following differential equations:

$$\begin{aligned}\dot{x}^1 &= \alpha(-x^1 + x^2 - H(x^1)) := f^0 \\ \dot{x}^2 &= x^1 - x^2 + x^3 &:= f^1 \\ \dot{x}^3 &= -\beta x^2 &:= f^2,\end{aligned}\tag{27}$$

where

$$H(x) = \begin{cases} ax + a - b, & x \leq -1 \\ bx, & |x| < 1 \\ ax - a + b, & x \geq 1. \end{cases}\tag{28}$$

By using the expression of Eq. (3), each f_k can be described as follows:

$$\begin{aligned}f_0 &= \begin{cases} -\alpha(a+1)x^1 + \alpha x^2 + \alpha(b-a) = f_0^0 \\ x^1 - x^2 + x^3 = f_0^1 \\ -\beta x^2 = f_0^2, \end{cases} \\ f_1 &= \begin{cases} -\alpha(b+1)x^1 + \alpha x^2 = f_1^0 \\ x^1 - x^2 + x^3 = f_1^1 \\ -\beta x^2 = f_1^2, \end{cases} \\ f_2 &= \begin{cases} -\alpha(a+1)x^1 + \alpha x^2 + \alpha(a-b) = f_2^0 \\ x^1 - x^2 + x^3 = f_2^1 \\ -\beta x^2 = f_2^2. \end{cases}\end{aligned}\tag{29}$$

In view of the characteristics of the nonlinear term H , it is clear that we must place the local sections at $x^1 = \pm 1$. Thus, the state space is segmented into three half-regions in \mathbb{R}^3 :

$$\begin{aligned}\Gamma_1 &: \left\{ \mathbf{x} \in \mathbb{R}^3 \mid x^1 < -1 \right\}, \\ \Gamma_2 &: \left\{ \mathbf{x} \in \mathbb{R}^3 \mid -1 \leq x^1 \leq 1 \right\}, \\ \Gamma_3 &: \left\{ \mathbf{x} \in \mathbb{R}^3 \mid x^1 > 1 \right\}.\end{aligned}\tag{30}$$

In the following, for simplicity we discuss the case where the intended UPO passes only Γ_1 and Γ_2 . Naturally, we can define a local section by the scalar

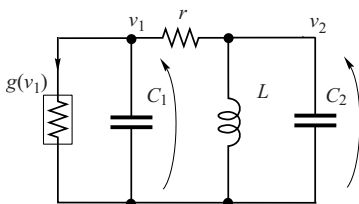


Fig. 2. Chua's circuit. A nonlinear conductor $g(v)$ has 3-segment piecewise linear characteristics.

function

$$q(\mathbf{x}) = q_0 = q_1 = x + 1 = 0 \quad (31)$$

and provide Π_0 at which the periodic flow from Γ_1 reaches Γ_2 . Therefore, the associated projection and the embedding are:

$$\begin{aligned} p : \mathbb{R}^3 &\rightarrow \mathbb{R}^2 \\ (x^1, x^2, x^3) &\mapsto (u^1, u^2) = (x^2, x^3), \end{aligned} \quad (32)$$

$$\begin{aligned} p^{-1} : \mathbb{R}^2 &\rightarrow \mathbb{R}^3 \\ (u^1, u^2) &\mapsto (x^1, x^2, x^3) = (-1, u^1, u^2), \end{aligned} \quad (33)$$

where we always let $x^1 = -1$. The Jacobians for these maps are

$$\frac{\partial p}{\partial \mathbf{x}_k} = \begin{pmatrix} 0 & 1 & 0 \\ 0 & 0 & 1 \end{pmatrix} \quad \text{and} \quad \frac{\partial p^{-1}}{\partial \mathbf{u}_k} = \begin{pmatrix} 0 & 0 \\ 1 & 0 \\ 0 & 1 \end{pmatrix}. \quad (34)$$

Similarly,

$$\frac{\partial q}{\partial \mathbf{x}_k} = (1 \ 0 \ 0). \quad (35)$$

Thus, we have

$$\frac{dq}{d\mathbf{x}_k} \cdot \mathbf{f}_k = f_k^0, \quad (36)$$

and

$$\mathbf{f}_k \cdot \frac{dq}{d\mathbf{x}_k} = \begin{pmatrix} f_k^0 & 0 & 0 \\ f_k^1 & 0 & 0 \\ f_k^2 & 0 & 0 \end{pmatrix}. \quad (37)$$

Consequently,

$$I_3 - \frac{1}{\frac{dq}{d\mathbf{x}_k} \cdot \mathbf{f}_k} \cdot \mathbf{f}_k \cdot \frac{dq}{d\mathbf{x}_k} = \begin{pmatrix} 0 & 0 & 0 \\ -f_k^1/f_k^0 & 1 & 0 \\ -f_k^2/f_k^0 & 0 & 1 \end{pmatrix}. \quad (38)$$

The remaining calculation of (22) is the variations $\partial \varphi_k / \partial \mathbf{x}_k$. They are computed from (16) by using the Runge-Kutta method. Its Jacobian matrix of \mathbf{f}_k is given by

$$\frac{\partial \mathbf{f}_0}{\partial \mathbf{x}_0} = \begin{pmatrix} -\alpha(a+1) & \alpha & 0 \\ 1 & -1 & 1 \\ 0 & -\beta & 0 \end{pmatrix}, \quad \frac{\partial \mathbf{f}_1}{\partial \mathbf{x}_1} = \begin{pmatrix} -\alpha(b+1) & \alpha & 0 \\ 1 & -1 & 1 \\ 0 & -\beta & 0 \end{pmatrix}. \quad (39)$$

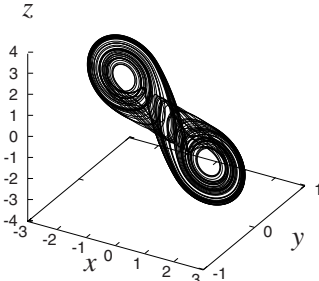


Fig. 3. A double scroll attractor of Chua's circuit. $\alpha = 9$, $\beta = 100/7$, $a = -5/7$, $b = -8/7$.

We fix the parameters as: $\alpha = 9$, $\beta = 100/7$, $a = -5/7$, $b = -8/7$. There is a double scroll attractor using this set of parameter values, as shown in Fig. 3.

Applying Newton's method formulated in Eq. (23), a pair of UPOs that cross the sections twice ($m = 2$) are calculated, as shown in Figs. 4 (a) and (b). These orbits are originally stable at $\alpha < 8.2$, and are calculated by the continuation method [29]. We can also calculate them by using the method discussed in Sec. 4.2 with $m = 2$ and $\epsilon = 10^{-12}$ specified therein. The location of the fixed point is also shown in Tab. 1. The eigenvalues of this fixed point are: $(\mu_1, \mu_2, \mu_3) = (1, -3.219297, -0.004119)$, and the period is $\tau = 2.425509$.

Table 1. A list of unstable periodic points.

| No. m | location | No. m | location |
|---------|----------------------------|---------|-----------------------------|
| (a) 2 | (1.0, 0.249220, -0.382555) | (g) 8 | (-1.0, 0.389678, 1.602575) |
| (b) 4 | (-1.0, 0.254159, 1.063931) | (h) 18 | (-1.0, 0.388208, 1.594470) |
| (c) 8 | (-1.0, 0.359790, 1.487480) | (i) 18 | (1.0, -0.278983, -1.161793) |
| (d) 8 | (-1.0, 0.374633, 1.539840) | (j) 18 | (1.0, -0.375425, -1.543004) |
| (e) 8 | (1.0, 0.093582, -0.107383) | (k) 18 | (-1.0, 0.257982, 1.079000) |
| (f) 8 | (-1.0, 0.271242, 1.131274) | (l) 20 | (1.0, -0.229638, -0.967268) |

Due to the symmetry of the system, these two attractors are symmetric with respect to the origin so that if one of them is obtained, the other can be obtained by simply inverting the sign of each coordinate. Nevertheless, the algorithm can detect both of them individually.

Figures 4 (c) and (d) show the orbits with $m = 4$ and Figs. 4 (e)–(h) show the orbits with $m = 8$, which clearly wanders between two areas. Figures 4 (i)–(n) show the orbits with $m = 8$, which travel through every Γ_1 – Γ_3 area. Moreover, Figs. 4 (o)–(w) show the orbits with $m = 18$, and Fig. 4 (x) shows the orbit with $m = 20$.

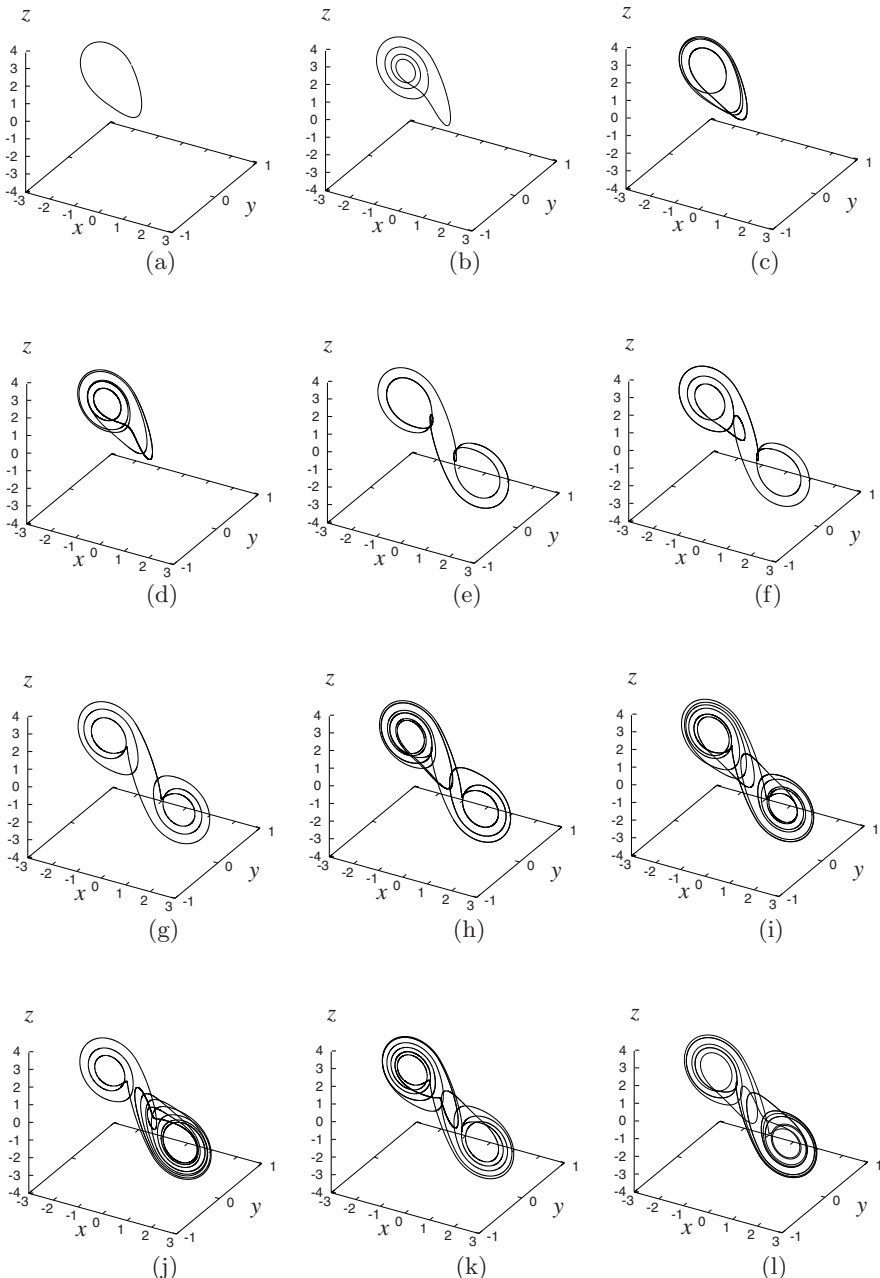


Fig. 4. Unstable periodic orbits in the double scroll attractor. $\alpha = 9$, $\beta = 100/7$, $a = -5/7$, $b = -8/7$.

In the numerical simulation, these orbits with the initial condition shown in Table 1 can be seen as a stable orbit for awhile but eventually it collapses and is absorbed by the chaotic attractor.

The accuracy of the multipliers are sensitive to the step size h of the Runge-Kutta method. This is perhaps a significant feature of the piecewise smooth systems. In the case of a pure nonlinear system, very accurate values of multipliers can be obtained using $h = 0.01$. If a more accurate solution is desired, a small value of h should be used. However, there is a lower limit for h in the Runge-Kutta method. The choice of h is not comparatively affected by the convergence rate of Newton's method. If more accurate data or the verification of the existence for UPOs are needed, the interval Newton's method is good to use [32].

5 Controlling Chaos of Piecewise Smooth Systems

The EFC [6] can be formulated in a very simple closed form by adding a control input term to Eq. (3):

$$\frac{d\mathbf{x}}{dt} = \mathbf{f}_k(\mathbf{x}) + \mathbf{K}(\hat{\mathbf{x}} - \mathbf{x}) \quad k = 0, 1, 2, \dots, m-1, \quad (40)$$

where $\hat{\mathbf{x}}$ is the target UPO and \mathbf{K} is a constant matrix. In [31], a method was proposed for stabilizing UPOs by a unified canonical feedback. In application of such feedback control technique for piecewise smooth systems was also discussed in [1].

By using EFC, we can stabilize any UPO calculated by the algorithm stated in Sec. 4.2. If one provides a signal generator that can store the data of several UPOs, the controlled system can stabilize a specified UPO from the chaotic region.

For realization of the control system by genuine electric circuits, storing UPO data and their high-speed reading/comparing is too difficult if only using analog elements. To overcome this difficulty, DSP (digital signal processor) seems to be suitable since a digital memory can utilize effectively without any overhead as compared with a computer system with a generic operating system.

A self-locating control of UPOs was proposed in [34]. It is a stabilizing method based on the OGY method [33] with Newton's algorithm. In contrast to this, our method provides automatic detection of UPOs by utilizing ergodicity of chaos and Newton's algorithm. Any parameter value is not be perturbed, which is advantageous since parameters may not be tunable in practice.

5.1 Stability analysis of EFC for piecewise smooth systems

Although some detailed stability analysis of EFC have already been given in [1, 31], we show another theoretical analysis in this section.

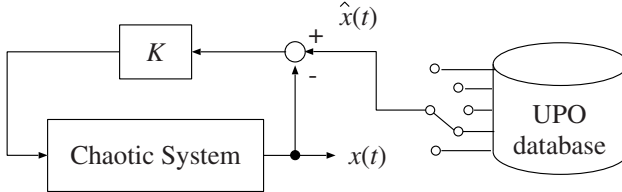


Fig. 5. A control system with the external force database.

We discuss a simple sufficient condition for the control strategy given in Eq. (40) in the case of piecewise smooth system, especially, Chua's circuit. For convenience, we consider a UPO crossing two half-regions. Then, the system equation (27) can be rewritten as

$$\begin{aligned}\dot{\mathbf{x}}(t) &= \mathbf{A}_0 \mathbf{x}(t) + \mathbf{P} && \text{if } \mathbf{x} \in \Gamma_1, & \Gamma_1 : \{\mathbf{x} \in \mathbb{R}^3 \mid x^1 < -1\} \\ \dot{\mathbf{x}}(t) &= \mathbf{A}_1 \mathbf{x}(t) && \text{if } \mathbf{x} \in \Gamma_2, & \Gamma_2 : \{\mathbf{x} \in \mathbb{R}^3 \mid -1 < x^1 < 1\},\end{aligned}\quad (41)$$

where, $\mathbf{x} = (x^1, x^2, x^3)^\top$ and

$$\mathbf{A}_0 = \begin{pmatrix} -\alpha(a+1) & \alpha & 0 \\ 1 & -1 & 1 \\ 0 & -\beta & 0 \end{pmatrix}, \quad (42)$$

$$\mathbf{A}_1 = \begin{pmatrix} -\alpha(b+1) & \alpha & 0 \\ 1 & -1 & 1 \\ 0 & -\beta & 0 \end{pmatrix}, \quad (43)$$

$$\mathbf{P} = \begin{pmatrix} \alpha(b-a) \\ 0 \\ 0 \end{pmatrix}, \quad (44)$$

where α, β, a, b are constants. Both \mathbf{A}_0 and \mathbf{A}_1 have a pair of stable complex eigenvalues and a real but unstable eigenvalue. Also, $\mathbf{x}_0(t)$ and $\mathbf{x}_1(t)$ are solutions of Eq. (41), satisfying

$$\mathbf{x}_0(t) = \varphi_0(t, \mathbf{x}_0(0)), \quad \mathbf{x}_1(0) = \mathbf{x}_0(\tau_0) = \varphi_0(\tau_0, \mathbf{x}_0(0)). \quad (45)$$

$$\mathbf{x}_1(t) = \varphi_1(t, \mathbf{x}_1(0)), \quad \mathbf{x}_0(0) = \mathbf{x}_1(\tau_1) = \varphi_1(\tau_1, \mathbf{x}_1(0)). \quad (46)$$

Each of $\varphi_0(t)$ and $\varphi_1(t)$ forms a periodic orbit. We rewrite these piecewise orbits as $\hat{\mathbf{x}}_0(t)$ and $\hat{\mathbf{x}}_1(t)$.

Now, we assume that $\hat{\mathbf{x}}_0(t)$ and $\hat{\mathbf{x}}_1(t)$ form an unstable periodic solution under appropriate parameter values. We try to stabilize this orbit by using the following state feedback:

$$\begin{aligned}\dot{\mathbf{x}}(t) &= \mathbf{A}_0 \mathbf{x}(t) + \mathbf{P} + \mathbf{K}(\hat{\mathbf{x}}_0(t) - \mathbf{x}(t)) && \text{if } x^1 < -1, \hat{x}^1 < -1 \\ \dot{\mathbf{x}}(t) &= \mathbf{A}_1 \mathbf{x}(t) + \mathbf{K}(\hat{\mathbf{x}}_0(t) - \mathbf{x}(t)) && \text{if } x^1 > -1, \hat{x}^1 < -1 \\ \dot{\mathbf{x}}(t) &= \mathbf{A}_1 \mathbf{x}(t) + \mathbf{K}(\hat{\mathbf{x}}_1(t) - \mathbf{x}(t)) && \text{if } x^1 > -1, \hat{x}^1 > -1 \\ \dot{\mathbf{x}}(t) &= \mathbf{A}_0 \mathbf{x}(t) + \mathbf{P} + \mathbf{K}(\hat{\mathbf{x}}_1(t) - \mathbf{x}(t)) && \text{if } x^1 < -1, \hat{x}^1 > -1,\end{aligned}\quad (47)$$

where we use

$$\mathbf{K} = \text{diag}\{K_{11}, K_{22}, K_{33}\}. \quad (48)$$

Firstly, we consider the first and the third cases of Eqs. (47):

$$\begin{aligned} \dot{\hat{\mathbf{x}}}_0(t) &= \mathbf{A}_0 \hat{\mathbf{x}}_0(t) + \mathbf{P} + \mathbf{K}(\hat{\mathbf{x}}_0(t) - \mathbf{x}_0(t)), \\ \dot{\hat{\mathbf{x}}}_1(t) &= \mathbf{A}_1 \hat{\mathbf{x}}_1(t) \mathbf{K}(\hat{\mathbf{x}}_1(t) - \mathbf{x}_1(t)), \end{aligned} \quad (49)$$

where $\hat{\mathbf{x}}_0$ and $\hat{\mathbf{x}}_1$ satisfy Eqs. (41) within each Γ_i , $i = 1, 2$; therefore,

$$\begin{aligned} \dot{\hat{\mathbf{x}}}_0(t) &= \mathbf{A}_0 \hat{\mathbf{x}}_0(t) + \mathbf{P} \\ \dot{\hat{\mathbf{x}}}_1(t) &= \mathbf{A}_1 \hat{\mathbf{x}}_1(t). \end{aligned} \quad (50)$$

Since the system is piecewise linear, the variation around the periodic solution at any instant t is written as

$$\begin{aligned} \mathbf{x}_0(t) &= \hat{\mathbf{x}}_0(t) + \boldsymbol{\xi}(t), \\ \mathbf{x}_1(t) &= \hat{\mathbf{x}}_1(t) + \boldsymbol{\zeta}(t). \end{aligned} \quad (51)$$

Substituting these equation into Eqs. (49) and then removing the relationship Eqs. (50) from the result, we have

$$\begin{aligned} \dot{\boldsymbol{\xi}}(t) &= (\mathbf{A}_0 - \mathbf{K})\boldsymbol{\xi}(t), \\ \dot{\boldsymbol{\zeta}}(t) &= (\mathbf{A}_1 - \mathbf{K})\boldsymbol{\zeta}(t). \end{aligned} \quad (52)$$

Suppose, in a simple design, that $K_{11} = K_{22} = K_{33} = K$. Then, the characteristic equations for Eqs. (52) become

$$\begin{aligned} \det [\mathbf{A}_0 - (\mu + K)I] &= 0, \\ \det [\mathbf{A}_1 - (\mu + K)I] &= 0. \end{aligned} \quad (53)$$

If we take a sufficiently large positive value for K , then all eigenvalues of the matrices $\mathbf{A}_0 - \mathbf{K}$ and $\mathbf{A}_1 - \mathbf{K}$ can become negative real since all coefficients of the characteristic equations can be regulated by K .

Similarly, we have the following equations from the second and the fourth cases of Eqs. (47):

$$\begin{aligned} \dot{\boldsymbol{\xi}}(t) &= (\mathbf{A}_0 - \mathbf{K})\boldsymbol{\xi}(t) + \mathbf{K}(\hat{\mathbf{x}}_1(t) - \hat{\mathbf{x}}_0(t)), \\ \dot{\boldsymbol{\zeta}}(t) &= (\mathbf{A}_1 - \mathbf{K})\boldsymbol{\zeta}(t) + \mathbf{K}(\hat{\mathbf{x}}_0(t) - \hat{\mathbf{x}}_1(t)). \end{aligned} \quad (54)$$

The remainders $\hat{\mathbf{x}}_1(t) - \hat{\mathbf{x}}_0(t)$ and $\hat{\mathbf{x}}_0(t) - \hat{\mathbf{x}}_1(t)$ are bounded for all t , because $\hat{\mathbf{x}}_0(t)$ and $\hat{\mathbf{x}}_1(t)$ are part of a periodic solution. Here, solutions of the variational equations (54) are not exploded. Thus, the control goal is achieved by choosing a sufficiently large value of K . For the cases of other UPOs wandering every half-region with an appropriate order, the stability analysis can be considered in the same way.

Note that the stability of the feedback system is confirmed only by the characteristic equations, while a Lyapunov function or relevant criterion is not necessary to use. Although the Poincaré mapping is required to calculate UPOs, it is not related to the control process.

As illustrated examples of the control strategy described by Eq. (40), we show a couple of simulations for the UPOs calculated in Section 4. Figures 6 (a) and (b) show simulation results of chaos stabilization for UPOs with $m = 10$ and 20, respectively. We chose a gain matrix as $\mathbf{K} = \text{diag}\{2, 2, 2\}$. The initial points are $(1, 1, 1)^\top$ and $(1, 1, 2)^\top$, respectively. The reference UPO signals were sampled by 30,000 points per cycle.

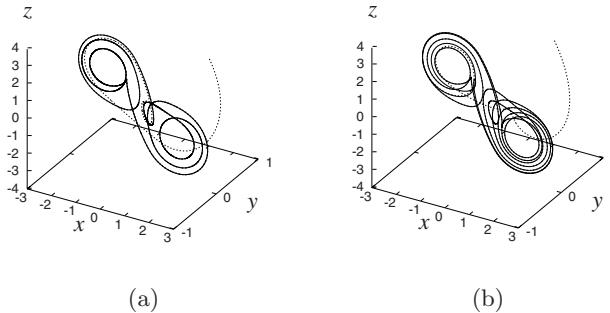


Fig. 6. Simulation results of the controlled Chua's circuit. (a) $m = 10$, the initial point is $(1, 1, 1)^\top$, (b) $m = 20$, the initial point is $(1, 1, 2)^\top$. The dashed and solid lines show the transient trajectory and the stabilized UPO, respectively.

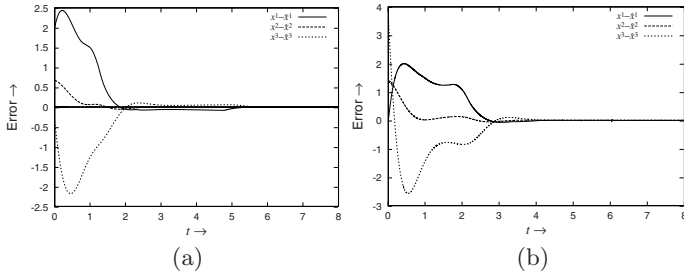


Fig. 7. Time response of errors according to Figs. 6 (a) and (b).

5.2 EFC for piecewise smooth systems

In this section, we discuss a more general case, i.e., piecewise smooth systems. It is assumed that each f_k in Eq. (3) contains some nonlinear terms. We

consider the dynamical behavior of the Alpazur oscillator and show the ability of EFC for this oscillator in this section.

Alpazur oscillator shown in Fig. 8 has been proposed and studied in [35]. It is a second-order piecewise dynamical system and has been analyzed in detail in [36].

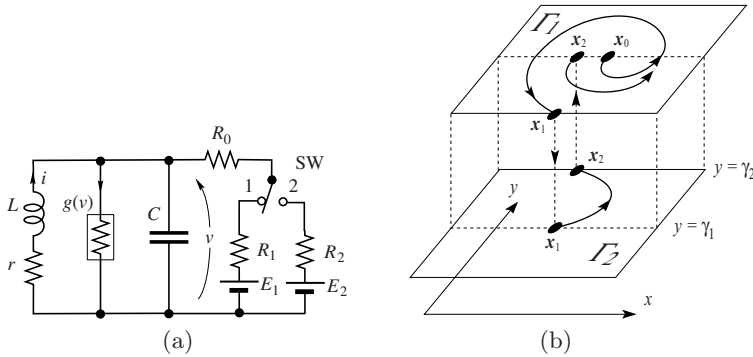


Fig. 8. (a) Alpazur oscillator, (b) a hysteresis characteristics realized by a switch.

Via suitable variable transformation, the circuit equation can be written in the following form:

$$\begin{cases} \frac{dx}{dt} = -kx - y \\ \frac{dy}{dt} = x + (1 - g_i)y - \frac{1}{3}y^3 + \delta_i, \quad k = 1, 2, \end{cases} \quad (55)$$

where subscription i is corresponding to the position 1 or 2 of the switch SW in the figure. This switch is controlled by the voltage v and it realizes hysteresis characteristics. Thus the whole dynamical system can be regarded as a hybrid system.

We explain the switching rule in Eq. (55) as follows. Firstly, we define two half planes:

$$\Gamma_1 = \{(x, y) \in \mathbb{R}^2 \mid y > \gamma_1\}, \quad \Gamma_2 = \{(x, y) \in \mathbb{R}^2 \mid y < \gamma_2\}. \quad (56)$$

Provided that $\gamma_2 > \gamma_1$, there exists an overlapped area within $\gamma_1 < y < \gamma_2$. If the flow on Γ_1 reaches the boundary $y = \gamma_1$, then the flow suddenly switches to the flow on Γ_2 without changing state variables. In the same manner, if the flow on Γ_2 reaches $y = \gamma_2$, then the flow switches to the flow on Γ_1 . We set parameters as $k = 0.1$, $g_1 = 0.2$, $g_2 = 2.0$, $h = -1.0$, $b = -0.1$, $\gamma_1 = 5$, $\gamma_2 = 0.5$. Figure 9 (a) shows the chaotic attractor with these parameters. By using the computation method mentioned above, UPOs embedded in the chaos are calculated, see Figs. 9 (b) and (c).

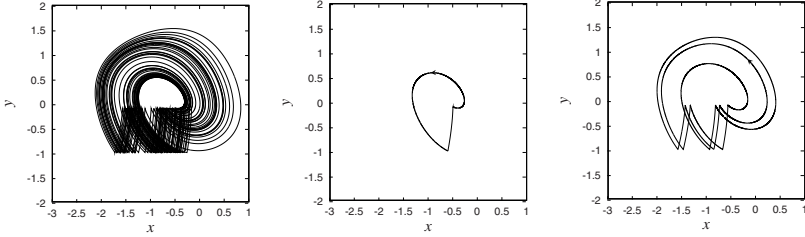


Fig. 9. (a) Chaos, (b) UPO, $m = 5$, $(x_0, y_0) = (-0.850783, -1)$, $\mu = 21.127059$.
(c) UPO, $m = 1$, $(x_0, y_0) = (-0.602357, -1)$, $\mu = 5.613888$.

We apply the control scheme (40) to the Alpazur oscillator. By a suitable choice of $K = \text{diag}\{\kappa_{11}, \kappa_{22}\}$, some UPOs can be stabilized by EFC. Since the system is piecewise smooth but nonlinear, the theoretical proof for the stability of EFC is difficult.

Figure 10 (a) shows the time response of the control input $\mathbf{K}(\mathbf{x} - \hat{\mathbf{x}})$ when EFC is applied to stabilize UPO shown in Fig. 9 (b). This result indicates that EFC is capable of stabilizing UPOs in piecewise smooth systems. We choose $\mathbf{K} = \text{diag}\{0, 1\}$, thus the control input is only added to the second equation at the right of Eq. (55) by only using information of $y(t)$.

In our experience, the EFC control is very effective as compared with the OGY method, because the error correction is always activated. Besides, the basin of attraction for the target can be achieved comparatively large by choosing large values for the diagonal elements in \mathbf{K} .

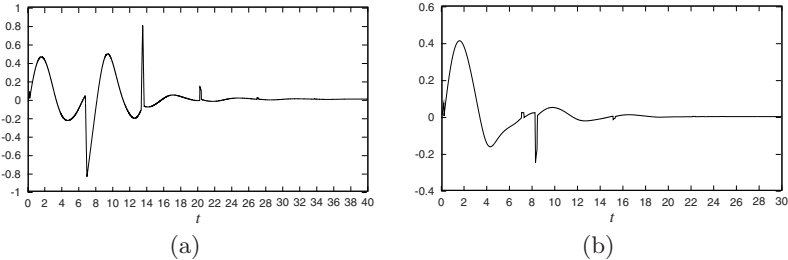


Fig. 10. Time response of Fig. 9 (b) and (c). $\kappa_{11} = 0, \kappa_{22} = 1.0$, $(x(0), y(0)) = (0, -1)$, $\kappa_{11} = 0, \kappa_{22} = 1.0$, $(x(0), y(0)) = (-0.3, -1)$.

6 Conclusions

We have proposed a simple yet efficient algorithm for calculating periodic orbits of piecewise smooth systems, particularly the unstable periodic orbits

embedded within a chaotic attractor. As an application, we have also discussed the stabilization of a calculated UPO from a chaotic region by a state feedback controller, along with some brief stability analysis on the controlled system.

References

1. Bernardo, M., Chen, G. (1999) Controlling bifurcations in nonsmooth dynamical systems. In *Controlling Chaos and Bifurcations in Engineering Systems*, ed. by Chen, G. Boca Raton, FL: CRC Press
2. Matsumoto, T., Komuro, M., Kokubu, H., Tokunaga, R., (1994) *Bifurcation*, Berlin: Springer
3. Saito, T., (1990) An approach toward higher dimensional hysteretic chaos generators. *IEEE Trans. Circ. Syst-I*, **37**:399–409
4. Kennedy, M. P. (1994) Chaos in the Colpitts oscillator. *IEEE Trans. Circ. Syst-I*, **41**:771–774
5. Yuan, G., Banerjee, S., Ott, E., Yorke, J. A. (1998) Border-collision bifurcations in the buck converter. *IEEE Trans. Circ. Syst-I*, **45**:707–716
6. Pyragas, K., (1992) Continuous control of chaos by self-controlling feedback. *Phys. Lett. A*, **170**:421–428
7. Kang, S. K., Chua, L. O. (1978) A global representation of multidimensional piecewise linear functions with linear partitions. *IEEE Trans. Circ. Syst.* **25**:938–940
8. Sontag, E. D. (1981) Nonlinear regulation: The piecewise linear approach. *IEEE Trans. Autot. Contr.*, **26**:346–357
9. Chua, L. O., Deng, A. C. (1986) Canonical piecewise-linear modeling. *IEEE Trans. Circ. Syst.*, **33**:511–525
10. Chua, L. O., Deng, A. C. (1988) Canonical piecewise-linear representation. *IEEE Trans. Circ. Syst.*, **35**:101–111
11. Pettit, N. B. O. L., Wellstead, P. E. (1995) Analyzing piecewise linear dynamical systems. *IEEE Contr. Syst.* **15**:43–50
12. Chua, L. O. (1969) *Introduction to Nonlinear Network Theory*. New York: McGraw-Hill
13. Sontag, E. D. (1996) Interconnected automata and linear systems: A theoretical framework in discrete-time. In *Hybrid Systems III - Verification and Control*, ed. by Henzinger, T. A., Sontag, E. D. Berlin: Springer, Lecture Notes in Computer Science **1066**, 436–448
14. Sontag, E. D. (1983) A Lyapunov-like characterization of asymptotic controllability. *SIAM J. Contr. Optim.*, **21**:462–471
15. Sontag, E. D. (1988) Controllability is harder to decide than accessibility, *SIAM J. Contr. Optim.* **26**:1106–1118
16. Blondel, V. D., Tsitsiklis, J. N. (1999) Complexity of stability and controllability of elementary hybrid systems. *Automatica*, **35**:479–489
17. Blondel, V. D., Bournez, O., Koiran, P., Tsitsiklis, J. N. (2000) The stability of saturated linear systems is undecidable. In *Proc. of Amer. Contr. Conference*, 1684
18. Banks, S. A., Khathur, S. A. (1989) Structure and control piecewise-linear systems. *Int. J. Contr.*, **50**:667–686

19. Johansson, M., Rantzer, A. (1998) Computation of piecewise quadratic Lyapunov functions for hybrid systems. *IEEE Trans. Auto. Contr.*, **43**:555–559
20. Johansson, M., Rantzer, A. (2000) Piecewise linear quadratic optimal control. *IEEE Trans. Auto. Contr.*, **45**:629–637
21. Cuzzola, F. A., Morari, M. (2001) A generalized approach for analysis and control of discrete-time piecewise affine and hybrid systems. In Proc. of 4th Int. Workshop on Hybrid Systems: Computation and Control. Berlin: Springer, 189–203
22. Wicks, M. A., Peleties, P. (1994) Construction of piecewise Lyapunov functions for stabilizing switched systems. In Proc. of Conference on Decision Contr., 3492–3497
23. Branicky, M. (1998) Multiple Lyapunov functions and other analysis tools for switched and hybrid systems. *IEEE Trans. Auto. Contr.* **43**:475–482
24. Pontryagin, L. S. (1962) Ordinary Differential Equations. New York: Addison-Wesley
25. Diakonos, F. K., Schmelcher, P., Biham, O (1998) Systematic computation of the least unstable periodic orbits in chaotic attractors. *Phys. Rev. Lett.*, **81**:4349–4352
26. Lathrop, D. P., Kostelich, E. J. (1989) Characterization of an experimental strange attractor by periodic orbits. *Phys. Rev. A*, **40**:4028–4031
27. Ogorzalek, M. J. (1997) Chaos and Complexity in Nonlinear Electronic Circuits. Singapore: World Scientific
28. Parker, T. S., Chua, L. O. (1986) Efficient solution of the variational equation for piecewise-linear differential equations. *J. Circ. Theory Appl.*, **14**:305–314
29. Parker, T. S., Chua, L. O. (1989) Practical Numerical Algorithms for Chaotic Systems. New York: Springer-Verlag
30. Chen, G., Dong, X. (1993) Controlling Chua’s circuit. *J. Circ. Sys. Comput.*, **3**:139–149
31. Chen, G., Dong, X. (1998) From Chaos to Order: Methodologies, Perspectives and Applications. Singapore: World Scientific
32. Galias, Z. (1998) Investigations of periodic orbits in electronic circuits with interval Newton method. In Proc. of 1998 IEEE ISCAS, vol. III, 370–373
33. Ott, E., Grebogi, C., Yorke, J. (1989) Controlling chaos. *Phys. Rev. Lett.*, **64**:1196–1199
34. Xu, D., Bishop, S. R. (1996) Self-locating control of chaotic systems using Newton algorithm. *Phys. Lett. A*, **210**:273–278
35. Kawakami, H., Lozi, R. (1992) Switched dynamical systems. In Proc. of RIMS Conference on Structure and Bifurcation of Dynamical Systems. Singapore: World Scientific, 39–58
36. Kousaka, T., Ueta, T., Kawakami, H., (1999) Bifurcation of switched nonlinear dynamical systems. *IEEE Trans. Circ. Syst.-II*, **7**:878–885

Formation Mechanisms and Control Methods of Beam Halo-Chaos in High-Current Ion Linacs

Jin-Qing Fang¹, Guanrong Chen², and Xinghuo Yu³

¹ China Institute of Atomic Energy
P. O. Box 275-27, Beijing 102413, P. R. China
fjq96@iris.ciae.ac.cn

² Department of Electronic Engineering
City University of Hong Kong, P. R. China

³ School of Electrical and Computer Engineering
Royal Melbourne Institute of Technology University
Melbourne, Australia

Abstract. This chapter introduces some potential applications of ion beam in high-current ion linacs, and discusses two key issues in such applications including the formation mechanisms of beam halo-chaos and its control methods. It is known that ion beam halo-chaos can be generated via different mechanisms, and recently some successful feedback methods have been developed for halo-chaos control, such as nonlinear feedback control, wavelet-based feedback control, switching manifold methods and time-delayed feedback self-control. Both analytical and numerical results have shown that these control methods are effective for suppressing beam halo-chaos.

1 Introduction

Recently, high-current, high-power, and high-duty ion linacs have become a focal point of intensive investigation in the fields of physics and engineering, particularly in variety of nuclear-energy research and development projects [1–5, 7–18, 26].

Some possible applications of ion beam in high-current ion linacs include: accelerator driven radioactive clean nuclear power systems, production of heavy ion drivers for thermonuclear energy, material testing facilities, production of tritium, transmutation of radioactive wastes, production of radioactive isotopes for medical use, spallation neutron sources, free-electron laser, and above all, scientific studies of high-energy and nuclear physics.

For space-charge dominated beams, nonlinear forces can modify the beam core density and create a halo surrounding a dense particle-core. This halo was first observed in a linacs, the LAMPF linacs, with 17mA current and 6 per cent duty factor [5], and then was simulated in many numerical studies afterwards.

Early observations of emittance growth and halo formation with particular reference to LAMPF simulation and observations were first reported

in [6]. It shows that radioactivation would be excessive even for a beam spill of 1 particle in 10^4 . Thus, the beam losses in it usually result in a radiation that damages the accelerator components and precludes human maintenance in the machine area. Therefore, beam halo-chaos has significantly limited the applications of high-intensity proton linacs. Today, this has become a key issue for high-power linacs. Some fundamental problems needed to be resolved are then not only to understand the phenomenon of beam halo-chaos formation but also to accomplish suppression and control of chaos toward practical applications.

Some mechanisms of beam halo-chaos formation have been studied via a set of two-dimensional (2D) and three-dimensional (3D) simulation models [10, 16]. To date, most research work has only focused on understanding the formation of beam halo-chaos. It is natural and indeed essential to first understand the mechanisms of intense beam losses that involve a variety of beam instabilities and some kind of halo-chaos formation. Main physical mechanisms of ion beam halo-chaos formation can be viewed from different angles. Beam halo-chaos may be generated when a beam is mismatched to a periodic focusing channel (PFC) or a focusing-defocusing (FODO) channel, exciting some sort of collective oscillations of the beam that are in resonance with the nonlinear oscillations of individual ions. Simulation studies mostly start with rms matched beam that are not stationary solutions of the underlying Vlasov equation. As a result, the initial beam undergoes some sort of redistribution in the phase space, masking the possible development of beam halos. Remarkable efforts have been devoted to a class of self-consistent 6D phase-space stationary distributions, both analytically and numerically. It was found that the coupling effect of the longitudinal, with transverse for elongated bunches and between them, cannot be neglected in the study of halo formation.

Beam halo-chaos is essentially a turbulent motion, i.e., a spatiotemporal chaotic motion in ion linacs; good examples include the LAMPF in Los Alamos [15]. This is because a matched beam, which enters a region of mismatch, will typically generate a complicated pattern of collective oscillations. In addition, the individual particles, which interact with these oscillations, may cause a coupling of all these modes. Normally, there is not enough time for the pattern to reach the new equilibrium in high current linacs, so the beam will undergo a very complicated turbulent motion that apparently ejects particles from the core, yielding some sort of halo-chaos.

In order to avoid serious radiation due to beam halo-chaos, further efforts have to be made to remove such halo-chaos by collimation. There have been several attempts, yet basically unsuccessful due to the fact that halo-chaos always regenerates [8]. Therefore, how to completely suppress and control beam halo-chaos in higher current ion linacs is an important and yet challenging subject for study, in both theoretical and practical considerations.

In recent years, the present authors have made special efforts to develop some effective control methods for suppressing and controlling beam halo-chaos, from a view point of chaos control [19, 26, 28, 29]. Specifically, some successful control methods such as nonlinear feedback control, wavelet-based feedback control, switching manifold control and time-delayed feedback self-control methods have been developed, for beam halo-chaos suppression in the PFCs, [19–26, 33, 37].

In this chapter, first, basic theoretical models for beam halo-chaos will be introduced, followed by a brief discussion on the chaos formation mechanisms. Then, some developed control methods for ion beam halo-chaos suppression in the PFCs will be described. Finally, some potential applications of halo-chaos control in new accelerator design and experiments will be discussed.

2 Basic Models and Analytic Methods

Since it is desirable for applications to have the maximum possible current in high-power accelerators, quite a lot of work are focused on the study of physical mechanisms for ion beam halo formation [3, 4, 15–17, 20]. However, the complex mechanisms have not been completely understood as of today.

Some basic models and theoretical methods for understanding the beam halo-chaos formation mechanisms are briefly reviewed in this section.

2.1 The particle-core model

The particle-core model has been used as a general theoretical framework for the study of beam halo-chaos formation [10–13, 15, 16]. It can provide significant insights of the dynamics of particles in the beam halo of a mismatched beam propagating through an axis-symmetric periodic focusing channel (PFC), uniform-focusing channel, and FODO channel. Main idea of this model can be described as follows.

First, consider the axis-symmetric model of breathing-mode round beams in high-current ion linacs. The dimensionless equation of the beam envelope through the periodic solenoidal focusing field, with the Kapchinsky-Vladimirsky (K-V) distribution, is given by [3–5, 7–15]:

$$\frac{d^2r_b}{ds^2} + k_z(s)r_b - \frac{K}{r_b} - \frac{\epsilon^2}{r_b^3} = 0. \quad (1)$$

in which dimensionless parameters and variables are used, defined by

$$\frac{s}{S} \rightarrow s, \quad \frac{r_b}{\sqrt{\epsilon S}} \rightarrow r_b, \quad \frac{SK}{\epsilon} \rightarrow K, \quad S^2 k_z \rightarrow k_z,$$

where ϵ is emittance of the beam current, t is time, r_b is beam radius and $s = z/\beta_b c t = z/S$ is the axial coordinate, in which β_b is the average axial

velocity of the beam particles, c is the speed of light, and S is the periodicity length for PFC; moreover, the periodic function $k_z(s) = k_z(s + S) = 2q^2B_z^2(s)/4\gamma_b^2\beta_b^2m^2c^4$ characterizes the strength of the focusing field, in which $k_z(s)$ can be written as $k_0^2 = k_z(s)$ with k_0 being the wave number of the transverse motion in the absence of space charge in the PFCs, $B_z(s) = B_z(0)$ is the magnetic field on the z -axis, q and m are the particle charge and rest mass, respectively, and $\gamma_b = (1 - \beta_b^2)^{-1/2}$ is the relativistic mass factor of the beam particles.

Note that the vacuum phase advance over one axial period of this focusing field is approximately given by $\sigma_0 = [S \int_0^S k_z(s)ds]^{1/2} = [\eta^2 k_z(0)]^{1/2}$, where η is the tune-depression, and, for PFCs, $k_0 = \sigma_0/S$. The perveance of the normalized beam, $K = 2q^2N_b/\gamma_b^3\beta_b^2mc^2$, is a measure of the beam self-field intensity, where N_b is the number of particles per unit axial length of the beam.

Based on the collective field described above, one can study the transverse motion of the test particles under their interaction with the field provided by the space charge of the beam-core, that is, for the equation in the x -coordinate [10]:

$$\frac{d^2x}{ds^2} + k_z(s)x - \frac{Kx}{a^2} = 0, \quad \text{if } r \leq a, \quad (2)$$

and

$$\frac{d^2x}{ds^2} + k_z(s)x - \frac{Kx}{r^2} = 0, \quad \text{if } r > a, \quad (3)$$

where a is the radius of the beam core and r , the particle radius. The equations for the y -coordinate are identical to Eqs. (2)-(3), with x being replaced by y .

A typical periodic focusing channel and periodic function $k_z(s)$ are shown in Fig. 1. This function represents a periodically interrupted or alternatively solenoidal focusing field, which interacts with individual particle motions.

Equations (1)-(3) can be used to study the halo formation via both theoretical analysis and numerical simulation. The main reason is that the K-V distribution is the simplest possible for analysis since its projection onto the real space has a uniform density and it has linear space charge forces. The stability of this K-V distribution has been analyzed and confirmed by numerical simulations.

2.2 Breathing model interaction with particle motion

Based on Eqs. (2)-(3), one may assume a core oscillation of the wave number p in the form of [11, 12]

$$r \rightarrow a(1 - \varepsilon \cos pz), \quad (4)$$

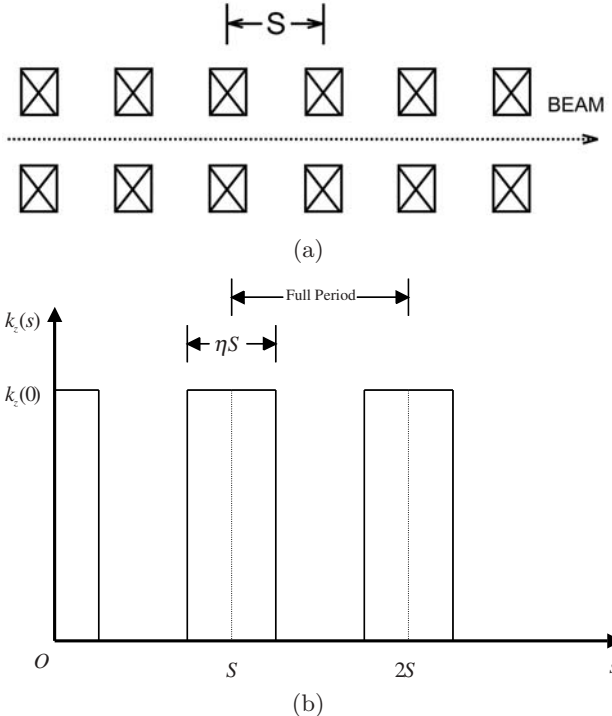


Fig. 1. (a) A periodic focusing channel; (b) the periodic function $k_z(s)$.

where a is a constant and ε is the relative oscillation amplitude. Then, one may expand r^{-2} in Eqs. (2)-(3) with the first-order term in ε . After some algebraic calculations, Eqs. (2)-(3) can be rewritten in a way as if r is replaced by a , in the following form:

$$\frac{d^2x}{ds^2} + q^2 x = -\frac{k_0}{a^2} x \left(1 - \frac{a^2}{r^2}\right) \Theta(r - a) + \frac{2\varepsilon k_0}{a^2} x \cos pz \Theta(a - r), \quad (5)$$

where $\Theta(u) = 1$ (or 0) for $u > 0$ (or $u < 0$), and $q = \sqrt{k_0^2 - k_0/a^2}$ is the oscillation wave number within the core.

With the radial forces of Eq. (5), it is seen that the angular momentum is constant. Using $Lqa^2 \equiv xy' - x'y = r^2\theta'$, the equation for the radial motion is rewritten as

$$\frac{d^2r}{ds^2} + q^2 \left(r - \frac{L^2 a^4}{r^3}\right) = -\frac{k_0}{a^2} r \left(1 - \frac{a^2}{r^2}\right) \Theta(r - a) + \frac{2\varepsilon k_0}{a^2} r \cos pz \Theta(a - r). \quad (6)$$

Here, the first term on the right makes the oscillation wave number depending on the amplitude, and the second term allows for energy transfer between the

core and the oscillating ion. It can be shown that the distribution in L for a K-V beam is uniform within the range $-\frac{1}{2} \leq L \leq \frac{1}{2}$.

Basic analysis for the above equation, with $L \neq 0$, can be carried out by applying the phase-amplitude method. The results in the largest effect for the case of $L = 0$ are as follows. Let

$$\frac{r}{a} = A \sin(qz + \alpha), \quad \frac{r'}{a} = qA \cos(qz + \alpha), \quad (7)$$

which will yield $A' \sin(qz + \alpha) + A\alpha' \cos(qz + \alpha) = 0$ for some A' and α' . One can then solve it for some expressions of A' and α' and then average over all oscillations except for the wave number $2q - p$, so as to obtain an integral of the motion. This allows one to write

$$h(w)\varepsilon \cos \psi = \Delta - b(w) - C/w, \quad (8)$$

where C is the integral constant, $w = r^2/a^2$, $\psi = (2q - p)z + 2\alpha$, and $\Delta = [1 + \sqrt{(1 + k_0^2/q^2)/2}]^{-1}$ is proportional to the resonance separation $p - 2q$, given as a relatively insensitive function of the tune depression q/k_0 . Here, since $h(w) = 1$ and $b(w) = 0$ for $w \leq 1$ and $w \geq 1$, one has

$$b(w) = \frac{2}{\pi w} \int_1^w \frac{du}{u} [(u-2) \tan^{-1} \sqrt{u-1} + \sqrt{u-1}], \quad (9)$$

$$h(w) = 1 - \frac{1}{\pi} \left[\tan^{-1} \sqrt{w-1} + \frac{(w-2)\sqrt{w-1}}{w^2} \right], \quad (10)$$

where $b(w)$ is related to the amplitude dependence of the single particle wave number, brought about by the nonlinearity of the particle motion outside the core.

Starting with the envelope equation for a breathing 2D beam, one can analyze the parametric resonance between the breaching mode and the nonlinear motion of an individual ion of amplitude larger than the core radius. The resulting phase space consists of an inner separatrix containing the core and an outer separatrix that becomes the locus near which the halo particles enter and cluster. Numerical simulations, saving with a “breathing” K-V beam, have confirmed the analytic prediction of the “peanut-shaped” 4D phase space, showing clearly the dominant behavior of the parametric resonance. A typical example is shown in Fig. 2.

The particle trajectories are most strongly affected by a parametric resonance, which occurs when the particle frequency is approximately half of the core frequency. This resonance is responsible for the growth of amplitudes that can form a halo. Particles that are initially nearest the core, and within the resonance-dominated region, are driven by the resonance. Acquiring large amplitudes is self limiting due to the nonlinear decrease of the space-charge force outside the core. The model predicts an important result that a maximum amplitude exists, which is the largest displacement on the separatrix

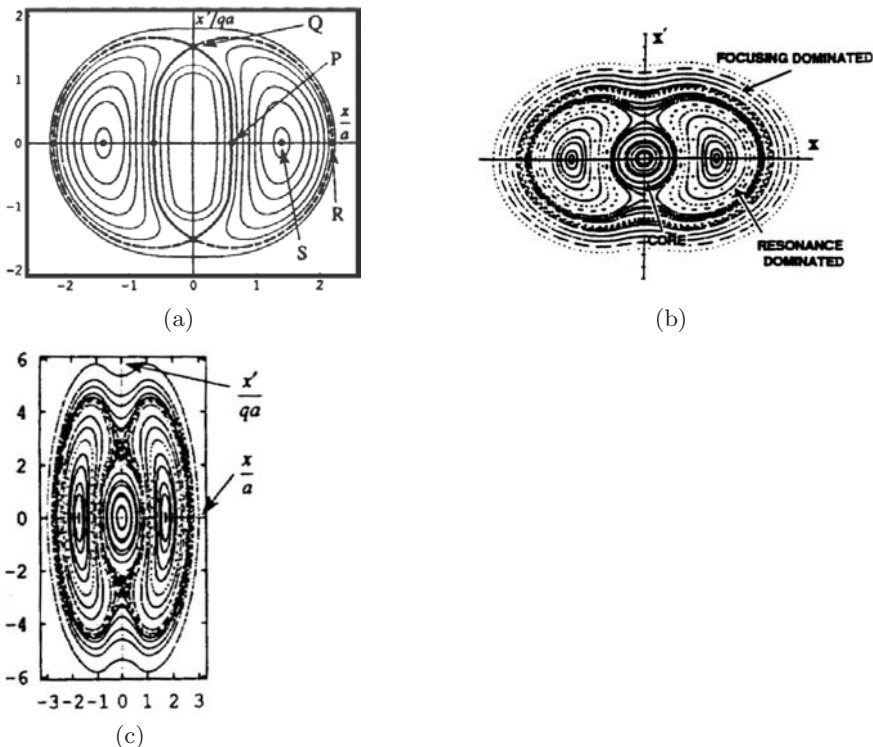


Fig. 2. Typical phase diagram of a particle in the (x, x') plane.

and is corresponding to a stroboscopic phase when the core has the minimum size.

Resonance-dominated particles will be cycling out and then come back as a result of the resonance. However, due to the amplitude-dependence of the frequency, a significant phase mixing occurs, and there usually will be some prides with amplitudes near the maximum value. It is found that these results are insensitive to details of the charge-distribution of the core. This was confirmed by a study of a model where the uniform core distribution is replaced by a Gaussian distribution. Although the Gaussian distribution is generally not an equilibrium distribution in a linear focusing channel, this replacement is still valid for testing the sensitivity of the results to the assumed core distribution.

In vicinity of the inner separatrix, particles are permitted to cross the separatrix and flow primarily along the outer separatrix (thick dashed curve in the figure). Evidence for chaos associated with the breakup of the separatrix is observed at low tune-depression ratios. The growth time for halo in the resonance-dominated region can be estimated from the model, as the average time required for particles within the resonance-dominated region to go from

the minimum to the maximum amplitude. It is found that this halo-growth time actually varies.

It is now clear that the parametric resonance model successfully predicts the location of the halo, but it has not addressed the diffusion of particles across the core boundary. Moreover, it has not been able to predict the circumstances that lead to a chaotic motion. Nevertheless, simulations have provided sufficient evidence that the fraction of the ions that enter the halo is surprisingly insensitive to the tune depression but it increases strongly as the mismatch becomes more severe. In addition, the motion starts to show chaotic behavior for tune depressions of 0.5 and below, a feature not addressed by the analytic model.

A further shortcoming of the analytic model is that it did not explain how ions were able to leave the core. This, however, was subsequently explained by analysis of the stability of a breathing K-V beam [11]. Simulations starting with a breathing K-V beam have confirmed that these instabilities led to oscillation-amplitude growth, where ions often enter the outer separatrix region, corresponding to halo formation for a sufficiently large mismatch.

2.3 Nonlinear resonances and induced chaos

The nonlinear resonances excited by the space charge force, which can lead to halo formation and induce chaos, have been further studied by both the perturbation-theoretic analysis and numerical methods [4, 12, 15, 22–26]. For an azimuthally symmetric beam evolving in a continuous focusing channel or a periodic focusing channel, Eqs. (1)–(3) depend only on the space charge turn $\eta = \sigma/\sigma_0$, where σ and σ_0 are the phase advances per unit lengths with and without space charge, respectively. For a matched beam, the envelope radius $r_b = \bar{r}_b$ is constant. For weak mismatches, the mismatch deviation is small, so the beam envelope radius can be written as

$$r_b(z) = \bar{r}_b + r, \quad r \ll \bar{r}_b.$$

Substituting this into Eq. (1), a linearized perturbation equation for the $r(z)$ can be obtained, which can be applied to study the oscillation modes of the envelope. Resonances between the particle motion and the space charge force can be defined by the turn divergence $\nu = k/k_c = \omega_p/\omega_c$, where k_c and ω_c denote the wave number and frequency of the particle-core oscillation, and ω_c the frequency of the particle oscillation. The two eigen-modes are given by $\nu_e = \eta/\sqrt{2(1 + \eta^2)}$ for the odd mode and $\nu_o = \eta/\sqrt{(1 + 3\eta^2)}$ for the even mode.

When the beam is mismatched, the range of the resonances excited by two eigen-frequencies of the beam envelope oscillation can be expressed as

$$\frac{\eta}{\sqrt{2(1 + \eta^2)}} \leq \nu_e < \frac{1}{\sqrt{2(1 + \eta^2)}}, \quad \text{for the even mode,} \quad (11)$$

and

$$\frac{\eta}{\sqrt{1+3\eta^2}} \leq \nu_o < \frac{1}{\sqrt{1+3\eta^2}}, \text{ for the odd mode.} \quad (12)$$

It is seen from the range of the resonances above that the nonlinear resonances of the testing particles only depend on the turn depression η associated with the space charge effect. In other words, it is the beam space charge effect that induces the nonlinear resonances. Calculation results from the relationship above are shown in Fig. 3.

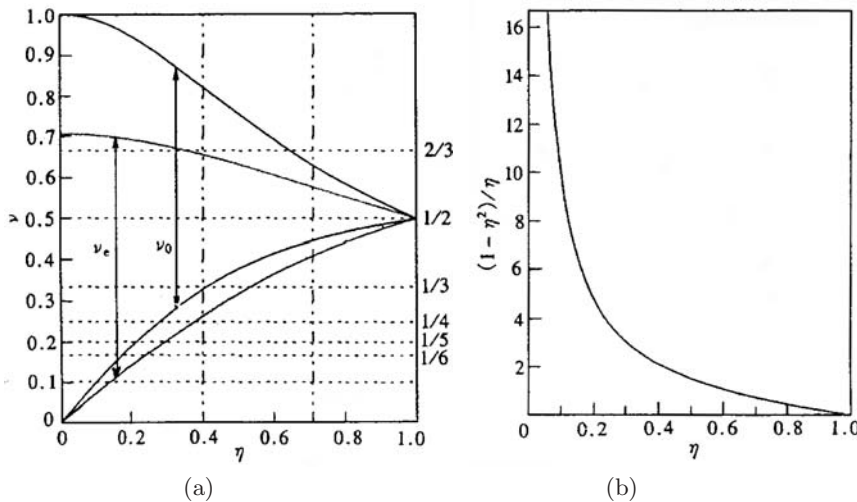


Fig. 3. The range of resonances vs. turn η : (a) and (b) $(1 - \eta^2)/\eta$ vs. η .

Figure 3(a) gives the range of the resonances that can be excited by the two eigen-modes as a function of the turn depression η , and it is constructed by the lower boundary of the even mode and the upper boundary of the odd mode. From the lower boundary of the even mode, one has

$$\eta \leq \sqrt{\frac{2\nu_e^2}{1 - 2\nu_e^2}}, \quad (13)$$

From the upper boundary of the odd mode, one has

$$\eta \leq \sqrt{\frac{1 - \nu_o^2}{3\nu_o^2}}. \quad (14)$$

Therefore, the initial values of η for the even and odd modes can be calculated respectively; for example, calculating $\eta \leq 0.6455$ for $2/3$ even mode

resonance, $\eta \leq 0.5345$ for 1/3 odd mode resonance, $\eta \leq 0.3780$ for 1/4 odd mode resonance, $\eta \leq 0.2949$ for 1/5 odd mode resonance, $\eta \leq 0.2425$ for 1/6 odd mode resonance, $\eta \leq 0.2425$ for 1/10 odd mode resonance. In this way, the whole range of resonance for initial values of η can be calculated.

There is a relationship for the phase advance with and without space charge

$$\sigma = (\sqrt{1 + u^2} - u)\sigma_0, \quad (15)$$

where $u = KS/2\epsilon\sigma_0$. Therefore, the relation between the current I and the turn η is

$$I = \frac{\epsilon\sigma_0}{S} \frac{I_0}{2} (\beta\gamma)^3 \frac{1 - \eta^2}{\eta}, \quad (16)$$

$(1 - \eta^2)/\eta$ vs. η is shown in Fig. 3(b).

One can use the formula given above to calculate the maximum current, avoiding the resonances in the whole range of resonances. For example, the maximum current is $I = 128.208mA$ if the beam energy is $40Mev$, $\sigma_0 = \pi/2$, $S = 0.4m$, $\epsilon = 10^{-7}m$. If the beam energy is selected as below $128mA$, the resonances with 2/3, 1/3, 1/4, 1/5, 1/6, 1/10 can be avoided.

It can be seen from Fig. 3 that when the turn depression $\eta \leq 0.1$, two eigen-frequencies of the even and odd modes for the beam-core envelope oscillations may excite 2/3, 1/2, 1/3, 1/4, 1/5, 1/6, 1/10 and some others resonances. If $\eta \leq 0.3$, they may excite 2/3, 1/2, 1/3, 1/4, 1/5 and some others resonances; if $\eta \geq 0.4$, however, 1/4, 1/5, and other strong resonances can be avoided; if $\eta \geq 0.7$, then 2/3, 1/3, 1/4, 1/5, 1/6, 1/10 and other resonances can be also avoided. Here, $\eta = \sqrt{0.5}$ can be used as a critical value for the high-current beam, that is, when $\eta \geq 0.7$, the space-charge dominated beam is converted to an emittance-dominated beam, and its envelope plasma oscillation becomes a betatron oscillation, so the aforementioned resonances can be avoided. Nevertheless, for the range of $0 < \eta < 1$, there are always resonances with $\nu_e = 1/2$ and $\nu_o = 1/2$, which implies that a half-integer resonances cannot be avoided sometimes.

The rms envelope equations can be numerically integrated without smooth approximation for the PFCs. It has been demonstrated that the resonance overlapping mechanism can lead to the formation of a halo area where the proton trajectories are chaotic. This chaotic behavior has been observed by using Poincaré sections, where $\hat{K} = \sigma_0^2(1 - \eta^2/\eta) = 3$. The numerical results have also been confirmed by analytical studies. As seen in Fig. 3, when $\eta \geq 0.7$, various resonances are excited at the same time for some initial conditions, and overlapping of these resonances will lead to form a chaotic area in which sensitive dependence on initial conditions and intermittencies have also been observed. It is known that nonlinear resonances can scatter particles around the beam core, and this halo formation is highly enhanced

when chaotic areas are found:

$$\text{nonlinear} - \text{resonances} \Rightarrow \text{chaos} \Rightarrow \text{halo} - \text{formation}$$

The links between these phenomena are now known clearly: the resonances overlapping mechanism explains the generation of the chaotic areas, and the diffusion in these areas (Arnold's web for $N > 2$) increases particle redistribution and halo generation.

The knowledge, described above, is gained for PFCs, FODO periods, and the continuous focusing channel, and has been used to avoid halo formation. The basic idea is simple: as halo comes mainly from particle diffusions in the chaotic areas, halo formation will be avoided if the resonances do not overlap. This has been demonstrated in [4], where defocusing octupoles were used to cancel both emittance growth and halo formation in a FODO channel tuned by $\sigma_0 = 100^\circ$. Other types of nonlinear correctors can also be used, e.g., modified octupoles have been proposed in [4] where effects of duodecapoles were demonstrated.

Some remarks are in order. For collisionless beams evolving in FODO channels (without acceleration), with the nonlinear space-charge forces, these systems are non-integrable. Some characters that are common to this class of systems include [4]: First, global properties of the systems are determined by the location and the size of the nonlinear resonances and by the resonance overlapping mechanism, which lead to the formation of chaotic areas. Second, particles diffusion and halo formation are enhanced in the chaotic areas (Arnold's web for $N > 2$). Third, beams that are not *a priori* unstable (beam current around $100mA$, $\sigma > 0$ on the axis) are in a regime of weak chaos. These systems usually have a mixture of quasi-periodic (KAM) and chaotic orbits, and a mixture of stable and unstable periodic orbits (fixed points). Fourth, the system flows are ergodic only in a subspace of the chaotic region but isolated adiabatic island exist within the entire regions (fortunately, these systems are generally not in a region of strong chaos).

2.4 Halo formation in three-dimensional bunches

A realistic treatment of halo formation must take into account 3D beam bunches and 6D phase space distributions. For this purpose, a 3D particle-in-cell (PIC) code HALO3D has been developed [12] and numerical studies were performed with a 3D beam bunch using the particle-core model, drawing attention to the existence and importance of a longitudinal halo for a spheroidal bunch. However, all studies based on the particle-core model do not address the question of whether halo formation is influenced by the density redistribution for a non-stationary beam, even if it is rms matched. In fact, halo formation in 2D due to the redistribution process in rms matched beams had been shown.

There are some continued efforts in studying the halo development mechanism in 3D bunches in the absence of the redistribution process [11, 14]. Such

an approach allows to study the fundamental mechanism of halo formation associated with beam mismatch. This method proves to be very efficient in 2D calculations. To accomplish this, it has been constructed, both analytically and numerically, a new class of stationary 6D phase space distributions for a spheroidal beam bunch. This analysis assumes smoothed external transverse and longitudinal restoring force gradients, k_Z, k_y, k_x . In general, the distribution can be chosen to have an approximately ellipsoidal boundary. However, for simplicity, the azimuthally symmetric case ($k_x = k_y$) was treated, so that the beam bunch is approximately spheroidal.

More precisely, consider the azimuthally symmetric 6D phase space distribution:

$$f(x, P) = N(H_0, H)^{1/2}, \quad (17)$$

where $H = k_x r^2/2 + k_z z^2/2 + e\Phi_s c(x) + mv^2/2$, and $p = mv$, $r^2 = x^2 + y^2$, with k_x, k_z being the smoothed transverse and longitudinal restoring force gradients respectively. The quantity $\Phi_s c(x)$ is the electrostatic potential due to the space charge of the bunch. The distribution can be normalized such that $\int dx \int dp f(x, p) = l$. Main result are summarized as follows:

1. The halo extent for a transverse halo increases slightly with increasing space charge. The increase is similar to the one seen from nonlinear stationary distributions in 2D simulations and non-stationary rms matched distributions [30]. However, the dependence on tune depression does not disappear with increasing mismatch, where no dependence on the tune depression for $p > 1.3$ was observed. In addition, the halo extent simply scales with the mismatch parameter. As was the case for the longitudinal halo, we found that the halo intensity is governed primarily by the mismatch. It is noted that the transverse halo develops significantly more slowly than the longitudinal halo for comparable mismatches. The halo usually saturates after a few hundred breathing periods. It is also noted that, for a pure transverse mismatch ($\mu_z = 1.0$), the transverse halo is observed even for $\mu_x = \mu_y = 1.15$. In general, the transverse halo closely duplicates all the features observed for nonlinear stationary distributions in 2D simulations. The agreement between 2D and 3D simulations is very good. The only two significant differences seen are related to the rate of halo development. In the 3D simulations, there is a clear dependence of halo intensity on the mismatch and tune depression, as shown in Figs. 4 and 5. Another difference is that the transverse halo in the 3D simulations develops significantly faster than in 2D, for comparable mismatches and turn depressions.
2. The longitudinal halo is its dependence on the mismatch when there is no mismatch in the radial direction. The number of particles in the halo drops dramatically with μ_Z . In fact, we see no halo for $\mu_z < 1.2$ (< 20

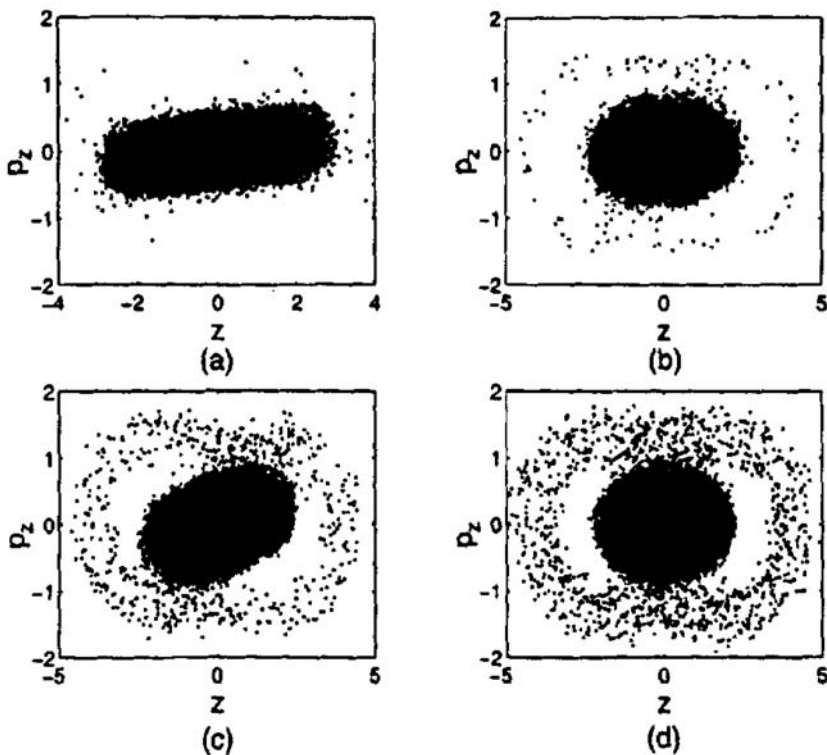


Fig. 4. Dependence of halo intensity on the mismatch for $c/a = 3$, $\eta_x = 0.65$, $\eta_z = 0.49$ (with 32768 particles plotted) for several mismatched μ . (a) $\mu = 1.1$ (b) $\mu = 1.2$. (c) $\mu = 1.3$ (d) $\mu = 1.4$

percent longitudinal mismatch). Note that the situation changes when the effect of coupling is significant.

3. There is clear coupling between the longitudinal and transverse motion. Due to the coupling between r and z , a transverse or longitudinal halo is observed even for a very small mismatch (less than 10 per cent) as long as there is a significant mismatch in the other plane. As an example, Fig. 6(a) shows a clear longitudinal halo for $\mu_z = 1.05$, $\mu_x = \mu_y = 1.5$ (5 percent longitudinal mismatch), and Fig. 6(b) shows a clear transverse halo for $\mu_z = 1.05$, $\mu_x = \mu_y = 1.5$ (5 per cent transverse mismatch). The effect of coupling is visible even for modest mismatches. For example, a 20 percent longitudinal mismatch is required to develop a longitudinal halo when the transverse mismatch is zero. However, when there is a mismatch in all directions, a halo is seen even when $\mu_z = \mu_x = \mu_y = 1.1$ (10 percent mismatch in all directions), as shown in Fig. 7. Such behavior clearly shows the importance of the coupling effect.

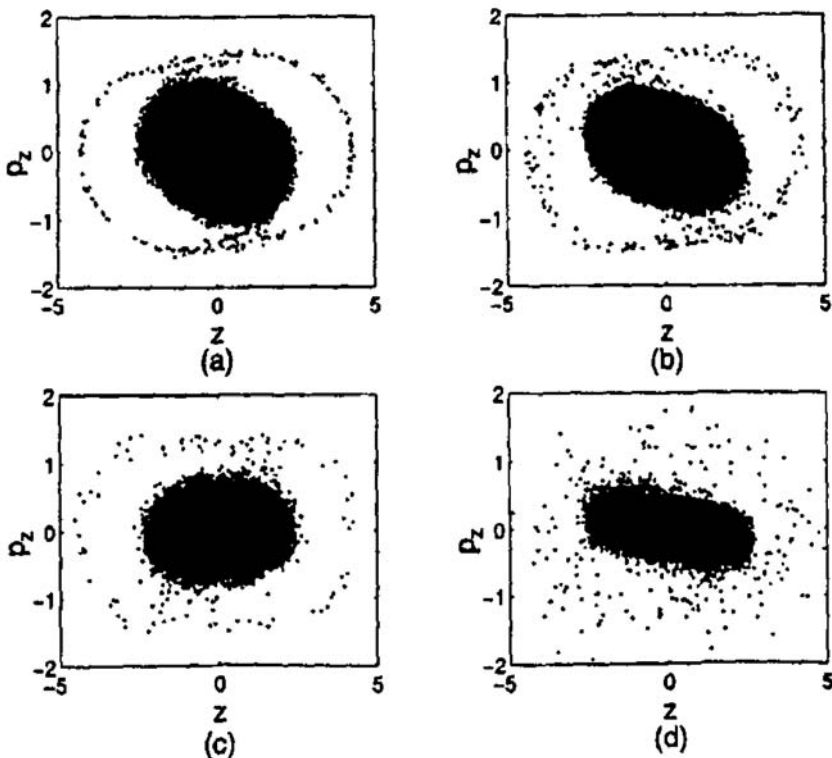


Fig. 5. Dependence of halo intensity on the tune depression for $c/a = 3$, $\mu = 1.2$.
 (a) $\eta = 1.2$ (b) $\eta = 0.87$ (c) $\eta = 0.49$ (d) $\eta = 0.32$

4. For halo structure, in the limit of low space charge the longitudinal phase space diagram closely resembles the filamentation process described in [5]. This results in that the phase space ellipse becomes distorted into a spiral-like structure depending on the mismatch factor, as can be seen in Fig. 8, for $c/a = 3$, $m = 0.87$, $m = 0.93$. As the particles are expelled from the core, they lead to a filamented core or produce new tails. The new tails are continuously pushed out from the core, but they always stay inside the original tail, as shown in Fig. 9.

This phenomenon provides a rough description of halo formation. When a significant portion of the particles are expelled from the origin, the particles inside the core see a reduced charge, which results in a new sets of expelled particles, which follow separatrices in the phase space that are closer to the core. For higher space charges, the beam undergoes more severe density redistribution and the detailed halo structure becomes more diffuse. The result is a peanut shaped diagram in longitudinal phase space without an obvious filamentation structure (Figs. 3, 4 and 5). The reason one does not observe

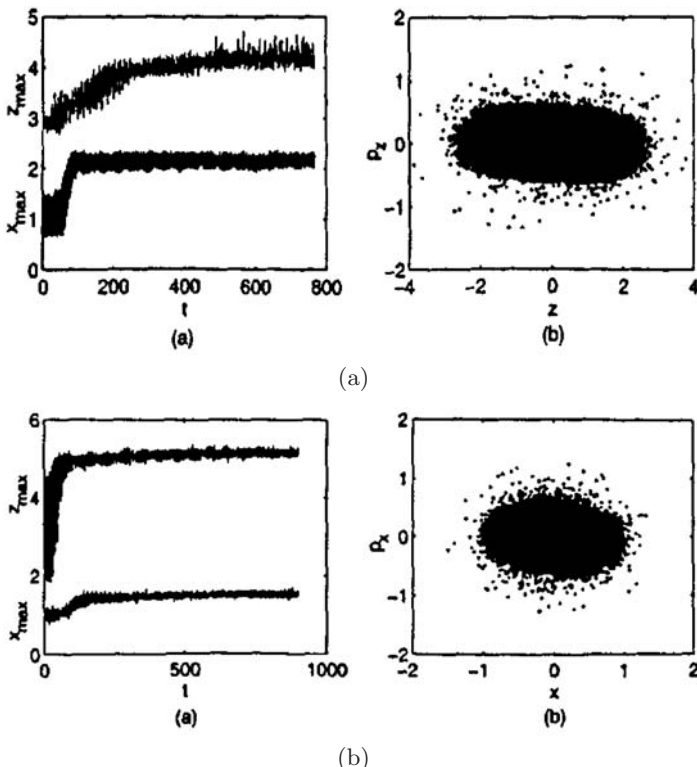


Fig. 6. (a) Longitudinal halo for $\mu_z = 1.05$, $\mu_x = \mu_y = 1.5$ (b) Transverse halo for $\mu_z = 1.05$, $\mu_x = \mu_y = 1.5$.

filamentation in this case is that most of the plotted particles are in the core. To get better resolution of the halo region, a low density phase-space cut was performed. In this procedure, a threshold phase-space density is chosen just above that in the halo, and all halo particles are plotted. In the high density region, only the fraction of the particles corresponding to the threshold density is plotted. The result is shown in Fig. 10, where the longitudinal phase-space diagram is shown, with and without the low density cut, for $c/a = 3$, $\mu = l.4$, $\eta_x = 0.65$, $\eta_z = 0.49$.

In this way, one sees how the spiral structure develops into the more familiar peanut diagram. This peanut diagram in the longitudinal phase space is very clear for relatively long bunches ($c/a > 3$). For short bunches, the diagram is distorted by the appearance of particles between the core and the halo in the limit of low space charges. This effect is probably related to the stronger coupling between the transverse and longitudinal motions for short bunches, and on its effect on the filamentation process.

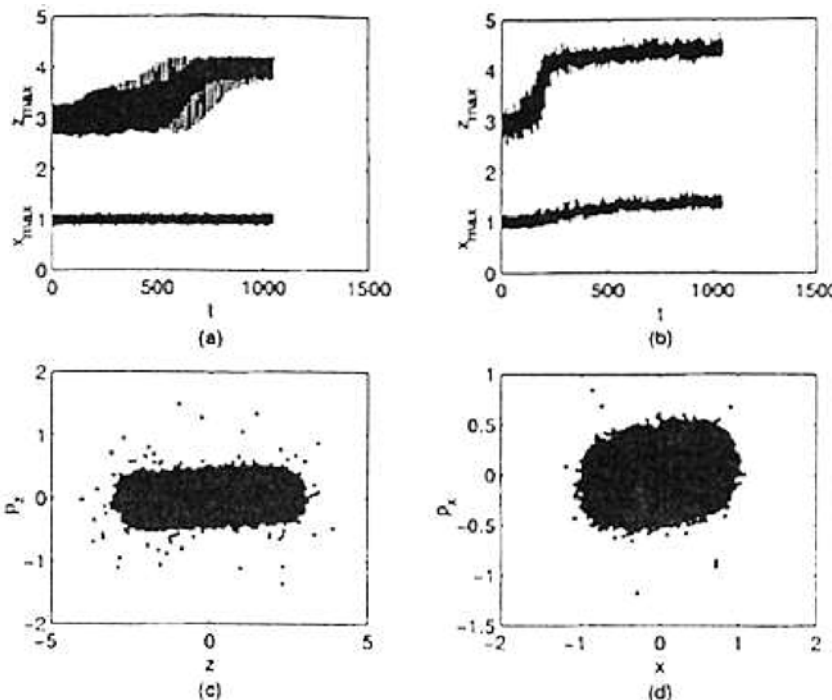


Fig. 7. There is a mismatch in all directions for $\mu_z = \mu_x = \mu_y = 1.1$ (10% mismatch in all directions).

In summary, most of the previous studies were concerned with halos in long beams. In the above-described work, it addresses the question of halo formation in a beam bunch that is of particular interest for accelerator production of the Tritium project, where relatively short bunches are proposed [35]. A new result, due to the coupling between the r and z planes, is that a transverse or longitudinal halo is observed for a mismatch less than 10 percent if the mismatch in the other plane is large.

To this end, the main conclusion is that the longitudinal halo is of great importance because it develops earlier than the transverse halo for elongated bunches with comparable longitudinal and transverse mismatches, and because it occurs even for mismatches in an order of 10 percent. In addition, controlling the longitudinal halo could be challenging if the phase width of the beam bunch in the RF bucket cannot be made sufficiently small.

Another conclusion is that halo formation depends on the distribution. Reported results about this issue are not self-consistent, and one still need to determine to what the extent the relatively rapid redistribution of the 6D phase space will contribute to the formation of halo chaos.

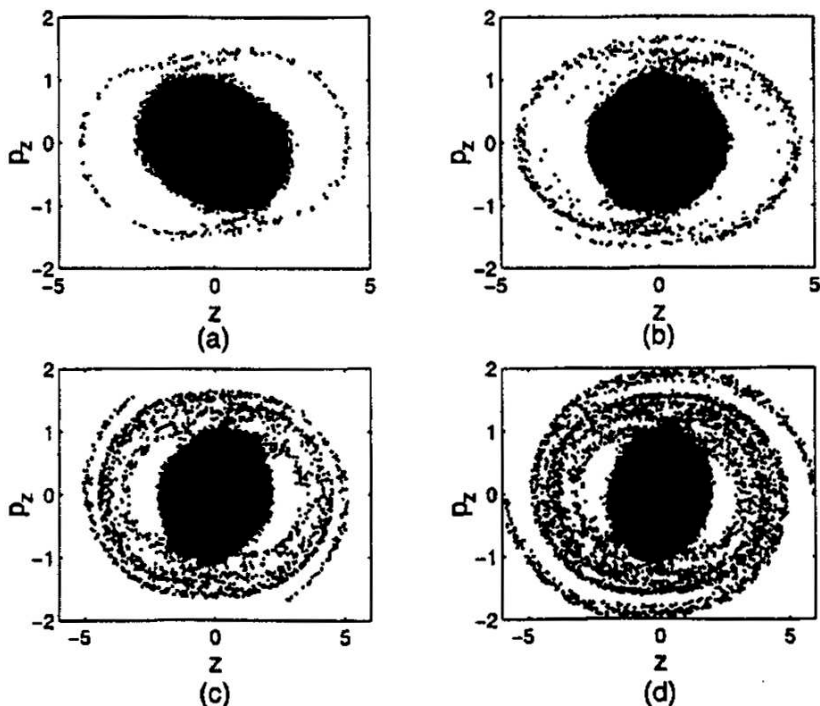


Fig. 8. Spiral-like structure, depending on the mismatch factor for $c/a = 3$, $m = 0.87$, $m = 0.93$ at $t = 900$, $c/a = 3$, $\eta_x = 0.93$. (a) $\mu = 1.2$ (b) $\mu = 1.3$ (c) $\mu = 1.4$ (d) $\mu = 1.6$.

2.5 Canonical transformation method

Recently, a canonical transformation method (CTM) has been developed to use the particle-core model for studying the dynamics of halo particles in a mismatched continuous beam propagating through an periodic-focusing channel. It is assumed that the beam-particle density and envelope are described by the K-V distribution function and envelope equation, in new phase-space variables, to minimize the flutter in the beam envelope and in the particle orbit in the PFCs so as to allow making stroboscopic plots. Applying this method, it is found that periodic focusing can be a possible mechanism for halo formation in a mismatched beam because in the PFCs certain particle initially not in the halo region can be brought into resonance with the core oscillation thereby generating halo particles [17].

Based on Eqs. (1)-(3), by introducing the variable transformation $u_e = x/a_m$ and $ds = d\tau/a_m^2$, where a_m is the envelope of the matched core defined

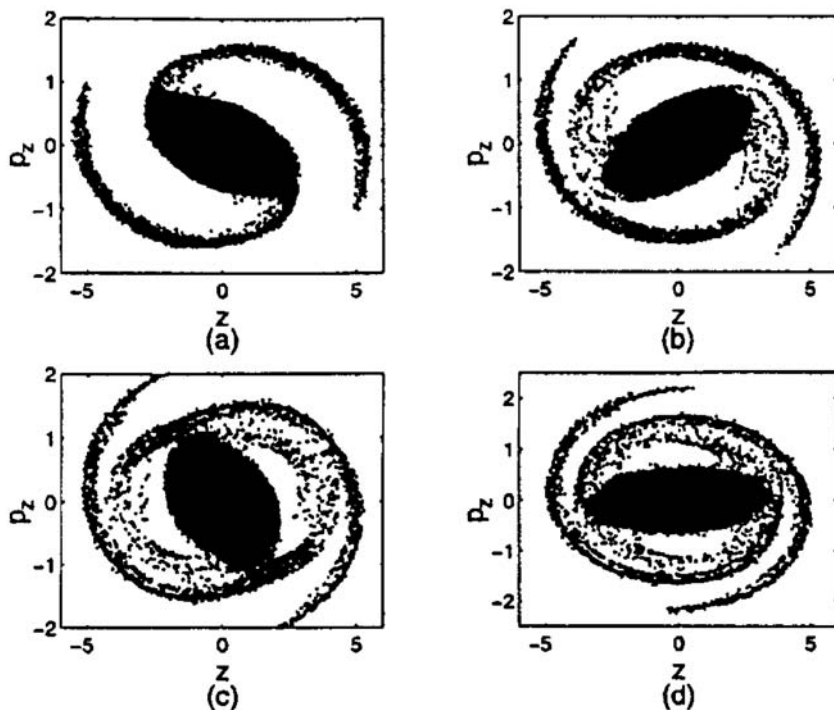


Fig. 9. Evaluation of filamentation for $c/a = 3$, $\eta_z x = 0.87$, $\mu = 1.6$. (a) $t = 250$ (b) $t = 350$ (c) $t = 450$ (d) $t = 550$.

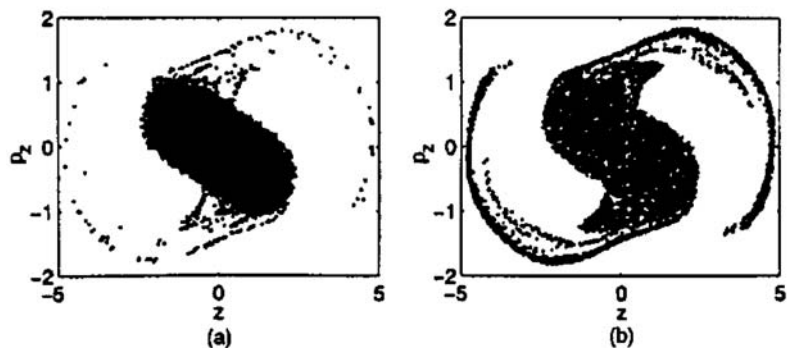


Fig. 10. Longitudinal phase-space diagram with and without the low density cut, for $c/a = 3$, $\mu = 1.4$, $\eta_x = 0.65$, $\eta_z = 0.49$.

by the condition $a_m(\tau) = a_m(\tau + 2\pi)$, Eq. (1) can be rewritten as

$$\frac{d^2 u_e}{ds^2} + u_e - \frac{1}{u_e^3} = k a_m^2 \left(\frac{1}{u_e} - u_e \right). \quad (18)$$

It should be noted that the form of Eq. (18) remains the same if a_m is any solution to Eq. (1). Choosing $w_e = du_e/ds$ as the conjugate variable of u_e , it can be proved that the change of variable here is in fact a canonical transformation.

Using the CTM, particles can be roughly categorized into four or five classes for small tune depression according to their motion in the phase diagram in the (x, x') plane, as shown by Fig. 11. Class-I particles remain inside the core. Class-II particles are outside the phase ellipse of the core but are not in resonance with the core oscillation because they experience less tune depression than the core particles. These particles stay close to the core. Class-III particles oscillate at frequencies near one-half of the core oscillation frequency, so they can resonate with the core motion to become halo particles. Class-IV particles oscillate with large amplitudes and are depressed least in tune, so they do not resonate with the core.

Figure 11 shows a stroboscopic plot of four paddles representing these four classes. In this example, particles start initially from rest with the values of u equal to 0.5551, 1.1203, 1.4281, and 3.4366, for Classes I, II, III, and IV, respectively. The particles of Classes II, III and IV appear to be scattered near the invariant curves of the Poincaré section for uniform-focusing channels.

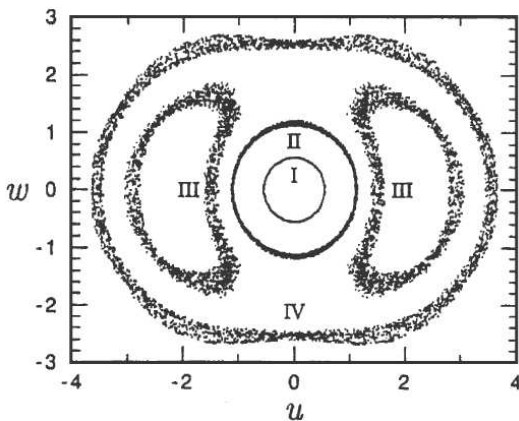


Fig. 11. Stroboscopic plot of four paddles representing the four classes of particles.

The particles of class V fall near the separatrices in a Poincaré section of the uniform-focusing case. Particles in this class can be driven into, and out of, resonance by the periodic focusing and the flutter, an effect not found in the uniform focusing systems. This discovery has a practical implication: since a

realistic beam inevitably has some tails instead of a sharp-edged density profile in the transverse direction, in a mismatched beam, some of the particles initially not in resonance with the core oscillation can be driven into the halo region by the mechanism discussed here.

Figure 12(a) is a stroboscopic plot of class-V particles with initial condition $(u, w) \approx (1.1607, 0)$. With large tune depression and strong focusing, the identification of particles' classes becomes ambiguous except for Class-I particles. For comparison, a plot made by strobing at the averaged envelope-oscillation period for the same particles is shown in Fig. 12(b), where one can see that points are more scattered and the 2:1 resonance is not apparent within the larger scattering of points shown in Figs. 12(a) and (b), which is mainly due to the phase shift between the strobing and the envelope oscillation as well as the projection.

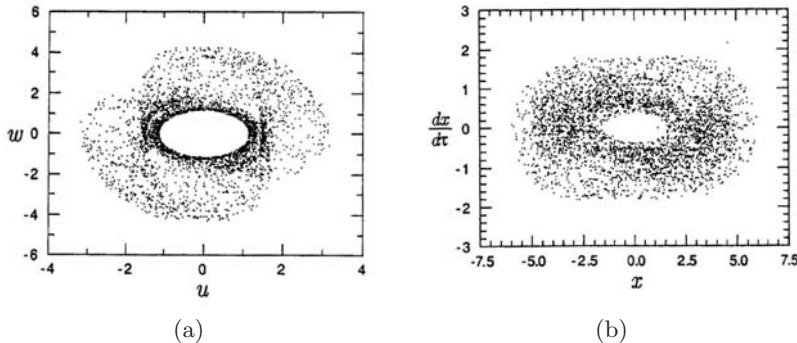


Fig. 12. Phase diagram (a) on the (w, u) plane. (b) on the (x, x') plane.

This approach allows one to perceive the dynamics of halo particles through the stroboscopic plots. The method is applicable to a wide range of parameter values without using any smooth approximation, and is not limited by the constraint that the frequency of core oscillation needs to be commensurable with that of the transverse focusing. Numerical examples were given for illustration and an analytical model was discussed to assist the understanding of halo formation. The parametric resonance (see Fig. 13), like the one studied in the uniform-focusing case, is still the main mechanism that causes the large-amplitude oscillation of halo particles. It has also been learned that certain particles with initial oscillation amplitudes slightly larger than the core radius, but not in the halo region, can be brought into resonance with the core oscillation by the fluctuation of the periodic focusing.

For periodic-focusing channels, the mechanism discussed above adds another possible process of halo formation. Application of this method to a quadrupole-focusing system was also studied. It was discussed that for a

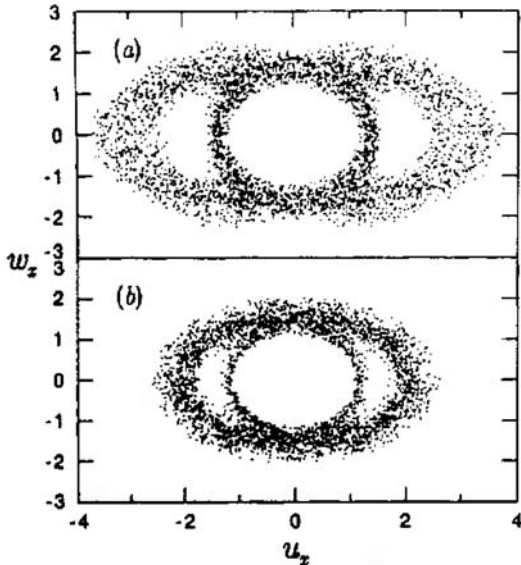


Fig. 13. The parametric resonance of halo particle with (a) the breathing mode and (b) the quadrupole mode oscillations of the beam envelope in a quadrupole-focusing channel.

problem of two degrees of freedom in the particle-core model, two dimensional plots can be easily understand but only for particles having zero or almost zero angular momentum. In that case, the x and v motions of particles can be treated separately, and it was found that particles made resonate with either the breathing mode or the quadrupole mode of the envelope oscillation, or a combination of these two modes, to move into beam halo.

2.6 The matrix transfer method

A first-order matrix transfer method has been proposed for analyzing intense ion beams in acceleration-deceleration systems, which can show a simple physical picture of the space charge effect for intense ion beams and of the edge field effect in thin lens [22]. This technique can be extended to proton beam transport in the PFCs, in which halo and chaotic motion were found [36–38].

To analyze the space charge effect produced by proton beam-self in the PFCs, one may employ the first-order matrix transfer theory for the intense proton beam. In this approach, assume that an external periodic focusing field and a round beam are axis-symmetric, and the velocity of the proton and the period (the interval between two peaks) of the external field are invariant in the PFCs. The space charge effects in the PFCs are described by a series of nonlinear thin lens placed at the beam peak and waist, respectively.

The effect of the nonlinear space charge for the thin lenses on proton leads to increasing $r' \rightarrow r + \Delta r$, where r' is the particle radius coordinate after the action of the thin lenses. Let

$$R_a = \sqrt{R_{max} R_{min}}, \quad \rho = \frac{R_{max}}{R_{min}}, \quad \beta = \frac{R_a}{\epsilon}, \quad (19)$$

where R_{max} and R_{min} are maximum and minimum radii of the beam envelope, respectively; ϵ the emittance of beam current, and ρ and ε some functions of the beam current intensity. Assume also that $\rho = \rho_0$.

Particle trajectory can be expressed in the phase plane (r, r') , where r denotes the transverse displacement (x or y) and $r' = dr/dz$. The action of external field can be expressed by a transport matrix. The matrix of the former half and latter half periods, M_{F0} and M_{L0} , are respectively described by

$$M_{F0} = \begin{bmatrix} \rho^{-1} \cos(\sigma_0/2) & \beta_0 \sin(\sigma_0/2) \\ -\beta_0^{-1} \sin(\sigma_0/2) & \rho \cos(\sigma_0/2) \end{bmatrix},$$

$$M_{L0} = \begin{bmatrix} \rho \cos(\sigma_0/2) & \beta_0 \sin(\sigma_0/2) \\ -\beta_0^{-1} \sin(\sigma_0/2) & \rho^{-1} \cos(\sigma_0/2) \end{bmatrix}.$$

Here, σ_0 is the phase advance per period for $I = 0$. Based on the transport matrix method, for K-V distribution, one has the following at $z = 0$ or $z = L$ (period length between two beam peaks):

$$\Delta r = \frac{wr}{R_a^2 \rho} = \frac{wr}{\beta \epsilon \rho}, \quad \text{if } |r| \leq R_a \sqrt{\rho}, \quad (20)$$

$$\Delta r = \frac{w}{r}, \quad \text{if } |r| > R_a \rho. \quad (21)$$

Moreover, let ρ_0 and ε_0 be values of ρ and ε corresponding to the beam current $I = 0$, and w be the quantity associated with the velocity of proton and beam current intensity.

On the other hand, if space charge effect is considered, the former half periodic matrix M_F and latter half periodic matrix M_L can be described by

$$M_F = \begin{bmatrix} \rho^{-1} \cos(\sigma/2) & \beta \sin(\sigma/2) \\ -\beta^{-1} \sin(\sigma) & \rho \cos(\sigma/2) \end{bmatrix},$$

$$M_L = \begin{bmatrix} \rho \cos(\sigma/2) & \beta \sin(\sigma/2) \\ -\beta^{-1} \sin(\sigma/2) & \rho^{-1} \cos(\sigma/2) \end{bmatrix}.$$

Here, σ is the phase advance per period for space charge effect on particles in the core. By using the matrix relationship, w is obtained as

$$w = 2\epsilon[\cos(\sigma/2) - \cos(\sigma_0/2)]/\sin(\sigma/2), \quad (22)$$

where σ_0 is the vacuum phase advance, σ is the phase advance caused for the space charge effect at one axial period for $r \ll R$.

The phase diagram in the phase space shows that nonlinear resonance takes place if $\sigma_0 < 90^\circ$ due to the nonlinear space charged effect. Figure 14(a) shows the resonance island with $1/8$ for $\sigma_0 = 60^\circ$ and $\sigma = 40^\circ$ ($\sigma = 45^\circ$, $\rho = 1.44$), and there are higher-order resonance islands. But, if $\sigma_o > 90^\circ$ and $\sigma < 90^\circ$, then $w > 0$, and the radius of proton must be expanded, as shown in Fig. 14(b). For $\sigma_o = 100^\circ$ and $\sigma = 70^\circ$, the radius of proton motion is increased due to the space charged effect, and scattering of protons occurs in radial directions, which leads to halo formation. There is clearly a resonance $1/4$ island ($\sigma = 90^\circ$), and $1/5$ ($\sigma = 72^\circ$) island is also taken place but it is not so clear due to its overlapping with the $1/4$ island. There is a large chaotic region near the $1/4$ resonance island. Moreover, this halo formation is highly enhanced since particle from the core can pass through this region to generate more halo. The main reasons for this are that the resonance overlapping forms chaotic areas and that diffusion in these areas (such as the Arnol'd web) increases proton redistribution and halo formation. That also explains why halo can regenerate in the PFCs. Yet, the general picture is not changed as σ is further decreased and σ_0 is kept a constant.

The method described above can be further extended, to study the behavior of high intense beams with more complicated but realistic distributions (such as the clock-shaped distribution) other than the K-V distribution.

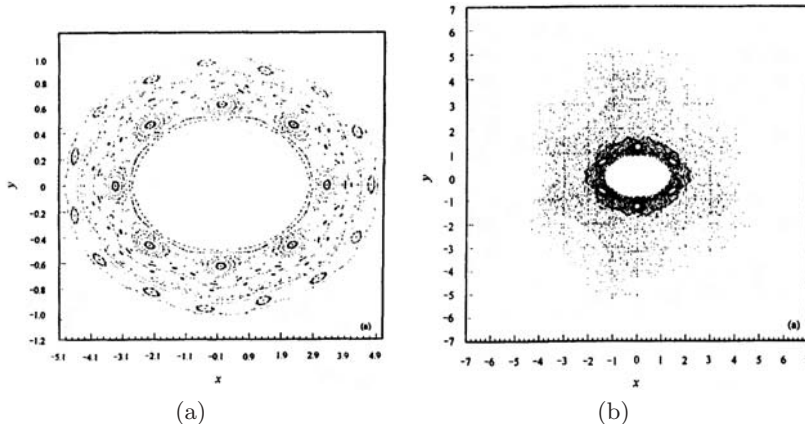


Fig. 14. (a) Resonance island with $1/8$ for $\sigma_o = 60^\circ$ and $\sigma = 40^\circ$ (b) $\sigma_o = 100^\circ$ and $\sigma = 72^\circ$.

3 Nonlinear Feedback Control of Beam Halo Chaos in PFCs

High current ion linacs have attracted increasing attention recently due to their possible applications in ion beam drivers, production of tritium, heavy

ion fusion, etc. In many cases involving high peak currents, their distribution spins off a cluster of particles in the form of the so-called ‘‘halo’’ surrounding a dense core. Nonlinear resonances and chaotic behaviors in the envelope oscillations of an intense beam, propagating through a periodic focusing field, have been found and analyzed [10–12], as discussed in detail above.

Halo chaos is essentially a turbulent or spatiotemporal chaotic motion in actual linacs. This is because a matched beam which enters a region of mismatch will undergo very complicated turbulent motion that apparently ejects particles from the core into some sort of halo. Many efforts on the removal of such halo chaos by collimation have been largely unsuccessful since halo almost always regenerates.

The question of how to remove halo chaos by applying nonlinear feedback control methods has been considered. In this pursuit, first consider a 2-D breathing mode round beams in high current ion. Consider the external periodic focusing field and the round beam to be axis-symmetric, and the proton velocity and the period of the external field are invariant in the PFCs. The control goal is to suppress the scattering of protons at radial direction and reach the match radius of proton beam. To do this, let $-G$ be the controller, which is added into the right-hand side of Eq. (1), and consider $\bar{k}_z(s)$ be the mean value of the periodic function $k_z(S)$ in the equation. Then, the controlled system is written as

$$\frac{d^2r_b}{ds^2} + \bar{k}_z(s)r_b - \frac{K}{r_b} - \frac{1}{r^3} = -G, \quad (23)$$

where notation as above.

In order to provide some ideas as what kind of controllers that may be able to control this nonlinear system, add a constant term α to both sides of Eq. (2) and then rewrite it as

$$\frac{d^2r_b}{ds^2} + \bar{k}_z(s)r_b + \alpha = \alpha + \frac{K}{r_b} + \frac{1}{r^3} - G, \quad (24)$$

in which the constant α is chosen such that the linear part on the left-hand side is stable. It is then easy to verify that $\alpha > \bar{k}_z^2/4$ guarantees this stability, since the two eigenvalues of this linear part on the left-hand side both have negative real parts. To ensure the entire controlled system to be stable, according to the Poincaré-Lyapunov theorem [27], a necessary condition, which the nonlinear part of the controlled system must satisfy, is

$$\lim_{\|r_b\| \rightarrow \infty} \frac{\|\alpha - G + k/r_b + 1/r_b^3\|}{\|r_b\|} = 0, \quad (25)$$

It is clear that a linear controller with the form $u = u(r_b) = ar_b + b$ cannot satisfy (25), namely, it is very unlikely capable of stabilizing the entire system (25) in the sense that $r_b \rightarrow 0$ as $t \rightarrow \infty$. Therefore, generally speaking,

nonlinear controllers are necessary, even in the simplest forms, perhaps associated with $(\cdot)^2$, $\exp(\cdot)$, $\sin(\cdot)$, where (\cdot) may be the error of feedback control such as $(r_b - a_m)$, (a_m is the match radius of beam under certain conditions).

It should be emphasized that the above qualitative analysis only provides some heuristic reasoning for choosing the controller structures. A rigorous mathematical verification of stability for those nonlinear controllers discussed above has been obtained recently, but it is omitted here. Successful simulation results obtained by some simple nonlinear controllers will be shown later in the following sections.

A Particle-in-Cell (PIC) simulation program has been developed for the PFCs, and has been used to simulate beam halo-chaos formation in the 4D phase space. The particle beam self-field satisfies the Poisson equation of potential:

$$\nabla^2 \varphi(\mathbf{r}, \mathbf{z}) = -\frac{\mathbf{q}}{\epsilon_0} \int \int \mathbf{f}(\mathbf{r}, \mathbf{r}_\perp; \mathbf{z}) d\mathbf{r}_\perp, \quad (26)$$

where $f(r, r_\perp; z)$ is the transverse distribution in the 4-D phase space and \mathbf{r}_\perp is the transverse dimensionless velocity. The self-field force acting on a particle then is

$$F_r = -q \nabla \varphi(\mathbf{r}, \mathbf{z}). \quad (27)$$

In simulations, the radial space-charge field of an axis-symmetric beam can be calculated from the Gaussian law by counting the number of particles in cells of a finite radial grid, which extends up to 5 times of the beam matched radius, in the particle simulation using the PIC method. One can then monitor the total energy through the transport channel and keep the total energy constant. In the simulation, 10^6 particles and 100 radial meshes were used over the length $r_b(0)$, which corresponds to the minimum radius of a matched beam.

In order to prevent activation of the beam pipe walls and components of a high power accelerator, beam loss must be minimized. To do so, apply a feedback controller, G , to the self-field force, that is,

$$F_r = -q \nabla \varphi(\mathbf{r}, \mathbf{z}) + \mathbf{G} \quad (28)$$

where G is a nonlinear controller to be designed. Some typical choices for G are

$$G = -g \sin(r_{rms} - a_m) \quad \text{and} \quad G = -g(r_{rms} - a_m)^2, \quad (29)$$

where a_m is the match radius of the beam envelope, r_{rms} is the root of mean square radii of particles, and g is the constant control gain.

As a control measure of halo-chaos, a halo intensity factor, H_{av} , is defined as the number of particles outside the boundary $r_b = 1.75r_b(0)$ divided by

all of particles participated in the simulation. The smaller the H_{av} , the better control performance. The primary results have shown that the nonlinear function controllers work well for suppressing or at least reducing the halo-chaos. For example, under a good control of the halo chaos, $H_{av} \leq 0.01$ is achieved using the feedback $G = -0.15(r_{rms} - a_m)^2$, which is applied sporadically every 5 pulses in PFC. Theoretical analysis and computer simulation results are summarized in [21–26].

4 Wavelet-Based Feedback Control

It was found that the wavelet-based feedback controller, as a special nonlinear function, is very effective for the control of beam halo chaos. The mother wavelet function takes the form of

$$f_{ab}(x) = -\frac{2}{a}[1 - (x - b)^2] \left\{ \exp\left[-\frac{(x - b)^2}{a}\right] \right\}, \quad (30)$$

while a simplified form is

$$f_{ab}(x) = \exp\left[-\frac{(x - b)^2}{a}\right], \quad (31)$$

and a general form is

$$f_{ab}(x) = C^{-\frac{(x - b)^2}{a}}, \quad (32)$$

where a and b are scaling and translation constants.

Wavelet-based feedback controller is designed as

$$G = -g[f_{ab}(r_{rms}) - f_{ab}(a_m)]. \quad (33)$$

The main reason of using wavelet function for controller design is that it has strong non-linearity and excellent localization property. It turns out that for halo-chaos control purpose, the translation can be very small. The general form of the wavelet-based controller is taken as Eq. (33) with $a = 2.8$ and $b = 0$, in which g is the control gain constant. When $r_{rms} \rightarrow a_m$ the goal of control is achieved, and in this case, it is clear that the control action is gradually vanished.

The main reasons for choosing r_{rms} for feedback control are: (i) r_{rms} is a global average statistical quantity of the particle beam, namely, the average root-mean-square radius of proton beam. Whether or not the system is under control, the change of r_{rms} is much more stable as compared to that of the maximum radius. (ii) r_{rms} reflects the spatial statistical correlation level in a particular position at a particular time. (iii) Since beam halo chaos is spatiotemporal chaos, it is very sensitive to external perturbation such as

mismatch factor, disturbance from the electromagnetic field, and noise. Using r_{rms} , which is insensitive to the external changes, to control beam halo chaos can reduce the sensitivity to external conditional variations, thereby increasing the stability of the controlled system. (iv) Since the proton distribution function is changing according to the nonlinear and mismatched effects of spatial electrons, it is natural to use statistical measurement and method for the study of halo-chaos control.

4.1 Main control results via wavelet-based feedback

In this section, main control results for the K-V distribution of initial proton beam are presented and compared before and after wavelet-based feedback controller (33).

Evolution of maximum proton beam radius

Figure 15 gives the evolution of maximum proton beam radius before and after the wavelet-based feedback controller (33) is applied.

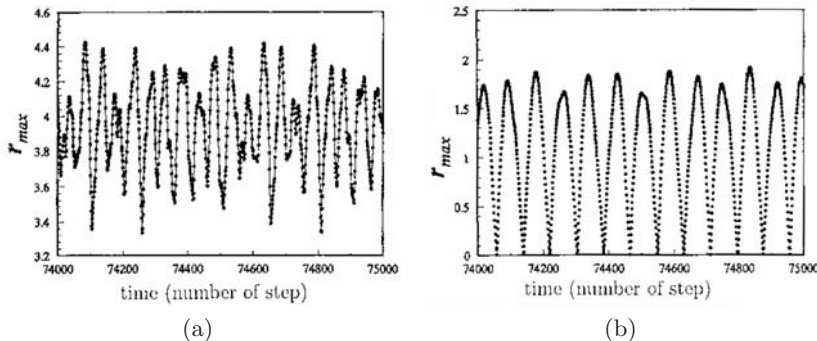


Fig. 15. Evolution of maximum proton beam radius r_{max} . (a) before control (b) after control.

The maximum radius of proton beam, r_{max} , changes irregularly without control, which indeed was of chaotic motion. It became relatively stable with very small magnitude, albeit showing little irregularity still after control. From the statistical point of view, the radius of its envelope has been significantly reduced by 4-5 times after control via (33) with (31) was turned on at the section of the 1200th periods.

Evolution of mean root-square radius r_{rms}

Figure 16 shows the evolution of the mean root-square radius, r_{rms} , of the proton beam, before and after the wavelet-based feedback controller (33) with (31) is applied.

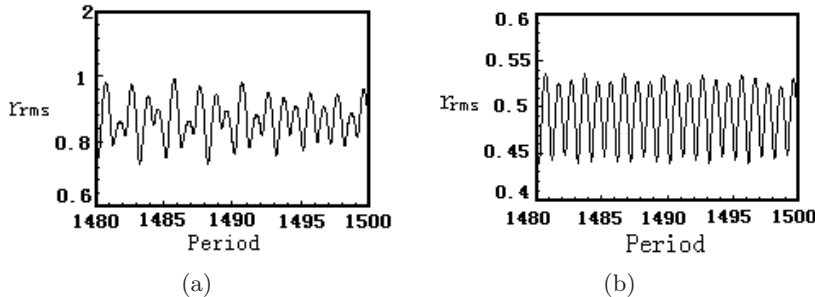


Fig. 16. Evolution of mean root-square radius r_{rms} of proton beam. (a) before control (b) after control.

It is clear from Fig. 16 that the evolution of mean-square radius of proton beam, r_{rms} , was chaotic, irregular, and scattered around with large radii before control, and yet it became almost quasi-periodic around the beam core with very small magnitudes after feedback control (33) with (31) was applied. The average value of r_{rms} is significantly reduced by 2-3 times. Therefore, it implies that beam halo-chaos is much suppressed.

Evolution of the mean-square momentum P_{av}^2 of proton beam

Figure 17 demonstrates the evolution of the mean-square momentum of the proton beam before and after controller (33) was applied.

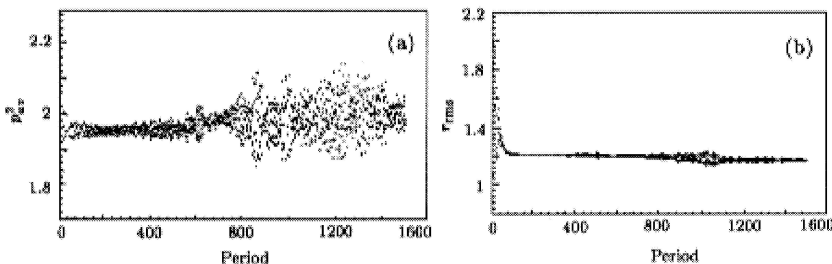


Fig. 17. Evolution of the mean-square momentum of proton beam. (a) before control (b) after control.

It is clear from Fig. 17 that the proton beam was scattered around with large radii due to the fact that the square of transverse mean-square momentum P_{av}^2 is very large (maximum about 2.2) before control, and yet it became very small (about 1.2) after the wavelet feedback control (33) with (31) was applied. The essential reason is that the transverse energy of proton beam, corresponding to P_{av}^2 , is reduced doubly.

Average value of halo-chaos strength factor H_{av}

Statistical average value of the beam halo chaos strength factor in each period, H_{av} , is the most important characteristic quantity for measuring its control results. Figures 18(a)-(b) show the changes of the H_{av} value with increasing numbers of the PFCs, and the comparison of the results obtained before and after control is applied, where the wavelet-based feedback controller with (33)and (31) was used to the PFCs during each period.

It can be seen from Fig. 18 that the H_{av} value significantly measures the effect on the beam halo-chaos by control. Obviously, the smaller the H_{av} , the better the control effect. Perfect control is achieved if $H_{av} \rightarrow 0$. A comparison between Fig. 18(a) and Fig. 18(b) implies that the wavelet-based feedback controller reduces the H_{av} value very effectively to zero after it was turned on. The values of H_{av} are reduced from the maximum of 0.14 to 0.00 in one cycle, meaning that halo-chaos is completely suppressed almost immediately.

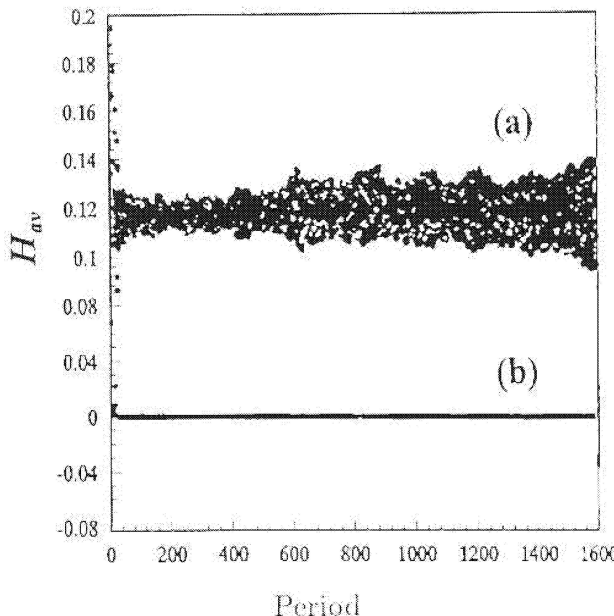


Fig. 18. Evolution of the H_{av} value. (a) before control (b) after control.

Phase portraits of halo-chaos

Figures 19 show the phase diagrams in the (Y, Y') space before and after control. One can see that not only the area of the phase diagram is largely reduced but also the density of proton-core is almost focused on the original core position. All results are summarized in Table 4.1, which shows that

the beam halo protons are almost suppressed, and the control effect of the wavelet-based feedback is extremely well for suppressing the beam halo chaos in the PFCs.

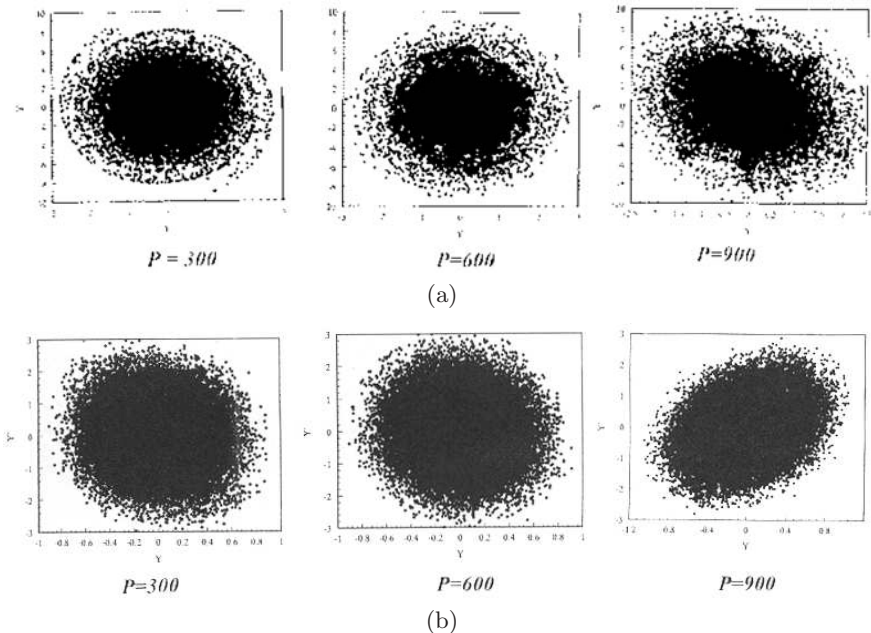


Fig. 19. Proton distribution diagram in the (Y, Y') space at the 1200th section. (a) before control (b) after control.

Table 1. Comparison: before and after wavelet feedback control

| Distr. | a | H_{av} , Bef/Aft | r_{max}/a_m Bef/Aft | ϵ_x , Bef/Aft | P_{av}^2 , Bef/Aft |
|-----------------|-----|--------------------|-----------------------|------------------------|----------------------|
| K-V | 2.8 | 1.29/0.00 | 5.20/2.00 | 2.84/1.0 | 3.63/1.31 |
| 3σ Gauss | 2.0 | 0.28/0.00 | 4.32/1.31 | 2.89/1.11 | 3.09/1.61 |
| Gauss | 0.7 | 0.31/0.00 | 4.95 /1.40 | 2.91/1.04 | 3.68/2.94 |
| Water-bag | 2.6 | 0.298/0.00 | 4.24/2.00 | 2.87/1.25 | 2.58/1.40 |
| Parabola | 0.5 | 0.24/0.00 | 5.20/1.00 | 2.84/1.00 | 3.62/1.31 |

The following conclusions are drawn from Table 1:

1. The control goal and other good quality and performance results can be achieved even after about a hundred iterations of control in the PFCs, when the wavelet-based feedback controller is periodically applied.

2. The root-square momentum of the protons can be significantly reduced by 2-3 times. So the transverse energy of protons is also much reduced correspondingly. Moreover, r_{max} is reduced by 2-3 times after controller was turned on at the 1200th section.
3. The radius of protons, in both x - and y -directions, can be significantly reduced. It is decreased by about 2-3 times after control.
4. After control is applied, almost all statistical properties of beam halo chaos are in good condition, such as the mean-square beam radius and the transverse energy, as well as the relative emittance, are effectively reduced by 2-3 times.
5. In addition, emittance as another quantity for measuring beam transport, ϵ_x and ϵ_y , are largely reduced (from 2.8 to 0.9) by the wavelet feedback control.

Comparison of single periodical control with multiple-periodical sporadic control

It should be pointed out that for controlling beam halo chaos, there are two ways of applying nonlinear control: the single periodical ($\Delta P = 1$) control (as seen in Table 1) and multiple-periodical sporadic interval ($\Delta P \geq 32$) control (as shown in Table 2).

Table 2. Fixed parameters of the wavelet function in the controller (33) with ($b = 0, a = 2.8, g = 15.5$) for the K-V distribution

| ΔP | H_{max} , Bef/Aft | r_{max}/a_m Bef/Aft | ϵ_x , Bef/Aft | P_{av}^2 , Bef/Aft |
|------------|---------------------|-----------------------|------------------------|----------------------|
| 1 | 0.148 / 0.000 | 5228 / 1.158 | 2.841 / 1.0023 | 3.651 / 1..367 |
| 2 | 0.148 / 0.000 | 5228 / 1.466 | 2.841 / 1.0035 | 3.651 / 1.649 |
| 3 | 0.148 / 0.000 | 5228 / 1.614 | 2.841 / 1.002 | 3.651 / 1.614 |
| 4 | 0.148 / 0.000 | 5228 / 1.563 | 2.841 / 1.000 | 3.651 / 1.562 |
| 6 | 0.148 / 0.000 | 5228 / 1.635 | 2.841 / 1.001 | 3.651 / 1.377 |
| 9 | 0.148 / 0.000 | 5228 / 1.713 | 2.841 / 1.003 | 3.651 / 1.623 |
| 11 | 0.148 / 0.000 | 5228 / 1.645 | 2.841 / 1.003 | 3.651 / 1.451 |

Table 2 shows a comparison of simulation results obtained before and after the wavelet-based feedback controller (33) with (31) was applied at the 1200th section. It is seen from Table 2 that multiple-periodical sporadic control can also reach the same good results as the single periodical control, but it has much higher economic impact on practical applications due to its simplicity in control fashion.

5 Switching Manifold Control Method

As seen from the above, the typical periodic function $k_z(s)$ represents a periodically interrupted or alternatively solenoidal focusing field. This function

as a switching function is a function of time; so its action results in dynamics that is an aggregation of the dynamical behaviors of two separate continuous-time dynamical systems:

$$(I) \quad \frac{d^2r_b}{ds^2} + k_z(0)r_b - \frac{K}{r_b} - \frac{1}{r_b^3} = 0, \quad (34)$$

$$(II) \quad \frac{d^2r_b}{ds^2} - \frac{K}{r_b} - \frac{1}{r_b^3} = 0. \quad (35)$$

For system (I), it is clear that it has two non-zero equilibria represented by

$$z_1 = \frac{\sqrt{\frac{K}{k_z(0)} + \sqrt{\frac{K^2}{k_z^2(0)} + \frac{4}{k_z(0)}}}}{2}, \quad (36)$$

$$z_2 = -\frac{\sqrt{\frac{K}{k_z(0)} + \sqrt{\frac{K^2}{k_z^2(0)} + \frac{4}{k_z(0)}}}}{2}. \quad (37)$$

Its phase plane portrait is depicted in Fig. 20(a).

For system (II), it does not have any finite equilibria, but instead, exhibits unstable motion. Its phase plane portrait is shown in Fig. 20(b).

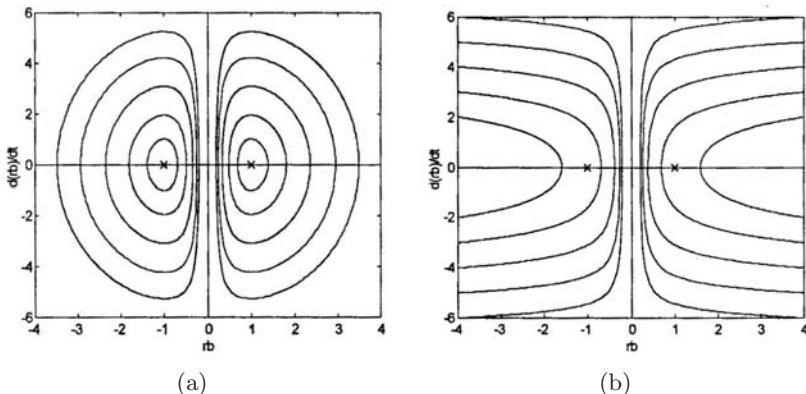


Fig. 20. Phase plane portrait. (a) for system (I), (b) for system (II).

Note that the behaviors of the halo chaos can be understood as a dynamical process, which switches between the motions shown in Figs. 20(a)-(b), in different regions of the phase plane. Because the switching occurs at a fixed time window (some kind of open-loop control), the combination of the “bursts” of system (II) and the “conservation” of energy of system (I), over different time intervals, creates chaotic dynamics as shown in Fig. 21.

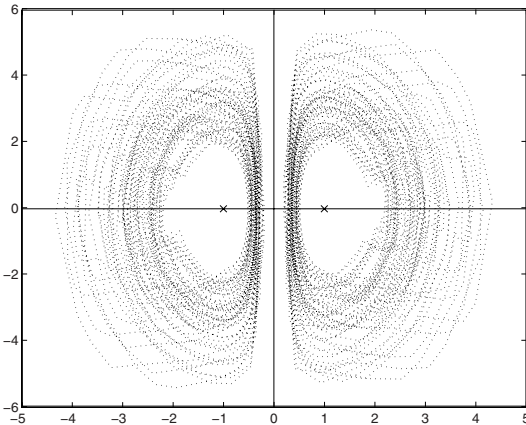


Fig. 21. Chaotic dynamics in the phase plane.

5.1 Switching control design

Here, a feedback law is introduced into the generation of the “switched signals” $k_z(s)$, so as to realize the suppression of halo chaos.

Given the completely different dynamical behaviors of systems (I) and (II), respectively, it is possible to use the concept of variable structure systems to piece together parts of the dynamical trajectories of the two systems, within different phase regions, to realize the suppression of halo chaos. The key issue is how to create a switching line such that this control idea can be realized.

First, consider the feasibility of the control. Since the system has two separate dynamical behaviors, divided by the axis $r_b = 0$, one can first focus on the region $r_b > 0$. As shown in Fig. 21, one may design a switching line,

$$g = \dot{r}_b + \lambda(r_b - z_1), \quad \lambda > 0, \quad (38)$$

such that $k_z(s)$ (considered as a control law) is switching between $k_z(0)$ and 0 according to the sign of g . Instead of “open-loop” switching according to the time sequences, such a sliding mode control effect can be created, as shown by the bold line in the Fig. 22. Any trajectory, as soon as it comes close enough to the “bold line,” will be attracted to it and stay on it thereafter. This is because there exists a domain of attraction around this part of the switching line. Once the sliding mode is reached, the trajectory will follow the dynamics $g = 0$, namely,

$$\dot{r}_b = -\lambda(r_b - z_1). \quad (39)$$

One can then easily see that following this dynamics, $r_b \rightarrow z_1$ asymptotically.

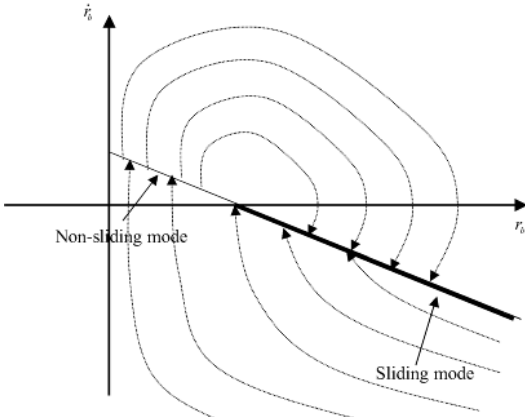


Fig. 22. A sliding mode shown by the bold line1. Switching between $k_z(0)$ and 0 according to the sign of g .

To design the switching control law, one may first reformulate the halo-chaos dynamics (34) and (35) as

$$\frac{d^2r_b}{ds^2} - \frac{K}{r_b} - \frac{1}{r_b^3} = u r_b, \quad (40)$$

where u is the switching controller, which can only take values between 0 and $-k_z(0)$. Note that if $u = -k_z(s)$, then the system ends up with halo-chaos (1). In this consideration, the switching controller u is designed as

$$u = \begin{cases} -k_z(0) & g > 0, \\ 0 & g < 0. \end{cases} \quad (41)$$

Such a switching controller will create the sliding region as shown in Fig. 22.

It should be noted that because of the limited switching values, the domain of attraction toward the sliding line can only be local. The exact size of the domain can be determined by using the equivalent control concept. The equivalent controller u_{eq} can be derived by solving $\dot{g} = 0$. Since

$$\dot{g} = \ddot{r}_b + \lambda \dot{r}_b = u r_b - \frac{K}{r_b} - \frac{1}{r_b^3} + \lambda \dot{r}_b, \quad (42)$$

one has

$$u_{eq} = r_b^{-1} \left(\frac{K}{r_b} + \frac{1}{r_b^3} - \lambda \dot{r}_b \right). \quad (43)$$

The domain of attraction for the sliding mode can then be constructed as follows [34]:

$$-k_z(0) < r_b^{-1} \left(\frac{K}{r_b} + \frac{1}{r_b^3} - \lambda \dot{r}_b \right) < 0. \quad (44)$$

The same control actions can be applied to the left-hand side of the phase portrait, so that trajectories starting from this part of the phase plane converge to z_2 , namely, $r_b \rightarrow z_2$. Figure 23 shows the control effects on the trajectories starting from two initial states in the left-hand and right-hand planes, respectively. One can see that halo-chaos has been well controlled into their corresponding small neighborhoods of equilibria.

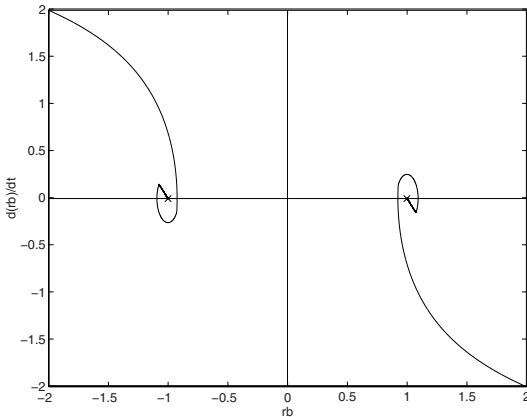


Fig. 23. Control effects on the trajectories.

In summary, different from the nonlinear feedback control and wavelet-based feedback control approaches described above for halo-chaos suppression [20–26], this effective control strategy is based on some successful concepts of variable structure systems and sliding mode control. The design is practical and the simulations are quite promising. Nevertheless, physical implementation of this control technique, like all the others, remains an important issue for further consideration.

6 Time-Delayed Self-Control Feedback Method

Another effective control is the so-called time-delayed self-control feedback control [37]. The time-delayed feedback method was firstly suggested by Pyragas [31, 32]. The method deals with a chaotic system that can be modelled by a set of nonlinear ordinary differential equations (ODE)

$$\frac{dy}{dt} = P(y, x) + gD(t), \quad \frac{dX}{dt} = Q(y, X). \quad (45)$$

The main feature of the method is that the controller with time delay feedback, $G = gD(t)$, is added to the right hand side of the first equation in (45), in which some scalar variable $y(t)$ can be measured as a system output.

The vector X describes the remaining variables of the system. $G(t) = gD(t)$ denotes an external continuous-time perturbation. It is interesting to note that, from an experimental point of view, the technique is based on the delay feedback perturbation

$$G(t) = gD(z) = g[y(t - \tau) - y(t)], \quad (46)$$

where g is gain, τ the period length or time. The perturbation above vanishes on the period- k unstable periodic orbit (UPO) when the delay time τ coincides with the period T_k of this UPO, $\tau = T_k$. There is no power dissipated in the feedback loop if stabilization is successful. This method can be implemented in experiment by a pure analog technique. Although it may fail for high-period orbits, it is suitable for control of halo-chaos, as to be further described below.

For the envelope equation (1) of proton beam, it can be transformed into the following set of ODEs:

$$\frac{dr_b}{ds} = v + G, \quad (47)$$

$$\frac{dv}{ds} = -k_z(s)r_b + \frac{K}{r_b} + \frac{1}{r_b^3}, \quad (48)$$

where $G = gD(z) = K[r_b(s - S) - r_b(s)]$, z is the axi-coordinate associated with time t , and S is the period length for the PFCs. The reason for this selection is that there is a periodic solution, $r_b(s + S) = r_b(s)$, when the proton beam is in the matched state, and the beam is in a chaotic status when it is in the unmatched state. The goal of controlling halo-chaos here is to turn the unmatched beam to become stable matched beam in the PFCs of the accelerator. The idea is to construct a time-delayed feedback perturbation in such a way that it does not change the desired unstable matched beam of the PFCs in the accelerator attractor, but only changes the corresponding Lyapunov exponents, λ , so that the beam becomes stable. Figure 24 shows evolution of the beam envelop radii before control and after the time-delayed control, with $r_b(s + S) = r_b(s)$ where $z = S$. Here, λ is changed from $\lambda = 0.002$ before control to $\lambda = -0.0043$ after control, under the time-delay feedback controller with the selected $g = 0.01$ for the set of the parameters (tune-depression $\eta = 0$, mismatch factor $M = 2$, vacuum phase advance $\sigma_0 = 115^\circ$, match radius $a_m = 0.7891642$, and perveance $k = 0.903079$). One can see that the original unstable envelope of orbit $r_b(s + S) = r_b(s)$ is stabilized after control, as shown in Fig. 24(a)-(b).

The above idea can be extended to the PIC simulation for control beam halo-chaos. In other words, one can verify if the above technique is also valid for the PIC simulation of beam halo-chaos. To do so, it is similar to wavelet-based feedback control that the mean root-square radius, r_{rms} , is taken as control variable and the control goal is to force $r_{rms} \rightarrow a_m$. Thus, one can

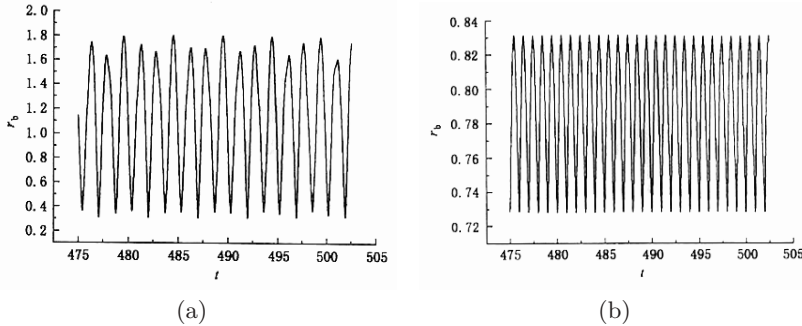


Fig. 24. Evolution of beam envelop radius (a) before control (b) After control.

use the same controlled equation as follows:

$$F_r = -q \nabla \varphi(\mathbf{r}, \mathbf{z}) + \mathbf{G}, \quad (49)$$

where the time-delayed controller is

$$G = g[r_{rms}(s + S) - r_{rms}]. \quad (50)$$

The simulation results for 5 kinds of initial proton beam distribution are listed in Table 3.

Table 3. Comparison of beam halo-chaos properties before and after the time-delay control with $g = 2.3$. B/A is short for before control / after control.

| Distribution | H_{av} , B/A | r_{max}/a_m , B/A | ϵ_x , B/A | P_{av}^2 , B/A | Evaluation |
|-----------------|----------------|---------------------|--------------------|------------------|------------|
| K-V | 0.15/0.00 | 5.19/1.14 | 2.87/1.00 | 2.98/0.87 | best |
| 3σ Gauss | 0.14/0.00 | 5.18/1.91 | 2.82/1.16 | 2.98/0.88 | best |
| Complete Gauss | 0.15/0.01 | 5.67 /3.04 | 2.90/1.16 | 3.05/1.02 | good |
| Water-bag | 0.11/0.00 | 4.24/1.69 | 2.86/1.21 | 2.15/0.77 | better |
| Parabola | 0.16/0.00 | 5.18/1.75 | 3.03/0.93 | 2.91/1.07 | better |

Figure 25 gives a comparison of the phase diagram in the (x, x') plane before and after the time-delayed control at $P=1200$ sections. It is seen from Fig. 25 that after control, the area of phase diagram in the (x, x') plane is doubly reduced to the fourth area before control. All simulation results demonstrate that the control has very good effect. It should be emphasized that one can use the same time-delayed controller to successfully achieve effective control for 5 kinds of different initial proton distributions. This method has some advantages for controlling the beam halo-chaos. It is technologically realizable and cost-effective since it is a simple linear controller with time-delayed and weak feedback.

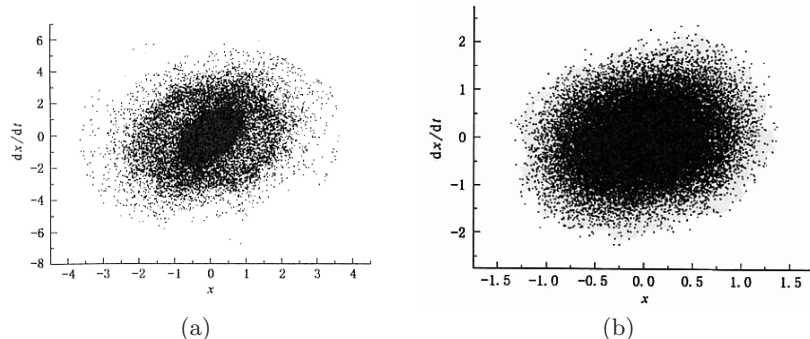


Fig. 25. Comparison of phase diagram in (x, x') space before control (left) and after control (right) at $P=1200$ sections.

7 Conclusions and Discussions

In this chapter, the mechanism of beam halo formation in high-current linear accelerator has been analyzed. It is shown that the halo-chaos formation depends not only on the nonlinear space charged effect but also on the interaction among the particles and the particle-core relation, which leads to particle transverse energy exchange. It has also confirmed by analysis and simulations that resonance overlapping forms chaotic areas and the “phase” mixing diffusion takes place in these areas.

One of the physical mechanism using feedback control indeed reveals the fact that the nonlinear feedback forces counteract the nonlinear effect of the beam space charge therefore reducing transverse energy of the proton beam, witnessed by the fact that the mean-square momentum of the proton beam is reduced significantly. In other words, the nonlinear feedback forces can suppresses the scattering of the transverse particles with higher energy. It should be pointed out that beam halo is also taken place in a cyclotron with intense beam current and is also a main reason of the beam losses, but the mechanism of halo formation here is different from that in a intensity linear accelerator, and the beam halo is not induced by resonance and chaos but the outward repellent motion and the vortex motion of the particles in the bunch [39, 40].

To control beam halo-chaos, several nonlinear feedback control methods have been proposed and verified, including a wavelet-based feedback control, switching manifold methods and time-delayed feedback self-control for suppressing halo chaos in proton beams, for five types of initial proton beam distributions. Particle-in-Cell (PIC) simulations have verified that these control methodologies are very effective for suppressing beam halo-chaos in high-current proton beam transport in the PFCs. These control methods should be useful in designing a new generation of accelerators. More importantly, these new methods can be easily tested in physical experiments. For example, ex-

ternal radio frequency fields can be coupled into the PFCs periodically and sporadically, and the parameters can be adjusted appropriately to achieve the goal of control. The time-delayed self-control feedback may be applied to experiment and design.

In summary, beam-halo chaos generation mechanisms and its effective suppression are difficult but very important topics for future research in new generation accelerator physics and nuclear energy industry, which pose a great challenge to control theorists and engineers in the beginning of the new century.

Acknowledgements.

This work was supported by the National Nature Science Foundation of China under Nos. 19875080, 70071047, 10247005 and also by Hong Kong Research Grant Council under CERG Grants CityU 1098/00E, 1018/01E and 1004/02E.

References

- Evans L. R., Graeyte, J. (1987) Beam-beam effects. In Proc. of the 1985 CERN Accelerator School, CERN, 87–03
- Sessler, A. M. (1972) Collective phenomena in accelerator. In Proc. of LINAC72 Conference, 291
- Lagniel, J. M. (1994) On halo formation from space-charge dominated beams. Nucl. Instrum. Meth., **A343**:46–53
- Lagniel J. M. (1993) Chaotic behavior and halo formation from 2D space-charge dominated beams. LNS/SM/93-12
- Jameson, R. A. (1994) Chaotic behavior induced by space charge. In Proc. of EPAC94 Conference, 1177
- Jameson, R. A. (1994) Frontiers of Accelerator Technology, ed. by Kurokawa, et al.. Proc. of the Joint US-CERN-Japan Intern'l School. Singapore: World Scientific, 430–560
- Reiser, M. (1991) Emittance growth in mismatched particle beams. Analytic Mode for Halo Formation – Proc. of Particle Accelerator Conference, 2497
- Kehne, D., Reiser, M., Rudd, H. (1993) Numerical and experimental studies of halo formation due to mismatch in a space-charge dominated electron beam. In Proc. of Particle Accelerator Conference, ed. by Corneliusen, 3657
- Reiser, M. (1994) Theory and Design of Charge Particle Beams. New York: Wiley
- Gluckstern, R. L. (1994) Analytic model for halo formation in high current ion linacs. Phys. Rev. Lett., **73**:1247–1250
- Gluckstern, R. L. (1996) Survey of halo formation studies in high intensity proton linacs. In Proc. of LINAC, 333–337
- Gluckstern, R. L., Fedotov, A. V., Kurennoy, S. S., Ryne, R. D. (1998) Halo formation in three-dimensional bunches. Phys. Rev. E, **58**:4977–4990
- Gluckstern, R. L., Kurennoy, S. (1997) In Proc. of the 1997 Particle Accelerator Conference, Vancouver, Canada

14. Fedotov, A. V., Gluckstern, R. L., Kurennoy, S. S., Ryne, R. D. (1999) Halo formation in three-dimensional bunches with various space. *Phys. Rev. ST Accel. Beams*, **2**:014201
15. Chen, C., Davidson, R. C. (1994) Nonlinear resonances and chaotic behavior in a periodically focused intense charged-particle beam. *Phys. Rev. E*, **72**:2195–2198
16. Fink, Y., Chen, C. (1997) Halo formation and chaos in root-mean-square matched beams propagating through a perioic solenoidal focusing channel. *Phys. Rev. E*, **55**:7557–7564
17. Wang, T. S. (2000) Particle-core study of halo dynamics in periodic-focusing channels. *Phys. Rev. E*, **61**:1855–1861
18. Fang, J. Q. (2000) A key problem of radioactive clear nuclear power apparatus drived by high-intensity accelerator: Formation mechanisms of beam halo-chaos and its contro strategy. *Nature (China)*, **22**:63–69
19. Fang, J. Q., Chen, G. (2000) Nonlinear feedback control of halo-chaos in high-intensity linacs. *High Power Laser and Particle Beams*, **12**:647–651
20. Fang, J. Q., Yuan, G., Weng, J. Q., Chen, G. (2000) Controlling beam halo-chaos using wavelet feedback method. *Nature (China)*, **22**:368–369
21. Fang, J. Q., *et al.* (2001) Controlling beam halo-chaos using wavelet function feedback method. *Acta Physica Sinica*, **50**:67–71
22. Fang, J. Q., *et al.* (2001) Physical mechanism of beam halo-chaos formation for high-current proton beam in a periodic-focusing channels and a nonlinear control strategy. *Progress in Nature Science*, **11**:6–13
23. Fang, J. Q., Luo, X. S., Chen, G., Weng, J. Q. (2001) Controlling beam halo-chaos. *Chinese Phys. Lett.*, **18**:1554–1557
24. Fang, J. Q., Chen, G., Zhou, L.-L. (2002) Complexity Analysis and control strategy for beam halo-chaos in ADS. *Int. J. Bifur. Chaos*, **12**(5):917–930
25. Fang, J. Q., Chen, G. (2002) Controlling halo-chaos via wavelet-based feedback. *Discrete Dynamics in Nature and Society*, **7**(3):165–175.
26. Fang, J. Q., Chen, G., Zhou, L.-L., Weng, J. Q. (2002) Nonlinear control of beam halo-chaos in accelerator driven nucleart power systems. *Commun. Theor. Phys.*, **37**:675–681
27. Verhust, F. (1996) *Nonlinear Differential Equations and Dynamical Systems*. 2nd ed. Berlin: Springer-Verlag
28. Ott, E., Grebogi, C., Yorke, J. A. (1990) Controlling chaos. *Phys. Rev. Lett.*, **64**:1196–1199
29. Chen, G., Dong, X. (1998) *From Chaos to Order: Methodologies, Perspectives and Applications*. Singapore: World Scientific
30. Okamoto, H., Ikegami, M. (1997) Simulation study of halo formation in breathing round beams. *Phys. Rev. E*, **55**:4694–4705
31. Pyragas, K. (1992) Continnons control of chaos by self-controlling feedback, *Phys. Lett. A*, **170**(6):421–428 and (1993), **181**:201
32. Pyragas, K. (1995) Control of chaos via extended delay feedback, *Phys. Lett. A*, **206**:323–330
33. Yu, X., Chen, G., Fang, J. Q. (2002) Stabilizing halo-chaos by variable structure control. In Proc. of 7th Int. Workshop on Variable Structure Systems. Sarajevo, Bosnia and Herzegovina, 345–352
34. Sira-Ramirez, H. (1989) A geometric approach to pulse-width modulated control in nonlinear dynamical systems. *IEEE Trans. Auto. Contr.*, **34**:184–187

35. ATP Conceptual Design Report, Los Alamos No. LAUR-97-1329, 1997
36. Ouyuan, H. F., Yu, Q. C. (2001) Studies on the Behavior of High Intense Beam in the Periodic Field (in Chinese). Beijing: Atomic Energy Press, NIC-01468, CNNC-0002, 121–130
37. Zhu, L.-W, Weng, J.-Q, Gao, Y., Fang, J. Q. (2002) Control of chaos via delayed self-controlling feedback. *Acta Physica Sinica*, **51**:1483–1488
38. Yu, Q. C., Ouyuan, H. F. (1992) Transport of charge particle beam in nonlinear periodic field (in Chinese). *High Energy and Nuclear Physics*, **17**:305–309
39. Ouyuan, H.-F. (2001) Effects of the space charge forces and the beam halo in an AVF cyclotron with intensity beam currents. *High Energy Physics & Nuclear Physics*, **25**:561–570
40. Ouyuan, H.-F. (2001) Effects of the space charge forces and the beam halo in a cyclotron. *High Energy Physics & Nuclear Physics*, **25**:674–679